Dissertation zur Erlangung des Doktorgrades
der Fakultät für Chemie und Pharmazie
der Ludwig-Maximilians-Universität
München

Reactor design, reaction engineering and cocatalyst development for photocatalytic water splitting half-reactions

Hugo Alejandro Vignolo González
aus
El Puerto, Valparaíso, Chile

2022

Erklärung

Diese Dissertation wurde im Sinne von §7 der Promotionsordnung vom 28. November 2011 von Frau Prof. Dr. Bettina V. Lotsch betreut.

Eidesstattliche Versicherung

Diese Dissertation wurde eigenhändig und ohne unerlaubte Hilfe erarbeitet.

München, den 16.09.2022

Hugo Alejandro Vignolo González

Dissertation eingereicht am:	22.09.2022
Erstgutachterin:	Hon.-Prof. Dr. Bettina V. Lotsch
Zweitgutachter:	Univ. Prof. Dr. Ulrich Heiz
Mündliche Prüfung am:	08.11.2022

Acknowledgements

I sincerely thank Bettina for her supervision. At the beginning of this PhD project, we embarked into the unknown territories of nanochemistry, having the two of us very dissimilar backgrounds. Although this in the end was more of an advantage, I thank her for having the courage, and the vision to take me as a PhD student in her group in first place, and for her thoughtfulness and patience to guide me through that journey.

I also thank the rest of my committee for accepting my invitation: Prof. Ulrich Heiz, Prof. Tomas Bein, Prof. Achim Hartschuh, Prof. Joost Wintterlin, and Prof. Ivana Ivanović-Burmazović. Thanks also to Dr. Liang Yao, for reading and supervising my thesis at early stages, to Prof. Bishnu Prasad-Biswal, for sharing substantial parts of his work to this thesis, and to Prof. Doris Grumelli, for voluntarily reviewing our manuscripts before publication.

I thank the people of the Lotsch group with whom we shared so many meaningful moments these years. In the (scientific) sweet and sour of pursuing a PhD, I will always remember more the good times and the laughs we shared, and generally all our interactions beyond science. In this regard and in no order, my warmest acknowledgements to Christian S., Sourav L., Stefan H., Stefan T., Claudia K., Viola D., Liang Y., Alex P., Andreas G., Takayoshi O., Andrés R., Alberto J., Marie D., and to the people with whom we shared a space for having made my days more amenable, Bishnu P., Rao L., Kenichi E., and Hien N.

I thank the fruitful day to day supervision of Sourav L, Takayoshi O., Alberto J., and Liang Y. Through your guidance and advise, I not only got an academic degree, but became a better scientist and person. A big thank also to my collaborators, and to colleagues from other research groups and technical support of the MPI-FKF, whose cooperation and kindness made my projects easier and expanded my vision of science.

Finalmente, y lo más importante, agradezco a Daruska por compartir la experiencia de este viaje conmigo en el día a día, para lo cual no existe idioma ni palabras para expresar mi amor y gratitud. A mis padres, herman@s, abuela, mis ya no tan pequeños sobrinos, cuñad@s, y familia y amig@s (en Chile, EE.UU. y Alemania) en general, por su apoyo incondicional, por darme fuerzas y motivación cuando pasé por momentos difíciles, y también por la alegría de compartir mis logros con ustedes. Los quiero mucho y también son parte de esto. Dedico también este logro a la memoria de Franz Miric y Hortensia López.

Table of Contents

Summary

Global warming concerns have brought energy conversion into the spotlight. The conversion of renewable energy into chemical energy carriers has required keen inventiveness of the scientific community to find feasible solutions within today´s global economy. The success of such solutions requires collective efforts of multiple stakeholders, but from a purely technical perspective, this translates to the search for materials that can readily split water using a renewable energy input. For example, by using the right combination of light absorbing and catalytically active materials — or simply photocatalysts — that can simultaneously harvest sunlight and catalyze water splitting (aka artificial photosynthesis). An efficient water splitting photocatalyst aims to transform as much power of the solar spectrum as possible into chemical energy stored in the form of hydrogen and oxygen. The efficiency of this conversion is the result of multiple steps ultimately related to the sequence of light absorption, charge separation and transport, and electron transfer reactions. A photocatalyst is a semiconductor material with properties (i.e., optical band gap and crystallinity) that facilitate that sequence. Photocatalyst optimization is the process of tweaking the rate of those multiple steps (i.e., through material properties) such that the losses along the sequence are minimized.

This work focuses on the optimization of the photocatalytic performance of TiO_2, WO_3, and covalent organic frameworks (COFs). Energy conversion efficiencies using these, and state of the art photocatalysts remain far from the target set for commercial feasibility. However, since the first water splitting experience on TiO_2, various materials have been also demonstrated promising photocatalytic properties for water splitting half reactions, like WO_3 and COFs. While both WO_3 and TiO_2 (band gap ~ 2.75 and 3.2 eV, respectively) are n-type semiconductors with valence bands that provide enough thermodynamic driving force for the oxygen evolution reaction (OER), WO_3 allows additional harvesting of the visible solar spectrum. COFs are crystalline organic semiconductors that can be synthesized from earth abundant elements which have demonstrated the photocatalytic hydrogen evolution reaction (HER). Differently to the existing myriad of inorganic HER photocatalysts, the superior chemical tunability of COFs allows rational design and almost unlimited options for the tailoring of their photocatalytic properties. Multiple strategies can be found in the literature to optimize the photocatalytic performance of TiO_2, WO_3 and

COFs by the modification of the light harvester material properties. The workflow presented herein differs from those, because it zooms to other aspects that are equally crucial to explain photocatalyst performance but that are typically less explored by material researchers. These are the increase of material photocatalytic performance upon decoration with cocatalysts (HER or OER electrocatalyst), and the intricate interplay between that performance and the nanoparticulate suspensions' multiphysics (optics, transport phenomena, and colloidal suspension stabilization). The latter rationalizes the photoreactor design presented along this work, which simplifies persisting instrumental problems and uncertainties of the artificial photosynthesis field related to reaction modeling, and the accuracy, reproducibility, and sensitivity of the quantification of photocatalyst performance.

Commercial TiO_2 (P25) is a standardized photocatalyst with the potential to benchmark photocatalytic OER rates among different laboratories, but it requires the addition of an OER catalyst to overcome water oxidation kinetic limitations. In this work a RuO_x cocatalyst is developed in-situ on P25 for such purpose. With the instrumentals developed for sensitive O_2 detection, the P25@RuO_2 benchmark is optimized in terms of activity and reproducibility (at simulated sunlight, AM1.5G) and its resulting external (0.2%) and internal photonic efficiency (16%) is presented. Along with the establishment of this OER benchmark, this work also drafts good practices for reporting OER rates (i.e., adventitious O_2 control), and innovative photoreactor engineering and optical modelling for the disentangling of the multiple factors determining photocatalysis physics. Using the same instrumentals for OER detection and a more elaborated cocatalyst tuning approach, a novel 2D RuO_x electrocatalyst (ruthenium oxide nanosheet, RONS) is added to WO_3 nanoparticles to enhance photocatalytic OER rates. First, the tuning of a top-down method to produce size-controlled unilamellar RONS is developed. Then, the composites resulting from RONS impregnation on WO_3 are compared to conventionally impregnated RuO_2 nanoparticles (RONP) on WO_3, the former displaying a 5-fold increase in photonic efficiency. These results are explained from the electrocatalytic properties at the RONS edges, and the optical properties of the resulting 2D/0D morphology of the RONS/WO_3 that decreases the optical losses due to parasitic cocatalyst light absorption.

COFs have enormous potential as photocatalysts by design. In this work the photocatalytic performance of a TpDTz COF is analyzed in terms of its interaction with a molecular HER cocatalyst (Ni-ME) and reaction modeling. The TpDTz COF/Ni-ME system, which is one of the few existing COF-molecular cocatalyst known to date that can produce hydrogen, shows relatively high HER photocatalytic activity (~1 mmol h^{-1} g^{-1}, AM1.5G) compared to other organic visible light responsive semiconductor benchmarks (i.e., like g-C_3N_4) and it operates in aqueous suspension (containing triethanolamine as electron donor). The TpDTz COF/Ni-ME surprisingly overperforms Pt modified TpDTz COF. Nonetheless, the COFs' charge transport properties are not well understood and most likely short-ranged. This blurs the experimental access to COFs' photocatalytic performance bottlenecks, including the prominent case of the TpDTz COF/Ni-ME system. Regardless of such difficulties, this work deepens the HER reaction understanding of the TpDTz COF/Ni-ME by analyzing dynamic HER reaction trends detected using the aforesaid photoreactor designs and instrumentals. From the modeled HER cycle kinetics and rapid dark step, the HER rate limiting step of the TpDTz COF/Ni-ME is placed at the electron transfer to the resting Ni-ME state. These HER mechanisms on COFs are experimentally challenging to access and are herein partially accessed in-situ from a reaction engineering and modelling perspective.

On the whole, this work is the culmination of a multidisciplinary effort to find new opportunities to understand and optimize materials used for energy conversion processes, ranging from fundamental material research, solid-state and optics physics, applied catalysis, to reactor engineering.

1. Introduction to Energy Conversion Photocatalysis

1.1 Sustainable Energy and Chemical Energy Conversion

Any functioning society needs energy. Energy is associated to quality of life and socio-economic development. In the year 2017, a global population of around 7.6 billion people consumed a total of 163,750 TW-hours/year, which is expected to increase 24% by the year 2040, due to ongoing global population growth, current standards of energy demand in developed nations, and socio-economic progress of underdeveloped nations.[1,2] Currently, such energy demands are met mostly by the burning of fossil fuels.[3,4] Energy production from fossil fuels is a CO_2 emission intensive activity — for example, on average 62 g of CO_2 per ton of cargo per km of route are released by a standard freight diesel truck, and 0.38 kg CO_2/kWh is released in modern gas fueled power plants.[5,6] Trends of energy production portfolios worldwide show that fossil fuel consumption are to keep increasing inexorably if different stakeholders (i.e., policy makers) do not agree on environmental restrictions on the release of CO_2 emissions to the atmosphere. The relation between anthropogenic CO_2 emissions and climate change is irrefutable. It has been warned that runaway of CO_2 emissions can produce immediate disruptions in the global climate. Changes of climate on a global scale will be irreversible after a net increase of 2 °C compared to preindustrial records, affecting life sustainability on earth in the long term.[3,4,7] An outlook of sustainability from a thermodynamic perspective can be applied to modern societies in this regard. Considering our global society as an open system bound to basic thermodynamics principles, sustainability refers to the balance of inputs (energy and mass) equaling growth rates and appropriate disposal of wastes.[2] Therefore, sustainable development of our society is almost inevitably linked to the way we produce energy. Shall we not move from rapid depletion of fossil fuels and the accumulation of its most distinctive greenhouse gas waste, CO_2, functioning of future generations will suffer of pressuring survival conditions and conflicts created by this imbalance.[2,4,7]

As depicted in Figure 1-1, renewable resources appear not only as less CO_2 intensive alternatives for energy production, but also as the most abundant, democratic, and constant energy input necessary to keep our life standards and leveraging of less developed nations. It must be kept in mind while analyzing Figure 1-1, that currently most of the CO_2 emissions from renewable resources result from infrastructure building, which

is assessed as part of the life cycle of the technology (i.e., for solar energy, ~ 100 gCO_2 kWh_e^{-1}); shall our energy portfolio contain less fossil fuel generated electricity, for example for photovoltaic (PV) panels manufacturing, renewables resources would emit at least two order of magnitude less CO_2 (< 10 gCO_2 kWh_e^{-1}) than the finite resources (with the exception of nuclear energy).[8]

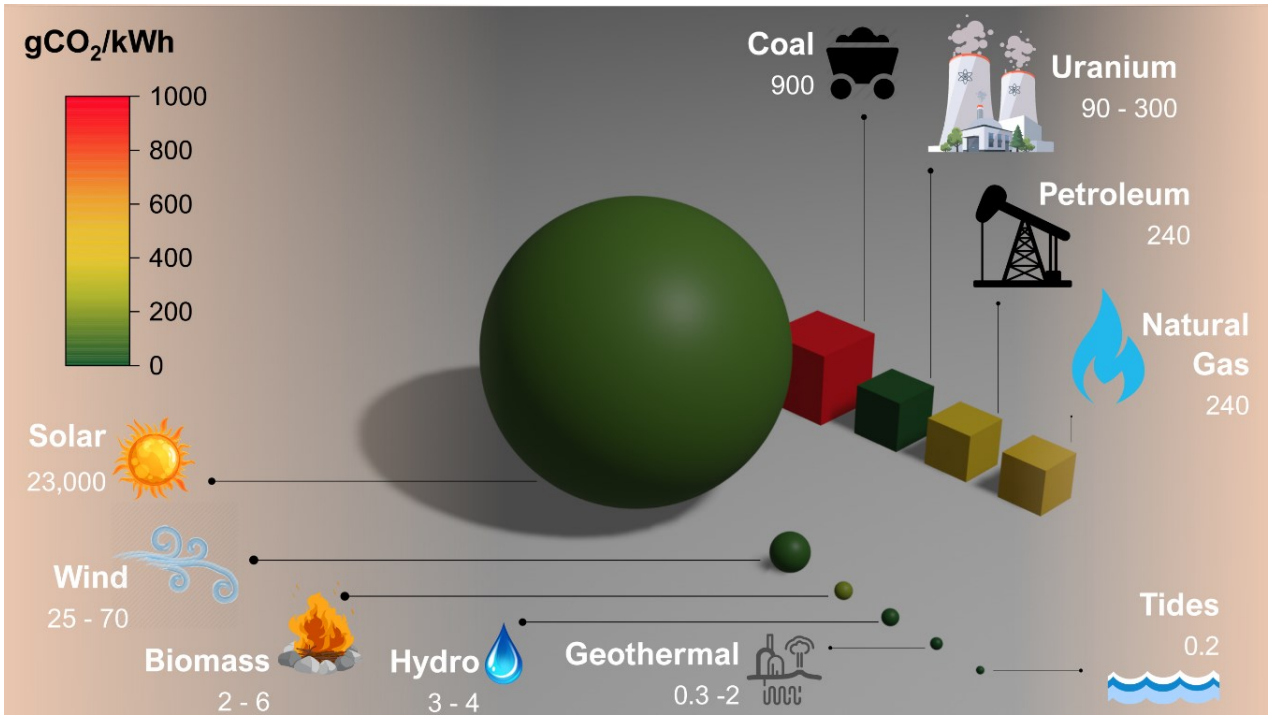

Figure 1-1. Comparison of finite (cubes, number in TW-year of reserve) and renewable (spheres, number in TW of total potential) global- exploitable energy resources. Global yearly consumption by 2020 is around 18 TW. Volume of 3D shapes is proportional to the magnitude of the resource. Surface color represents gCO_2 emission per kWh generated of electricity (color bar on the left).[1,5,6,8]

This necessary transition to renewable energy generation is occurring but at slow pace.[4,7] The first challenge and why going renewable is not likely to happen overnight, it is due to its multidimensional nature (science, engineering, politics, social, economics) that involves profound changes in country politics and infrastructure.[2,4] A second challenge is that most renewable resources are intermittent and cannot be used on demand like fossil fuels (i.e., solar and wind).[9,10] Since electricity cannot be stored without means of conversion mediated by energy carriers or other forms, like capacitors or batteries, renewable electricity generation without conversion is economically and logistically impaired. A third major challenge to cut off CO_2 emissions is not directly related to electricity generation

and storage, but what is due to technical reasons — areas so called "hard to decarbonize". For example, air transport and cargo trucks technology nowadays cannot shift from running on diesel and kerojet, to conventional batteries due to the relatively low energy densities scale up with mass of the latter.[3–5,10] In this context, to move toward a more sustainable society, technologies for converting renewable energy to high energy density and viable distribution chemical energy carriers like H_2 tackle the challenges of energy storage and distribution to non-stationary consumers, simultaneously. Chemical energy conversion is then predicted as one of the pivotal technological changes driving the transition to a CO_2 emission free energy grid, as shown in Figure 1-2. Among other energy carriers, green H_2 production has an additional benefit in decreasing CO_2 emissions because it is also a feedstock for multiple other chemical industries, like NH_3 production — nowadays, H_2 as a feedstock production comes mostly from steam reforming which is another main contributor for CO_2 total emissions.[10,11] Green H_2 may also have a role in reverting climate change because of its applications in CO_2 recycling, for example hydrogenation to CH_3OH or Fischer-Tropsch fuels. It is therefore rational that in literature this model of society having green H_2 as the central drive, so called "hydrogen society" or "hydrogen economy", is referred to as a synonym of sustainable energy systems.[4,12]

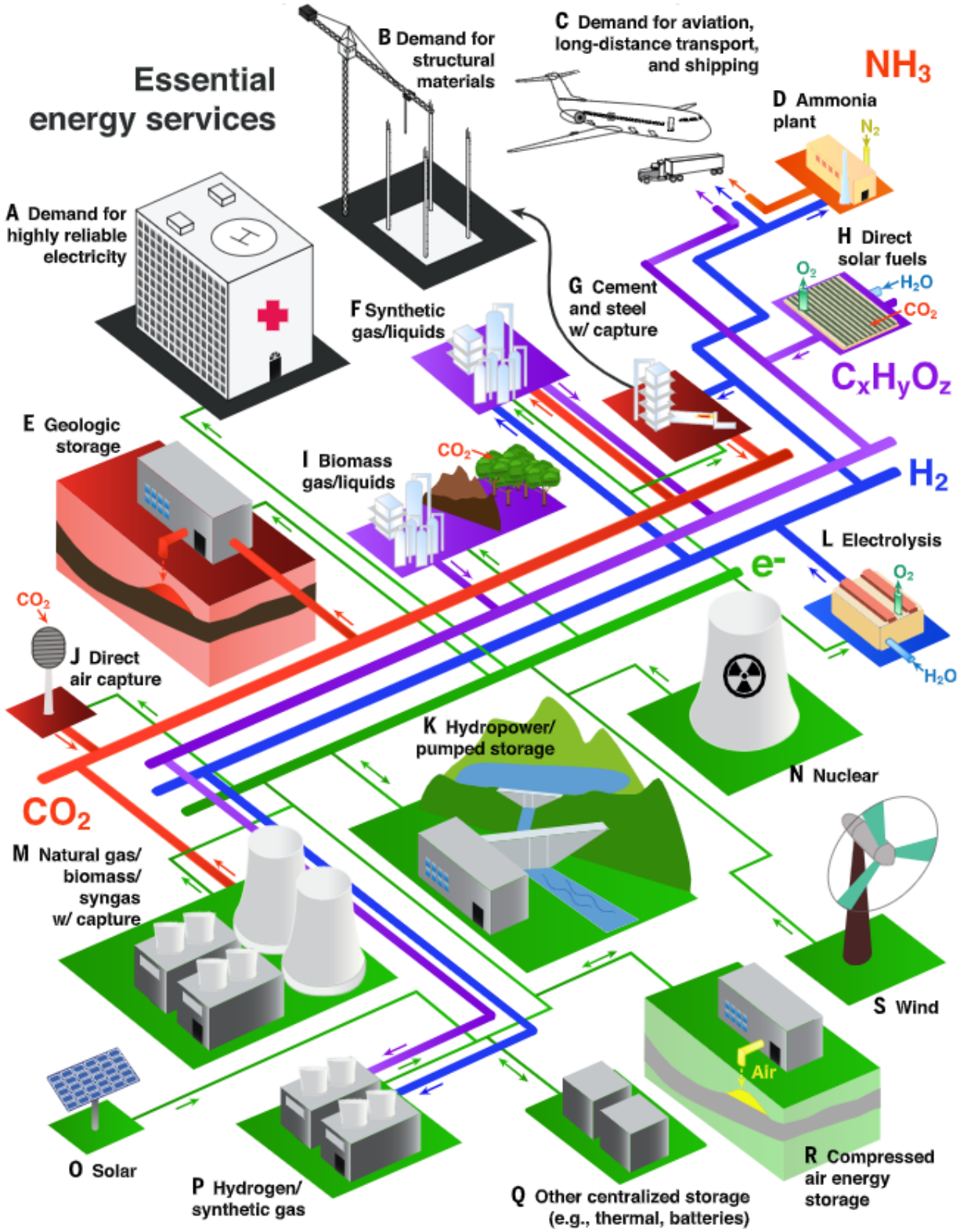

Figure 1-2. Schematic of an integrated system that can provide essential energy services without adding any CO_2 to the atmosphere (A to S). Colours indicate the dominant role of specific technologies and processes. Green, electricity generation and transmission; blue, hydrogen production and transport; purple, hydrocarbon production and transport; orange, ammonia production and transport; red, carbon management; and black, end uses of energy and materials. Reproduced from Davis et al (2018).[10]

1.2 Green Hydrogen Market

Without means of storage, renewable energy still has made its way through the market mostly due to the steep decrease in the levelized cost of energy (LCOE) for wind and solar energy in the last decades. [2,9,10] There has been evident progress in smart electrical grids and others similar technologies to take advantage of this cheap and clean resource on demand as much as possible.[2,9,10] However, there is still a surplus of renewable electricity at peaks of generation that evidences again the techno-economic importance of energy conversion. This peak of renewable generation has triggered among other trends the spurt of battery applications (i.e., light weight transportation), and the drop of the estimated cost of H_2 from electricity to relatively competitive prices of < 4.0 USD/Kg; H_2 as a commodity has a current production cost from fossil fuels via steam reforming of around 0.8 - 1.5 USD/Kg.[13,14] In addition to electricity prices, efficiency of conversion together with investment costs is also a key factor in determining techno-economic feasibility of green H_2 production. Nowadays, given its simplicity, robust operation, and STH efficiencies around 10 - 30%, water electrolysis is the most prevalent technology driving the transition to green H_2.[12,15–18] H_2 production price from electrolysis depends on the price of local electricity and the investment for infrastructure. By 2020, in some regions with abundant solar energy from PV, electrolysis can produce H_2 at prices as low as 1-2 USD/Kg.[13,14] The electrocatalytically produced H_2 price by 2040 - 2050 will eventually decrease below the projected price of fossil H_2 production (optimally produced, 0.8 USD/Kg).[14] Following such takeover of the H_2 market as a commodity, whose predicted trends are presented in Figure 1-3a, green H_2 production is also expected to compete as an efficient energy carrier, meaning that the cost of energy stored in production/consumption cycles of H_2 in USD/kWh will eventually compete with the ones of fossil fuels and batteries, for example, in the field of heavy-duty transportation.[9–11]

Water electrolysis is an electrochemical process in which water is converted to H_2 and O_2 via two parallel redox reactions mediated by heterogeneous catalysts and externally applied voltage (Figure 1-3b). Most efficient catalysts for the hydrogen evolution reaction (HER) are Pt- and Ni-based materials, while Ru- and Ir-based compounds (in acidic media and using proton exchange membranes, PEM) are typically used as catalysts for the oxygen evolution reaction (OER).[19–22] Projected prices of H_2 from electrolysis are to keep

their decreasing trend with the condition that key persisting limitations of current technology are solved. These limitations are associated mainly to the compromise of efficiency, corrosion, and price of OER catalysts.[12,15,17,19,20] For the moment, OER performance of alternative and cheaper materials based on earth abundant element, like Mn and Co, is still under-developed for industrial scale applications (i.e., oxides or layered double hydroxides).[20] Other limitations of electrolysis are its requirement for HER/OER reactions balance (alkaline or proton exchange membrane, PEM), and scale-up complications.[12,15,16,18]

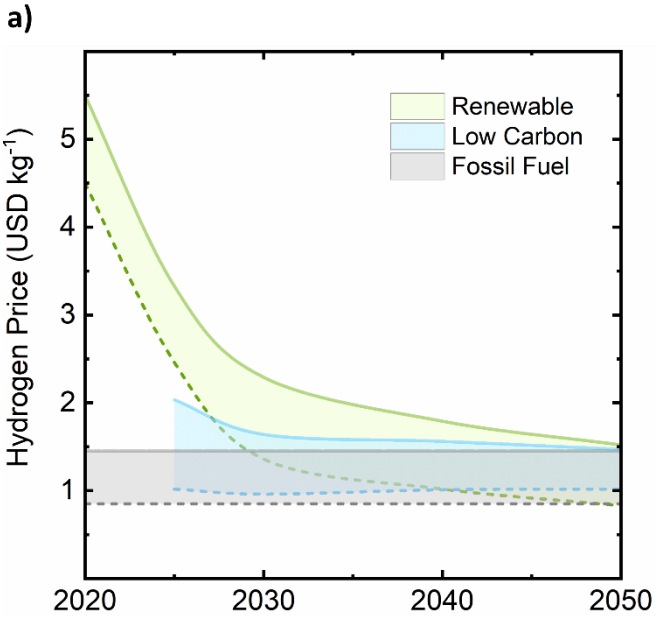

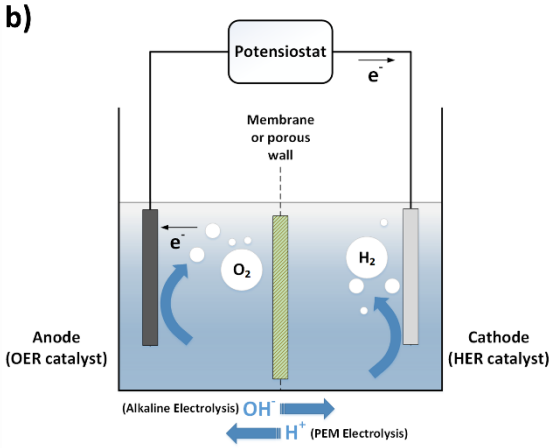

Reaction at	Alkaline Electrolysis	PEM Electrolysis
Anode	$2\ OH^- \rightarrow H_2O + ½\ O_2 + 2\ e^-$	$H_2O \rightarrow 2\ H^+ + ½\ O_2 + 2\ e^-$
Cathode	$H_2O + 2\ e^- \rightarrow H_2 + 2\ OH^-$	$2\ H^+ + 2\ e^- \rightarrow H_2$
Overall Cell	$H_2O \rightarrow H_2 + ½\ O_2$	

Figure 1-3. (a) Hydrogen production costs by production pathway. Band represents estimated cost at average location (solid line) and optimal location (dashed) lines. Green hydrogen refers to PV based hydrogen generation (green). Fossil Fuel refers to conventional natural gas reformation (grey). Low carbon refers to conventional production aided with CO_2 capture (light blue). Key price assumptions are: 2.6 – 6.8 USD Mmbtu^{-1} for natural gas, and in USD/kWh: 25 – 73 (year 2020), 13 – 37 (year 2030), and 7 - 25 (year 2040) for LCOE od PV electricity. Adapted from Hydrogen Council, McKinsey & Company (2021).[14] **(b)** Schematic illustration of alkaline water electrolysis and PEM water electrolysis. Adapted from Kumar and Himabindu (2019).[15]

1.3 Artificial photosynthesis

1.3.1 Background

Aside from conventional electrolysis, H_2 and other chemicals may be produced directly from sunlight, which is widely known as artificial photosynthesis. The definition of artificial photosynthesis is any reaction whose overall Gibbs energy change is positive and driven by sunlight ($\Delta G_r > 0$), and whose spontaneous backward processes are — at least partially—

kinetically suppressed.[23] In photosynthetic systems, the maximum chemical energy stored in a molecule of product that can generate useful work if reacted reversibly backwards is given by ΔG_r ($\Delta G°_r$ refers to the ΔG_r at standard conditions). The efficiency of the conversion process, or so called solar to chemical efficiency (STC), considering the solar input, is then given by:[24,25]

$$STC = \frac{r_c \times \Delta G_r}{P_{sun} \times A} \qquad \text{Equation 1-1}$$

r_c : production rate of the chemical of interest (mol h^{-1})

ΔG_r : Gibbs energy of the reaction (J mol^{-1})

P_{sun}, A : the energy flux of the sunlight (100 mW cm^{-2}), and the area of illumination

Artificial photosynthesis differs from natural photosynthesis mainly on the tailoring of a range of products different than biomass. Artificial photosynthesis is mediated by *human-made* or *human-modified* materials, typically heterogeneous photocatalysts.[23,26] The most meritorious photosynthetic system in terms of energy stored per molecule of product, and the aforesaid market and environmental value of the product, is photocatalytic H_2 generation from water, or photocatalytic overall water splitting (POWS).[12,16,27–29] Other less conventional forms of artificial photosynthesis include photocatalytic NH_3 dehydrogenation and CO_2 reduction to CH_3OH.[30,31]

$$H_2O \rightarrow H_2 + ½\ O_2 \quad (\Delta G°_r = 237\ kJ\ mol^{-1})$$
$$NH_3(aq) \rightarrow 3/2\ H_2(g) + ½\ N_2(g) \quad (\Delta G°_r = 27\ kJ\ mol^{-1})$$
$$CO_2 + 2\ H_2O \rightarrow CH_3OH_{(aq)} + 3/2\ O_2 \quad (\Delta G°_r = 703\ kJ\ mol^{-1})$$

The underlying principle of POWS is the generation of electron-hole (e^--h^+) pairs (or excitons) when light is absorbed on the light-harvester material, i.e., on a semiconductor. In the absence of intermediate levels (i.e., surface traps), the photogenerated electron-hole pair potential is given by the conduction (E_{CB}) and valence band (E_{VB}) level,

respectively. The energy of the absorbed photon ($h\nu$) must be equal or greater than the material bandgap ($E_g = E_{CB} - E_{VB}$).

Light absorption: $h\nu$ + photocatalyst → photocatalyst + e^- + h^+ ($h\nu > E_g$)

In a single step POWS, two redox reactions occur simultaneously on the photocatalyst surface triggered by the photogenerated electron-hole pair (electrochemical) potential. These reactions are usually referred to as hydrogen evolution and oxygen evolution reactions (HER and OER, respectively).

HER: $4\ H^+ + 4\ e^- \rightarrow 2\ H_2$ (0 – 0.059 x pH, V versus NHE)

OER: $2\ H_2O + 4\ h^+ \rightarrow O_2 + 4\ H^+$ (1.23 – 0.059 x pH, V versus NHE)

In the absence of kinetic limitations, thermodynamics of this simplified POWS process requires 4 photons with energy at least higher than 1.23 eV (~ 1,000 nm) per molecule of water split, which represents an ideal maximum of STH efficiency from the solar spectrum of 47%.[18] However, in a laboratory scale, state of the art optimized POWS systems for H_2 production have only achieved ~ 0.4 % STH efficiencies with one-step systems.[16,18,24,32] The limitations of real POWS systems are associated to recombination of photogenerated charges, and spontaneous backwards reactions (i.e., H_2O formation).[16,18] On the one hand, and despite the progress achieved compared to the initiatory POWS systems, economic feasibility of POWS requires STH efficiencies higher than 5%. [16,18] On the other hand, given the low cost of infrastructure and scale-up advantages of POWS compared to electrolysis, significant efforts worldwide are still devoted to find more efficient materials. Recently, these scale-up concepts have been tested on an industrial scale POWS facility (> 100 m^2 of photocatalyst panels), which has proven H_2 production at 0.3% STH efficiencies under realistic conditions (i.e., considering product separation and atmospheric conditions).[33,34] As this performance remains roughly one order of magnitude lower than the aforesaid POWS target for economic feasibility, compared to electrolysis, artificial photosynthesis is only an emerging technology for green H_2 production. Nowadays, artificial photosynthesis

research focuses on addressing fundamental material challenges on a laboratory scale to find more efficient particulate systems.[16,18]

1.3.2 Semiconductor based POWS principles

As previously described, the principle of POWS is the photogeneration of electron-hole pairs. Upon illumination with photons of energies above the band gap of the light absorber material, for example a direct band gap semiconductor, a shift of the population of electrons (n) and holes (p) at thermal equilibrium takes place. Electron-hole populations at thermal equilibrium (n_0, p_0) are described by the Fermi level of the semiconductor (E_f), band alignment (E_{VB} and E_{CB}), and Fermi statistics.[17,35,36] Most semiconductors are extrinsic due to doping or crystal defects, meaning that the intrinsic concentration of electrons and holes is unbalanced. Typically, in extrinsic semiconductors at room temperature the increase of minority carriers (Δn, or Δp) under illumination largely exceeds the minority carrier population under thermal equilibrium. For example, in an n-type semiconductor, $\Delta p >> p_0$, $\Delta n << n_0$ and $\Delta n \sim \Delta p$. In practice, this can be interpreted as regions of the illuminated n-type semiconductor having an excess population of minority carrier (Δp) at the E_{VB} level. Likewise, Δn are at the E_{CB} level since hot electrons relaxation is typically considered ultra-fast. Therefore steady illumination generates a perturbed equilibrium that is usually redefined by quasi-Fermi levels under illumination ($E_{f,n}$ and $E_{f,p}$ for electrons and holes, respectively).[17,35–37] Quasi-Fermi levels are a simplification of the distribution of Δn *and* Δp, which are local densities resulting from electron-holes generated in proximity (exciton) at local photogeneration rates following light absorption. The quasi-Fermi level representation is a way to describe the net driving force for locally generated electron-hole pairs to separate and migrate in space.[37–39] The elementary driving force is the difference between the electrochemical potentials of E_{CB} and E_{VB} relative to the reduction and oxidation electrochemical reactions at the semiconductor surface, respectively. Then, a fraction of generated excitons separates, meaning that the driving force for charge migration is enough to overcome the exciton binding energy, which is the minimum energy to ionize the exciton from its lower energy state. This binding energy is determined by coulombic interactions, which depend on the electronic properties of the material structure, like dielectric constant and carrier's effective mass.[36,40] For strongly bound

excitons, the probability of radiative recombination is high.[41–43] After separation, surviving free Δn and Δp can migrate independently according to charge carrier dynamic principles (diffusion-drift) to the surface of the photocatalyst. Free charge carrier recombination (for example, radiative or via crystal defects) is still typically the fastest pathway, which is characterized by short minority carrier lifetimes.[36,41,43–45] From the minority charge carrier lifetime and its transport properties a dimensional length scale arises, known as the minority carrier diffusion length (L_D). L_D yields a rough estimation of how far from its generation a free minority charge carrier can travel before recombining with the majority charge carrier in the bulk of the semiconductor.[36] In POWS, free electron and holes reaching the surface can also recombine, for example via the semiconductor surface trap states, or engage simultaneously in OER and HER reactions.[36,37]

Charge separation is also affected by the (ideal) equilibration of charge carrier's chemical potential at the interface of the semiconductor with surrounding photocatalytic media (electrolyte) — the first described by E_f under dark conditions, and the latter by redox pairs' reaction potentials (i.e., O_2/H_2O) present in the elctrolyte.[17,37,39,46] Under steady illumination and in the absence of kinetic barriers for electron transfer, the chemical potential of the charge carriers in the semiconductor is defined by $E_{f,n}$ and $E_{f,p}$. This process is known as Fermi levels equilibration. The Fermi level equilibration condition at the photocatalyst interface with photocatalytic media, or with the energy level of decorated metals, triggers an additional effect crucial in describing charge dynamic trends and exciton separation, known as band bending. Band bending refers to the shift of the E_{CB} and E_{VB} isolated energy levels after the previously described electron chemical potential equilibration at interfaces and influences the charge carrier net electrical fields along the photocatalyst. Nonetheless, the extent of band bending induced by the semiconductor-electrolyte contact is small in nanoparticulate (diameter < 100 nm) photocatalysts in the absence of semiconductor-metal contacts (< 10 mV).[46,47] If a photocatalyst is composed of semiconductor-metal contacts on its surface, depending on the dimensions and the chemical and electrical properties of the metal, when immersed in an electrolyte, the resulting band bending magnitude along the photocatalyst may switch locally from the one previously described for a semiconductor-electrolyte contact, to band bending dominated by homogeneous semiconductor-metal junction.[36,46,48–50] The latter

may trigger drastic changes in the band bending magnitude in the photocatalyst (i.e., up to 1 V if a Schottky junction is expected), significantly affecting the driving force for exciton separation and migration of free charge carriers.[36,46,48,50]

Fermi level equilibration, light absorption, and other intrinsic properties of the semiconductor mentioned previously, like exciton binding energy, transport properties and minority carrier lifetime (or diffusion length) result in a net movement of charges towards the surface of the photocatalyst. This whole process from light absorption to steady surface reaction at HER and OER active sites can be seen as balanced flow of free charges along the light-harvester, which is accompanied by the evolution of gaseous H_2 and O_2 products. A depiction of simplified POWS and the breakdown of its elemental steps are presented in Figure 1-4 and Figure 1-5.

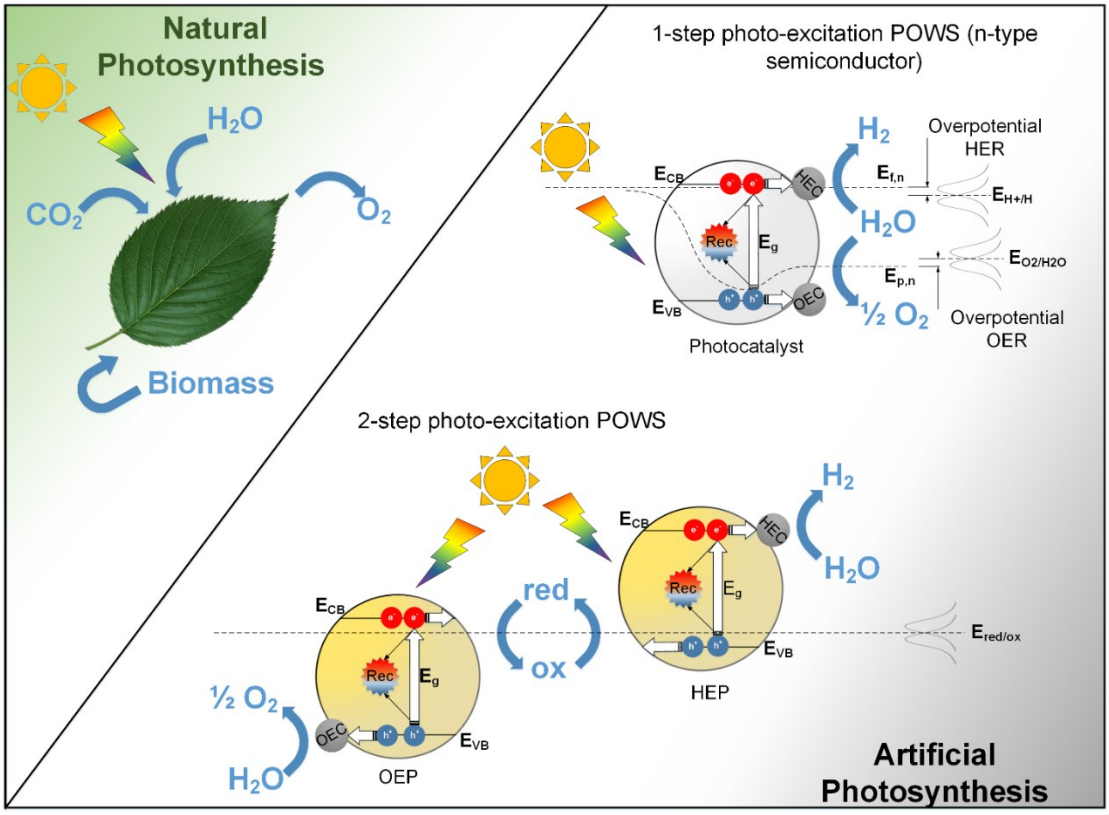

Figure 1-4. Schematic view of natural and artificial photosynthesis. Photocatalytic overall water splitting (POWS) systems are represented as 1-step and 2-step photoexcitation (aqueous red/ox mediator, z-scheme). Dashed lines represent quasi-Fermi levels under illumination for an n-type semiconductor (band bending not represented). Z-scheme OER and HER reaction ignores n- or p-type extrinsic behaviour (no overpotential assumed for red/ox reactions). Acronyms: E_{VB} and E_{CB}, valence and conduction band levels; E_g, semiconductor bandgap; HEP, hydrogen evolution photocatalyst; OEP, oxygen evolution photocatalyst; HEC, hydrogen evolution catalyst; OEC,

oxygen evolution catalyst; ox, oxidant; red, reductant; $E_{f,n}$ and $E_{p,n}$, semiconductor quasi-Fermi levels of electron and holes; $E_{H+/H}$, $E_{OH-/H2O}$ and $E_{red/ox}$, HER, OER and redox shuttle reaction energy levels.[17,18]

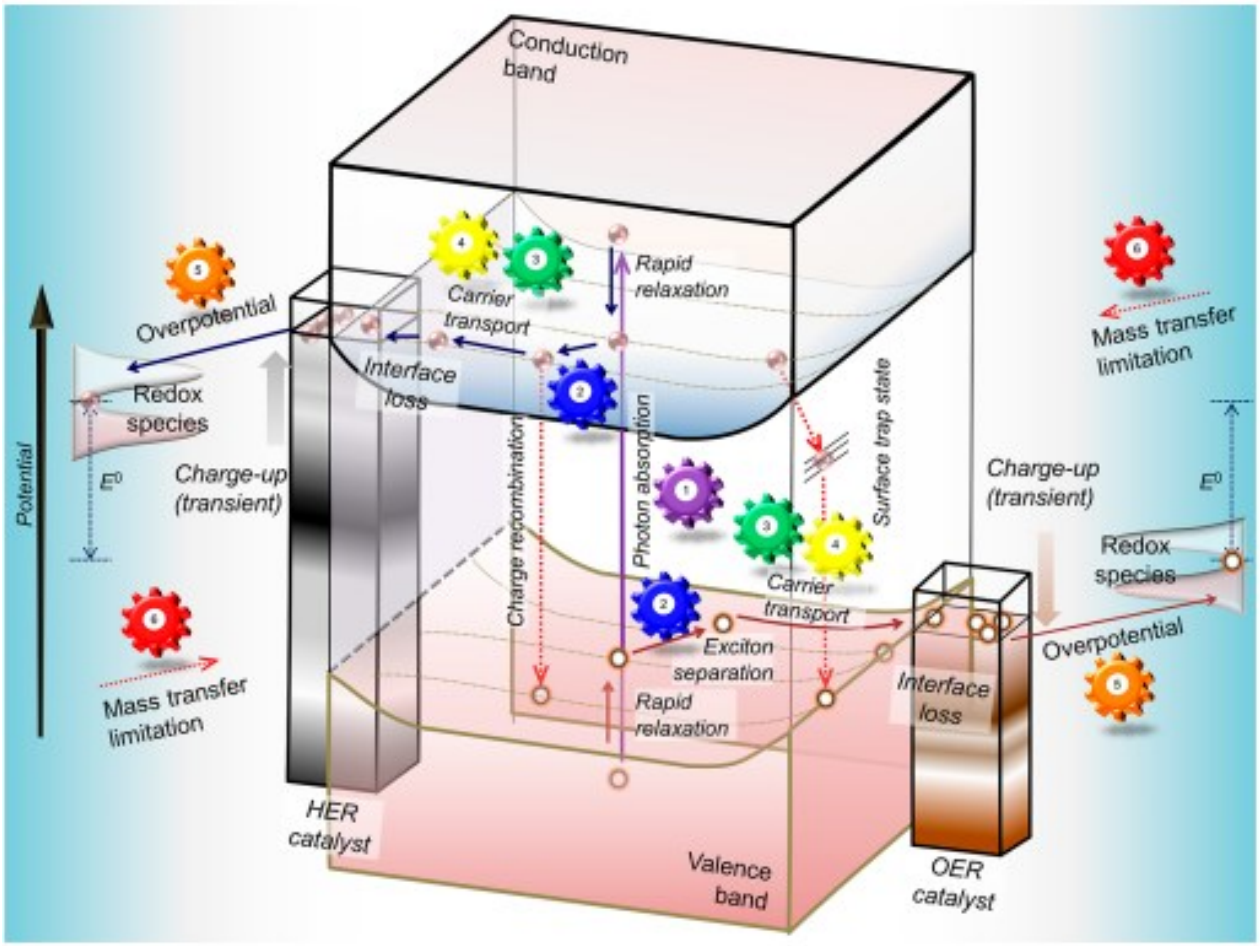

Figure 1-5. Schematic image of the mechanistic aspects of the photocatalytic water splitting process. The gear with the number indicates the order of the photocatalytic process to be successful for overall water splitting. Reproduced from Takanabe et al (2017).[36]

Additionally, depletion of photogenerated charges at the photocatalyst surface follows electrocatalysis principles, for example Butler-Volmer.[51] Consequently, like overpotential in electrocatalysis accounting for kinetic barriers in electron transfer, photocatalytic HER and OER rates require an excess of reduction/oxidation potential of surface electron/holes relative to the redox potential of HER/OER reactions.[52–54] Different to the ideal case where $E_{f,n}$ and $E_{f,p}$ equilibrate with HER and OER potential, this required excess of potential establishes a dynamic offset between such levels at the photocatalyst surface. In POWS, this overpotential requirement leads to accumulation of carriers at the interface to extract

them as steady HER and OER currents (redox rates), which produces a potential irreversible loss and a build-up of potential close to the photocatalyst surface.[36,40] The latter also increases surface charge recombination and reduces charge transport and separation from the bulk of the photocatalyst. Therefore, the overpotential requirement can be interpreted as a kinetic limit or boundary condition for the resulting HER and OER currents at the photocatalyst surface, which controls the overall POWS efficiency. Furthermore, the HER and OER electrocatalytic rates triggered by the aforesaid photo-physics and electrochemical principles are also coupled to mass transfer of adsorbates in solution to the photocatalyst surface (ions involved, like H^+). Ion's transport phenomena, depending on reaction rates and transport properties (including drift and semiconductor internal fields) may generate reaction or mass transfer dominated regimes.[36,40,50,55]

1.3.3 POWS efficiency and optimization

As it has been now described, POWS is a multiphysics problem involving multiple timescales. Light absorption takes place in a rapid time scale between fs and ps, while charge carrier dynamics (separation, diffusion, and transport) occurs within a broad time scale frame between 10^{-9} and 10^{-3} s.[36,50] Surface reaction and mass transport phenomena is referred to typically as the slowest processes because they occur between 10^{-3} and 10^{0} s time scale.[36] These steps in different time scales influence one another, resulting in an overall efficiency that is controlled by one or multiple bottlenecks as the gears depiction of Figure 1-5 suggests.[36,40,50,55] A photocatalyst efficiency can be conveniently divided as follows. η_{abs}: light absorption at the semiconductor generating electron-hole pairs (exciton), η_{sep}: exciton separation and migration to the semiconductor surface, which is limited by bulk charge recombination, and η_{cat}: redox reactions for proton reduction or water oxidation, which includes interfacial potential losses (overpotential) and surface charge recombination.[52–54] Using the irradiated photon rate into a suspension as the solar input (as photon flux I_0), resulting POWS rates (based on HER rates, r_{H2}) can be seen as:

$$r_{H2} = {}^{I_0}/_{2} \times \eta_{abs} \times \eta_{sep} \times \eta_{cat} \qquad \text{Equation 1-2}$$

It is clear from Equation 1-1 and Equation 1-2 that the overall STH in a photocatalyst is a convolution of η_{cat}, η_{sep} and η_{abs}. Semiconductor engineering as the light absorber POWS material is necessary to achieve high η_{sep} and η_{abs}. However, in most semiconductors, typical engineering of band alignment allowing visible light absorption and proper bands potential for redox reactions, among other light absorber beneficial features, contribute to but do not necessarily ensure efficient POWS.[16,18] At most bare semiconductor active sites, the activation energies for HER and OER reactions is relatively high (high overpotentials), making charge transfer sluggish and kinetically hindered by surface recombination (low η_{cat}).[52–54] Few materials can harvest light and provide suitable redox active sites. Consequently, to achieve higher STH efficiencies, hydrogen evolution and oxygen evolution cocatalyst (HEC and OEC) addition is most of the times imperative to enable redox reactions at the photocatalyst surface through mechanisms involving lower kinetic barriers for electron transfer.[52–54] Although some cocatalysts may also have direct effects improving η_{sep} due to beneficial modifications of the electric field along the photocatalyst (i.e., via Schottky contact band bending), the most desired attribute of a cocatalyst is their relatively low electrochemical overpotential for HER or OER reactions, which enhances η_{cat}.[47,56–58] The latter may also trigger a drastic indirect improvement of η_{sep} due to the lower accumulation of charges necessary at the photocatalyst surface for efficient charge transfer. Therefore, besides light harvester optimization, addition of an appropriate cocatalyst is one of the most successful strategies to obtain efficient POWS composite materials.[52–54]

Another approach to increase STH efficiencies in POWS is inspired by natural photosynthesis, where light absorption occurs in two steps (PS-I and PS-II). POWS can also be tailored in two steps, which is typically performed via a z-scheme.[16,18,27,59] In a redox shuttle mediated z-scheme, as depicted in Figure 1-4, light simultaneously excites the OER photocatalyst (OEP) and HER photocatalyst (HEP), whose charge balance is mediated by the reversible oxidation/reduction of a shuttle acting as electron acceptor/donor. Besides reversibility and stability, a suitable redox shuttle must have an electrochemical redox potential in-between HER and OER, for example KIO_3/I^-.[59–62]

$$3\ IO_3^- + 3\ H_2O + 6\ e^- \rightarrow I^- + 6\ OH^-\ (+0.67\ V\ versus\ NHE,\ at\ pH = 7)$$

The use of a redox shuttle introduces more backward reaction possibilities, additional multi-electrons processes, and doubles the theoretical number of photons required per molecule of H_2 produced. This approach requires fine control of the undesired processes to successfully achieve POWS, like a shuttle short-circuit.[18] Still, it opens the possibility to independently tune the OEP and HEP systems for visible response with less constrain on band alignment, and thus on the semiconductor choice.

1.3.4 Inorganic Light harvesters

Since the pioneering work of Honda and Fujishima using TiO_2 in 1972, scientists have been looking for more efficient inorganic semiconductors, both from a narrower band gap (η_{abs}) and lower recombination rates (η_{sep}) perspective.[18,63] TiO_2 by then was the first ever reported OWS materials. In that work, photocurrents were measured with an external bias voltage using TiO_2 photoanodes. Later TiO_2 and other Ti based materials were screened for POWS with modest STH limited to the UV region. It was then demonstrated that oxides of other transition metals (like Ta^{5+} and W^{6+}) and conventional metal cations (like Ga^{3+} and Sn^{4+}) were also active in the UV region.[18] These *d0* and *d10* type materials owe their activity to electronic structures of conduction and valence band, which come mostly from *d* (CB of the transition metal) and *sp* (VB of the anion) hybridized orbitals.[18,64] This alignment sets a minimum bandgap of around 3 eV if both HER and OER are to occur on the same material, with only moderate reduction potential of the $E_{CB} \sim 0.1$ - 0.2 eV relative to the H^+/H energy level. In time, tuning of such compounds (among other aspects later described in this chapter) into more innovative highly crystalline structures like metal doped perovskites ($SrTiO_3$:Al) have demonstrated high intrinsic efficiencies above 30% in the UV region, and more recently close to 100% (apparent quantum yield, AQY).[18,65,66] However, as high as intrinsic efficiency can be, meaning the ratio of produced hydrogen molecules to half the photons of a certain wavelength absorbed by the light harvester, STH is still limited by the absorption spectra (low η_{abs}). For example, for a theoretical 100% AQY in a one-step semiconductor material but with a band gap below 400 nm, the light absorption spectra represent only a small fraction of the total solar power input (5%), thus the system overall STH outcome of only 2%.[18] In parallel, numerous efforts have been

made to engineer the semiconductor band gap to harvest a wider light spectrum. The most established approach to obtain POWS activity at lower band gaps (<3 eV) is tuning the O_{2p} hybrid levels to shift the E_{VB} bands up in potential. This branched to a new type of crystals that are oxygen deficient and/or that contain N_{2p} orbitals, like TaON and other oxynitrides.[18,60,67,68]

Another material breakthrough in artificial photosynthesis occurred with the experimental demonstration of redox shuttles in POWS. This was first demonstrated by the work of Abe et al (2001) on specific Anatase/Rutile phases of TiO_2, which yielded only modest STH efficiencies.[59,61,69] Z-scheme materials have diversified in time following similar principle as one-step materials but allowing independent optimization of HEP and OEP regarding band levels and other favorable crystal aspects. Z-scheme materials now include as OEP: TiO_2 (rutile), WO_3 and $BiVO_4$; and as HEP: TiO_2 (anatase), TaON, and $SrTiO_3$.[59,60,62,68,70,71] This approach has been the most successful so far and has achieved STH efficiencies in the range of 1%.

It must be stressed that high STH efficiencies depend on multiple other aspects different from the visible light response and band alignment of the semiconductor chosen. To control backward processes, like charge recombination, and improve beneficial transport properties, like small exciton binding energies and high carrier mobility, special attention must be paid also to material crystallinity, crystal phases, morphology, size, electron mediator, and cocatalyst decoration.[16,18,32] As previously described, cocatalyst decoration is a critical aspect to facilitate photocurrents of H_2 and O_2 at lower overpotential at the photocatalyst surface, and charge separation. Material research of the cocatalysts constituent is discussed separately in Section 1.3.6.

1.3.5 Organic Light harvesters

In parallel to inorganic semiconductor materials, crystalline, semi-crystalline and amorphous organic polymers have also been investigated in the field of artificial photosynthesis.[72–74] Organic polymers appear attractive in comparison to inorganic semiconductors given their higher degree of molecular tunability. In organic polymers, the levels of highest occupied and lowest unoccupied molecular orbitals (HOMO/LUMO) have in practice similar implications as E_{CB} and E_{VB} in semiconductors generating a potential to

drive redox reactions, like HER and OER.[72,75,76] Yet, the specific principles by which excitons in organic polymer light harvesters separate and migrate to the surface differ significantly from the inorganic semiconductor counterpart. In comparison to typical inorganic semiconductors used for POWS, organic semiconductors suffer from large exciton binding energies, and low carrier mobility due to, among other factors, the influence of intermediate trap ("deep traps") energy levels between HOMO/LUMO.[75,77,78] Carbon nitride-based materials are one of the first that emerged as an alternative organic light harvester due to favorable electronic properties, crystallinity, suitable band gap, stability, non-toxicity, and abundance.[72,79,80] Since the work of Wang, Antonietti, et al (2009) that showed photocatalytic HER on graphitic carbon nitrides (g-C_3N_4) for the first time, other variations of conjugated polymers have shown favorable properties for single or hybrid light-harvesters composites. Among others CN_xH_y optimizations, control of surface area, conduction band level via doping, and enhanced charge separation are crucial for their use in POWS. [72,73,79,81–83] Despite of some encouraging results and the higher level of tunability of CN_xH_y based materials when compared to inorganic semiconductors, benchmark STH efficiencies and stability of the latter are still significantly higher.[72,73,84] One explanation for this difference is the ability of inorganic semiconductor to remain stable at highly oxidative valence band levels, meaning E_{VB} deeper than 2.5 V vs NHE.[18,74,85]

In addition to CN_xH_y, 2D covalent organic frameworks (COFs) have been screened in photocatalysis studies with organic light harvesters. 2D COFs are highly crystalline and porous 2D polymers with covalently linked building blocks in-plane and interlayer π-stacking out-of-plane.[76,86,87] Given their controlled and versatile bottom-up synthesis, unlimited building block combinations and rapidly developing new linkages, the tunability of COFs optical and photocatalytic properties is particularly high. Furthermore, their backbone structure allows a precise control of their micro- mesopore diameter, and a diverse addition of cocatalyst (externally physiosorbed, chemisorbed, or covalently linked).[76,78,86,87] Compared to other polymeric semiconductors like graphene or CN_xH_y based materials, COFs' chemical and crystal tunability is significantly higher and more versatile. However, despite such versatility, COFs are for the moment not considered photosynthetic materials yet, because most of their screening in half-reaction are

performed with sacrificial agents. For example, photocatalytic HER using TEOA as sacrificial agent.[88,89] It is later explained in Section 1.3.8 that in most cases, the use of sacrificial agents provides insightful information for HER and OER half-reactions screening on a photocatalysts, but the energy contained in the products is less than the solar input ($\Delta G_r < 0$).[23,29] Although COFs have been consistently showing high HER half-reaction rates in presence of sacrificial agents, COF systems discussed along this thesis (like in Chapter 4) will be presented as potential photosynthetic systems only. On the other hand, the use of COFs as a tunable polymeric semiconductor is a proof of concept that a bottom-up approach is feasible to understand artificial photosynthesis more rationally. For example, correlating quantitatively changes in the COF structure to improvements of specific photocatalytic properties, like exciton lifetime, migration, and trapping.[75,76,78,86] Differently, changes in the structure of a conventional inorganic semiconductor likely modifies multiple photocatalytic properties at the same time. Given that POWS involves multiple entangled steps, COFs as light harvesters offer an earth-abundant based alternative that can be rationally bottom-up approached to eventually achieve higher STH efficiencies.

Homogeneous light-harvesters, namely organic dyes, have a different light excitation mechanism based on photochemical principles. Some dyes have applications in photocatalysis for energy conversion, like $[Ru(bpy)_3]^{2+}$.[70,90,91] Contrarily to the heterogenous organic polymers described so far, dyes application in POWS are limited to sensitization.[18,91,92] References to pure dyes used as light harvester in this work are likewise purely conceptual to half-reaction and cocatalyst screening.

1.3.6 Heterogeneous cocatalyst

It has been established that a suitable cocatalyst addition can drastically increase η_{cat} and η_{sep} in POWS. Cocatalyst addition with a suitable band alignment with a particular light harvester can also create a Schottky contact eventually favorable for η_{sep}. The most desired attribute of cocatalysts in POWS is their low electrochemical overpotential requirement to generate high HER or OER currents or, put simply, low electrocatalytic overpotential — other roles of cocatalysts can be found in literature.[21,54] In electrocatalysis, overpotential is the potential difference between a half-reaction's thermodynamically determined potential, and the potential at which the redox event is experimentally observed at a

certain (low) current density (i.e., 10 mA cm^{-2}).[21,52–54] This difference depends among other factors on the electrocatalyst activity and the excess potential needed for electron-transfer processes, as typically described in Butler-Volmer equations and accessed experimentally by a Tafel Analysis (through the observed exchange current, j_0, and Tafel slope).[21,22,36,40] At a more fundamental level, this difference comes from energetic barriers occurring at different steps of a particular reaction mechanisms on the electrocatalyst surface, for example of the Volmer step for HER. A Volmer mechanism assumes the M-H bond formation (Volmer step) as the rate limiting step (RLS) for HER, which is likely the case for Tafel slopes larger than 118 mV s^{-1}.[22,54,93] When an electrocatalytic process is drastically dominated by one reaction RLS, that RLS activation energy (ΔG_{act}) defines the kinetic relation (in the absence of mass transfer limitations and ohmic drops) between measured currents and the applied overpotential relative to the half-reaction potential (η_a). Material electrocatalytic performance is then described by the relation between this ΔG_{act} or similar process with an energetic barrier (like the one calculated from the M-H bond length in a Volmer HER mechanism) and the observed η_a at a certain current density (or alternatively ΔG_{act} versus j_0).[22,54] Results from the body of knowledge of electrochemistry resemble typical volcano plots used in conventional heterogenous catalysis for an optimum of ΔG_{act}, as shown in Figure 1-6a and Figure 1-6b.

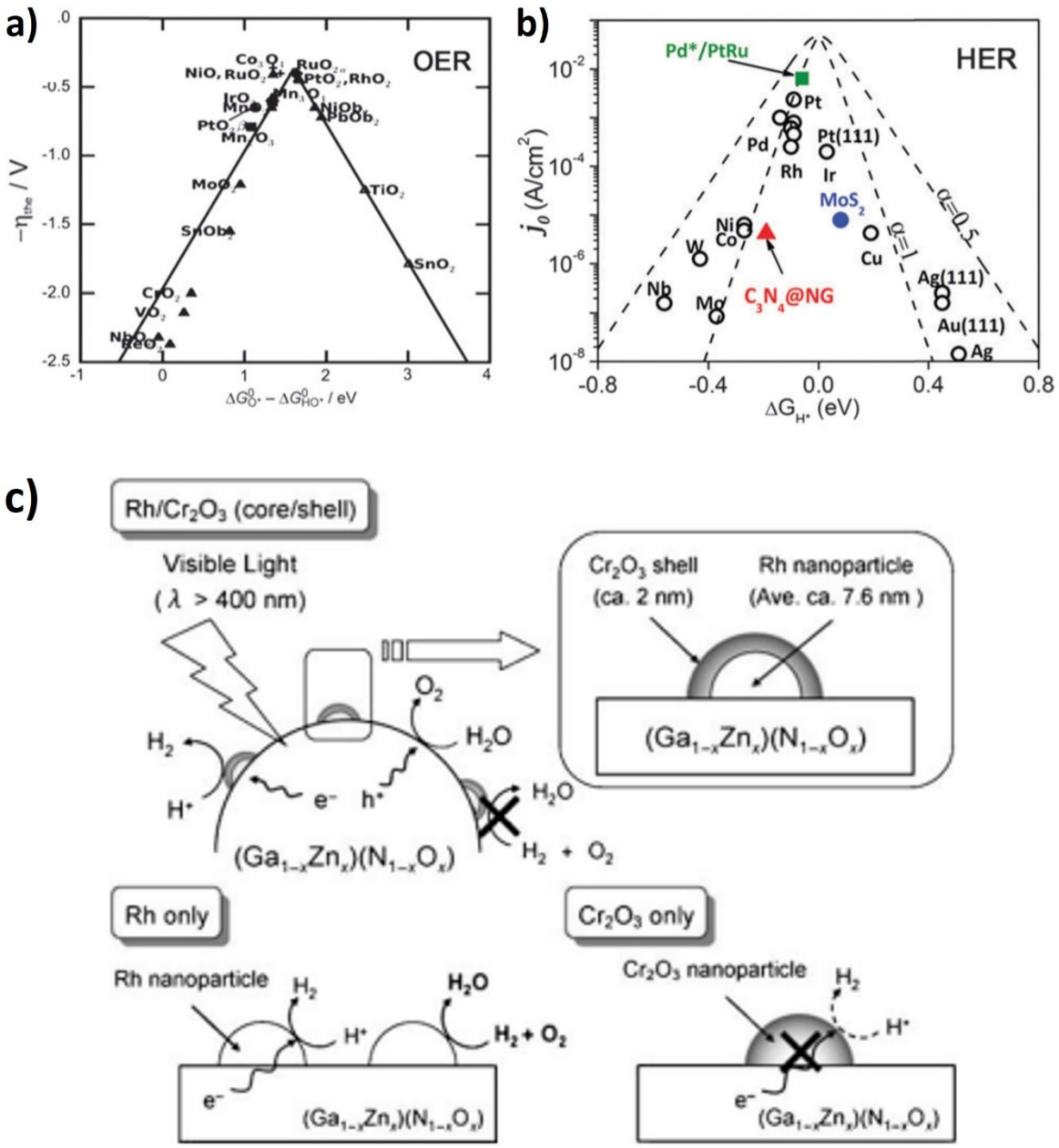

Figure 1-6. (a) Electrocatalytic trends towards OER of different oxides (as the theoretical overpotential at a current density of 10 mA cm^{-2}, η_{the}) plotted against the limiting step activation energy ($\Delta G^{\circ}_{O^*}$ - $\Delta G^{\circ}_{HO^*}$). Reproduced from Jaramillo, Nørskov, Rossmeisl et al (2011).[22,94] **(b)** Electrocatalytic trends towards HER of different metals, alloy compounds, and non-metallic materials (as exchange current density, j_0), plotted against their computationally predicted limiting step activation energy (reduction of adsorbed H^+, ΔG_{H^*}). Reproduced from Zhang Qiao, Zheng et al. (2013).[22,95] (c) A schematic reaction mechanism of OWS on Rh/Cr_2O_3-loaded $(Ga_{1-x}Zn_x)(N_{1-x}O_x)$ and the corresponding processes on supported Rh NPs and Cr_2O_3 NPs. Reproduced from Maeda, Domen et al. (2006).[96]

Accordingly, cocatalyst development in photocatalysis has been linked to η_{cat} and thus to materials with low electrochemical overpotential for HER and OER reactions. The most efficient HER cocatalysts in photocatalysis are noble metals, like Pt, Pd, and Rh, while for

OER the most efficient cocatalysts are noble metal oxides, like RuO_x, IrO_x, and PtO_x.[25,52–54,62,68,97] Other less active cocatalyst, but also used in photocatalysis due to their low prices and abundances are NiO_x (HER) and CoO_x (OER).[18,98] Most common methods found in literature to create active junctions of such materials and heterogeneous light harvesters (inorganic or organic) are impregnation-calcination, photo-deposition, and hydrothermal methods. These methods can readily load cocatalyst nanoparticles directly on the surface of a semiconductor light harvester from precursor salts like $RuCl_3$, $IrCl_3$, and H_2PtCl_6.[21,54] Another aspect of cocatalyst development, besides η_{cat}, is the prevention of backward reactions. In a real POWS system, HER cocatalysts speed up the spontaneous formation of water at room temperature from H_2 and O_2 recombination. In this regard, a significant achievement in cocatalyst development for POWS is the creation of a cocatalyst that limits backward reactions. In POWS, HER cocatalyst deposition is in most cases imperative, but materials like Pt are also active catalysts for H_2O formation. This has been demonstrated to be one of the major obstacles to achieve POWS with inorganic semiconductors, both in one-step and two-step excitation schemes.[18,33,34,62,96,99] Water formation at the HER catalyst was first prevented with in-situ formation of a covering layer of adsorbates preventing O_2 permeation. This was discovered by Abe, Sayama and Arakawa (2003). In their work, a KIO_3/I^- redox shuttle was used as mediator in photocatalysis experiments on a TiO_2(Rutile)/TiO_2(Anatase) z-scheme.[59,69] The formation of a I^- layer around the photocatalyst was theorized to prevent O_2 diffusion to Pt active sites.[59,69] The role of these adsorbate protective layers has been also hinted by POWS obtained in one-step excitation on TiO_2 in the presence of Cl^- and HCO_3^- salts.[100,101] This idea was later further rationalized and controlled by Maeda, Domen et al (2006), which is described in Figure 1-6c.[96,99] In of their work, a CrO_x layer was created around a NiO_x HER catalyst to allow selective permeation of H^+ to the Pt active site. This method was named as core-shell cocatalyst. In time, the core-shell approach has expanded to other variations using more elaborated types of HEC cores (Rh, Pt) and passivating shells (CrO_x, TiO_2).[33,62,65,66,99,102]

1.3.7 Molecular cocatalysts

Another type of cocatalyst-light harvester interaction can be obtained by using molecular catalysts. Molecular catalysts have the advantage of exploiting specific organic

coordination to achieve highly specific and well-defined reaction mechanisms preventing product recombination. Given the organic complexes exposing individual atoms, metal center exposure far higher compared to inorganic cocatalysts, and high turnover frequency numbers are normally expected.[52,54,103] Molecular catalysts can perform highly active charge transfer from light harvesters in different combinations of phases with their light harvester: homogeneous or heterogeneous systems.[103–106] Their nature involves unique reaction mechanisms with multiple steps and lower activation energies, which can activate metals centers that are far from the volcano optimum of Figure 1-6.[103–106] Due to aforesaid advantages, numerous applications can be found in the field of CO_2 reduction and HER half-reactions in the presence of sacrificial electron donors (i.e., using cobaloxime, DuBois or thiolate complexes).[52,54,103] Molecular catalysts on the other hand, due to electron-transfer issues and stability, must seemingly be anchored to a heterogeneous light-harvester for POWS systems.[103,106] This anchoring presents several challenges, and its only application seems to be limited to very inefficient single-step systems, and as a HER cocatalyst in z-schemes.[103,106] Despite the low STH efficiencies of systems reported using molecular catalysts, their advantages in selectivity, well understood reaction mechanisms, and tunable charge-transfer makes them still attractive and worthwhile studying in artificial photosynthesis applications.

1.3.8 Half-reactions versus artificial photosynthesis

POWS is thermodynamically and kinetically a burdensome multiphysics problem. At early stages of material screening of photocatalytic activity for energy applications, POWS is extremely challenging and unlikely to happen readily in most existing semiconductors. Therefore, at early stages of material development, it is justified to study only half-reactions separately with the aid of suitable sacrificial agents.[24,107] In case of HER, the sacrificial agent is an electron donor (SED), while in OER the sacrificial agent is an electron acceptor (SEA). When HER or OER are tried photocatalytically with sacrificial agents, they are widely known as half-reactions studies of water splitting. The agents used for accepting or donating electrons are chemicals that ideally do not impose kinetic or thermodynamic limitations when reduced or oxidized. This with the purpose of studying the HER or OER reaction of interest as the limiting step, for mechanistic studies, or feasibility and material

first optimization screening. Different to redox shuttle reduction/oxidation, sacrificial agent reduction/oxidation is an irreversible process, whose overall free energy change is downhill (ΔG_r is < 0).[23,29] Therefore, in such cases the produced H_2 or O_2 gas do not store sunlight as chemical energy, since they happen spontaneously because of a sunlight-accelerated exergonic reaction. This is the reason why most sacrificial systems are not interesting in the context of artificial photosynthesis, and optimization of half-reactions does not necessarily translate later to more efficient POWS. Half-reaction screening also likely generates artificial inflation of HER and OER rates due to O_2 and H_2 resulting from decomposition of sacrificial agents after oxidation/reduction.[107,108] In other cases, like HER in the presence of methanol as SED, HER photocatalytic rate inflation occurs due to proton reduction triggered by radical decay of the first oxidized SED species, known as current doubling.[108–110] Half-reaction screening is however an insightful approach to obtain information about reaction mechanisms, and to optimize certain aspects of novel materials at early stages, like band structure. However, full optimization of half-reactions should not be the goal. When possible, good practices in the field dictate that after successful half-reactions screening, posterior optimization should move quickly to POWS.[24–26,111,112] In case the intended application is ultimately a z-scheme, half-reaction screening should be preferentially performed with redox shuttles as electron donor/acceptors. The use of redox shuttles for half-reaction studies provides conditions much more like POWS, including challenges of backward reactions.

1.4 State of the art systems for POWS-related applications

1.4.1 Half-reaction: Hydrogen Evolution Reaction (HER)

Currently, publications dealing with the HER half-reaction with inorganic semiconductors materials are less abundant in the context of energy conversion. This is, because since their first application in photocatalytic water splitting, the body of knowledge of the field has progressed enough to achieve overall water splitting in the absence of sacrificial agents or electrochemical bias.[18,63] For example, few years after the discovery of the Honda and Fujishima effect, TiO_2 was proven to produce abundant H_2 purely photocatalytically using CH_3OH and other carbohydrates as SED (with Pt and RuO_2 as cocatalyst).[113] Few decades later, the work of Abe et al (2005, 2003) achieved POWS using phase controlled TiO_2 and

Pt HER cocatalyst in a z-scheme.[59,69] Since then, most applications of TiO_2 in energy conversion have focused directly on POWS. HER half-reaction publications with TiO_2 are nowadays mostly focused on mechanistic aspects, exploration of different crystal structures (including defects such as oxygen vacancies), band-alignment, and optics studies, among others.[114–118] This also applies for other more novel inorganic semiconductor, for example niobium based layered perovskites. Niobium based layered perovskites are a family of 2D materials widely known to work not only for photocatalytic HER in the presence of SED, but also in one-step and two-step light absorption systems for POWS.[119] Still, HER half-reaction study using layered perovskite niobates ($KCa_2Na_{n-3}Nb_nO_{3n+1}$, n = 3 or 4) was recently published by Suzuki, Abe, et al (2018).[120] In this study the effect of N-doping win the presence of K^+ ions was explored to increase light absorption in the visible range. N-doping is generally a straightforward technique to control the optical bandgap in semiconductors, but in niobates is challenging with ordinary solid-state synthesis methods due to undesired reduction of Nb^{+5} of Nb^{+4}. In this work, the latter was prevented with the use of a KCl flux and a NH_3 stream during synthesis, and the material was later decorated with platinum. The published photocatalytic HER rates on this material in the presence of methanol as electron donor are modest, which does not suggest that a potential application to POWS would be obviously outstanding with this material.[120] However, this study demonstrated first that rational tuning of the niobates' optical bandgap using a more elaborated synthesis technique was possible, which could be subsequently linked to better photocatalytic HER and OER rates. In this way, the artificial photosynthesis research community recognizes that HER half-reaction studies on inorganic semiconductors are crucial for the progress of the field, if a novel property of a particular material is promising for a posterior POWS application. For example, noble metal free materials, like Zn(O,S)/graphene-oxide or B/P-based, can photocatalytically produce HER under visible light.[121,122] Eventual POWS applications of earth-abundant element-based systems like these would significantly decrease the cost of the produced hydrogen.[81,95,121,122]

As previously described in Section 1.3.5, along with the search of cheaper inorganic semiconductors, carbon nitrides and covalent organic frameworks (COFs) are widely used as alternative HER organic semiconductors.[72,76,79,81] Following the pivotal work of Wang,

Antonietti, et al (2009) in HER photocatalysis using melon, multiple other carbon nitrides have been tested for HER.[79,81–83] To date, most CN_xH_y type materials that are phocatalytically active for hydrogen evolution are amorphous or semi-crystalline and contain hydrogen in their structure due to the synthesis conditions, like melon. This limited crystallinity has only shown moderate activity of melon-based materials compared to inorganic semiconductors. Most successful strategies to increase photocatalytic activity of carbon nitride systems is to use alternative synthesis methods to obtain more crystalline structures, like poly-heptazine imide (PHI) 2D-frameworks.[73,82,83] The highest reported HER photocatalytic activity in the visible range using CN_xH_y -based materials belongs to one of these semi-crystalline structures. In the work of Lin, Wang et al (2016), a crystalline Tri-s-triazine-Based framework showed an AQY of roughly 50% at 420 nm, using a combination of TEOA and K_2HPO_4 as sacrificial agent and additive for charge migration, respectively.[123] Owing to their high photocatalytic rates and ongoing improvements in synthesis methods, most recent publications of CN_xH_y -based materials for HER half-reactions are focused on more crystalline structures, like cation-doped-PHI and triazine frameworks.[75,82,83]

Covalent organic frameworks (COFs) on the other hand are still consistently published in photocatalytic HER studies as heterogeneous organic light-harvester.[76,86,87] Even though it has been established that COF applications in photocatalytic HER studies still demand the use of strong SED, COFs have several advantages over CN_xH_y -based materials, as described in Section 1.3.5 .[75,76,86,87,124] Such potential has justified the interest in COFs as a conceivable future photosynthetic and organic system, based solely on moderate HER half-reaction activity evidence. Photocatalytic HER with COFs under visible light was first published by Stegbauer, Lotsch, et al (2014). In this work a hydrazone-based COF (TFPT-COF) showed an AQY of ~2% at 400 nm, using Pt as HER cocatalyst and 10 %v/v TEOA as SED. This pivotal work showed that the TFPT-COF suffered deactivation, but it was also demonstrated to be reversible with mild post catalysis treatment.[125] Although photocatalytically HER rates cannot be compared directly, qualitatively, the HER rates obtained with this system (i.e., in units of μmol h^{-1} g^{-1}) were comparable to the benchmarks of graphene and C_3N_4-based materials at the time.[25,125] In another similar work, Vyas, Lotsch, et al (2015) demonstrated that the nitrogen content of an azine-based

COF (N_x-COF, with *x* being the number of N atoms in the linker unit) had an almost unique effect on COF crystallinity and charge migration. This crystallinity tuning of the N_x-COF linked to nitrogen content (from N_0 to N_3) was accompanied by a roughly two-order of magnitude increase in photocatalytic HER rate.[80] This demonstrated the COF chemical tunability potential. Later, these azine-based COFs were also combined with a cobaloxime molecular cocatalyst for photocatalytic HER, in the work of Banerjee, Lotsch, et al (2017).[105] Optical and photophysical characterization of the N_2-COF employed, suggested that electronic interaction with the cobaloxime was favorable in an outer-sphere model for electron transfer (N_2-COF@cobaloxime). Despite the moderate HER rates achieved, this work proved that COFs and cocatalysts can be tuned simultaneously and rationally to a molecular level to obtain a noble-metal free molecular cocatalysts. In the work of Wang, Copper, et al (2018) it was demonstrated that on top of crystallinity, other COF properties could also be rationally tuned to improve photocatalytic HER rates even further.[74,87] In this work a COF based on dibenzo[*b*,*d*]thiophene sulfone (DBTS) exhibited photocatalytic HER rates an order of magnitude higher than the benchmark of N_3-COF in similar photocatalytic media. Likewise, the DBTS COF crystallinity was required to achieve an optimal HER rate, but also, its backbone was proven to enhance other beneficial properties for photocatalysis, like hydrophilicity, pore size, and wettability. Another recent application of COFs in photocatalytic HER is the functionalization of a Thiazolo[5,4-d]thiazole-Bridged COF (TpDTz-COF) with a physiosorbed, nickel-based molecular cocatalyst (Ni-Me). Compared to the noble-metal-free benchmark at the time, the N_2-COF@cobaloxime system, the TpDTz-COF@Ni-Me system achieved even higher and more stable HER rates (with TEOA as SED).[89] Another example of COF-cocatalyst tunability is the linkage of cocatalyst to the COF backbone. Following such trends on molecular catalyst-COF interactions, Gottschling, Lotsch et al (2020) published a COF-42 modification with click chemistry, which covalently linked aforesaid cobaloxime cocatalyst to the COF backbone.[88] This approach showed that engineering of COF-cocatalyst interaction was possible and key to improve turnover number and frequency of the attached cobaloxime (TON and TOF, respectively), compared to the physiosorbed equivalent. This showed again further evidence of rational COF tunability for photocatalysis, which justifies their screening for HER half-reactions with sacrificial agents in the context of artificial photosynthesis.

1.4.2 Half-reaction: Oxygen Evolution Reaction (OER)

Like the HER half-reaction, the OER half-reaction screening with inorganic semiconductors materials is progressively less abundant for the purpose of showing artificial photosynthesis potential. Similar to the example of HER half-reaction screening on TiO_2 presented in the previous section, TiO_2 was also long ago described to produce oxygen in the presence of an SEA (like $AgNO_3$).[117] Although the techniques used at the time to quantify photocatalytically produced oxygen had not been yet refined, qualitative OER results with such materials were later indirectly confirmed by the POWS work of Abe et al (2003, 2005).[59,69,117,126] Following this z-scheme composed of two different phases of TiO_2 and a Pt cocatalyst (described in Section 1.3.5 and Section 1.3.6), other inorganic semiconductors have been quickly screened showing not only a significant increase in OER half-reaction rates, but also POWS efficiencies far higher than the pioneering work of Abe et al in (2003, 2005).[16,18] These more modern OEP materials include visible light responsive semiconductors like WO_3, $BiVO_4$ and TaON. As it will be described in Section 1.4.3, most photocatalysis applications of these materials in the context of artificial photosynthesis have focused directly on POWS.[62,67,68] On the other hand, like the HER half-reaction, recent OER half-reaction publications with TiO_2 and newer materials are focused on preliminary bandgap engineering, characterization of reaction mechanism, and other specific applications. For example, the work of Suzuki, Abe, et al (2017) with layered perovskite niobates also screened improved photocatalytic OER with $AgNO_3$ as SEA resulting from their bandgap engineering work.[120] Also using $AgNO_3$ as SEA, Jadhav, Domen et al (2020) have recently published a layered perovskite ($BaTaO_2N$) with an astounding photocatalytic OER efficiency (AQY~11%) in the visible range (420 nm).[127] Other works have also screened photocatalytic OER half-reaction in more realistic POWS conditions using IO_3^- as electron acceptor. Iwase, Abe et al (2017) published a study screening different cocatalysts on TaON.[60] TaON is a material previously used for POWS that when decorated with RuO_2 cocatalyst acts as an efficient OEP.[60,67,68] RuO_2 as a cocatalyst is widely known to play a beneficial role in both water oxidation and IO_3^- reduction in OEP systems. In this way, the work of Iwase, Abe et al (2017) further expanded the characterization of cocatalysts in a TaON based OEP system, which was restricted only to photocatalytic OER in the presence

of IO_3^-.[60] Another type of photocatalytic OER screening is benchmarking and standardization, with the goal of facilitating comparison of material efficiencies among different laboratories. In 2020 Vignolo, Lotsch et al published a OER benchmark for photocatalysis, using a commercial form of TiO_2 (P25), for standardization of photocatalytic rates.[25] This study is presented in detail in Chapter 5.

As OER is a kinetically and thermodynamically much more challenging process than HER, it is well established in the research community that discovery or optimization of OER materials have a higher merit than HER investigations, particularly on inorganic materials. Due to these challenges of the OER half-reaction, OER is regularly considered the POWS bottleneck when compared to rapid timescales of photogenerated charge recombination.[128] A secondary POWS challenge is the prevention of water formation at HER centers. Depending on the SEA used for OER screening, and if general strategies to design the HEP system prevent water formation successfully, OER optimization has a more immediate impact in posterior POWS application than HER does. It is then not surprising that in some studies, tuning of specific photocatalytic properties are performed with the goal of optimizing OER rates, which later shows a direct impact on POWS. In these studies, the OER optimized system using IO_3^- (or other irreversible SEA like $AgNO_3$) is later coupled to a particular HEP system, showing typically that the OER optimal system correlates with the most efficient POWS.[68,129–131]

Alternatively, organic semiconductors have not overcome this OER bottleneck yet, given their limited compromise between stability and oxidative HOMO level. A handful of CN_xH_y based materials and even less COF systems have achieved photocatalytic OER at efficiencies comparable to inorganic systems.[18,75,81,132] A significant research resource is being dedicated to inorganic systems, but their scarce literature in water oxidation mechanism and stability issues make them impractical for POWS application.[26,74,85] Therefore, it is expected that exploration of more efficient materials for photocatalytic OER screening keeps taking place on inorganic and especially on organic semiconductors in the long term.

1.4.3 Photocatalytic Overall Water Splitting (POWS)

As described in previous sections, most efficient one-step light absorption systems have been achieved with optimization of multiple properties of *d0* and *d10* type of semiconductors.[18] Active systems in the UV region are typically $SrTiO_3$ and Ta-based systems. Benchmarks of these systems show STH efficiencies in the range of 0.1 - 0.5%.[18,34,65,66] For example, Kato, Kudo et al (2003) demonstrated an AQY as high as 57% for 270 nm with Lanthanum doped $NaTaO_3$ ($NaTaO_3$:La) as light absorber and NiO as cocatalyst.[133] Approaches introducing additional levels above O_{2p} orbitals have also achieved great progress in STH efficiencies, for example, with N_{2p} levels like LaTaON. The band gap narrowing approaches have achieved STH in a similar range of 0.1 - 1%.[18] On the other hand, some of the most active systems are either are not well understood, like p-n type heterojunctions (GaN:Mg/InGaN:Mg) and organic semiconductors (g-C_3N_4-CDots), or they lack stability, like *d7* materials (CoO).[18,134,135] In general, one-step systems are limited by the tradeoff between charge recombination and visible light response.[32] Regardless of these limitations, Goto, Domen et al (2018) have shown a scalable hydrogen production prototype using Al-doped $SrTiO_3$ light harvester ($SrTiO_3$:Al) decorated with a core-shell HER cocatalyst (Rh/Cr_2O_3).[34] This one-step light absorption tandem supported on a panel-like reactor achieved a STH of 0.4%, which is like the material performance at laboratory scale (STH=0.65%). The panel has been put to operation later at a 100 m^2 scale, with a robust performance at ambient pressures with minimal losses of energy due to product separation.[33,34] Wang, Domen et al (2018) and Abe et al (2011, 2011, 2017) have also presented other band gap engineered Ta-based materials, which at laboratory scales show high STH efficiencies, like nitrides (i.e., Ta_3N_5) and oxynitrides (i.e., TaON).[60,67,68,98] Another approach to achieve POWS in one-single step was first presented by Ohno, Matsumura et al (1996), using a mixed phase TiO_2 decorated with platinum.[136] In previous sections, it is described that passivating layers (i.e., core-shell cocatalysts) can prevent backward water formation in POWS. Following this approach, I^- is intendedly added as an additive to shield the HER cocatalyst center from evolved O_2, in this case Pt. If besides Pt shielding, I^- oxidation is kinetically limited compared to water oxidation at the semiconductor surface, even if inefficient, POWS may overcome backward reactions. This effect was further refined by controlling I^- oxidation on the same material by Abe, Ohtani et al (2003), but remained unexploited for almost a decade due to the limited light

absorption range of TiO_2.[70] With the advent of 2D visible light active semiconductors, like layered niobates, this approach was revisited by Oshima, Maeda, et al (2019).[137] In this study, $KCa_2Nb_3O_{10}$ was used as the light harvester. If compared to TiO_2, layered niobates not only owe their higher photocatalytically activity to suitable electronic structure and visible light response. 2D light harvester like layered niobates also prevent charge recombination due to short charge migration lengths, and further control of water formation at HER cocatalyst (Pt) due to enhanced shielding of Pt centers at the interlayer space. In addition to Pt shielding, Oshima, Maeda, et al (2019) explored the specific effect of in-situ Na cation exchange by replacing the KI additive by NaI, which improved POWS rates significantly. The Na/K exchange in the structure was proven and enhanced the hydration of the interlayer space, which was believed to increase the availability of protons at the Pt center. The published AQY of POWS in this study is significantly lower than other benchmarks of one-step POWS systems. Still, this study demonstrated that layered niobates like $KCa_2Nb_3O_{10}$ show an alternative approach to achieve POWS in a single step given the peculiar properties of their interlayer space.

Alternatively, two-step excitation systems have achieved STH efficiencies higher than 1% with a much wider variety of visible-light active semiconductors. Similar to scalable one-step POWS with Al:$SrTiO_3$, Wang, Domen et al (2016) have proposed a POWS solar panel printed with a two-step light absorption POWS system in a z-scheme.[62] The system is composed of $BiVO_4$:Mo as OEP (RuO_x cocatalyst), and TaON:La,Rh as HEP ($Ru/Cr_2O_3/TiO_2$ cocatalyst). This z-scheme was relayed with a Au solid layer shuttle. As a result, a STH efficiency of 1.1% was obtained with similar advantages for industrial scalability as with their work with $SrTiO_3$:Al.[34,62] In a lab scale, similar approaches of two-step excitation systems have been attempted by other authors, but to date and to our knowledge, the benchmark of 1% has not been exceeded. For example, other works have explored different combinations of WO_3 (IrO_2/PtO_x cocatalyst), H_2WO_4 and H_4WO_5 as OEP, and $SrTiO_3$:Rh (Ru cocatalyst) and $H_xNb_yO_z$ (Pt cocatalyst) as HEP.[68,131,138–140] Particularly, the interlayer properties of layered niobates exploited for one-step POWS using I^- as additive, are also advantageous to prevent backward reactions in z-schemes POWS. This in addition to visible light response and the short migration lengths required. For example, one of the HEP systems published by Abe et al was composed of layered $H_4Nb_6O_{17}$ as light

harvester with interstitially decorated Pt cocatalyst.[91] In this work, the STH efficiency achieved was modest (<0.01%) and required dye-sensitization. In the same direction, the works of Fujito, Abe et al (2018) and Oshima, Maeda et al (2018), have tried variations of layered niobates (i.e., $KCa_2Nb_3O_{10}$) to improve exciton lifetime.[137,139,140] Although STH efficiencies of these visible-light-responsive z-schemes based on layered niobates have remained low, it has established another valid approach to suppress backward reactions at the HER cocatalyst in a z-scheme, different to the well-established core-shell cocatalyst approaches, and research on these materials is still going on.

1.5 References

1. Ahmad, T. & Zhang, D. A critical review of comparative global historical energy consumption and future demand: The story told so far. *Energy Reports* **6**, 1973–1991 (2020).
2. Tester, J. W., Drake, E. M., Driscoll, M. J., Golay, M. W. & Peters, W. A. *Choosing Among Options*. (The MIT Press, 2012).
3. Walsh, B. *et al.* Pathways for balancing CO2 emissions and sinks. *Nat Commun* **8**, 14856 (2017).
4. Ozin, G. & Ghoussoub, M. *The Story of CO2: Big Ideas for a Small Molecule*. (University of Toronto Press, Higher Education Division, 2020).
5. Pachauri, R. K. & Meyer, L. A. *IPCC, 2014: Climate Change 2014: Synthesis Report. Contribution of Working Groups I, II and III to the Fifth Assessment Report of the Intergovernmental Panel on Climate Change*. (2014).
6. Steen, M. *Greenhouse Gas Emissions from Fossil Fuel Fired Power Generation Systems*. https://publications.jrc.ec.europa.eu/repository/handle/JRC21207 (2017).
7. Bosetti, V. *et al.* COP21 climate negotiators' responses to climate model forecasts. *Nat Clim Chang* **7**, 185–189 (2017).
8. Perez, R. & Perez, M. Energy Reserves from page 4. *Int. Energy Agency SHC Program. Sol. Updat* **62**, (2015).
9. Guerra, O. J. Beyond short-duration energy storage. *Nat Energy* **6**, 460–461 (2021).
10. Davis, S. J. *et al.* Net-zero emissions energy systems. *Science (1979)* **360**, (2018).
11. van Renssen, S. The hydrogen solution? *Nat Clim Chang* **10**, 799–801 (2020).
12. Hisatomi, T. & Domen, K. Introductory lecture: Sunlight-driven water splitting and carbon dioxide reduction by heterogeneous semiconductor systems as key processes in artificial photosynthesis. *Faraday Discuss* **198**, 11–35 (2017).
13. Flis, G. & Deutsch, M. *Agora Energiewende, Agora Industry (2021): 12 Insights on Hydrogen*. www.agora-industry.de (2021).
14. McKinsey & Company & Hydrogen Council. *Hydrogen Insights A perspective on hydrogen investment, market development and cost competitiveness*. www.hydrogencouncil.com. (2021).

15. Shiva Kumar, S. & Himabindu, V. Hydrogen production by PEM water electrolysis – A review. *Mater Sci Energy Technol* **2**, 442–454 (2019).
16. Wang, Q. & Domen, K. Particulate Photocatalysts for Light-Driven Water Splitting: Mechanisms, Challenges, and Design Strategies. *Chem Rev* **120**, 919–985 (2020).
17. Kuang, Y., Yamada, T. & Domen, K. Surface and Interface Engineering for Photoelectrochemical Water Oxidation. *Joule* **1**, 290–305 (2017).
18. Chen, S., Takata, T. & Domen, K. Particulate photocatalysts for overall water splitting. *Nature Publishing Group* **2**, 1–17 (2017).
19. Mavrič, A. & Cui, C. Advances and Challenges in Industrial-Scale Water Oxidation on Layered Double Hydroxides. *ACS Appl Energy Mater* **4**, 12032–12055 (2021).
20. Oh, N. K. *et al.* Highly efficient and robust noble-metal free bifunctional water electrolysis catalyst achieved via complementary charge transfer. *Nat Commun* **12**, 4606 (2021).
21. Roger, I., Shipman, M. A. & Symes, M. D. Earth-abundant catalysts for electrochemical and photoelectrochemical water splitting. *Nat Rev Chem* **1**, 3 (2017).
22. Jiao, Y., Zheng, Y., Jaroniec, M. & Qiao, S. Z. Design of electrocatalysts for oxygen- and hydrogen-involving energy conversion reactions. *Chem Soc Rev* **44**, 2060–2086 (2015).
23. Osterloh, F. E. Photocatalysis versus Photosynthesis : A Sensitivity Analysis of Devices for Solar Energy. *ACS Energy Lett.* **2**, 445−453 (2017).
24. Wang, Z. *et al.* Efficiency Accreditation and Testing Protocols for Particulate Photocatalysts toward Solar Fuel Production. *Joule* **5**, 344–359 (2021).
25. Vignolo-González, H. A. *et al.* Toward Standardized Photocatalytic Oxygen Evolution Rates Using RuO2@TiO2 as a Benchmark. *Matter* **3**, 464–486 (2020).
26. Antonietti, M. & Savateev, A. Splitting Water by Electrochemistry and Artificial Photosynthesis: Excellent Science but a Nightmare of Translation? *Chemical Record* **18**, 969–972 (2018).
27. Wang, Z., Li, C. & Domen, K. Recent developments in heterogeneous photocatalysts for solar-driven overall water splitting. *Chem Soc Rev* **48**, 2109–2125 (2019).

28. Butburee, T., Chakthranont, P., Phawa, C. & Faungnawakij, K. Beyond Artificial Photosynthesis: Prospects on Photobiorefinery. *ChemCatChem* **12**, 1873–1890 (2020).
29. Tachibana, Y., Vayssieres, L. & Durrant, J. R. Artificial photosynthesis for solar water-splitting. *Nat Photonics* **6**, 511–518 (2012).
30. Iwase, A., Ii, K. & Kudo, A. Decomposition of an aqueous ammonia solution as a photon energy conversion reaction using a Ru-loaded ZnS photocatalyst. *Chemical Communications* **54**, 6117–6119 (2018).
31. White, J. L. *et al.* Light-Driven Heterogeneous Reduction of Carbon Dioxide : Photocatalysts and Photoelectrodes. (2015) doi:10.1021/acs.chemrev.5b00370.
32. Wang, Z., Li, C. & Domen, K. Recent developments in heterogeneous photocatalysts for solar-driven overall water splitting. *Chem Soc Rev* **48**, 2109–2125 (2019).
33. Nishiyama, H. *et al.* Photocatalytic solar hydrogen production from water on a 100-m2 scale. *Nature* **598**, 304–307 (2021).
34. Goto, Y. *et al.* A Particulate Photocatalyst Water-Splitting Panel for Large-Scale Solar Hydrogen Generation. *Joule* **2**, 509–520 (2018).
35. Tan, H. L., Abdi, F. F. & Ng, Y. H. Heterogeneous photocatalysts: an overview of classic and modern approaches for optical, electronic, and charge dynamics evaluation. *Chem Soc Rev* **48**, 1255–1271 (2019).
36. Takanabe, K. Photocatalytic Water Splitting: Quantitative Approaches toward Photocatalyst by Design. *ACS Catal* **7**, 8006–8022 (2017).
37. Laurence M. Peter. Part 1 Fundamental Aspects of Photocatalysis. *Royal Society of Chemistry* 1–28 (2016).
38. Cass, M. J. *et al.* Microwave Reflectance Studies of Photoelectrochemical Kinetics at Semiconductor Electrodes. 2. Hydrogen Evolution at p-Si in Ammonium Fluoride Solution. *J Phys Chem B* **107**, 5864–5870 (2003).
39. Hisatomi, T., Minegishi, T. & Domen, K. Kinetic Assessment and Numerical Modeling of Photocatalytic Water Splitting toward Efficient Solar Hydrogen Production. *Bull Chem Soc Jpn* **85**, 647–655 (2012).

40. Takanabe, K. Transferring Knowledge of Electrocatalysis to Photocatalysis: Photocatalytic Water Splitting. in *Nanotechnology in Catalysis* 891–906 (Wiley-VCH Verlag GmbH & Co. KGaA, 2017). doi:10.1002/9783527699827.ch33.
41. Chen, P. *et al.* Approaching the intrinsic exciton physics limit in two-dimensional semiconductor diodes. *Nature* **599**, 404–410 (2021).
42. Merkl, P. *et al.* Ultrafast transition between exciton phases in van der Waals heterostructures. *Nature Materials* vol. 18 691–696 Preprint at https://doi.org/10.1038/s41563-019-0337-0 (2019).
43. Voznyy, O., Sutherland, B. R., Ip, A. H., Zhitomirsky, D. & Sargent, E. H. Engineering charge transport by heterostructuring solution-processed semiconductors. *Nat Rev Mater* **2**, 17026 (2017).
44. Zhou, X. & Dong, H. A Theoretical Perspective on Charge Separation and Transfer in Metal Oxide Photocatalysts for Water Splitting. *ChemCatChem* **11**, 3688–3715 (2019).
45. Tang, K. W. *et al.* Transport Modeling of Locally Photogenerated Excitons in Halide Perovskites. *J Phys Chem Lett* **12**, 3951–3959 (2021).
46. Zhang, Z. & Yates, J. T. Band Bending in Semiconductors: Chemical and Physical Consequences at Surfaces and Interfaces. *Chem Rev* **112**, 5520–5551 (2012).
47. Li, L., Salvador, P. A. & Rohrer, G. S. Photocatalysts with internal electric fields. *Nanoscale* **6**, 24–42 (2014).
48. Lin, F. & Boettcher, S. W. Adaptive semiconductor/electrocatalyst junctions in water-splitting photoanodes. *Nat Mater* **13**, 81–86 (2014).
49. Pan, Z. *et al.* Mutually-dependent kinetics and energetics of photocatalyst/co-catalyst/two-redox liquid junctions. *Energy Environ Sci* **13**, 162–173 (2020).
50. Garcia-Esparza, A. T. & Takanabe, K. A simplified theoretical guideline for overall water splitting using photocatalyst particles. *J Mater Chem A Mater* **4**, 2894–2908 (2016).
51. Shinagawa, T., Garcia-Esparza, A. T. & Takanabe, K. Insight on Tafel slopes from a microkinetic analysis of aqueous electrocatalysis for energy conversion. *Sci Rep* **5**, 1–21 (2015).

52. Yang, J., Wang, D., Han, H. & Li, C. Roles of Cocatalysts in Photocatalysis and Photoelectrocatalysis. *Acc Chem Res* **46**, 1900–1909 (2013).
53. Yang, J. *et al.* Roles of cocatalysts in semiconductor-based photocatalytic hydrogen production. *Philosophical Transactions of the Royal Society A: Mathematical, Physical and Engineering Sciences* **371**, 20110430 (2013).
54. Ran, J., Zhang, J., Yu, J., Jaroniec, M. & Qiao, S. Z. Earth-abundant cocatalysts for semiconductor-based photocatalytic water splitting. *Chem. Soc. Rev.* **43**, 7787–7812 (2014).
55. Qureshi, M. *et al.* Contribution of electrolyte in nanoscale electrolysis of pure and buffered water by particulate photocatalysis. *Sustain Energy Fuels* **2**, 2044–2052 (2018).
56. Dias, P., Andrade, L. & Mendes, A. Hematite-based photoelectrode for solar water splitting with very high photovoltage. *Nano Energy* **38**, 218–231 (2017).
57. Kim, J. H. & Lee, J. S. Elaborately Modified BiVO 4 Photoanodes for Solar Water Splitting. *Advanced Materials* **31**, 1806938 (2019).
58. Yan, F. *et al.* Schottky or Ohmic Metal-Semiconductor Contact: Influence on Photocatalytic Efficiency of Ag/ZnO and Pt/ZnO Model Systems. *ChemSusChem* **7**, 101–104 (2014).
59. Abe, R., Sayama, K. & Sugihara, H. Development of new photocatalytic water splitting into H2 and O2 using two different semiconductor photocatalysts and a shuttle redox mediator IO3-/I-. *Journal of Physical Chemistry B* **109**, 16052–16061 (2005).
60. Iwase, Y., Tomita, O., Higashi, M. & Abe, R. Enhanced oxygen evolution on visible light responsive TaON photocatalysts co-loaded with highly active Ru species for IO 3 − reduction and Co species for water oxidation. *Sustain Energy Fuels* **1**, 748–754 (2017).
61. Abe, R., Sayama, K., Domen, K. & Arakawa, H. A new type of water splitting system composed of two different TiO2 photocatalysts (anatase , rutile) and a IO-3/I- shuttle redox mediator. *Chem Phys Lett* **344**, 339–344 (2001).

62. Wang, Q. *et al.* Scalable water splitting on particulate photocatalyst sheets with a solar-to-hydrogen energy conversion efficiency exceeding 1%. *Nat Mater* **15**, 611–615 (2016).
63. FUJISHIMA, A. & HONDA, K. Electrochemical Photolysis of Water at a Semiconductor Electrode. *Nature* **238**, 37–38 (1972).
64. Inoue, Y. Photocatalytic water splitting by RuO2-loaded metal oxides and nitrides with d0- and d10 -related electronic configurations. *Energy Environ Sci* **2**, 364 (2009).
65. Takata, T. *et al.* Photocatalytic water splitting with a quantum efficiency of almost unity. *Nature* **581**, 411–414 (2020).
66. Ham, Y. *et al.* Flux-mediated doping of $SrTiO_3$ photocatalysts for efficient overall water splitting. *J Mater Chem A Mater* **4**, 3027–3033 (2016).
67. Maeda, K., Abe, R. & Domen, K. Role and function of ruthenium species as promoters with TaON-based photocatalysts for oxygen evolution in two-step water splitting under visible light. *Journal of Physical Chemistry C* **115**, 3057–3064 (2011).
68. Abe, R., Higashi, M. & Domen, K. Overall water splitting under visible light through a two-step photoexcitation between TaON and WO3 in the presence of an iodate-iodide shuttle redox mediator. *ChemSusChem* **4**, 228–237 (2011).
69. Abe, R., Sayama, K. & Arakawa, H. Significant effect of iodide addition on water splitting into H2 and O2 over Pt-loaded TiO2 photocatalyst : suppression of backward reaction. *Chem Phys Lett* **371**, 360–364 (2003).
70. Abe, R., Shinmei, K., Koumura, N., Hara, K. & Ohtani, B. Visible-light-induced water splitting based on two-step photoexcitation between dye-sensitized layered niobate and tungsten oxide photocatalysts in the presence of a triiodide/iodide shuttle redox mediator. *J Am Chem Soc* **135**, 16872–16884 (2013).
71. Suzuki, H., Nitta, S., Tomita, O., Higashi, M. & Abe, R. Highly Dispersed RuO_2 Hydrates Prepared via Simple Adsorption as Efficient Cocatalysts for Visible-Light-Driven Z-Scheme Water Splitting with an IO_3^-/I^- Redox Mediator. *ACS Catal* **7**, 4336–4343 (2017).
72. Fang, Y., Fu, X. & Wang, X. Diverse Polymeric Carbon Nitride-Based Semiconductors for Photocatalysis and Variations. *ACS Mater Lett* **2**, 975–980 (2020).

73. Lin, L., Yu, Z. & Wang, X. Crystalline Carbon Nitride Semiconductors for Photocatalytic Water Splitting. *Angewandte Chemie* **131**, 6225–6236 (2019).
74. Wang, Y. *et al.* Current understanding and challenges of solar-driven hydrogen generation using polymeric photocatalysts. *Nat Energy* **4**, 746–760 (2019).
75. Banerjee, T., Podjaski, F., Kröger, J., Biswal, B. P. & Lotsch, B. v. Polymer photocatalysts for solar-to-chemical energy conversion. *Nat Rev Mater* **6**, 168–190 (2021).
76. Banerjee, T., Gottschling, K., Savasci, G., Ochsenfeld, C. & Lotsch, B. v. H2 Evolution with Covalent Organic Framework Photocatalysts. *ACS Energy Lett* **3**, 400–409 (2018).
77. Rahman, M. Z. & Mullins, C. B. Understanding Charge Transport in Carbon Nitride for Enhanced Photocatalytic Solar Fuel Production. *Acc Chem Res* **52**, 248–257 (2019).
78. Keller, N. & Bein, T. Optoelectronic processes in covalent organic frameworks. *Chem Soc Rev* **50**, 1813–1845 (2021).
79. Wang, S., Zhang, J., Li, B., Sun, H. & Wang, S. Engineered Graphitic Carbon Nitride-Based Photocatalysts for Visible-Light-Driven Water Splitting: A Review. *Energy and Fuels* **35**, 6504–6526 (2021).
80. Vyas, V. S. *et al.* A tunable azine covalent organic framework platform for visible light-induced hydrogen generation. *Nat Commun* **6**, 8508 (2015).
81. Wang, X. *et al.* A metal-free polymeric photocatalyst for hydrogen production from water under visible light. *Nat Mater* **8**, 76–80 (2009).
82. Schlomberg, H. *et al.* Structural Insights into Poly(Heptazine Imides): A Light-Storing Carbon Nitride Material for Dark Photocatalysis. *Chemistry of Materials* **31**, 7478–7486 (2019).
83. Kröger, J. *et al.* Photocatalytic Hydrogen Evolution: Interfacial Engineering for Improved Photocatalysis in a Charge Storing 2D Carbon Nitride: Melamine Functionalized Poly(heptazine imide). *Adv Energy Mater* **11**, 2170028 (2021).
84. Martin, D. J., Reardon, P. J. T., Moniz, S. J. A. & Tang, J. Visible light-driven pure water splitting by a nature-inspired organic semiconductor-based system. *J Am Chem Soc* **136**, 12568–12571 (2014).

85. Sivula, K. Are Organic Semiconductors Viable for Robust, High-Efficiency Artificial Photosynthesis? *ACS Energy Lett* **5**, 1970–1973 (2020).
86. Huang, X. & Zhang, Y.-B. Covalent Organic Frameworks for Sunlight-driven Hydrogen Evolution. *Chem Lett* **50**, 676–686 (2021).
87. Wang, X. *et al.* Sulfone-containing covalent organic frameworks for photocatalytic hydrogen evolution from water. *Nat Chem* **10**, 1180–1189 (2018).
88. Gottschling, K. *et al.* Rational Design of Covalent Cobaloxime–Covalent Organic Framework Hybrids for Enhanced Photocatalytic Hydrogen Evolution. *J Am Chem Soc* **142**, 12146–12156 (2020).
89. Biswal, B. P. *et al.* Sustained Solar H2 Evolution from a Thiazolo[5,4-d]thiazole-Bridged Covalent Organic Framework and Nickel-Thiolate Cluster in Water. *J Am Chem Soc* **141**, 11082–11092 (2019).
90. Morris, N. D., Suzuki, M. & Mallouk, T. E. Kinetics of electron transfer and oxygen evolution in the reaction of [Ru(bpy) 3] 3+ with colloidal iridium oxide. *Journal of Physical Chemistry A* **108**, 9115–9119 (2004).
91. Abe, R., Shinmei, K., Hara, K. & Ohtani, B. Robust dye-sensitized overall water splitting system with two-step photoexcitation of coumarin dyes and metal oxide semiconductors. *Chemical Communications* 3577 (2009) doi:10.1039/b905935k.
92. Youngblood, W. J. *et al.* Photoassisted Overall Water Splitting in a Visible Light-Absorbing Dye-Sensitized Photoelectrochemical Cell. *J Am Chem Soc* **131**, 926–927 (2009).
93. Sarkar, S. & Peter, S. C. An overview on Pd-based electrocatalysts for the hydrogen evolution reaction. *Inorg Chem Front* **5**, 2060–2080 (2018).
94. Man, I. C. *et al.* Universality in Oxygen Evolution Electrocatalysis on Oxide Surfaces. *ChemCatChem* **3**, 1159–1165 (2011).
95. Zheng, Y. *et al.* Hydrogen evolution by a metal-free electrocatalyst. *Nat Commun* **5**, 3783 (2014).
96. Maeda, K. *et al.* Noble-Metal/Cr2O3 Core/Shell Nanoparticles as a Cocatalyst for Photocatalytic Overall Water Splitting. *Angewandte Chemie* **118**, 7970–7973 (2006).
97. Dilla, M. *et al.* The fate of O2 in photocatalytic CO2 reduction on TiO2 under conditions of highest purity. *Phys.Chem.Chem.Phys.* **21**, 15949–15957 (2019).

98. Wang, Z. *et al.* Overall water splitting by Ta3N5 nanorod single crystals grown on the edges of KTaO3 particles. *Nat Catal* **1**, (2018).
99. Sakamoto, N. *et al.* Highly dispersed noble-metal/chromia (core/shell) nanoparticles as efficient hydrogen evolution promoters for photocatalytic overall water splitting under visible light. *Nanoscale* **1**, 106 (2009).
100. Huang, L. *et al.* Cl− making overall water splitting possible on TiO2-based photocatalysts. *Catal. Sci. Technol.* **4**, 2913–2918 (2014).
101. Sayama, K. & Arakawa, H. Effect of carbonate salt addition on the photocatalytic decomposition of liquid water over Pt – TiO catalyst. **93**, 1647–1654 (1997).
102. Maeda, K. *et al.* Photocatalytic overall water splitting promoted by two different cocatalysts for Hydrogen and Oxygen evolution under visible light. *Angewandte Chemie - International Edition* **49**, 4096–4099 (2010).
103. Morikawa, T., Sato, S., Sekizawa, K., Arai, T. & Suzuki, T. M. Molecular Catalysts Immobilized on Semiconductor Photosensitizers for Proton Reduction toward Visible-Light-Driven Overall Water Splitting. *ChemSusChem* **12**, 1807–1824 (2019).
104. Banerjee, T. *et al.* Single-Site Photocatalytic H2 Evolution from Covalent Organic Frameworks with Molecular Cobaloxime Co-Catalysts. *J Am Chem Soc* **139**, 16228–16234 (2017).
105. Banerjee, T. *et al.* Single-Site Photocatalytic H 2 Evolution from Covalent Organic Frameworks with Molecular Cobaloxime Co-Catalysts. *J Am Chem Soc* **139**, 16228–16234 (2017).
106. Ivanova, I., Kandiel, T. A., Cho, Y.-J., Choi, W. & Bahnemann, D. Mechanisms of Photocatalytic Molecular Hydrogen and Molecular Oxygen Evolution over La-Doped NaTaO 3 Particles: Effect of Different Cocatalysts and Their Specific Activity. *ACS Catal* **8**, 2313–2325 (2018).
107. Costantino, F. & Kamat, P. v. Do Sacrificial Donors Donate H2 in Photocatalysis? *ACS Energy Lett* 242–246 (2021) doi:10.1021/acsenergylett.1c02487.
108. Schneider, J. & Bahnemann, D. W. Undesired Role of Sacrificial Reagents in Photocatalysis. *J. Phys. Chem. Lett.* **4**, 3479–3483 (2013).
109. Hainer, A. S. *et al.* Photocatalytic Hydrogen Generation Using Metal-Decorated TiO 2 : Sacrificial Donors vs True Water Splitting. *ACS Energy Lett* **3**, 542–545 (2018).

110. Walenta, C. A. *et al.* Why co-catalyst-loaded rutile facilitates photocatalytic hydrogen evolution. *Physical Chemistry Chemical Physics* **21**, 1491–1496 (2019).
111. Kisch, H. & Bahnemann, D. Best Practice in Photocatalysis: Comparing Rates or Apparent Quantum Yields? *Journal of Physical Chemistry Letters* **6**, 1907–1910 (2015).
112. Qureshi, M. & Takanabe, K. Insights on measuring and reporting heterogeneous photocatalysis: Efficiency definitions and setup examples. *Chemistry of Materials* **29**, 158–167 (2017).
113. Kawai, T. & Sakata, T. Conversion of carbohydrate into hydrogen fuel by a photocatalytic process. *Nature* **286**, 474–476 (1980).
114. Scanlon, D. O. *et al.* Band alignment of rutile and anatase TiO2. *Nat Mater* **12**, 798–801 (2013).
115. Miyoshi, A., Nishioka, S. & Maeda, K. Water Splitting on Rutile TiO2 -Based Photocatalysts. *Chem. Eur.J. 2018,* **24**, 18204–18219 (2018).
116. Hashimoto, K., Irie, H. & Fujishima, A. TiO2 Photocatalysis : A Historical Overview and Future Prospects. **44**, 8269–8285 (2006).
117. Oosawa, Y. & Grätzel, M. Effect of surface hydroxyl density on photocatalytic oxygen generation in aqueous TiO2 suspensions. *Journal of the Chemical Society, Faraday Transactions 1: Physical Chemistry in Condensed Phases* **84**, 197 (1988).
118. Ajmal, A., Majeed, I., Malik, R. N., Idriss, H. & Nadeem, M. A. Principles and mechanisms of photocatalytic dye degradation on TiO2 based photocatalysts: A comparative overview. *RSC Adv* **4**, 37003–37026 (2014).
119. Nunes, B. N., Lopes, O. F., Patrocinio, A. O. T. & Bahnemann, D. W. Recent advances in niobium-based materials for photocatalytic solar fuel production. *Catalysts* **10**, (2020).
120. Suzuki, H., Tomita, O., Higashi, M., Nakada, A. & Abe, R. Improved visible-light activity of nitrogen-doped layered niobate photocatalysts by NH3-nitridation with KCl flux. *Appl Catal B* **232**, 49–54 (2018).
121. Rahman, M. Z., Kibria, M. G. & Mullins, C. B. Metal-free photocatalysts for hydrogen evolution. *Chem Soc Rev* **49**, 1887–1931 (2020).

122. Shi, L. *et al.* n-type boron phosphide as a highly stable, metal-free, visible-light-active photocatalyst for hydrogen evolution. *Nano Energy* **28**, 158–163 (2016).
123. Lin, L., Ou, H., Zhang, Y. & Wang, X. Tri- s -triazine-Based Crystalline Graphitic Carbon Nitrides for Highly Efficient Hydrogen Evolution Photocatalysis. *ACS Catal* **6**, 3921–3931 (2016).
124. Burger, B. *et al.* A mobile robotic chemist. *Nature* **583**, 237–241 (2020).
125. Stegbauer, L., Schwinghammer, K. & Lotsch, B. v. A hydrazone-based covalent organic framework for photocatalytic hydrogen production. *Chem. Sci.* **5**, 2789–2793 (2014).
126. Borgarello, E., Kiwi, J., Pelizzetti, E., Visca, M. & Grätzel, M. Photochemical cleavage of water by photocatalysis. *Nature* **289**, 158–160 (1981).
127. Jadhav, S. *et al.* Efficient photocatalytic oxygen evolution using BaTaO 2 N obtained from nitridation of perovskite-type oxide. *J Mater Chem A Mater* **8**, 1127–1130 (2020).
128. Inoue, H. *et al.* The water oxidation bottleneck in artificial photosynthesis: How can we get through it? An alternative route involving a two-electron process. *ChemSusChem* **4**, 173–179 (2011).
129. Miyoshi, A. *et al.* Nitrogen/fluorine-codoped rutile titania as a stable oxygen-evolution photocatalyst for solar-driven Z-scheme water splitting. *Sustain Energy Fuels* **2**, 2025–2035 (2018).
130. Suzuki, H., Tomita, O., Higashi, M. & Abe, R. Design of nitrogen-doped layered tantalates for non-sacrificial and selective hydrogen evolution from water under visible light. *J Mater Chem A Mater* **4**, 14444–14452 (2016).
131. Suzuki, H., Tomita, O., Higashi, M. & Abe, R. Tungstic acids H2WO4 and H4WO5 as stable photocatalysts for water oxidation under visible light. *J Mater Chem A Mater* **5**, 10280–10288 (2017).
132. Sachs, M. *et al.* Understanding structure-activity relationships in linear polymer photocatalysts for hydrogen evolution. *Nat Commun* **9**, 4968 (2018).
133. Kato, H., Asakura, K. & Kudo, A. Highly efficient water splitting into H2 and O2 over lanthanum-doped NaTaO3 photocatalysts with high crystallinity and surface nanostructure. *J Am Chem Soc* **125**, 3082–3089 (2003).

134. Zhan, X. *et al.* Efficient CoO nanowire array photocatalysts for H2 generation. *Appl Phys Lett* **105**, (2014).
135. Liao, L. *et al.* Efficient solar water-splitting using a nanocrystalline CoO photocatalyst. *Nat Nanotechnol* **9**, 69–73 (2014).
136. Ohno, T., Saito, S., Fujihara, K. & Matsumura, M. Photocatalyzed Production of Hydrogen and Iodine from Aqueous Solutions of Iodide Using Platinum-Loaded TiO 2 Powder. *Bull Chem Soc Jpn* **69**, 3059–3064 (1996).
137. Oshima, T., Wang, Y., Lu, D., Yokoi, T. & Maeda, K. Photocatalytic overall water splitting on Pt nanocluster-intercalated, restacked KCa2Nb3O10 nanosheets: The promotional effect of co-existing ions. *Nanoscale Adv* **1**, 189–194 (2019).
138. Tomita, O. *et al.* Improved photocatalytic water oxidation with Fe3+/Fe2+ redox on rectangular-shaped WO3 particles with specifically exposed crystal faces via hydrothermal synthesis. *Chem Lett* **46**, 221–224 (2017).
139. Hojo, K. *et al.* An Improved Z-Scheme for Overall Water Splitting Using Dye-Sensitized Calcium Niobate Nanosheets Synthesized by a Flux Method. *ACS Appl Energy Mater* **4**, 10145–10152 (2021).
140. Fujito, H. *et al.* Layered Perovskite Oxychloride Bi 4 NbO 8 Cl: A Stable Visible Light Responsive Photocatalyst for Water Splitting. *J Am Chem Soc* **138**, 2082–2085 (2016).

2. Theory of Photocatalyst Engineering for Energy Conversion

Within the context of energy conversion reactions, in this section, we list the principles by which a given photocatalyst can be externally optimized for different purposes, i.e., to increase its solar to chemical efficiency. In this chapter, a semi-quantitative description of external methods for photocatalyst optimization is given, assuming that the internal basic aspects of a heterogeneous light-harvester are previously settled. Coarse-grain models are used along this chapter to describe the approximate expected behavior when a photocatalyst is decorated with a cocatalyst material, or when the photocatalytic suspension properties or reactor design are considered on the photocatalyst overall performance. This section does not consider multi-physics modeling resolution, or mechanistic description of single photocatalysis steps described conceptually in the previous sections. Nonetheless, it facilitates understanding of the underlying basic principles to rationally elaborate the methods for photocatalyst decoration, photo reactor design, and reaction instrumentals discussed in Chapter 4 and Chapter 6 for WO_3 and TiO_2 based OER systems, and a COF based HER system in Chapter 5.

In what follows we present a list of coarse-grain models to account for the external performance modification of a given light-harvester, including reaction media. Such description is presented in a bottom-up approach order, that in heterogeneous catalysis this is, starting from the fundamental thermodynamics and dynamic processes involving rapid time scales and short length scales, to then describe measurable changes occurring in a macro scale. Accordingly, a standard charge carrier dynamics model for inorganic semiconductors is developed semi-quantitatively (Section 2.1 and Section 2.2), to relate η_{sep} and η_{cat} — separation and catalytic efficiencies defined for photocatalysis in Chapter 1, respectively — formally to modifications to surface reaction, for example, by means of heterogeneous cocatalyst decoration. Such model is refined from other literature sources and applied to the WO_3/RuO_2 photocatalytic OER system, later analyzed in Chapter 6. Secondly, such concepts are expanded to the thiazolo[5,4-d]thiazole-linked COF presented in Chapter 5 as the light absorber in a photocatalytic HER scheme, considering the different nature of charge carrier dynamics in organic polymers (Section 2.3). Opposite to the many examples in the literature where COFs reach their optimal HER photocatalytic performance when decorated with Pt, the thiazolo[5,4-d] thiazole-linked COF performs more optimally

when combined with an in-situ formed Nickel HER molecular catalyst. The essence of the latter result is expanded connecting the aforesaid concepts developed for η_{sep} and η_{cat}, and the original work presented in Chapter 4 (Section 2.4). From Section 2.5 to Section 2.7, crucial phenomena external to the photocatalyst material are presented and unraveled in their multiple and subtle interconnections to the very nature of charge carrier dynamics, and the way they affect η_{sep}, η_{cat} and light absorption efficiency (η_{abs}). The external phenomena in question appear along Chapters 4 to Chapter 6, and are: mass transfer, photon fate and reactor optics, and colloidal stabilization of nanosized photocatalysts. Mass transfer is an integral constituent of the resulting η_{sep} and η_{cat} of a photocatalyst. Reactor optics is a concept that is crucial to understand η_{abs} from a perspective different to the light-harvester optical band gap. Colloidal stabilization of a nanosized photocatalyst is crucial to prevent material aggregation and agglomeration in suspension, which has consequences in all the aspects just described. Finally, in Section 2.8, the figure of merits that define overall photocatalytic performance are presented, whose quantification are based on measurable quantities and capture the convolution of all the steps that shape photocatalysis.

2.1 Charge transport in inorganic semiconductors

The initiating phenomena in photocatalysis happen with the irradiation of photons above the optical band gap of the starting semiconductor material (or also organic polymer). The key parameter in a heterogeneous light-harvester is the extinction coefficient ($k(\lambda)$).[1-3] k describes among other crucial properties the optical band gap (E_g) and optical depth ($\alpha(\lambda)$) in a material, the second meaning the average extinction of photons traveling in the light harvester medium.[1,4,5] Additionally, a fraction of photons reaching the photocatalyst surface are scattered away. To disentangle the scattering effect from photon absorption, additional optical experiments and modeling are required using also other material properties, like the refractive index ($n(\lambda)$).[2,3,6] This optical modeling of scattering and absorbed photon fraction is later described in Section 2.6. For decorated materials, cocatalyst on the surface of the light harvester may also shield the light from reaching the actual light harvester, which is known as parasitic light absorption and produces optical losses.[7-11] For the moment, to calculate photogeneration of charges, we consider only the

intensity of the fraction of incident photons whose fate is not being scattered away or parasitically absorbed (I). Using such, the exciton generation rate function G (using radial depth coordinate r) in a photocatalyst nanoparticle (radius r_0) can be obtained from Lambert-Beer's law.[12,13]

$$G = \alpha \times I\left[exp(-\alpha r) + exp\big(-\alpha(r_0 - r)\big)\right] \quad \text{Equation 2-1}$$

Equation 2-1 considers that I is isotropic and steady around the nanoparticle. I is at the same time a local quantity which depends on the irradiated photons to the photocatalytic suspension, and light extinction along the suspension geometry (described in Section 2.6).[12,13] Following light absorption, it is assumed that the dominant charge transport in typical inorganic semiconductors is separated electron-holes. This assumption for inorganic semiconductors is justified given that bound excitons have short lifetimes, and due to the fast carrier mobility and high dielectric constants of inorganic semiconductors.[14-18] This results in low exciton binding energies in inorganic semiconductors (typically 10 meV), which can be readily overcome at the typical magnitudes of electric fields triggered, for example, under the influence of Fermi level equilibration at semiconductor contacts.[1,4,14,15] Then, at the space domain of a nanoparticle geometry, the equations governing movement of free charges are the Poisson equation for electric field, and the continuity equation for free electron (n) and holes (p) as follows (in cartesian coordinates),

$$\nabla \cdot \nabla(\phi) = -\frac{q}{\varepsilon_0 \varepsilon_r}(p + n + N_A + N_D) \quad \text{Equation 2-2}$$

$$\frac{dn}{dt} = -\frac{1}{q}\nabla \cdot J_n - R + G \quad \text{Equation 2-3}$$

$$\frac{dp}{dt} = -\frac{1}{q}\nabla \cdot J_p - R + G \quad \text{Equation 2-4}$$

Where q is the fundamental electron charge, J_n and J_p are the electron and hole current densities, N_A and N_D are the acceptor and donor concentration of the semiconductor, ε_0

and ε_r are the vacuum and relative permittivity constant of the material, respectively.[1,4,19] $R(n,p)$ is a scalar function that is the sum of all types of recombination processes in the light harvester bulk that are dependent on local electron and hole excess concentrations (i.e., Shockley-Read-Hall, or radiative).[1,4,19] G is the scalar function for the exciton generation rate described in Equation 2-1 in spherical coordinates (depending on the photocatalyst geometry, G may also depend on the spherical angular coordinates).[1,4,19] The electron-hole fluxes are obtained from the following diffusion-drift expressions,

$$J_n = q(\mu_n n E + D_n \nabla n) \qquad \text{Equation 2-5}$$

$$J_p = q(\mu_p p E + D_p \nabla p) \qquad \text{Equation 2-6}$$

$$E = -\nabla \phi \qquad \text{Equation 2-7}$$

Where μ_p, μ_n are the electromobility constants of electron and holes in the semiconductor, and D_h, D_n the electron and holes diffusivity.[1,4,19] With this set of equations plus the boundary conditions at the light-harvester surface, the distribution of electron and holes along the photocatalyst geometry can be estimated from fundamental physical properties only. The boundary conditions can be obtained from the Fermi level equilibration at the interface of the light harvester with the electrolyte (photocatalytic solution media, or just solution), or with a decorated cocatalyst.[4,20]

For homogeneous and symmetrical semiconductor-solution (-electrolyte) and semiconductor-metal (-cocatalyst) interfaces, the band bending region can be estimated based on a depletion layer width (W_d, or accumulation in p-type semiconductors).[4,20] W_d is calculated using some of the semiconductor electrical properties described above, plus the emission barrier height at the contact interface.[4,20] For homogeneous interfaces, the carrier density and thus band bending in the dark can be predicted based on W_d and a depletion region, without solving the set of carrier transport presented in Equation 2-2 to Equation 2-7. For example, in photocatalysis using bare semiconductor nanoparticles, band bending is obtained from the 3D Poisson-Boltzmann equation, assuming an ideal Schottky contact at the semiconductor-solution interface. The analytical solution for the band bending

magnitude (V_{BB}) versus nanoparticle radial coordinate r (spherical coordinates) is presented in Equation 2-8 for dark conditions.[4,20]

$$V_{BB}(r) = \frac{kT}{6q}\left[\frac{r-(r_0-W_d)}{L_D}\right]^2\left[\frac{1+2(r_0-W_d)}{r}\right] \quad \text{Equation 2-8}$$

Where r_0 is the nanoparticle radius, and L_d is the *Debye Length*, which like W_d, is a dimensional number dependent on the same material properties described above in carrier transport equations. Other similar expressions can be obtained for ideal 2D and 3D geometries of semiconductor-metal Schottky and ohmic contacts.[4,20,21] However, in photocatalysis the geometry of decorated cocatalyst typically produce metal-semiconductor contours with characteristic lengths smaller than the semiconductor W_d, whose band bending is then inhomogeneous.[22-24] Band bending under inhomogeneous and asymmetrical conditions can only be estimated from the resolution of charge carrier dynamics principles (Equation 2-2 to Equation 2-7) considering the semiconductor and contact geometry.[4,25] Additionally, the inhomogeneous band bending of the semiconductor around a nanosized cocatalyst metal contact, when immersed in an electrolyte leads to the pinch-off effect.[4,22,25] The pinch-off effect is the inhomogeneous band bending regime where the semiconductor-solution junction properties dominate the semiconductor-metal junction, typically reducing the effective barrier height of the ideal Schottky junction in n-type semiconductors.[22-24]

To account for inhomogeneous and asymmetrical band bending, which is the case by default in photocatalysis, the semiconductor-metal and semiconductor-solution contacts must be modelled locally. Assuming an n-type semiconductor forming a Schottky contact at the interface with a metal or solution, and no surface trap states or fermi level pinning, the emission barrier height of the contact (Φ_B, for metal or solution) becomes a local boundary condition. The surface electron and hole densities at thermal equilibrium ($n_0|_Q$, $p_0|_Q$), at each point $Q(x,y,z)$ that belongs to the surface of the contact between the semiconductor and the photocatalytic solution or metal ($S_{contact}$) is defined as,

$$n_0|_Q = N_C \exp\left(\frac{\phi_B}{k_B T}\right) \quad ,(Q \in S_{contact}) \qquad \text{Equation 2-9}$$

$$p_0|_Q = N_V \exp\left(\frac{E_g - \phi_B}{k_B T}\right) \quad ,(Q \in S_{contact}) \qquad \text{Equation 2-10}$$

Where N_C and N_V are the density of states of conduction and valence band, respectively, E_g is the semiconductor optical band gap, and k_B is the Boltzmann constant, and $S_{contact}$ is the geometrical surface of the contacts (metal or solution).[4,20] The Dirichlet boundary conditions in Equation 2-9 and Equation 2-10 are a way of representing the concentration of electrons and holes at the semiconductor surface that produces a zero current of charge carriers going across the contact emission barrier height.[4,20,25] The set of equations above defines a relative potential difference at the surface compared to the Fermi level of the semiconductor, thus an additional condition is needed to obtain a mathematical solution at absolute potential levels. At no illumination, this last boundary condition is that the chemical potential of electrons described by the Fermi level of the majority carrier (E_F) must be aligned with the redox couple potential of the surrounding solution (E_{sol}).[4,23,26] This is, assuming an n-type semiconductor, the condition at which the electron transfer rates of oxidation and reduction of the dominant redox species are equal.[23,26] In photocatalytic systems where more than one dominant redox couple exists, for example in one-step POWS systems ($E_{H/H+}$ and $E_{O2/H2O}$), the condition of net zero current in dark leads to a non-equilibrium equilibration potential E_{sol} in between both energy levels.[23] Additionally in the dark, no generation or excess of electron-holes ($G=0$) perturbs the net zero current condition.

$$E_F = E_{sol} \qquad \text{Equation 2-11}$$

With the set of equations above, self-contained numerical solutions can be obtained for any geometry and combinations of semiconductor-metal and semiconductor-solution contacts present in photocatalysis.[4,20,25] Numerical solutions of interest showing geometry dependent band bending under dark conditions can be found in the literature.[4,20,25,26]

2.2 Interface reaction and cocatalyst role in inorganic semiconductors

Under illumination, the charge generation rate is different than zero (G, in Equation 2-1) producing excess of electron and holes for which the bulk recombination term (R) is also different than zero, yet the latter not necessarily annihilates all photogenerated charges. The band bending solution in the dark at the surface contact (metal or solution) no longer holds, because the surviving photogenerated charges in the bulk will migrate according to the charge dynamic principles in Section 2.1, for which a charge extraction boundary condition is needed at the surface to describe no charge accumulation. This leads to the change of the Dirichlet to a Neumann-Robin condition at the semiconductor-solution and semiconductor-metal interfaces, accounting for electron-holes at the surface at concentrations different from the ones described by the surface equilibrium in the dark, which is no net current around the potential barrier. Therefore, under illumination, the surface potential condition of the contact is not Fermi level equilibration with E_{sol} anymore. An additional boundary condition involving the surface potential is required to complete the degrees of freedom of the transport problem (like in Equation 2-11). For simplicity, it is typically found in the literature that the semiconductor contact, with metal or solution, are treated as sinks for holes and electrons with no surface recombination ($R_s = 0$), which are assumed to operate at overpotentials commonly found in electrochemistry for HER/OER reactions.[1,4,19] This approach therefore interprets electron and holes currents at the contacts as charge extraction at the constant overpotential set (the semiconductor-solution interface can be treated as an ideal Schottky contact deriving the emission/recombination velocities from a pseudo-first order electron transfer rate).[1,4,19] This is an unrealistic condition but makes the system simple enough to calculate numerical solutions without the input of reaction kinetics parameters that are challenging to be accessed experimentally. Any careful attempt to include electron transfer kinetics would need to deal with potential effects due to the formation of Helmholtz layers at the photocatalytic solution (electrolyte) surrounding the surface of the photocatalyst, or complex reaction mechanisms for OER reaction.[1,4,19,23,27] For example, the work of Pan, Domen, Hu, et al (2020) has embraced partially such intricacies of POWS interface reactions under electrochemical principles.[23] They have modelled multiple coarse-grain electron transfer steps involved in Al-doped $SrTiO_3$/Pt and Ta_3N_5/Pt photocatalyst

junctions, which are studied immersed in an aqueous solution.[23] Their mathematical model is further validated experimentally via photoelectrochemistry open circuit experiments on a model material ($SrTiO_3$/Pt) at electrolytes purged at different gas atmosphere, mimicking dark conditions in photocatalysis.[23] Some of their findings have refuted persisting misconceptions within the research field. For example, they highlight the importance of the pinch-off effect and the adaptive junction behavior of semiconductor-metal photocatalyst junctions in charge-separation, and the non-equilibrium condition when two redox couples are present in solution.[22,23,25] Although their findings are pivotal and have generated a more realistic working model for POWS photocatalyst, their models are based on analytical expressions that ignore the cocatalyst geometry.[23] Therefore, their assessment of cocatalyst performance is only qualitative and cannot differentiate the multiple roles of a cocatalyst in an actual photocatalytic system. Other similar analytical solutions in the literature deal with transport equations under illumination and assume simple homogeneous geometries, whose most important inputs are typically migration length, optical depth, and depletion layer width (like the Gartner 1-D solution).[20,28,29] Yet, the extent of analytical solution applications to real photocatalysis conditions is only qualitative and cannot realistically isolate the charge separation and catalytic effects of cocatalyst addition.

It must be noted that different to photoelectrochemistry, where the convoluted cocatalyst role effects can be broken down experimentally (i.e., with contacts measuring the potential drop at the semiconductor-cocatalyst interface), in particulate suspension photocatalysis isolated cocatalysts effects are for the moment accessible only via modeling and simulations addressing the actual photocatalyst geometry.[19,23,26] In the context of photocatalysis numerical simulations, reaching an estimation of the free charge's potential may justify aforesaid simplifications that neglect reaction kinetics at the surface by introducing the fixed overpotential boundary condition (Dirichlet boundary condition).[1,4,19] Such models at a constant parameter input of overpotential do not only target the influence of the pinch-off effect but estimate in full the charge separation effect of adding a cocatalyst to tune the surface reaction, for example, increasing locally the emission barrier of the ideal Schottky contact relative to E_{sol}.[1,4,19] The emission barrier at the semiconductor-metal-solution interface versus semiconductor-solution can be up to 1 eV

higher at homogeneous ideal conditions.[1,4,19,25,30] Equation 2-8 shows that for a bare semiconductor nanoparticle in contact with only solution, the magnitude of band bending is dependent on the nanoparticle radius and the emission barrier height. For typical nanoparticle sizes in photocatalysis (< 100 nm) and photocatalytic solutions, photocatalytic solution induced band bending is only in the order of 10 mV.[20,21,31] Depending on the inhomogeneous geometry of the metal cocatalyst and its work function, this band bending magnitude can be increased significantly by adding a metal contact, changing the η_{sep} of the resulting photocatalyst.[1,4,19,25,31]

In the literature about charge transport modeling in photoelectrochemistry, quantitative solutions can be found describing the enhancement of charge separation by different types of metal cocatalyst geometries (ohmic or Schottky contact), which reflects on variations of simulated quantum efficiencies (from extracted electron-hole currents at the contact surface, and illumination input in Equation 2-1).[19,23,26,32-34] For the first time, such numerical simulation concepts were explored by Garcia-Esparza and Takanabe (2016) for photocatalytic systems, particularly a POWS system.[1,4] In their work numerical simulations of transport using a TaON/Pt system are presented, with a simplified boundary condition assuming a fixed overpotential and charge extraction described by a thermionic kinetic process.[1,4] Their POWS numerical simulations ignore the actual catalytic role of cocatalyst addition, which is simplified to the assumption of a typical overpotential for HER on platinum (nanoparticle), close to 0 mV, and 300 mV for OER on TaON. They describe for example, that for n-type semiconductors decorated with HER cocatalysts, an ohmic junction is preferred instead of a Schottky junction to promote electron migration to the HER site, which can also be found in other experimental literature sources.[1,4,35] Their work also predicts a maximum of 15% quantum efficiency for Pt cocatalyst nanoparticles of sizes of 10 - 20 nm separated at an angle of 90° on the TaON nanoparticles (100 nm) surface. In their work the effect of other semiconductor engineering aspects different than cocatalyst addition are also quantitatively predicted, like donor density in an n-type semiconductor.[1,4]

Following on the work of Garcia-Esparza and Takanabe (2016) that addresses actual photocatalyst geometries and same equations for charge carrier dynamics described in this and the previous section, we add an additional level of complexity to at least capture

semi-quantitatively the catalytic role of cocatalyst decoration on semiconductor nanoparticles. For such, boundary conditions are treated as actual Neumann-Robin conditions, accounting also for surface recombination. For simplicity, the general terminology for the transport equations above is now specified for one of the well understood systems that will be presented in Chapter 6. This system is photocatalytic (AM 1.5 G) OER half-reaction on bare WO_3 as light harvester (100 nm nanoparticles), and WO_3 decorated with RuO_2 (10 nm nanoparticles) as a cocatalyst for water oxidation. In this system there is typically no pH adjustment, and KIO_3 (10 mM) is used as an electron acceptor, which is assumed to dominate the solution redox energy level ($E_{sol} \sim E_{IO3-/I-}$ = 0.67 V versus NHE, at pH =7).[36-39]

The change to a Neuman-Robin boundary condition (J_n and J_p are currents density of electron and holes following Equation 2-5 and Equation 2-6) can be modeled for example assuming a second order electron transfer rate constant (k_{red} and k_{ox} for reductive and oxidative outer sphere processes, respectively) to the solution acceptor/donor molecule ($[IO_3]/[I^-]$, $[OH^-]/[O_2]$), and with a thermionic kinetic process for a semiconductor-cocatalyst Schottky contact (v_n and v_p are the emission/recombination velocities across the barrier for electrons and holes, respectively).[19,23,26,28,33] Such process is assumed arbitrarily as an outer sphere mechanism for simplicity. Additionally, recombination at the semiconductor surface must be considered, for example via intermediate energy level traps or surface states (R_s).[4,19] For the bare semiconductor the system is completed by replacing the Dirichlet surface conditions (Equation 2-9 to Equation 2-11) with the following equations at each point $Q(x,y,z)$ that belongs to the surface of the contact between WO_3 and the photocatalytic solution (S_{sol}),

$$\vec{J}_n\big|_Q \cdot \vec{n}|_Q = k_{red}[IO_3{}^-]\big(n|_Q - n_0|_Q\big) + R_S|_Q \qquad ,(Q \in S_{sol}) \qquad \text{Equation 2-12}$$

$$\vec{J}_p\big|_Q \cdot \vec{n}|_Q = k_{ox}[OH^-]\big(p|_Q - p_0|_Q\big) + R_S|_Q \qquad ,(Q \in S_{sol}) \qquad \text{Equation 2-13}$$

Where $\vec{n}$ is the local normal vector to the surface of the contact, and IO_3^- and OH^- are acceptor and donor species, respectively. k_{red} and k_{ox} are the coarse grain 2nd-order

electron transfer constants for IO_3^- reduction and water oxidation, respectively.[12,13,23,26,29,33] The mass action law above assumes a single electron transfer event as the rate limiting step (RLS), with the remaining sequence of multiple electron steps in a pseudo steady state. For example, some mechanisms for water oxidation place the RLS at the oxidation of OH^- to $OH^\cdot$ step.[23,26,29,33]

With this model accumulation of n and p at the contact sets the electron and hole currents leaving the surface, which must match the rate of recombination and reaction events (right side of Equation 2-12 and Equation 2-13). According to a classical Marcus outer sphere mechanism, k_{red} and k_{ox} are also dependent on the driving force between energy levels of the redox reactions involved ($E_{IO3-/I-}$ and $E_{H2O/OH-}$) and the energy of surface electrons and holes (trapped or bulk).[12,13] OER is very unlikely to occur via outer sphere since the k_{red} and k_{ox} are typically several orders of magnitude slower than surface recombination.[12,13,40,41] Additionally, as both outer sphere reactions occur at almost no spatial separation and in the absence of external voltage bias like in photoelectrochemical systems, regardless of band bending induced by the semiconductor-solution contact, both electrons and holes still need to migrate their way through to the same homogeneous contact surface. The consequence of the latter would be poor charge separation and fast charge recombination (i.e., radiative decay), with the only possibility of active site dissociation being local fluctuations of $[IO_3]/[I^-]$ and $[OH^-]/[O_2]$ adsorbed on the semiconductor surface, which would enable potentially more favorable direct (but inelastic) mechanisms for charge transfer.[20,23,29]

Indeed, materials like WO_3 and TiO_2 have surface traps (like surface bridging oxygen sites), whose predicted reaction mechanisms for electron transfer involve far lower kinetic barriers, i.e., for both water oxidation and IO_3^- reduction.[12,13,29,40-43] Instead of the outer sphere mechanisms in Equation 2-12 and Equation 2-13, reaction pathways are faster via aforesaid metal oxide semiconductor surface traps, which also involve spatial active site separation.[12,13,29,40-43] However, such mechanisms known in literature as indirect charge transfer still require high activation energies in WO_3 compared to typical electrocatalysts (i.e., RuO_2) and present a minimal active site separation on the sub-nanometer scale, therefore limiting charge separation also.[12,13,40,41,44,45] The implications of electron transfer occurring via surface traps are discussed at the end of this section. For simplicity, it is

temporarily assumed that on a bare WO_3 surface, IO_3^- reduction occurs readily according to Equation 2-12 and Equation 2-13, and that the bottleneck for charge extraction is water oxidation, whose timescale is similarly slow via surface trap or outer sphere, the latter captured by k_{ox}.

Low photocatalytic OER rates on bare WO_3 can be explained primarily using the set of equations above based on the typical timescales of k_{ox} versus rapid recombination. Sluggish water oxidation rates on WO_3 are supported by electrocatalysis experiments found in the literature.[38,39,44] The electrocatalytic overpotential for water oxidation for bare WO_3 (photo)anodes is on the order of 1 V.[38,39,44] This poor catalytic behavior of WO_3 for water oxidation can be captured for example with the Tafel exchange current in electrocatalysis (i_0).[1] For a small i_0 value of WO_3, the amount of overpotential needed to observe any OER rate in photocatalysis is unrealistically high since the charge accumulation needed at the surface translates to increased bulk recombination on the carrier pathway to the surface (due to loss of band bending), and surface recombination that also increases with n and p densities at the surface.[1,38,39,44]

Consequently, our photocatalytic system model predicts that OER will not be observed practically on WO_3 without decoration with a proper cocatalyst. If WO_3 is decorated with RuO_2, at the RuO_2/WO_3 contact (assumed as Schottky for simplicity), the first effect on the boundary condition is the local change in the emission barrier that creates an additional gradient to migrate holes at the surface to the RuO_2 sites, and electrons to neighboring reduction sites.[4,19] For a system with decorated cocatalyst, the following boundary conditions must be considered at the semiconductor-cocatalyst contact (S_{cat}),

$$J_n|_Q \cdot \vec{n}|_Q = v_n\left(n|_Q - n_0|_Q\right) + R_S|_Q \qquad (Q \in S_{cat}) \qquad \text{Equation 2-14}$$

$$J_p\big|_Q \cdot \vec{n}|_Q = v_p\left(p|_Q - p_0|_Q\right) + R_S|_Q \qquad (Q \in S_{cat}) \qquad \text{Equation 2-15}$$

The catalytic role of the RuO_2 sites can be described semi-quantitatively by using the representation found in the literature that considers OER catalyst as hole sinks. In our system, RuO_2 can store holes by generating higher valence Ru species, and their accumulation in the cocatalyst phase builds up an energy level (E_{cat}) such that eventually

the stored holes can be quenched steadily by water oxidation at the metal-solution interface.[32-34,46-49] On the one hand, in view of the pinch-off effect and the ability of some metallic cocatalyst to engage in parallel redox reactions, like Pt/PtO_x catalysts and the reactions leading to multiple Pt oxidation states, often in the literature 0D models of photocatalyst nanoparticles assume that the cocatalyst junction approximates the limit of an adaptive junction. Therefore, in such models it is expected minimal influence of the cocatalyst in band bending.[22-24] On the other hand, RuO_2 catalysts have chemical properties that approximate better the definition of a buried junction (shifting potential), meaning that conventional anhydrous RuO_2 (rutile) is dense, ion impermeable, and highly conductive.[32-34,46,47] Accordingly, and alike to other sources in the literature, we consider RuO_2 cocatalysts as a buried junction in our model, from the perspective that it is rather likely that a RuO_2 phase conducts and stores holes close to the metal-solution interface, which does not happen via chemical transformation to intermediate Ru species that are electrolyte-permeable.[32-34,46,47] The main implication of considering RuO_2 as a buried junction in our model is that the potential barrier is fixed relative to E_{cat}, and E_{cat} must match thermionic kinetics in Equation 2-14 and Equation 2-15, and electrochemistry kinetics.[34,49] Additionally, the model presented in this section deals directly with the cocatalyst geometry and local band bending, hence it does not require assumptions about the outcome of the band bending magnitude.

The resulting model for a WO_3/RuO_2 junction is presented in Figure 2-1, which depicts all the crucial mathematical objects described in Section 2.1 and 2.2.

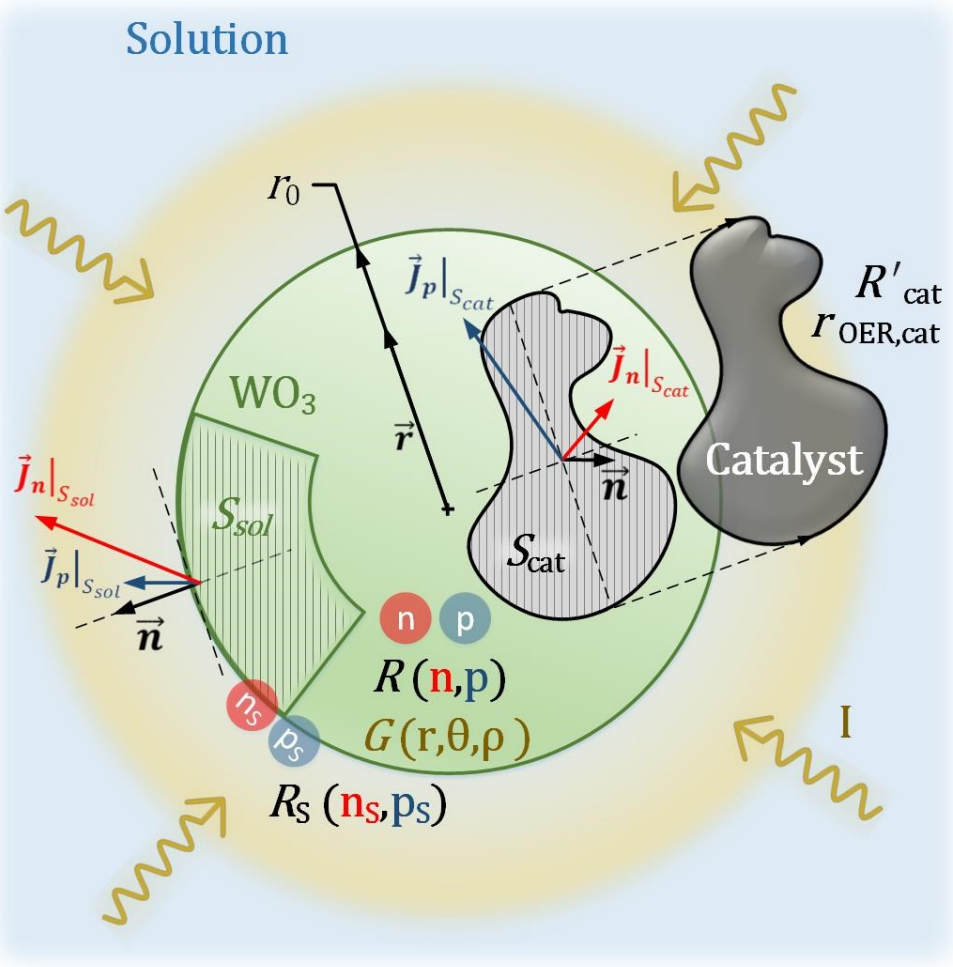

Figure 2-1. Depiction of charge carrier dynamics modelling of a WO_3/cocatalyst junction in photocatalysis. The WO_3 nanoparticle (radius r_o) spherical surface that is in contact with the photocatalytic solution is S_{sol}, while the patch that corresponds to the contact with the arbitrary cocatalyst shape is S_{cat}. The cocatalyst volume is mapped in spherical coordinates (radial coordinate r, angle coordinates ϑ and ρ). n (red) and p (blue) are local electron-hole densities, and n_s and p_s their corresponding surface value. Scalar functions G and R are the generation rate (depends on irradiated photon flux I), and the recombination rate (depends on n and p), respectively. Boundary conditions at contact surfaces are visualized as the carrier current (J_n and J_p) and the normal surface vector ($\vec{n}$) at an arbitrary point on the contact surface. $r_{OER,RuO2}$ and R'_{cat} are the frequency of OER and recombination events on the cocatalyst phase, respectively. The solution of the transport problems yields the n and p distribution along the WO_3 volume.

On the one hand, cocatalyst decoration creates another pathway for recombination at the RuO_2 site (R'_{cat}, defined as an absolute # of events per unit of time).[10,45] On the other hand, kinetic barriers for water oxidation decrease dramatically such that at steady state, the accumulation of holes in the catalyst produces significant OER rates ($r_{OER,RuO2}$, defined as an absolute # of events per unit of time).[10,45] $r_{OER,RuO2}$ depends on the difference between E_{cat} and the oxidation potential of water ($|E_{cat} - E_{H2O/OH-}|$), for example following

Butler-Volmer equations.[10,24,37,45] Different to the electron transfer rate constants defined in Equation 2-12 and Equation 2-13 for single events per carrier at the semiconductor surface (k_{red} and k_{ox}), due to the difficulty in describing electron and hole densities in a semi-metal material like RuO_2, the dependence of $r_{OER,RuO2}$ to accumulation of charges is kept as an implicit function of $|E_{cat} - E_{H2O/OH-}|$, as in electrocatalysis.[24,37] To complete the solution to the transport equations, boundary conditions in in Equation 2-14 and Equation 2-15 must also accomplish that electron and holes rates going across the contact emission barrier set by E_{cat} match the recombination and catalytic event frequency at the cocatalyst phase.[4,19,32-34] Then the charge transfer at the semiconductor-cocatalyst interface can be described as follows,

$$\oiint_{S_{cat}} v_p(p - p_0)\, dS = R'_{cat} + r_{OER,RuO2}(|E_{cat} - E_{H2O/OH}|) \qquad \text{Equation 2-16}$$

$$\oiint_{S_{cat}} v_n(n - n_0)\, dS = R'_{cat} \qquad \text{Equation 2-17}$$

$$E_{CB}|_Q - E_{cat} = \phi_B \qquad (Q \in S_{sol}) \qquad \text{Equation 2-18}$$

The equations presented in this and the previous section for charge carrier dynamics include transient states. Still, in photocatalysis the solution to such equations is typically of interest only at steady-state conditions. To obtain steady-state solutions directly, time derivatives (dp/dt, dn/dt) in Equation 2-3 and Equation 2-4 can be cancelled out, which should be consistent with neutrality of photogenerated charges and currents leaving the surface. Therefore, the boundary conditions involving electron currents (Equation 2-14) can be replaced directly by the equality to hole currents, as in Equation 2-19

$$\oiint_{S_{cat}+\,S_{sol}} J_n \cdot \vec{n}\, dS = -\oiint_{S_{cat}+\,S_{sol}} J_p \cdot \vec{n}\, dS \qquad \text{Equation 2-19}$$

Given the previous models and photocatalytic OER rates on bare (negligible) and decorated WO_3 nanoparticles that will be presented in Chapter 6, it can be inferred that the addition of cocatalyst has two major positive effects. One has already been described and relates to separation efficiency (η_{sep}) and the immediate effect of increased local band bending facilitating migration of holes to the cocatalyst surface, due to a higher emission barrier and the larger separation of HER and OER active sites. η_{sep} increases indirectly also because of the cocatalyst catalytic role, due to less hole surface accumulation on the cocatalyst decorated WO_3. The η_{sep} can now be defined more formally as the surface integrated hole-current density leaving the entire photocatalyst surface ($S_{cat+sol} = S_{cat} + S_{sol}$) divided by the total absorbed photons by the WO_3 nanoparticle volume (V_{WO3}), which for holes leads to Equation 2-20 (equivalent for electrons in steady state).

$$\eta_{sep} = \frac{\oiint_{S_{cat+sol}} J_h \cdot \vec{n}\, dS}{\oiiint_{V_{WO3}} G\, dV} \qquad \text{Equation 2-20}$$

The second effect is attributed directly to the cocatalyst catalytic role and the increase of η_{cat}, which can be understood from lower cocatalyst kinetic barriers for water oxidation compared to bare WO_3. For bare WO_3, η_{cat} is defined as the ratio of surface charge transfer versus charge transfer plus surface recombination, which for holes leads to Equation 2-21 (equivalent for electrons in steady state).

$$\eta_{cat,WO_3} = \frac{\oiint_{S_{sol}} k_{ox}[OH^-](p - p_0)\, dS}{\oiint_{S_{sol}} (k_{ox}[OH^-](p - p_0) + R_S) dS} \qquad \text{Equation 2-21}$$

While for RuO_2 decorated WO_3, the same definition leads to

$$\eta_{cat,WO_3+RuO_2} = \frac{4 \times r_{OER,RuO2} + \oiint_{S_{sol}} k_{ox}[OH^-](p - p_0)\, dS}{\oiint_{S_{sol}} (k_{ox}[OH^-](p - p_0) + R_S) dS + R'_{cat} + 4 \times r_{OER,RuO2}} \qquad \text{Equation 2-22}$$

The effect of cocatalyst addition is evident in improving the η_{cat} (OER) of semiconductors with poor electrocatalytic activity for water oxidation, like WO_3. Given the evidence from the electrochemistry and photoelectrochemistry literature, it is expected that the photocatalytic differences in OER rates after RuO_2 decoration on WO_3 come from the fact that $\eta_{\mathrm{cat,WO3+RuO2}} \gg \eta_{\mathrm{cat,WO3}}$.[38,39,44] The performance of different OER cocatalysts decorated on the same WO_3 light harvester can also be understood from these equations, considering the cocatalyst differences in electrical and catalytic properties, and geometry. Withal, we can also reassure based on the concepts presented in this section the holistic approach highlighted in the literature, that while good electrocatalytic activity of cocatalysts is a requirement, it does not ensure good photocatalytic performance.[4,10,45] Besides electrocatalytic activity, cocatalyst performance is bound to the right interfacial electrical properties that favor overall charge separation and prevent charge recombination.[4,10,45]

To date, no numerical simulation has been performed on the photocatalytic system like the one presented above without the input of a fixed overpotential to model interface reaction. Regardless of such lack of quantitative results, our model can be described semi-quantitatively by the introduction of quasi-Fermi levels ($E_{\mathrm{F,n}}$ and $E_{\mathrm{F,p}}$ for electrons and holes, respectively).[4,19,23] If the solution to transport equations and boundary conditions above gives a full description of electron and hole densities (n and p) along the photocatalyst geometry, the solution can be expressed as

$$n = N_C \exp\left(\frac{E_{F,n} - E_{CB}}{k_B T}\right) \qquad \text{Equation 2-23}$$

$$p = N_V \exp\left(\frac{-E_{F,p} + E_{CB} - E_g}{k_B T}\right) \qquad \text{Equation 2-24}$$

The semi-quantitative description of quasi-Fermi levels following the principles in the set of equations above and numerical results from the literature, can be found in Figure 2-2 for bare and decorated WO_3 in the region close to the semiconductor-cocatalyst and semiconductor-solution contact.[4,19,23]

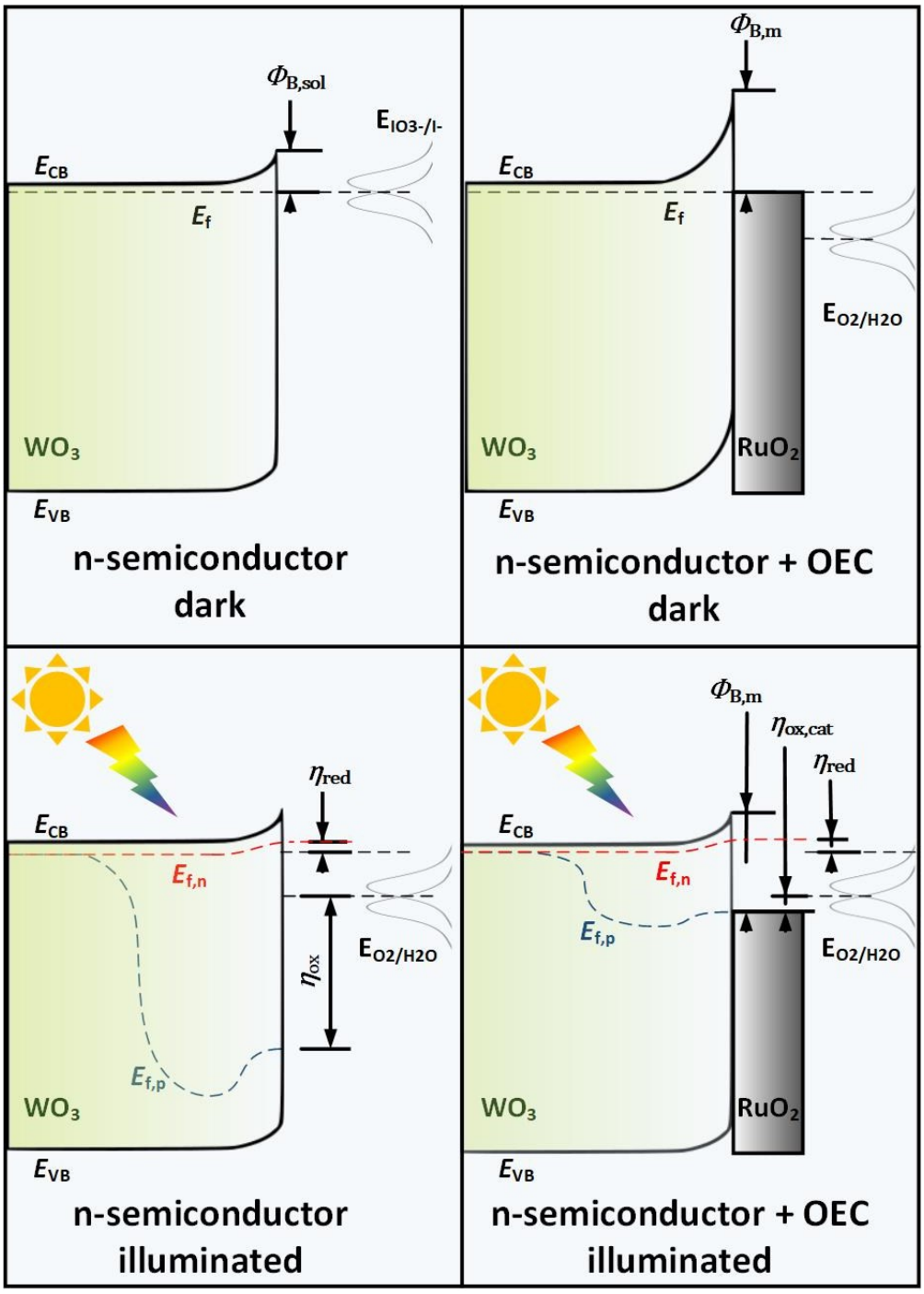

Figure 2-2. Depiction of quasi-Fermi levels of a WO_3 in photocatalysis in the absence of and presence of cocatalyst decorated on the WO_3 surface, and at dark and illuminated conditions. Dashed lines represent Fermi levels (black, under dark condition) and quasi-Fermi levels (under illumination, red for electrons, blue for holes). Acronyms: E_{VB} and E_{CB}, valence and conduction band levels; $E_{f,n}$ and $E_{p,n}$, semiconductor quasi-Fermi levels of electron and holes; $E_{IO3-/I-}$ and $E_{OH-/H2O}$, redox shuttle and OER reaction energy levels, respectively; η_{ox}, η_{red}, oxidation and reduction overpotential at bare WO_3 surface; $\eta_{ox,cat}$, oxidation overpotential at bare RuO_2, $\Phi_{B,sol}$, $\Phi_{B,m}$, emission barrier height of WO_3 contact with solution and RuO_2, respectively.

In addition to such local 1D predictions in Figure 2-2 based on $E_{F,n}$ and $E_{F,p}$ (dashed lines represent arbitrary pathways with arbitrary units for energy levels, describing the distance to the photocatalyst surface with arbitrary units also), a qualitative carrier potential distribution along a photocatalyst geometry (cross-section) is presented in Figure 2-3 (roughly approximated to similar numerical simulations in the literature).[1,4] As previously mentioned in this section, electron transfer events on bare WO_3 are more likely to occur via surface traps. Surface traps of WO_3 acting as active sites lead to similar equations compared to the cocatalyst phase, including active site spatial separation, but with far lower electrocatalytic activity compared to RuO_2.

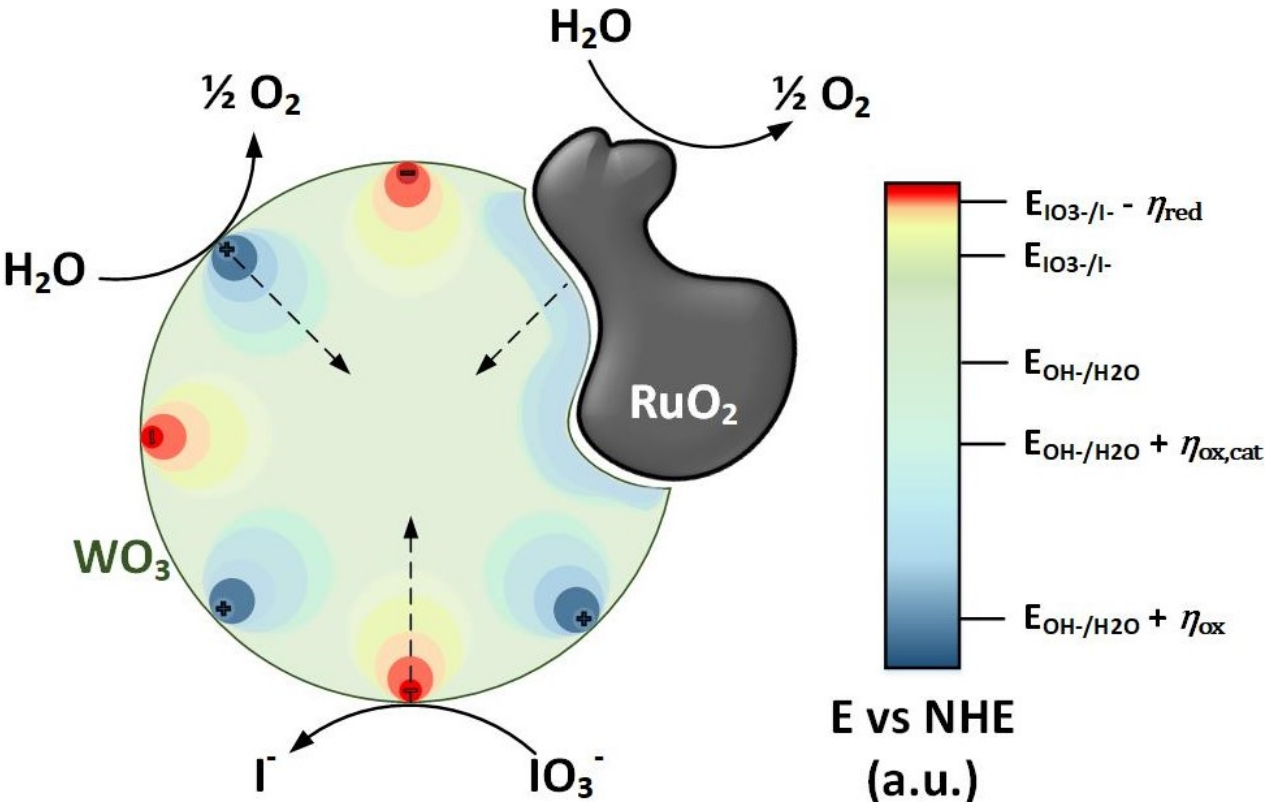

Figure 2-3. Qualitative description of charge carrier distributions under illumination along a WO_3/cocatalyst junction geometry (cross-section). Colour bar on the right indicates in arbitrary units the relevant energy levels in Figure 2-2. Colormap of cross section of WO_3 phase indicates the charge carrier densities expressed in electrical potential. Model considers spatial separation of WO_3 reduction and oxidation active sites. Dashed arrows depict qualitatively the arbitrary pathways used to graph $E_{f,n}$ and $E_{f,p}$ in Figure 2-2, assuming that the RuO_2 phase is arbitrarily far enough to not interfere with the charge distribution obtained along the dashed arrow lines on bare WO_3, compared to the undecorated WO_3 case.

The representation in Figure 2-3 considers active site separation via traps for WO_3 and an arbitrary RuO_2 cocatalyst junction shape (dashed arrows depict qualitatively the arbitrary pathways used to graph $E_{f,n}$ and $E_{f,p}$ in Figure 2-2). It can be inferred from Figure 2-3, that the color areas representing charge build-up (dark blue close to the bare WO_3 oxidation site, and dark red close to the bare WO_3) are high recombination rates zones. Whereas the areas close to the RuO_2 cocatalyst are expected to build less potential due to the smaller electrocatalytic overpotential requirement for water oxidation and upward band bending that facilitates hole migration to the RuO_2 sites.

The effect of different levels of cocatalyst loadings (i.e., cocatalyst/semiconductor %wt) in photocatalysis can also be derived from the principles exposed in this section, since it is expected that at a high loading, recombination rates due to oxidative potential build up will increase more than accessible cocatalyst active sites for water oxidation, which predicts an optimum of η_{cat} versus cocatalyst loading. Excessively high cocatalyst loading eventually turns out detrimental even if the additional cocatalyst material maintains its size, just increasing the coverage of well dispersed water oxidation sites on the light-harvester support, due to less distant active sites, and hindering of IO_3^- reduction sites.[1,4]

In cases where the local band bending around the cocatalyst does not favor proper migration of free charge carriers to their respective surface active-site, like the $Pt/SrTiO_3$ HER junction in POWS, the pinch-off effect still mitigates increased band bending, if the cocatalyst patches remain small enough ($< W_{\text{d}}$ of the light-harvester).[22-24] The latter case is also unfavored at high cocatalyst loadings when the additional decorated material increases its patch size, diminishing the pinch-off effect and thus separation efficiency. At high loading also, the decorated cocatalyst affects light absorption phenomena on the light-harvester support and thus η_{abs}. The detrimental optical effect resulting from cocatalyst decoration, previously described as parasitic light absorption, can be found in the literature, and is described in detail in Chapter 6.[7-11]

The role of anhydrous RuO_2 (rutile) is primarily a water oxidation catalyst, which is held along this and the previous section, but it also presents mild electrocatalytic activity for IO_3^- reduction.[38,39,50,51] The role of anhydrous RuO_2 (rutile) as a bifunctional catalyst also for IO_3^- reduction is not represented simultaneously in this section but is discussed in Chapter 6 as another beneficial effect in efficiency of OEP systems using KIO_3 as the

electron acceptor. Electrocatalysts that only enhance IO_3^- reduction like PtO_x and $RuO_2{\cdot}nH_2O$ are also employed as OEC on WO_3 and TaON photocatalytic systems.[38,39,50,51] PtO_x and $RuO_2{\cdot}nH_2O$ reduction catalyst can also be described using the concepts of this section, modifying the previously described equations accordingly. In such cases the electron transfer bottleneck results in IO_3^- reduction instead of water oxidation, and the overpotential at the catalyst (E_{cat}) is defined relative to the $E_{IO3-/I-}$ level, while water oxidation turns less sluggish compared to recombination events at the bare WO_3 semiconductor surface active sites. Nevertheless, upward band bending produced at the semiconductor-cocatalyst Schottky contact that is also a reduction site is not necessarily beneficial.[4,34,35] As predicted for example in the work of Garcia-Esparza and Takanabe (2016), in such case a semiconductor-cocatalyst ohmic contact is preferred to conduct electrons to the cocatalyst reduction active sites, and the Schottky behavior of an IO_3^- reduction catalyst like $RuO_2{\cdot}nH_2O$ (and neighboring semiconductor-solution Schottky contact) may even produce negative effects in charge separation.[4,34,35] In other similar cases where a high work function metal contact is expected to catalyze reduction reactions on an n-type semiconductor, for example the Pt/$SrTiO_3$ HER junction in POWS, the pinch-off effect and adaptive junction nature of the cocatalyst avoid the likely loss of η_{sep} triggered by unfavorable upward band bending.[23]

The overall efficiency of the entire photocatalytic process is defined in later sections as apparent quantum efficiency of OER reaction, which is the product of η_{abs}, η_{sep} and η_{cat} altogether. Other effects of cocatalyst addition like surface plasmon resonance or charge collection are not discussed along this document but can be found in multiple other sources in the literature.[4,8,10,45]

2.3 Charge transport in covalent organic frameworks

The charge transport models described in Section 2.1 and Section 2.2 only hold for free charge carriers, which is very often not the sole, or most dominant, means of charge transport in organic semiconductors.[52,53] In organic semiconductors, the concept of HOMO/LUMO still relates to E_V and E_C to define a fundamental driving force for the redox reactions at the surface of a particular photocatalyst — the local E_V and E_C energy levels in COFs are typically accessible only using theoretical models, i.e., density functional theory

(DFT).[52-57] Different to inorganic semiconductors, though, the generated exciton is at the organic semiconductor's backbone is not necessarily E_V and E_C delocalized bands.[52-57] Next, in organic semiconductors due to high effective masses of charge carriers and low permittivity of the medium (ε_R typically below 5), large exciton binding energies (Ex_{BE}) are typically expected (0.1 - 1 eV).[52,53] Depending on the interaction between the exciton and the organic semiconductor backbone, either free charge carriers (in acceptor/donor COF systems), excitonic (i.e., Frenkel) or polaronic transport may be the fastest means of charge transport.[52-55,58] A clear definition of relevant material physico-chemical properties in organic semiconductors to elucidate exciton transport and separation mechanisms are not as straightforward as in their highly crystalline inorganic counterparts.[52] For example, in crystalline inorganic semiconductors with well-defined high intrinsic charge densities (N_A/N_D approximately between 10^{15} and 10^{20} m^{-3}), high permittivity (ε_R in the range of 10 - 15), and high carrier mobility (μ_p/μ_n approximately between 10^0 and 10^4 $m^2\ V^{-1}\ s^{-1}$), upward (n-type) or downward (p-type) band bending is typically expected at the photocatalyst-solution interface, promoting facile exciton dissociation (Ex_{BE} < 25 meV) and free minority charge transport to the interface.[1,4] On the other hand, in organic semiconductors, due to the vaguely characterized low intrinsic density of charge carriers, large Ex_{BE}, and complex non-linear exciton-exciton and exciton-backbone interactions (i.e., involving self-trapping or exciton-exciton annihilation), the type of transport and charge separation toward the photocatalyst-solution interface becomes highly speculative.[52,53,55] Such organic semiconductors' properties defining the type of charge transport and separation are indeed challenging to access quantitatively via experiments or theory, like accurate exciton binding energy determination, and yet crucial for quantification of performance using transport models like the one presented in Section 2.1.[52,55] Organic semiconductors also present irregular geometries, including intricate porosity at different length scales, which impedes a clear cut definition of analytical surface geometries. Because of aforesaid reasons, trying to rigorously quantify the effect of organic semiconductors external modifications (like cocatalyst addition) based on free charge carrier transport only is unrealistic, and challenging even if the charge transport mechanism is properly represented.

As described in Section 1.3.5 and Section 1.4.1, the potential of COFs as organic semiconductor systems in photocatalysis is widely accepted in the literature due to their chemical tunability and high cristallinity.[59,60] Although COFs' crystallinity is superior compared to other organic semiconductors, which has been proven experimentally to enhance overall photocatalytic HER rates on COFs (using SED like TEoA), COFs still have far inferior dielectric behavior and larger exciton binding energies than regular inorganic semiconductors.[52,59,60] In some cases, COFs charge transport nature can be modulated, for example including acceptor/donor functional groups in the COF backbone to promote exciton separation and facilitate free charge carrier transport instead of short-lived excitonic transport.[52,55,59,61] Yet, the partial consensus in the literature is that bulk transport in COFs is likely excitonic, and that the specific mechanisms of charge transport and separation at the COF-solution interface are still challenging to interrogate and define accurately.[52,53,62,63] Qualitatively, this behavior translates to photocatalytic reactions being confined to a narrow region where excitons can survive and migrate to the COF photocatalyst surface reaction sites.[52,55,63] A more fundamental description of the steps involved in COF photocatalysis can be found in the review of Banerjee and Lotsch et al (2020).[52]

Exciton generation rates in COFs may follow a similar light extinction as in the previous section, whose trend and optical bandgap can still be roughly described based on the COF absorption coefficient. In a COF photocatalyst, the absorption of a photon due to the functional groups of the backbone promotes the jump of electrons from the local E_V and E_C bands, generating a localized exciton bound by strong coulombic interactions, and whose mobility mechanism involves hoping instead of band transport.[52,55,63] Due to their porosity and irregular surfaces, COF geometries have far more intricacies than inorganic particles that are considered perfectly spherical — or light-harvesters with other low-dimensional structures —which is challenging for quantification of the fraction of scattered and absorbed photons at a COF surface. Ignoring such irregularities and the complexity in predicting scattered photons at COFs' outer surface, exciton generation may still follow an approximation like Equation 2-1 for COF particles.

Following light absorption, the high Ex_{BE} and low intrinsic density of carriers in COFs are expected to produce negligible charge depletion/accumulation at the interface of COF-

suspensions from Fermi level equilibration, and from short exciton (or minority free charge carrier) lifetimes regardless of the type of bulk charge transport.[52,55] Also owing to their low permittivity and slow carrier (or exciton diffusion) mobility, migration lengths and depletion/accumulation regions in COFs are in the order of 1 - 10 nm only.[52,63] Charge or exciton migration lengths in COFs are also highly sensitive to the balance of charge mobility and trap recombination.[52,61,63] These factors limit photocatalytic reactions in COFs to a highly local region close to the surface. In this region, additional effects favorable for charge separation and/or free charge carrier transport may still occur due to adsorption of acceptor/donor molecule pairs on the surface, deposition of metal centers (like Pt nanoparticles), and surface defects.[52] Due to the locality of photocatalytic reactions close to the COF-solution interface, COFs hierarchical porosity and wettability, among other COF interfacial properties, have a key role to modulate charge transport, electron transfer reactions, and mass transfer phenomena involved in half-reactions for energy conversion, like HER.[52,56,57,59]

2.4 Interface reaction and the role of molecular cocatalysts in covalent organic frameworks

Simplification of the charge transport intricacies in COFs to a generic excitonic reaction scheme is still well accepted in organic polymer photocatalysis literature, for example in the work of Sachs, Cooper et al (2020), and other similar sources.[57,58,64,65] In these HER coarse-grain models, it is assumed that a first reaction step is triggered by unspecific surface excitons (COF^*), which are quenched in the presence of an electron donor (i.e., TEoA or TEA) and can happen oxidatively or reductively. Assuming arbitrarily a reductive quenching pathway, a reduced charge carrying COF is produced after hole quenching (COF^-). The latter state subsequently enables proton reduction.[57,58,64,65] It must be noted that the quenching mechanism may also occur oxidatively.[65-67] Using these models, a simplified assessment of the electron transfer to protons or a (molecular) catalyst intermediate can be performed, assuming rapid timescales of charge generation and transport and hole quenching compared to proton or molecular catalyst reduction.[57,58,64,65]

This type of modelling is presented in Chapter 4, through the work of Prasad-Biswal, Vignolo-Gonzalez, Lotsch et al (2019). A thiazolo[5,4-d]thiazole-linked COF (TpDTz) was

used as the light-harvester of a photocatalytic HER system in a 10% TEoA (SED, [D]) aqueous solution.[57] In this work, the TpDTz COF is proven to produce hydrogen more efficiently with an in-situ assembled molecular Nickel catalyst (Nickel-Mercapto-Ethanol, Ni-ME) than with traditional Pt decorated nanoparticles (~ 5 nm), the latter presenting minimal enhancement of HER rates measured on bare TpDTz COF at optimal loadings (1 wt% Pt/COF). A simplified version of this system is presented in Figure 2-4 (full description can be found in in Chapter 4).[57]

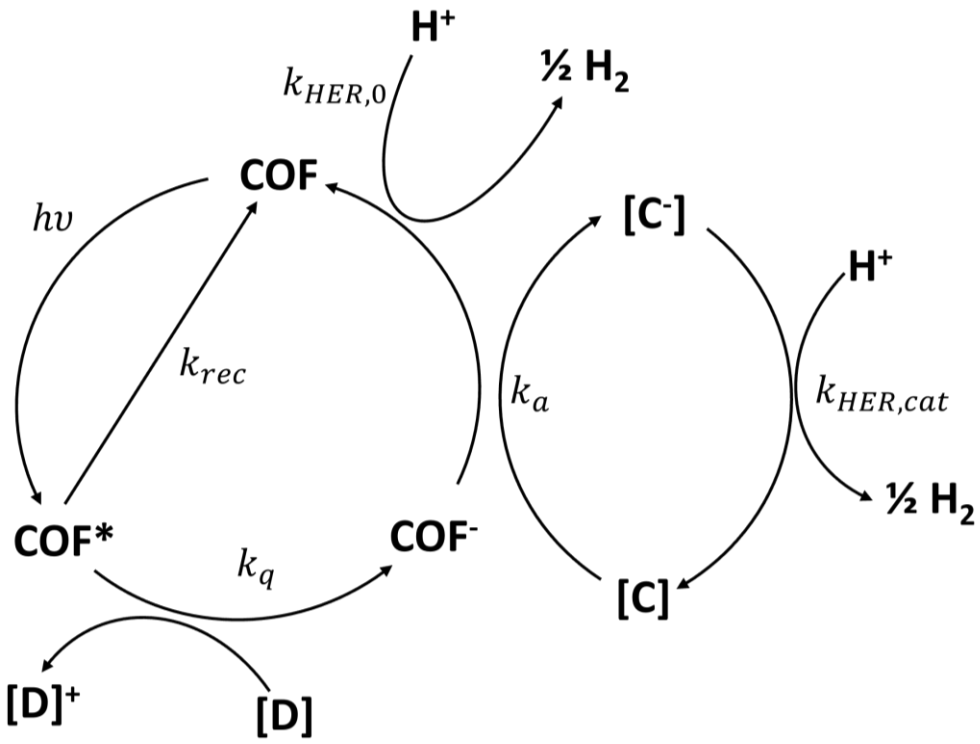

Figure 2-4. Coarse-grain microkinetic model of HER mechanism of the TpDTz COF and Ni-ME catalyst. Simplified from Chapter 4.

Although it is difficult to define η_{sep} semi-quantitatively for this system using charge transport principles (like in Section 2.2), the consistent increase of HER rates on the TpDTz COF by adding the Ni-ME catalyst ([C]) to the photocatalytic suspension can be partially explained based on a rough definition of η_{cat} as follows. First, charge transport close to the TpDTz COF surface is assumed generic and faster relative to surface electron transfer events like proton reduction and hole quenching, which defines the number of excitons or density of separated charge carrier pairs density at the COF surface, which we name as an average generic surface exciton density (n_s). The n_s is defined by the generation rate

in the bulk (G, i.e., using Equation 2-1) and the separation efficiency η_{sep}, which are unknown implicit functions. Similar to the Robin-Neumann boundary condition in Equation 2-12 and Equation 2-13, n_s sets a charge extraction condition that maintains the photocatalyst at steady state. An outer sphere mechanism for the electron transfer from the COF to the Ni-ME catalyst or proton reduction at the bare COF sites (k_a and $k_{HER,0}$ second order constants, respectively) is assumed, and a pseudo-first order dark HER step for the reduced catalyst state ($k_{HER,cat}$) at the local concentration of [H^+] ions.[57,64] Electron-hole recombination and donor quenching (k_{rec} and k_q second order constants, respectively) are considered in a fast pseudo-steady state ensuring no accumulation of [COF^-] in time ($d[COF^-]/dt = 0$), and proton reduction does not consider current doubling from radical decay of the donor or competing undesired reactions, like oxygen reduction or recombination of [COF^-] with [D^+]. Then, the charge extraction boundary condition is defined for all the photogenerated excitons along the COF volume (V_{COF}) that reach the surface of the COF.

$$\iiint_{V_{COF}} G\, dV \cdot \eta_{sep}(n_s) = n_s \left(k_{rec} + k_q[D][COF]_0(1-f)\right) \qquad \text{Equation 2-25}$$

Where the implicit average η_{sep} function is expected to depend on n_s.[68] For simplicity, a mean field approximation is assumed for the entire COF surface. The quenching is assumed to happen at a rate proportional to quenching active sites on the surface ([COF]$_0$), donor concentration in solution ([D]), and n_s. The fraction of the COF surface being blocked by the [COF^-] is f, which is assumed to compete with adsorption of [D], which is assumed to be at adsorption/desorption equilibrium. Using the pseudo-steady state condition of COF surface occupations, the stationary fraction f can be calculated for the bare COF system as

$$f_{COF} = \frac{n_s k_q[D]}{n_s k_q[D] + k_{HER,0}[H^+]} \qquad \text{Equation 2-26}$$

And for the system with molecular catalyst

$$f_{COF+Cat} = \frac{n_s k_q [D]}{n_s k_q [D] + k_a [C]}$$ Equation 2-27

Under the approximation that the electron transfer to the catalyst and direct proton reduction are far slower than donor quenching ($f \sim 1$), and that recombination dominates the boundary condition in Equation 2-25, it can be predicted that the n_s satisfying the boundary condition does not change significantly in the absence or presence of Ni-ME catalyst (ignoring local charge separation effects due to Ni-ME adsorption). For the Ni-ME system, the latter approximation causes that the Ni-ME catalyst reduction rate is only proportional to the amount of active [C] with a pseudo-first-order constant invariant with time. In Chapter 4 and Appendix C, following such approximation of the electron transfer rates to the molecular Ni-ME catalyst, the molecular part of the system is solved analytically satisfying most of the observations on photocatalytic HER experiments on the COF + Ni-ME system. A microkinetic analysis (MKA) was used to solve the behavior of gounrd-state and reduced cocatalyst [C(t)] and [C^*(t)] in time for a system with slow deactivation (k_d first order catalyst deactivation constant) and $k_{HER,cat} \gg k_a \gg k_d$.[57] The resulting change of catalytic performance of the TpDTz COF system due to presence of Ni-ME or another molecular catalyst of similar nature can be approximated to

$$\frac{\eta_{cat\ COF}}{\eta_{cat\ COF+Cat}} \sim \frac{k_{HER,0}}{k_{HER,cat}[C^-]}$$ Equation 2-28

In the previous scenario, direct proton reduction at the TpDTz COF is unlikely since the COF surface lacks any active site capable of lowering the activation energy of outer-sphere proton reduction mechanisms. Consequently, only trace level HER rates are reported on bare TpDTz COF, whereas the Ni-ME catalyst being a potent single-site water reduction electrocatalyst has an evident effect on photocatalytic HER rates, which is approximately 10^3 times higher at the maximum [C^*(t)] than the one of bare COF.[57] It must be noted that the maximum [C^*(t)] in time and the timescale of activation is implicit in the dynamic behavior of [C^*(t)], which depends also on the electron transfer rate to the resting state

species [C(t)] (redefined as first order constant k_a in the original work).[57] In fact, in this system, when the source of protons was changed to D_2O, the results suggest that k_a is likely the rate limiting step instead of $k_{HER,cat}$.[57] Optimal ranges of pH (8.5), TEoA concentration (10 vol%) and cocatalyst load (10 wt%) had been identified to maximize HER rates (941 μmol g^{-1} h^{-1}), as well as the influence of other SEDs (i.e., TEA), yet the rationalization of such trial-and-error optimization is not trivial using the surface exciton models just described.[57] Different to D_2O/H_2O experiments where only $k_{HER,cat}$ is expected to change significantly due to kinetic isotope effects (apparent $k_{HER,cat}(H_2O)/k_{HER,cat}(D_2O) \sim 1.6$), varying other factors like pH have multiple simultaneous effects difficult to deconvolute without the input of other (unknown) reaction parameters (for example, the Ni-Me(hexamer) coordination equilibrium constants).[52,57,58,69] Such variables may also affect other aspects of η_{sep} that are not captured by the model, like improved charge separation due to changes in adsorbed TEoA molecules at different concentrations, or changes of E_{sol} at different pH and TEoA concentrations.[52,57,58] Additionally, HER rates from adventitious sacrificial process are likely to change also for example, by changing the sacrificial agent type and amount.[70,71]

In Chapter 4, it will be shown in detail that others similar Ni-based complexes with different ligands (like 2-mercaptophenol, Ni-MP), and other earth-abundant metal centered complexes (like Cu-ME) were also tested on the TpDTz COF as cocatalysts. Such complexes are typically reported in literature as effective HER single site electrocatalysts and may follow similar coarse grain reactions mechanisms like the one of Ni-ME.[57,69,72,73] Although a high $k_{HER,Cat}$ is expected on those under photocatalytic conditions, results show at at least one order of magnitude decrease of HER rates compared to the Ni-ME (Co-ME, 84 μmol g^{-1} h^{-1}) and in some cases no difference to the bare TpDTz COF (~ 1 - 10 μmol g^{-1} h^{-1}).[57] This suggests that the k_a may not only be the limiting step for Ni-ME catalysts, but also for other complexes.[57] Particularly in cases where cocatalysts enhance TpDTz COF activity but with activation timescales in the order of 10 h or longer, the reaction model described in this section may explain lower HER based on less optimal k_a compared to Ni-ME, for example due to higher electron transfer from the COF to the metal complex in the presence of a different ligand field.[57,64] In such case, the build-up of [C^-(t)] is expected to plateau at lower HER rates and at timescales where cocatalyst deactivation becomes competitive

(> 25 h). In systems for which no activity improvement is observed in the presence of a cocatalyst, like the TpDTz COF with Ni-MP cocatalyst system, the explanation might be related to photocatalysis conditions different to the reported electrocatalysis optimal conditions and unfavorable for both $k_{\mathrm{HER,cat}}$ and k_{a} in the Ni-MP case, like basic pH or aqueous media, or simply poor cocatalyst complexation.[57]

In the specific case of TpDTz COF, Pt underperformance compared to the Ni-ME catalyst entails multiple reasons and cannot be explained solely using the quantitative approaches just described. As explained in Chapter 4, Ni-ME and Pt HER reaction mechanisms are inherently different in nature (i.e., homogeneous versus heterogeneous), and fundamental differences in charge separation are expected from metallic nanoparticles deposited on the surface.[52] Based on the original explanation presented in Chapter 4, and based on the concepts of Section 2.1 and Section 2.2, the type of light harvester-cocatalyst junction may explain qualitatively the difference between Pt and Ni-ME performances as follows.[57] Pt induced charge separation may exist due to the large work function of Pt (6.35 eV) and mild n-type behavior of the TpDTz COF, which depending on the extent of the pinch-off effect at such small Pt islands (~ 5 nm), it may produce a buried Schottky-like junction (COF-Pt-solution) with a higher potential barrier than the original COF-solution interface.[52,57,60] This type of junction generally described in Section 2.2 may induce an increased electric field potential gradient for electrons in the opposite direction from the Pt center, i.e., to the center of the COF particle. On the other hand, the Ni-ME molecular catalyst can be approximated to an adaptative junction with almost no effect on the bare COF-solution band bending.[49,57] If this behavior is expected for the COF-Pt interface, the potential build-up at the COF-Pt interface is more likely to increase recombination and parasitic light absorption than actual enhancement of HER rates. Pt poor performance is also influenced by its dispersion after photo-deposition, which is localized on the external surface of the TpDTz COF.[57] In this scenario, only electrons generated within the TpDTz COF migration length can be transferred to the Pt centers, which is likely only few nanometers from the external surface of the COF, thus misspending recombined excitons deeper at the TpDTz COF (effective) optical radial depth.[52,57] On the other hand, the Ni-ME cocatalyst can exploit the TpDTz COF porosity since it can homogeneously diffuse to portions of the TpDTz COF deeper at the optical radial depth.[52,57]

2.5 Mass transfer

In a photocatalytic system, the reactants transport system from the bulk of the photocatalytic solution (i.e., liquid media at the center of a reaction vessel) to a low-dimensional photocatalyst (i.e., nanoparticle) is coupled to the surface redox reaction rates.[1,4,74,75] Although mass transfer is not immediately related to the photocatalyst material properties, it affects indirectly its resulting η_{sep} and η_{cat}.[1,4] For example, at sub-microscopic scales and near the photocatalyst surface where transport is dominated by diffusion of solvated molecules, ion transport gradients (i.e., OH^- ions to the RuO_x OER center at the surface of WO_3) translate to ohmic and charge recombination losses.[1,4,74,75] Ion mass transfer can be accounted for by coupling charge transport equations in Section 2.2 to Section 2.3 to the Nernst-Planck-Poisson equation for electric field and diffusion-drift flux, which happens within the liquid immediate domain around the photocatalyst surface (near-surface region).[1,4,74] Nevertheless, estimation of ion gradients suggest that even at high HER/OER photocatalytic rates (> 150 $\mu mol_{H2}\ h^{-1}\ cm^{-2}$) on the most efficient POWS catalysts reported to date (like $CrO_x/Pt/SrTiO_3$), the resulting limitations from ohmic losses are below 1 mV, which is a far lower contribution to overpotentials observed at HER/OER active-sites.[74] Therefore, within the research field of artificial photosynthesis, limitations caused by ion transport at microscopic scales in observed HER and OER rates is unlikely.[74]

Besides ion transport, transport of other soluble species also play an important role in observed photocatalytic rates, for example dissolved gases and sacrificial agents.[75-77] Also, other types of mass transport are present in photocatalytic solutions which can be defined qualitatively by transport resistances based on macroscopic mass transfer coefficients.[76-78] One type of mass transport was already described as microscopic in scale and occurs in the region where nanoparticles behave like Brownian particles.[74,75] Within this limit and further from the photocatalyst surface, a net photocatalytic rate maybe approximated to a continuous point source for products ($\dot{m}_i$, representing for example HER or OER rates), and stoichiometric sink for reactants (like OH^-, H^+, or TEoA). Such resulting rate is dependent on both surface redox reactions, and their conjugation with local transport of products/reactants to/from the solution bulk with meso-scale phenomena, like turbulent

eddies streams produced by solution stirring.[79-83] This is referred to in literature as solid-liquid transport resistance.[76,78] The magnitude of this transport resistance (R_{bulk}) can be derived from of the coupling of fluid dynamics (i.e., described by Langevin equations) and molecular transport principles (like molecular diffusion or Nernst-Planck equations) within the Brownian motion region, and the outer region described by continuity equations (like Navier-Stokes or Lattice Boltzmann).[78-83] The second resistance is typically referred to as a classical liquid-gas interface, which is characterized as a series of two resistances, which corresponds to a liquid mass transfer coefficient (k_{l}) and gas transfer coefficient (k_{g}), and an interface equilibrium described by Henry's Law.[76,78] A graphical representation of aforesaid mass transport phenomena at different length-scales in photocatalysis is shown in Figure 2-5.

If the resulting overall transport resistance (R_{total}, equal to R_{bulk} for solubilized reactants/products in liquid phase with no vapor pressure) is small for example for liquid-phase reactants ($[c]_{\mathrm{react}}$), reaction rates at the surface of the photocatalyst can be approximated as if they occur at nearly the same concentration of reactants in the bulk ($[c]_{\mathrm{react,bulk}} \sim [c]_{\mathrm{react,surface}}$). Whereas at high transport resistance, liquid-phase reactants will form a gradient competing with surface reaction rates and observed HER or OER rates will have different extents of transport limitations, which in the most extreme case is a fully transport limited system where a boundary layer may form around the catalyst and the observed HER or OER rates correspond only to transport rates ($[c]_{\mathrm{react,bulk}} \gg [c]_{\mathrm{react,surface}}$).

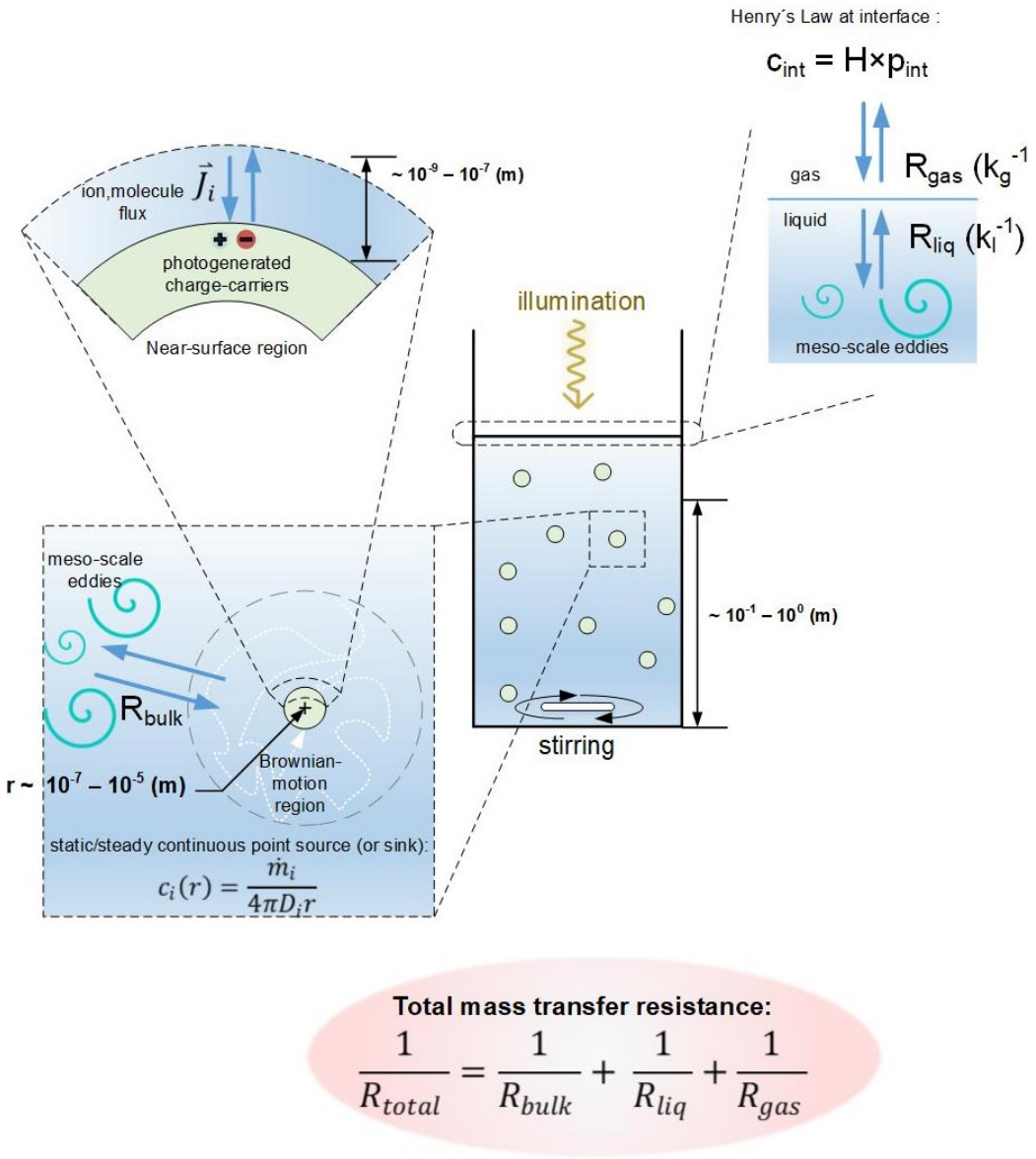

Figure 2-5. Qualitative description of mass transfer phenomena in a nanoparticulate suspension photocatalysis. R_{bulk} refers to the mass transport resistance between meso-scale mixing region and the Brownian-motion regime of the photocatalyst nanoparticles. At the liquid-gas interface, mass transport resistance at R_{liq} and R_{gas} is governed by the classical liquid-gas mass transfer coefficients (k_l, k_g), with an equilibrium condition at the interface given by Henry´s law (c_{int} and p_{int} are the liquid and partial pressure of a reactant in equilibrium at the interface, and H the corresponding Henry´s Constant). Ohmic losses from ion flux (J_i) in the near-surface region of the photocatalyst is not considered limiting. Within the Brownian motion region and far from the photocatalyst surface, a continuous point source or sink expression is highlighted ($\dot{m}_i$). Steady concentration of a generic reactant i within this region is obtained at steady conditions at a radial distance r from the nanoparticle. D_i refers to the diffusion coefficient of the reactant i in the liquid solution.

It has been reported in literature and in Chapter 4 that in HER photocatalytic system in the presence of SED, that SED transport — which is far slower than H^+ transport due to low diffusion rates of typical SED (i.e., binary diffusion coefficients in water, $D_{ethanol}$ ~ 1x10$^-$

^{9} m^2 s^{-1}, D_{H+} ~ 1x10^{-8} m^2 s^{-1}, at 25 °C and diluted conditions) — may limit the apparent HER rates.[76,78,84,85] In such cases, increasing the degree of meso-scale mixing, i.e., with liquid stirring, is necessary to achieve higher HER rates. For example, the reported HER rates on TpDTz COF - NiME system in Chapter 4 were obtained at 400 RPM magnetic stirring (asymptotic HER maximum versus stirring RPM), whereas at no stirring, the reaction rate observed was 50% less (~ 500 μmol h^{-1} g^{-1}).[57] This observation is in line with other similar HER systems in the literature suggesting that the SED transport (or also NiME transport to the TpDTz COF) is partially limiting.[57,76] In such cases, photocatalytic solution engineering (i.e., pH and buffering) and the means of meso-scale mixing (i.e., stirring) will produce observable effects on HER rates. Macro-scale liquid mixing limitation contributions can be ignored since most photocatalytic reactions in lab-scale reactors (i.e., top illumination) occur at optical depths in the order of millimeters, therefore not needing significant convective or vortex type of transport.[77,83,86] The limiting transport in HER photocatalytic suspensions is mostly associated to R_{bulk} of the SED since interface transport for H_2 is inherently fast due to relatively high diffusivity of H_2 in water and low Henry's constants (in aqueous media, H_{H2} ~ 8x10^{-6} mol m^{-3} Pa^{-1}), or sometimes because of spontaneous formation of a H_2 bubble phase.[87,88] Gas phase transport resistances are typically ignored due to facile gas mixing, and in continuous flow reactors, the headspace of a photocatalytic cell can be considered in most cases as an ideally mixed region.[3,57]

Differently, O_2 transport plays an important role in most photocatalytic OER system.[3,78] Different to H_2 transport in HER, the type of meso-scale mixing can also affect desorption of dissolved O_2 from OER photocatalytic reaction to the gas phase, due to relatively lower diffusivity and Henry's constants compared to H_2 in water (in aqueous media, H_{O2} ~ 1x10^{-5} mol m^{-3} Pa^{-1}).[3,78,87] This has two main implications in OER experiments. Firstly, developing a O_2 accumulation gradient from OER in the vicinity of the photocatalyst may produce ORR, which will affect significantly interface faradaic losses, charge recombination, and in POWS system product recombination (water formation).[23,89] Secondly, it has practical implications in OER measurements, since most reliable OER quantification systems are based on headspace O_2 detection, and OER rates will show typically a delay after illumination starts, due to the necessary buildup of dissolved O_2 in liquid phase such that O_2 desorption to the gas phase becomes stationary.[3,78,90,91] In such systems, regular

stirring has observable effects on R_{bulk} due to meso-scale eddies, but only a mild increase in k_l and k_g is expected at the highest stirring velocities feasible in lab-scale photocatalytic reactors (< 1000 RPM).[3,78] This has led to engineering of continuous flow reactors where bubbles of inert gas (i.e., N_2, Ar, or He) are forced into the liquid, which increases interface transport effective area, and depending on the bubble size, may also have positive effects on R_{bulk} due to more intimate mechanical interaction of the bubbles with the photocatalyst Brownian particle domain compared to the eddies induced by regular magnetic stirring.[3,78-83] In the literature, full mathematical descriptions of interface transport enhancement in OER due to bubbling can be found.[78] Following such principles, in Chapter 5 and 6 a bubbling reactor is used to avoid dissolved O_2 gradients affecting adventitious ORR, minimize the effects of reactor leaks; and make the OER detection more precise, fast, and able to capture kinetic processes without dealing with complicated dissolved O_2 detection.

2.6 Photon fate and reactor optics

In Section 2.1, the relation between local light absorption rates at the photocatalyst surface and exciton generation rates within a photocatalyst (G) has been established. Photocatalysis differs from electrocatalysis due to the convolution of redox reactions with electron-hole generation and separation at the same photocatalyst material. Due to this, photocatalysis is highly dependent on optics phenomena due to the strong dependence of the term G on local light intensity conditions in a photoreactor, which makes the core of photocatalysis a problem that requires multiple input to predict photocatalytic performance, including reactor optics and previously discussed mass transfer. Due to the high uncertainty in the models' assumptions, inputs estimations, material variability, and nonlinear relations between inputs and photocatalytic performance (described in Section 2.1 and 2.2), reported photocatalytic rates in literature for different materials are highly dependent not only on the incident light used (typically AM 1.5G) but also the photo reactor geometry, conditions, and optical properties of the photocatalytic suspensions.[1,3,91,92] It is generally accepted in the research field of artificial photosynthesis that there is no straightforward method to deconvolute intrinsic photocatalytic HER and OER rates from the features of the photo reactor used to measure them. Simplified reaction models approximate a photocatalyst internal quantum yield (QY) as a semi-empirical relation that

roughly extrapolate wavelength dependent performance to other geometries, for example assuming a charge-recombination limited regime ($QY \sim I^{0.5}$) or surface reaction limited regime ($QY \sim I$).[12,13,93] This simplification reduces greatly the level of complexity described in Section 2.1 and Section 2.2 for the relation between G and photocatalytic performance. However, even these simplified representations require local quantification of I, which is formally derived in suspensions as the local volumetric rate of photon absorption (*LVRPA,* or *LVREA* for energy absorption).[77,94] In photocatalysis, the experimentally measured production rate of a species *i* at a particular wavelength (r_i, *i.e.,* r_{HER}) comes from the spatial integration of local reaction rates (QY as a function of the local *LVRPA* and λ, the first dependent on reactor coordinates x,y, and z, and λ).[3,77,94] The relation between local reaction rates occurring at different local *LVRPA* and observable apparent quantities is as follows,

$$AQY(\lambda) = \frac{r_i(\lambda)}{A \times I_{avg}(\lambda)} = \frac{\iiint LVRPA(\lambda, x, y, z) \times QY(LVRPA, \lambda) dx dy dz}{A \times I_{avg}(\lambda)} \quad \text{Equation 2-29}$$

Where the apparent quantum yield (AQY) is the observed ratio between the measured rate of product (r_i), and the average incident light intensity in photon basis at the liquid interface (I_{avg}) multiplied by the illuminated area (A). When wavelength dependance is also ignored, the ratio obtained for a particular spectrum (i.e., AM 1.5G) becomes an apparent quantum efficiency.[3,90] The *LVRPA* in a reactor can be obtained from optical modeling of photocatalytic suspension, a radiation balance, and proper boundary conditions.[77,94] If the *LVRPA* and rates are estimated in a photoreactor at different wavelengths, a more fundamental relation between *QY* and *LVRPA* can be fitted semi-empirically for wavelength and incident light intensity measurements, as described by Equation 2-29. The QY is the minimum level of complexity to describe a photocatalyst performance independent of the reactor geometry used in the measurement. However, the *LVRPA* is hard to estimate or measure directly due to the influence of light-scattering.[3,77,90-92,94] There are three approaches in the literature to deal with this problem, which are depicted in Figure 2-6.

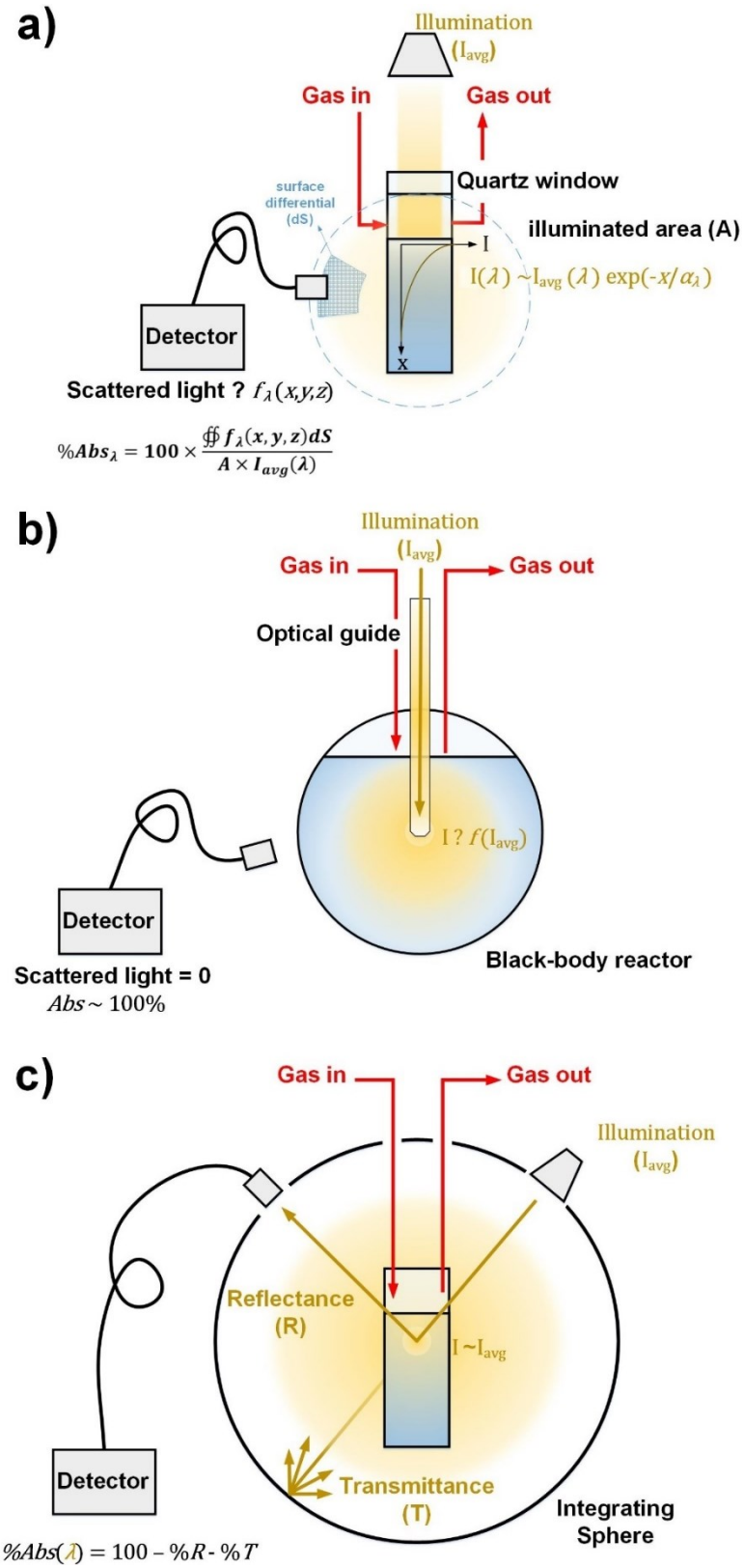

Figure 2-6. Photoreactor design benchmark. **(a)** Top-illuminated reactor, **(b)** black body reactor, and **(c)** integrating sphere embedded cuvette-reactor. The depicted detector aims to visualize scattered light readouts. In all reactors, *Gas in* and *Gas out* represent gas streams used to measure product rates, and light intensity beam is I_{avg}. *I* is the actual intensity distribution along the photocatalytic suspension geometry. In a), α is the suspension extinction coefficient, and *f* the fraction of scattered light distribution per surface area around the reactor.

The first approach is the use of optically simpler reactors where symmetry is desirable and scattered light leaves the reactor, like conventional top-illuminated borosilicate or quartz reactors (Figure 2-6a). In this design *LVRPA* through the reactor is easier to model, and its intricacies have less direct influence on the photocatalytic performance of a particular photocatalyst.[3,77,90-92,94] This allows comparison of photocatalytic rates obtained from different materials in a single cell, if the same incident light is used, and if the influence of scattered light in the overall photocatalytic performance is overlooked.[3,90-92] For such, performance of different materials in a cell (i.e., STH) must be measured at least in a regime where light extinction is maximum (optimal photonic efficiency).[3,92] However, quantitative comparison of photocatalytic performance of different materials among different groups (i.e., based on optimal photonic efficiency), might be possible only if identical standardized cells are used, or if scattered light is estimated from optical modeling and/or local scattered light measurements.[3,90-92] Estimation of scattered light in this type of reactor would allow comparison of internal indicators that only consider effectively absorbed light.[3,90] Such internal indicators provide a criterion more suitable to compare photocatalytic performance of different materials among different groups, because the consequences of the photo reactor geometry differences in terms of scattered light are extracted.[3,90-92]

The second type of reactor is called black-body reactor (Figure 2-6b). This design aims to minimize the scattered light to a minimum allowing measurement of average internal indicators directly, like QY.[95-97] However, in black-body reactors, such internal indicators estimations are highly dependent on the photo reactor cell used, when compared to conventional top-illuminated reactors, due to the *LVRPA*–geometry dependency, and geometrical intricacies of black-body reactors.[77,94-97] As the expected *LVRPA* in the black-body reactor type is then highly burdensome, the obtained QY in this design cannot be easily resolved in terms of *LVRPA* dependency, but only in terms of I_{avg}.[95-97] Additionally, black-body reactors must be tuned in volume for each type of sample ensuring that scattered light is zero and that the product rate does not change with the increase in photocatalytic suspension volume.[95-97]

A third reactor type is an integrating sphere embedded cell, in which a minimal optical depth of sample ensures an almost homogeneous light intensity through the sample ($\sim I_{avg}$), and where both products and scattered light are measured simultaneously (Figure 2-6c).[98,99] Such model is the most appropriate to study intrinsic photocatalytic performance, but the hardware necessary is limiting for most research groups and requires fine tuning of optics and analytics.[98,99] To the best of our knowledge, its use in high throughput material screening in the field of artificial photosynthesis is still limited to few studies only.[99]

Among the three types of reactors, the use of conventional top-illuminated photo reactors has prevailed in the artificial photosynthesis research community, which compromises to the uncertainty of scattered light over the aforesaid disadvantages of black-body and integrating sphere embedded reactors.[3,90-92] The top-illuminated photo reactor design is the choice used in the studies presented in Chapter 4 to Chapter 6. However, the extent of scattered light and light extinction is rarely characterized in the literature employing this design, thus photocatalytic performance assessment in top-illuminated reactors is most typically based on apparent indicators as figures of merits (like *AQY* or *EQE*).[3,90-92] As apparent indicators have implicit the influence of the external optical properties of the system on η_{abs}, comparison based on external indicators is still qualitative since it ignores external inflation or deflation of the η_{abs} of the photocatalyst material under study, as for examples by the amount of light scattered out the reactor.[1,3,99] Benchmark of materials photocatalytic performance must address the η_{abs} of different materials, but η_{abs} should only be a consequence of the material intrinsic optical properties (i.e., optical band gap), and ideally should not be influenced by the differences in η_{abs} due to the external photo reactor optics. η_{abs} manipulation by means of external optics, i.e., by the increasing of photocatalytic suspension volume, among others, comes nearer to photo reactor optimization.[90,92]

Benchmark of materials performance using the existing conventions in artificial photosynthesis (i.e., using optimal photonic efficiency) is qualitative even if the same reactor design is used.[3,90-92] For example, the same reactor geometry among different groups may differ in illumination conditions (i.e., homogeneity, collimation, and intensity), or even within the same group; photocatalytic suspension properties using different

materials will differ (i.e., suspension absorptance) and η_{abs} is still influenced by external optics phenomena.[3,90-92] An exception to the latter would be experiments conducted in top-illuminated reactors where scattered light is either measured or simulated, for example to estimate the *LVRPA* necessary to extract a *QY*.[77,94,99] However, conventional *LVRPA* estimation based on deterministic radiation balances resolution based on finite elements modelling is computationally heavy (small grids) and impractical for most systems given the assumptions used, for example for boundary conditions.[77,94]

An alternative optics modelling is presented in Chapter 5 to quantify practically the scattered light in photocatalytic OER experiments on commercial TiO_2 decorated with RuO_x.[3] This optical model is based on a stochastic representation of photon trajectories using probability estimations of scattering or absorption events, based on the refractive index (n) and absorption coefficient (k) of the nanoparticulate photocatalyst, Mie/Rayleigh scattering phenomena in aqueous media, and Fresnel boundary conditions for photons reaching interfaces (like liquid-glass, and gas-liquid).[2,3,6,100] The probability transition matrix based on optics phenomena (master equation) defines step by step the photon fate for each irradiated photon in terms of absorption or scattering type of events, and the angle of the latter, using the generation of a set of random numbers.[2,3,6,100] For each event, the random number generation also defines the trajectory length given the inverse of the total extinction coefficient.[2,3,6,100] After performing multiple simulations for single irradiated photons ($\sim 10^6$), a statistical distribution of the number and type of events at different reactor points and wavelengths narrows monotonically, which defines convergence.[2,3,6,100] This type of modelling is generally referred to in literature as kinetic Monte-Carlo methods and provide facile estimations of light scattering and light extinction profiles necessary for performance assessment in nearly symmetrical reactors, which can be double checked experimentally with partial scattered light measurements (like in Chapter 5, with a spectrophotometer).[3] Nonetheless, the main drawback of this approach is its dependance of the sometimes intricate photocatalyst geometry, and previously measured optical properties (n and k).[2,3,6,100]

Additionally, the extent of parasitic light absorption — meaning the amount of light that is absorbed by the cocatalyst material and that does not generate useful excitons for photocatalysis — requires careful attention since it is also associated to optical losses and

thus η_{abs}.[7,8,11,101] Parasitic light absorption is discussed in detail in Chapter 6. Parasitic light absorption modelling requires the definition of the same *n* and *k* parameters for the cocatalyst material and more refined models for optical cross-section at typically small length scales (< 10 nm) of for example OER junctions, like TiO_2/RuO_x or WO_3/RuO_x. In such cases quantitative modeling of simultaneous light interaction with the light harvester and cocatalyst components of a photocatalyst composite is highly challenging. As an alternative, in Chapter 6, light interaction with the individual photocatalyst composite components (e.g., WO_3 and RuO_2) is modeled using the previously mentioned stochastic methods, and numerical simulations when the cocatalyst dimension is small (e.g., ruthenium oxide nanosheets of thickness ~ 1 nm). Optical modelling of these scenarios for the incident photons can still partially explain the different contributions to parasitic light absorption of a particular photocatalyst.

Complementary to optical modelling, optics assessment of photocatalytic suspensions is also possible by means of ex-situ UV-vis transmission and diffuse transmission measurements. The latter differs from the former in the additional use of an integrating sphere device. This type of optical assessment, as explained in Chapter 6 and in the literature, may provide qualitative estimations of suspension optical depths, suspension absorptance in photocatalysis, and the extent of parasitic light absorption.[90,92,98,99,102] Optics criteria for optical reactor design can be found in Chapter 5, and Appendices C and D.

2.7 Colloidal stabilization

It has been established in Section 2.1 and Section 2.2. that the solution redox level (E_{sol}) plays an important role in Fermi level equilibration, and in Section 2.5 that electrolyte composition can affect ion transport properties. Additionally, ions in solution can affect other important aspects of photocatalytic reactions. For example, among other effects in photocatalysis induced by the modification of the electrolyte, differences due to interaction with active sites and properties of the electrical double layer (EDL).[1,27,74] The EDL is a type of ions distribution in a solvent, emerging from ion adsorption on a heterogenous phase, like the surface of a photocatalyst, and coulombic forces affecting the arrangement of ions around the first layer of adsorbed ions (Figure 2-7a).[27] Charge carrier dynamic principles

and reaction mechanisms in Section 2.1 and Section 2.2 must also consider the potential drop along the EDL and organizational effects in interfacial electron transfer reactions (i.e., λ in Marcus equations).[27,103,104] Although these are crucial aspects to be considered when describing interfacial electron transfer reactions involved in HER and OER photocatalytic rates, quantitative description of such phenomena in particulate suspensions are hard to access quantitatively, and thus typically restricted to rationalization of trial-and-error observations in photocatalytic experiments, for example, using knowledge from similar electrochemical systems or theoretical approaches.[1,27,36,74]

Nevertheless, engineering of some aspects of the EDL is feasible in photocatalysis. One of them is related to agglomeration control of low-dimensional heterogeneous materials used to harvest light, like nanoparticle metal oxides.[27,105,106] Given the area/volume ratio of low-dimensional materials (i.e., $6/D_p$ in nanoparticles of diameter D_p), a significant surface contribution to the free energy of the nanomaterial-solution system takes place when low-dimensional materials are embedded in solution.[105,107] This results in a significant tendency of low-dimensional materials to form agglomerates to reduce the free energy of the nanomaterial-solution interface and reach thermodynamic equilibrium (i.e., Helmholtz or Gibbs surface free energy).[105-107] Agglomeration of low-dimensional materials in photocatalytic suspension is undesired because of multiple factors related to the increased hydrodynamic radius of agglomerated material, including light shielding, mass transport resistance, heterogeneity during in-situ cocatalyst photodeposition, and sedimentation of material to less illuminated areas of photoreactors (Figure 2-7b).

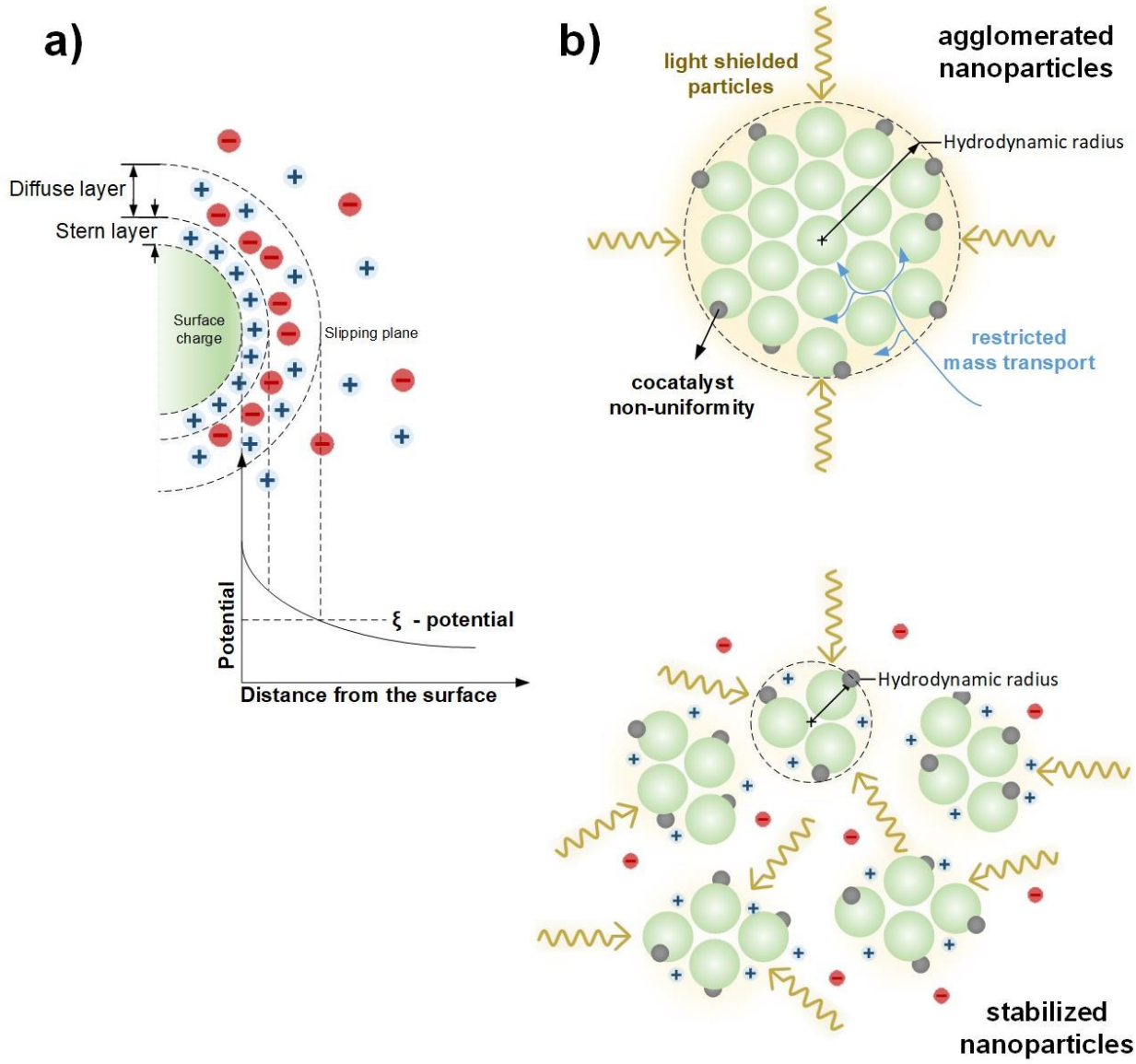

Figure 2-7. Influence of electrical double layer on photocatalyst nanoparticles agglomeration. (a) z-potential and electrical double layer representation, and **(b)** relevant differences in photocatalysis between the agglomerated and properly stabilized condition of the photocatalyst nanoparticles colloid (in yellow, optics related; in blue, mass transfer related; in black, photo deposited cocatalyst dispersion related).

This behavior is well described in the DLVO theory of colloids (named after the authors initials) and quantifies the kinetics of nanoparticles forming agglomerates and aggregates, based on the existence of two energy minimums (primary and secondary) when multiple nanoparticles are in proximity and surrounded by solution.[105-107] Primary (irreversible aggregation) and secondary (reversible agglomeration) minimums are separated by a dominant kinetic barrier, and aggregates are formed when the barrier is overcome.[105-107] Agglomeration refers to particle clusters at the necessary proximity to reach the secondary

energy minimum, in which they are loosely bound.[105-107] Different to irreversible aggregation, redispersion of agglomerates is possible at least temporarily if an appropriate external shear force is applied, for example by means of mechanical ultrasonication (US) or vortexing.[105-107] However, in photocatalysis, suspensions might only be initially mechanically dispersed, and the prevention of agglomeration while practical photocatalytic or cocatalyst photodeposition experiments can only be controlled by the colloidal stability of the suspension. To produce colloidally stable suspensions, the suspended single nanomaterials (i.e., single nanoparticles) should remain in average at distances further from the secondary minimum proximity.[105-108] Agglomeration and aggregation of low-dimensional materials in photocatalytic experiments are prevented, if sufficiently high kinetic barriers prevent such proximity.[108]

In the DLVO model, the kinetic barriers are described primarily by competitive van der Waals (attraction) and coulombic forces (repulsion).[105-107,109] The moderate addition of ions to the photocatalytic suspension can prevent agglomeration due to lowering of the photocatalyst surface energy (thermodynamic effect), and modification of the EDL potential to increase repulsion forces (kinetic effect).[27,105,106] The key parameter in the DLVO model to quantify aforesaid trends is the zeta potential (*ζ-potential*), which is the potential at the slipping plane of the EDL (Figure 2-7a) and whose magnitude to ensure a stable colloid is approximately |*ζ-potential*| > 30 mV.[105-107,110-112] The *ζ-potential* is a function that depends mostly on the material surface charge, and solvent type, pH and ionic strength.[110-112] In OER systems like in Chapter 6 (WO_3 nanoparticles decorated with RuO_x as cocatalyst), the same SEA ions ($K^+IO_3^-$) in aqueous solution can maintain the resulting photocatalytic suspensions well dispersed, due to the increase of the *ζ-potential* in a wide pH range at 10 mM KIO_3. In other cases in the literature, added salinity (NaCl) and pH are manipulated to improve the photocatalyst stability.[110-112] In Chapter 5, an alternative mechanism of stabilization is presented for a TiO_2 based photocatalytic suspension (TiO_2 as commercial 20 nm nanoparticles, known as P25), where the measured *ζ-potential* in aqueous suspension is close to zero at neutral conditions (iso-electric point at pH = 6.8). The *ζ-potential* of the P25 suspension increases slightly (~ 15 - 20 mV at pH = 7) at mild salinity (< 100 mM NaCl) and becomes sufficiently high only at extreme pH and salinity that are impractical in OER photocatalysis.[3,110-112] In such case, additional

(electro)steric stabilization effects are necessary to prevent agglomeration, which in the case of P25 is evidenced by the dramatic decrease of agglomerate radius (from 1-2 μm to 75 - 100 nm at pH = 7) with the addition of an inorganic bulky ion that is inert to the highly oxidative valence band of TiO_2 (tetra-sodium pyrophosphate, TSPP).[3]

Other factors affecting colloidal stability of photocatalytic suspensions are temperature and suspension density. Although the photocatalytic reaction temperature is typically chosen in view of charge carrier dynamics and reaction kinetics considerations, and the suspension density in view of optimal light extinction, low temperature and low suspension densities are primarily the first approach to prevent material agglomeration and aggregation, because of less frequent Brownian-particles collisions.[105-108]

2.8 Performance indicators

It has been described along this chapter that photocatalysis is composed by multiple elementary steps, sometimes grouped conveniently to define singular process efficiencies, for example η_{cat} and η_{sep}.[1] Nevertheless, photocatalytic performance in particulate suspension is described only by few figures of merit and typically refers to the overall efficiency of the process.[3,90-92] The first input in photocatalytic performance measured in most typical top-illumination reactors is the incident photon rate (I_0) from a light source (i.e., Xe lamps), and its wavelength distribution ($I´(r,\lambda)$ in mW m^{-2} nm^{-1}) whose radial dependency comes from the beam 2D distribution. We set as an arbitrary convention that I and $I´$ refer to photon basis (# of photons per area per time) or energy basis (power per area per time) light intensities, respectively. The spectral distribution is typically measured by spectrophotometer fibers and manipulated by means of optical filters, like solar terrestrial distribution (AM 1.5G filter), visible light (cut-off 420 nm filter), or central wavelength (CWL) filters (i.e., 20 nm band filters). Additionally, the incident photon rate is dependent on the light source 2D beam distribution (radial, and also angular in low cost housed Xe lamps) and collimation, which are dependent on the type and quality of the light source, and reactor optical design. Light sources used in this study are Xe lamps with less than 5° divergence, and an average spot heterogeneity varying from 2% (AAA quality solar simulator) to more than 20% (housed Xe lamps).[3,57] Therefore, the incident photon rate I_0 (in in 10^{-6} μE h^{-1} units) is defined as,

$$I_0(\lambda) = \frac{3600}{N_a}\int_0^r\int_{\lambda_1}^{\lambda_2} I'(\lambda, r)\frac{\lambda}{hc}\pi r\, d\lambda\, dr = \frac{3600 \times A}{N_a}\int_{\lambda_1}^{\lambda_2} I'(\lambda)_{avg}\frac{\lambda}{hc}d\lambda \qquad \text{Equation 2-30}$$

Where h and c are the Planck and light speed constants, and λ the characteristic wavelength (i.e., average) between λ_1 and λ_2. The second key input for assessing performance is the product rate output (r_i for species i). Particularly in artificial photosynthesis applications, due to the low product formation rate, this can only be calculated from direct analytics detecting the target analytes, like H_2 or O_2 gas. Depending on the reactor type, r_i can be calculated from molar accumulation in a close system at nearly constant headspace moles (batch reactors at constant volume, P and T) from:

$$r_i = N_T \times \frac{dx_i}{dt} \qquad \text{Equation 2-31}$$

Where N_T is the total number of moles in the headspace, and x_i the molar fraction of the target analyte. The molar fraction can be tracked for example with discrete points sampled by a gas chromatograph (GC), and the time derivative can be approximated to discrete slopes ($\Delta x_i/\Delta t$, where Δt is the detection interval). Additional *point-to-point* corrections are needed when product sampling is destructive, meaning that an amount of sample is extracted out of the reactor for detection and is replenished with inert gas to maintain the pressure of the closed system. In case leaks of the same measured species are present like in OER experiments, a leakage slope obtained under dark conditions is also necessary in photocatalytic rates calculations.

For reactors that are also kept at constant at constant volume, P and T, but flow conditions (in flow F_{in}), the product rate can be calculated dynamically directly from a steady-state mass balance,

$$r_i = \frac{F_{in} \times \left(x_{out,i} - x_{in,i}\right) \times 10^{-6}}{\left(1 - x_{out,i} \times 10^{-6}\right)} \qquad \text{Equation 2-32}$$

Where $x_{i,\mathrm{in}}$ and $x_{i,\mathrm{out}}$ refer to the species *i* molar fraction at the inlet and outlet of reactor, respectively, which are tracked with instrumental analytics before and after illumination like in batch reactors. Flow reactors' retention times are defined as $N_{\mathrm{T}}/F_{\mathrm{in}}$, which is required to correct transient-state equilibration, for example assuming ideal mixing. Qualitatively, the mass balance in Equation 2-32 does not require transient-state corrections for times after illumination at least two times the retention time. It should be recognized that the average production rates (described previously as dependent on *LVRPA* spatial distribution) are not fixed amounts but dynamic trends, which is captured more appropriately at flow conditions.[3,77,94] Or else, when the target is to calculate performance indicators based on accumulation of products rather than rates, batch reactors should be preferred. Details of dimensions, drawings, and type of photoreactors can be found in Chapter 5, and Appendices B to D.

To avoid ambiguity, it now follows a list of typical performance indicator definitions that are found throughout this work, and pertinent to the fields of artificial photosynthesis and photocatalysis. Definitions are gathered from different literature sources to more accurately emphasize the ideas and calculations stated in the forthcoming Chapters 4 to Chapter 6 and adapted to specific reactions under study, like flow conditions. Although in the artificial photosynthesis research field the terms apparent quantum yield (*AQY*) and external quantum efficiencies (*EQE*) are most of the time used interchangeably, in the most rigorous sense the term *AQY* should be used only if information of reaction versus monochromatic light (or narrow wavelength band) is available[57,94,98,113,114]. The same distinction applies to internal quantum efficiency (*IQE*) and quantum yield (*QY*, also internal quantum yield). Another strong assumption for the estimations of Turnover Frequency (*TOF*) and Turnover Number (*TON*) below is the definition that all cocatalyst centers are exposed to liquid media, which translates into a lower limit of *QY*, and it refers to the space averaged observed value ignoring the *LVRPA* dependency at different wavelengths.

Apparent Quantum Yield (AQY, in photocatalytic OER)[90,92,98]:

$$AQY(\lambda)\% = \frac{4 \times r_{O_2}}{I_0(\lambda)}$$ Equation 2-33

$I_0(\lambda)$: Incident photon rate at a specified wavelength λ (i.e. 10^{-6} μE h^{-1})

Quantum Yield (Φ, in photocatalytic OER)[90,92,98]

$$\Phi(\lambda)\% = \frac{4 \times r_{O_2}}{I_{abs}(\lambda)}$$ Equation 2-34

$I_{abs}(\lambda)$: Total absorbed photon rate at a specified wavelength λ (i.e. 10^{-6} μE h^{-1})

Photonic efficiency (ξ_e)[90,92,98]

$$\xi_e(\lambda_i, \lambda_j)\% = \frac{4 \times r_{O_2}}{I_0(\lambda_i, \lambda_j)}$$ Equation 2-35

$I_0(\lambda_i, \lambda_j)$: Incident photon rate at a specified wavelength range between λ_i and λ_j (i.e. 10^{-6} μE h^{-1})

Quantum efficiency (QE)[90,92,98]

$$\mathrm{QE}(\lambda_i, \lambda_j)\% = \frac{4 \times r_{O_2}}{I_{abs}(\lambda_i, \lambda_j)}$$ Equation 2-36

$I_{abs}(\lambda_i, \lambda_j)$: Absorbed photon rate at a specified wavelength range between λ_i and λ_j

Turnover Frequency (TOF_{avg}) and Turnover Number (TON_{avg})[57,115]

$$\boldsymbol{TON_{avf}} = \int_{\boldsymbol{t=0}}^{\boldsymbol{t_f}} r_{O_2}(t)dt \Big/ \mu\text{mol of cocatalyst}$$ Equation 2-37

$$\boldsymbol{TOF_{avg}} = {}^{r_{O_2}}/_{\mu\text{mol of cocatalyst}}$$ Equation 2-38

Relative photonic efficiency (ξ'_e, using benchmark)[3]

$$\xi'_e(\lambda_i, \lambda_j) = \frac{\frac{r_{opt,x}}{I_{0,x}(\lambda_i, \lambda_j)}}{\frac{r_{opt,0}}{I_0}}$$ Equation 2-39

I_0 : Incident photon rate for OER benchmark at near AM 1.5G conditions

$I_{0,x}(\lambda_i, \lambda_j)$: Incident photon rate for a material x to be normalized, at a specified wavelength range between λ_i and λ_j . Equal to I_0 if AM 1.5G is also used for material x.

$r_{opt,0}$: Optimal photocatalytic OER production rate of OER benchmark in [10^{-6} µmol h^{-1}], at a condition where adding more suspension volume or more photocatalyst density at constant I_0 at the liquid gas-interface produces no further increase of measured OER.

$r_{opt,x}$: Optimal photocatalytic OER production rate of material x to be normalized in [10^{-6} µmol h^{-1}] at a condition where adding more suspension volume (or other forms of catalyst load) at constant $I_{0,x}(\lambda_i, \lambda_j)$ at the liquid gas-interface produces no further increase of measured OER.

2.9 Detection of photocatalytic rates

Regardless of the focus of photocatalyst engineering, the latter should aim to rationally and sequentially tailor material components or morphologies based for example on its optical properties, charge carrier dynamics, and electron transfer reactions kinetics at their active centers. Correct orchestration of this properties is captured altogether by the figures of merit described in the previous section, which relies on the detection of photocatalytic rates. Within the field of artificial photosynthesis, quantification of photocatalytic HER rates in the presence of hole scavengers and under *close-to-solar spectrum* illumination (AM 1.5G standard, or wavelength bands, with intensities ~ 100 mW cm^{-2}) is a relatively straightforward measurement using commercially available equipment.[90,91] The most standard HER measurement in suspension photocatalysis is the top-illuminated borosilicate or quartz batch photo reactor, which accumulates hydrogen in an inert atmosphere that is

kept at constant temperature and pressure.[90,91] Hydrogen build-up due to illumination is tracked typically with discrete sampling injected to a gas chromatograph (GC) that separates the sample mixture. Analytical GC exploits the different affinities of different analytes to a column (packed or capillary) that is flown with a carrier gas at a temperature program. When successful separation occurs, the GC column elutes pulse distributions (i.e., gaussian peaks) at different times for each analyte (retention time), whose area is proportional to the injected molecules of analyte. For gas detection in photocatalysis (i.e., H_2 and O_2), a GC device is typically equipped with a thermal conductivity detector (TCD), which is considered a universal detector. Commercial availability and tailoring of the GC-TCD detection technique has allowed facile material screening and has contributed to enormous advances in for example, HER photocatalysis using engineered organic polymers (i.e., carbon nitrides) as light-harvesters.[57,59,116] The standard sensitivity of a GC-TCD equipment is limited by the contrast of thermal conductivity of the analytes compared to a reference gas (sometimes same as carrier gas in GC). Other commercial gas detection techniques based on plasma generation and high voltage can expand sensitivity to certain type of analytes, like flame ionization detectors (FID). FID detected currents from collection of ionized carbon containing analytes on a hydrogen flame are significantly higher than the ones measured on TCD detector. GC-TCD/FID machines are widely available and allow also trace detection (around 1 – 10 ppm levels at standard conditions) of CO_2 reduction products in photocatalysis, like CO.

Mass spectrometry (MS) is another universal detection technique based on ion collection that is usually coupled to GC analysis, which provides resolution of the molecular weight (m) and charge (z) of ionized analytes. In commercial GC-MS devices, analytes are ionized at high temperature (> 200 °C) by chemical sources or high voltage (~ 1 keV), and the current at different m/z channels is collected selectively in a high vacuum chamber (< 10^{-4} Pa), typically using quadrupole mass analyzers, which provides additional insight into fragmentation patterns of molecules eluted at different retention times. GC-MS applications in quantification of permanent gas, like H_2 or O_2, requires careful attention of parent peaks which typically limits GC-MS to qualitative analysis like molecule identification and isotope labeling.

Despite the many options for tailoring commercially existing GC-TCD/FID and GC-MS devices (or combinations of them), their main limitation is that H_2 and O_2 detection can only be optimized at the expense of the other, and with only moderate results for lower detection limits (LDL), for example by using a carrier gas that enhances thermal conductivity differences with the target analytes. Particularly in POWS applications, only highly active materials like $BiVO_4$ or WO_3 for OEP, or $SrTiO_3$ or TaON for HEP, or finely tuned $SrTiO_3$ (i.e., Al doped) in one-step, can be measured practically with GC-TCD configurations,[88,90,91,117,118] whereas photocatalytic activities of other novel materials at earlier stages of optimization is inaccessible given the sensitivity limits of for example GC-TCD devices.[119,120]

Expanding the existing detection sensitivity in the research field of artificial photosynthesis not only allows POWS detection at trace levels. It also allows product rate quantification at earlier stages of photocatalyst optimization for half-reactions, or alternatively, finer quantification of dynamic production rates allowing reaction kinetic studies on moderately active materials, as shown in Chapter 4 for the case of HER rates detection on TpDTz COF with a Ni-ME cocatalyst.

An alternative and to achieve the goal of universal trace detection, alternative detectors have entered GC applications, like the barrier ionization discharge detector (BID). An example of this configuration can be found in Appendix A. This platform was built in tandem with a GC manufacturer (Shimadzu) in an autosampler configuration and duplicated with a MS detector line allowing molecular mass resolution for when isotope experiments are required.[121] Given the high sensitivity of the BID detector, the amount of sample required is 250 µL at standard conditions to achieve an lowest detection limit of 0.5 ppm for H_2, in contrast to regular TCD detectors that require 3 mL of sample at standard conditions to achieve an LDL of 50 ppm for H_2. The latter feature has a significant impact in batch measurements.

The BID detector is based on metastable helium plasma generation, which allows strong ionization of any type of molecule, including simultaneous high response to H_2 and O_2.[119-121] The BID detector is also more sensitive than an FID detector to carbon containing molecules, like CO.[119-121] Such GC-BID detection platform had only few precedents in artificial photosynthesis works that were motivated by the need of simultaneous trace

detection of H_2 and O_2 from emerging POWS materials with low or moderate activity (~1 μmol g_{cat}^{-1} h^{-1}).[114,119,120,122]

The aforesaid configuration of the BID detector stands out even more for its O_2 detection sensitivity, whose tuning of LDL for O_2 (2 ppm) can outperform the one of a TCD detector up to two orders of magnitude. At this sensitivity, special features in auto-sampling to control adventitious O_2 background are also required which is considered in the design of the proposed GC-MS/BID platform. For example, these features of the GC-BID/MS for O_2 detection are exploited in the experiments where OER cocatalyst (i.e., Ru-based) engineering at early stages is reliant on feedback from photocatalysis experiments producing only traces of O_2. Trace O_2 detection can be complemented with photoluminescence (PL) based O_2 sensors, whose principle is an excited dye decay in the presence of O_2.[3,123] Such technology was adapted from commercial PL sensors (Presens) allowing for accurate temperature and pressure compensation. The PL detection is considered an online sensor given that it is not an invasive technique and that it has high dynamic resolution (3 s, $\tau_{90\%}$ ~ 10 s), and similar lowest detection limit to a BID detector.[3,123] An example of this redundant O_2 detection presented in Chapter 5 and Chapter 6 also required reactor engineering to make compatible a simple optical design and chemical inertness (borosilicate glass), with high purity gas handling standards (tightly sealed glass-metal connections) and trace product detection. The OER reactor design to be coupled to the GC-BID/MS platform considered a continuous flow bubbling configuration to overcome mass transfer limitations described in Section 2.5, and a convenient trade-off between rapid assembly-purging-methods, high throughput data collection and reactor cleaning, and controlled leakage rates ($<10^{-9}$ He atm L min^{-1}).

3.0 References

1. Takanabe K. Photocatalytic Water Splitting: Quantitative Approaches toward Photocatalyst by Design. *ACS Catalysis* 2017, **7**(11)**:** 8006-8022.
2. Miranda-Muñoz JM, Carretero-Palacios S, Jiménez-Solano A, Li Y, Lozano G, Míguez H. Efficient bifacial dye-sensitized solar cells through disorder by design. *Journal of Materials Chemistry A* 2016, **4**(5)**:** 1953-1961.
3. Vignolo-González HA, Laha S, Jiménez-Solano A, Oshima T, Duppel V, Schützendübe P*, et al.* Toward Standardized Photocatalytic Oxygen Evolution Rates Using RuO2@TiO2 as a Benchmark. *Matter* 2020, **3**(2)**:** 464-486.
4. Garcia-Esparza AT, Takanabe K. A simplified theoretical guideline for overall water splitting using photocatalyst particles. *Journal of Materials Chemistry A* 2016, **4**(8)**:** 2894-2908.
5. Takanabe K. Transferring Knowledge of Electrocatalysis to Photocatalysis: Photocatalytic Water Splitting. *Nanotechnology in Catalysis*. Wiley-VCH Verlag GmbH & Co. KGaA: Weinheim, Germany, 2017, pp 891-906.
6. Li Y, Carretero-Palacios S, Yoo K, Kim JH, Jiménez-Solano A, Lee C-H*, et al.* Maximized performance of dye solar cells on plastic: a combined theoretical and experimental optimization approach. *Energy & Environmental Science* 2016, **9**(6)**:** 2061-2071.
7. Kempler PA, Gonzalez MA, Papadantonakis KM, Lewis NS. Hydrogen Evolution with Minimal Parasitic Light Absorption by Dense Co–P Catalyst Films on Structured p-Si Photocathodes. *ACS Energy Letters* 2018, **3**(3)**:** 612-617.
8. Morawiec S, Holovský J, Mendes MJ, Müller M, Ganzerová K, Vetushka A*, et al.* Experimental quantification of useful and parasitic absorption of light in plasmon-enhanced thin silicon films for solar cells application. *Scientific Reports* 2016, **6**(1)**:** 22481-22481.
9. Abe R, Shinmei K, Koumura N, Hara K, Ohtani B. Visible-light-induced water splitting based on two-step photoexcitation between dye-sensitized layered niobate and tungsten oxide photocatalysts in the presence of a triiodide/iodide shuttle redox mediator. *Journal of the American Chemical Society* 2013, **135**(45)**:** 16872-16884.

10. Ran J, Zhang J, Yu J, Jaroniec M, Qiao SZ. Earth-abundant cocatalysts for semiconductor-based photocatalytic water splitting. *Chem Soc Rev* 2014, **43**(22)**:** 7787-7812.
11. Yang J, Wang D, Han H, Li C. Roles of Cocatalysts in Photocatalysis and Photoelectrocatalysis. *Accounts of Chemical Research* 2013, **46**(8)**:** 1900-1909.
12. Liu B, Nakata K, Zhao X, Ochiai T, Murakami T, Fujishima A. Theoretical Kinetic Analysis of Heterogeneous Photocatalysis: The Effects of Surface Trapping and Bulk Recombination through Defects. *The Journal of Physical Chemistry C* 2011, **115**(32)**:** 16037-16042.
13. Liu B, Zhao X, Terashima C, Fujishima A, Nakata K. Thermodynamic and kinetic analysis of heterogeneous photocatalysis for semiconductor systems. *Physical Chemistry Chemical Physics* 2014, **16**(19)**:** 8751-8751.
14. Akselrod GM, Deotare PB, Thompson NJ, Lee J, Tisdale WA, Baldo MA*, et al.* Visualization of exciton transport in ordered and disordered molecular solids. *Nature Communications* 2014, **5**(1)**:** 3646-3646.
15. Tang KW, Li S, Weeden S, Song Z, McClintock L, Xiao R*, et al.* Transport Modelling of Locally Photogenerated Excitons in Halide Perovskites. *The Journal of Physical Chemistry Letters* 2021, **12**(16)**:** 3951-3959.
16. Chen P, Atallah TL, Lin Z, Wang P, Lee SJ, Xu J*, et al.* Approaching the intrinsic exciton physics limit in two-dimensional semiconductor diodes. *Nature* 2021, **599**(7885)**:** 404-410.
17. Merkl P, Mooshammer F, Steinleitner P, Girnghuber A, Lin KQ, Nagler P*, et al.* Ultrafast transition between exciton phases in van der Waals heterostructures. *Nature Materials*: Nature Publishing Group; 2019. pp. 691-696.
18. Voznyy O, Sutherland BR, Ip AH, Zhitomirsky D, Sargent EH. Engineering charge transport by heterostructuring solution-processed semiconductors. *Nature Reviews Materials* 2017, **2**(May)**:** 1-10.
19. Cass MJ, Duffy NW, Peter LM, Pennock SR, Ushiroda S, Walker AB. Microwave Reflectance Studies of Photoelectrochemical Kinetics at Semiconductor Electrodes. 2. Hydrogen Evolution at p-Si in Ammonium Fluoride Solution. *The Journal of Physical Chemistry B* 2003, **107**(24)**:** 5864-5870.

20. Zhang Z, Yates JT. Band Bending in Semiconductors: Chemical and Physical Consequences at Surfaces and Interfaces. *Chemical Reviews* 2012, **112**(10)**:** 5520-5551.
21. Bisquert J, Garcia-Belmonte G, x000E, Fabregat-Santiago F. Modelling the electric potential distribution in the dark in nanoporous semiconductor electrodes. *Journal of Solid State Electrochemistry* 1999, **3**(6)**:** 337-347.
22. Laskowski FAL, Oener SZ, Nellist MR, Gordon AM, Bain DC, Fehrs JL*, et al.* Nanoscale semiconductor/catalyst interfaces in photoelectrochemistry. *Nature Materials* 2020, **19**(1)**:** 69-76.
23. Pan Z, Yanagi R, Wang Q, Shen X, Zhu Q, Xue Y*, et al.* Mutually-dependent kinetics and energetics of photocatalyst/co-catalyst/two-redox liquid junctions. *Energy & Environmental Science* 2020, **13**(1)**:** 162-173.
24. Walter MG, Warren EL, McKone JR, Boettcher SW, Mi Q, Santori EA*, et al.* Solar Water Splitting Cells. *Chemical Reviews* 2010, **110**(11)**:** 6446-6473.
25. Tung RT. The physics and chemistry of the Schottky barrier height. *Applied Physics Reviews* 2014, **1**(1)**:** 011304-011304.
26. Gaudy YK, Haussener S. Utilizing modeling, experiments, and statistics for the analysis of water-splitting photoelectrodes. *Journal of Materials Chemistry A* 2016, **4**(8)**:** 3100-3114.
27. Waegele MM, Gunathunge CM, Li J, Li X. How cations affect the electric double layer and the rates and selectivity of electrocatalytic processes. *The Journal of Chemical Physics* 2019, **151**(16)**:** 160902-160902.
28. Hisatomi T, Minegishi T, Domen K. Kinetic Assessment and Numerical Modeling of Photocatalytic Water Splitting toward Efficient Solar Hydrogen Production. *Bulletin of the Chemical Society of Japan* 2012, **85**(6)**:** 647-655.
29. Laurence MP. Part 1 Fundamental Aspects of Photocatalysis. *Royal Society of Chemistry* 2016**:** 1-28.
30. Uddin MT, Nicolas Y, Olivier C, Toupance T, Müller MM, Kleebe H-J*, et al.* Preparation of RuO2/TiO2 Mesoporous Heterostructures and Rationalization of Their Enhanced Photocatalytic Properties by Band Alignment Investigations. *The Journal of Physical Chemistry C* 2013, **117**(42)**:** 22098-22110.

31. Li L, Salvador PA, Rohrer GS. Photocatalysts with internal electric fields. *Nanoscale* 2014, **6**(1)**:** 24-42.
32. Mills A, Duckmanton PA, Reglinski J. A simple, novel method for preparing an effective water oxidation catalyst. *Chemical Communications* 2010, **46**(14)**:** 2397-2398.
33. Mills TJ, Lin F, Boettcher SW. Theory and Simulations of Electrocatalyst-Coated Semiconductor Electrodes for Solar Water Splitting. *Physical Review Letters* 2014, **112**(14)**:** 148304-148304.
34. Nellist MR, Laskowski FAL, Lin F, Mills TJ, Boettcher SW. Semiconductor–Electrocatalyst Interfaces: Theory, Experiment, and Applications in Photoelectrochemical Water Splitting. *Accounts of Chemical Research* 2016, **49**(4)**:** 733-740.
35. Yan F, Wang Y, Zhang J, Lin Z, Zheng J, Huang F. Schottky or Ohmic Metal-Semiconductor Contact: Influence on Photocatalytic Efficiency of Ag/ZnO and Pt/ZnO Model Systems. *ChemSusChem* 2014, **7**(1)**:** 101-104.
36. Iqbal A, Bevan KH. Simultaneously Solving the Photovoltage and Photocurrent at Semiconductor–Liquid Interfaces. *The Journal of Physical Chemistry C* 2018, **122**(1)**:** 30-43.
37. Fajardo AM, Lewis NS. Free-Energy Dependence of Electron-Transfer Rate Constants at Si/Liquid Interfaces. *The Journal of Physical Chemistry B* 1997, **101**(51)**:** 11136-11151.
38. Suzuki H, Nitta S, Tomita O, Higashi M, Abe R. Highly Dispersed RuO2 Hydrates Prepared via Simple Adsorption as Efficient Cocatalysts for Visible-Light-Driven Z-Scheme Water Splitting with an IO3-/I- Redox Mediator. *ACS Catalysis* 2017, **7**(7)**:** 4336-4343.
39. Abe R, Higashi M, Domen K. Overall water splitting under visible light through a two-step photoexcitation between TaON and WO3 in the presence of an iodate-iodide shuttle redox mediator. *ChemSusChem* 2011, **4**(2)**:** 228-237.
40. Montoya JF, Salvador P. The influence of surface fluorination in the photocatalytic behaviour of TiO2 aqueous dispersions: An analysis in the light of the direct–indirect kinetic model. *Applied Catalysis B: Environmental* 2010, **94**(1-2)**:** 97-107.

41. Monllor-Satoca D, Gómez R, González-Hidalgo M, Salvador P. The "Direct–Indirect" model: An alternative kinetic approach in heterogeneous photocatalysis based on the degree of interaction of dissolved pollutant species with the semiconductor surface. *Catalysis Today* 2007, **129**(1-2)**:** 247-255.
42. Dimitrijevic NM, Vijayan BK, Poluektov OG, Rajh T, Gray KA, He H*, et al.* Role of Water and Carbonates in Photocatalytic Transformation of CO ₂ to CH ₄ on Titania. *Journal of the American Chemical Society* 2011, **133**(11)**:** 3964-3971.
43. Berardo E, Zwijnenburg MA. Modeling the Water Splitting Activity of a TiO ₂ Rutile Nanoparticle. *The Journal of Physical Chemistry C* 2015, **119**(24)**:** 13384-13393.
44. Can F, Courtois X, Duprez D. Tungsten-Based Catalysts for Environmental Applications. *Catalysts* 2021, **11**(6)**:** 703-703.
45. Roger I, Shipman MA, Symes MD. Earth-abundant catalysts for electrochemical and photoelectrochemical water splitting. *Nature Reviews Chemistry* 2017, **1**(1)**:** 3-3.
46. Kim JH, Lee JS. Elaborately Modified BiVO 4 Photoanodes for Solar Water Splitting. *Advanced Materials* 2019, **31**(20)**:** 1806938-1806938.
47. Kuang Y, Yamada T, Domen K. Surface and Interface Engineering for Photoelectrochemical Water Oxidation. *Joule* 2017, **1**(2)**:** 290-305.
48. Laskowski FAL, Nellist MR, Qiu J, Boettcher SW. Metal Oxide/(oxy)hydroxide Overlayers as Hole Collectors and Oxygen-Evolution Catalysts on Water-Splitting Photoanodes. *Journal of the American Chemical Society* 2019, **141**(4)**:** 1394-1405.
49. Lin F, Boettcher SW. Adaptive semiconductor/electrocatalyst junctions in water-splitting photoanodes. *Nature Materials* 2014, **13**(1)**:** 81-86.
50. Iwase Y, Tomita O, Higashi M, Abe R. Enhanced oxygen evolution on visible light responsive TaON photocatalysts co-loaded with highly active Ru species for IO 3 – reduction and Co species for water oxidation. *Sustainable Energy & Fuels* 2017, **1**(4)**:** 748-754.
51. Maeda K, Abe R, Domen K. Role and function of ruthenium species as promoters with TaON-based photocatalysts for oxygen evolution in two-step water splitting under visible light. *Journal of Physical Chemistry C* 2011, **115**(7)**:** 3057-3064.

52. Banerjee T, Podjaski F, Kröger J, Biswal BP, Lotsch BV. Polymer photocatalysts for solar-to-chemical energy conversion. *Nature Reviews Materials* 2021, **6**(2)**:** 168-190.
53. Keller N, Bein T. Optoelectronic processes in covalent organic frameworks. *Chemical Society Reviews* 2021, **50**(3)**:** 1813-1845.
54. Guiglion P, Butchosa C, Zwijnenburg MA. Polymer Photocatalysts for Water Splitting: Insights from Computational Modeling. *Macromolecular Chemistry and Physics* 2016, **217**(3)**:** 344-353.
55. Wang H, Jin S, Zhang X, Xie Y. Excitonic Effects in Polymeric Photocatalysts. *Angewandte Chemie International Edition* 2020, **59**(51)**:** 22828-22839.
56. Gottschling K, Savasci G, Vignolo-González H, Schmidt S, Mauker P, Banerjee T*, et al.* Rational Design of Covalent Cobaloxime–Covalent Organic Framework Hybrids for Enhanced Photocatalytic Hydrogen Evolution. *Journal of the American Chemical Society* 2020, **142**(28)**:** 12146-12156.
57. Biswal BP, Vignolo-González HA, Banerjee T, Grunenberg L, Savasci G, Gottschling K*, et al.* Sustained Solar H2 Evolution from a Thiazolo[5,4-d]thiazole-Bridged Covalent Organic Framework and Nickel-Thiolate Cluster in Water. *Journal of the American Chemical Society* 2019, **141**(28)**:** 11082-11092.
58. Sachs M, Sprick RS, Pearce D, Hillman SAJ, Monti A, Guilbert AAY*, et al.* Understanding structure-activity relationships in linear polymer photocatalysts for hydrogen evolution. *Nature Communications* 2018, **9**(1)**:** 4968-4968.
59. Banerjee T, Gottschling K, Savasci G, Ochsenfeld C, Lotsch BV. H2 Evolution with Covalent Organic Framework Photocatalysts. *ACS Energy Letters* 2018, **3**(2)**:** 400-409.
60. Huang X, Zhang Y-B. Covalent Organic Frameworks for Sunlight-driven Hydrogen Evolution. *Chemistry Letters* 2021, **50**(4)**:** 676-686.
61. Jin S, Supur M, Addicoat M, Furukawa K, Chen L, Nakamura T*, et al.* Creation of Superheterojunction Polymers via Direct Polycondensation: Segregated and Bicontinuous Donor–Acceptor π-Columnar Arrays in Covalent Organic Frameworks for Long-Lived Charge Separation. *Journal of the American Chemical Society* 2015, **137**(24)**:** 7817-7827.

62. Jakowetz AC, Hinrichsen TF, Ascherl L, Sick T, Calik M, Auras F*, et al.* Excited-State Dynamics in Fully Conjugated 2D Covalent Organic Frameworks. *Journal of the American Chemical Society* 2019, **141**(29)**:** 11565-11571.
63. Flanders NC, Kirschner MS, Kim P, Fauvell TJ, Evans AM, Helweh W*, et al.* Large Exciton Diffusion Coefficients in Two-Dimensional Covalent Organic Frameworks with Different Domain Sizes Revealed by Ultrafast Exciton Dynamics. *Journal of the American Chemical Society* 2020, **142**(35)**:** 14957-14965.
64. Banerjee T, Haase F, Savasci G, Gottschling K, Ochsenfeld C, Lotsch BV. Single-Site Photocatalytic H2 Evolution from Covalent Organic Frameworks with Molecular Cobaloxime Co-Catalysts. *Journal of the American Chemical Society* 2017, **139**(45)**:** 16228-16234.
65. Wang Y, Vogel A, Sachs M, Sprick RS, Wilbraham L, Moniz SJA*, et al.* Current understanding and challenges of solar-driven hydrogen generation using polymeric photocatalysts. *Nature Energy* 2019, **4**(9)**:** 746-760.
66. Haase F, Banerjee T, Savasci G, Ochsenfeld C, Lotsch BV. Structure–property–activity relationships in a pyridine containing azine-linked covalent organic framework for photocatalytic hydrogen evolution. *Faraday Discussions* 2017, **201:** 247-264.
67. Stegbauer L, Schwinghammer K, Lotsch BV. A hydrazone-based covalent organic framework for photocatalytic hydrogen production. *Chem Sci* 2014, **5**(7)**:** 2789-2793.
68. Zhang Y, Sajjad MT, Blaszczyk O, Parnell AJ, Ruseckas A, Serrano LA*, et al.* Large Crystalline Domains and an Enhanced Exciton Diffusion Length Enable Efficient Organic Solar Cells. *Chemistry of Materials* 2019, **31**(17)**:** 6548-6557.
69. Zhang W, Hong J, Zheng J, Huang Z, Zhou JS, Xu R. Nickel−Thiolate Complex Catalyst Assembled in One Step in Water for Solar H2 Production. *J Am ChemSoc* 2011, **133:** 20680−20683-20680−20683.
70. Schneider J, Bahnemann DW. Undesired Role of Sacrificial Reagents in Photocatalysis. *J Phys Chem Lett* 2013, **4:** 3479-3483.
71. Costantino F, Kamat PV. Do Sacrificial Donors Donate H2 in Photocatalysis? *ACS Energy Letters* 2021**:** 242-246.

72. Kagalwala HN, Gottlieb E, Li G, Li T, Jin R, Bernhard S. Photocatalytic Hydrogen Generation System Using a Nickel-Thiolate Hexameric Cluster. *Inorganic Chemistry* 2013, **52**(15)**:** 9094-9101.
73. Stewart MP, Ho M-H, Wiese S, Lindstrom ML, Thogerson CE, Raugei S*, et al.* High Catalytic Rates for Hydrogen Production Using Nickel Electrocatalysts with Seven-Membered Cyclic Diphosphine Ligands Containing One Pendant Amine. *Journal of the American Chemical Society* 2013, **135**(16)**:** 6033-6046.
74. Qureshi M, Garcia-Esparza AT, Shinagawa T, Sautet P, Le Bahers T, Takanabe K. Contribution of electrolyte in nanoscale electrolysis of pure and buffered water by particulate photocatalysis. *Sustainable Energy & Fuels* 2018, **2**(9)**:** 2044-2052.
75. Iqbal A, Bevan KH. The impact of boundary conditions on calculated photovoltages and photocurrents at photocatalytic interfaces. *MRS Communications* 2018, **8**(2)**:** 466-473.
76. Nadeem MA, Khan MA, Ziani AA, Idriss H. An Overview of the Photocatalytic Water Splitting over Suspended Particles. *Catalysts* 2021, **11**(1)**:** 60-60.
77. Zalazar CS, Romero RL, Martín CA, Cassano AE. Photocatalytic intrinsic reaction kinetics I: Mineralization of dichloroacetic acid. *Chemical Engineering Science* 2005, **60**(19)**:** 5240-5254.
78. Hernández S, Bensaid S, Armandi M, Sacco A, Chiodoni A, Bonelli B*, et al.* A new method for studying activity and reaction kinetics of photocatalytic water oxidation systems using a bubbling reactor. *Chemical Engineering Journal* 2014, **238:** 17-26.
79. Yoshida H, Kinjo T, Washizu H. Numerical simulation method for Brownian particles dispersed in incompressible fluids. *Chemical Physics Letters* 2019, **737:** 136809-136809.
80. Mynam M, Sunthar P, Ansumali S. Efficient lattice Boltzmann algorithm for Brownian suspensions. *Philosophical Transactions of the Royal Society A: Mathematical, Physical and Engineering Sciences* 2011, **369**(1944)**:** 2237-2245.
81. Wengeler R, Nirschl H. Turbulent hydrodynamic stress induced dispersion and fragmentation of nanoscale agglomerates. *Journal of Colloid and Interface Science* 2007, **306**(2)**:** 262-273.

82. Amanulla CH, Nagendra N, Suryanarayana Reddy M. Computational analysis of non-Newtonian boundary layer flow of nanofluid past a semi-infinite vertical plate with partial slip. *Nonlinear Engineering* 2018, **7**(1)**:** 29-43.
83. Mao Z, Yang C. Computational chemical engineering – Towards thorough understanding and precise application. *Chinese Journal of Chemical Engineering* 2016, **24**(8)**:** 945-951.
84. Fischer SA, Dunlap BI, Gunlycke D. Correlated dynamics in aqueous proton diffusion. *Chemical Science* 2018, **9**(35)**:** 7126-7132.
85. Ubbelohde AR. The mutual diffusion coefficient of ethanol–water mixtures: determination by a rapid, new method. *Proceedings of the Royal Society of London A Mathematical and Physical Sciences* 1974, **336**(1606)**:** 393-406.
86. Fitschen J, Hofmann S, Wutz J, Kameke Av, Hoffmann M, Wucherpfennig T*, et al.* Novel evaluation method to determine the local mixing time distribution in stirred tank reactors. *Chemical Engineering Science: X* 2021, **10:** 100098-100098.
87. Sander R. Compilation of Henry's law constants (version 4.0) for water as solvent. *Atmospheric Chemistry and Physics* 2015, **15**(8)**:** 4399-4981.
88. Goto Y, Hisatomi T, Wang Q, Higashi T, Ishikiriyama K, Maeda T*, et al.* A Particulate Photocatalyst Water-Splitting Panel for Large-Scale Solar Hydrogen Generation. *Joule* 2018, **2**(3)**:** 509-520.
89. Chen S, Takata T, Domen K. Particulate photocatalysts for overall water splitting. *Nature Publishing Group* 2017, **2:** 1-17.
90. Qureshi M, Takanabe K. Insights on measuring and reporting heterogeneous photocatalysis: Efficiency definitions and setup examples. *Chemistry of Materials* 2017, **29**(1)**:** 158-167.
91. Wang Z, Hisatomi T, Li R, Sayama K, Liu G, Domen K*, et al.* Efficiency Accreditation and Testing Protocols for Particulate Photocatalysts toward Solar Fuel Production. *Joule* 2021, **5**(2)**:** 344-359.
92. Kisch H, Bahnemann D. Best Practice in Photocatalysis: Comparing Rates or Apparent Quantum Yields? *Journal of Physical Chemistry Letters* 2015, **6**(10)**:** 1907-1910.

93. Emeline AV, Ryabchuk VK, Serpone N. Dogmas and Misconceptions in Heterogeneous Photocatalysis. Some Enlightened Reflections. *The Journal of Physical Chemistry B* 2005, **109**(39)**:** 18515-18521.
94. Cabrera MI, Alfano OM, Cassano AE. Novel Reactor for Photocatalytic Kinetic Studies. *Industrial & Engineering Chemistry Research* 1994, **33**(12)**:** 3031-3042.
95. Emeline AV, Zhang X, Jin M, Murakami T, Fujishima A. Application of a "black body" like reactor for measurements of quantum yields of photochemical reactions in heterogeneous systems. *Journal of Physical Chemistry B* 2006, **110**(14)**:** 7409-7413.
96. Megatif L, Dillert R, Bahnemann DW. Reaction rate study of the photocatalytic degradation of dichloroacetic acid in a black body reactor. *Catalysts* 2019, **9**(8)**:** 635-652.
97. Megatif L, Dillert R, Bahnemann DW. Determination of the quantum yield of a heterogeneous photocatalytic reaction employing a black body photoreactor. *Catalysis Today* 2019.
98. Serpone N. Relative photonic efficiencies and quantum yields in heterogeneous photocatalysis. *Journal of Photochemistry and Photobiology A: Chemistry* 1997, **104:** 1-12.
99. Kunz LY, Diroll BT, Wrasman CJ, Riscoe AR, Majumdar A, Cargnello M. Artificial inflation of apparent photocatalytic activity induced by catalyst-mass-normalization and a method to fairly compare heterojunction systems. *Energy and Environmental Science* 2019, **12**(5)**:** 1657-1667.
100. Miranda-Muñoz JM, Esteso V, Jiménez-Solano A, Lozano G, Míguez H. Finite Size Effects on Light Propagation throughout Random Media: Relation between Optical Properties and Scattering Event Statistics. *Advanced Optical Materials* 2020, **8**(1)**:** 1901196-1901196.
101. Yang J, Yan H, Zong X, Wen F, Liu M, Li C. Roles of cocatalysts in semiconductor-based photocatalytic hydrogen production. *Philosophical Transactions of the Royal Society A: Mathematical, Physical and Engineering Sciences* 2013, **371**(1996)**:** 20110430-20110430.

102. Serpone N, Salinaro A. Terminology, relative photonic efficiencies and quantum yields in heterogeneous photocatalysis. Part I: Suggested protocol (Technical Report). *Pure and Applied Chemistry* 1999, **71**(2)**:** 303-320.
103. Bangle RE, Schneider J, Piechota EJ, Troian-Gautier L, Meyer GJ. Electron Transfer Reorganization Energies in the Electrode–Electrolyte Double Layer. *Journal of the American Chemical Society* 2020, **142**(2)**:** 674-679.
104. Guidelli R, Compton RG, Feliu JM, Gileadi E, Lipkowski J, Schmickler W*, et al.* Defining the transfer coefficient in electrochemistry: An assessment (IUPAC Technical Report). *Pure and Applied Chemistry* 2014, **86**(2)**:** 245-258.
105. Hotze EM, Phenrat T, Lowry GV. Nanoparticle Aggregation: Challenges to Understanding Transport and Reactivity in the Environment. *Journal of Environmental Quality* 2010, **39**(6)**:** 1909-1924.
106. Endres SC, Ciacchi LC, Mädler L. A review of contact force models between nanoparticles in agglomerates, aggregates, and films. *Journal of Aerosol Science* 2021, **153:** 105719-105719.
107. Tsuda A, Konduru NV. The role of natural processes and surface energy of inhaled engineered nanoparticles on aggregation and corona formation. *NanoImpact* 2016, **2:** 38-44.
108. Henry C, Minier J-P, Pozorski J, Lefèvre G. A New Stochastic Approach for the Simulation of Agglomeration between Colloidal Particles. *Langmuir* 2013, **29**(45)**:** 13694-13707.
109. Kim H-Y, Sofo JO, Velegol D, Cole MW, Lucas AA. Van der Waals Dispersion Forces between Dielectric Nanoclusters. *Langmuir* 2007, **23**(4)**:** 1735-1740.
110. Jiang J, Oberdörster G, Biswas P. Characterization of size, surface charge, and agglomeration state of nanoparticle dispersions for toxicological studies. *Journal of Nanoparticle Research* 2009, **11**(1)**:** 77-89.
111. Suttiponparnit K, Jiang J, Sahu M, Suvachittanont S, Charinpanitkul T, Biswas P. Role of Surface Area, Primary Particle Size, and Crystal Phase on Titanium Dioxide Nanoparticle Dispersion Properties. *Nanoscale Research Letters* 2010, **6**(1)**:** 27-27.

112. Zhang B, Zhang C, He H, Yu Y, Wang L, Zhang J. Electrochemical Synthesis of Catalytically Active Ru/RuO 2 Core−Shell Nanoparticles without Stabilizer. *Chemistry of Materials* 2010, **22**(13)**:** 4056-4061.
113. Braslavsky SE, Braun AM, Cassano AE, Emeline AV, Litter MI, Palmisano L*, et al.* Glossary of terms used in photocatalysis and radiation catalysis (IUPAC Recommendations 2011). *Pure and Applied Chemistry* 2011, **83**(4)**:** 931-1014.
114. Dilla M, Moustakas NG, Becerikli AE, Peppel T, Springer A, Schlo R*, et al.* Judging the feasibility of TiO2 as photocatalyst for chemical energy conversion by quantitative reactivity determinants. *Phys Chem Chem Phys* 2019, **21:** 13144-13150.
115. Wachs IE, Phivilay SP, Roberts CA. Reporting of reactivity for heterogeneous photocatalysis. *ACS Catalysis* 2013, **3**(11)**:** 2606-2611.
116. Kröger J, Jiménez - Solano A, Savasci G, Rovó P, Moudrakovski I, Küster K*, et al.* Photocatalytic Hydrogen Evolution: Interfacial Engineering for Improved Photocatalysis in a Charge Storing 2D Carbon Nitride: Melamine Functionalized Poly(heptazine imide). *Advanced Energy Materials* 2021, **11**(6)**:** 2170028-2170028.
117. Takata T, Jiang J, Sakata Y, Nakabayashi M, Shibata N, Nandal V*, et al.* Photocatalytic water splitting with a quantum efficiency of almost unity. *Nature* 2020, **581**(7809)**:** 411-414.
118. Wang Q, Hisatomi T, Jia Q, Tokudome H, Zhong M, Wang C*, et al.* Scalable water splitting on particulate photocatalyst sheets with a solar-to-hydrogen energy conversion efficiency exceeding 1%. *Nature Materials* 2016, **15**(6)**:** 611-615.
119. Pougin A, Dilla M, Strunk J. Identification and exclusion of intermediates of photocatalytic CO2 reduction on TiO2 under conditions of highest purity. *Physical Chemistry Chemical Physics* 2016, **18:** 10809-10817.
120. Dilla M, Schlçgl R, Strunk J. Photocatalytic CO2 Reduction Under Continuous Flow High-Purity Conditions : Quantitative Evaluation of CH4 Formation in the Steady-State. *ChemCatChem* 2017, **9:** 696-704.
121. Antoniadou M, Zachariadis GA, Rosenberg E. Investigating the performance characteristics of the barrier discharge ionization detector and comparison to the

flame ionization detector for the gas chromatographic analysis of volatile and semivolatile organic compounds. *Analytical Letters* 2019, **52**(17)**:** 2822-2839.

122. Dilla M, Jakubowski A, Strunk J, Ristig S, Strunk J, Schlögl R. The fate of O2 in photocatalytic CO2 reduction on TiO2 under conditions of highest purity. *PhysChemChemPhys* 2019, **21:** 15949-15957.
123. Detz RJ, Abiri Z, Kluwer AM, Reek JNH. A Fluorescence-Based Screening Protocol for the Identification of Water Oxidation Catalysts. *ChemSusChem* 2015, **8**(18)**:** 3057-3061.

3. Research Objective and Methods

It has become apparent that material research and optimization in artificial photosynthesis entails simultaneous tuning of multiple aspects of a photocatalyst. As will be described in Chapter 4 and Chapter 6, such tuning can focus on light absorption and charge separation to obtain higher photonic efficiencies in measured HER rates (TpDTz COF with Ni-ME cocatalyst) or cocatalyst engineering to obtain higher OER rates while keeping the light-harvester material unchanged (WO_3 nanoparticles decorated by ruthenium oxide nanosheets). In Chapter 5 it will be shown that photocatalyst engineering can also focus on a material benchmark for photocatalytic OER rates with moderate external photonic efficiency, yet with a reproducible internal quantum efficiency (commercial TiO_2 nanoparticles decorated with RuO_x clusters). In all these cases, where the detection platforms allow so, OER and HER rate measurements can unravel additional information on photocatalytic reaction kinetics, for example by means of reactant isotope labeling (like D_2O, or $H_2{}^{18}O$) or dynamic reaction trend modelling and analysis.[1,2]

The first goal of this thesis is to prove that alternative detection techniques used in gas chromatography, like a barrier ionization discharge detector (BID), can be a more suitable option compared to existing commercial detectors for the purpose of universal, simultaneous, precise, and sensitive detection of all gas products involved in artificial photosynthesis. Additionally, sensitive detection and analyte mass identification by a coupled mass spectrometer (MS) will enable the use of flow reactors to study reaction rates dynamically.

In Section 2.3 it is described the artificial photosynthesis potential of COF materials is described by the tailoring of their optoelectronic properties to enhance η_{abs} and η_{sep}. The TpDTz COF used as a model system to prove HER photocatalytic rates fine detection has a suitable optical bandgap (2.2 eV) and photocatalytic properties for HER. The Ni-ME cocatalyst is described in Section 2.4 as necessary to enable the immediate increase of η_{cat}, and indirect improvement of η_{sep} due to less accumulation of surface excitons. The GC-BID scheme is a crucial asset for the results presented in Chapter 4. In Chapter 4, the BID detector is used to track traces of produced H_2 under illumination in a flow

configuration more convenient for rate quantification and dynamic reaction trend measurements, which provides a crucial input to fit mathematical models of electron transfer mechanisms between the TpDTz COF and the Ni-ME cocatalyst; whereas the MS detector is used to check a necessary condition for water-proton reduction (*m*/*z* shift of H_2 signal when D_2O replaces H_2O). The GC-MS/BID hardware implementation has been not only refinement in detection of HER rates, but it has also deepened top-down approaches to unravel and simplify intricate multiphysics problems in photocatalysis, like the microkinetic model elaborated for the TpDTz COF with Ni-ME cocatalyst in Chapter 4. Such models are fundamentally difficult to resolve without rigorous means of product detection.

Besides setup sensitivity, which is granted for both HER and OER reactions using the proposed GC-BID/MS and photo reactor platform just described, in Chapter 5 we list other considerations that must be considered in the field of OER. For example, the need of minimizing the influence of adventitious OER rates from sacrificial electron acceptor reduction (i.e., IO_3^- shuttle) and external O_2 leakages. Additionally, as described in Section 2.6, comparison of HER and OER photocatalytic rates among different groups is not a trivial problem due to the presence of light scattering in the standard photo reactor design in the literature.

In this way, the second goal of this thesis is to establish a combination of material research and best practices in photocatalysis to elaborate a reproducible benchmark (TiO_2/RuO_2) for photocatalytic water oxidation, facilitating comparison of OER rates among different groups.

In Chapter 5, a benchmark photocatalyst for water oxidation is presented to answer to this problematic (TiO_2/RuO_2). This investigation on this model TiO_2/RuO_2 OER system aims to normalize OER rates obtained for other novel materials. The decoration of a RuO_2 cocatalyst on P25 is necessary to overcome kinetic water oxidation limitations affecting the intrinsic η_{abs} and η_{sep} of the base P25 material, as described in Section 2.1 and Section 2.2.[3,4] Together with showing the avenues for comparison of rates in the field, i.e., using the concepts of relative optimal photonic efficiency and internal quantum efficiency,

Chapter 5 also highlights a set of best practices of our research group that has made our OER rates quantification reliable even in the presence of parasitic reactions of sacrificial agents.[5,6] The properties crucial for photocatalysis of the chosen RuO_2 cocatalysts are also tracked for photocatalytic OER performance (hydrothermally and photo-deposited on P25) and simultaneously characterized (i.e., crystallinity and uniformity on P25) using conventional techniques like powder X-ray diffraction (PXRD), UV-Vis powder diffuse reflectance spectroscopy (PDRS), and transmission electron microscopy (TEM) for morphology. Additionally, techniques more sensitive to the surface features of the photocatalyst were performed on the TiO_2/RuO_2 system, to access the very nature of the catalyst decorated. These techniques correspond to X-ray photoelectron spectroscopy (XPS), and complementary techniques to TEM, like energy dispersive X-ray spectroscopy (TEM-EDX), and Fast Fourier Transform (TEM-FFT). As a result, the developed OER cocatalyst deposited on P25 presented is identified unequivocally as a combination of Ru^0 and anhydrous RuO_2, whose role in photocatalysis is well identified in literature as charge separation (i.e., Schottky junction) and lower activation energy for electron transfer reactions (HER and OER), respectively.

The cocatalyst research in Chapter 5 aims to find a highly reproducible TiO_2/RuO_2 composite, whose optimization process considers photonic efficiency as a requirement of a minimum detectable quantity only. This approach ignores more fundamental aspects of cocatalyst properties engineering to obtain higher photonic efficiencies suitable for industrial POWS applications, like cocatalyst structure and morphology, and the applicability of the light-harvester in real artificial photosynthesis where visible light response is desired. Regarding the latter, the light harvester of the system is switched to WO_3. WO_3 is one of the most active visible light responsive OER materials, commercially available (100 nm nanoparticles), and like TiO_2, suitable to work with IO_3^- as electron acceptor shuttle.[7-11]

Consequently, the third goal of this thesis is to expand the concepts in Chapter 5 to a more contingent optimization goal for the field of artificial photosynthesis, in this case, a morphology engineered cocatalyst that rationally increases the OER photonic efficiency

of WO_3, based on the cocatalyst low-dimensional shape (nanosheets) and electrocatalytic properties.

The multiple roles of the RuO_2 cocatalyst in enhancing the η_{abs} and η_{sep} of the base WO_3 light-harvester are described in Section 2.2. Taking advantage of our accumulated expertise in OER photocatalysis best practices and cocatalyst characterization, including fine and high throughput detection methods, in Chapter 6 a ruthenium oxide cocatalyst is engineered in morphological and structural properties away from the default 0D cocatalyst shape of conventional deposition methods, and decorated on WO_3 to rationally optimize photocatalytic OER rates. In Chapter 6, WO_3 is decorated with a conventional form of anhydrous RuO_2 via impregnation-calcination methods (RONP), to produce a baseline anisotropic and randomly distributed RuO_2 cocatalyst nanoparticle previously reported in the literature.[7,9] This baseline material is coined as 0D/0D in terms of low-dimensional morphology (WO_3/RONP). Then, a top-down approach to produce ruthenium oxide nanosheets (RONS) is developed. RONSs are a mixed valence ruthenate (Ru(III) and Ru(IV)).[12] It is then identified that the resulting 0D/2D morphology from the WO_3 impregnated with RONS colloids (WO_3/RONS) has two main features that increase OER rates up to 5 times compared to the baseline composite (WO_3/RONP). Firstly, the RONS is a more electrocatalytically active material compared to conventional RuO_2 rutile, due to the previously reported edge structure of the ruthenate constituent of the RONS.[12] Secondly, WO_3/RONS has less parasitic light absorption. This beneficial optical trade arises as a combination of RONS optical properties, and the beneficial light-shielded cocatalyst arising from the 0D/2D morphology, which controls the parasitic light absorption of the cocatalyst and thus minimizes optical losses — associated to η_{abs}— of the resulting photocatalyst. The presented 0D/2D morphology in Chapter 6 has no precedent in the field of OER photocatalysis and it has been developed owing to a unique combination of multidisciplinary material research and relying on the OER detection techniques presented hereto. These results highlight the importance of rational cocatalyst tuning as an integral part of photocatalyst optimization to obtain higher photonic efficiencies.

3.4 References

1. Biswal BP, Vignolo-González HA, Banerjee T, Grunenberg L, Savasci G, Gottschling K*, et al.* Sustained Solar H2 Evolution from a Thiazolo[5,4-d]thiazole-Bridged Covalent Organic Framework and Nickel-Thiolate Cluster in Water. *Journal of the American Chemical Society* 2019, **141**(28)**:** 11082-11092.
2. Vignolo-González HA, Laha S, Jiménez-Solano A, Oshima T, Duppel V, Schützendübe P*, et al.* Toward Standardized Photocatalytic Oxygen Evolution Rates Using RuO2@TiO2 as a Benchmark. *Matter* 2020, **3**(2)**:** 464-486.
3. Dilla M, Jakubowski A, Strunk J, Ristig S, Strunk J, Schlögl R. The fate of O2 in photocatalytic CO2 reduction on TiO2 under conditions of highest purity. *PhysChemChemPhys* 2019, **21:** 15949-15957.
4. Dilla M, Moustakas NG, Becerikli AE, Peppel T, Springer A, Schlo R*, et al.* Judging the feasibility of TiO2 as photocatalyst for chemical energy conversion by quantitative reactivity determinants. *Phys Chem Chem Phys* 2019, **21:** 13144-13150.
5. Costantino F, Kamat PV. Do Sacrificial Donors Donate H2 in Photocatalysis? *ACS Energy Letters* 2021**:** 242-246.
6. Schneider J, Bahnemann DW. Undesired Role of Sacrificial Reagents in Photocatalysis. *J Phys Chem Lett* 2013, **4:** 3479-3483.
7. Abe R, Higashi M, Domen K. Overall water splitting under visible light through a two-step photoexcitation between TaON and WO3 in the presence of an iodate-iodide shuttle redox mediator. *ChemSusChem* 2011, **4**(2)**:** 228-237.
8. Abe R, Sayama K, Sugihara H. Development of new photocatalytic water splitting into H2 and O2 using two different semiconductor photocatalysts and a shuttle redox mediator IO3-/I. *Journal of Physical Chemistry B* 2005, **109**(33)**:** 16052-16061.
9. Suzuki H, Nitta S, Tomita O, Higashi M, Abe R. Highly Dispersed RuO2 Hydrates Prepared via Simple Adsorption as Efficient Cocatalysts for Visible-Light-Driven Z-Scheme Water Splitting with an IO3-/I- Redox Mediator. *ACS Catalysis* 2017, **7**(7)**:** 4336-4343.

10. Fujioka Y, Frantti J, Asiri AM, Obaid AY, Jiang H, Nieminen RM. Structural Properties of Pure and Nickel-Modified Nanocrystalline Tungsten Trioxide. *The Journal of Physical Chemistry C* 2012, **116**(32)**:** 17029-17039.
11. Fujioka Y, Frantti J, Nieminen RM, Asiri AM. Formation of ruthenium cluster on nanocrystalline tungsten trioxide. *Journal of Physical Chemistry C* 2013, **117**(15)**:** 7506-7510.
12. Laha S, Lee Y, Podjaski F, Weber D, Duppel V, Schoop LM*, et al.* Ruthenium Oxide Nanosheets for Enhanced Oxygen Evolution Catalysis in Acidic Medium. *Advanced Energy Materials* 2019, **9**(15)**:** 1803795-1803795.

4. Insights into Photocatalytic Hydrogen Evolution Rates on Covalent Organic Frameworks through Homogeneous Reaction Modelling

The work in this chapter was reproduced and adapted from:

Sustained Solar H_2 Evolution from a Thiazolo[5,4-*d*]thiazole-Bridged Covalent Organic Framework and Nickel-Thiolate Cluster in Water

Bishnu P. Biswal, Hugo A. Vignolo-González*, Tanmay Banerjee, Lars Grunenberg, Gökcen Savasci, Kerstin Gottschling, Jürgen Nuss, Christian Ochsenfeld, and Bettina V. Lotsch

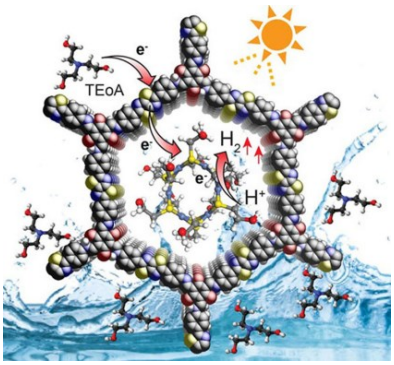

published in *J. Am. Chem. Soc.* 2019, 141, 28, 11082–11092
DOI: 10.1021/jacs.9b03243
https://pubs.acs.org/doi/full/10.1021/jacs.9b03243
Numbering of figures and headings were changed
Adapted with permission from ACS and First Author
(Electronic Supporting Information in Appendix B)

* Hugo A. Vignolo-González conceived the reactor engineering design and construction used for photocatalytic rate measurements, including data processing and refining, and photocatalysis figures of merit calculations and analysis. Coarse grain reaction mechanisms of molecular Ni-Me catalyst were drafted in collaboration with the First Author, Tanmay Banerjee and Bettina V. Lotsch. Mathematical modelling and data fitting were solely performed by Hugo A. Vignolo-González, and reaction insights into reaction rate limiting steps were elaborated in collaboration with the First Author, Tanmay Banerjee and Bettina V. Lotsch.

4.1 Abstract

Solar hydrogen (H_2) evolution from water utilizing covalent organic frameworks (COFs) as heterogeneous photosensitizers has gathered significant momentum by virtue of the COFs' predictive structural design, long-range ordering, tunable porosity, and excellent light-harvesting ability. However, most photocatalytic systems involve rare and expensive platinum as the co-catalyst for water reduction, which appears to be the bottleneck in the development of economical and environmentally benign solar H_2 production systems. Herein, we report a simple, efficient, and low-cost all-in-one photocatalytic H_2 evolution system composed of a thiazolo[5,4-*d*]thiazole-linked COF (**TpDTz**) as the photoabsorber and an earth-abundant, noble-metal-free nickel-thiolate hexameric cluster co-catalyst assembled *in situ* in water, together with triethanolamine (TEoA) as the sacrificial electron donor. The high crystallinity, porosity, photochemical stability, and light absorption ability of the **TpDTz** COF enables excellent long-term H_2 production over 70 h with a maximum rate of 941 μmol h^{-1} g^{-1}, turnover number TON_{Ni} > 103, and total projected TON_{Ni} > 443 until complete catalyst depletion. The high H_2 evolution rate and TON, coupled with long-term photocatalytic operation of this hybrid system in water, surpass those of many previously known organic dyes, carbon nitride, and COF-sensitized photocatalytic H_2O reduction systems. Furthermore, we gather unique insights into the reaction mechanism, enabled by a specifically designed continuous-flow system for non-invasive, direct H_2 production rate monitoring, providing higher accuracy in quantification compared to the existing batch measurement methods. Overall, the results presented here open the door toward the rational design of robust and efficient earth-abundant COF–molecular co-catalyst hybrid systems for sustainable solar H_2 production in water.

4.2 Introduction

The conversion and storage of solar energy in the form of chemical bonds in "solar fuels" like H_2 through light-driven water reduction has evolved into a key technology over the past decade due to the fast depletion of fossil energy sources and rapid global climate change.[1-6] To drive the proton reduction half-reaction in an efficient way, the major challenge is to find a catalytic system that is robust and highly active, but at the same time low-cost and earth-abundant, in combination with a strongly absorbing, chemically

stable photosensitizer (PS).[7,8] In this regard, covalent organic frameworks (COFs)[9-12] have recently emerged as an exciting class of photoactive materials for light-driven H_2 production due to their tunable light-harvesting[13] and charge-transport properties.[14] In contrast to other porous materials, COFs are known for being mechanically robust and offering large accessible surface areas. By virtue of their modular geometric and electronic structures, COFs have attracted significant interest for a range of applications including adsorption, storage and separation,[15-19] chemical sensing,[20,21] electronics,[22,23] and catalysis.[24] In spite of their versatility, there are only few reports on COFs utilized as photoabsorbers for photocatalytic H_2 evolution so far.[25-30] Although it is rare and expensive, all except one of these works has employed metallic platinum as the co-catalyst to reduce water efficiently, which appears to be the bottleneck in the development of scalable, economical solar H_2 production. In addition, the use of nanoparticulate Pt co-catalysts precludes obtaining detailed insights into the nature of the catalytic sites and the intricacies of the photocatalytic cycle. Inspired by natural photosynthesis,[31] researchers worldwide are motivated by this shortcoming to search for single-site, earth-abundant, non-precious metal-based co-catalysts with well-defined catalytic centers. So far, only one molecular co-catalyst–COF system for photocatalytic H_2 evolution has been demonstrated.[32] This system is based on an azine-linked COF (N2-COF)[26] acting as the PS and a cobaloxime molecular proton reduction catalyst, which shows a H_2 evolution rate of 782 μmol h^{-1} g^{-1} and a turnover number TON_{Co} = 54.4. However, the limited photostability and especially the utilization of an organic solvent (acetonitrile/water mixture; 4:1) were major concerns.[32]

Notably, a majority of molecular catalysts decompose during prolonged catalysis, are inherently insoluble in water, and require the addition of organic solvents to accomplish water reduction.[33-37] With cobaloxime-based systems, for example, the catalyst often converts to an inactive form within a few hours (<6 h) of H_2 evolution, possibly due to ligand decomposition or hydrogenation.[38,39]

To overcome these issues, the development of a scalable, earth-abundant, and low-cost co-catalyst system which is soluble in water and can be coupled efficiently to a molecularly defined heterogeneous photoabsorber is in high demand. In this regard, Ni-based synthetic photocatalytic H_2 evolution catalysts[40-42] have attracted significant interest

because of their robust and oxygen-tolerant nature and, importantly, their structural similarity to the active site in [Ni-Fe] hydrogenase.[43-46]

Likewise, small molecules and polymers containing fused (bi)heterocyclic thiazolo[5,4-*d*]thiazole (TzTz) moieties have received much attention as semiconductors in organic electronics lately because of their n-type character featuring high oxidative stability and their rigid planar structure.[47] The latter enables efficient intermolecular π–π overlap that affords high electron and hole mobility.[47-50] Such TzTz moieties further feature excellent photoabsorbing ability, which is likewise beneficial for photocatalysis.[7] Nevertheless, TzTz-based COFs have not been explored so far. Notably, thus far, only a very limited number of COFs bearing photoactive functionalities such as triazine,[25,26] diacetylene,[27] or sulfone moieties[28] have been shown to produce H_2 from water, with the noble metal Pt acting as co-catalyst.

Combining these aforementioned leverages, in this work, we present a light-driven hybrid proton reduction system employing a newly designed TzTz-linked COF (**TpDTz**) as a photoabsorber and a molecular Ni-thiolate cluster (NiME)[51] assembled *in situ* from a Ni(II) salt and 2-mercaptoethanol (ME). The combination of the NiME cluster co-catalyst and **TpDTz** COF enables sustained H_2 evolution with an excellent rate (941 μmol h^{-1} g^{-1}) and a TON_{Ni} > 103 (70 h) in the presence of triethanolamine (TEoA) as the sacrificial electron donor (SED) in water under AM 1.5 light illumination. We thus report a single-site heterogeneous COF-based photocatalyst system that operates with a noble-metal-free co-catalyst in *water* as the solvent. We further carve out structure–property–activity relationships by comprehensively screening the parameter space of this heterogeneous–homogeneous hybrid photocatalytic system, including pH, SED, co-catalyst metal centers, different N/S-containing chelating ligands for co-catalysts, and a variety of PSs. Also, our study is built on a continuous-flow photocatalytic reactor system which enables a non-invasive and direct monitoring of the H_2 evolution rate with high accuracy, in contrast to the routinely used standard photocatalytic batch reactors, and this allows gathering unique insights into the photocatalytic reaction modeling and kinetics. The results and understanding presented here thus contribute toward the rational development of robust and efficient single-site hybrid photocatalytic systems as a sustainable solution for solar H_2 production in water.

4.3 Results and discussion

4.3.1 COF synthesis and characterization

The precursor 4,4′-(thiazolo[5,4-*d*]thiazole-2,5-diyl)dianiline (**DTz**) was synthesized as described in the Supporting Information (Appendix B) and characterized using single-crystal X-ray diffraction, nuclear magnetic resonance (NMR) spectroscopy, Fourier transform infrared (FTIR) spectroscopy, and mass spectrometry. **TpDTz** COF was synthesized by solvothermally reacting 1,3,5−triformylphloroglucinol; **Tp** (1.0 equiv) and **DTz** (1.5 equiv) in the presence of 6 M aqueous acetic acid using an *o*-dichlorobenzene and *N,N*-dimethylacetamide solvent combination in a high-precision glass vial, which was sealed and heated to 120 °C for 3 days (**Figure 4-1** and Appendix B, section B.2). Following a similar protocol, **TpDTP** COF with a similar pore size was synthesized as a reference,[52] with the **DTz** linker replaced with the linear terphenyl linker. To verify crystallinity and phase purity, the as-synthesized **TpDTz** COF was analyzed via powder X-ray diffraction (PXRD). The PXRD pattern exhibits an intense first peak at 2.56° 2θ corresponding to the 100 reflection along with other diffraction peaks at 4.41, 5.23, 6.90, and 9.10° 2θ, attributed to the 110, 200, 210, and 220 reflections, respectively. In addition, at ∼26° 2θ a broad set of reflections is visible, with 00l being the most intense, which corresponds to the π–π stacking of the 2D layers (**Figure 4-1**c). The experimental PXRD pattern is in good agreement with the simulated AA eclipsed stacking model (Figure B-6). The lattice parameters of **TpDTz** COF were extracted by Pawley refinement in the hexagonal space group *P*6/*m* (*a* = *b* = 39.27 Å, *c* = 3.46 Å, α = β = 90°, and γ = 120°) (**Figure 4-1**c). The relatively high level of order observed with PXRD may originate from effective π–π stacking interactions facilitated by the planarity of the **DTz** linker and, thus, the 2D layers. The measured pore aperture is ∼3.4 nm, and the π–π stacking distance between individual layers is ∼3.5 Å for **TpDTz** COF, as obtained from the structural model. The FTIR spectrum of the as-synthesized **TpDTz** COF shows bands at ∼1254 cm^{-1} (−C–N), ∼1571 cm^{-1} (C═C), and ∼1618 cm^{-1} (C═O) (Figure B-9), which confirms the formation of the proposed β-ketoenamine-linked framework. The TzTz moiety was identified by appearance of C═N vibrations (∼1660 cm^{-1}) and C–S stretching bands between 650 and

700 cm^{-1}. The structural composition of **TpDTz** COF was further confirmed by ^{13}C cross-polarization magic-angle spinning (CP-MAS) NMR spectroscopy (**Figure 4-2**a). The spectrum shows signals corresponding to the heterocyclic TzTz ring of the **DTz** building unit (δ ≈ 151 ppm), together with a characteristic signal of the carbonyl carbon (C═O) at ~184 ppm, which further supports formation of the β-ketoenamine moiety. ^{15}N NMR spectroscopy confirms the presence of two different kinds of nitrogen atoms with chemical shifts of −93 and −243 ppm, corresponding to the TzTz and enamine (═C–NH−) moieties, respectively (**Figure 4-2**a). All assignments are supported by quantum-chemical calculations of NMR chemical shifts (Tables S4 and S5) at the B97-2/pcS-2//PBE0-D3/def2-TZVP level using the FermiONs++ program package[53,54] based on a selected molecular model system (Figure B-49). The corresponding structures were optimized at the PBE0-D3/def2-TZVP level using Turbomole (version 7.0.3).[55,56] Scanning electron microscopy (SEM) images of **TpDTz** COF reveal a flower-like morphology composed of flakes with 1–3 μm lateral dimensions (Figure B-11). Transmission electron microscopy (TEM) images confirm the layered morphology of the crystalline network with clearly visible 2D honeycomb-type pores oriented perpendicular to the crystallographic *c* axis with a periodicity of ~3.3 nm (**Figure 4-2**c). In order to evaluate the thermal stability of **TpDTz** COF, we further performed thermogravimetric analysis (TGA) in air. The TGA profile suggests that the COF pores are guest free and the material is thermally stable up to ~400 °C (Figure B-10).

The permanent porosity of **TpDTz** COF was assessed by Ar adsorption analysis measured at 87 K (**Figure 4-2**b and Figure B-13). A Brunauer–Emmett–Teller (BET) surface area of 1356 $m^2\ g^{-1}$ was obtained for **TpDTz** COF, which is comparable to some of the most porous β-ketoenamine-based porous COFs previously synthesized via solvothermal methods.[27,28,57] The experimental pore size of 3.4 nm obtained from the adsorption isotherm using the quenched solid state density functional theory (QSDFT) cylindrical-slit adsorption kernel for carbon (inset of **Figure 4-2**b) is in excellent agreement with the pore size obtained from the structure model (~3.4 nm) and TEM (~3.3 nm). Further, the measured water adsorption isotherm (total uptake 309 $cm^3\ g^{-1}$, 25 wt% at STP) of **TpDTz** COF suggests its relatively hydrophilic nature, induced by the polar N/S containing TzTz group and should thus lead to higher dispersibility of the COF in water

during photocatalysis,[28,29] as opposed to the non-TzTz **TpDTP** COF (total uptake 75 cm^3 g^{-1}, 6 wt% at STP) with similar pore sizes (Figure B-15). This fact is also supported by the higher CO_2 uptake for **TpDTz** COF compared to **TpDTP** COF (Figure B-16).

Since chemical stability is a crucial criterion for any material to be considered for practical applications, we investigated the chemical stability of **TpDTz** COF under strongly acidic (12 M HCl) conditions and in boiling water up to 7 days. The retention of all characteristic peaks in the PXRD pattern suggests a high chemical stability under the tested conditions (Figure B-7). It is important to note that **TpDTz** COF is stable only under mild basic conditions (1 M KOH) for up to 3 days, while at harsher basic conditions (12 M KOH for 7 days) the framework decomposes. The high chemical tolerance of **TpDTz** COF is ascribed to the combined effect of the stabilizing enol-to-keto tautomerism[57] and the planarity of the TzTz moiety,[47-50] which allows for strong π–π interactions between the layers.

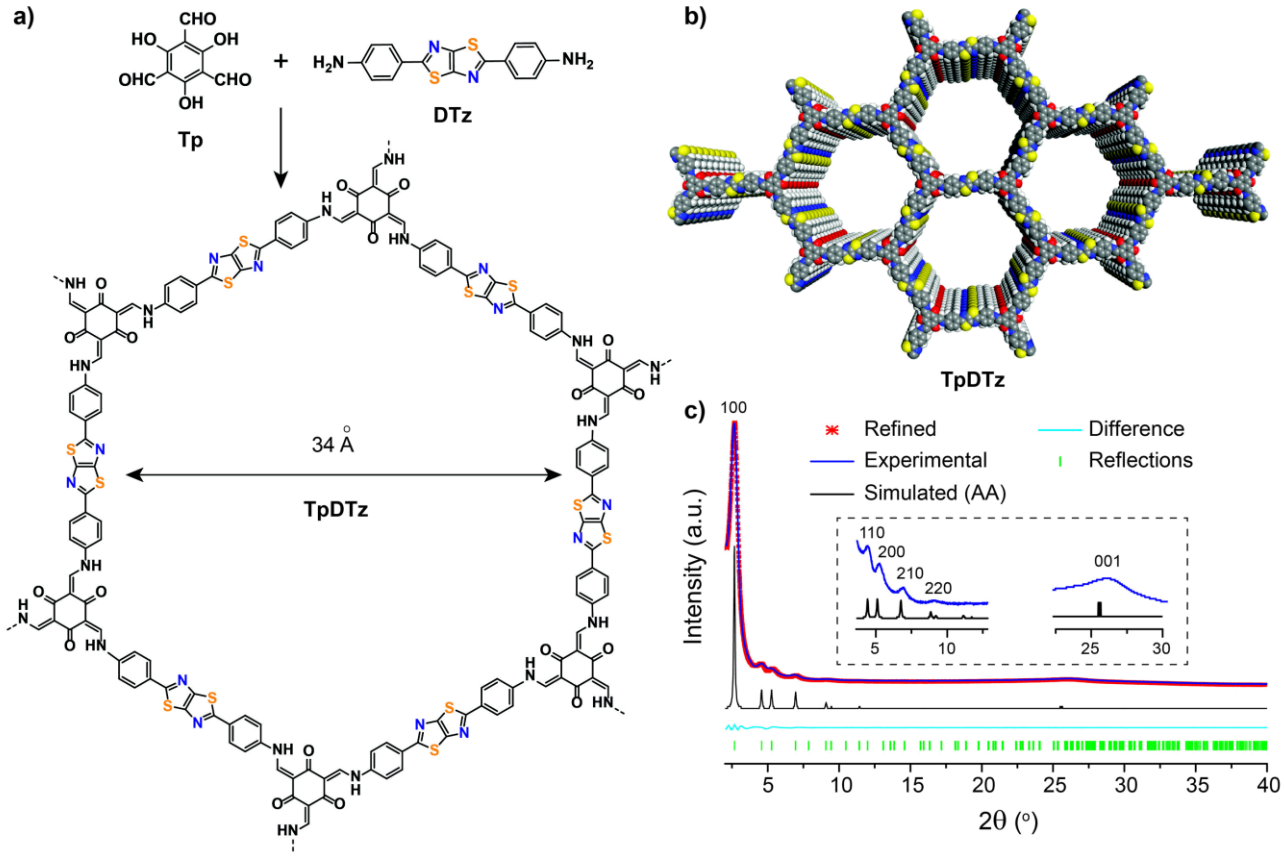

Figure 4-1. Synthesis and structural characterization of TpDTz COF. (a) Schematic representation of TpDTz COF synthesis. **(b)** Space-filling model of TpDTz COF pores with π–π stacking of successive 2D layers (gray, C; blue, N; red, O; yellow, S; and white, H). **(c)** Indexed PXRD patterns of TpDTz COF with corresponding Pawley refinement (red) showing good fit to the experimental data (blue) with minimal differences (cyan); the inset shows close-up of the indexed experimental (blue) and simulated (black) PXRD patterns based on Pawley fits [final R_{wp} = 2.59% and R_p = 1.89%].

4.3.2 Opto-electronic properties and photocatalysis

The UV–vis diffuse reflectance (DR) spectrum of **TpDTz** COF reveals efficient light absorption extending into the orange parts of the visible spectrum with an absorption edge at ~598 nm (Figure 2d). Kubelka–Munk analysis yields a direct optical band gap of ~2.07 eV. In contrast, **TpDTP** COF shows a blue-shifted absorption band edge at ~531 nm, corresponding to a larger optical band gap of ~2.28 eV (Figure B-18), due to the absence of light harvesting TzTz units. The measured photoluminescence (PL) spectra (Figure B-19) reflect this trend; **TpDTz** COF has a significantly red-shifted emission (λ_{max} = 690 nm) compared to **TpDTP** COF (λ_{max} = 630 nm). The fluorescence decays can be fitted with triexponential functions, and the amplitude-weighted average lifetimes for **TpDTz** and **TpDTP** COFs are 94 and 115 ps, respectively (Figure B-20). Emission intensities were too low to measure accurate absolute emission quantum yields. The short excited-state lifetimes together with low emission quantum yields suggest more pronounced non-radiative rates in the COF systems, relative to the radiative rates, similar to our previously reported N3-COF system.[26,30]

Cyclic voltammograms (CV) of **TpDTz** COF films were measured to estimate the band positions and the thermodynamic driving force for H_2 evolution. The voltammogram of a **TpDTz** COF-modified FTO working electrode[58,59] shows an irreversible reduction wave with an onset potential of $E_{red,onset} \approx -1.24$ V vs saturated calomel electrode (SCE) (**Figure 4-2**e and Figure B-22). From the optical bandgap (E_g = 2.07 eV) determined from the UV–vis DR spectrum, the valence band (VB) and conduction band (CB) edges of **TpDTz** COF can be estimated to be $E_{CB} = -3.46$ eV and $E_{VB} = -5.53$ eV vs the vacuum level, following the equations $E_{CB} = -(E_{red,onset\ vs\ SCE} + 4.7)$ eV and $E_{VB} = E_{CB} - E_{g,opt}$.[60-63] Quantum-chemical calculations of vertical ionization potentials and electron affinities on a **TpDTz** pore model (Figure B-53), cut from a supercell built using the 2D periodic optimized unit cell of the **TpDTz** COF (Figure B-52), support these findings (Table B-8). Based on a comparison of these values with the oxidation potential of TEoA (0.57 V vs SCE)[63] and the reduction onset potential of the NiME molecular catalyst system (−0.75 V vs SCE) (Figure B-21), it is likely that **TpDTz** COF can transfer electrons to the NiME co-catalyst system, forming a reduced Ni(I) center and thereby enabling H_2 evolution in

successive steps.[51,60] Also, TEoA can efficiently quench the photoexcited holes in the COF thereby replenishing its photoactivity.

Owing to the planar and conjugated structure, the electron-deficient nature of the heterocyclic backbone, and the optimal band gap and hence light absorption ability, the TzTz-linked **TpDTz** COF was investigated as the heterogeneous photoabsorber for photocatalytic H_2 evolution in combination with the Ni-thiolate hexameric cluster (NiME) co-catalyst in water. The NiME cluster co-catalyst has a cyclic hexameric structure composed of six Ni(II) ions forming a planar ring, and the Ni centers are bridged by 12 ME units, which has been confirmed by DFT calculation and single-crystal X-ray diffraction analysis by others (Figure B-35).[51,64] This NiME cluster co-catalyst has been shown to produce H_2 actively when sensitized by an organic xanthene dye (erythrosin B).[51] However, the generation of unstable PS radical species upon photochemical quenching of the excited-state dye (PS*) leads to a fast decomposition and hence poor photochemical stability of organic dye PSs, which hinders the long-term performance of the photocatalytic system.[40,51] The strategy of combining a photochemically stable COF photoabsorber with the Ni-thiolate cluster co-catalyst in water could thus be a viable path to impart better long-term stability for H_2 production.

The beauty of the aforesaid NiME complex lies in its simple, quick *in situ* synthesis in water upon addition of a Ni(II) salt and ME at room temperature. This *in situ* assembly strategy is different from those of most other Ni(II) and Co(II) co-catalyst complexes, featuring arduous *ex situ* synthesis and purification of a water-soluble analogue, thus adding to the cost-effectiveness of the NiME cluster co-catalyst approach.[32,40-42]

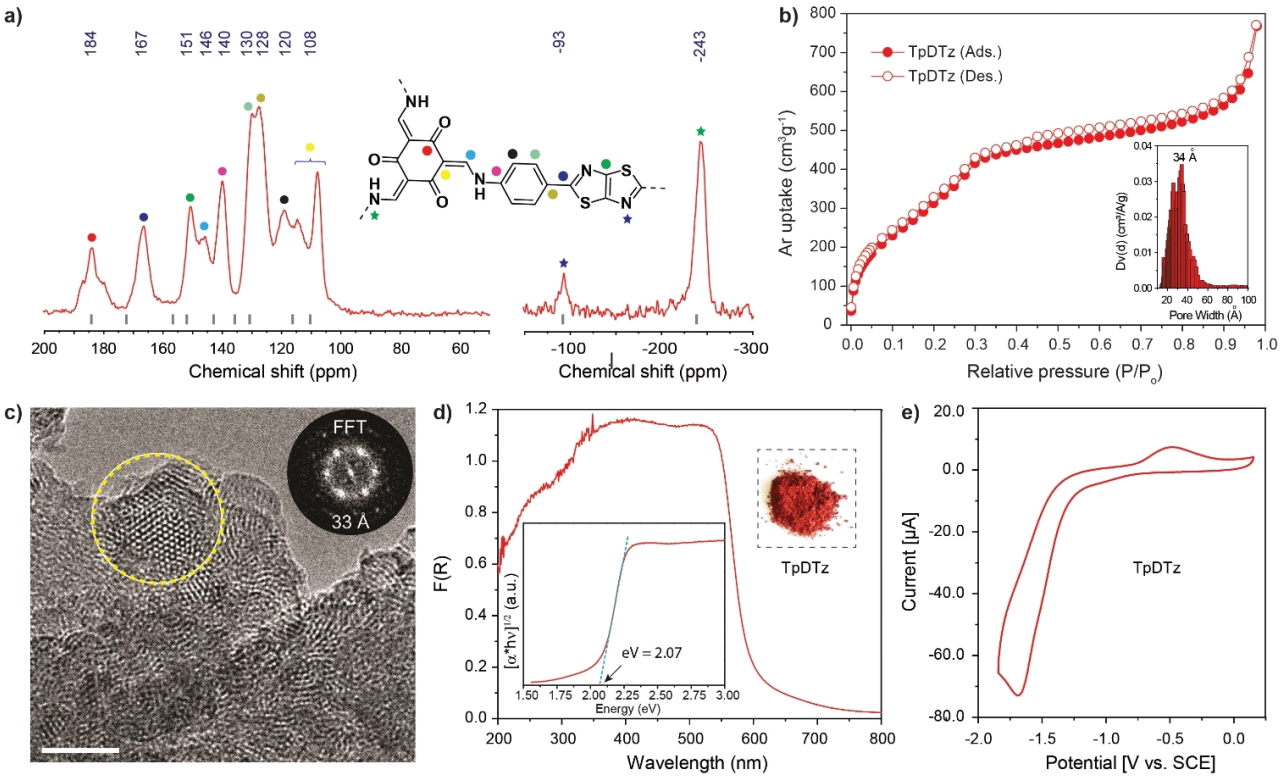

Figure 4-2. Structural characterization of TpDTz COF. (a) ^{13}C and ^{15}N CP-MAS solid-state NMR spectra of TpDTz COF. Calculated NMR chemical shifts for the TpDTz-NMR model (Figure B-49) obtained at the B97-2/pcS-2//PBE0-D3/def2-TZVP level of theory (Tables S4 and S5) are shown as gray dashes. **(b)** Argon adsorption–desorption isotherm for TpDTz COF recorded at 87 K; inset shows calculated pore size distribution of TpDTz COF according to the QSDFT method. **(c)** TEM image of TpDTz COF showing the hexagonal pore structure with a periodicity of ~3.3 nm (scale bar, 100 nm). **(d)** UV–vis diffuse reflectance (DR) spectrum for TpDTz COF measured in the solid state; insets show a plot of the Kubelka–Munk function to extract the direct optical band gap and a photograph of TpDTz COF powder. **(e)** Cyclic voltammogram (CV) of a TpDTz COF-modified FTO working electrode in 0.1 M NBu_4PF_6 as the supporting electrolyte in anhydrous acetonitrile at a scan rate of 100 mV/s.

In addition, this cluster has been shown to be a potent H_2 evolution co-catalyst producing H_2 immediately after light illumination in the presence of a PS and SED, and hence does not require any photodeposition, nor does it show an activation time, contrary to Pt-based photocatalytic systems.[25-30]

For better measurement accuracy and to gain insights into the photocatalytic mechanism, we developed a continuous-flow system to monitor the H_2 evolution performance of the hybrid photocatalytic system (**Figure 4-3** and Figure B-23). In this measurement system, the molar flow entering the system, the pressure (0.5 bar), and the temperature (25 °C) of the reactor are continuously controlled, while bypassing some of the out-flow to an open sampling loop gas chromatograph (GC) autosampler. In this way, the rate of

H_2 production (R_{H2}) can be monitored directly using only two experimental inputs: F_{in} from the mass flow controller, and $x_{H2,ppm}$ from an online GC (BID) detection system (Equation 4-1), where F_{in} is the carrier gas (in this case He) flow in to the system and $x_{H2,ppm}$ is the molar fraction of H_2 at the outlet.

$$R_{H_2} = \frac{F_{in} \times x_{H_2 ppm} \times 10^{-6}}{\left(1 - x_{H_2 ppm} \times 10^{-6}\right)} \qquad \text{Equation 4-1}$$

Typically, the run-to-run error with this method is below 3%, compared to at least 15–20% error with a standard batch system. Also, this continuous-flow system is independent of experimental conditions and does not require human intervention when sampling or local derivative approximations as with regular batch system measurements (Figure B-34). In addition to the better accuracy of this method in monitoring kinetic trends in the photocatalytic H_2 evolution process, the method also keeps the media unperturbed — since the presence of the GC sampling line does not affect the hydrogen balance — thus completely eliminating typical sampling losses and mathematical and experimental uncertainties associated with batch photocatalytic reactor systems.

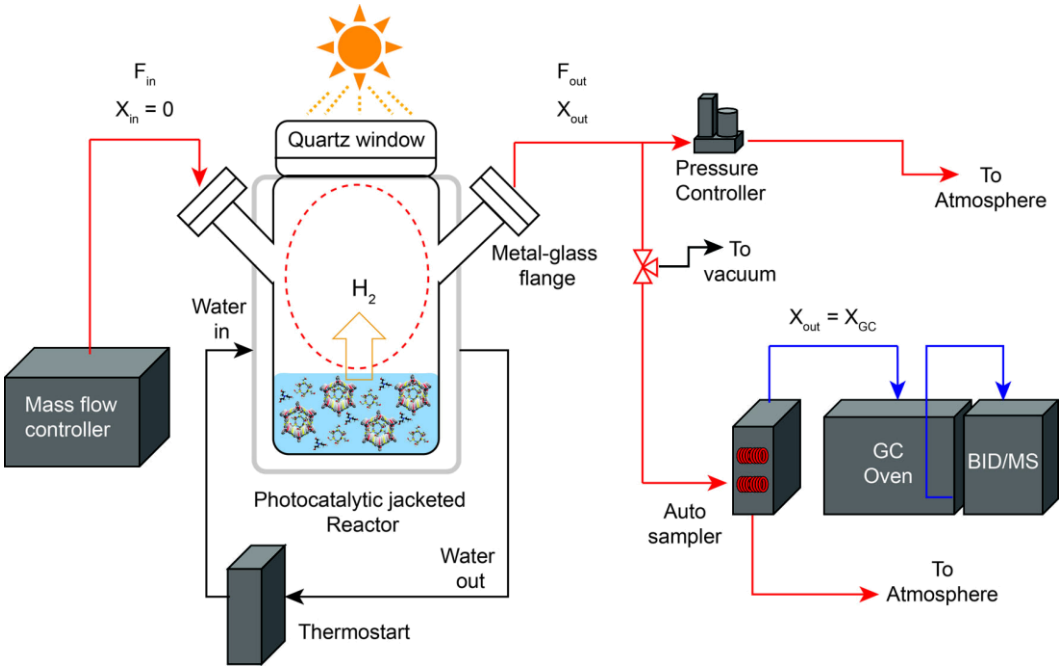

Figure 4-3. Continuous-flow photocatalytic reactor design. Schematic diagram of the designed continuous-flow photocatalytic reactor system (red streamlines are the continuous-flow pathway of gas). In contrast, the batch configuration involves mass flow controllers as dead-ends after back purging the initial headspace and replaces the autosampler by a septa-port or a manual sampling valve.

In a typical photocatalytic experiment using our hybrid system, 5 mg of **TpDTz** COF was dispersed in 10 mL of H_2O containing TEoA (10 vol%) as the SED, and the pH was adjusted to 8.5 by adding HCl. $Ni(OAc)_2 \cdot 4H_2O$ (10 wt%, 0.5 mg) and ME (10 equiv, 1.4 µL) were then charged to instantaneously form the brown-colored NiME cluster co-catalyst. When irradiated with 100 mW/cm^2 AM 1.5 radiation, the resulting mixture produces H_2 actively over a period of at least 70 h—with ~40% of the highest production rate still preserved after this time—in a single run without adding additional TEoA or co-catalyst (**Figure 4-4**a). A maximum H_2 evolution rate of 941 µmol g^{-1} h^{-1} with a TON_{Ni} > 103 (70 h) and a TOF = 2.3 h^{-1} when the system is fully active were obtained. A mathematically projected (Appendix B, section B.8) TON_{Ni} > 443 (890 µmol of total H_2 evolution) can be obtained for the photocatalytic H_2 evolution performance corresponding to a complete depletion of the co-catalyst. The relation between co-catalyst, SED, and observed activity loss of the system in time was confirmed by *in situ* addition of loss-equivalent amounts of ME or TEoA independently after 72 h of illumination, which did not change the deactivation trends observed (Appendix B, section B.8). It must be noted that the TON_{Ni} mentioned above is only a lower limit calculated based on the total amount of Ni(II) salt used for the photocatalysis experiment. Under identical conditions the erythrosin B (EB) dye-sensitized system[18] produces H_2 with a maximum rate of 49,297 µmol g^{-1} h^{-1} (attained in 1 h); however, the rate rapidly drops off, and the whole system becomes completely inactive within 7 h. A TON_{Ni} > 36.5 (73 µmol of total H_2 evolution) was obtained after 7 h (TOF_{Ni} = 31.9 h^{-1}), which is 12 times lower than the value projected for the **TpDTz** COF-sensitized system (Figure 4a). These results demonstrate the added value of using a heterogeneous PS to stabilize charge transfer in photocatalytic hybrid systems.

Also, the **TpDTz** COF-NiME photocatalytic system produces H_2 at a 17% higher maximum rate and has a TON nearly 8-fold as high as our previously reported N2-COF-cobaloxime-based system (782 µmol h^{-1} g^{-1}, TON_{Co} = 54.4), while operating in water.[32] The H_2 evolution rate and the sustained activity of this simple **TpDTz** COF-NiME system are competitive with and even superior to those of many COF-based photocatalytic systems (Table B-3) and other benchmark photocatalytic systems involving metallic Pt or molecular Ni co-catalysts. Examples include g-C_3N_4/Pt (840 µmol g^{-1} h^{-1}),[65] TP-BDDA/Pt (324 µmol g^{-1} h^{-1}),[27] N2-COF/Pt (480 µmol g^{-1} h^{-1}),[26] crystalline poly(triazine imide)/Pt (864 µmol g^{-}

^{1} h^{-1}),[66] sg-CN-Ni (103 µmol g^{-1} h^{-1}),[67] $Ni_{12}P_5$/g-C_3N_4(536 µmol g^{-1} h^{-1}),[68] $^{NCN}CN_x$-NiP (763 µmol g^{-1} h^{-1}),[69] and carbon quantum dots (CQDs)-Ni (398 µmol g^{-1} h^{-1}).[70]

Control experiments were performed by sequentially removing one of the components, i.e., **TpDTz** COF, TEoA, $Ni(OAc)_2 \cdot 4H_2O$, and ME, at a time from our photocatalytic system to identify their importance and role for the H_2 evolution. Indeed, no H_2 evolution was observed for a period of 12 h unless all individual components act in concert, signifying that each is essential for the photocatalytic system to work and efficiently produce H_2 (Figure B-27).

Furthermore, a 1:10 metal-to-ligand molar ratio and 10 wt% of catalyst with respect to the PS were observed to elicit the best photocatalytic performance (Figure B-28 and Figure B-29). To confirm water as the source of H_2, the photocatalytic reaction was performed in D_2O under identical conditions (**Figure 4-4**a). A production rate for D_2 in D_2O similar to that for H_2 in H_2O was observed over 72 h, taking batch-to-batch variations into account. This result suggests that water is the hydrogen source responsible for the production of H_2, assuming that no significant proton/deuterium exchange processes in the individual components are at play. This finding was further confirmed by an almost complete disappearance of the $m/z = 2$ signal for H_2 in a mass spectrometric measurement of the headspace gas of the photocatalytic reaction performed in D_2O (Figure B-26). Note that D_2 is evolved with a time lag compared to H_2, which is likely due to the kinetic isotope effect (KIE) of deuterium as described below. Further, H_2 evolution experiments performed under multiple light *on–off* cycles over a period of 26 h (**Figure 4-4**b) suggests a purely light driven H_2 evolution process in water. Once the catalytic system is fully active, H_2 evolution activity is seen to be restored even after a prolonged light *off* period.

SED and the reaction pH are known to have a profound influence on the activity of many H_2 production systems.[26,27,32] In our case, we observed a similar effect; the rate of H_2 generated from the photochemical reaction is the highest (941 µmol g^{-1} h^{-1}) at pH 8.5 using TEoA as SED. However, at acidic conditions (pH 6.5) there was negligible H_2 evolution (16 µmol g^{-1} h^{-1}). This could be attributed to the protonation of TEoA or due to inhibition of proton loss from one-electron oxidized $TEoA^+$.[35] Notable H_2 evolution is observed over 24 h under alkaline conditions (pH 11), albeit at lower rates (308 µmol g^{-1} h^{-1}) as compared to pH 8.5 (Figure B-30). This is possibly due to the reduced driving

force for protonation of the Ni hydride intermediate co-catalyst species at higher pH to subsequently generate H_2. Triethylamine (TEA) and Na_2S were also explored as potential SEDs. Interestingly, they produce H_2 but with significantly lower rates of 84 μmol g^{-1} h^{-1} and 7 μmol g^{-1} h^{-1}, respectively (Figure B-31). Higher TEoA concentrations were found to decrease H_2 evolution rates; a TEoA concentration of 10 vol% in water was observed to result in the maximum H_2 production rate (Figure B-32).

H_2 evolution rates of the photocatalytic systems containing **TpDTz** COF PS and different Ni(II)co-catalysts were measured (**Figure 4-4**c). Different sulfur-containing compounds, such as thiourea (TU) and 2-mercaptophenol (MP), were explored as potential ligands for *in situ* formation of Ni(II)co-catalyst complexes. However, neither NiTU nor NiMP produced any H_2 with **TpDTz** COF, possibly due to unfavorable complexation of the ligands with Ni(II) in water: TU and MP are known to be poorer complexation agents as compared to ME.[71] Also, a reported *ex situ* synthesized Ni(*abt*)$_2$ -complex[42] was studied as a potential H_2 evolution co-catalyst under our experimental conditions, but no H_2 evolution was seen, most likely due to its poor solubility in water. It is also interesting to note that **TpDTz** COF produces H_2 with a significantly smaller rate of 23 μmol g^{-1} h^{-1} with metallic Pt co-catalyst and TEoA at pH 8.5 over a period of 24 h as compared to that with NiME. The significant difference between H_2 evolution of the molecular co-catalyst and photodeposited Pt nanoparticles is difficult to explain by a single effect.[32,70] However, it may be argued that the higher activity of the NiME co-catalyzed system in contrast to the surface bound Pt nanoparticles (Figure B-48) is due to a more effective blocking of charge carrier recombination since the co-catalyst is physically separated from the framework (physisorbed), which may support better charge separation. We further screened the H_2 evolution activity of other transition metal-ME complexes, such as CoME and CuME, with **TpDTz** COF as the PS following a similar method as that of NiME. Although all systems produced H_2, they do so with a much lower rate following the order NiME (941 μmol g^{-1} h^{-1}) > CoME (85 μmol g^{-1} h^{-1}) > CuME (52 μmol g^{-1} h^{-1}). This could be due to the poor solubility of CoME and CuME clusters in water compared to the NiME, which is in accordance with the reported dye sensitized molecular -system[51] (**Figure 4-4**d).

We then evaluated the H_2 evolution ability of the NiME cluster co-catalyst with a variety of photoabsorbing materials; **TpDTP** COF,[52] N3-COF,[26] an amorphous porous polymer

containing TzTz groups (TzTz-POP-3),[72] and the diamine linker **DTz** were tested under identical conditions. Even though N3-COF is considered one of the most active COFs for photocatalytic H_2 generation (reported rate of 1700 μmol g^{-1} h^{-1} when co-catalyzed by Pt), (10b) with NiME co-catalyst it produces H_2 only at a very low rate of 40 μmol g^{-1} h^{-1} (**Figure 4-4**e). Under similar conditions **TpDTP** COF produces H_2 at a rate of 160 μmol g^{-1} h^{-1}, which is nearly 6 times less compared to that of the **TpDTz** COF sensitized system. The marked difference in photocatalytic activity between **TpDTz** COF and **TpDTP** COF may in part be rationalized by the reaction conditions which were not optimized specifically for **TpDTP** COF, but also by their different photon absorption characteristics. A redshift of ~67 nm is observed for **TpDTz** COF with respect to **TpDTP** COF, which indicates that **TpDTz** COF absorbs photons more effectively in the visible range. This said, increased reactivity is only expected if the conduction band is not significantly lowered to maintain the thermodynamic driving force for the HER. In addition to that, the higher crystallinity and the higher BET surface area of 1356 m^2 g^{-1} for **TpDTz** COF versus 736 m^2 g^{-1} for **TpDTP** COF, along with a better dispersibility of the more hydrophilic **TpDTz** COF in aqueous solution, are likely determining factors for the enhanced photocatalytic activity. Notably, the amorphous polymer TzTz-POP-3 and the diamine linker **DTz** are completely inactive at producing H_2 with the NiME co-catalyst (**Figure 4-4**e). Overall, the significantly lower reactivity of other PSs in producing H_2 with the NiME co-catalyst is rationalized by a combined effect of unfavorable charge-transfer processes, reduced light harvesting, low crystallinity and surface area, and poor dispersibility in water.

The apparent quantum efficiency (AQE) was calculated using four different bandpass filters with central wavelengths (±20 nm) at 400, 500, 550, and 600 nm to quantify the spectral contribution toward H_2 evolution activity of the **TpDTz** COF photoabsorber. **Figure 4-4**f shows that **TpDTz** COF has a maximum AQE of 0.2% at 400 nm. Under AM 1.5 illumination, the AQE was estimated to be 0.044%, which is higher than that of our previously reported N2-COF-cobaloxime H_2 evolution system (0.027%).[32]

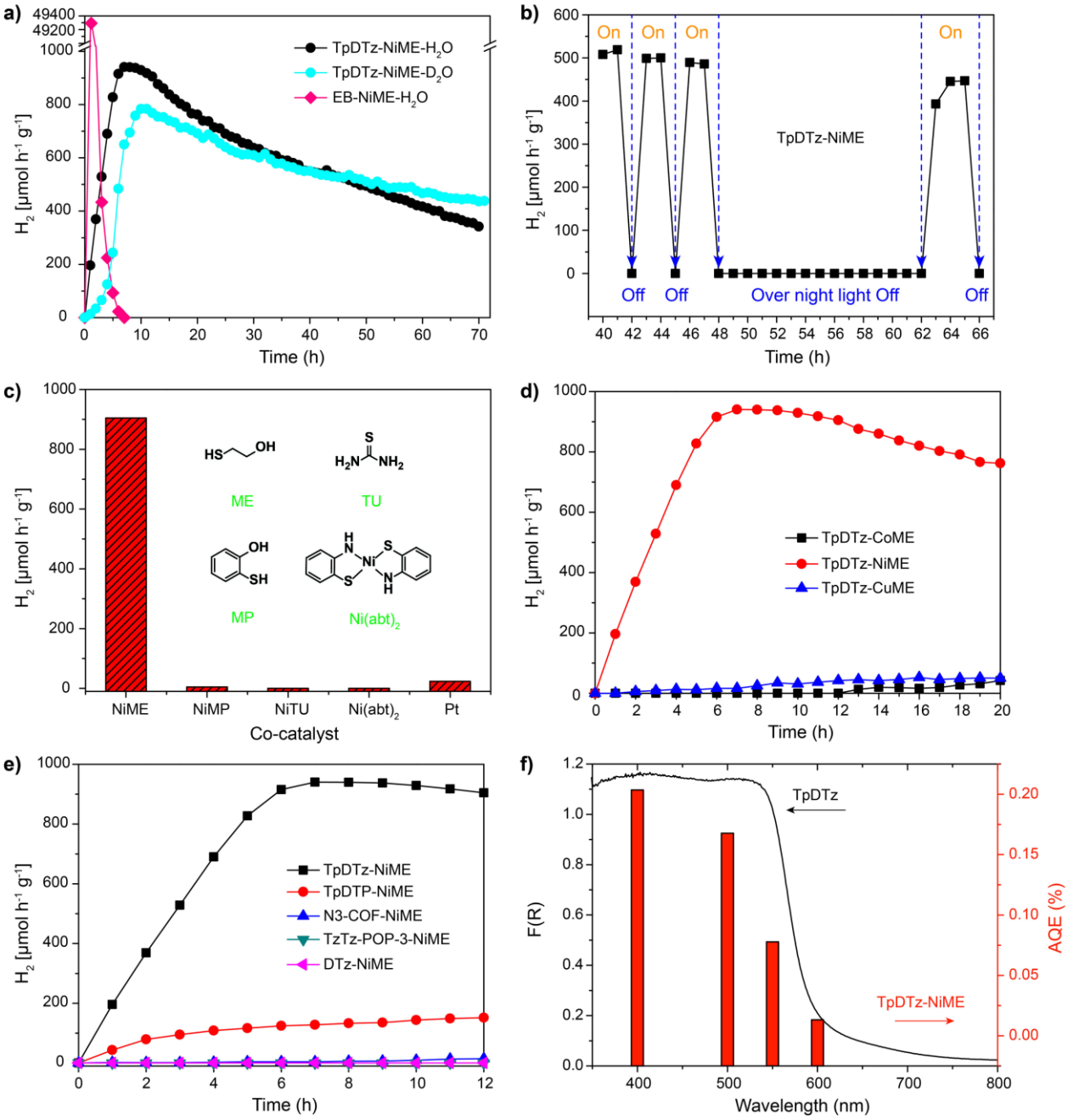

Figure 4-4. Photocatalytic H_2 evolution. (a) Comparison of photocatalytic H_2 evolution rates in water (H_2O) and deuterium oxide (D_2O), using TpDTz COF over 72 h and EB dye under AM 1.5 light irradiation [COF photosensitizer: 5 mg of TpDTz COF in 10 mL of H_2O/D_2O with 10 vol% TEoA, 0.5 mg of $Ni(OAc)_2$, and 1.4 µL of ME at a final pH of 8.5; dye photosensitizer: 1.33 mg of EB in 10 mL of H_2O with 10 vol% TEoA, 0.5 mg of $Ni(OAc)_2$, and 1.4 µL of ME at a final pH of 8.5]. **(b)** Light *on–off* cycles for photocatalytic H_2 evolution experiments with TpDTz COF in water over 26 h. **(c)** Photocatalytic H_2 evolution with TpDTz COF in water using different co-catalysts. **(d)** Photocatalytic H_2 evolution with TpDTz COF in water using different metal-ME co-catalysts. **(e)** Photocatalytic H_2 evolution from water using different photosensitizers. **(f)** Overlay of the UV–vis DR spectra of TpDTz COF with apparent quantum efficiency (AQEs) for the photocatalytic H_2 evolution reaction with TpDTz COF at four different incident light wavelengths.

We further verified the photochemical stability of **TpDTz** COF after a 72 h long photocatalysis experiment. The isolated **TpDTz** COF sample was fully characterized using PXRD, ssNMR, SEM, and TEM, and it was found that the framework structure, crystallinity, and morphology of **TpDTz** COF are retained (Appendix B, section B.9), thus supporting the high chemical stability of this COF (*vide supra*). A small additional signal at 56.6 ppm in the ^{13}C ssNMR spectrum possibly corresponds to trapped ME molecules inside the **TpDTz** COF pore. This, together with the observation of traces of Ni in the post-photocatalytic **TpDTz** COF using SEM-EDAX (Figure B-46) may hint to chemisorption of small amounts of co-catalyst to the COF walls. However, ^{15}N ssNMR of the **TpDTz** COF sample does not show any noteworthy difference in the chemical shifts of the N signals before and after photocatalysis (Figure B-41), suggesting that there is no substantial direct interaction between the residual Ni and the nitrogen centers of the COF. Also, the as-recovered **TpDTz** COF sample does not produce any H_2 under identical photocatalytic conditions except for the absence of $Ni(OAc)_2{\cdot}4H_2O$ and 2-ME ligand. This suggests that the interaction between **TpDTz** COF and NiME is mostly physical, and no lasting chemical interaction exists between the two components. Our finding thus suggests an outer-sphere electron transfer to be at play, which nevertheless is efficient enough to allow facile charge transfer from the photoabsorber to the NiME co-catalyst (**Figure 4-5**a).

To obtain deeper insights into the photocatalytic mechanism, an overall coarse-grain mathematical model (Supporting Information eq S6.2) of the photocatalytic reaction was developed (see Appendix B, section B.8 for details) by taking advantage of the quantification of hydrogen evolution rates in our flow detection platform. Our model was based on three primary experimentally observed trends: the activation time required by the photocatalytic system to reach maximum rates in the first run (**Figure 4-4**a), the absence of this activation time during light *on–off* cycles or long dark periods before illumination (**Figure 4-4**b), and the KIE in D_2O, namely, smaller deuterium evolution rates and delayed response, together with the observation of a similar initial activation time as with H_2O (**Figure 4-4**a). A possible reaction model is outlined in **Figure 4-5**b. The absence of an activation time during light *on–off* cycles (**Figure 4-4**b) suggests a light enhanced formation of a catalyst resting state [R] of the NiME complex upon illumination, as seen by the initial activation time required for the system to reach maximum efficiency.

The reaction network can then be reduced to the following core steps using a microkinetics analysis. For the heterogeneous (COF) fast cycle: COF photoexcitation ($h\nu$), exciton recombination in the COF (k_{rec}), reductive quenching of the COF (k_q), and electron transfer from $COF^{\bullet-}$ to [R] to form the active intermediate species [I] (k_a). Quantum-chemical calculations on the **TpDTz** pore model system (Figure B-55) identify the lowest photoexcitation energy to be 2.30 eV (Table B-9), the difference density of this excited state (Figure B-57) visualizing the exciton. The spin density of the radical anion as a result of the reductive quenching of this state is shown in Figure B-58. For the homogeneous (catalyst) cycle: formation of a rapidly coordinated complex [Ni-L] (K_{eq}), slow assembly of the catalytically active species (k_T, k_T^{-1}), an apparent first-order activation step from [R] to [I] (k_a), an irreversible deactivation step [D] (k_d), and the closing of the catalytic cycle via a dark step that produces H_2 (k_{HER}). If in such a system k_T and k_T^{-1} are significantly slower compared to the rest of the steps, the *on–off* behaviour can be explained, because in the absence of light the dark equilibrium is slow and the amount of [R] and [I] will not change significantly over time. Furthermore, the absence of HER in the dark during the light *on–off* cycles observed in **Figure 4-4**b suggests that a k_{HER}-limited homogeneous cycle is unlikely. Then, once nickel enters the cycle as [R] more rapidly due to a light-shifted equilibrium, [R] will build up until the rate of [D] leaving the system irreversibly is equal to the rate of formation of [R], [I] being stationary. This will lead to an expression for activation of the photocatalytic system such that the activation curve is an exponential asymptote with time constant t_a, which is dominated by electron-transfer rate k_a, a linear deactivation with an apparent time constant t_d, an HER apparent kinetic constant R_{H2},max, and the apparent transient time t_0 only which corresponds to the initial time delay necessary for the intermediate [I] to be pseudo-stationary (Supporting Information eq S6.2). Our model further provides an accurate fit to the data obtained in both H_2O and D_2O, in line with an expected trend of a KIE. In this case, R_{H2},max, t_d, and t_0 changed as expected, but the time constant for the activation step (t_a) being independent of the isotopic mass is almost unchanged (Table B-2), further corroborating our proposed rate-limiting steps (RLS). Our reaction model not only explains these qualitative trends but also provides an accurate fit with standard errors below 5% for different data sets. It is important to note that acquiring detailed insights into the H_2/D_2 evolution reaction

mechanism for the **TpDTz** COF-NiME photocatalytic system became possible only with the use of a flow reactor system.

Our reaction modelling results suggest that as long as a slow catalyst activation time is observed, the RLS of the system is seemingly the electron transfer from the COF to the NiME complex. While this outcome is fully consistent with the assumed outer-sphere electron-transfer process, it reinforces the idea of studying the kinetics of such processes in more detail as this will be crucial to improve the HER rate by rational design of the COF–co-catalyst interface.

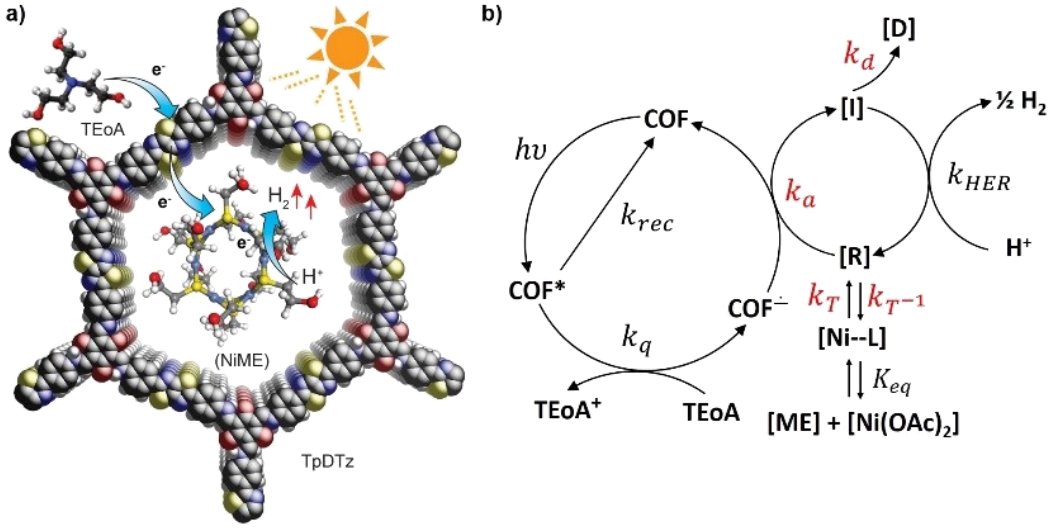

Figure 4-5. Reaction limitations insights. (a) General schematic of the proposed pathway for H_2 evolution (color code: gray, C; red, O; yellow, S; blue, N; and light pink/white, H). **(b)** Proposed key steps of the photocatalytic H_2 evolution reaction with TpDTz COF and NiME cluster co-catalyst. [Ni-L] denotes a ligand-coordinated co-catalyst state which is attained fast compared to the [R] state, [R] denotes the catalyst resting state, which is catalytically active nickel cluster species, [D] denotes the deactivated species, and [I] denotes an intermediate reduced catalyst species able to run the HER step.

4.4 Conclusions

We report the first COF photosensitizer and noble-metal-free molecular co-catalyst photocatalytic system for sustained solar H_2 production from water. This single–site system comprises the newly designed N/S-containing **TpDTz** COF PS that absorbs strongly in the visible region of the solar spectrum and is robust for long-term hydrogen evolution. In combination with an earth-abundant Ni-thiolate cluster co-catalyst which self-assembles in water, we obtain solar H_2 evolution rates as high as 941 µmol h^{-1} g^{-1} and a TON_{Ni} >

103 (70 h) with persistent H_2 evolution for more than 70 h in a single run, which surpasses many benchmark photocatalytic H_2 evolution systems based on COFs and carbon nitrides. To map out the parameter space of this hybrid photocatalytic system, we comprehensively screened the influence of various reaction components, including pH, SED, co-catalyst metal centers, different N/S-containing chelating ligands, and a variety of PSs on the photocatalytic activity. In addition, we have introduced a newly designed continuous-flow system enabling the non-invasive, direct detection of the H_2 production rate. This platform not only provides higher accuracy in quantification; it also paves the way for unprecedented insights into the reaction mechanism which are difficult to obtain with the existing batch measurement methods. Microkinetic modeling of the reaction system suggests that an outer-sphere electron transfer from the photoabsorber to the catalyst is the rate-limiting step, thus spotlighting the importance of the rational design of the COF–co-catalyst interface.

4.5 Acknowledgments

B.P.B. acknowledges the Alexander von Humboldt foundation for a research fellowship. B.V.L. acknowledges financial support by an ERC Starting Grant (project COF Leaf, grant number 639233), the Deutsche Forschungsgemeinschaft (DFG, German Research Foundation) - project number 358283783 - SFB 1333, and the Max Planck Society. B.V.L. and C.O. acknowledge further support by the cluster of excellence e-conversion (EXC 2089) and the Center for Nanoscience (CeNS). C.O. acknowledges financial support as a Max-Planck-Fellow at the Max Planck Institute for Solid State Research, Stuttgart. We thank Viola Duppel for recording the SEM and TEM images, Igor Moudrakovski for solid-state NMR measurements, Marie-Luise Schreiber for elemental analysis, and Prof. Dr. Ulrich Starke and Dr. Kathrin Müller for XPS data

4.6 References

1. Alstrum-Acevedo JH, Brennaman MK, Meyer TJ. Chemical Approaches to Artificial Photosynthesis. 2. *Inorganic Chemistry* 2005, **44**(20)**:** 6802-6827.

2. Lewis NS, Nocera DG. Powering the planet: Chemical challenges in solar energy utilization. *Proceedings of the National Academy of Sciences* 2006, **103**(43)**:** 15729-15735.
3. Bard AJ, Fox MA. Artificial Photosynthesis: Solar Splitting of Water to Hydrogen and Oxygen. *Accounts of Chemical Research* 2002, **28**(3)**:** 141-145.
4. Author NG. 2013.
5. Hoffert MI, Caldeira K, Jain AK, Haites EF, Harvey LDD, Potter SD*, et al.* Energy implications of future stabilization of atmospheric CO2 content. *Nature* 1998, **395**(6705)**:** 881-884.
6. Vyas VS, Lau VW-h, Lotsch BV. Soft Photocatalysis: Organic Polymers for Solar Fuel Production. *Chemistry of Materials* 2016, **28**(15)**:** 5191-5204.
7. Banerjee T, Gottschling K, Savasci G, Ochsenfeld C, Lotsch BV. H2 Evolution with Covalent Organic Framework Photocatalysts. *ACS Energy Letters* 2018, **3**(2)**:** 400-409.
8. Zou X, Zhang Y. Noble metal-free hydrogen evolution catalysts for water splitting. *Chemical Society Reviews* 2015, **44**(15)**:** 5148-5180.
9. Côté AP, Benin AI, Ockwig NW, O'Keeffe M, Matzger AJ, Yaghi OM. Porous, Crystalline, Covalent Organic Frameworks. *Science* 2005, **310**(5751)**:** 1166-1170.
10. Feng X, Ding X, Jiang D. Covalent organic frameworks. *Chemical Society Reviews* 2012, **41**(18).
11. Xu S-Q, Zhan T-G, Wen Q, Pang Z-F, Zhao X. Diversity of Covalent Organic Frameworks (COFs): A 2D COF Containing Two Kinds of Triangular Micropores of Different Sizes. *ACS Macro Letters* 2015, **5**(1)**:** 99-102.
12. Kandambeth S, Dey K, Banerjee R. Covalent Organic Frameworks: Chemistry beyond the Structure. *Journal of the American Chemical Society* 2018, **141**(5)**:** 1807-1822.
13. Keller N, Calik M, Sharapa D, Soni HR, Zehetmaier PM, Rager S*, et al.* Enforcing Extended Porphyrin J-Aggregate Stacking in Covalent Organic Frameworks. *Journal of the American Chemical Society* 2018, **140**(48)**:** 16544-16552.
14. Feng X, Liu L, Honsho Y, Saeki A, Seki S, Irle S*, et al.* High-Rate Charge-Carrier Transport in Porphyrin Covalent Organic Frameworks: Switching from Hole to

Electron to Ambipolar Conduction. *Angewandte Chemie International Edition* 2012, **51**(11)**:** 2618-2622.

15. Doonan CJ, Tranchemontagne DJ, Glover TG, Hunt JR, Yaghi OM. Exceptional ammonia uptake by a covalent organic framework. *Nature Chemistry* 2010, **2**(3)**:** 235-238.
16. Oh H, Kalidindi SB, Um Y, Bureekaew S, Schmid R, Fischer RA*, et al.* A Cryogenically Flexible Covalent Organic Framework for Efficient Hydrogen Isotope Separation by Quantum Sieving. *Angewandte Chemie International Edition* 2013, **52**(50)**:** 13219-13222.
17. Biswal BP, Chaudhari HD, Banerjee R, Kharul UK. Chemically Stable Covalent Organic Framework (COF)-Polybenzimidazole Hybrid Membranes: Enhanced Gas Separation through Pore Modulation. *Chemistry - A European Journal* 2016, **22**(14)**:** 4695-4699.
18. Ji W, Xiao L, Ling Y, Ching C, Matsumoto M, Bisbey RP*, et al.* Removal of GenX and Perfluorinated Alkyl Substances from Water by Amine-Functionalized Covalent Organic Frameworks. *Journal of the American Chemical Society* 2018, **140**(40)**:** 12677-12681.
19. Sun Q, Aguila B, Earl LD, Abney CW, Wojtas L, Thallapally PK*, et al.* Covalent Organic Frameworks as a Decorating Platform for Utilization and Affinity Enhancement of Chelating Sites for Radionuclide Sequestration. *Advanced Materials* 2018, **30**(20).
20. Das G, Biswal BP, Kandambeth S, Venkatesh V, Kaur G, Addicoat M*, et al.* Chemical sensing in two dimensional porous covalent organic nanosheets. *Chemical Science* 2015, **6**(7)**:** 3931-3939.
21. Gao Q, Li X, Ning G-H, Leng K, Tian B, Liu C*, et al.* Highly photoluminescent two-dimensional imine-based covalent organic frameworks for chemical sensing. *Chemical Communications* 2018, **54**(19)**:** 2349-2352.
22. Keller N, Bessinger D, Reuter S, Calik M, Ascherl L, Hanusch FC*, et al.* Oligothiophene-Bridged Conjugated Covalent Organic Frameworks. *Journal of the American Chemical Society* 2017, **139**(24)**:** 8194-8199.

23. Dogru M, Bein T. On the road towards electroactive covalent organic frameworks. *Chem Commun* 2014, **50**(42)**:** 5531-5546.
24. Ding S-Y, Gao J, Wang Q, Zhang Y, Song W-G, Su C-Y*, et al.* Construction of Covalent Organic Framework for Catalysis: Pd/COF-LZU1 in Suzuki–Miyaura Coupling Reaction. *Journal of the American Chemical Society* 2011, **133**(49)**:** 19816-19822.
25. Stegbauer L, Schwinghammer K, Lotsch BV. A hydrazone-based covalent organic framework for photocatalytic hydrogen production. *Chem Sci* 2014, **5**(7)**:** 2789-2793.
26. Vyas VS, Haase F, Stegbauer L, Savasci G, Podjaski F, Ochsenfeld C*, et al.* A tunable azine covalent organic framework platform for visible light-induced hydrogen generation. *Nature Communications* 2015, **6**(1).
27. Pachfule P, Acharjya A, Roeser J, Langenhahn T, Schwarze M, Schomäcker R*, et al.* Diacetylene Functionalized Covalent Organic Framework (COF) for Photocatalytic Hydrogen Generation. *Journal of the American Chemical Society* 2018, **140**(4)**:** 1423-1427.
28. Wang X, Chen L, Chong SY, Little MA, Wu Y, Zhu W-H*, et al.* Sulfone-containing covalent organic frameworks for photocatalytic hydrogen evolution from water. *Nature Chemistry* 2018, **10**(12)**:** 1180-1189.
29. Banerjee T, Lotsch BV. The wetter the better. *Nature Chemistry* 2018, **10**(12)**:** 1175-1177.
30. Haase F, Banerjee T, Savasci G, Ochsenfeld C, Lotsch BV. Structure–property–activity relationships in a pyridine containing azine-linked covalent organic framework for photocatalytic hydrogen evolution. *Faraday Discussions* 2017, **201:** 247-264.
31. Barber J, Tran PD. From natural to artificial photosynthesis. *Journal of The Royal Society Interface* 2013, **10**(81).
32. Banerjee T, Haase F, Savasci G, Gottschling K, Ochsenfeld C, Lotsch BV. Single-Site Photocatalytic H2 Evolution from Covalent Organic Frameworks with Molecular Cobaloxime Co-Catalysts. *Journal of the American Chemical Society* 2017, **139**(45)**:** 16228-16234.

33. Zhang P, Wang M, Dong J, Li X, Wang F, Wu L*, et al.* Photocatalytic Hydrogen Production from Water by Noble-Metal-Free Molecular Catalyst Systems Containing Rose Bengal and the Cobaloximes of BFx-Bridged Oxime Ligands. *The Journal of Physical Chemistry C* 2010, **114**(37)**:** 15868-15874.
34. Fihri A, Artero V, Razavet M, Baffert C, Leibl W, Fontecave M. Cobaloxime-Based Photocatalytic Devices for Hydrogen Production. *Angewandte Chemie International Edition* 2008, **47**(3)**:** 564-567.
35. Du P, Knowles K, Eisenberg R. A Homogeneous System for the Photogeneration of Hydrogen from Water Based on a Platinum(II) Terpyridyl Acetylide Chromophore and a Molecular Cobalt Catalyst. *Journal of the American Chemical Society* 2008, **130**(38)**:** 12576-12577.
36. Lazarides T, McCormick T, Du P, Luo G, Lindley B, Eisenberg R. Making Hydrogen from Water Using a Homogeneous System Without Noble Metals. *Journal of the American Chemical Society* 2009, **131**(26)**:** 9192-9194.
37. Probst B, Rodenberg A, Guttentag M, Hamm P, Alberto R. A Highly Stable Rhenium−Cobalt System for Photocatalytic H2 Production: Unraveling the Performance-Limiting Steps. *Inorganic Chemistry* 2010, **49**(14)**:** 6453-6460.
38. Hawecker J, Lehn JM, Ziessel RF. Efficient Homogeneous Photochemical Hydrogen Generation and Water Reduction Mediated by Cobaloxime or Macrocyclic Cobalt Complexes. *Nouv J Chim* 1983, **7**(5)**:** 7.
39. McCormick TM, Han Z, Weinberg DJ, Brennessel WW, Holland PL, Eisenberg R. Impact of Ligand Exchange in Hydrogen Production from Cobaloxime-Containing Photocatalytic Systems. *Inorganic Chemistry* 2011, **50**(21)**:** 10660-10666.
40. Han Z, McNamara WR, Eum M-S, Holland PL, Eisenberg R. A Nickel Thiolate Catalyst for the Long-Lived Photocatalytic Production of Hydrogen in a Noble-Metal-Free System. *Angewandte Chemie International Edition* 2012, **51**(7)**:** 1667-1670.
41. Rao H, Yu W-Q, Zheng H-Q, Bonin J, Fan Y-T, Hou H-W. Highly efficient photocatalytic hydrogen evolution from nickel quinolinethiolate complexes under visible light irradiation. *Journal of Power Sources* 2016, **324:** 253-260.

42. Das A, Han Z, Brennessel WW, Holland PL, Eisenberg R. Nickel Complexes for Robust Light-Driven and Electrocatalytic Hydrogen Production from Water. *ACS Catalysis* 2015, **5**(3)**:** 1397-1406.
43. Bouwman E, Reedijk J. Structural and functional models related to the nickel hydrogenases. *Coordination Chemistry Reviews* 2005, **249**(15-16)**:** 1555-1581.
44. Fontecilla-Camps JC, Volbeda A, Cavazza C, Nicolet Y. Structure/Function Relationships of [NiFe]- and [FeFe]-Hydrogenases. *Chemical Reviews* 2007, **107**(10)**:** 4273-4303.
45. Tard C, Pickett CJ. Structural and Functional Analogues of the Active Sites of the [Fe]-, [NiFe]-, and [FeFe]-Hydrogenases. *Chemical Reviews* 2009, **109**(6)**:** 2245-2274.
46. Carroll ME, Barton BE, Gray DL, Mack AE, Rauchfuss TB. Active-Site Models for the Nickel–Iron Hydrogenases: Effects of Ligands on Reactivity and Catalytic Properties. *Inorganic Chemistry* 2011, **50**(19)**:** 9554-9563.
47. Bevk D, Marin L, Lutsen L, Vanderzande D, Maes W. Thiazolo[5,4-d]thiazoles – promising building blocks in the synthesis of semiconductors for plastic electronics. *RSC Advances* 2013, **3**(29).
48. Dessì A, Calamante M, Mordini A, Peruzzini M, Sinicropi A, Basosi R*, et al.* Thiazolo[5,4-d]thiazole-based organic sensitizers with strong visible light absorption for transparent, efficient and stable dye-sensitized solar cells. *RSC Advances* 2015, **5**(41)**:** 32657-32668.
49. Olgun U, Gülfen M. Effects of different dopants on the band gap and electrical conductivity of the poly(phenylene-thiazolo[5,4-d]thiazole) copolymer. *RSC Adv* 2014, **4**(48)**:** 25165-25171.
50. Woodward AN, Kolesar JM, Hall SR, Saleh N-A, Jones DS, Walter MG. Thiazolothiazole Fluorophores Exhibiting Strong Fluorescence and Viologen-Like Reversible Electrochromism. *Journal of the American Chemical Society* 2017, **139**(25)**:** 8467-8473.
51. Zhang W, Hong J, Zheng J, Huang Z, Zhou J, Xu R. Nickel–Thiolate Complex Catalyst Assembled in One Step in Water for Solar H2 Production. *Journal of the American Chemical Society* 2011, **133**(51)**:** 20680-20683.

52. Zhu Y, Zhang W. Reversible tuning of pore size and CO2adsorption in azobenzene functionalized porous organic polymers. *Chem Sci* 2014, **5**(12)**:** 4957-4961.
53. Kussmann J, Ochsenfeld C. Pre-selective screening for matrix elements in linear-scaling exact exchange calculations. *The Journal of Chemical Physics* 2013, **138**(13).
54. Kussmann J, Ochsenfeld C. Preselective Screening for Linear-Scaling Exact Exchange-Gradient Calculations for Graphics Processing Units and General Strong-Scaling Massively Parallel Calculations. *Journal of Chemical Theory and Computation* 2015, **11**(3)**:** 918-922.
55. Ahlrichs R, Bär M, Häser M, Horn H, Kölmel C. Electronic structure calculations on workstation computers: The program system turbomole. *Chemical Physics Letters* 1989, **162**(3)**:** 165-169.
56. TURBOMOLE V7.3 2018, a development of University of Karlsruhe and Forschungszentrum Karlsruhe GmbH, 1989-2007, TURBOMOLE GmbH, since 2007; available from \\ http://www.turbomole.com.
57. Kandambeth S, Mallick A, Lukose B, Mane MV, Heine T, Banerjee R. Construction of Crystalline 2D Covalent Organic Frameworks with Remarkable Chemical (Acid/Base) Stability via a Combined Reversible and Irreversible Route. *Journal of the American Chemical Society* 2012, **134**(48)**:** 19524-19527.
58. Peng L-Z, Liu P, Cheng Q-Q, Hu W-J, Liu YA, Li J-S*, et al.* Highly effective electrosynthesis of hydrogen peroxide from oxygen on a redox-active cationic covalent triazine network. *Chemical Communications* 2018, **54**(35)**:** 4433-4436.
59. Wei P-F, Qi M-Z, Wang Z-P, Ding S-Y, Yu W, Liu Q*, et al.* Benzoxazole-Linked Ultrastable Covalent Organic Frameworks for Photocatalysis. *Journal of the American Chemical Society* 2018, **140**(13)**:** 4623-4631.
60. Cardona CM, Li W, Kaifer AE, Stockdale D, Bazan GC. Electrochemical Considerations for Determining Absolute Frontier Orbital Energy Levels of Conjugated Polymers for Solar Cell Applications. *Advanced Materials* 2011, **23**(20)**:** 2367-2371.
61. Calik M, Auras F, Salonen LM, Bader K, Grill I, Handloser M*, et al.* Extraction of Photogenerated Electrons and Holes from a Covalent Organic Framework Integrated

Heterojunction. *Journal of the American Chemical Society* 2014, **136**(51)**:** 17802-17807.

62. Zhao W, Zhuang X, Wu D, Zhang F, Gehrig D, Laquai F*, et al.* Boron-π-nitrogen-based conjugated porous polymers with multi-functions. *Journal of Materials Chemistry A* 2013, **1**(44).
63. Pellegrin Y, Odobel F. Sacrificial electron donor reagents for solar fuel production. *Comptes Rendus Chimie* 2017, **20**(3)**:** 283-295.
64. Gould RO, Harding MM. Nickel and palladium complexes of 1-hydroxyethane-2-thiol and analogues. Part I. Crystal structure of cyclohexakis[bis-(μ-1-hydroxyethane-2-thiolato)-nickel(II)]. *J Chem Soc A* 1970, **0**(0)**:** 875-881.
65. Zhang J, Chen X, Takanabe K, Maeda K, Domen K, Epping JD*, et al.* Synthesis of a Carbon Nitride Structure for Visible - Light Catalysis by Copolymerization. *Angewandte Chemie International Edition* 2010, **49**(2)**:** 441-444.
66. Schwinghammer K, Tuffy B, Mesch MB, Wirnhier E, Martineau C, Taulelle F*, et al.* Triazine-based Carbon Nitrides for Visible-Light-Driven Hydrogen Evolution. *Angewandte Chemie International Edition* 2013, **52**(9)**:** 2435-2439.
67. Indra A, Menezes PW, Kailasam K, Hollmann D, Schröder M, Thomas A*, et al.* Nickel as a co-catalyst for photocatalytic hydrogen evolution on graphitic-carbon nitride (sg-CN): what is the nature of the active species? *Chemical Communications* 2016, **52**(1)**:** 104-107.
68. Kasap H, Caputo CA, Martindale BCM, Godin R, Lau VW-h, Lotsch BV*, et al.* Solar-Driven Reduction of Aqueous Protons Coupled to Selective Alcohol Oxidation with a Carbon Nitride–Molecular Ni Catalyst System. *Journal of the American Chemical Society* 2016, **138**(29)**:** 9183-9192.
69. Zeng D, Ong W-J, Zheng H, Wu M, Chen Y, Peng D-L*, et al.* Ni12P5 nanoparticles embedded into porous g-C3N4 nanosheets as a noble-metal-free hetero-structure photocatalyst for efficient H2 production under visible light. *Journal of Materials Chemistry A* 2017, **5**(31)**:** 16171-16178.
70. Martindale BCM, Hutton GAM, Caputo CA, Reisner E. Solar Hydrogen Production Using Carbon Quantum Dots and a Molecular Nickel Catalyst. *Journal of the American Chemical Society* 2015, **137**(18)**:** 6018-6025.

71. Nanda J, Sapra S, Sarma DD, Chandrasekharan N, Hodes G. Size-Selected Zinc Sulfide Nanocrystallites: Synthesis, Structure, and Optical Studies. *Chemistry of Materials* 2000, **12**(4)**:** 1018-1024.

72. Biswal BP, Becker D, Chandrasekhar N, Seenath JS, Paasch S, Machill S*, et al.* Exploration of Thiazolo[5,4-d

]thiazole Linkages in Conjugated Porous Organic Polymers for Chemoselective Molecular Sieving. *Chemistry - A European Journal* 2018, **24**(42)**:** 10868-10875.

5. Toward Standardized Photocatalytic Oxygen Evolution Rates

The work in this chapter was reproduced and adapted from:

Toward Standardized Photocatalytic Oxygen Evolution Rates Using RuO_2@TiO_2 as a Benchmark

Hugo A. Vignolo-González*, Sourav Laha, Alberto Jiménez-Solano, Takayoshi Oshima, Viola Duppel, Peter Schützendübe and Bettina V. Lotsch

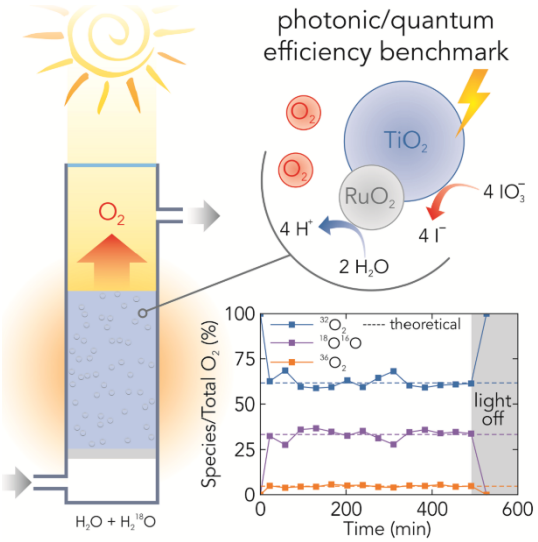

published in *Matter*. 2020, 3, 2, 464-486
DOI: 10.1016/j.matt.2020.07.021
https://doi.org/10.1016/j.matt.2020.07.021
Numbering of figures and headings were changed
Adapted with permission from Cell Press
(Electronic Supporting Information in Appendix C)

* H.A.V.-G. conceptualized and executed the ideas on material preparation, photocatalytic rates standardization, reactor engineering, and instrumental analysis; H.A.V.-G. and A.J.-S. conceptualized QE measurements; A.J.-S. modeled photocatalytic suspension optically and performed optical measurements; S.L. performed benchmark characterization and analysis, and supervised and improved material preparation; data analysis was performed by H.A.V.-G. A.J.-S., S.L., and T.O.; V.D. performed and analyzed TEM, TEM-EDX, and TEM-FFT experiments; P.S. performed XPS measurements; H.A.V.-G., A.J.-S., S. L., T.O., and B.V.L. discussed the concepts and manuscript target; H.A.V.-G. and T.O. wrote the original draft; H.A.V.-G., A.J.-S., S.L., T.O., and B.V.L. wrote, complemented, an edited the manuscript in different stages; B.V.L. and T.O. supervised the work.

5.1 Abstract

Quantitative comparison of photocatalytic performances across different photocatalysis setups is technically challenging. Here, we combine the concepts of relative and optimal photonic efficiencies to normalize activities with an internal benchmark material, RuO_2 photodeposited on a P25-TiO_2 photocatalyst, which was optimized for reproducibility of the oxygen evolution reaction (OER). Additionally, a general set of good practices was identified to ensure reliable quantification of photocatalytic OER, including photoreactor design, photocatalyst dispersion, and control of parasitic reactions caused by the sacrificial electron acceptor. Moreover, a method combining optical modeling and measurements was proposed to quantify the benchmark absorbed and scattered light (7.6% and 81.2%, respectively, of λ = 300–500 nm incident photons), rather than just incident light (≈AM 1.5G), to estimate its internal quantum efficiency (16%). We advocate the adoption of the instrumental and theoretical framework provided here to facilitate material standardization and comparison in the field of artificial photosynthesis.

5.2 Introduction

Global anthropogenic CO_2 emission rates grow at alarming rates. Along with increasing the share of renewables on energy portfolios worldwide, it is projected that renewable-to-chemical energy conversion is essential to control the global temperature rise.[1–3] In this context, artificial photosynthesis has gained attention in the last decades as it tackles larger-scale solar energy storage by producing chemical fuels such as hydrogen from abundant water and sunlight.[4–6] Nevertheless, the pinnacle of artificial photosynthesis, namely photocatalytic overall water splitting (POWS), not only drives an overall thermodynamically uphill chemical reaction using sunlight but also involves the kinetically highly challenging water oxidation reaction. Due to the latter, POWS has been blended with different branches of material research in order to achieve technically feasible applications. Since the first experiments with TiO_2 in 1972 by Honda and Fujishima that showed OWS for the first time, a large number of other semiconductor materials have been tested for POWS on a lab scale, reaching several milestones in solar-to-hydrogen efficiency (STH). Although the most efficient materials are still relatively far from the

commercial target of 2–4 US dollars per kilogram of H_2, the prospects of POWS using particle suspensions still look promising considering their low cost and STH efficiencies that are nowadays closer to the technical target of 5%-10%.[5,7–12]

Despite the evident progress in this field, a gap persists when comparing photocatalytic STH and other indicators of different materials synthesized and characterized under different groups' standards. An International Union of Pure & Applied Chemistry (IUPAC) report recommends to use so called "internal" quantum yield (Φ), which is defined as the ratio between the number of products formed or reactant consumed and the number of photons absorbed at a certain wavelength.[13,14] However, in heterogeneous suspension systems, it is very challenging to quantify the number of absorbed photons due to light scattering and/or reflection. As a compromise, photonic efficiencies (ξ_e) or apparent quantum yields (AQY), which consider total incident photons instead of absorbed photons in the yield ratio, are conventionally used. Hence, the key prefix "internal" or "apparent" (or "external") are used broadly to distinguish between absorbed or incident photons in the denominator. Strictly, the term "yield" should be restricted to the cases where the wavelength of such photons is narrowly bounded (i.e., in the limit of a single, specific wavelength), while "efficiency" refers to polychromatic light. Notwithstanding, photonic efficiency and external quantum efficiency (EQE) have been commonly used as equivalent external indicators to AQY when specifying a wavelength range, and likewise, internal quantum efficiency (IQE) has been commonly used interchangeably with internal quantum yield as an internal indicator.[13–17] Regardless of the consensus on terminology used to describe photocatalytic activity, along with the problem of light scattering, photocatalytic activity is dependent on many other factors, e.g., light intensity, extinction coefficient, reactants, and reactor design, most of which are either difficult to determine or to standardize.[13,15,18–20] These facts blur the current state of the art in the field. As a response to this challenge, several efforts have been made to create a platform for comparing photocatalytic activities under standardized conditions.[15,17] For example, a recent work proposed that materials should be compared only by photonic efficiencies at plateaus of photocatalytic production (or consumption) rate versus catalyst loading, which is defined as optimal photocatalytic rate (r_{opt}), then divided by the total incident photons to calculate the optimal photonic efficiency ($\xi_{e,opt}$).[13,15] However, this is a simplistic approach to

describe performance as compared with the more reliable internal indicators such as Φ. The Φ of a material is a more complex function of local light intensity at each wavelength, whose integration along the reactor suspension and light spectra gives the total photocatalytic rate observed.[21,22] However, assuming such averaging when comparing ξ_e at the optimal regime at least gives a glimpse at which material is more active than another overall, including the influence of a specific reaction cell in a regime where light cannot be further extinguished. It must be noted that this optimal ξ_e approach does not fully resolve the aforementioned light absorption quantification intricacies, and while technically challenging, internal quantum yield, or alternatively IQE, should be the preferred indicators for material comparison among different groups because such indicators suffer from less influence of the setup on their estimation.[13,15,20,23]

Alternatively, other novel hardware-based approaches can be also found in the literature to screen Φ directly, such as the integrating sphere embedded reactor,[17,23] and the black-body reactor.[22,24,25]When compared with the optimal photonic efficiency approach, hardware-based approaches are useful and even more powerful complementary techniques to quantify Φ functions directly if the locally absorbed photon flux profile along the photoreactor cell is accessible. Nevertheless, typical applications of the black-body reactor design suffer from unaccountable light distributions,[24,25] which is key to reporting a meaningful Φ function,[21,25,26] whereas the integrating sphere design restrictions in terms of photoreactor design make it less amenable to the comprehensive standardization of photocatalytic rates.[17,23] In this context, if Φ (or IQE) quantification is technically not possible, a possible methodology to reflect experimental discrepancies in different groups without imposing a particular photoreactor design is to include an internal standard material in the optimal photonic efficiency approach, assuming that its intrinsic Φ is measurable and universally consistent. To introduce this idea, let us imagine a generic newly developed photocatalyst within a research group 1, namely Material A, which is measured relative to an internal standard (Material "zero") in a specific setup 1 ($r^1_{opt,A}$ versus $r^1_{opt,0}$) to produce a reaction of interest (i.e., oxygen evolution reaction [OER]) at a reproducible incident light condition I_0 (i.e., AM 1.5G); and a similar study on Material B in a certain research group 2 ($r^2_{opt,B}$ versus $r^2_{opt,0}$), as depicted in Figure 5-1. If optimal photocatalytic OER rates of both Materials A and B are normalized

as $r'_{opt,A} = r^1_{opt,A}/r^1_{opt,0}$ and $r'_{opt,B} = r^2_{opt,B}/r^2_{opt,0}$—or, equivalently, $\xi'_{e,A} = \xi_e{}^1_{opt,A}/\xi_e{}^1_{opt,0}$ and $\xi'_{e,B} = \xi_e{}^2_{opt,B}/\xi_e{}^2_{opt,0}$ in the case of Materials A or B using a light standard different than I_0 (from now on defined generically as relative photonic efficiency, ξ'_e)—and as long as the internal standard has the same Φ property in both cases, the normalized rates r'_{opt} show semiquantitatively whether A or B has the higher apparent activity relative to the other material. For this comparison, there would be no other particular constraint on reaction media or reactor design for groups A or B, but general good experimental practices,[13,15,27] and that catalyst A, catalyst B, and the standard 0 are at the optimal point of their respective setups.

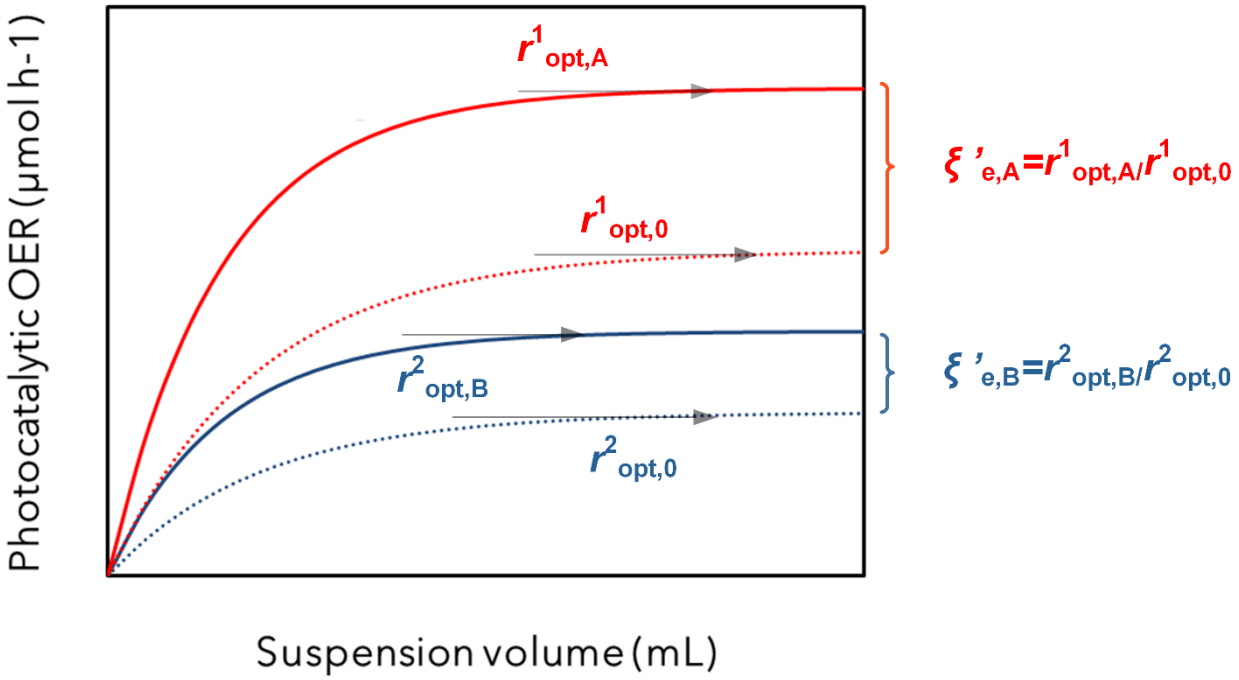

Figure 5-1. Photocatalytic activity versus photocatalytic suspension volume representation. Definition of optimal oxygen evolution reaction (OER) photocatalytic rate (r_{opt}), and relative photonic efficiencies (ξ'_e) using a unique illumination standard for materials A, B and benchmark (zero). Adapted from Qureshi and Takanabe.[13]

In 2003 and subsequently in 2011, similar photocatalysis standardization attempts had been developed in the field of photocatalytic degradation under ISO Standards, whereby acetaldehyde photodegradation on P25 Degussa (Evonik), a commercial form of TiO_2 (20-nm nanoparticles, 80% anatase, 20% rutile), was used as a standard system.[15,28,29] The foundations of these studies were laid by a comprehensive article by Serpone et al. in 1997 who developed the concept of relative photonic efficiencies (ξ'_e) providing actual

quantitative trends of P25 light absorption and scattering photocatalytic rates, and set the standard terminology for the field.[17] To the best of our knowledge, however, such methodologies have never been adapted to actual photosynthetic systems, presumably because of the fact that there is an inherent difference between photocatalytic degradation and energy conversion. Unlike photocatalytic degradation, artificial photosynthesis requires an activation step (in other words co-catalyst deposition) that is ideally simple, reproducible (optically and chemically), and robust, i.e., that maintains the nature of its surface chemistry whatever synthetic methodology is followed, which excludes doping or thermal sintering approaches. These restrictions most likely have hindered the concept of a benchmark photocatalyst in the field of artificial photosynthesis.

Here, we propose RuO_2 deposited on P25 as a benchmark photocatalyst for OER, which involves a kinetically challenging 4-electron transfer process, as an OER benchmark sufficiently active to estimate the required $r_{opt,0}$ reliably, to calculate relative photonic efficiencies as described in Figure 5-1. P25 as a commercial form of TiO_2 has been widely used as a photocatalyst including in different direct solar energy conversion studies.[30–37] P25 eliminates typical reproducibility problems that come with material synthesis because of its standardized fabrication. We identify optimal conditions from literature to deposit RuO_2 on colloidally stabilized P25 in a highly reproducible manner and thoroughly characterize the benchmark photocatalyst and its OER rates. In addition to the quantification of OER rates of reproducible optimal samples using the optimal photonic efficiency concept, isotopic labeling was performed under *operando* conditions to unequivocally associate such rates with water oxidation, as schemed in Figure 5-2. This result underpins our suggested best practices, which materialize in a set of recommendations that solve typical reproducibility weaknesses in the field. In addition, light absorption assessment is a feature in photocatalysis that is not frequently included in photocatalyst screening. Here, we present a method to estimate IQE by means of scattered light measurements and optical modeling, which estimated the absorbed and scattered light in the system as depicted in Figure 5-2. This IQE modeling is a measurement of efficiency that is more reactor independent and is measured under *operando* conditions for this benchmark, which opens a second door to a more powerful way of comparing materials among different groups in the field of artificial photosynthesis.

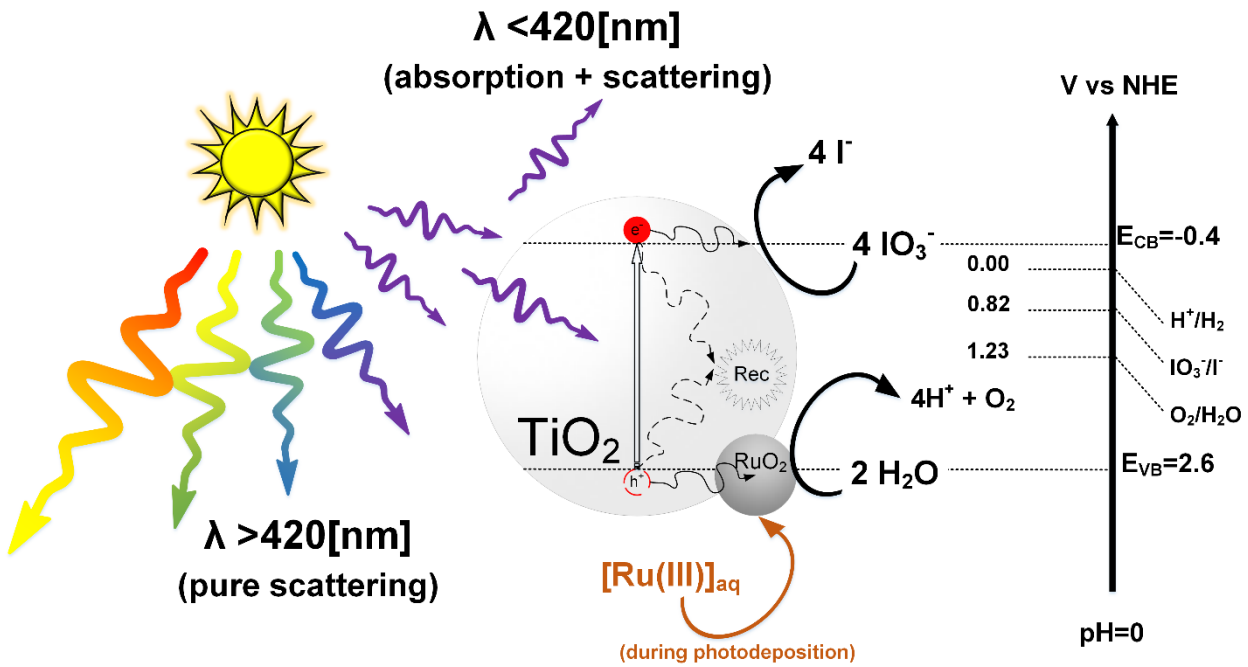

Figure 5-2. Band diagram (not to scale), light absorption, and reaction representation of P25/RuO_2 Benchmark for photocatalytic OER.

5.3 Results and discussion

5.3.1 Co-catalyst loading, dispersion environment and characterization

A catalyst/co-catalyst system that is maximally reproducible, robust, and error-tolerant regarding its synthesis while showing good OER rates is instrumental in its use as a benchmark system for determining relative photonic efficiencies. With this set of requirements in mind, two different deposition methods in liquid suspension were screened using only P25 and a Ru(III) precursor as the light harvester and co-catalyst tandem, respectively: photodeposition (PD) and low-temperature hydrothermal (HT) decoration.[12,38–41] Detailed deposition procedures can be found in Experimental Procedures (Appendix C). Having identified the optimal dispersion condition, the loading amount of Ru was optimized for each method separately (Figure C-2). The optimal nominal Ru(III)/P25 weight contents found are 0.15%, 0.30%, and 0.50% for photodeposition (PD), hydrothermal-microwave (HT-MW), and hydrothermal-heating-block (HT-HB) methods, respectively (nominal contents are calculated from initial Ru(III) mass in solution). Real Ru/P25 weight contents are measured with inductively coupled plasma-

optical emission spectrophotometry (ICP-OES) analysis (Table C-1). According to literature and our UV-visible (UV-vis) experiments (Figure C-3), excessive loading of ruthenium (Ru) species leads to a decrease in overall activity due to the black color of the product that competes with P25 light absorption while producing no reaction.[37,39] Having identified optimal Ru levels during deposition, we scaled the *ex situ* production of two samples that showed the highest activity at screening conditions, which allows decoupling of Ru deposition from photocatalytic OER rate measurements. These samples were deposited *ex situ* as follows: 0.15% nominal Ru loading using PD in the absence of dispersing agent (Ru0.15/P25-PD) and 0.3% nominal Ru% using the HT-MW method (Ru0.3/P25-HT-MW); for scale-up details of the methods, see Experimental Procedures (Appendix C).

A problem usually overlooked in the catalyst deposition on a semiconductor and that we have found much more relevant is the aggregation of semiconductor nanoparticles. The lack of homogeneity in deposition environment should alter the size and/or dispersion of catalyst, and we will show below that achieving a well-dispersed state for the photodeposited Ru species is key for using this system as a benchmark. In the particular case of P25, poor stability in suspension has been evidenced in pure aqueous media at neutral conditions (zeta-potential close to zero.[42,43] Accordingly, while depositing catalyst in pure water containing a catalyst precursor, sedimentation of P25 is significant, particularly when the suspension density is close to 1 mg mL^{-1}. However, this is a non-trivial problem to tackle, since organic dispersants are undesired due to their hole-scavenging nature. From the inorganic dispersants in literature, tetrasodium pyrophosphate (TSPP, $Na_4P_2O_7 \cdot 10H_2O$) was chosen among other inorganic dispersing agents because of its proven drastic effect in colloidally stabilizing TiO_2 nanoparticles at relatively low concentrations.[44] This is crucial, as the agglomerate size and homogeneity affect the dispersion of decorated co-catalyst and the optics of light absorption. In fact, the addition of TSPP visually increases sedimentation time significantly if suspension density is kept around 0.5 mg mL^{-1} of P25 in water.[44] In addition to this, we also performed dynamic light-scattering (DLS) experiments as a quantitative technique to obtain the %number distribution of different samples in suspension. It can be seen in Figure 5-3a that the micron-size agglomerates of P25 (alternatively P25 diameter distribution in percent is 1,351 nm [82%], 264 nm [12%], 5,520 nm [6%]) disappeared

after the incorporation of 1 mM TSPP, which according to the original study is a result of electrostatic stabilization due to physisorption of highly charged $P_2O_7^{4-}$ ions on the P25 surface. On the other hand, excessive addition of $P_2O_7^{4-}$ ions to photocatalytic media is not desired either, because it can block active sites by adsorption.[45,46] Not surprisingly, the effect of TSPP was found to be beneficial for photocatalytic activity around this optimum concentration of 1 mM but not beyond (Figure C-4). We therefore consider the addition of 1 mM TSPP as dispersing agent during photodeposition as a variation of the PD method, from now on defined simply as PD∗. Accordingly, a third *ex situ* sample was produced at 0.15% nominal Ru using PD with 1 mM TSPP as dispersing agent (Ru0.15/P25-PD∗).

The addition of TSPP had a positive impact on dispersion not only during co-catalyst deposition (Figure 5-3a and Figure C-4) but also after the deposition. The qualitative effect of dispersing agent on agglomeration of the *ex situ* sample suspensions was measured by DLS and is presented in Figure 5-3b – Figure 5-3d for the samples PD∗, HT-MW, and PD, respectively (gray distribution is no TSPP, pink distribution is 1 mM TSPP). These results show that after *ex situ* deposition, the addition of TSPP in all three samples is still beneficial in diminishing agglomerate size during the photocatalytic OER activity measurements.

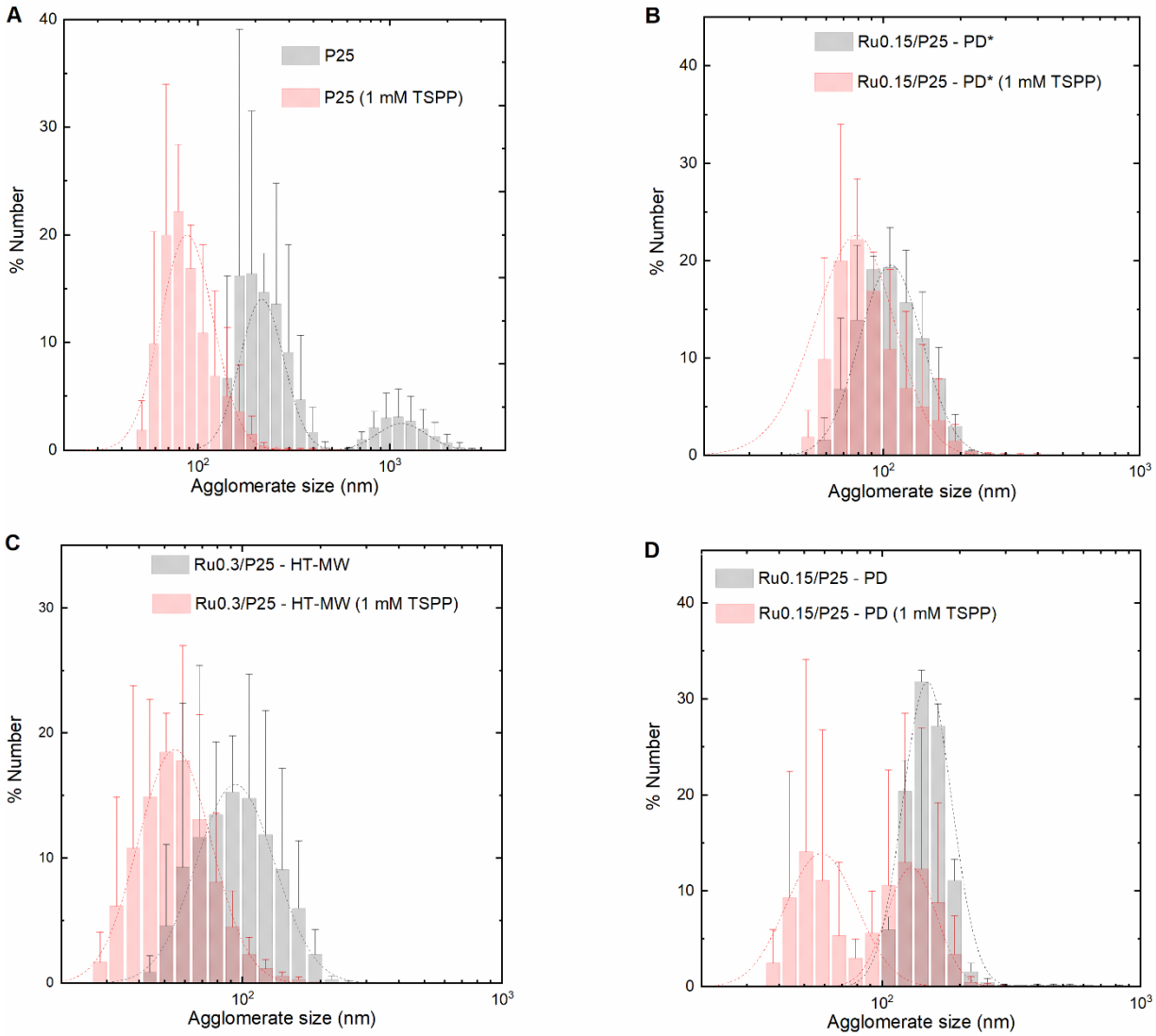

Figure 5-3. Dynamic light scattering (DLS) number % distribution of agglomerate size at 0.5 mg mL^{-1}. Three candidate P25/RuO_2 *ex situ* deposited samples and P25 suspensions were freshly prepared and sonicated under the exact photocatalytic conditions (10 mM KIO_3), at 0 and 1 mM TSPP (gray and pink, respectively) to obtain percent number distribution of agglomerate size. Suspension of P25 also contained Ru(III) precursor (0.02 mM $RuCl_3 \cdot xH_2O$ [0.15% Ru]). Dashed lines are log-normal fittings, and error bars correspond to ± SEM of duplicate datasets (10 redundant DLS measurements each). The *ex situ* deposited samples were previously prepared and collected using the following methods: **(a)** P25 blank, **(b)** 0.15% nominal Ru using PD with 1 mM TSPP (PD* method, sample Ru0.15/P25-PD*), **(c)** 0.3% nominal Ru% using the HT-MW method (Ru0.3/P25-HT-MW), and **(d)** 0.15% nominal Ru loading using PD in the absence of TSPP (Ru0.15/P25-PD).

To thoroughly characterize the benchmark material candidate, we used a comprehensive set of characterization techniques including powder X-ray diffraction (PXRD), transmission electron microscopy (TEM) coupled with energy-dispersive X-ray spectroscopy (TEM-EDX) and fast Fourier transformation (TEM-FFT), and X-ray photoelectron spectroscopy (XPS). As mentioned earlier, the PXRD pattern (Figure C-7) of P25 confirms that it is a mixture of

both anatase and rutile phases of TiO_2. On the other hand, no apparent change was observed in the PXRD patterns of PD∗ and HT-HB, which indicates low overall amounts of deposited Ru species on P25. TEM images of all the materials along with the TEM-FFTs of PD and HT-HB are shown in Figure 5-4a, and the corresponding TEM-EDX data are presented in Figure C-6. The TEM images underline the well-dispersed nature of the deposited Ru species. Especially the addition of TSPP during photodeposition made larger Ru particles scarcely visible on TEM images. As both samples PD and PD∗ have a similar real Ru content (ICP-OES, Table C-1) after deposition, it can be hypothesized that the sample using TSPP during photodeposition had a larger active surface of Ru species than the one without TSPP. The larger agglomerate size of P25 without TSPP restricted the Ru species to form only at the outer surface of those agglomerates, forming larger-sized clusters observable in the TEM as nanoparticles (Figure C-8). In contrast, at smaller P25 agglomerate sizes, the Ru species are formed on a larger surface area exhibiting smaller characteristic particle sizes (subnanometer). The d-spacings determined from the TEM-FFTs indicate deposition of metallic Ru and rutile RuO_2 nanoparticles using PD and HT-HB, respectively (samples $Ru^0$1.0/P25-PD and Ru1.0/P25-HT-HB).[47,48] In agreement with the above observations, XPS reveals the presence of only metallic Ru (Ru(0)) in PD, but the presence of both Ru(0) and Ru(IV) are observed in samples HT-HB and Ru 0.15/P25-PD∗ (Figure 5-4b; for detailed analysis see Supplemental Information, Appendix C). No trace of P, Cl, K, or Na was observed by the XPS peak analysis or ICP-OES measurements. Competing Ru(III) reduction to Ru(0) (at ~0.5 eV versus normal hydrogen electrode [pH 0]) is possible through the photoinduced formation of electron-hole pairs and the relatively small concentration of sacrificial electron acceptor (SEA) during the photodeposition process.[49]

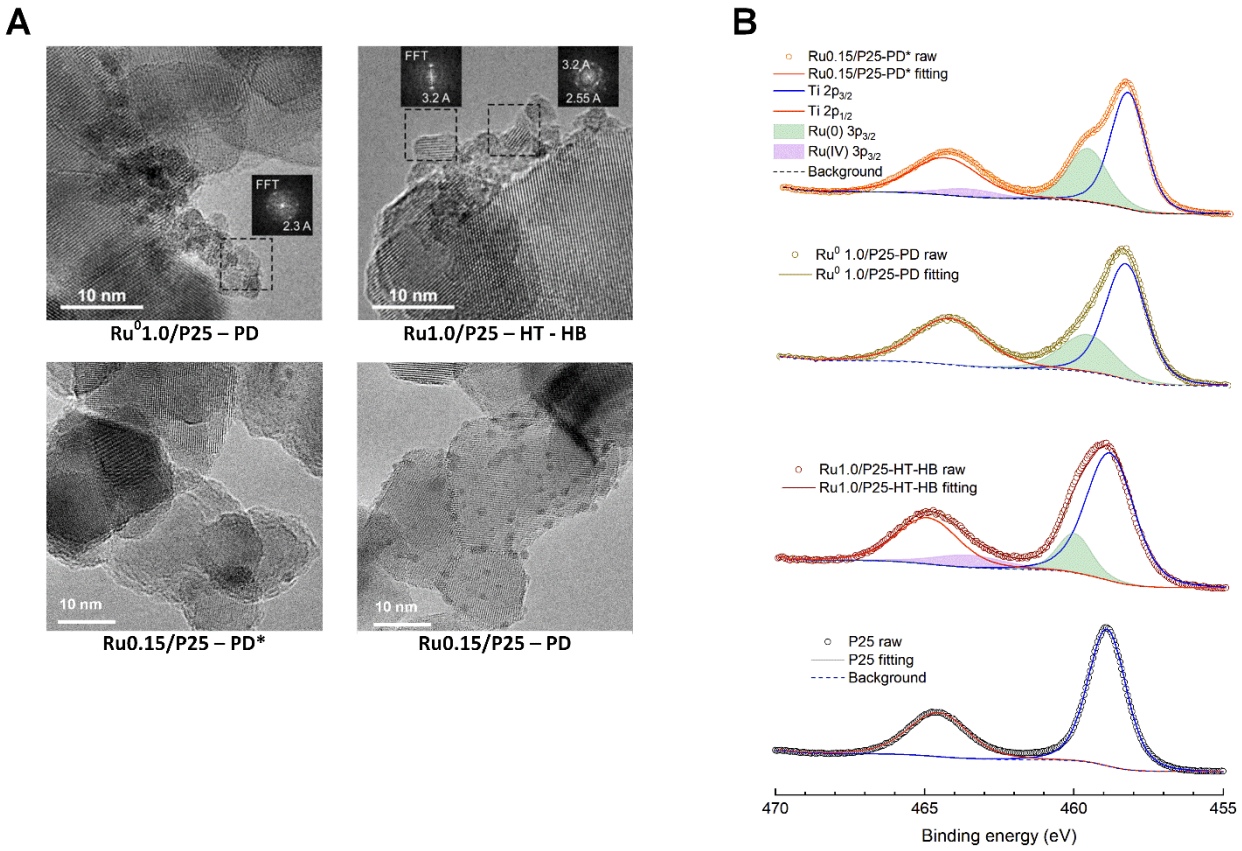

Figure 5-4. Heterojunction characterization of P25/RuO_2 ex-situ deposited samples. (a) TEM images showing the d-spacings obtained by fast Fourier transformation of the regions containing metallic Ru^0 (2.3 Å) and RuO_2 (3.2 Å) nanoparticles on P25. Reference samples are 1% PD Ru in methanol medium ($Ru^0$1.0/P25-PD), and HT deposited RuO_2 on P25 (Ru1.0/P25-HT-HB). TEM-EDX data of both are presented in Figure C-6. Ru0.15/P25-PD∗ and Ru0.15/P25-PD are the Ru% optimal samples PD *ex situ* with and without TSPP, respectively (scale bars, 10 nm). **(b)** XPS spectra of $Ru^0$1.0/P25-PD, Ru1.0/P25-HT-HB, Ru0.15/P25-PD∗, and P25 blank.

5.3.2 Photocatalytic OER detection platform

To allow for the precise quantification of OER photocatalytic rates on *ex situ* deposited RuO_2 on P25 samples, we developed a continuous-flow high-purity glass reactor[50] suitable for OER kinetic studies, optimized with a specific focus at overcoming O_2 mass transfer limitations, air leakages, and dead volumes (Figure 5-5 and Figure C-16). We also explored reactor-engineering concepts to optimize and combine trace detection and on-line analysis, which is flexible and sensitive enough to sample a wide range of reaction rates and reactor geometries; from an optics perspective, it is also simple enough to reproduce and model photon fate. The minimum O_2 detection limit of the three detection devices at the reactor outlet is around 1 ppmv, which is measured on top of a consistent background

amount of around 5 ppmv (for details see Experimental Procedures, Appendix C). At typical flow rates of 10–20 NmL min^{-1}, the minimum detectable activity can be as low as 0.02 μmol_{O2} h^{-1}, with an instrumental time resolution of 3 s. To the best of our knowledge, a comparably sensitive and versatile design has not yet been reported for photocatalysis, and resembles just vaguely other prototypes in the literature that also explored some forms of bubble-induced on-line photocatalytic OER.[51,52]

It is worth noting that the high sensitivity of our setup allowed us to identify several OER quantification abnormalities that may disguise the actual activity of P25. For instance, sodium persulfate and silver nitrate are widely used sacrificial electron acceptors; however, we observed O_2 evolution even without light absorber under illumination (Figure C-1). Compared with the measured OER rates in the case with light absorber (bare P25), the fraction of that OER rate evolved in the absence of light absorber was 72% and 0% for persulfate and KIO_3, respectively. Because $AgNO_3$ produces significant optical changes through Ag^0 deposition during its photoreduction, it was not considered for Ru deposition in this study, yet we quantified its OER background in the absence of P25 and obtained an amount similar to the one of persulfate, using an alternative detection of dissolved O_2 in liquid (for details of O_2 detection see Experimental Procedures, Appendix C). The parasitic O_2 amounts detected in the presence of persulfate and $AgNO_3$ are far beyond our instrumental error; therefore, it likely results from spontaneous SEA decomposition.[53] After trying different combinations of blanks and light conditions, we have identified that moderate KIO_3 concentrations (<20 mM) and AM 1.5G (I_0) have no significant background except in the presence of bare P25. Additionally, KIO_3 is not only an SEA but also a potential redox/shuttle for future photocatalytic OWS studies.[54] This is why we chose this diluted aqueous KIO_3 solution as a standard reaction medium.

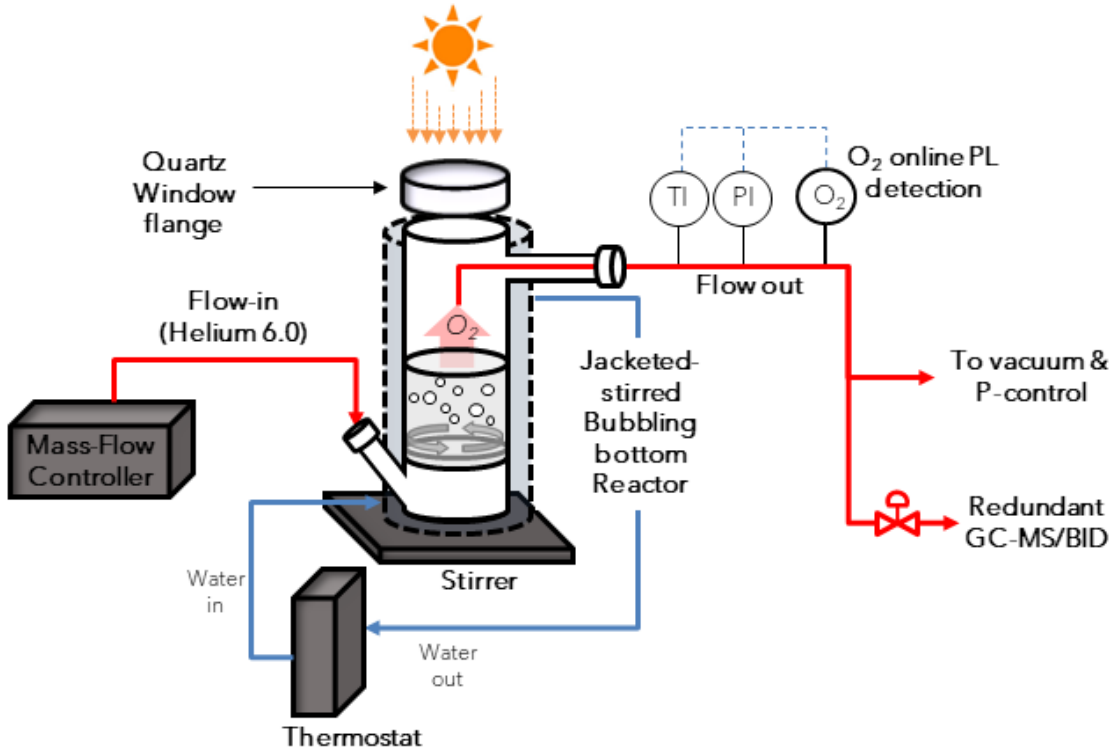

Figure 5-5. Schematic experimental set-up for direct on-line quantification of photocatalytic OER rates. Red lines are inert gas pathways. A controlled helium flow of 10–20 NmL min^{-1} bubbles through the liquid hold-up of the reactor through a porous frit, which is stirred and irradiated with a Xe lamp using an AM 1.5G spectra filter and an incident light intensity of 100 mW cm^{-2}.

5.3.4 Optimal photonic efficiencies and reproducibility of optimal samples

Using the setup described in Figure 5-5, the full curve of optimal photonic efficiency (equivalent trend to optimal photocatalytic OER rate r_{opt}) of the sample Ru0.15/P25-PD∗ (*ex situ* photodeposited at 1 mM TSPP) is presented in Figure 5-6a, and a summary of r_{opt} of all *ex situ* samples using the same methodology is shown in Figure 5-6b. The suspension conditions are 10 mM KIO_3, using the 0 and 1 mM of TSPP levels that were screened before to show differences on the sample agglomerate size (Figure 5-3), and a unique I_0 illumination standard (AM 1.5G). The sample Ru0.15/P25-PD∗ was preliminarily screened as the benchmark candidate, which is now justified given it has the highest r_{opt} measured at 1 mM TSPP (but not beyond, see Figure C-4); from now on this set of suspension conditions is simply referred to as benchmark standard.

From these results, it is evident that the optimal photonic efficiency of Ru species formed on Ru0.15/P25-PD∗ (photodeposition using 1 mM TSPP) and Ru0.15/P25-PD (photodeposition without TSPP) are far larger than those observed when using HT deposition methods, the latter being only 44% better than P25 without co-catalyst. The better results for the PD∗ over the PD method were already explained by agglomerate size measurements (DLS) on P25 with and without dispersing agent (Figure 5-3a), and further supported by TEM. A higher dispersion of the co-catalyst was seen in TEM images using TSPP (Figure C-8). On the other hand, the use of TSPP at 1 mM (but not beyond, see Figure C-4) versus 0 mM concentration during OER photocatalytic activity measurements has a minor positive impact only on photonic efficiency, on both Ru0.15/P25-PD and Ru0.15/P25-PD∗ samples, which was also supported by the small differences in agglomerate size of the samples observed by DLS when using dispersing agent (Figure 5-3b and Figure 5-3d); thus, this impact was expected to be less significant. This is consistent with our observations that the drastic change of distribution of Ru species formed at drastically different agglomerate sizes (Figure 5-3a) is what makes the sample Ru0.15/P25-PD∗ almost twice as active as Ru0.15/P25-PD. Therefore, the choice of Ru0.15/P25-PD∗ as the optimal benchmark is justified because of photonic efficiency and sample homogeneity. The use of dispersing agent during photocatalytic OER rate measurements is still positive due to the additional colloidal stabilization and higher photonic efficiency, and is thus justified to be included as part of the benchmark conditions (later justified for IQE estimations also).

More importantly, the PD method proved highly reproducible and robust to slight changes in setup during *ex situ* deposition (such as suspension volume, reactor geometries, and different AM 1.5G solar simulators). Although not optimal compared with PD∗ from an activity or dispersion point of view, the batch-to-batch variation statistics of the sample Ru0.15/P25-PD already shows a narrow normal distribution in Figure 5-6c and Figure 5-6d. On the other hand, a batch duplicate using the PD∗ method showed a difference in the r_{opt} experiment (at benchmark conditions) of only around 4%, and hence even better reproducibility than the PD method.

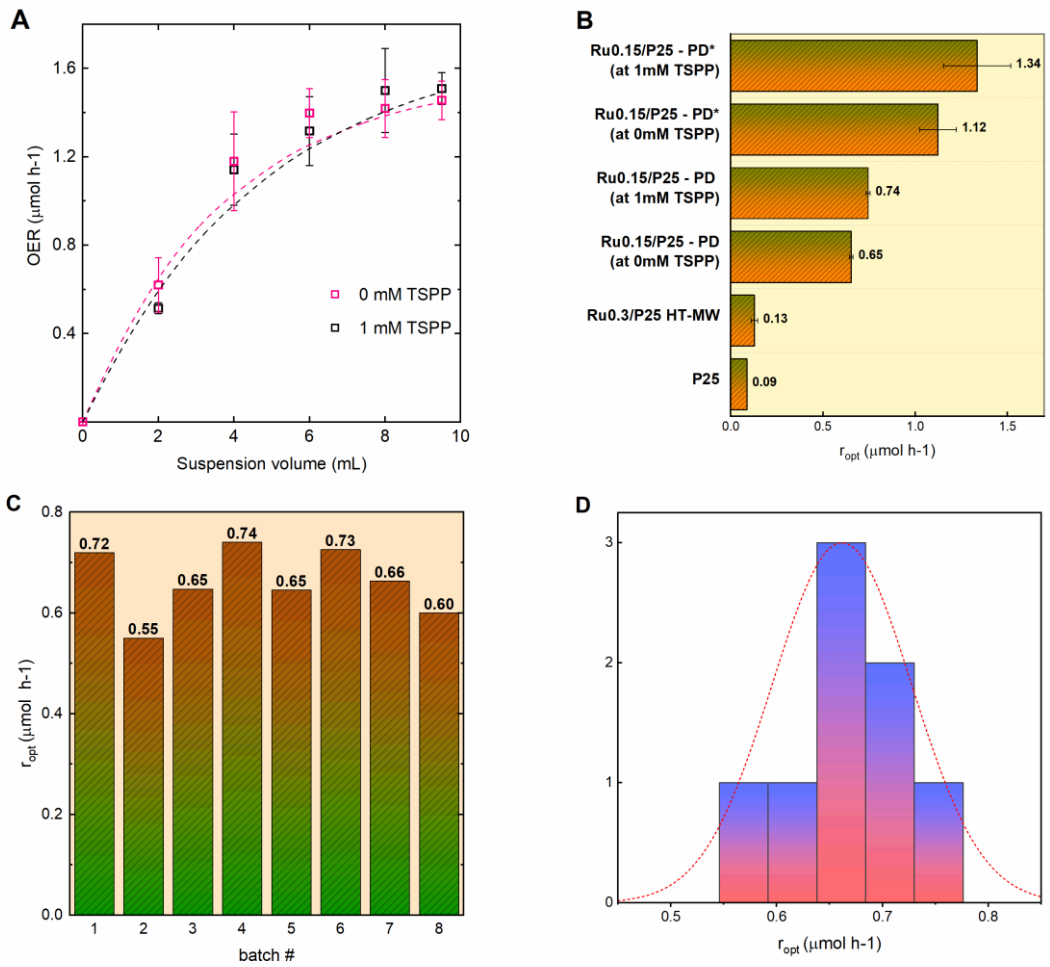

Figure 5-6. Comparison of photocatalytic OER methods and reproducibility. (a) Characteristic curve of optimal sample Ru0.15/P25-PD∗ (produced *ex situ* using 1 mM TSPP, details in Experimental Procedures**,** Appendix C), at 0.5 mg mL^{-1} and AM 1.5 conditions, at 10 mM KIO_3 using two levels of dispersant (dashed lines are fitted exponential apparent extinction curves, and data points are presented as mean ± SEM of duplicated measurements). **(b)** Comparison of overall activity using other deposition methods using the r_{opt} definition (error bars represent mean ± SEM of duplicated measurements). **(c)** Batch-to-batch variation of photocatalytic activity of sample Ru0.15/P25-PD produced *ex situ* (details in Experimental Procedures, Appendix C), then tested at 0.5 mg mL^{-1} and AM 1.5 conditions, at 10 mM KIO_3 and no dispersant. **(d)** Histogram representation of batch-to-batch variation in photocatalytic activity of sample Ru0.15/P25-PD (mean and SD values of fitted normal distribution in red dashed line are 0.65 and 0.05 µmol h^{-1}, respectively).

5.3.4 Benchmark photocatalytic water oxidation performance

Based on its high reproducibility and external photonic efficiency, Ru0.15/P25-PD* was chosen as a suitable OER benchmark. We present its dynamic rate measurements along with other performance indicators at photocatalytic conditions for longer time on-stream (14 h) in Figure 5-7. The results show no major deactivation in time and also a turnover number (TON_{avg}) of over 600 when the light was turned off, which is roughly one order of magnitude higher than the TON of a similar OER model system using a dye photoabsorber and a molecular water oxidation catalyst, near its full deactivation point.[52] This hints that the RuO_2/P25 tandem of our proposed benchmark is self-corrosion and agglomeration resistant at this timescale. A drop of 12% activity after the first 20 min is observed, which is usually ignored in the r_{opt} calculations because only the final stable values of OER rates are recorded in such cases. This drop might be attributed to I^- being backward oxidized.[55] We also present quantitative analysis using two complementary detection methods for O_2 by means of gas chromatography (GC). The signal of O_2 was quantified by highly sensitive barrier discharge ionization detection (BID) and mass spectrometry (MS), whose net response was different by only 8% and 10%, respectively, from the one measured with a photoluminescence sensor that quantifies O_2 based on the effect of dynamic luminescence quenching by molecular oxygen (PST9); this instrumental error of the three complementary detection devices was included in the statistics of r_{opt}.[50] Additionally, using this same platform a quantitative *operando* isotope labeling experiment was included using $H_2{}^{18}O$ water in a ratio 1:3 with respect to regular Milli-Q water. This experiment is key to unambiguously and quantitatively confirming that nearly all of the oxygen measured indeed comes from water oxidation. Similar attempts were tried in previous photocatalytic water oxidation studies, yet in our experiments a quantitative O_2 species population analysis in realistic reaction medium is provided.[56,57] The population of O_2 species presented in Figure 5-8 ($^{32}O_2$ = 61.8%, $^{16}O^{18}O$ = 33.4%, and $^{36}O_2$ = 4.7%) is fairly similar to the theoretical one assuming a mean field approximation and no kinetic isotope effect ($^{32}O_2$ = 60.2%, $^{16}O^{18}O$ = 34.7%, and $^{36}O_2$ = 5%). Although in terms of relative ratios of $^{16}O^{18}O$ and $^{36}O_2$ labeled species to $^{32}O_2$ this difference corresponds to 20% and 30% error respectively, showing a slight overpopulation of regular $^{32}O_2$, this deviation can be corrected considering a kinetic isotope effect (KIE). The isotope effect is predicted by

literature placing the rate-limiting step on the direct nucleophilic attack of the H_2O molecule to the photogenerated hole at surface lattice O sites, in which case both relative ratio errors drop to less than 2% and thus is contained in the instrumental error (Figure 5-8).[58,59] This result indeed validates all the blanks and choices made during the development of this methodology, including leakage and reaction control of the SEA.[53] Note that our RuO_2/P25 is active for OER not only with KIO_3, but also other commonly used SEAs such as $Na_2S_2O_8$ and $AgNO_3$, which opens up a platform for other groups to compare photocatalytic performances with an arbitrary SEA.

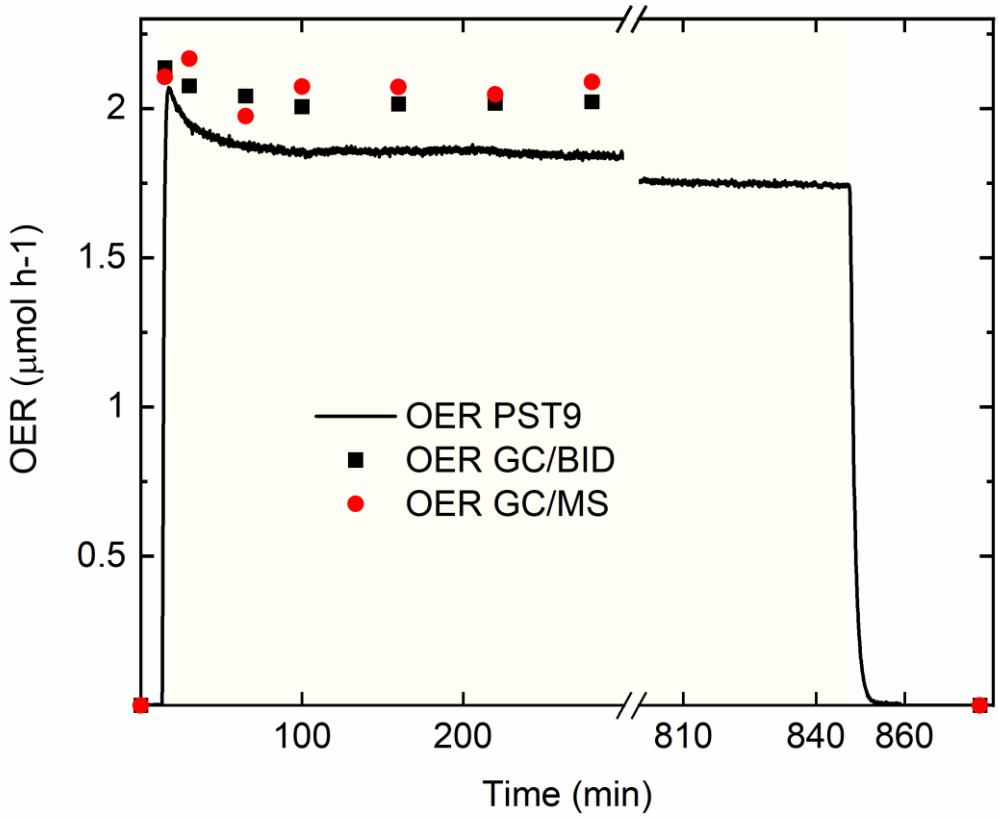

Figure 5-7. Quantitative analysis with the complementary GC-MS/BID system at longer Time on Stream. AM 1.5G, 1-sun Illumination, 5 mg Ru0.15/P25-PD*, 10 mL H_2O (10 mM KIO_3, 1 mM TSPP). After 14 h illumination (yellow graph background indicates light-on time interval), max. TOF_{avg} 49 h^{-1}, final $TON_{avg} \approx 600$, final TOF_{avg} = 86% of max. TOF_{avg}. Max. observed ξ_e(AM 1.5G) = 0.2%, ξ_e(AM 1.5G, λ < 420 nm) = 3.8%, max. observed IQE (AM 1.5G) = 16%.

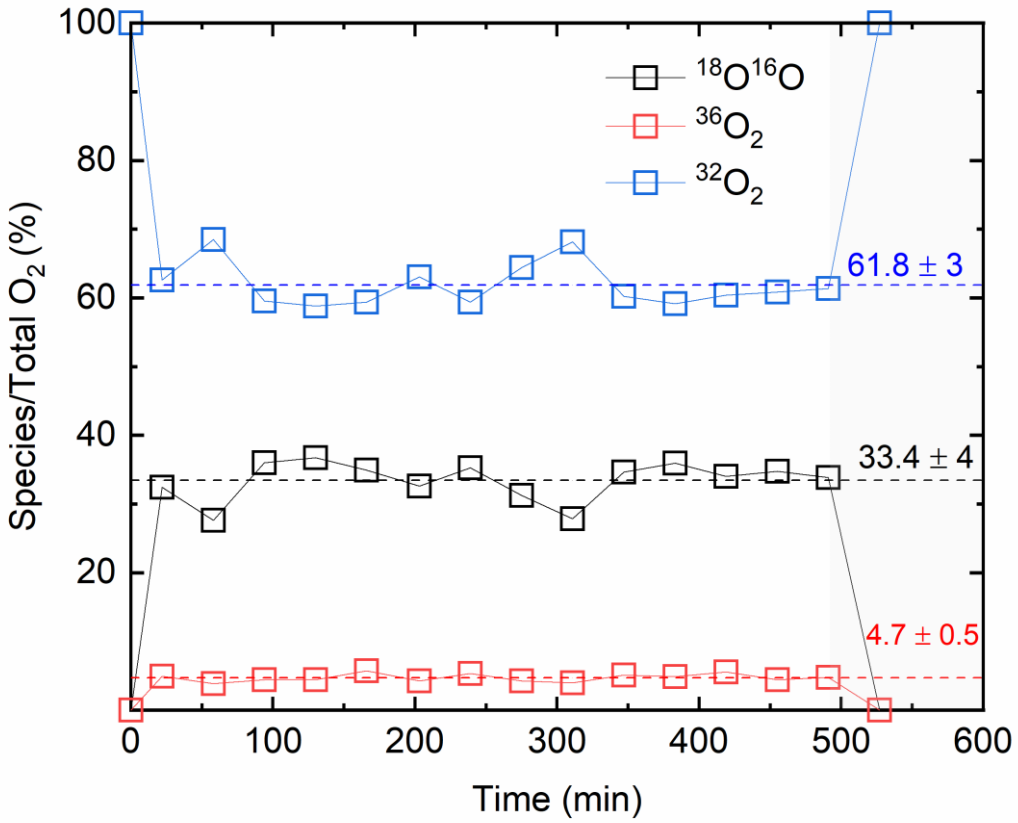

Figure 5-8. Isotopic mass distribution at O_2 retention time of GC. For channels *m*/*z* = 32 ($^{32}O_2$), *m*/*z* = 34 ($^{16}O^{18}O$), and *m*/*z* = 36 ($^{36}O_2$), obtained by integration of molecule counting around O_2 retention time, after 12 min of sample illumination during 500 min under identical conditions (gray graph background indicates light-off time interval), but 4-mL suspension using a ratio of 1:3 in weight of $H_2{}^{18}O$ (97%^{18}O) to H_2O (in dashed lines, O population statistic of mean ± SD).

5.3.5 Benchmark quantum efficiency

While the use of relative photonic efficiencies as reporting standard allows for a better cross-laboratory comparability of photocatalytic rates, IQEs have the advantage of being a more objective measure of a material's intrinsic photocatalytic activity, as the effect of scattering/reflection is excluded. As such, the difference between photonic efficiency and IQE signifies limitations of the overall reaction system in terms of light-management and suspension properties, which can then be optimized separately. The IQE of the benchmark sample under standardized conditions was estimated using stochastic optical modeling of the photon fate in the reaction system validated with *operando* measurements of side-scattered light. This is a key estimation that not only tells us about a measure of efficiency

of this benchmark that is more independent of the light-management design of the setup but also provides an additional criterion for standardization. Based on this model, the predicted side-scattered photon probability at different wavelengths and depths from the liquid-gas interface (0–32 mm, scheme in Figure C-12) is contrasted with experimentally measured light profiles under *operando* conditions, together with incident light *in situ* before the measurement, using a spectrophotometer, which is presented in Figure C-13. These results show a good agreement between the theory and experimental values for this section of the reactor, without any type of curve fitting besides position fine adjustment and normalization. The trend obtained for this section is extrapolated to the rest of the geometry and presented as overall probabilities of an incident photon to be reflected, scattered, or absorbed, which is presented in Figure 5-9.

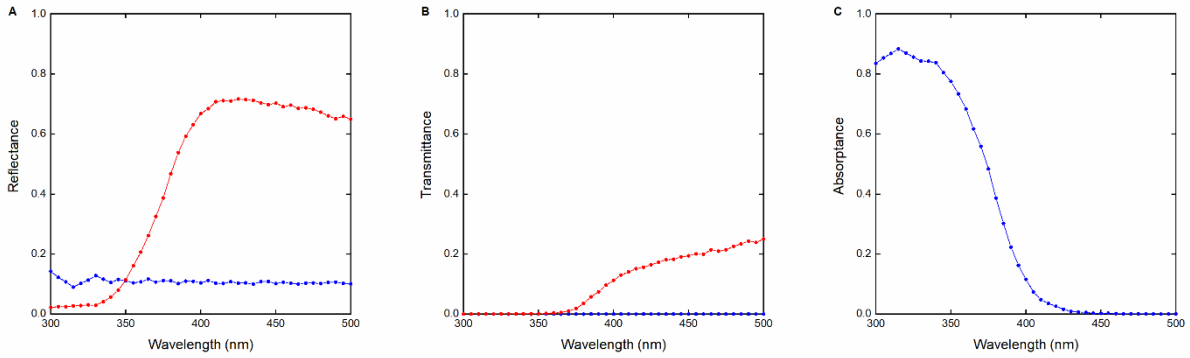

Figure 5-9. Predicted photon-fate vs wavelength in real reaction media. **(a)** Theoretical specular (blue) and diffuse (red) reflectance, **(b)** ballistic (blue) and diffuse (red) transmittance, and **(c)** absorptance. Suspension absorptance was used to calculate the rate of photons absorbed by the suspension for internal quantum efficiency (IQE) calculations.

The fraction of light that is absorbed by the suspension is only around 8.9% (Figure C-15). When quantified as absorbed photon flux, the IQE (AM 1.5G) of the system for this reactor geometry is estimated as 16%, versus the estimations for ξ_e(AM 1.5G) = 0.2% and ξ_e(AM 1.5G, λ < 420 nm) = 3.8%. Notwithstanding, this result should be taken as a spatial and spectral average IQE at this very AM 1.5G spectrum, geometry, and light intensity, since the actual quantum yield Φ of the material is a function of wavelength and local absorbed photon rate. This can be seen specifically from Figure C-14 showcasing that most of the photon absorption below 400 nm takes place in the first 2 mm of suspension, and we can expect that the observed IQE is an integration of the contribution of each slice

of suspension at different wavelength and light intensities.[21,26] Additionally, it can be seen in Figure C-15 and Figure 5-6a that the IQE measured at 10 mL is not a constant, because when compared with the trends of solar spectrum weighted integrated absorptance (SSWIA), defined as

$$\mathrm{SSWIA} = \frac{\int_{300}^{500} A(\lambda)\mathrm{AM1.5}G(\lambda)\mathrm{d}\lambda}{\int_{300}^{500} \mathrm{AM1.5}G(\lambda)\mathrm{d}\lambda} \qquad \text{Equation 5-1}$$

where $A(\lambda)$ is the absorptance of the suspension predicted for the points of r_{opt} measured at less suspension volume, it is clear that the ratio of r_{opt} to SSWIA is not preserved, which hints at the expected dependence of IQE on the local light intensity. In practical terms, though, even if what is preserved is the Φ function of the benchmark rather than a constant IQE, this IQE number (16%) may still be roughly extrapolated to other setups where the light absorption profile of a suspension or homogeneous solution can also be quantified (i.e., using an integrating sphere), as a complementary and more meaningful comparison to the proposed ξ'_e normalization. The normalization based on relative photonic efficiencies ξ'_e proposed here simplifies the comparison of photocatalytic activities obtained for different materials tested in different experimental setups because it captures overall differences in light absorption and scattering for both material and benchmark, as long as the Φ of the benchmark is preserved. On the other hand, the IQE of the benchmark reported here is a trend that is more likely to be preserved quantitatively regardless of slight differences in experimental setups. While Φ is technically challenging to be measured for most heterogeneous suspensions, we still recommend that IQEs should be primarily compared if possible, as IQE is an indicator closer to Φ than ξ_e and involves less averaging, and thus is less influenced by the reactor design, which is ultimately desired for a more rigorous standardization among groups.

5.4 Conclusion

We have established a photocatalytic OER benchmark system based on a photodeposition method to produce a material with appreciable and reproducible OER activity, obtained from a suitable commercial reactant that is widely accessible. Using a modified photodeposition protocol complemented by colloidal stabilization under the optimized conditions (loading of 0.15 w/w % of Ru(III) to P25, a suspension density of 0.5 mg of P25 per mL of an aqueous solution containing 10 mM KIO_3 as SEA and 1 mM TSPP as a dispersing agent), the collected material can be used as a photocatalytic OER benchmark in an activity screening platform by normalizing the photocatalytic OER rates of an arbitrary sample in an arbitrary setup against this benchmark measured under the same experimental conditions. Equally important, we present a set of best practices in the field to make photocatalytic OER quantification in general more reliable, including on-line OER detection, accurate subtraction of leakage backgrounds, elimination of parasitic O_2 background and minimization of sacrificial use, suspension stability measures, and complementary OER measurements to validate quantification. Importantly, we reveal that typical SEAs such as persulfate and silver nitrate can evolve O_2 even without light absorber, which advocates for a more careful use of SEAs in general. Finally, we present two novel *operando* techniques to corroborate first that O_2 was produced solely from water oxidation (^{18}O isotope labeling using on-line GC-MS) and that the interplay of light scattering and absorption plays an important role in determining measured photonic and internal quantum efficiencies of the benchmark, as verified by photon fate modeling and side-scattered light measurements. Both techniques play a central role in the determination of the IQE of the benchmark, which is an indicator closer to quantum yield, the gold standard in photocatalysis. Although not much literature is devoted to quantitatively accessing quantum yields in heterogeneous photocatalysis, this is the ultimate performance indicator for the field of artificial photosynthesis because it is reactor independent. We recommend the direct comparison of quantum yield or, alternatively, IQE, to primarily evaluate photocatalyst OER efficiencies, which can be benchmarked with the IQE estimations presented here. Alternatively, for materials whose light absorption cannot be readily quantified, the relative photonic efficiency method presented here is a first step toward standardizing photocatalytic activity results. Therefore, reporting relative

photonic efficiencies would greatly simplify the comparison of results reported by different groups. It is our hope that the methodology presented here fosters and facilitates both the creation and use of photocatalytic benchmarks and at the same time opens up new avenues to reliably compare photocatalytic performance indicators across different laboratories by means of quantum yield estimations or, alternatively, IQE.

5.5 Acknowledgements

Financial support is gratefully acknowledged from the Max Planck Society, an ERC Starting Grant (project COF Leaf, grant number 639233), the Cluster of Excellence e-conversion, and the Center for Nanoscience. A.J.-S. gratefully acknowledges a postdoctoral scholarship from the Max Planck Society. We thank Prof. Schütz (Max Planck Institute for Intelligent Systems, Stuttgart, MPI-IS) for allowing XPS analysis at their facilities. The authors are grateful to Dr. Gunther Richter for helpful discussion of XPS data and the MPI-IS for the XPS infrastructure support. The authors thank M.-L. Schreiber for performing ICP analysis.

5.6 References

1. Walsh, B. *et al.* Pathways for balancing CO2 emissions and sinks. *Nat Commun* **8**, 14856 (2017).
2. Peters, G. P. *et al.* Carbon dioxide emissions continue to grow amidst slowly emerging climate policies. *Nature Climate Change* vol. 10 3–6 Preprint at https://doi.org/10.1038/s41558-019-0659-6 (2020).
3. Bosetti, V. *et al.* COP21 climate negotiators' responses to climate model forecasts. *Nat Clim Chang* **7**, 185–189 (2017).
4. Osterloh, F. E. Photocatalysis versus Photosynthesis : A Sensitivity Analysis of Devices for Solar Energy. *ACS Energy Lett.* **2**, 445−453 (2017).
5. Wang, Q. & Domen, K. Particulate Photocatalysts for Light-Driven Water Splitting: Mechanisms, Challenges, and Design Strategies. *Chem Rev* **120**, 919–985 (2020).
6. Chen, X., Shen, S., Guo, L. & Mao, S. S. Semiconductor-based Photocatalytic Hydrogen Generation. *Chem Rev* **110**, 6503–6570 (2010).

7. Roger, I., Shipman, M. A. & Symes, M. D. Earth-abundant catalysts for electrochemical and photoelectrochemical water splitting. *Nat Rev Chem* **1**, 3 (2017).
8. Chen, S., Takata, T. & Domen, K. Particulate photocatalysts for overall water splitting. *Nature Publishing Group* **2**, 1–17 (2017).
9. Ma, Y. *et al.* Titanium Dioxide-Based Nanomaterials for Photocatalytic Fuel Generations. *Chem. Rev.* **114**, 9987−10043 (2014).
10. Linsebigler, A. L., Lu, G. & Yates, J. T. Photocatalysis on TiOn Surfaces: Principles, Mechanisms, and Selected Results. *Chem. Rev.* **95**, 735–758 (1995).
11. Goto, Y. *et al.* A Particulate Photocatalyst Water-Splitting Panel for Large-Scale Solar Hydrogen Generation. *Joule* **2**, 509–520 (2018).
12. Wang, Q. *et al.* Scalable water splitting on particulate photocatalyst sheets with a solar-to-hydrogen energy conversion efficiency exceeding 1%. *Nat Mater* **15**, 611–615 (2016).
13. Qureshi, M. & Takanabe, K. Insights on measuring and reporting heterogeneous photocatalysis: Efficiency definitions and setup examples. *Chemistry of Materials* **29**, 158–167 (2017).
14. Braslavsky, S. E. *et al.* Glossary of terms used in photocatalysis and radiation catalysis (IUPAC Recommendations 2011). *Pure and Applied Chemistry* **83**, 931–1014 (2011).
15. Kisch, H. & Bahnemann, D. Best Practice in Photocatalysis: Comparing Rates or Apparent Quantum Yields? *Journal of Physical Chemistry Letters* **6**, 1907–1910 (2015).
16. Cabrera, M. I., Alfano, O. M. & Cassano, A. E. Novel Reactor for Photocatalytic Kinetic Studies. *Ind Eng Chem Res* **33**, 3031–3042 (1994).
17. Serpone, N. Relative photonic efficiencies and quantum yields in heterogeneous photocatalysis. *J Photochem Photobiol A Chem* **104**, 1–12 (1997).
18. Grewe, T., Meggouh, M. & Tüysüz, H. Nanocatalysts for Solar Water Splitting and a Perspective on Hydrogen Economy. *Chem Asian J* **11**, 22–42 (2016).
19. Schlögl, R. Heterogeneous catalysis. *Angewandte Chemie - International Edition* **54**, 3465–3520 (2015).
20. Wachs, I. E., Phivilay, S. P. & Roberts, C. A. Reporting of reactivity for heterogeneous photocatalysis. *ACS Catal* **3**, 2606–2611 (2013).

21. Emeline, A. V, Ryabchuk, V. K., Serpone, N. & May, R. V. Dogmas and Misconceptions in Heterogeneous Photocatalysis . Some Enlightened Reflections. *J. Phys. Chem. B* **109**, 18515–18521 (2005).
22. Emeline, A. V., Zhang, X., Jin, M., Murakami, T. & Fujishima, A. Application of a 'black body' like reactor for measurements of quantum yields of photochemical reactions in heterogeneous systems. *Journal of Physical Chemistry B* **110**, 7409–7413 (2006).
23. Kunz, L. Y. *et al.* Artificial inflation of apparent photocatalytic activity induced by catalyst-mass-normalization and a method to fairly compare heterojunction systems. *Energy Environ Sci* **12**, 1657–1667 (2019).
24. Megatif, L., Dillert, R. & Bahnemann, D. W. Reaction rate study of the photocatalytic degradation of dichloroacetic acid in a black body reactor. *Catalysts* **9**, 635–652 (2019).
25. Megatif, L., Dillert, R. & Bahnemann, D. W. Determination of the quantum yield of a heterogeneous photocatalytic reaction employing a black body photoreactor. *Catal Today* 0–1 (2019) doi:10.1016/j.cattod.2019.06.008.
26. Ollis, D. F. Kinetic disguises in heterogeneous photocatalysis. *Top Catal* **35**, 217–223 (2005).
27. Wang, Z., Li, C. & Domen, K. Recent developments in heterogeneous photocatalysts for solar-driven overall water splitting. *Chem Soc Rev* **48**, 2109–2125 (2019).
28. ISO - International Organization for Standardization. Fine Ceramics (Advanced Ceramics, Advanced Technical Ceramics) — Test Method for Air-Purification Performance of Semiconducting Photocatalytic Materials — Part 1: Removal of Nitric Oxide. (2016).
29. ISO - International Organization for Standardization. Fine ceramics (Advanced Ceramics, Advanced Technical Ceramics) — Test method for Air-Purification Performance of Semiconducting Photocatalytic Materials — Part 2: Removal of acetaldehyde. (2019).
30. Pougin, A., Dilla, M. & Strunk, J. Identification and exclusion of intermediates of photocatalytic CO2 reduction on TiO2 under conditions of highest purity. *Physical Chemistry Chemical Physics* **18**, 10809–10817 (2016).

31. Dilla, M. *et al.* The fate of O2 in photocatalytic CO2 reduction on TiO2 under conditions of highest purity. *Phys.Chem.Chem.Phys.* **21**, 15949–15957 (2019).
32. Dilla, M. *et al.* Judging the feasibility of TiO2 as photocatalyst for chemical energy conversion by quantitative reactivity determinants. *Phys. Chem. Chem. Phys.* **21**, 13144–13150 (2019).
33. Dilla, M., Schlçgl, R. & Strunk, J. Photocatalytic CO2 Reduction Under Continuous Flow High-Purity Conditions : Quantitative Evaluation of CH4 Formation in the Steady-State. *ChemCatChem* **9**, 696–704 (2017).
34. Huang, L. *et al.* Cl− making overall water splitting possible on TiO2-based photocatalysts. *Catal. Sci. Technol.* **4**, 2913–2918 (2014).
35. Hashimoto, K., Irie, H. & Fujishima, A. TiO2 Photocatalysis : A Historical Overview and Future Prospects. **44**, 8269–8285 (2006).
36. Li, R. *et al.* Achieving overall water splitting using titanium dioxide-based photocatalysts of different phases. *Energy Environ. Sci.* **8**, 2377–2382 (2015).
37. Wenderich, K. & Mul, G. Methods, Mechanism, and Applications of Photodeposition in Photocatalysis: A Review. *Chem Rev* **116**, 14587–14619 (2016).
38. Mills, A., Duckmanton, P. A. & Reglinski, J. A simple, novel method for preparing an effective water oxidation catalyst. *Chemical Communications* **46**, 2397–2398 (2010).
39. Mi, S. Y., Liu, Y. X. & Wang, W. D. Photo-depositing Ru and RuO2 on Anatase TiO2 Nanosheets as Co-catalysts for Photocatalytic O2 Evolution from Water Oxidation. *Chinese Journal of Chemical Physics* **29**, 585–590 (2016).
40. Jiao, Y., Jiang, H. & Chen, F. RuO2/TiO2/Pt ternary photocatalysts with epitaxial heterojunction and their application in CO oxidation. *ACS Catal* **4**, 2249–2257 (2014).
41. Xiang, G., Shi, X., Wu, Y., Zhuang, J. & Wang, X. Size effects in Atomic-Level Epitaxial Redistribution Process of RuO2 over TiO2. *Sci Rep* **2**, 801 (2012).
42. Teleki, A., Wengeler, R., Wengeler, L., Nirschl, H. & Pratsinis, S. E. Distinguishing between aggregates and agglomerates of flame-made TiO2 by high-pressure dispersion. *Powder Technol* **181**, 292–300 (2008).
43. Suttiponparnit, K., Jiang, J., Sahu, M. & Suvachittanont, S. Role of Surface Area , Primary Particle Size , and Crystal Phase on Titanium Dioxide Nanoparticle Dispersion Properties. *Nanoscale Res Lett* **6**, 1–8 (2011).

44. Jiang, J., Oberdörster, G. & Biswas, P. Characterization of size, surface charge, and agglomeration state of nanoparticle dispersions for toxicological studies. *Journal of Nanoparticle Research* **11**, 77–89 (2009).
45. Zhao, D. *et al.* Surface modification of TiO2 by phosphate: Effect on photocatalytic activity and mechanism implication. *Journal of Physical Chemistry C* **112**, 5993–6001 (2008).
46. Ajmal, A., Majeed, I., Malik, R. N., Idriss, H. & Nadeem, M. A. Principles and mechanisms of photocatalytic dye degradation on TiO2 based photocatalysts: A comparative overview. *RSC Adv* **4**, 37003–37026 (2014).
47. Persson, K. Materials Data on RuO2 (SG:136) by Materials Project. **4**, (2016).
48. Persson, K. Materials Data on Ru (SG:194) by Materials Project. **4**, (2016).
49. Povar, I. & Spinu, O. Ruthenium redox equilibria: 3 . Pourbaix diagrams for the systems Ru-H2O and Ru-Cl - -H2O. *J. Electrochem. Sci. Eng.* **6**, 145–153 (2016).
50. Biswal, B. P. *et al.* Sustained Solar H2 Evolution from a Thiazolo[5,4-d]thiazole-Bridged Covalent Organic Framework and Nickel-Thiolate Cluster in Water. *J Am Chem Soc* **141**, 11082–11092 (2019).
51. Hernández, S. *et al.* A new method for studying activity and reaction kinetics of photocatalytic water oxidation systems using a bubbling reactor. *Chemical Engineering Journal* **238**, 17–26 (2014).
52. Limburg, B., Bouwman, E. & Bonnet, S. Rate and Stability of Photocatalytic Water Oxidation using [Ru(bpy)3] 2+ as Photosensitizer. *ACS Catal. 2016,* **6**, 5273−5284 (2016).
53. Schneider, J. & Bahnemann, D. W. Undesired Role of Sacrificial Reagents in Photocatalysis. *J. Phys. Chem. Lett.* **4**, 3479–3483 (2013).
54. Abe, R., Sayama, K., Domen, K. & Arakawa, H. A new type of water splitting system composed of two different TiO2 photocatalysts (anatase , rutile) and a IO-3/I- shuttle redox mediator. *Chem Phys Lett* **344**, 339–344 (2001).
55. Abe, R., Sayama, K. & Arakawa, H. Significant effect of iodide addition on water splitting into H2 and O2 over Pt-loaded TiO2 photocatalyst : suppression of backward reaction. *Chem Phys Lett* **371**, 360–364 (2003).

56. Bui, T. D., Yagi, E., Harada, T., Ikeda, S. & Matsumura, M. Isotope tracing study on oxidation of water on photoirradiated TiO 2 particles. *Appl Catal B* (2012) doi:10.1016/j.apcatb.2012.07.014.
57. Ding, Q. *et al.* Unravelling the water oxidation mechanism on NaTaO3–based photocatalyst. *J Mater Chem A Mater* (2020) doi:10.1039/c9ta14235e.
58. Miyoshi, A., Nishioka, S. & Maeda, K. Water Splitting on Rutile TiO2 -Based Photocatalysts. *Chem. Eur.J. 2018,* **24**, 18204–18219 (2018).
59. Valdés, Á., Qu, Z. W., Kroes, G. J., Rossmeisl, J. & Nørskov, J. K. Oxidation and photo-oxidation of water on TiO2 surface. *Journal of Physical Chemistry C* **112**, 9872–9879 (2008).

6. Morphology matters: 0D/2D Composites for Enhanced Photocatalytic OER Rates

The work in this chapter was reproduced and adapted from:

Morphology Matters: 0D/2D WO_3 Nanoparticle-Ruthenium Oxide Nanosheet Composites for Enhanced Photocatalytic Oxygen Evolution Reaction Rates

Hugo A. Vignolo-González, Andreas Gouder, Sourav Laha, Viola Duppel, Sol Carretero-Palacios, Alberto Jiménez-Solano, Takayoshi Oshima, Peter Schützendübe, Bettina V. Lotsch.

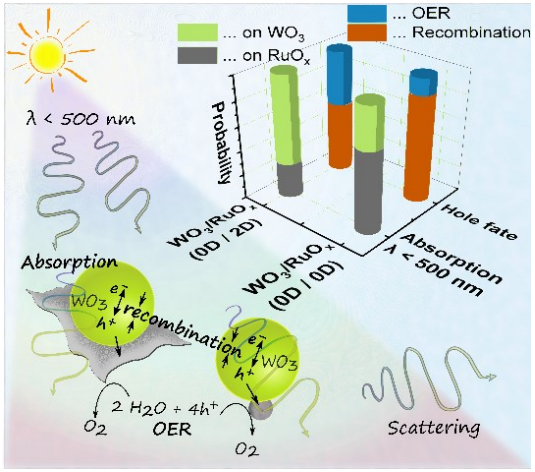

Accepted in *Adv. Energy Mater.*
DOI: 10.1002/aenm.202203315
https://doi.org/10.1002/aenm.202203315
Numbering of figures and headings were changed
Adapted with permission from Wiley-Adv. Energy Mater.
(Electronic Supporting Information in Appendix D)

6.1 Abstract

In the field of artificial photosynthesis with semiconductor light harvesters, the default cocatalyst morphologies are isotropic, zero-dimensional (0D) nanoparticles. Herein we present the use of highly anisotropic 2D ruthenium oxide nanosheet (RONS) cocatalysts as an approach to enhance photocatalytic oxygen evolution (OER) rates on commercial WO_3 nanoparticles (0D light harvester). At optimal cocatalyst loadings and identical photocatalysis conditions, WO_3 impregnated with RONS (RONS/WO_3) shows a 5-fold increase in normalized photonic efficiency compared to when it is impregnated with conventional ruthenium oxide (rutile) nanoparticles (RONP/WO_3). We attribute the superior RONS/WO_3 performance to two special properties of the RONS: (i) lower electrochemical water oxidation overpotential for RONS featuring highly active edge sites, and (ii) decreased parasitic light absorption on RONS. We present evidence that OER photocatalytic performance can be doubled with control of RONS edges and show that compared to WO_3 impregnated with RONP, the advantageous optical properties and geometry of RONS decrease the fraction of light absorbed by the cocatalyst, thus reducing the parasitic light absorption on the RONS/WO_3 composite. Therefore, the results presented in the current study will promote engineering of cocatalyst morphology as a complementary concept to optimize light harvester-cocatalyst composites for enhanced photocatalytic efficiency.

6.2 Introduction

Artificial photosynthesis has grown in the last decades due to its potential to store solar energy on large scale and long term by producing clean chemical fuels, such as hydrogen, with the energy input of sunlight.[1–3] Conversion of water into H_2 and O_2 utilizing sunlight is one of the most challenging yet rewarding photosynthetic processes, which is generally known as photocatalytic overall water splitting (POWS).[3–6] Water splitting is a thermodynamically uphill chemical reaction composed of simultaneous hydrogen evolution and oxygen evolution reactions (HER and OER). The OER is kinetically slower since it requires 4-electron transfer to oxidize water, and therefore, water oxidation is consistently referred to as the main kinetic bottleneck of water splitting.[2,7–10] When studying OER half-reactions, only a handful inorganic photocatalysts can harvest light efficiently, generate

sufficiently oxidative holes, and catalyze water oxidation without a dedicated cocatalyst, all on the same material, i.e., $BiVO_4$, Ta_3N_5, and rutile-TiO_2.[11–15] For most semiconductor light harvesters though, the addition of a cocatalyst that reduces the electrochemical overpotential for water oxidation is imperative to overcome kinetically sluggish hole-transfer at the light harvester surface. Reducing the overpotential for water oxidation at the expense of requiring an additional hole-transfer step at the light harvester/cocatalyst junction can be a beneficial compromise, if other aspects of the created interface are properly controlled (i.e., band alignment) or even improved, for example by reducing electron-hole recombination losses through improved charge carrier separation at the new interface.[16–18] Common OER light harvesters include TiO_2 (UV), TaON, and WO_3;[13,19–22] and the most efficient OER cocatalysts are noble metal oxides, like RuO_x and IrO_x.[11,13,21,23] Optimization of the cocatalyst component of these hybrid photocatalytic systems is crucial to improve photocatalytic OER performance. In addition to cocatalyst load, close attention should be paid to tuning the deposition method, cocatalyst structure (e.g., core-shell structure), and chemical composition.[14,24,25] Such features, among others, have a direct impact on optical and photocatalytic properties of the light harvester/cocatalyst junction which ultimately govern activity, for example light absorption and charge transfer.[5,11,26,27] It is well established in literature that impregnation-calcination, photo-deposition, and hydrothermal methods can readily load active cocatalyst nanoparticles (0D morphology) directly on the surface of a semiconductor light harvester from precursor salts like $RuCl_3$, $IrCl_3$, and H_2PtCl_6.[21,23,28,29] However, despite their simplicity, reproducibility, and high degree of cocatalyst dispersion on a light harvester support, these methods generally suffer from the lack of control of cocatalyst morphology, and particle size uniformity.[11,26,30] Cocatalyst loading relates to reaction active sites. Yet, excessive loading typically results in aggregation of the cocatalyst and excessive coverage of the semiconductor, which slows down the surface redox reactions due to inaccessible active sites and hinders light absorption on the semiconductor.[11,31] A moderately better trade-off in terms of 0D cocatalyst uniformity and dispersion on the support can be achieved with the use of colloidal impregnation of previously synthesized nanoparticles (NPs) or nanoclusters instead of precursor salts.[30,32–35]

Alternatively, 1D (i.e., nanotubes) and 2D (i.e., nanosheets) materials put forward an intriguing assortment of new functionalities if used as water oxidation cocatalysts in photocatalysis, like enhanced conductivity and charge storage capacity.[36–38] Among other types of 2D inorganic structures, ruthenium oxide nanosheets (RONSs) appear especially attractive — not only promoting rapid transfer of photogenerated charge carriers across the cocatalyst/light harvester interface, but also enhancing electrocatalytic water oxidation.[39,40] Lee and co-workers used RONS as a matrix together with inorganic photocatalysts, and observed activity increase due to the rapid charge transfer from the photocatalyst to the RONS interfaces.[40]

Our group also recently reported excellent performance of RONS as an electrochemical water oxidation catalyst.[39,40] The lower overpotential for electrocatalytic water oxidation attributed theoretically to the RONS edges is desired to utilize transferred photo-generated holes more efficiently. It has also been reported that RONS is more optically transparent compared to rutile ruthenium oxide nanoparticles (RONP).[37,41] This is advantageous to control the prevalent problem of light shielding that the latter produces on a particular light harvester support (parasitic light absorption).[11,31,34] Light absorption on the cocatalyst of a hybrid photocatalyst is often referred to in the literature as light shielding.[11,31,34,42] Out of the total light absorbed by a photocatalyst composite, in the absence of sensitization effects (i.e., plasmonics), only the fraction absorbed by the light harvester generates photocurrents. Therefore, in artificial photosynthesis, light absorption on conventional cocatalysts like RuO_x at wavelengths below the light harvester optical band gap is considered parasitic.[11,31,42,43] Although parasitic light absorption has not been formally addressed in any artificial photosynthesis performance indicator in literature to date, it is important because it relates directly to the photocatalyst solar-to-chemical efficiency.[21,44–48] Therefore, to improve the efficiency of a hybrid photocatalyst, parasitic light absorption losses should be controlled, for example, by the usage of more optically transparent cocatalyst materials like RONS.[37,41,42] The usage of 2D cocatalysts is, in any case, an emerging trend in other areas of photocatalysis. Their screening for example in HER applications evidences that 2D cocatalysts on light harvester composites produce higher rates compared to conventional 0D cocatalysts.[40,49–51]

This article highlights the combination of a 0D light harvester (commercial WO_3) and 2D (RONS) water oxidation cocatalyst (0D/2D) as a more efficient composite OER photocatalyst (RONS/WO_3) compared to its 0D/0D (RONP/WO_3) morphology equivalent (depicted in Figure 6-1). We explain the observed higher photocatalytic OER rates on RONS/WO_3 compared to RONP/WO_3, decoupling the effects of two main observations: Firstly, taking into account the chemically distinct nature of RONS and RONP, we investigate the influence of the high electrocatalytic activity at the RONS' edge sites, evidenced by higher photocatalytic activity of samples with RONS having smaller lateral size.[39] Secondly, we study the influence of advantageous optical properties, arising from the 0D/2D composite morphology on photocatalysis, which we quantify as reduced (parasitic) light absorption on RONS.

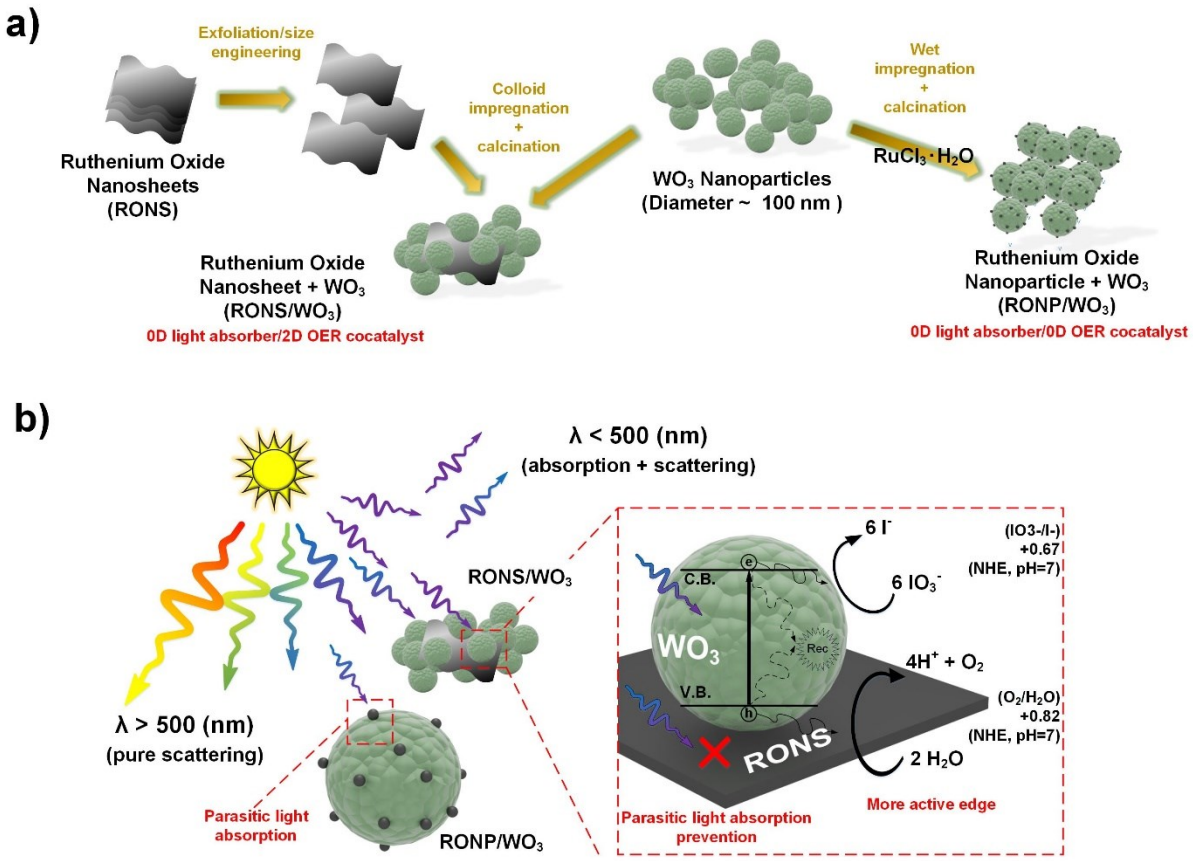

Figure 6-1. Schematics of 0D/2D and 0D/0D morphologies for light harvester/cocatalyst composites. (a) Synthesis procedure of 0D/2D and conventional 0D/0D hybrid heterostructures. (**b**) Advantages of photocatalytic water splitting using a WO_3 nanoparticle on ruthenium oxide nanosheet (RONS/WO_3) morphology (0D/2D) versus conventional (0D/0D) ruthenium oxide nanoparticle on WO_3 surface decoration (RONP/WO_3).

6.3. Results and Discussion

6.3.1 Structure, Morphology and Optical Properties

Ruthenium Oxide Nanosheets (RONS). The nanosheets were prepared by exfoliation of proton exchanged $NaRuO_2$, which was synthesized as described in the literature.[39,52] The resulting $H_xNa_yRuO_2 \cdot zH_2O$ (proton exchanged $NaRuO_2$) was suspended in ultrapure water (1 mg mL^{-1}) and tetrabutylammonium hydroxide (TBAOH, 2.5 mM) to obtain suspended unilamellar RONS (see details in Experimental Section, Appendix D).[39] The reported exfoliation procedure has an efficiency of ~20%, meaning the mass fraction of the initial precursor $H_xNa_yRuO_2 \cdot zH_2O$ that turns into a stable RONS colloid.[39] To make this exfoliation process more efficient, reproducible, shorter, and most importantly, to allow control of RONS lateral size, two other exfoliation variants were identified. One variant replaced previously reported daily cycles of shaking-ultrasonication of the colloids by timed vortexing (8 h) immediately followed by ultrasonication (1 h).[39] This method favors higher and more reproducible exfoliation efficiencies (~40%) suitable for the extensive photocatalysis screening of this study. The second variant is similar to the first but introduced the additional removal of unexfoliated material after vortexing of the colloid (8 h) to obtain a stable colloid stock. The obtained colloid stock is split for different ultrasonication durations (0, 1, 2 and 3 h), to obtain ultrasonication-time-dependent RONS lateral size but at low exfoliation efficiency (~5%). This method is used to explore nanosheet edge effects exclusively (see details of exfoliation in Methods Section, Appendix D). Atomic force microscopy (AFM, Figure 6-2a) and scanning electron microscopy (SEM, Figure 6-2b) images are used to display the 2D morphology of single RONS. As previously reported, the nanosheet thickness is ~1-2 nm, with a lateral size distribution dependent on the exfoliation procedure and roughly spanning from 100 nm to 1 μm.[39] Powder X-ray diffraction (PXRD) pattern in Figure D-1 reveals that bulk $NaRuO_2$ and $H_xNa_yRuO_2 \cdot zH_2O$ have similar crystallinity to the ones of our previous work.[39]

RONS/WO_3 and RONP/WO_3 Composites. Among other OER light harvesters, WO_3 has a moderate band gap (2.75 eV), high thermal and photocorrosion stability, a highly oxidative valence band, and is commercially available. WO_3 has a conduction band with suitable electronic properties to reduce an IO_3^- redox shuttle instead of irreversible sacrificial

electron acceptors typically used in OER experiments, such as $AgNO_3$.[20,22,28,29,53] These attributes of WO_3 have made it a typical choice as oxygen evolution photocatalyst to achieve efficient POWS z-schemes (see summary of WO_3 photosynthetic applications in Table D-1).[13,20,29] Accordingly, WO_3 was chosen as light harvester for RONP and RONS in lieu of other semiconductors, used in the form of commercial nanopowders (particle size < 100 nm) to better benchmark its cocatalyst-dependent activity. The structure and morphology of commercial WO_3 nanopowders were characterized by PXRD, transmission electron microscopy (TEM), and SEM, and are presented in Figure D-2 to Figure D-10. PXRD and TEM fast Fourier transform (TEM-FFT) of WO_3 powders show patterns and d-spacing in agreement with a monoclinic phase with space group $P2_1/n$ (d_{020} = 3.7 Å) reported in the literature for this commercial form of WO_3 (Figure D-2 and Figure 6-2c).[54–56] Previously exfoliated RONS suspensions were used to impregnate WO_3 nanoparticles (RONS/WO_3) as a cocatalyst for OER. Impregnation of WO_3 by RONS was performed by mixing of the RONS colloid with an aqueous suspension of WO_3 at room temperature to form a homogeneous slurry. The slurry was then dried-off at 100 °C and under manual stirring, and grinded with pestle-mortar to obtain a fine-homogeneous powder. The wet WO_3 impregnation with RONP (RONP/WO_3) was performed similarly but replacing the RONS colloid with a $RuCl_3 \cdot H_2O$ aqueous solution as the Ru precursor. RONS/WO_3 and RONP/WO_3 impregnated samples were adjusted to nominal %wt Ru/WO_3 loadings of 0.05, 0.1, 0.2, 0.4, 0.6, 1, 2 and 3. Finally, the obtained RONS/WO_3 and RONP/WO_3 powders were calcinated at 400 °C for 1.5 h (see details of the WO_3 impregnation in Experimental Section, Appendix D, and in Figure D-3 and Figure D-4).

Inductively coupled plasma – optical emission spectrometry (ICP-OES) elemental analysis was performed to confirm the Ru loading of the produced RONS/WO_3 and RONP/WO_3 samples (see details of Ru loading estimations and ICP-OES analysis in Experimental Section, Appendix D, and in Figure D-4). The relative error between nominal and ICP-OES measured Ru loadings of RONS/WO_3 and RONP/WO_3 samples is on average 7% and 6%, respectively. Therefore, unless stated otherwise, the nominal amount is used to refer to the Ru loadings of RONS/WO_3 and RONP/WO_3 samples. Energy dispersive X-ray spectroscopy with SEM (SEM-EDX elemental maps) and TEM (TEM-EDX) were performed to characterize RONS/WO_3 and RONP/WO_3 morphology, structure, and cocatalyst

dispersion. SEM-EDX and TEM-EDX analyses in Figure D-5 to Figure D-10 reveal that both decorated cocatalyst compositions contain Ru. As shown in Figure 6-2c, the decorated cocatalyst nanoparticle size of the RONP/WO_3 sample is approximately 10 nm, with a d-spacing (3.2 Å) corresponding to that of anhydrous RuO_2 rutile (d_{110} = 3.17 Å), which is consistent with the literature.[21,57] At high cocatalyst loadings on WO_3 (3 %wt Ru), RONP has the same d-spacing, but with some portion increasing in particle size, isotropically or as short nanorods (Figure D-5 and Figure D-6). SEM images of RONS/WO_3 samples like in Figure 6-2d reveal an apparently less uniform cocatalyst distribution compared to RONP/WO_3 samples, with a nanosheet morphology akin to pure RONS in Figure 6-2a and Figure 6-2b. Although the detection of RONS with SEM-EDX and TEM-EDX elemental maps is technically difficult (i.e., due to the low RONS thickness) at low magnifications (Figure D-9), nanosheets identified by imaging were confirmed by TEM-EDX and SEM-EDX local analysis and X-ray photoelectron spectroscopy (XPS). In RONS/WO_3, the increased thickness (~10 nm) of certain spots containing RONS indicate its partial restacking during the colloid impregnation (Figure D-8), which partially supports the RONS' lack of uniformity on WO_3. RONS colloids are stable during the WO_3 impregnation due to the presence of TBAOH, but partial RONS restacking instead of association with WO_3 NPs is still expected toward the dry-off step. This competition between WO_3 NPs adsorption on RONS and RONS restacking occurs because the surfaces of both RONS and WO_3 are anionic, which was confirmed by the zeta-potential measurements in Figure D-11a (at pH = 7, -49 mV for RONS, and -58 mV for WO_3).[37,58,59] Therefore, the self-assembly of the 0D/2D structure (depicted in Figure 6-1) from these surfaces with the same charge relies on adhesion phenomena toward the dry-off step, and weak attractive electrostatic interactions between the surfaces of WO_3 and RONS in colloidal suspension, the latter mediated for example by counter ions.[60–62] These pathways for the self-assembly of iso-charged surfaces have been reported in the literature for similarly synthesized RONS and other 2D composites.[37,60–63] Dynamic light scattering observations in Figure D-11b suggest an additive model for adsorption of WO_3 NP on RONS, which supports the idea that the aforesaid interactions between the WO_3 and RONS surfaces are effective for self-assembly.[59,64] Self-assembly is further supported by multiple SEM images and SEM-EDX analysis of bulk powders of RONS/WO_3 samples (Figure D-8 and Figure D-10). The latter systematically shows that

RONS (or restacked RONS) were always found to be surrounded by WO_3 (single NP or aggregates) after calcination. Additional insights into the RONS/WO_3 morphology were obtained by TEM and TEM-EDX (Figure D-7), which confirm the 0D/2D morphology. This morphology, regardless of partial restacking of RONS, resembles the target of 0D/2D morphology with a hybridized RONS/WO_3 interface similar to that depicted in Figure 6-1. Furthermore, SEM-EDX and TEM-EDX qualitatively confirmed the relative Ru content of different RONS-like structures as shown in Figure 6-2d and Figure 6-2e (and Figure D-7 and Figure D-10), which points to RONS layers surrounded by WO_3 NP. This morphology is similar to a previously reported 0D light harvester/RONS hybrid junction, proven to be photocatalytically active.[40] The as-obtained 0D/2D morphology of the WO_3 NP-RONS composite has to the best of our knowledge not been used in artificial photosynthesis until now.

XPS was performed on RONS/WO_3 and RONP/WO_3 samples to check for the Ru oxidation state of RONP and RONS after impregnation, which is presented in Figure D-12 (Ru $3d_{5/2}$ signal). XPS analysis reveals that after the calcination, the RONP/WO_3 Ru $3d_{5/2}$ signal is centered at 280.5 eV, which corresponds to anhydrous RuO_2 (Figure D-12), [19,21,29] whereas the RONS/WO_3 Ru $3d_{5/2}$ signal that is centered at 280.7 eV (Figure D-12) is a superposition of Ru(III) and Ru(IV) peaks ($RuOOH_x$, $0<x<1$).[39,65] WO_3 background together with the low amount of RONS in the RONS/WO_3 sample (3 %wt Ru), make it difficult to resolve this broad and low intensity signal to individual peaks. These Ru(III) and Ru(IV) individual peaks are still visible in XPS of pure exfoliated RONS and correspond to the Ru $3d_{5/2}$ signals as previously reported for RONS (Figure D-13). [39,65] XPS suggests that the fundamental chemical difference between RONP and RONS is the presence of trivalent Ru together with tetravalent Ru in RONS ($RuOOH_x$, $0<x<1$) whereas only tetravalent Ru is present in RONP. The properties of $RuOOH_x$ are described in our previous work (more catalytically active edge of the (110) facet).[39] Therefore, within the photocatalysis framework of this article it is considered that at equivalent Ru loading, RONS/WO_3 and RONP/WO_3 are mainly different in cocatalyst uniformity on WO_3, morphology, and differences in composition and edge properties of RONS and RONP, as discussed above. Multiple consequences in optics, electronics, and photocatalytic aspects can result from such differences, for example different photogenerated charge migration trends at the junction of RONS/WO_3 and

RONP/WO_3. Among all those we find that two properties of RONS/WO_3 and RONP/WO_3 are significantly different, namely reduced parasitic light absorption and water oxidation overpotential in RONS/WO_3.

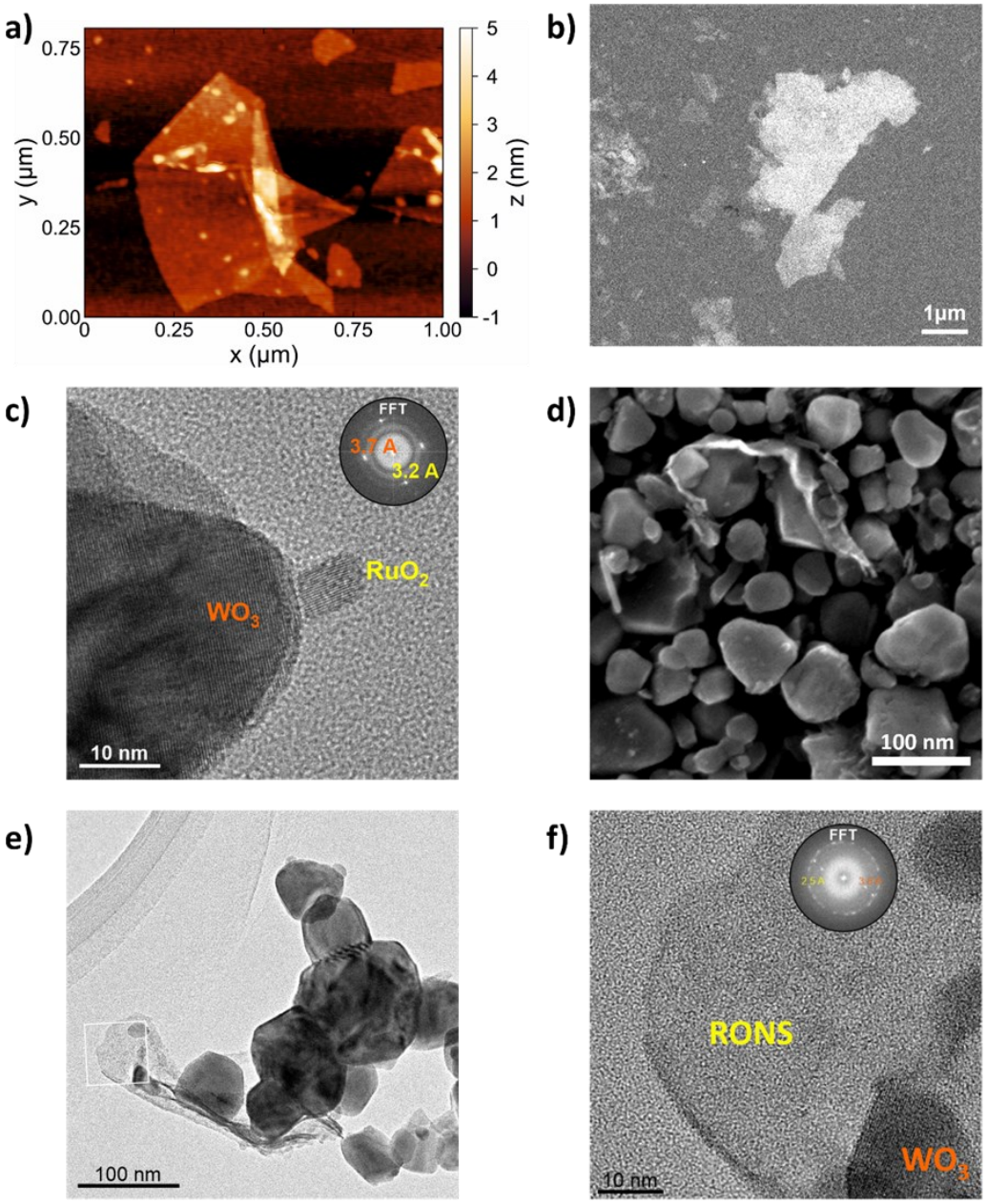

Figure 6-2. Light harvester/cocatalyst composite morphologies and properties. (a) AFM image (height profile in color map), and **(b)** SEM image of exfoliated ruthenium oxide nanosheets (RONS) obtained with an energy and angle selective detector (EsB). **(c)** TEM image of RONP/WO_3 sample after $RuCl_3 \cdot xH_2O$ wet impregnation (0.4 %wt Ru), showing the d-spacings obtained by fast Fourier transformation (FFT) of the regions containing ruthenium oxide nanoparticles (RONP, d_{110} = 3.18 Å). **(d)** SEM image of RONS/WO_3 sample after RONS wet impregnation (3 %wt Ru), obtained with an Inlens detector. EDX analysis can be found in Figure D-10. **(e)** TEM image of RONS/WO_3 sample after RONS wet impregnation (3 %wt Ru), and **(f)** zoom-in of the demarcated area (white square) showing the d-spacings obtained by fast Fourier transformation (FFT) of the regions containing RONS. TEM-EDX analysis can be found in Figure D-7.

Optical Properties of RONS/WO_3 and RONP/WO_3. Knowledge of the optical properties of RONS and RONP is crucial to quantify differences in parasitic light absorption in a photocatalysis environment. Ruthenium oxide materials like RONS and RONP typically exhibit black color and a narrow optical band gap (< 0.5 eV).[37,66–68] Diffuse reflectance UV-vis spectra of bare and impregnated WO_3 powders are shown in Figure D-14, which shows the WO_3 optical band gap (2.75 eV in Tauc plot), and qualitatively no evident change of absorption band edges of the composites due to RONP or RONS impregnation. The latter confirms that RONP and RONS have optical band gaps in the IR range. The resulting broad absorption of ruthenium oxide between 450-800 nm is less for RONS/WO_3 than for RONP/WO_3, both having equal cocatalyst loading (3 %wt Ru). This difference is also evident to the bare eye (Figure D-14). To properly quantify such observations suggesting that parasitic light absorption in RONS/WO_3 is less pronounced than for RONP/WO_3, UV-Vis diffuse reflectance and transmittance (*T+R*) was measured on suspensions of both samples at equivalent Ru content (nominal %wt Ru), at each of the Ru loading levels used for the WO_3 impregnation with cocatalyst (see depiction of experiments in Figure D-15). Suspensions containing samples like in photocatalysis conditions were introduced into an integrating sphere and absorptance ($A = 1 - (R + T)$) was measured in the range of 300 to 800 nm (see details of UV-vis measurements in Experimental Section, Appendix D). In addition to the absorptance of RONS/WO_3 and RONP/WO_3 photocatalysis samples (Figure D-16a and Figure D-17b), the absorptance of pure RONS colloidal suspensions was measured (Figure D-16b and Figure D-16c). The mass of Ru contained in the pure RONS colloids is equivalent to the one of RONS/WO_3 composites at each Ru loading level (%wt Ru). The WO_3 background used for absorptance correction can be found in Figure D-17a for different suspension densities. Above the absorption range of WO_3 (λ > 450 nm) and at equivalent Ru mass in suspension, for example at 2 %wt Ru, pure RONS absorbs roughly 45% less light than RONP/WO_3 (in Figure D-16b, average of the 500-800 nm wavelength range). Although this is in line with the previously reported high optical transparency of RONS, below 600 nm the pure RONS absorptance increases and begins to approach the one of RONP/WO_3 at equivalent Ru mass in suspension.[37,41]. When comparing pure RONS versus RONS/WO_3 at equivalent Ru mass in suspension in the same wavelength range, the average light absorption on WO_3-supported RONS is reduced by ~

30-40% at loadings > 0.6 %wt Ru (Figure D-16c). In this wavelength range (500-800 nm), such decrease in cocatalyst light absorption can be explained by the scattering of photons reaching the surrounding WO_3 nanoparticles of the RONS/WO_3 composite. In absorptance measurements, this event favors ultimately photon scattering out of the suspension over absorption on the exposed surface of RONS. For every wavelength and at equivalent cocatalyst load, RONS/WO_3 samples present always the lowest cocatalyst light absorption when compared to pure RONS or RONP/WO_3 (Figure D-16). This is a convolution of geometrical aspects (cocatalyst exposure), cocatalyst transparency (i.e., due to chemical and geometrical differences compared to RONP), and the fate of photons impinging on the WO_3 part of the composites.

To deconvolute these different contributions to the decreased cocatalyst light absorption of the RONS/WO_3 samples, we model light interaction with the photocatalyst components considering two possible scenarios (see details of optical modelling in Method Section, Appendix D). In a first scenario, we explain the lower cocatalyst light absorption of pure RONS versus RONP/WO_3 (Figure D-16b). For such, we model the photons that impinge on exposed RONS and RONP to study the influence of RONS morphology and optical properties on cocatalyst light absorption. In a second scenario, we explain the lower cocatalyst light absorption of pure RONS versus RONS/WO_3 (Figure D-16c). For such, we model the photons that impinge on WO_3 to study the influence of lower RONS exposure to photons on cocatalyst light absorption. The modelled scenarios rationalize UV-Vis experimental observations and suggest that the RONS high transparency and optically shielded RONS (by WO_3 NPs) may effectively control parasitic light absorption on the RONS/WO_3 samples during photocatalysis (see optical modelling analysis in Supporting Information, Appendix D, and in Figure D-18 to Figure D-20).

The optics quantitative analysis presented hitherto considers a wavelength range where WO_3 only scatters photons (500-800 nm), because we cannot directly access the fraction of light that is parasitically absorbed in RONS/WO_3 and RONP/WO_3 samples when WO_3 also absorbs light. On the one hand, it can be assumed that the lower cocatalyst light absorption of RONS/WO_3 at wavelengths above 500 nm may result in less optical losses during photocatalysis (see optical modelling analysis in Supporting Information, Appendix D). On the other hand, light absorption on WO_3 is the utmost requirement for

photocatalysis, hence parasitic light absorption is only relevant if estimated for wavelengths below 500 nm. In later sections, we derive from the aforesaid quantitative observations at wavelengths between 500 and 800 nm an upper limit of parasitic light absorption for the relevant photons (400 to 500 nm) irradiated on RONS/WO_3 and RONP/WO_3 suspensions.

6.3.2 Photocatalytic Properties of RONS/WO_3 and RONP/WO_3

It is well documented that the ruthenium oxide/WO_3 heterojunction favors charge separation in WO_3 and lowers the overpotential of water oxidation.[11,31,69] However, if ruthenium oxide loading is too high, further increase of OER rates is limited by parasitic light absorption and increased surface recombination at the ruthenium oxide centers, and shields WO_3 active sites.[11,31,69] Previously described optical and photocatalytic differences of RONS and RONP are key to explain dissimilar OER rates after the WO_3 impregnation, and why their optimal ruthenium oxide loadings on WO_3 differs. It must be noted that the less uniform cocatalyst distribution of RONS/WO_3 compared to the highly dispersed RONP/WO_3 may also play a role in photocatalytic activity, as well as additional electrochemical cocatalyst differences.[38,52]These additional differences are not considered quantitatively in the OER photocatalytic rate analysis presented in this section, in view of the larger impact expected from the well-established lower water oxidation overpotential of RONS compared to RONP as discussed below, and the suppressed parasitic light absorption of the RONS.[38,39,52,70,71]

Photocatalytic OER Rates and Cocatalyst Performance on WO_3. To probe the immediate influence of optics and electrochemical properties on the photocatalytic properties in water oxidation, RONP/WO_3 and RONS/WO_3 were tested for photocatalytic OER activity. Photocatalysis was performed in a water suspension (ultrapure water, 0.5 mg mL^{-1}) under attenuated simulated sunlight (65 mW cm^{-2}) and using KIO_3 as electron acceptor (10 mM). OER rates were measured in a continuous photocatalytic high throughput cell described in our previous work.[21] The maximum OER rate in time was recorded for both samples at different loadings, and at plateau of photonic efficiency versus suspension volume (optimal photonic efficiency, ξ_e), which is shown in Figure 6-3a.[21,45] At loadings of 1 %wt Ru/WO_3

for both RONS and RONP, which is optimal only for RONP, the RONS/WO_3 sample shows a 3.5-fold increase in ξ_e compared to RONP/WO_3 (0.13% and 0.038%, respectively). Upon the impregnation of WO_3 with additional RONS, the resulting optimally loaded RONS/WO_3 sample (2 %wt Ru/WO_3) shows a 5-fold increase in ξ_e (0.19%) compared to the optimally loaded RONP/WO_3. This optimal ξ_e of the RONS/WO_3 sample remained constant at a higher RONS loading of 3 %wt Ru/WO_3. The fact that the photocatalytic activity of RONS plateaus at Ru loadings on WO_3 up to 3-times higher than optimally loaded RONP/WO_3 is explained later based on the RONS optical properties.

The dynamic OER rate measurement of RONS/WO_3 can be found in a long illumination test in Figure D-21, which shows that RONS/WO_3 is stable under photocatalysis conditions (7 h). No signs of deactivation were observed on RONP/WO_3 either after long illumination times. Under the same conditions, bare WO_3 has no activity above our detection limits, and ξ_e of a RuO_2/TiO_2 benchmark (AM 1.5G, 300-800 nm) for rate standardization is 0.27% ± 0.05% (*relative optimal photonic efficiency*, ξ'_e). Optimal photonic efficiencies ξ_e in Figure 6-3a are reported using good practices for measuring OER rates (see Supporting Information for details, Appendix D).[21,45,46,72] These practices include normalization of OER rates, minimization of artificial O_2 rates from electron acceptor decomposition, and ^{18}O labeling experiments (Figure D-22 and Table D-2). Normalized activities of RONP/WO_3 (ξ'_e = 0.15) and RONS/WO_3 (ξ'_e = 0.8) in Figure 6-3a were later refined with photocatalytic OER measurements in a second reactor cell with more controlled optics (see Supporting Information for details, Appendix D). To fully assess standardized performance indicators, photonic efficiency and apparent quantum yield (AQY) results obtained in this alternative cell for RONP/WO_3 and RONS/WO_3 OER are presented in Figure D-23a and Figure D-23b, respectively (lamp spectra in Figure D-24).

In Figure 6-3a it is shown that ξ'_e of RONS/WO_3 even surpasses the one of WO_3 impregnated at optimal loadings of PtO_x (ξ'_e = 0.47, 1% wt Pt) and $RuO_2 \cdot nH_2O$ (ξ'_e = 0.32, 0.5-1% wt Ru); details of PtO_x and $RuO_2 \cdot nH_2O$ can be found in the Experimental Section. PtO_x and $RuO_2 \cdot nH_2O$ are the most active inorganic 0D cocatalysts on WO_3 reported to date for photocatalytic OER using IO_3^- as an electron acceptor.[19,20,28,29] However, both PtO_x and $RuO_2 \cdot nH_2O$ are inherently different cocatalysts. They are benchmarked on WO_3, but they should not be compared directly with RONP (or RONS). While anhydrous RuO_2 (RONP) is

a well-established water oxidation electrocatalyst with moderate additional activity for IO_3^- reduction, PtO_x and $RuO_2{\cdot}nH_2O$ are primarily cocatalysts for reduction of IO_3^-.[19,20,28,29] Even so, RONP and other RuO_x species are considered bifunctional cocatalysts that promote, to different extents, both water oxidation and IO_3^- reduction.[19,20,29] To rule out that higher OER rates on RONS/WO_3 are just the consequence of the previously reported faster IO_3^- reduction rates on certain RuO_x catalysts, (photo)electrochemical measurements (Linear Sweep Voltammetry, LSV) were performed on WO_3, RONS/WO_3, RONP/WO_3, and PtO_x/WO_3. Dark LSV measurements show that RONS (and RONP) electrocatalytic activity relates mostly to water oxidation, being the RONS the electrocatalyst with the lowest IO_3^- reduction and the highest water oxidation activity (Figure D-25a and Figure D-25b). Under chopped illumination (Figure 6-3b), RONS/WO_3 also exhibits the highest water oxidation photocurrent (10 μA cm^{-2} at a potential of 0.5 V *vs.* Ag/AgCl). These observations denote that higher photocatalytic OER rates of RONS/WO_3 versus RONP/WO_3 are unequivocally related to the beneficial optical properties of RONS/WO_3, and the higher water oxidation electrocatalytic activity of the RONS (see details of the electrochemistry and photoelectrochemistry analysis in Supporting Information, Appendix D). In the next sections, these two features of RONS/WO_3 are discussed in the context of photocatalysis.

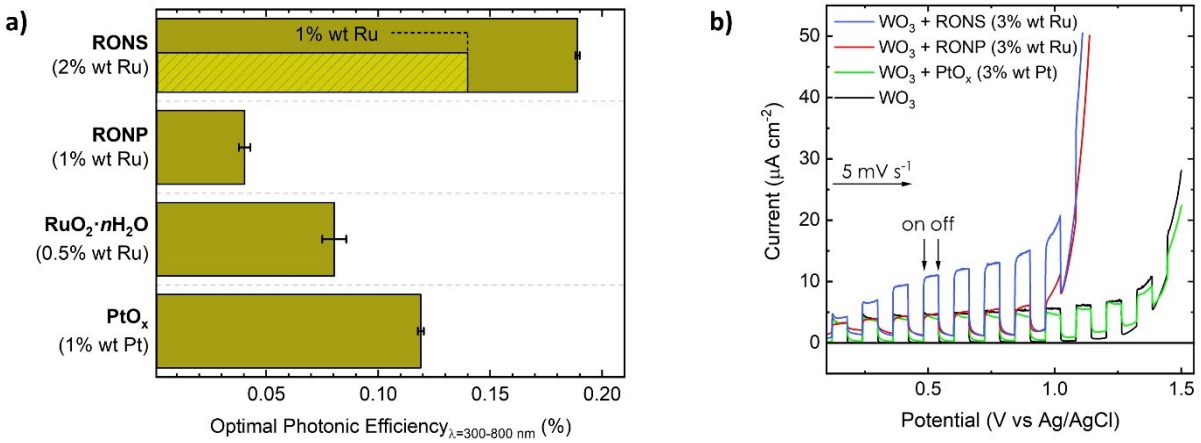

Figure 6-3. Activity benchmark of different cocatalysts on WO_3. (a) Comparison of photocatalytic OER activity of different cocatalysts optimally loaded on WO_3, using the concept of optimal photonic efficiency (ξ_e). Inset within the RONS bar shows activity of the RONS loaded on WO_3 at 1% wt Ru. Photocatalysis conditions: 10 mL ultrapure water, 10 mM KIO_3, 0.5 mg mL^{-1} of sample and attenuated solar spectra (Figure D-24, 65 mW cm^{-2}). Error bars represent mean ± standard error of the mean of the average activity of two independent batches of sample (see

details in Experimental Section, Appendix D). Optimal photonic efficiency of RuO_2/TiO_2 benchmark for rate standardization is 0.27% (relative optimal photonic efficiency, ξ'_e). ξ'_e of WO_3 impregnated with optimal cocatalyst loadings of RONS (2% wt Ru), RONP (1% wt Ru), PtO_x (1% wt Pt) and $RuO_2{\cdot}nH_2O$ (0.5% wt Ru) are, respectively, 0.80, 0.15, 0.48 and 0.32. **(b)** LSV profiles for WO_3 + cocatalyst electrodes in 0.1 M aqueous Na_2SO_4 solution, and curves under chopped AM 1.5G irradiation (dashed-dot lines). Scan rate: 5 mV s^{-1}

Lower Water Oxidation Overpotential of RONS edges. The first key aspect for the higher photocatalytic OER activities of RONS/WO_3 is the higher electrocatalytic activity of the RONS edges when compared to anhydrous RuO_2 (0.76 V lower overpotential for water oxidation).[39] It is expected in WO_3 photocatalysis that this "electrocatalytic advantage" of RONS over RONP facilitates a more efficient extraction of the photogenerated holes reaching the cocatalyst/WO_3 interface; assuming that water oxidation controls hole extraction rates.[11,31,73,74] Higher cocatalyst electrocatalytic activity simultaneously reduces accumulation of photogenerated holes at the cocatalyst/WO_3 interface, which indirectly reduces charge recombination in WO_3.[73–75] Altogether, the more active RONS edge is then necessary to rationalize the higher RONS/WO_3 photocatalytic OER rates.

To prove this effect in photocatalysis, RONS colloids displaying controlled nanosheet lateral sizes were impregnated at equal loading on WO_3. Nanosheets with different lateral sizes were obtained by varying the ultrasonication time of a unique RONS colloid stock, which was previously prepared by vortexing/centrifugation. Subsequent ultrasonication of the stock decreases the sheets' lateral dimension, which increases the edge-to-volume ratio of RONS that we have linked to its higher cocatalyst water oxidation activity (see details of RONS exfoliation in Experimental Section, Appendix D). We measured photocatalytic OER rates of RONS/WO_3 samples impregnated with such RONS colloid stock (at 20 and 50 mM TBAOH), at equal cocatalyst loading (~0.25 %wt Ru, Figure D-26), but different ultrasonication duration before WO_3 impregnation. Results showing the OER rate differences with ultrasonication times are presented in Figure 6-4a. At 20 mM TBAOH, the maximum OER activity of RONS/WO_3 was obtained for the colloid vial sonicated for 1 h (50% increase compared to no sonication). Lateral size distributions obtained from AFM images of the RONS before impregnating of WO_3 are displayed in Figure 6-4b for the same samples screened in Figure 6-4a. The most significant decrease in nanosheet lateral size occurs after 1 h of ultrasonication of the colloid stock (Figure D-27 and Figure 6-4b). The corresponding RONS/WO_3 sample shows the highest photocatalytic OER activity (Figure

6-4a). The optimal ultrasonication time of the RONS colloid used to produce RONS/WO_3 photocatalysis samples relates to an observed compromise between RONS lateral size and agglomeration (see details of the RONS size dependent photocatalysis studies in Supporting Information, Appendix D, and in Figure D-27 and Figure D-28). Still, our results show that the maximum activity is linked to the sharpest decrease in nanosheet lateral size, and thus that more active edge sites play a role in photocatalysis. This observation is supplemented with the second experiment at identical conditions but increasing the TBAOH concentration (50 mM) to stabilize the small agglomerates during extended ultrasonication. Accordingly, the experiment at 50 mM TBAOH shows a ~100% increase in activity at 2 h of ultrasonication (Figure 6-4a) of the colloid compared to no ultrasonication. Additionally, photocatalysis experiments were performed using an OER suitable dye ($[Ru(bpy)_3]^{2+}$ $2Cl^-$) as light harvester instead of WO_3 (and $Na_2S_2O_8$ as sacrificial electron acceptor),[76,77] to isolate the edge effects from other influences such as those due to RONS/WO_3 hybridization efficiency during the impregnation step (Figure D-29). The trend obtained is similar, presumably because agglomeration of RONS colloids during ultrasonication still reduces the surface area for hole transfer to $[Ru(bpy)_3]^{2+}$. Dye experiments likewise show such distinctive increase of OER rates with ultrasonication time and hence confirm that more RONS edges increases photocatalytic OER rates (Figure D-29c).

Parasitic Light Absorption on RONS/WO_3 and RONP/WO_3. We quantify in this section the impact of parasitic light absorption on the superior photocatalytic performance of RONS/WO_3, by building upon the cocatalyst light absorption differences of RONP/WO_3 and RONS/WO_3 analyzed in previous sections (500-800 nm range). We have established that such trends result from multiple optical differences between RONP and RONS that arise, for example, from different electric properties. We extrapolate the experimentally measured cocatalyst absorptance (%) for each cocatalyst loading to photocatalysis conditions as an estimation of parasitic light absorption (see Methods Section for calculations and assumptions details, Appendix D). This estimation sets an upper limit for the fraction of the irradiated relevant photons (400–500 nm) being absorbed by the

cocatalyst during photocatalysis, which we define as the parasitic light absorption fraction (f_{RuO2}).

Figure 6-4c shows the trends of photocatalytic OER rates and f_{RuO2} of RONP/WO_3 and RONS/WO_3 versus different cocatalyst loadings (rates at optimal cocatalyst loading are used to calculate optimal photonic efficiencies in Figure 6-3a). Meaningful comparison of two photocatalyst material performances requires calculations of the internal photonic efficiency or quantum yields, and thus the quantification of suspension absorptance under photocatalysis conditions.[21,72] Given that both RONP/WO_3 and RONS/WO_3 samples have an identical WO_3 light harvester support, their photocatalytic OER rates can be compared directly since differences in light absorptance of RONP/WO_3 and RONS/WO_3 suspensions come primarily from optical losses related to f_{RuO2}. Plateauing of OER rates with cocatalyst loading for RONP/WO_3 (1 %wt Ru) and RONS/WO_3 (2 %wt Ru) occurs around f_{RuO2} = 20-30%. Optimal cocatalyst loading of RONP/WO_3 and RONS/WO_3 cannot be explained quantitatively based on this optical limit only. In addition to the fraction of photons effectively absorbed by WO_3, the cocatalyst effect on internal photonic efficiency is also dependent on charge carrier dynamics of photogenerated charges. OER rates at the cocatalyst/WO_3 junction depend on multiple (opto)electronic factors such as cocatalyst/WO_3 band alignment, charge separation and water oxidation overpotential of the cocatalyst.[11,16,17,31] For example, assuming a recombination-limited model mediated by hole-trapping at the surface of the semiconductor, OER rates are proportional to active sites for water oxidation.[16,73,74] In this scenario, based on mass action law, the coarse grain probability of hole transfer to ruthenium oxide depends linearly on the concentration of photogenerated holes at the WO_3 surface, and cocatalyst availability.[73,74] At the same time, OER rates must satisfy the electrochemical relation between water oxidation rates at the cocatalyst surface and the available overpotential of the surface hole.[11,31] OER rates also improve with cocatalyst addition, due to the heterojunction properties that may generate a significant upward band bending (i.e., 1.22 V for RuO_2/TiO_2).[69,78,79] This likely upward band bending at the ruthenium oxide/WO_3 junction reduces charge recombination due to electric field induced electron-hole separation.[69,78–80] Altogether, at low cocatalyst loadings and proper band alignment, OER rates are expected to increase with cocatalyst addition. This can be seen in Figure 6-4c for both RONP/WO_3 and RONS/WO_3. At loadings of

< 0.2 wt% Ru, photocatalytic OER rates increase sharply with cocatalyst load, with little influence of adverse effects like parasitic light absorption (f_{RuO2} < 10%). On the other hand, OER rates plateau with more ruthenium oxide centers at high loads, because of multiple factors, like the increasing formation of unavailable cocatalyst active sites.[11,31,69] Excessive ruthenium oxide loading increases the nanoparticle size of RONP and likely leads to restacking of RONS. All these factors create an intricate relation between parasitic light absorption, photogenerated charge carrier dynamics, and optimal cocatalyst loading. Likewise, junction properties controlling OER rates are intrinsically different between RONP/WO_3 and RONS/WO_3. [39–41,50,52] For example, the edge of RONS has a lower water oxidation overpotential compared to rutile RuO_2, which was described formerly as another factor to explain higher OER activities of RONS/WO_3.[39] Regardless of such complexities, the common parasitic light absorption threshold of 20-30% described in Figure 6-4c still emerges as the limiting factor for cocatalyst load in both RONP/WO_3 and RONS/WO_3. Parasitic light absorption partially explains the higher optimal cocatalyst loadings of RONS/WO_3. Due to the beneficial optical properties of RONS, RONS/WO_3 shows an evident stretch of the f_{RuO2} function versus cocatalyst loading, which also translates to less optical losses and overall higher OER rates on RONS/WO_3.

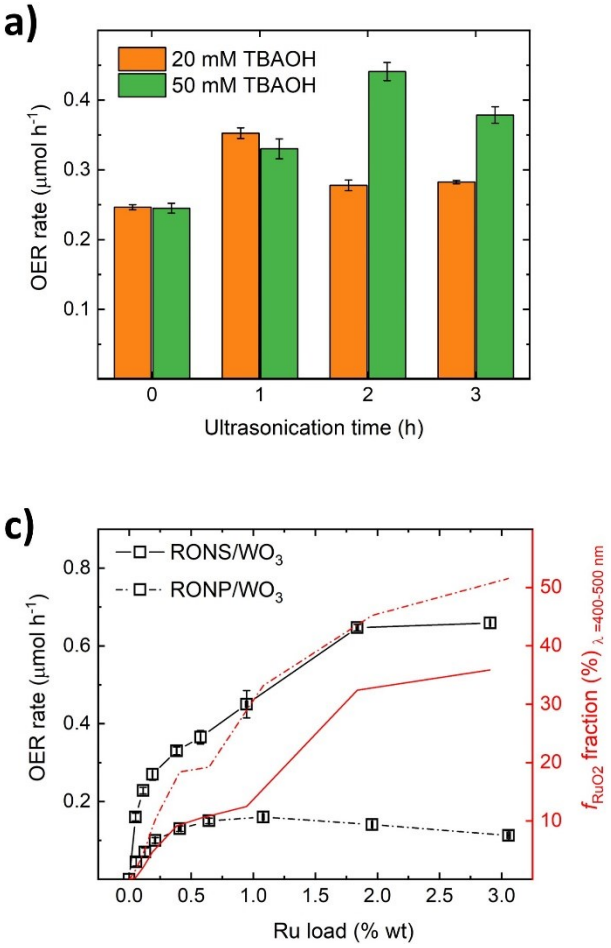

Figure 6-4. Influence of lower cocatalyst water oxidation overpotential and parasitic light absorption on photocatalytic OER rates. (a) Comparison of photocatalytic OER rates at equal loading of RONS on WO_3 (0.25-0.33 %wt Ru, Figure D-26), exfoliated using only 12 h vortexing, but later ultrasonicated at different times (x-axis) before the WO_3 colloid impregnation. TBAOH concentrations during exfoliation are 20 mM and 50 mM. Photocatalysis conditions: 10 mL ultrapure water, 10 mM KIO_3, 0.5 mg mL^{-1} of sample and attenuated solar spectra (Figure D-24, 65 mW cm^{-2}). Error bars represent mean ± standard error of the mean of the average activity of two independent batches of sample (see details in Experimental Section, Appendix D). **(b)** Nanosheet lateral size distribution from AFM images of the vortexed exfoliated RONS at different ultrasonication times and 20 mM TBAOH (x-axis in (a)). Solid lines correspond to the distribution fit (triple exponential, 95% confidence band in colored area). Example of surveyed AFM images, including sample after 3 h of ultrasonicated, can be found in Figure D-27. **(c)** Photocatalytic OER rates versus the cocatalyst loadings impregnated on WO_3 (x-axis considers Ru loadings measured by ICP-OES elemental analysis, Figure D-4c). Photocatalysis conditions: 10 mL ultrapure water, 10 mM KIO_3, 0.5 mg mL^{-1} of sample and attenuated solar spectra (Figure D-24, 65 mW cm^{-2}). Error bars represent mean ± standard error of the mean of the average activity of two independent batches of sample (see details in Experimental Section, Appendix D). Secondary y-axis (red) represents the fraction of irradiated light that is parasitically absorbed by the cocatalyst (f_{RuO_2}) versus cocatalyst loading, estimated from UV-vis measurements (Figure D-16a and Figure D-17c) and optical modelling (Figure D-18c), and extrapolated to the wavelength range of 400-500 nm (see Methods Section for f_{RuO_2} calculations and assumptions details, Appendix D).

6.4 Conclusion

We have established that a 2D morphology presents evident advantages compared to conventional 0D morphologies in Ru-based cocatalysts to obtain higher photocatalytic OER on a commercial light harvester (WO_3). RONS impregnated on WO_3 (RONS/WO_3, 2 %wt Ru) show a 5-fold increase in photonic efficiency compared to RONP impregnated on WO_3 (RONP/WO_3, 1 %wt Ru) – both at their optimal Ru loading. We have demonstrated that this increase of photocatalytic OER performance is related to more beneficial optical and electrochemical properties of RONS for water oxidation. We have quantified the former and the latter using the concepts of controlled parasitic light absorption (f_{RuO2}), and lower electrochemical overpotential for water oxidation at RONS edges, respectively. A low electrochemical overpotential at the RONS edge was previously identified under electrocatalytic water splitting conditions and assigned to higher activity of the RONS edges. We have systematically demonstrated the impact of RONS edges on photocatalytic OER rates for the first time, which we have controlled indirectly by engineering the RONS exfoliation/aggregation state and size. In addition, we introduced and quantified the concept of the fraction of parasitic light absorption by the cocatalyst, f_{RuO2}, which is barely discussed in photocatalysis literature, and we show here that it has quantitative impact on light absorption efficiency by the light absorber. The optical properties established for RONS and the 0D/2D as compared to the conventional 0D/0D morphology allow us to rationalize the observed correlation between catalytic activity and catalyst loading, a concept that may generate particular interest in the context of earth-abundant cocatalysts for artificial photosynthesis. While we have demonstrated that 2D RONS show higher activity as OER cocatalyst than 0D RONP, we have also shown that RONS stand out in a photocatalysis benchmark against other reported 0D cocatalysts on WO_3, such as PtO_x, and $RuO_2 \cdot nH_2O$, under the photocatalysis conditions used in this study. Finally, we present an alternative to the regular light harvester chemical, structural, and electronic tuning by adding the concept of morphology tuning to identify more efficient composite catalyst systems for artificial photosynthesis. On the one hand, the use of 1D and 2D morphologies in semiconductors light harvesters typically exhibits beneficial properties for example, to decrease photogenerated charge recombination. This has been widely exploited in artificial photosynthesis (i.e., as 2D light harvester/0D cocatalyst). On the other hand, the use of cocatalysts with 2D morphology (rather than 0D) like RONS is an emerging trend in

photocatalysis but rarely applied yet to energy conversion systems. Based on results from related fields of study, we believe that synergies in simultaneous light harvester and cocatalyst morphology design present unique opportunities to assemble more efficient inorganic photosynthetic systems.[14,42] The results presented herein and other interesting properties of 2D materials mentioned in this article thus open multiple possibilities for cocatalyst morphology engineering.

6.5 Acknowledgements

A.G and S.L contributed equally to this work. Financial support is gratefully acknowledged from the Max Planck Society, the Cluster of Excellence "e-conversion" (EXC 2089/1–390776260), and the Center for Nanoscience. S.L. is thankful to the Science and Engineering Research Board (SERB), Government of India, for the award of a Ramanujan Fellowship (RJF/2021/000050). A.J.-S. gratefully acknowledges Spanish Ministry of Universities for funding through a Beatriz Galindo Research fellowship BG20/00015. We thank Prof. Gisela Schütz (Max Planck Institute for Intelligent Systems, MPI-IS, Stuttgart) for access to XPS analysis at their facilities. The authors are grateful to Dr. Gunther Richter for helpful discussion of XPS data and the MPI-IS for the XPS infrastructure support. The authors thank Andres Rodríguez-Camargo for FTIR and PXRD measurements and Marie-Luise Schreiber for extensive ICP-OES elemental analysis.

6.6 References

1. Hisatomi, T. & Domen, K. Introductory lecture: Sunlight-driven water splitting and carbon dioxide reduction by heterogeneous semiconductor systems as key processes in artificial photosynthesis. *Faraday Discuss* **198**, 11–35 (2017).
2. Grewe, T., Meggouh, M. & Tüysüz, H. Nanocatalysts for Solar Water Splitting and a Perspective on Hydrogen Economy. *Chem Asian J* **11**, 22–42 (2016).
3. Kim, J. H., Hansora, D., Sharma, P., Jang, J. W. & Lee, J. S. Toward practical solar hydrogen production-an artificial photosynthetic leaf-to-farm challenge. *Chem Soc Rev* **48**, 1908–1971 (2019).
4. Osterloh, F. E. Photocatalysis versus Photosynthesis : A Sensitivity Analysis of Devices for Solar Energy. *ACS Energy Lett.* **2**, 445−453 (2017).
5. Wang, Z., Li, C. & Domen, K. Recent developments in heterogeneous photocatalysts for solar-driven overall water splitting. *Chem Soc Rev* **48**, 2109–2125 (2019).
6. Nadeem, M. A., Khan, M. A., Ziani, A. A. & Idriss, H. An overview of the photocatalytic water splitting over suspended particles. *Catalysts* **11**, 1–25 (2021).

7. Kärkäs, M. D., Johnston, E. V., Verho, O. & Akermark, B. Artificial photosynthesis: From nanosecond electron transfer to catalytic water oxidation. *Acc Chem Res* **47**, 100–111 (2014).
8. Wang, Q. & Domen, K. Particulate Photocatalysts for Light-Driven Water Splitting: Mechanisms, Challenges, and Design Strategies. *Chem Rev* **120**, 919–985 (2020).
9. Idriss, H. The elusive photocatalytic water splitting reaction using sunlight on suspended nanoparticles: Is there a way forward? *Catal Sci Technol* **10**, 304–310 (2020).
10. Sivula, K. Are Organic Semiconductors Viable for Robust, High-Efficiency Artificial Photosynthesis? *ACS Energy Lett* **5**, 1970–1973 (2020).
11. Mei, B., Han, K. & Mul, G. Driving Surface Redox Reactions in Heterogeneous Photocatalysis: The Active State of Illuminated Semiconductor-Supported Nanoparticles during Overall Water-Splitting. *ACS Catal* **8**, 9154–9164 (2018).
12. Miyoshi, A., Nishioka, S. & Maeda, K. Water Splitting on Rutile TiO2 -Based Photocatalysts. *Chem. Eur.J. 2018,* **24**, 18204–18219 (2018).
13. Chen, S., Takata, T. & Domen, K. Particulate photocatalysts for overall water splitting. *Nature Publishing Group* **2**, 1–17 (2017).
14. Wang, Q. *et al.* Scalable water splitting on particulate photocatalyst sheets with a solar-to-hydrogen energy conversion efficiency exceeding 1%. *Nat Mater* **15**, 611–615 (2016).
15. Wang, Z. *et al.* Overall water splitting by Ta3N5 nanorod single crystals grown on the edges of KTaO3 particles. *Nat Catal* **1**, (2018).
16. Pan, Z. *et al.* Mutually-dependent kinetics and energetics of photocatalyst/co-catalyst/two-redox liquid junctions. *Energy Environ Sci* **13**, 162–173 (2020).
17. Garcia-Esparza, A. T. & Takanabe, K. A simplified theoretical guideline for overall water splitting using photocatalyst particles. *J Mater Chem A Mater* **4**, 2894–2908 (2016).
18. Lin, F. & Boettcher, S. W. Adaptive semiconductor/electrocatalyst junctions in water-splitting photoanodes. *Nat Mater* **13**, 81–86 (2014).

19. Maeda, K., Abe, R. & Domen, K. Role and function of ruthenium species as promoters with TaON-based photocatalysts for oxygen evolution in two-step water splitting under visible light. *Journal of Physical Chemistry C* **115**, 3057–3064 (2011).
20. Abe, R., Higashi, M. & Domen, K. Overall water splitting under visible light through a two-step photoexcitation between TaON and WO3 in the presence of an iodate-iodide shuttle redox mediator. *ChemSusChem* **4**, 228–237 (2011).
21. Vignolo-González, H. A. *et al.* Toward Standardized Photocatalytic Oxygen Evolution Rates Using RuO2@TiO2 as a Benchmark. *Matter* **3**, 464–486 (2020).
22. Erbs, W., Desilvestro, J., Borgarello, E. & Graetzel, M. Visible-light-induced oxygen generation from aqueous dispersions of tungsten(VI) oxide. *J Phys Chem* **88**, 4001–4006 (1984).
23. Dilla, M. *et al.* The fate of O2 in photocatalytic CO2 reduction on TiO2 under conditions of highest purity. *Phys.Chem.Chem.Phys.* **21**, 15949–15957 (2019).
24. Maeda, K., Teramura, K., Saito, N., Inoue, Y. & Domen, K. Improvement of photocatalytic activity of (Ga1−xZnx)(N1−xOx) solid solution for overall water splitting by co-loading Cr and another transition metal. *J Catal* **243**, 303–308 (2006).
25. Maeda, K. *et al.* Noble-Metal/Cr2O3 Core/Shell Nanoparticles as a Cocatalyst for Photocatalytic Overall Water Splitting. *Angewandte Chemie* **118**, 7970–7973 (2006).
26. Wenderich, K. & Mul, G. Methods, Mechanism, and Applications of Photodeposition in Photocatalysis: A Review. *Chem Rev* **116**, 14587–14619 (2016).
27. Wang, W. & Qi, L. Light Management with Patterned Micro- and Nanostructure Arrays for Photocatalysis , Photovoltaics , and Optoelectronic and Optical Devices. **1807275**, 1–29 (2019).
28. Ma, S. S. K., Maeda, K., Abe, R. & Domen, K. Visible-light-driven nonsacrificial water oxidation over tungsten trioxide powder modified with two different cocatalysts. *Energy Environ Sci* **5**, 8390–8397 (2012).
29. Suzuki, H., Nitta, S., Tomita, O., Higashi, M. & Abe, R. Highly Dispersed RuO_2 Hydrates Prepared via Simple Adsorption as Efficient Cocatalysts for Visible-Light-Driven Z-Scheme Water Splitting with an IO_3^-/I^- Redox Mediator. *ACS Catal* **7**, 4336–4343 (2017).

30. Munnik, P., de Jongh, P. E. & de Jong, K. P. Recent Developments in the Synthesis of Supported Catalysts. *Chem Rev* **115**, 6687–6718 (2015).
31. Ran, J., Zhang, J., Yu, J., Jaroniec, M. & Qiao, S. Z. Earth-abundant cocatalysts for semiconductor-based photocatalytic water splitting. *Chem. Soc. Rev.* **43**, 7787–7812 (2014).
32. Kawawaki, T. *et al.* Controlled colloidal metal nanoparticles and nanoclusters: recent applications as cocatalysts for improving photocatalytic water-splitting activity. *J Mater Chem A Mater* **8**, 16081–16113 (2020).
33. Maeda, K. Z-Scheme Water Splitting Using Two Different Semiconductor Photocatalysts. *ACS Catal* **3**, 1486–1503 (2013).
34. Yang, J., Wang, D., Han, H. & Li, C. Roles of Cocatalysts in Photocatalysis and Photoelectrocatalysis. *Acc Chem Res* **46**, 1900–1909 (2013).
35. Sakamoto, N. *et al.* Highly dispersed noble-metal/chromia (core/shell) nanoparticles as efficient hydrogen evolution promoters for photocatalytic overall water splitting under visible light. *Nanoscale* **1**, 106 (2009).
36. Oh, S. M., Patil, S. B., Jin, X. & Hwang, S. J. Recent Applications of 2D Inorganic Nanosheets for Emerging Energy Storage System. *Chemistry - A European Journal* **24**, 4757–4773 (2018).
37. Hong, H. *et al.* Enhanced interfacial electron transfer between thylakoids and RuO2 nanosheets for photosynthetic energy harvesting. *Sci Adv* **7** (2021).
38. Sugimoto, W., Iwata, H., Yasunaga, Y., Murakami, Y. & Takasu, Y. Preparation of Ruthenic Acid Nanosheets and Utilization of Its Interlayer Surface for Electrochemical Energy Storage. *Angewandte Chemie International Edition* **42**, 4092–4096 (2003).
39. Laha, S. *et al.* Ruthenium Oxide Nanosheets for Enhanced Oxygen Evolution Catalysis in Acidic Medium. *Adv Energy Mater* **9**, 1803795 (2019).
40. Lee, J. M. *et al.* A Conductive Hybridization Matrix of RuO2Two-Dimensional Nanosheets: A Hybrid-Type Photocatalyst. *Angewandte Chemie - International Edition* **55**, 8546–8550 (2016).
41. Roh, J. W., Shin, W. H., Kim, H.-S., Kim, S. Y. & Kim, S. Simultaneous Enhancement of Electrical and Optical Properties of Transparent Conducting RuO2 Nanosheet films by Facile Ultraviolet-Ozone Irradiation. *Applied Sciences* **10**, 4127 (2020).

42. Kempler, P. A., Gonzalez, M. A., Papadantonakis, K. M. & Lewis, N. S. Hydrogen Evolution with Minimal Parasitic Light Absorption by Dense Co–P Catalyst Films on Structured p-Si Photocathodes. *ACS Energy Lett* **3**, 612–617 (2018).
43. Morawiec, S. *et al.* Experimental quantification of useful and parasitic absorption of light in plasmon-enhanced thin silicon films for solar cells application. *Sci Rep* **6**, 22481 (2016).
44. Braslavsky, S. E. *et al.* Glossary of terms used in photocatalysis and radiation catalysis (IUPAC Recommendations 2011). *Pure and Applied Chemistry* **83**, 931–1014 (2011).
45. Kisch, H. & Bahnemann, D. Best Practice in Photocatalysis: Comparing Rates or Apparent Quantum Yields? *Journal of Physical Chemistry Letters* **6**, 1907–1910 (2015).
46. Qureshi, M. & Takanabe, K. Insights on measuring and reporting heterogeneous photocatalysis: Efficiency definitions and setup examples. *Chemistry of Materials* **29**, 158–167 (2017).
47. Gottschling, K. *et al.* Rational Design of Covalent Cobaloxime–Covalent Organic Framework Hybrids for Enhanced Photocatalytic Hydrogen Evolution. *J Am Chem Soc* **142**, 12146–12156 (2020).
48. Biswal, B. P. *et al.* Sustained Solar H2 Evolution from a Thiazolo[5,4-d]thiazole-Bridged Covalent Organic Framework and Nickel-Thiolate Cluster in Water. *J Am Chem Soc* **141**, 11082–11092 (2019).
49. Jo, Y. K., Lee, J. M., Son, S. & Hwang, S. 2D inorganic nanosheet-based hybrid photocatalysts: Design, applications, and perspectives. *Journal of Photochemistry and Photobiology C: Photochemistry Reviews* **40**, 150–190 (2019).
50. Lim, J. *et al.* Two-dimensional RuO2 nanosheets as robust catalysts for peroxymonosulfate activation. *Environ Sci Nano* **6**, 2084–2093 (2019).
51. Chen, G. *et al.* Ball-milling combined calcination synthesis of MoS2/CdS photocatalysts for high photocatalytic H2 evolution activity under visible light irradiation. *Appl Catal A Gen* **443–444**, 138–144 (2012).

52. Fukuda, K. *et al.* Synthesis of nanosheet crystallites of ruthenate with an α-NaFeO 2-related structure and its electrochemical supercapacitor property. *Inorg Chem* **49**, 4391–4393 (2010).
53. Abe, R., Sayama, K. & Sugihara, H. Development of new photocatalytic water splitting into H2 and O2 using two different semiconductor photocatalysts and a shuttle redox mediator IO3-/I-. *Journal of Physical Chemistry B* **109**, 16052–16061 (2005).
54. Fujioka, Y. *et al.* Structural Properties of Pure and Nickel-Modified Nanocrystalline Tungsten Trioxide. *The Journal of Physical Chemistry C* **116**, 17029–17039 (2012).
55. Fujioka, Y., Frantti, J., Nieminen, R. M. & Asiri, A. M. Formation of ruthenium cluster on nanocrystalline tungsten trioxide. *Journal of Physical Chemistry C* **117**, 7506–7510 (2013).
56. Persson, K. Materials Data on RuO2 (SG:136) by Materials Project. **4**, (2016).
57. Kim, A. *et al.* Selective CO 2 methanation on Ru/TiO 2 catalysts: unravelling the decisive role of the TiO 2 support crystal structure. *Catal Sci Technol* **6**, 8117–8128 (2016).
58. Zhang, B. *et al.* Electrochemical Synthesis of Catalytically Active Ru/RuO 2 Core−Shell Nanoparticles without Stabilizer. *Chemistry of Materials* **22**, 4056–4061 (2010).
59. Praus, P. *et al.* Synthesis and properties of nanocomposites of WO3 and exfoliated g-C3N4. *Ceram Int* **43**, 13581–13591 (2017).
60. Lee, J. M. *et al.* A Linker-Mediated Self-Assembly Method to Couple Isocharged Nanostructures: Layered Double Hydroxide-CdS Nanohybrids with High Activity for Visible-Light-Induced H 2 Generation. *Chemistry - A European Journal* **20**, 17004–17010 (2014).
61. Parapat, R. Y., Saputra, O. H. I., Ang, A. P., Schwarze, M. & Schomäcker, R. Support effect in the preparation of supported metal catalysts *via* microemulsion. *RSC Adv.* **4**, 50955–50963 (2014).
62. Hemmingson, S. L. & Campbell, C. T. Trends in Adhesion Energies of Metal Nanoparticles on Oxide Surfaces: Understanding Support Effects in Catalysis and Nanotechnology. *ACS Nano* **11**, 1196–1203 (2017).

63. Wang, P., Jia, C., Huang, Y. & Duan, X. Van der Waals Heterostructures by Design: From 1D and 2D to 3D. *Matter* **4**, 552–581 (2021).
64. Dvorský, R., Trojková, J., Praus, P. & Luňáček, J. Analysis of mechanisms of composite particles modification in liquid dispersions. *Mater Res Bull* **48**, 2286–2288 (2013).
65. Morgan, D. J. Resolving ruthenium: XPS studies of common ruthenium materials. *Surface and Interface Analysis* **47**, 1072–1079 (2015).
66. Ko, D.-S. *et al.* Understanding the structural, electrical, and optical properties of monolayer h-phase RuO2 nanosheets: a combined experimental and computational study. *NPG Asia Mater* **10**, 266–276 (2018).
67. de Almeida, J. S. & Ahuja, R. Electronic and optical properties of RuO2 and IrO2. *Phys Rev B* **73**, 165102 (2006).
68. El-Tantawy, F. *et al.* Optical properties of nanostructured ruthenium dioxide thin films via sol–gel approach. *Journal of Materials Science: Materials in Electronics* **28**, 52–59 (2017).
69. Gu, Q., Gao, Z., Yu, S. & Xue, C. Constructing Ru/TiO2 Heteronanostructures Toward Enhanced Photocatalytic Water Splitting via a RuO2/TiO2 Heterojunction and Ru/TiO2 Schottky Junction. *Adv Mater Interfaces* **3**, 1500631 (2016).
70. Yang, J. *et al.* Roles of cocatalysts in semiconductor-based photocatalytic hydrogen production. *Philosophical Transactions of the Royal Society A: Mathematical, Physical and Engineering Sciences* **371**, 20110430 (2013).
71. Zhao, G. & Xu, X. Cocatalysts from types, preparation to applications in the field of photocatalysis. *Nanoscale* **13**, 10649–10667 (2021).
72. Wang, Z. *et al.* Efficiency Accreditation and Testing Protocols for Particulate Photocatalysts toward Solar Fuel Production. *Joule* **5**, 344–359 (2021).
73. Liu, B. *et al.* Theoretical Kinetic Analysis of Heterogeneous Photocatalysis: The Effects of Surface Trapping and Bulk Recombination through Defects. *The Journal of Physical Chemistry C* **115**, 16037–16042 (2011).
74. Liu, B., Zhao, X., Terashima, C., Fujishima, A. & Nakata, K. Thermodynamic and kinetic analysis of heterogeneous photocatalysis for semiconductor systems. *Physical Chemistry Chemical Physics* **16**, 8751 (2014).

75. Takanabe, K. Photocatalytic Water Splitting: Quantitative Approaches toward Photocatalyst by Design. *ACS Catal* **7**, 8006–8022 (2017).
76. Lewandowska-Andralojc, A. & Polyansky, D. E. Mechanism of the quenching of the tris(bipyridine)ruthenium(II) emission by persulfate: Implications for photoinduced oxidation reactions. *Journal of Physical Chemistry A* **117**, 10311–10319 (2013).
77. Limburg, B., Bouwman, E. & Bonnet, S. Rate and Stability of Photocatalytic Water Oxidation using [Ru(bpy)3] 2+ as Photosensitizer. *ACS Catal. 2016,* **6**, 5273−5284 (2016).
78. Uddin, M. T. *et al.* Preparation of RuO2/TiO2 Mesoporous Heterostructures and Rationalization of Their Enhanced Photocatalytic Properties by Band Alignment Investigations. *The Journal of Physical Chemistry C* **117**, 22098–22110 (2013).
79. Hermans, Y. *et al.* Energy-Band Alignment of BiVO 4 from Photoelectron Spectroscopy of Solid-State Interfaces. *The Journal of Physical Chemistry C* **122**, 20861–20870 (2018).
80. Li, L., Salvador, P. A. & Rohrer, G. S. Photocatalysts with internal electric fields. *Nanoscale* **6**, 24–42 (2014).

7. Conclusion and outlook

This thesis has demonstrated the impact of rational cocatalyst tailoring and reaction engineering on photocatalyst efficiency. Through these two, the concept of photocatalyst optimization (i.e., for higher energy conversion efficiency) has been expanded to go beyond the more conventional design/tuning of the light absorber material properties.

The unique light harvesting properties of the studied TpDTz COF and its interaction with a noble-metal-free molecular cocatalyst (Ni-ME) has led to sustained photocatalytic HER rates. This endeavor relied on the engineering of a continuous-flow system, which facilitated the dynamic and sensitive detection of H_2 production rates. This platform was first introduced during these HER measurements on the TpDTz COF/Ni-ME system and highlighted the importance of photoreactor design and trace detection. The proposed trace detection method provided high accuracy, sensitivity, and reproducibility in H_2 and O_2 quantification through a novel gas chromatography setup (GC-MS/BID). Its implications proved an alternative approach to access the HER reaction mechanism which is difficult to obtain for COFs from high-throughput detection techniques (i.e., batch photoreactors), or fundamental complimentary studies of COF charge transport properties (i.e., via electrochemistry and carrier lifetime detection).[1,2] With the aid of isotope labeling (D_2O) and microkinetic modeling of the HER reaction dynamic trends, assuming rapid photo physics and charge dynamics at the COF, the rate limiting step of the system is targeted at the outer-sphere electron transfer from the TpDTz COF to the Ni-ME catalyst. This methodology aims to guide the efforts of more fundamental techniques on the COFs' charge dynamics based on the identified HER bottleneck.[2,3] Through reaction engineering, the fundamental photocatalytic properties of COFs and cocatalysts were partially bridged to the macroscopic observations of photocatalytic rates at *operando* conditions. This approach has been followed by subsequent studies on other HER organic semiconductors that aim to gain insight into steps of the photocatalytic process.[4,5]

Although artificial photosynthesis is an ever-growing field of study for heterogeneous catalysis, literature on standardization of photocatalytic rates has been scarce and hard to implement in practical terms to energy conversion materials. Based on the systematic work presented on a RuO_x cocatalyst photodeposited on commercial TiO_2 (P25), which was tracked using a modified bubbling reactor coupled to the previously presented detection

instrumentals, a water oxidation benchmark (RuO_2@TiO_2) was developed. The RuO_2@TiO_2 is the first in the field of photocatalytic water oxidation and aims to standardize OER rates obtained by different research groups. Together with avenues for comparison of OER rates in the field, this investigation on RuO_2@TiO_2 highlighted a set of best practices of our research group that has made our OER rates quantification reliable even in the presence of parasitic reactions of sacrificial agents. More recent and comprehensive publications on photocatalysis protocols for energy conversion align with this RuO_2@TiO_2 work.[6-8] Additionally, the optical modelling of photocatalytic suspensions and the ^{18}O labeling techniques are powerful *operando* techniques that have inspired subsequent works on reaction mechanisms and the reporting of photonic efficiency.[6,9] The role of RuO_x was assumed to be water oxidation given the evidence at the time of the RuO_2@TiO_2 benchmark publication. Yet, the unambiguous presence of metallic Ru and RuO_2 identified by XPS and SEM-FFT analysis may have unexplored effects in charge separation at the benchmark, which have been better described now along this work. Future applications of this system to actual energy conversion may include the streamlining of the nature of high RuO_x cocatalyst activity and how it couples to TiO_2, whose role as photocatalyst and light absorber are still under constant scrutiny.[10,11]

As a concluding work, inspired by the expertise of our research group gathered through years in the field of photocatalytic HER and OER reaction and cocatalyst engineering, a multidisciplinary analysis is presented to tailor a RuO_x 2D OER cocatalyst (RONS). It has been demonstrated through this work on WO_3 as light absorber, that photocatalytic performance can be drastically enhanced by the fine and rational tuning of the cocatalyst properties beyond the conventional impregnation techniques. Cocatalyst morphology approaches like the one presented for RONS had been previously explored in the artificial photosynthesis field, which eventually led to the workhorse core-shell cocatalyst.[12] However, not only the core-shell approach but the myriad of cocatalyst material research in literature tends to overlook other types of low-dimensionalities of the cocatalyst component different than nanoparticles (0D). The alternative to the latter has been proven successful after impregnating WO_3 with the engineered RONS. The RONS/WO_3 composites not only outperforms the reference RONP/WO_3 composite produced from conventional impregnation of WO_3 with RuO_2 nanoparticles, but also other well established cocatalysts

that exploit external effects to boost WO_3 photocatalytic activity, like PtO_x and hydrous RuO_2. The immediate impact of this work relates to a possible takeover of the RONS as the cocatalyst of choice in z-schemes that use WO_3 as the oxygen evolution photocatalyst and IO_3^-/I^- redox shuttles.[13-15] Although other potential cocatalyst roles of semi metallic materials have been discussed during this work, the RONS role found in this work primarily points to the lower electrochemical overpotential requirement at the RONS edge and the controlled parasitic light absorption given by the 0D/2D morphology of the RONS/WO_3 composites (f_{RuO2}). f_{RuO2} is a novel concept that was introduced through this work to quantify cocatalyst light absorption (~20-30% at optimally loaded RONS and RONP on WO_3) and has no precedent in the photocatalysis literature. Another expected impact expected on the energy conversion field is the possibility of simultaneous light harvester and cocatalyst morphology engineering, which represents a unique opportunity to assemble more efficient synergetic photosynthetic composites based also on a #D/#D morphology degree of freedom. Additionally, in other areas of photocatalysis where cocatalysts can be synthesized from cheap earth abundant elements, and where optical losses due light absorption on the cocatalyst component are crucial, the reduced parasitic light absorption of the 0D/2D morphology may allow higher cocatalyst loads than the 0D/0D morphology. Reduction of parasitic light absorption may not be restricted to the 0D/2D morphology and promises almost endless possibilities to tailor not only optics, but also charge dynamics and electron transfer aspects present in photocatalysis.

This thesis puts together a top-down interpretation of photocatalyst optimization in an energy conversion context. This work shall not be viewed as a competition to more traditional approaches to discover new photocatalysts based for example on their advantageous intrinsic light absorption and band alignment properties. Neither it competes with approaches tuning material properties (i.e., chemical composition, crystalline phases, junctions, size, etc.) of existing photocatalysts to achieve photocatalytic properties (i.e., band gap, binding energy, charge mobility, etc.) that ensure a better energy conversion efficiency trade off. Instead, this works aims to complement those views on the same problem. Synergies coming from combining the different approaches available to find efficient water splitting photocatalysts may eventually launch artificial photosynthesis to the pool of solutions that will combat global warming.

7.1 References

1. Banerjee T, Podjaski F, Kröger J, Biswal BP, Lotsch BV. Polymer photocatalysts for solar-to-chemical energy conversion. *Nature Reviews Materials* 2021, **6**(2)**:** 168-190.
2. Keller N, Bein T. Optoelectronic processes in covalent organic frameworks. *Chemical Society Reviews* 2021, **50**(3)**:** 1813-1845.
3. Jakowetz AC, Hinrichsen TF, Ascherl L, Sick T, Calik M, Auras F*, et al.* Excited-State Dynamics in Fully Conjugated 2D Covalent Organic Frameworks. *Journal of the American Chemical Society* 2019, **141**(29)**:** 11565-11571.
4. Kröger J, Jiménez‐Solano A, Savasci G, Rovó P, Moudrakovski I, Küster K*, et al.* Photocatalytic Hydrogen Evolution: Interfacial Engineering for Improved Photocatalysis in a Charge Storing 2D Carbon Nitride: Melamine Functionalized Poly(heptazine imide). *Advanced Energy Materials* 2021, **11**(6)**:** 2170028-2170028.
5. Gottschling K, Savasci G, Vignolo-González H, Schmidt S, Mauker P, Banerjee T*, et al.* Rational Design of Covalent Cobaloxime–Covalent Organic Framework Hybrids for Enhanced Photocatalytic Hydrogen Evolution. *Journal of the American Chemical Society* 2020, **142**(28)**:** 12146-12156.
6. Welter ES, Kött S, Brandenburg F, Krömer J, Goepel M, Schmid A*, et al.* Figures of Merit for Photocatalysis: Comparison of NiO/La-NaTaO3 and Synechocystis sp. PCC 6803 as a Semiconductor and a Bio-Photocatalyst for Water Splitting. *Catalysts* 2021, **11**(11)**:** 1415.
7. Wang Z, Hisatomi T, Li R, Sayama K, Liu G, Domen K*, et al.* Efficiency Accreditation and Testing Protocols for Particulate Photocatalysts toward Solar Fuel Production. *Joule* 2021, **5**(2)**:** 344-359.
8. Kunz LY, Diroll BT, Wrasman CJ, Riscoe AR, Majumdar A, Cargnello M. Artificial inflation of apparent photocatalytic activity induced by catalyst-mass-normalization and a method to fairly compare heterojunction systems. *Energy and Environmental Science* 2019, **12**(5)**:** 1657-1667.
9. Mo Z, Di J, Yan P, Lv C, Zhu X, Liu D*, et al.* An All-Organic D-A System for Visible-Light-Driven Overall Water Splitting. *Small* 2020, **16**(48)**:** 2003914.

10. Hashimoto K, Irie H, Fujishima A. TiO2 Photocatalysis : A Historical Overview and Future Prospects. 2006, **44**(12)**:** 8269-8285.
11. Jadhav AR, Bui VQ, Cho Y, Liu Y, Kumar A, Kim H*, et al.* Unveiling a Three Phase Mixed Heterojunction via Phase-Selective Anchoring of Polymer for Efficient Photocatalysis. *Advanced Energy Materials* 2022, **12**(15)**:** 2102116.
12. Zhang B, Zhang C, He H, Yu Y, Wang L, Zhang J. Electrochemical Synthesis of Catalytically Active Ru/RuO 2 Core−Shell Nanoparticles without Stabilizer. *Chemistry of Materials* 2010, **22**(13)**:** 4056-4061.
13. Tomita O, Nitta S, Matsuta Y, Hosokawa S, Higashi M, Abe R. Improved photocatalytic water oxidation with Fe3+/Fe2+ redox on rectangular-shaped WO3 particles with specifically exposed crystal faces via hydrothermal synthesis. *Chemistry Letters* 2017, **46**(2)**:** 221-224.
14. Can F, Courtois X, Duprez D. Tungsten-Based Catalysts for Environmental Applications. *Catalysts* 2021, **11**(6)**:** 703-703.
15. Abe R, Higashi M, Domen K. Overall water splitting under visible light through a two-step photoexcitation between TaON and WO3 in the presence of an iodate-iodide shuttle redox mediator. *ChemSusChem* 2011, **4**(2)**:** 228-237.

Appendix A. Gas Chromatography and Instrumental Developments

A gas chromatography setup (GC) was tailored in tandem with a GC supplier (Shimadzu) to expand the sensitivity of H_2, O_2, N_2, CO and CH_4 detection available in the market. As only commercial parts could be provided by Shimadzu, a significant part of the conceptual and practical tailoring of the existing detection and auto sampling technologies was performed *in the house* by our research group and as part of this doctoral dissertation. Reactor and instrumental interfaces necessary for the coupling of photocatalysis experiments and the intended trace analysis platform were designed and assembled from isolated commercial parts entirely by our group and as part of this doctoral dissertation. As this machine necessary for trace analysis had no precedent in the literature about photocatalysis, the setup was assembled in two stages to first prove a minimalistic configuration, which was later upgraded to the final intended configuration.

For the detection setup design, it was considered that the analytes were contained in a gas sample that is a moisturized CO_2/inert gas mixture. The detection setup was accompanied by an automatic autosampler (JAS) that consisted of helium primed rotation valves within a heated housing (three VICI Valco 6-port, 2 position), and minimal sampling-loop volume (250 µL). The heated housing, and all transfer lines are actively heated at 70°C. The two lines were thought parallel and identical, and meant to separate the target gas analytes to two redundant detectors. The autosampler box and the GC oven are interfaced with an Advanced Flow Controller unit (AFC), to control different injector settings, like column velocity, split ratio, and purging. A conventional quadrupole mass spectrometer (MS) was chosen as the first detector, and a barrier ionization discharge (BID) detector as the second detector. Given that both detectors track the sample composition from the same source, MS techniques performed in this platform and presented along this dissertation can be considered at *operando* conditions. The resulting machine was coined GCMSBID. Initially, a unique Molsieve column (MS-5a) was considered for analyte separation that could only work with forward elution of polar vapors in the gas matrix (i.e., moisture), for which a temperature program of the oven operating up to 120 °C was necessary. This was considered the default method for HER, OER and water splitting measurements, and its analysis time was around 40 min. An alternative method allowed quicker measurements in detriment of the momentary buildup of water. The

shortening of the measurement time (15 min) in this second configuration was achieved by limiting the maximum temperature of the oven to 70 °C. Due to this, the alternative method could only sample consecutively thrice, due to the buildup of vapors in the MS-5a columns, and then a measurement using the default method was necessary. When highly volatile and poler solvents were used, like acetonitrile, the use of an external sample upstream the autosampler valve was necessary, which could only be used in continuous flow measurements.

Although CO_2 reduction experiments are not shown along this thesis, CO, H_2 and CH_4 coming from photocatalytic reduction of CO_2 was possible. The CO_2 atmosphere needed for such measurements required priming of the MS-5a column, for which the GCMSBID machine had a second calibration due to the change of polarity of the MS-5a column when primed with CO_2. After a batch of CO_2 reduction experiments, the MS-5a column needed a high temperature bake out due to the strong CO_2 adsorption on the column active film (300 °C). This GC workflow is les conventional than the use of shincarbon columns in the market for CO_2 reduction experiments, where CO_2 can be eluted without using column baking. However, shincarbon columns cannot separate O_2/N_2, which is crucial for water splitting and OER measurements. Priming and bake out of the MS-5a, and its two calibration curves (the first with Helium as balance gas, and the second with CO_2 as balance gas), were in the end proven more practical than installing and removing a shincarbon column between regular and CO_2 reduction experiments. The flow of gas streams at the GCMSBID plus autosampler is sketched in Figure A-1.

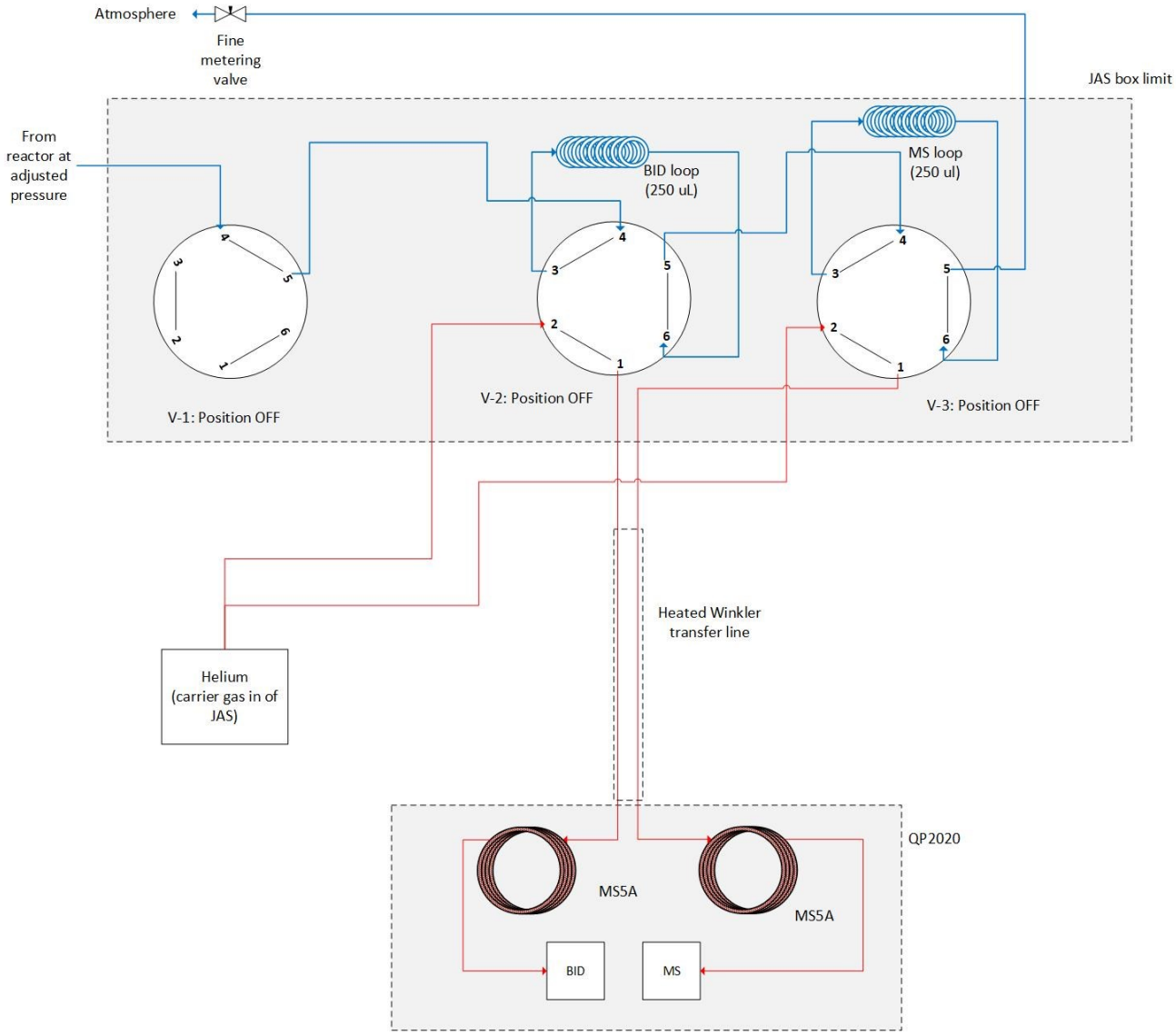

Figure A-1. GCMSBID and autosampler flow diagram. Red streams refer to carrier gas lines, while blue streams refer to sample gas lines. Machine configuration in the diagram is in sampling loop flushing mode. Injection mode is obtained by rotation of Valve V-3 and V-2 position. Within battery limit in dashed lines, hardware was designed and installed by Shimadzu.

The pressure of the sampling loop is regulated via an automated back pressure controller (Brooks SL series + PLC box), which is used to maintain the photoreactor pressure upstream the autosampler box (typical setpoint was 0.5 barg). The flow through the loop was measured and set to around 1 mL min^{-1}, by means of a fine metering valve (Swagelok) discharging to a vacuumed suction close to atmospheric pressure. The sampling loop priming was set to 1 min, allowing roughly 1.5 mL of sample to displace the total volume of the autosampler (0.5 mL of the loop, plus small contributions from dead volumes). In

between sampling, the loop was prevented from air contamination using a water seal and a check valve discharge.

This first configuration was used for experiments in Chapter 4 and Chapter 5, which is shown in Figure A-2. The calibration of the BID detector was performed using a split ratio of 10, meaning the ratio of injected sample entering the column, and a 7-level curve (0, 5, 10, 20, 50, 100, 1000 ppm) for H_2 and O_2, and a 5-level curve for CO and CH_4 (0, 5, 10, 20, 200 ppm). A minimum peak area around 2 ppm of O_2 is typically present and used as the instrument zero, which comes from the adventitious air introduced to the gas stream by the autosampler valve rotation. O_2 concentration in the reactor headspace at trace level is tracked redundantly using a photoluminescence flow-through sensor (Presence PL sensor, PST9) located upstream the JAS sample box. Three points were used per level for the GCMSBID calibration. The resulting accuracy was R^2>0.999 for all the analytes above, with a relative difference at each level below 2%. When the reactor pressure was set to a pressure different to the one by default, the GCMSBID calibration curves needed remeasuring at the desired alternative pressure, accounting for roughly a 20% increase in the detector signal per 1 (barg). In flow mode, the reactor inflow was controlled with a He/CO_2 gas mixer with a humidifying membrane (Cellkraft P-2), or alternatively with a single mass flow controller (MFC, Bronkhorst El-line). Valves and piping were a combination of vacuum standards (KF flange 10/16, metal-metal, glass-metal), and compression fitting (i.e., Swagelok or Let-lok). For photoreactor cooling and illumination, existing water recirculator-thermostat (Lauda Eco Silver) and a housed Xe lamp (450 W, Oriel Instruments) were used.

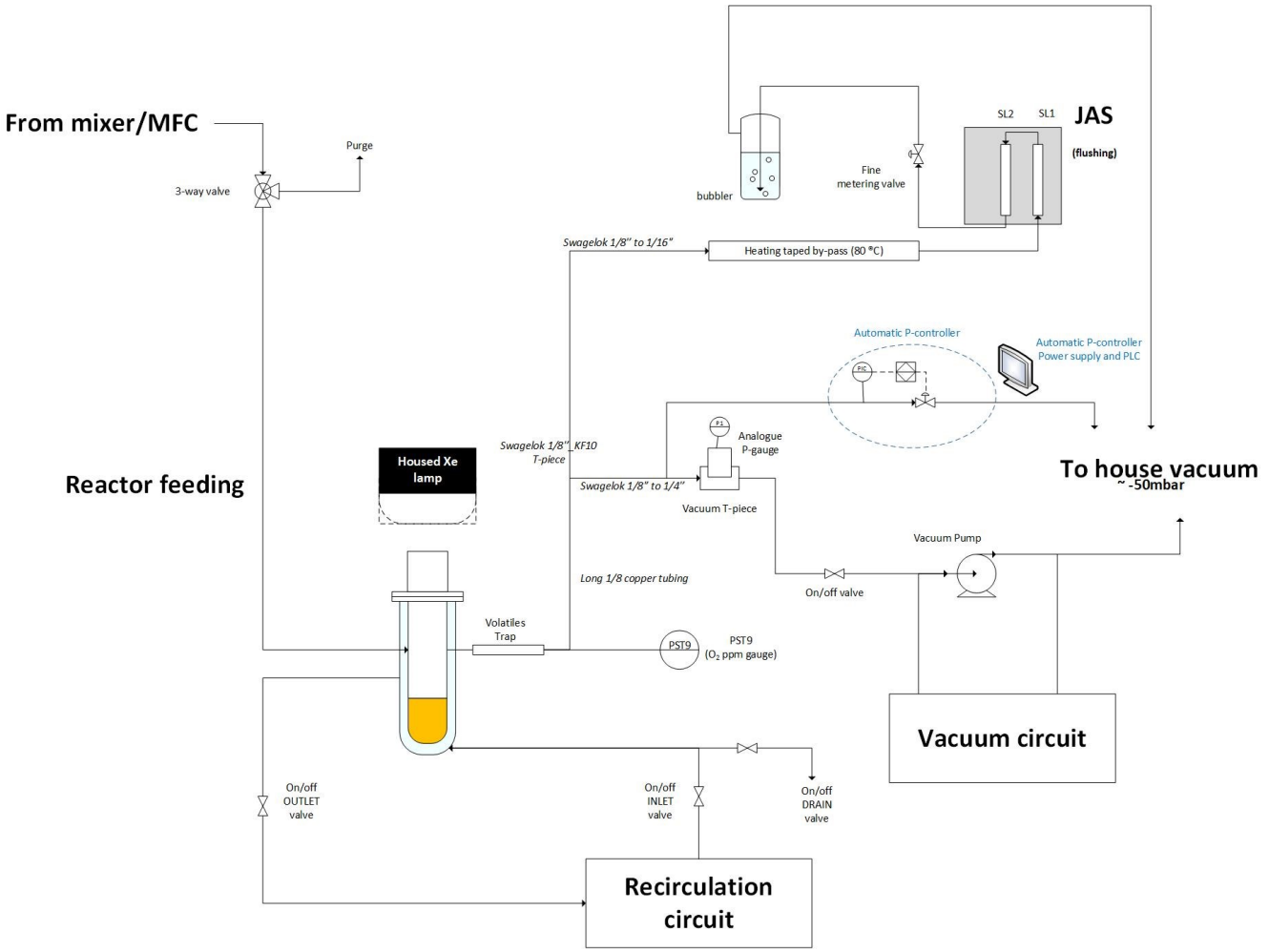

Figure A-2. Reactor instrumentation and simplified analytics flow diagram

Later, the developed GCMSBID device was upgraded aiming to the following goals. First, to avoid high temperature and baking procedures, a backflush unit was installed. The backflush consisted of the installation of a pre-column (Qbond), and automatic and controlled depressurization of the GC injector. Injection occurs first at the set split ratio (i.e., 10), and column velocity. During injection, the Advanced Pressure Control (APC) unit controlling the node pressure between the two columns is kept turned off, which means that the pre-column and MS-5a columns are in series. At a cut-off time of around 3.9 min, the node pressure control of the node between the two columns is activated, and the injector depressurized. This ensures proper elution of H_2, O_2, N_2, CO and CH_4 from the Qbond to the MS-5a column, while CO_2, moisture, and other vapors remain in the Qbond, and are then flushed backwards with the inversion of the Qbond flow direction. This allows a unique calibration for the GCMSBID setup, because the CO_2 and polar vapors in the injected sample do not contact the MS-5a column, which ends in a fixed analysis time around 10 minutes. Additionally, a vacuum system (Pfeiffer vacuum controller plus a membrane pump) was installed at the discharge of the JAS autosampler to allow any upstream pressure at the reactor, which was later decreased from the typical setpoint of 0.5 (barg) to 0.15 (barg). The discharge pressure of the JAS autosampler is kept at around 200 (mbar) of absolute pressure. The sampling loop flushing flow and sampling time allowed a similar volume displacement as in the previous configuration, also controlled by a fine metering valve, but with a mass flow gauge to read the sampling loop flow flushing in real time (Alborg). Additionally, a set of APC channels were connected to the sampling loop lines, to decouple the reactor pressure from the pressure of the loop before injection to the column. This system uses a miniature check valve downstream the sampling loop, which allows a reproducible 1 (kPa) injection pressure in the loop after flushing, which is achieved at minimal dead volumes and without the need of external vacuum control or transducers. This pressure injection control allows reactor pressure manipulation preserving the calibration curve obtained at a different and arbitrary pressure of the sample. The flow of gas streams at the upgraded GCMSBID plus autosampler is sketched in Figure A-3. In addition to the practical advantages already described, after this upgrade and using the same existing calibration method, the resulting R^2 after linear fitting increased (>0.9999), and the relative error from calibration points at each concentration

level lowered (<1%). This is a measure of higher reproducibility of the upgraded GCMSBID station.

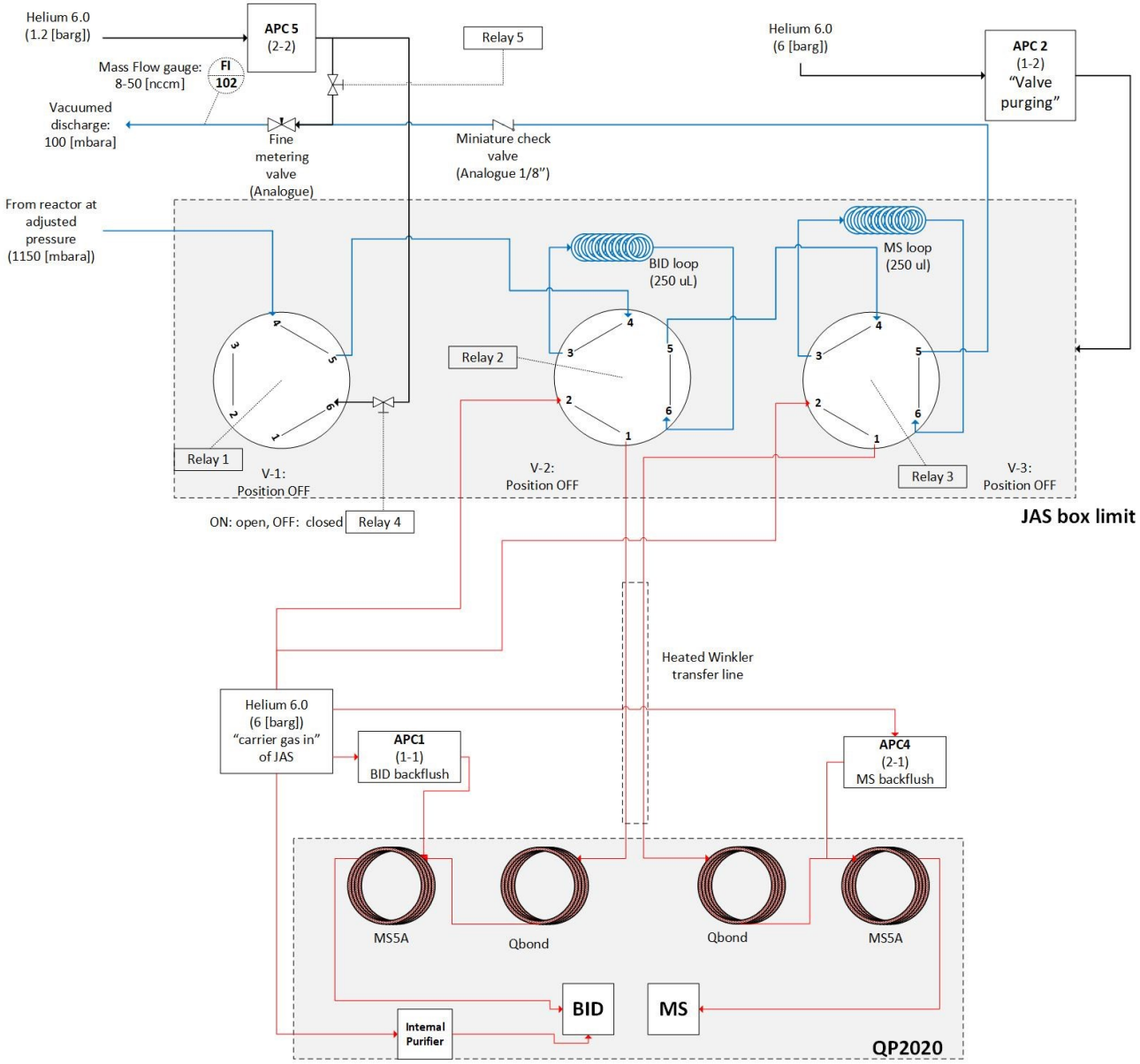

Figure A-3. GCMSBID and autosampler flow diagram after upgrade. Red streams refer to carrier gas lines, while blue streams refer to sample gas lines, and black streams refer to sampling loop pressure control. Machine configuration in the diagram is in sampling loop flushing mode. Before this configuration, machine is in stand-by. Stand-by mode is obtained by rotation of valve V-1, and Relay 4 open injecting pure carrier gas from an APC channel at pressure equivalent to the one upstream in the reactor cell. After changing to sampling loop flushing, and after the time the loop is fully primed with reactor sample (as depicted), pressure control takes place. Pressure control is achieved by rotating V-1 back to stand by position, but with relay 5 open, relay 4 closed, and the APC is depressurized to an injection pressure of 1 kPa. Injection mode after pressure control is obtained by rotation of Valve V-3 and V-2 position. Back flush is activated 3.9 min after injection, which happens when the injection of carrier gas is depressurized keeping a constant split ratio at the Qbond column, and same MS-5A column velocity, but a negative Qbond column velocity. Within battery limit in dashed lines, hardware was designed and installed by Shimadzu.

This upgraded configuration was used for experiments in Chapter 6, which is shown including reactor streamlines in Figure A-4. The light source presented in the measurements of Chapter 6 were also upgraded from the housed Xe lamps used in Chapter 4 and Chapter 5. The average spot heterogeneity of housed lamps was 20% at its default beam focusing when the Xe lamps is newly installed, but it can get up to 50% if the beam is defocused for example, to compensate power losses that come with lamp aging. In Chapter 6, photocatalytic measurements are performed using an actual solar simulator instead, with a beam heterogeneity of less than 2% (AAA quality solar simulator, Newport Instruments). Xe lamp technologies are highly collimated by default, which means that the beam divergence is typically less than 5°.

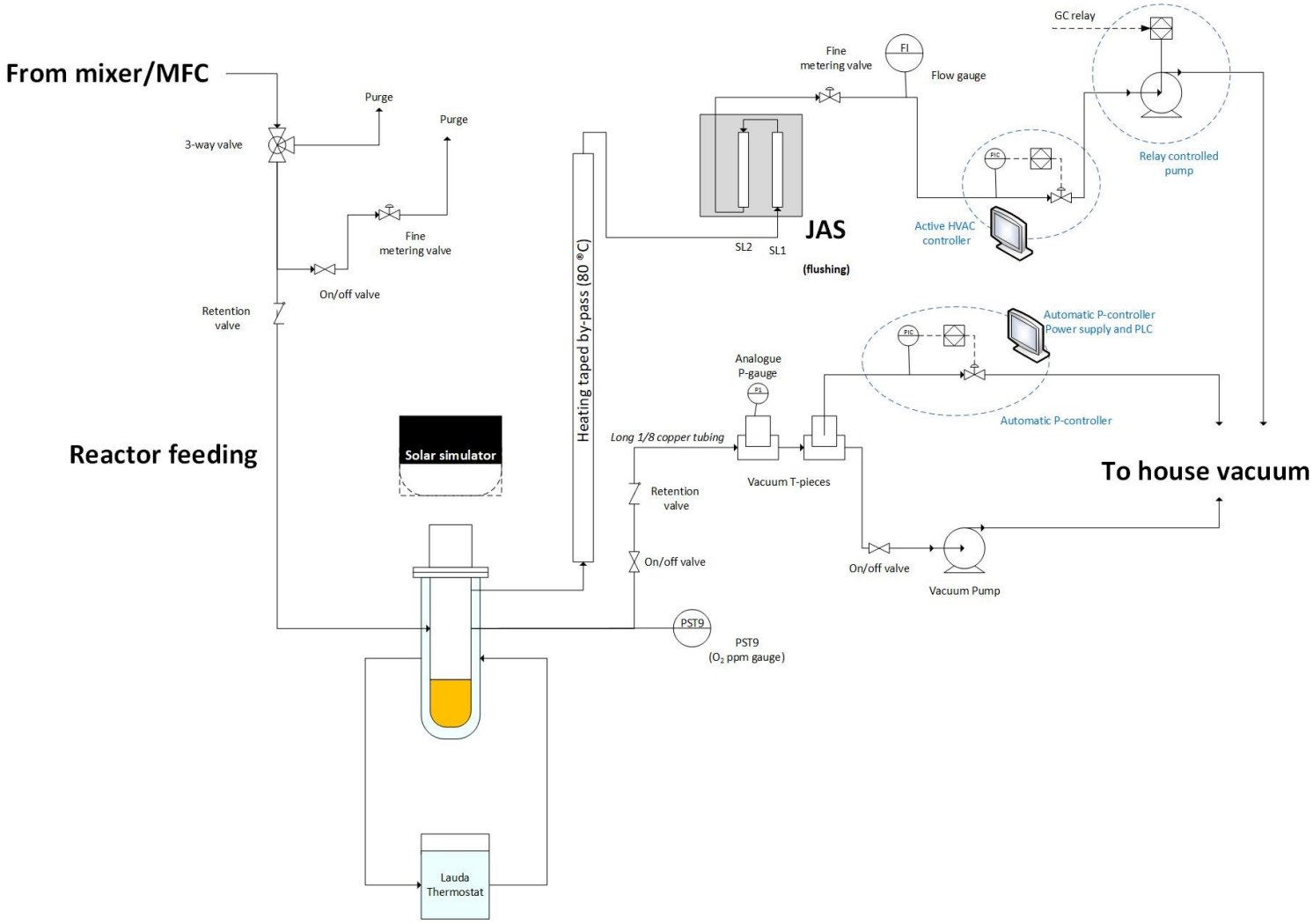

Figure A-4. Reactor instrumentation and simplified analytics flow diagram after upgrade

Appendix B. Supplementary and Experimental Section/Methods - Chapter 4

The work in this chapter was reproduced and adapted from the supplemental material of:

Sustained Solar H_2 Evolution from a Thiazolo[5,4-*d*]thiazole-Bridged Covalent Organic Framework and Nickel-Thiolate Cluster in Water

Bishnu P. Biswal, Hugo A. Vignolo-González, Tanmay Banerjee, Lars Grunenberg, Gökcen Savasci, Kerstin Gottschling, Jürgen Nuss, Christian Ochsenfeld, and Bettina V. Lotsch

B.1 Materials

1,3,5–triformylphloroglucinol (Tp) was synthesized using the previously reported literature protocol.[1] All commercially available reagents and solvents were used without further purification. Commercially available starting materials were bought from Sigma-Aldrich, TCI chemicals and Fisher Scientific depending upon their availability.

B.2 General instrumentation and methods

Powder X-ray diffraction (PXRD) patterns were collected at room temperature on a Stoe Stadi P diffractometer (Cu-Kα1, Ge(111)) in Debye-Scherrer geometry. The sample was measured inside a sealed glass capillary (1.0 mm) with spinning for improved particle statistics. Molecular modeling of the TpDTz COF was carried out using of BIOVA Materials Studio 2017 (17.1.0.48. Copyright © 2016 Dassault Systèmes) suite and the structure and unit cell parameters were relaxed using force fields (Forcite, universal force fields with Ewald electrostatic and van der Waals summations method). The unit cells of the model was then refined in the 2θ range 2-40° with the experimentally obtained PXRD pattern of TpDTz COF in the Reflex module of the BIOVA Materials Studio 2017, with fixed atom coordinates. The obtained structural models were checked for bond length and bond angle consistency in the structure.

Fourier transform infrared (FT-IR) spectra were recorded in attenuated total reflection (ATR) geometry on a PerkinElmer UATR Two equipped with a diamond crystal. The spectra were background corrected. FTIR data are reported with a wave number (cm^{-1}) scale.

Thermogravimetric analyses (TGA) were carried out on a TG50 analyzer (Mettler-Toledo) and a SDT Q600 TG-DTA analyzer in air at a heating rate of 5 ºC min^{-1} within a temperature range of 25−800 °C.

Electrospray ionization (ESI) mass spectrometry was performed on a Thermo Finnigan LTQ FT in positive and negative mode. Samples were dissolved in a mixture of acetonitrile and water.

Diffuse reflectance UV–visible absorption spectra were collected on a Cary 5000 spectrometer (referenced to barium sulphate). Absorption spectra were calculated from the reflectance data using the Kubelka-Munk function.

X-ray photoelectron spectroscopy (XPS) measurements were performed with an Axis Ultra system from Kratos equipped with a monochromatized Al Kα source. Detail scans were acquired with a pass energy of 20 eV. The peaks were fitted after subtraction of a Shirley background. A Gauss/Lorentz ratio of 30% was used for all peaks and the full width half maximum was used as a free fitting parameter.

Elemental analysis (EA) was carried out with an Elementar vario EL (Elementar Analysensysteme, Hanau, Germany).

Inductively coupled plasma atomic emission spectroscopy (ICP-AES) was done on a VARIAN VISTA RL simultaneous spectrometer (Agilent Technologies, Santa Clara, California, USA) with a CCD-detector.

Steady-state and time-resolved emission. Steady-state and time-resolved emission data were collected at room temperature using an Edinburgh FLS980 spectrometer. For steady-state emission, samples were excited using light output from a housed 450 W Xe lamp passed through a single grating (1800 l/mm, 250 nm blaze) Czerny-Turner monochromator and finally a bandwidth slit. Emission from the sample was passed through a double grating (1200 l/mm, 500 nm blaze) Czerny-Turner monochromator (appropriate bandwidth) and finally detected by a cooled microchannel plate photomultiplier tube (MCP-PMT) detector. The dynamics of emission decay were monitored by using the FLS980's time-correlated single-photon counting capability (1024 channels; 50 ns window) with data collection for 5000 counts. Excitation was provided by an Edinburgh EPL-375 picosecond pulsed laser diode (375 $\pm$ 6 nm, pulse width - 68 ps) and a cooled microchannel plate photomultipler tube (MCP-PMT) was used as the detector. Kinetics were fit with a tri exponential function by using the Edinburgh software package, whenever required. Amplitude average lifetimes were calculated using the expression given below

$$\tau_{av} = \frac{\sum_i a_i \tau_i}{\sum_i a_i}$$

SEM measurements were executed with a Zeiss Merlin or a VEGA TS 5130MM (TESCAN) instrument equipped with an X-MaxN20 (Oxford) EDX detector.

TEM was performed with a Philips CM30 ST (300kV, LaB6 cathode). The samples were prepared dry onto a copper lacey carbon grid (Plano). EDX was obtained on a Noran System Seven (NSS) Si(Li) detector.

Argon (Ar) adsorption analyses were performed at 87 K on a Quantachrome Instruments Autosorb iQ MP automatic volumetric instrument. All the COF samples were outgassed for 12 h at 120 °C under vacuum prior to the gas adsorption studies. The surface areas were evaluated using the Brunauer-Emmett-Teller (BET) model applied between P/P_0 values of 0.05 and 0.2 for mesoporous COFs. The pore size distributions were calculated using the Quenched Solid State Density Functional Theory (QSDFT) cylindrical-slit adsorption kernel for carbon implemented in the ASiQwin software v 3.01.

H_2O adsorption measurements were performed at 293K with a sample weight of 10 – 15 mg and preheating at 120 °C for 12 h.

CO_2 adsorption measurements were performed at 273K with a sample weight of 10 – 15 mg and preheating at 120 °C for 12 h.

Liquid and solid state NMR spectra. All liquid state NMR measurements were performed on a JEOL ECZ 400S 400 MHz spectrometer (magnetic field 9.4 T). ^{1}H, ^{13}C and ^{15}N measurements were performed in 5 mm NMR tubes using deuterium field lock. An appropriate number of accumulations have been made to achieve sufficient signal-to-noise ratio. ssNMR was recorded on a Bruker Avance III 400 MHz spectrometer (magnetic field 9.4 T). Chemical shifts (δ) are given in ppm relative to TMS; coupling constants J are given in Hertz (Hz). $(CD_3)_2SO$ [$\delta(^{1}H)$ = 2.50 ppm, $\delta(^{13}C)$ = 39.6 ppm] was used as solvent, lock and internal standard. For ssNMR spectroscopy, the samples were packed in 4 mm ZrO_2 rotors, which were spun in a Bruker WVT BL4 double resonance MAS probe. Chemical shift was referenced relative to tetramethylsilane (^{13}C), and CH_3NO_2 (^{15}N) as an external standard. The spinning rate was ^{13}C NMR and 8 kHz for ^{15}N measurements. A standard cross-polarization sequence with a 2 ms ramped contact pulse was used for ^{13}C and a total

of 4096-8192 scans were routinely accumulated. ^{15}N solid state NMR spectra were obtained with ramped cross-polarization and contact pulses of 3-8 ms optimized for the best signal. Both ^{13}C and ^{15}N measurements were performed at conditions of high-power broadband proton decoupling (SPINAL 64) with the spectral conditions being optimized for the shortest relaxation delay by measuring the ^{1}H T_1 relaxation time. Carbon chemical shifts are expressed in parts per million (δ scale).

Quantum-chemical calculations. The structure for the TpDTz-NMR model was optimized on PBE0-D3/def2-TZVP level of theory.[2-5] Structures for the TpDTz and TpDTP pore model were optimized on RI-PBE-D3/def2-TZVP level of theory. NMR chemical shifts were obtained on B97-2/pcSseg-2 level of theory[6,7] using previously obtained structures. Calculated ^{13}C-NMR chemical shifts were corrected by 3.12 ppm to account for a systematic offset in comparison to experimentally obtained NMR chemical shifts. Structure optimizations were performed using the Turbomole program package in version 7.0.3,[8,9] NMR chemical shifts were calculated using the FermiONs^{++} program package.[10,11]

B.3 Synthetic Procedures

Synthesis of 4,4'-(thiazolo[5,4-*d*]thiazole-2,5-diyl)dianiline (DTz): In a 100 ml round bottom flask a mixture of glacial acetic acid (15 mL), iron powder (Fe; 161.7 mmol; 9 g) and 2,5-bis(4-nitrophenyl)-3a,6a-dihydrothiazolo[5,4-*d*]thiazole (3.23 mmol, 1.25 g) was stirred at 60 ºC for 48 h under Ar atmosphere. Afterwards, the acid was neutralized using NaOH (12 M) and water. The Fe powder was separated from the suspension using a magnetic rod and the residual yellow solid was collected through filtration and dried under vacuum to obtain the crude product. The compound was purified using column chromatography with hexane: ethyl acetate (10:90) as eluent (314 mg, ~30% yield). FT-IR (solid): ν_{max} = 3411, 3303, 3196, 2922, 2850, 1603, 1521, 1453, 1422, 1290, 1219, 1176, 1126, 1002, 881, 823, 660, 624, 612, 590, 508, 444 cm^{-1}.

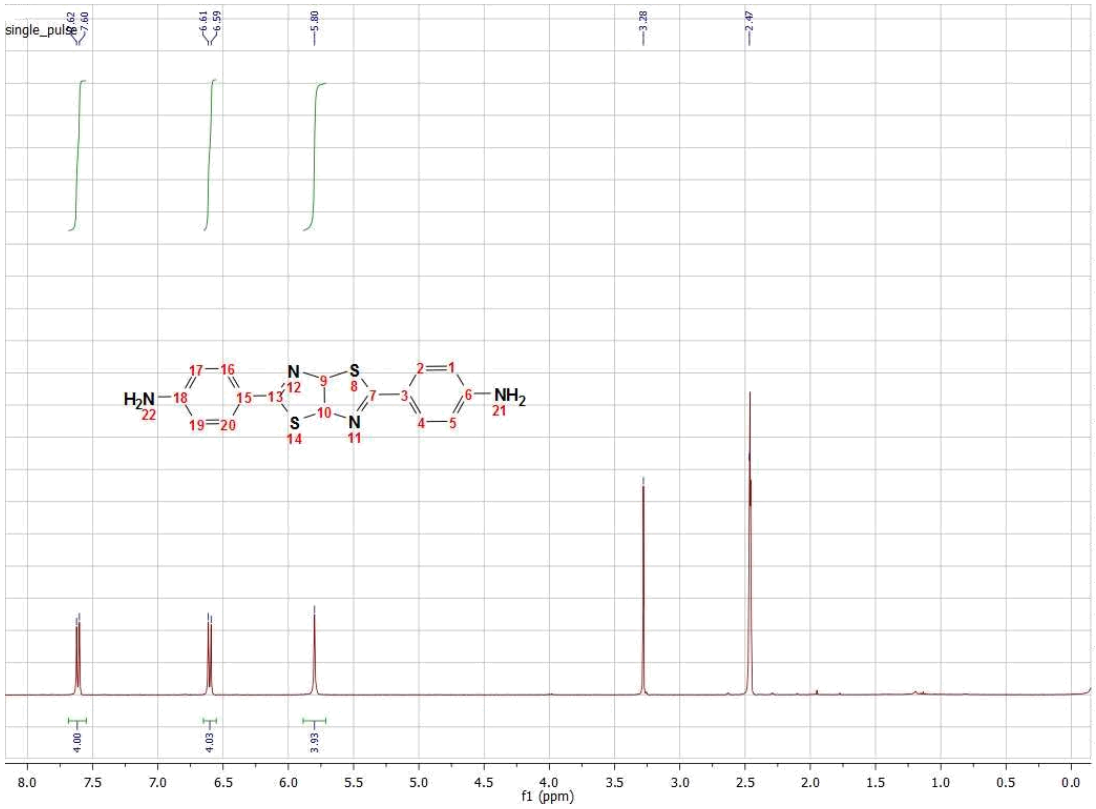

Figure B-1. ^{1}H NMR spectrum of DTz measured in $(CD_3)_2SO$

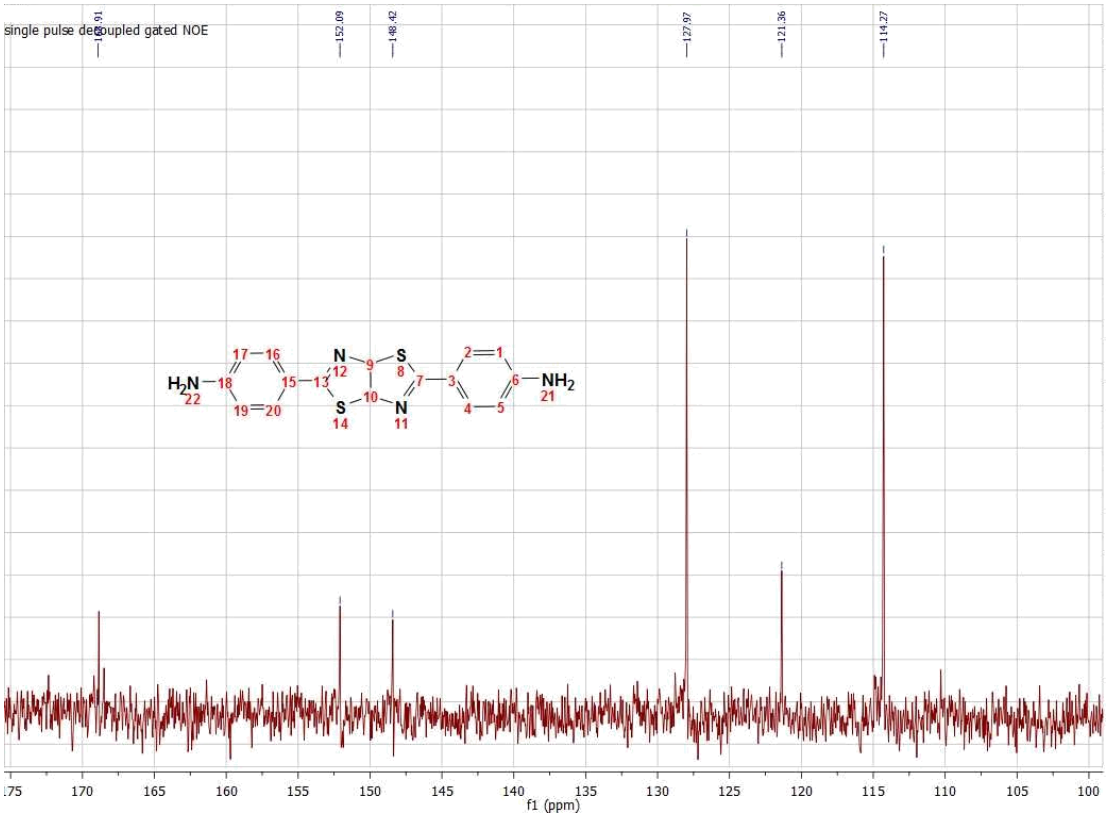

Figure B-2. ^{13}C NMR spectrum of DTz measured in $(CD_3)_2SO$.

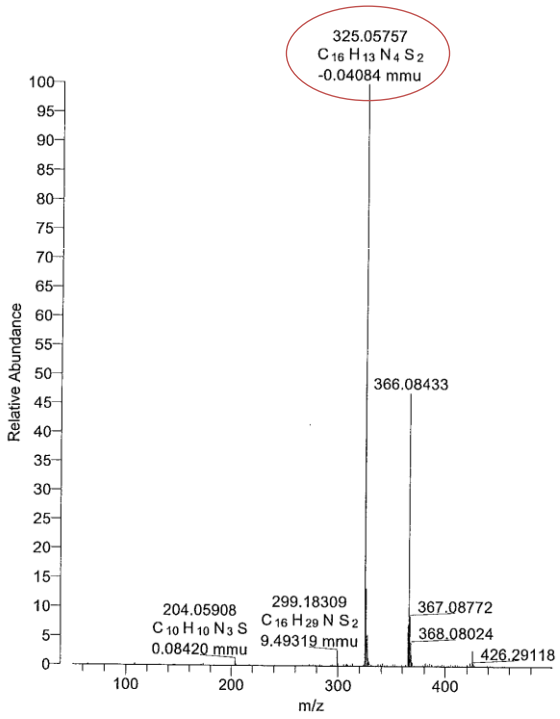

Figure B-3. ^{13}C NMR spectrum of DTz measured in $(CD_3)_2SO$. Mass spectrum of DTz (Exact Mass: 324.05, the circled peak corresponds to the compound mass).

Crystallographic details of 4,4'-(thiazolo[5,4-d]thiazole-2,5-diyl)dianiline (DTz): Crystals suitable for single-crystal X-ray diffraction were selected under high viscosity oil, and mounted with Paratone-N oil on a loop made of Kapton foil (Micromounts™, MiTeGen, Ithaca, NY). Diffraction data were collected at 100 K with a SMART APEXII CCD X-ray diffractometer (Bruker AXS, Karlsruhe, Germany), using graphite-monochromated Mo-Kα radiation, and an N-Helix low-temperature device (Oxford Cryosystems, Oxford, U.K.).[12] The reflection intensities were integrated with the SAINT subprogram in the Bruker Suite software[13], a multi-scan absorption correction was applied using SADABS[14], and the structures were solved by direct methods and refined by full-matrix least-square fitting with the SHELXTL software package.[15,16] Hydrogen atoms bonded to carbon and nitrogen atoms were added to the structure model on calculated positions using a riding model. The molecular structure is shown in Figure B-4, crystal data and data collection details are given in Table B-1.

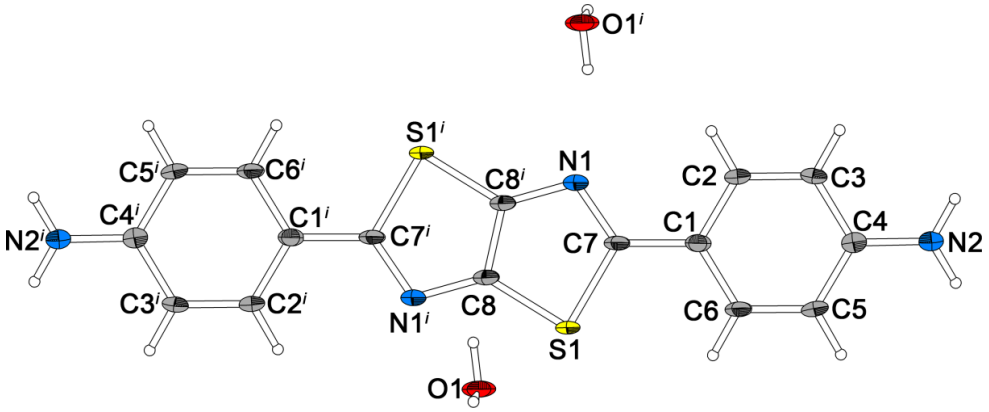

Figure B-4. Mass spectrum of DTz (Exact Mass: 324.05, the circled peak corresponds to the compound mass). Molecular structure of DTz with atom labels (symmetry code i = –x, –y, –z) and 50 % probability ellipsoids for non-H atoms.

Table B-1. Crystal data, data collection and refinement details for DTz at100 K.

Empirical formula	$C_{16}H_{12}N_4S_2$; 2 H_2O	
Formula weight	360.45	
Space group (no.), Z	$P\bar{1}$ (2), 1	
Lattice parameters /Å, /°	a = 3.974(3)	α = 117.275(8)
	b = 10.235(8)	β = 93.726(9)
	c = 11.097(9)	γ = 93.395(9)
V/Å^3	398.3(5)	
ρ_{xray} /g×cm^{-3}	1.503	
Crystal size /mm^3	0.16×0.10×0.05	
Diffractometer	SMART APEX II, Bruker AXS	
X-ray radiation, λ /pm	MoKα, 71.073	
Absorption correction	Multi-scan, SADABS	
2θ range /°	4.15 ≤ 2θ ≤ 52.63	
Index ranges	–4 ≤ h ≤ 4, –12 ≤ k ≤ 12, –13 ≤ l ≤ 13	
Reflections collected	3151	
Data, R_{int}	1591, 0.030	
No. of parameters	115	
Transmission: t_{min}, t_{max}	0.082, 0.150	
Final R indices [I > 2σ(I)]	R1 = 0.059, wR2 = 0.156	

R indices (all data)	R1 = 0.062, wR2 = 0.159
Deposition no.	**CCDC- 1898622**

Synthesis of TpDTz COF: The synthesis of TpDTz was achieved by reacting *1,3,5*–triformylphloroglucinol (Tp) (1 eq., 7.5 mg, 0.035 mmol) and DTz (1.5 eq., 17.5 mg, 0.053 mmol) in the presence of catalytic amount (0.1 ml) of aqueous acetic acid (6M) using *o*-dichlorobenzene and N,N-dimethylacetamide (DMAc) (1:3 by vol., 2 ml) as the solvent combination in a Biotage 5 ml high precision glass vial, which was further sealed and heated at 120 ºC for 3 days. The resulting deep reddish powder was washed with DMAc, acetone and tetrahydrofuran (THF) to isolate highly crystalline TpDTz COF with ~80% isolated yield. Elem. Anal. Calcd.: C, 61.38; H, 3.28; N, 13.01; O, 7.43; S, 14.90. Found (average of 4 TpDTz COF samples): C, 52.61; H, 3.74; N, 13.20; S, 14.78.

Synthesis of TpDTP COF: The synthesis of TpDTP was achieved by reacting Tp (1 eq., 7.5 mg, 0.035 mmol) and 4,4''-diamino-*p*-terphenyl (DTP) (1.5 eq., 14.5 mg, 0.055 mmol) in the presence of a catalytic amount (0.1 ml) of aqueous acetic acid (6M) using *o*-dichlorobenzene and N,N-dimethylacetamide (DMAc) (1:3 by vol., 2 ml) as the solvent combination in a Biotage 5 ml high precision glass vial, which was further sealed and heated at 120 ºC for 3 days. The resulting faint yellow powder was washed with DMAc, acetone and tetrahydrofuran (THF) to isolate crystalline, porous TpDTP COF with ~83% isolated yield.

Synthesis of N3-COF: The N3-COF was synthesized adopting our previously reported procedure.[17]

Synthesis of TzTz-POP-3: The synthesis of TzTz-POP-3 was carried out according to a literature procedure.[18] In detail, a Pyrex tube (o.d. × i.d. = 1 × 0.8 cm^2 and length 18 cm) was charged with 1,3,5-tris(4-formylphenyl)benzene (30 mg, 76.84 μmol, 1 eq.), dithiooximide (DTO) (13.8 mg, 115.26 μmol, 1.5 eq.) and 2 ml of nitrobenzene. This mixture was sonicated for 10 min. in order to get a homogenous dispersion. The tube was then flash frozen at 77 K (liquid N_2 bath) and degassed by three freeze-pump-thaw cycles. The tube was sealed under vacuum and then heated at 150 ºC for 4 days. A brownish yellow colored precipitate was collected by filtration and washed with ethanol, DMAc and acetone several times until the filtrate became colorless, dried at 150 ºC under vacuum for 12 h to obtain TzTz-POP-3.

Synthesis of Ni(*abt*)$_2$: The synthesis of Ni(*abt*)$_2$ was carried out according to a literature procedure.[19] In detail, 2-aminothiophenol (*abt*; 236 mg, 1.89 mmol) and potassium hydroxide (110 mg, 2 mmol) were dissolved in 5 mL of 20% aqueous ethanol. To this solution, a solution of Ni(OAc)$_2$.4H$_2$O (235 mg, 0.94 mmol) in 5 mL of 2.5 M aqueous ammonia was added dropwise with stirring. A yellow colored precipitate was formed immediately, then the solution was stirred for 30 min, and the precipitate was collected by filtration. The precipitate was suspended in 15 mL of water containing 200 mg of potassium hydroxide, and air was bubbled through the solution for overnight, resulting in the formation of a dark blue precipitate. The precipitate was collected by filtration and crystallized from diethyl ether to give dark blue microcrystals of Ni(*abt*)$_2$ (190 mg, 65%). Elem. Anal. Calcd: C, 47.25; H, 3.30; N, 9.18; Ni, 19.24; S, 21.02. Found: C, 47.78; H, 3.25; N, 9.21; Ni, 18.18 (found from ICP); S, 21.12.

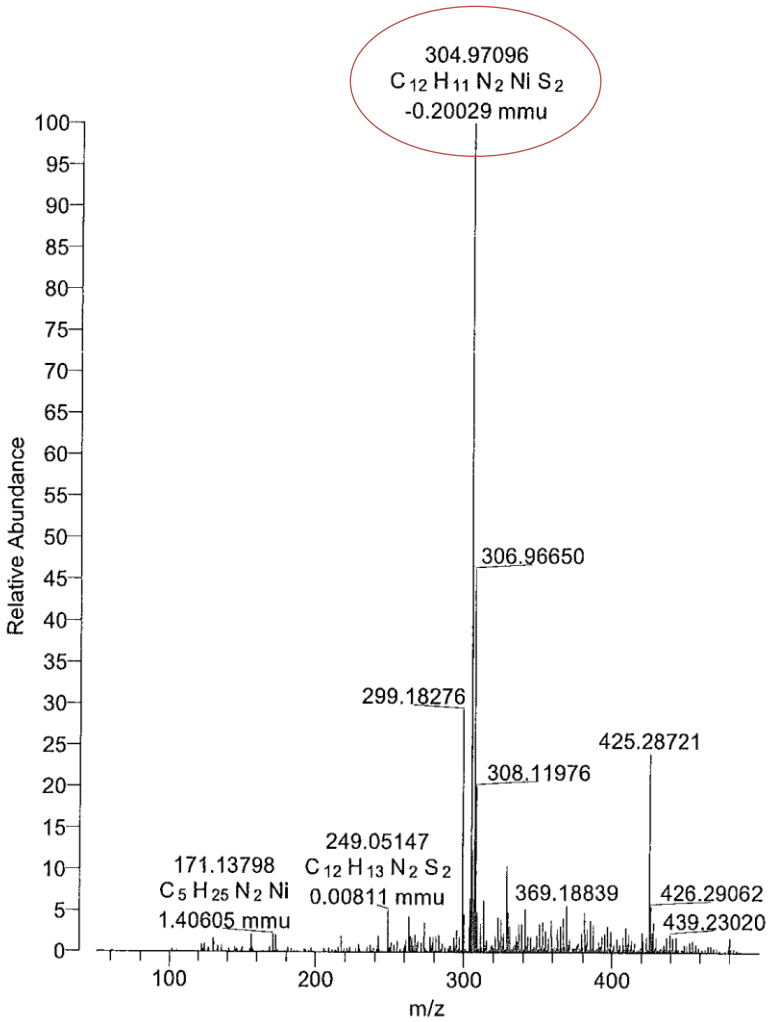

Figure B-5. Mass spectrum of Ni(abt)$_2$ (Exact Mass: 303.96, the circled peak corresponds to the complex mass).

B.4 Powder X-ray diffraction

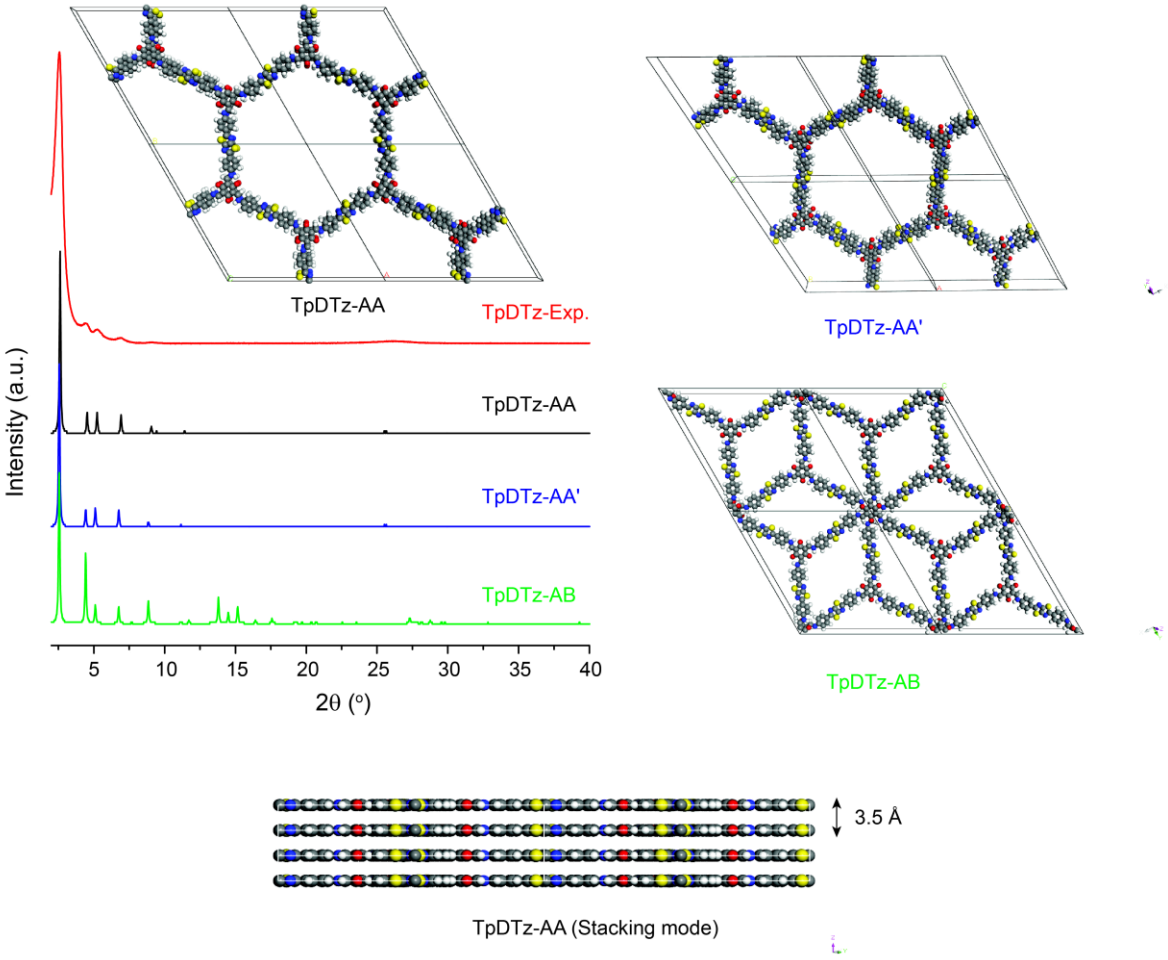

Figure B-6. Experimental (red) compared with simulated (AA) eclipsed (black), (AA') 2Å slip-eclipsed (blue), and (AB) staggered (green) PXRD profiles of TpDTz COF with corresponding optimized structure models.

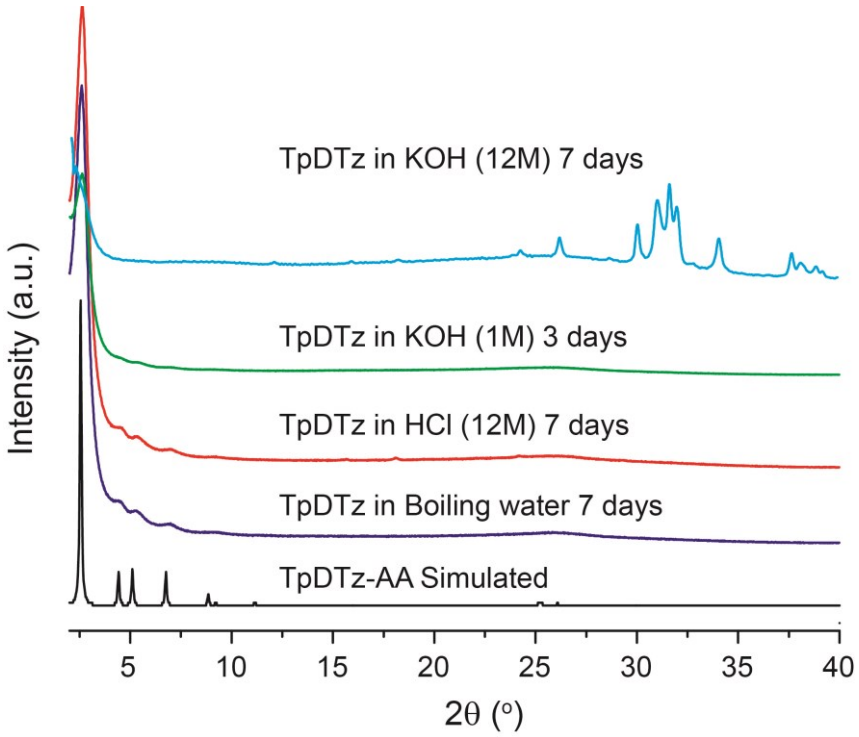

Figure B-7. PXRD confirms the chemical stability of TpDTz COF in boiling water and concentrated HCl (12M). Note: TpDTz COF is unstable upon 12M KOH treatment for 7 days and moderately stable in 1M KOH for 3 days.

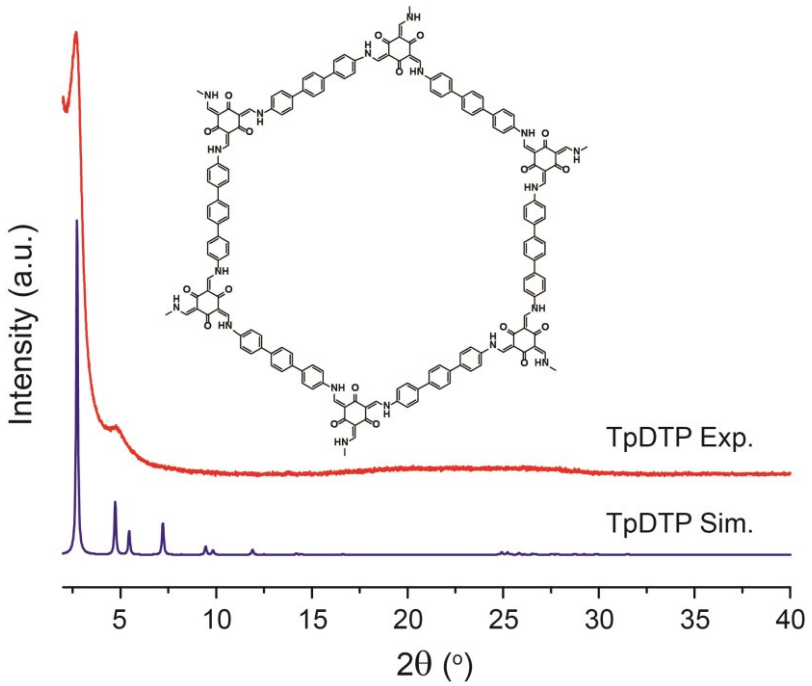

Figure B-8. Comparison of the experimental and simulated PXRD patterns of TpDTP COF; inset is the chemical structure of one pore.

B.5 FTIR spectra and TG analysis

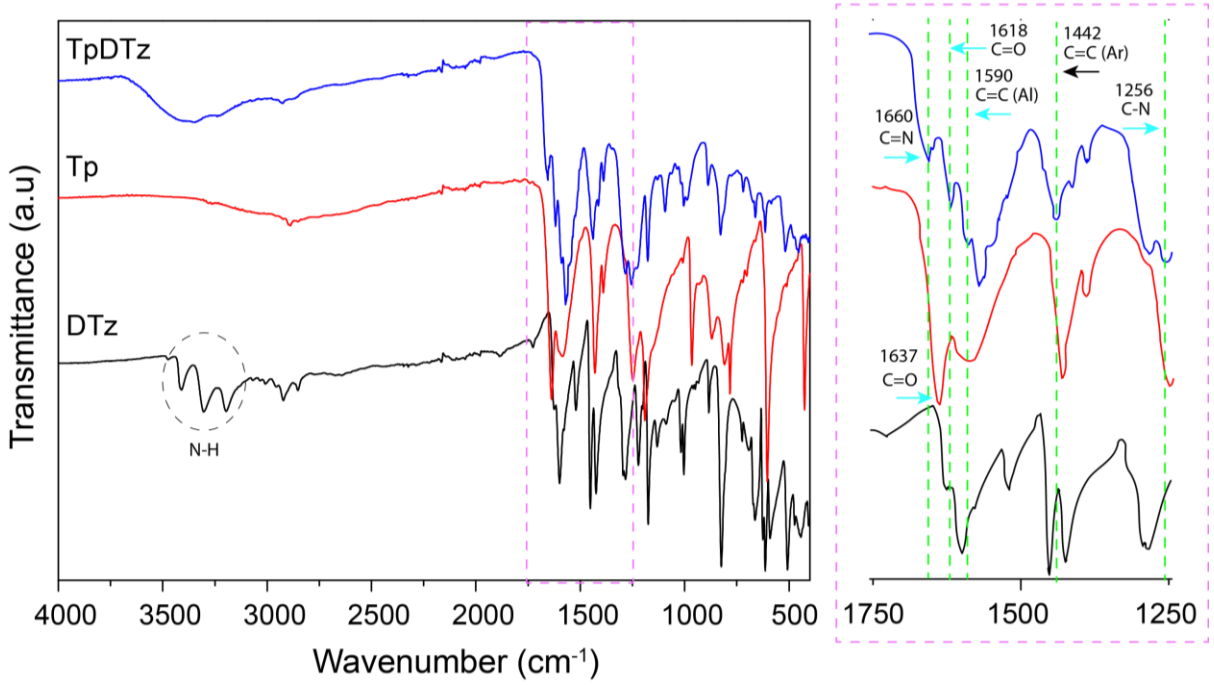

Figure B-9. Comparison of FT-IR spectra of TpDTz COF and respective starting materials (Tp and DTz).

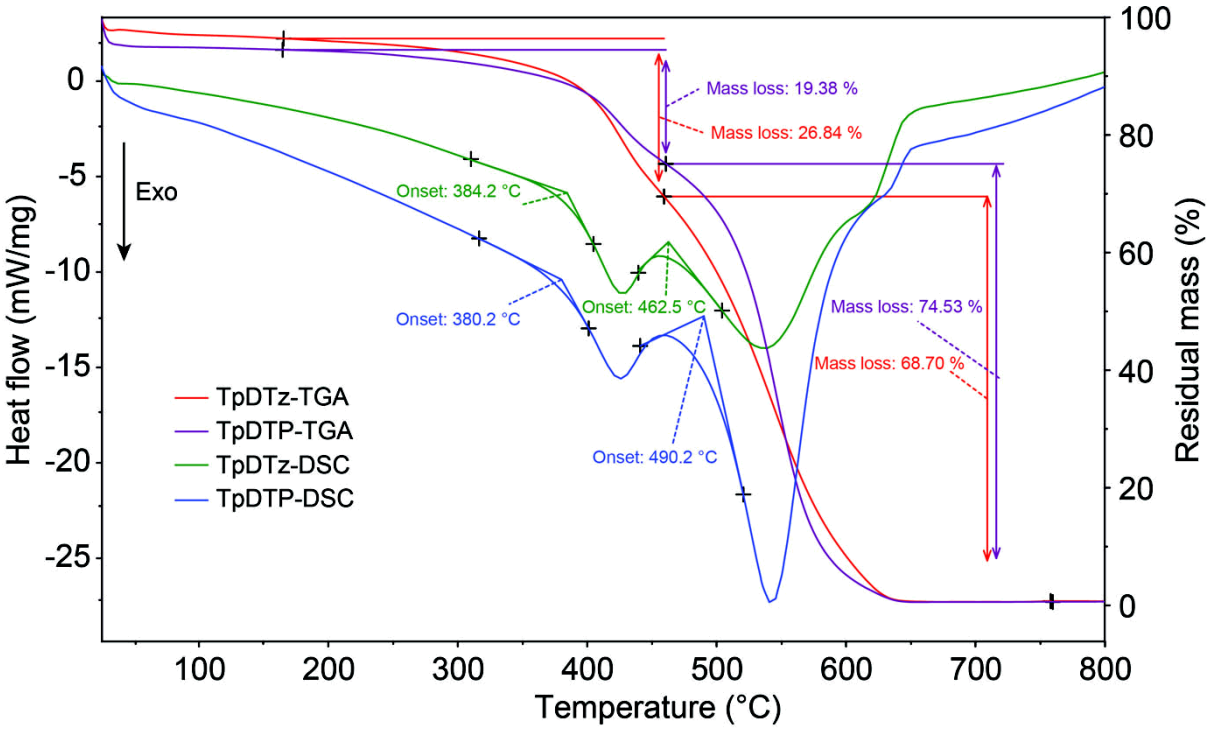

Figure B-10. Comparison of TGA and DSC profiles of TpDTz and TpDTP COF.

B.5 SEM and TEM analyses

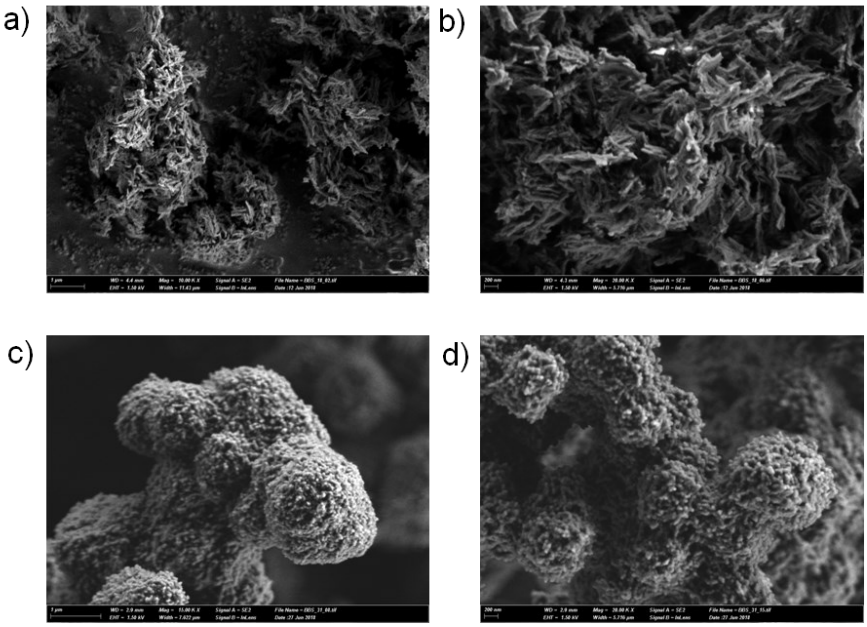

Figure B-11. SEM images **(a), (b)** TpDTz and **(c), (d)** TpDTP respectively. [Scale bar: a; c) 1 µm and c, d) 80 nm]

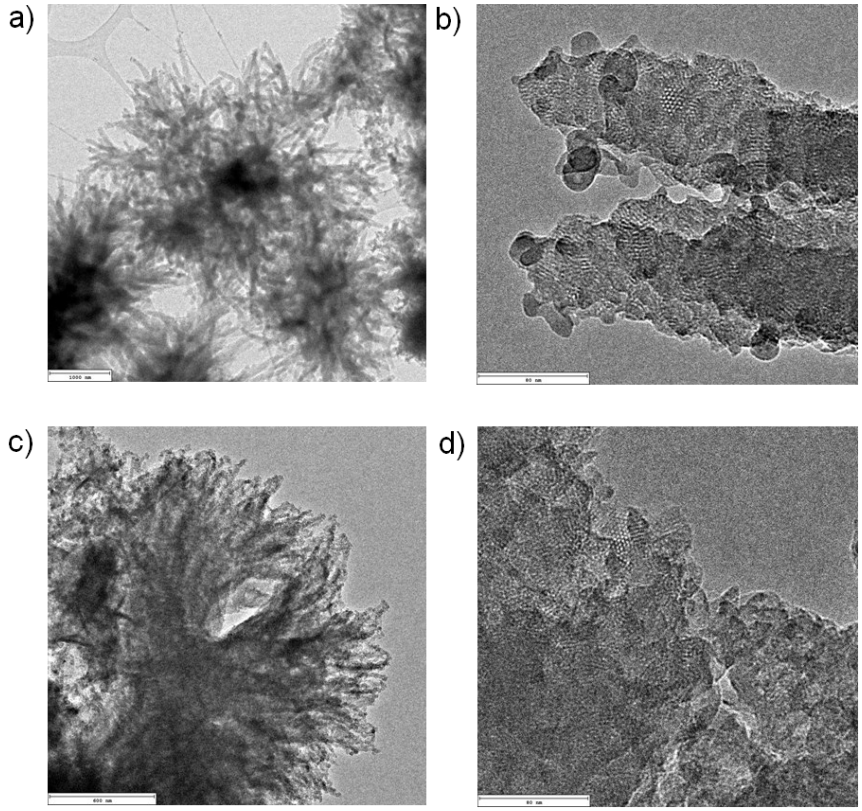

Figure B-12. TEM images **(a), (b)** TpDTz and **(c), (d)** TpDTP respectively. [Scale bar: a; 1 µm, b) 80 nm, c) 600 nm and d) 80 nm]

B.6 Gas and vapour adsorption in COFs

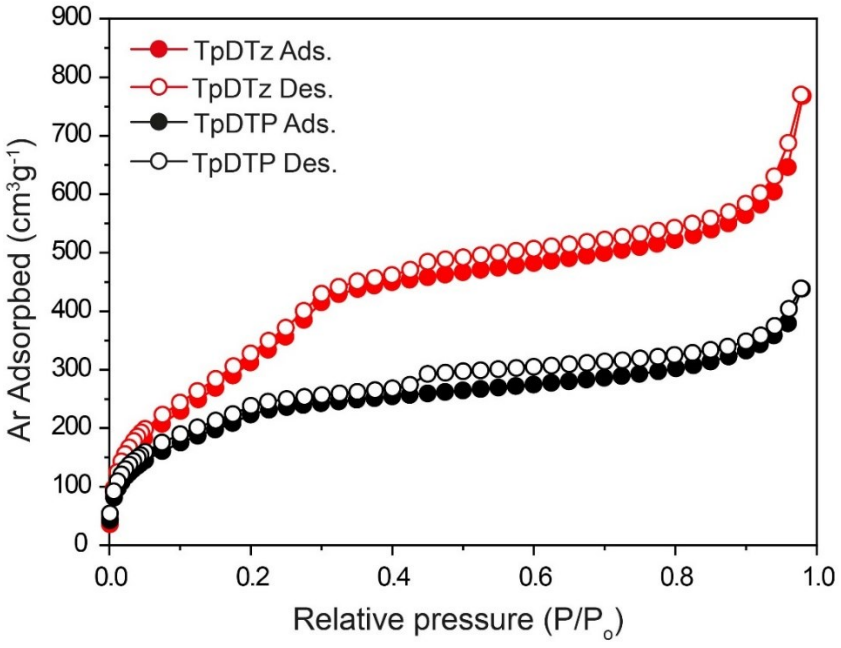

Figure B-13. Comparison of the Ar adsorption-desorption isotherms of TpDTz and TpDTP COF.

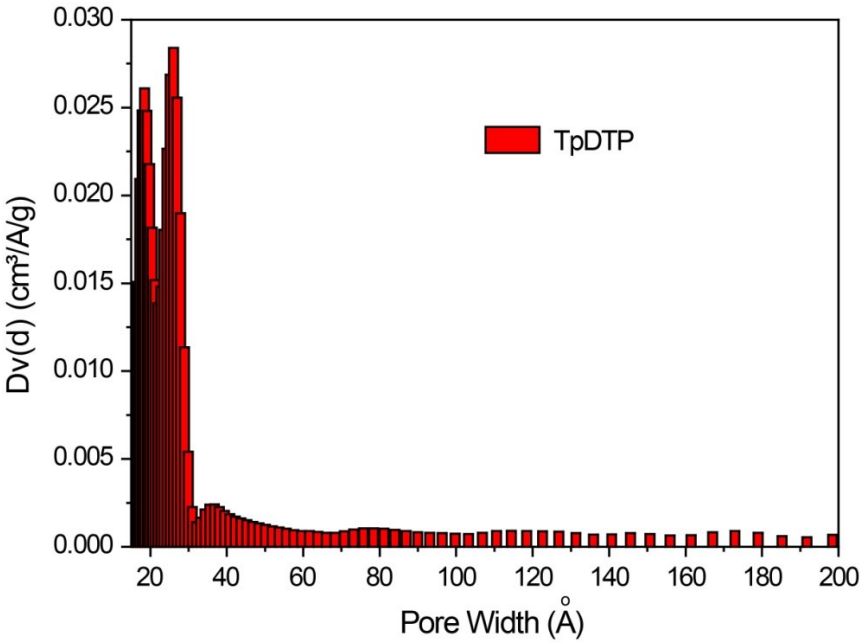

Figure B-14. Pore size distributions of TpDTP COF (two maxima at 19 and 27 Å) calculated from Ar adsorption-desorption data using the QSDFT cylindrical-slit adsorption kernel for carbon.

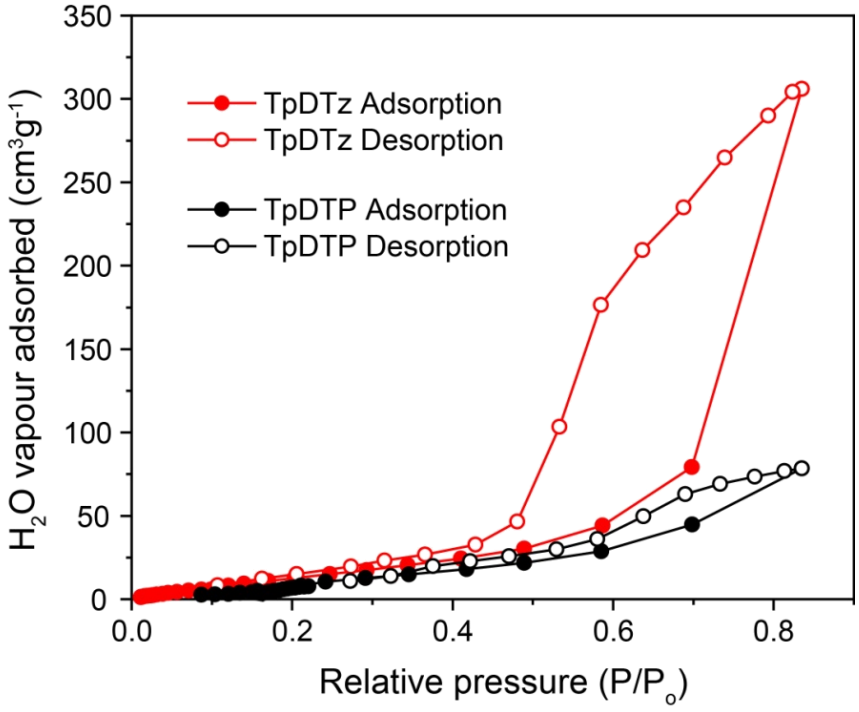

Figure B-15. Comparison of the H2O adsorption-desorption isotherms of TpDTz and TpDTP COF recorded at 293 K.

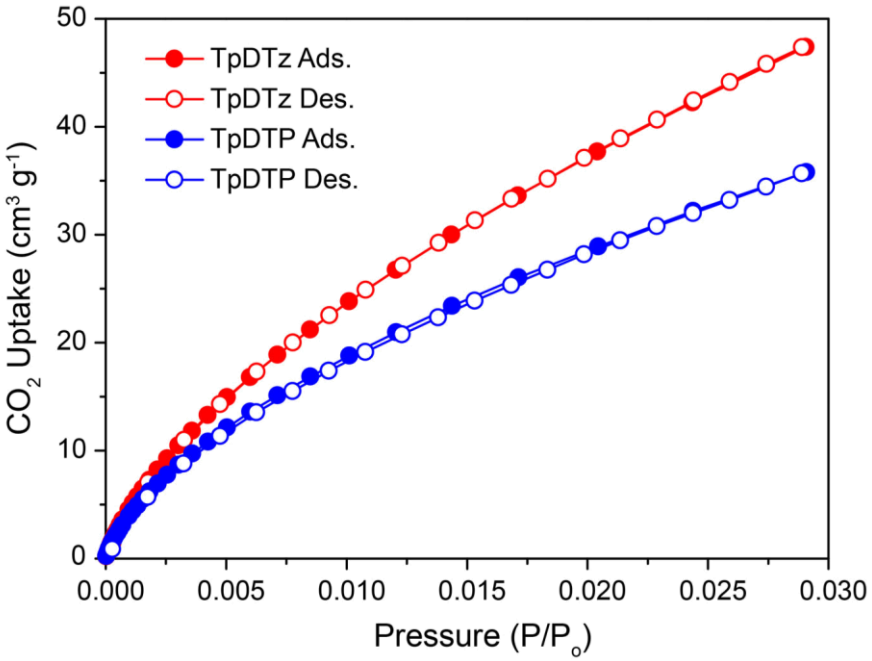

Figure B-16. Comparison of the CO2 adsorption isotherms of TpDTz and TpDTP COF recorded at 273 K.

B.7 Optical and electronic properties

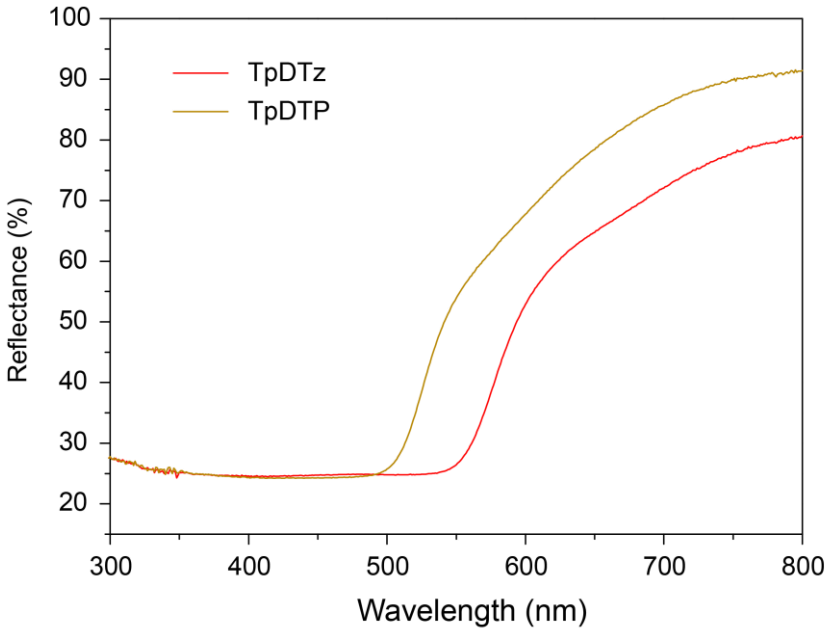

Figure B-17. Comparison of the UV–vis DRS spectra for TpDTz (red) and TpDTP (yellow) COF measured in the solid state.

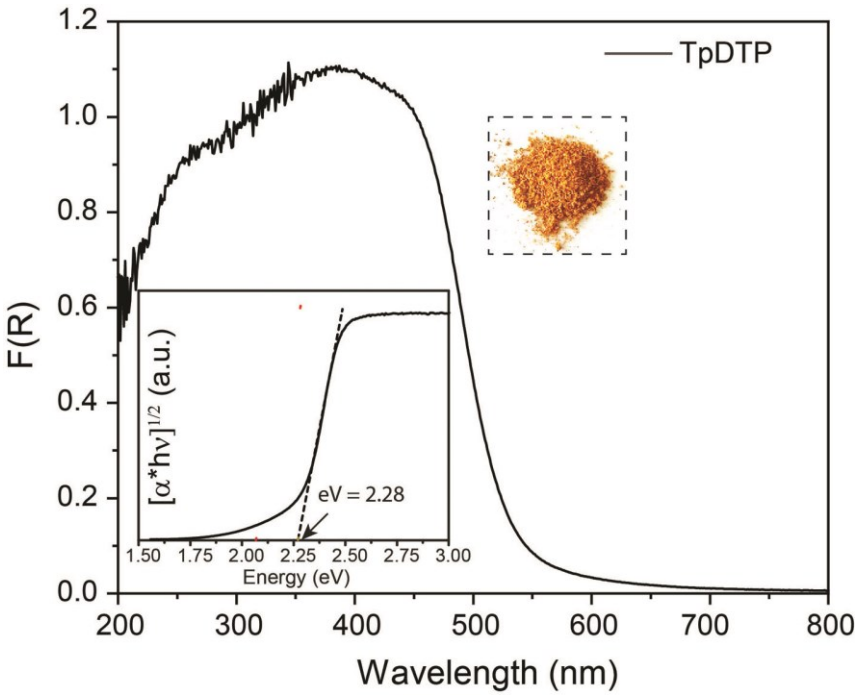

Figure B-18. UV–vis DRS spectra for TpDTP COF measured in the solid state, inset: plot indicates the Kubelka-Munk function for a direct gap, from which an optical band gap size of 2.28 eV is extracted, and the photograph of TpDTP COF powder placed within a dashed box.

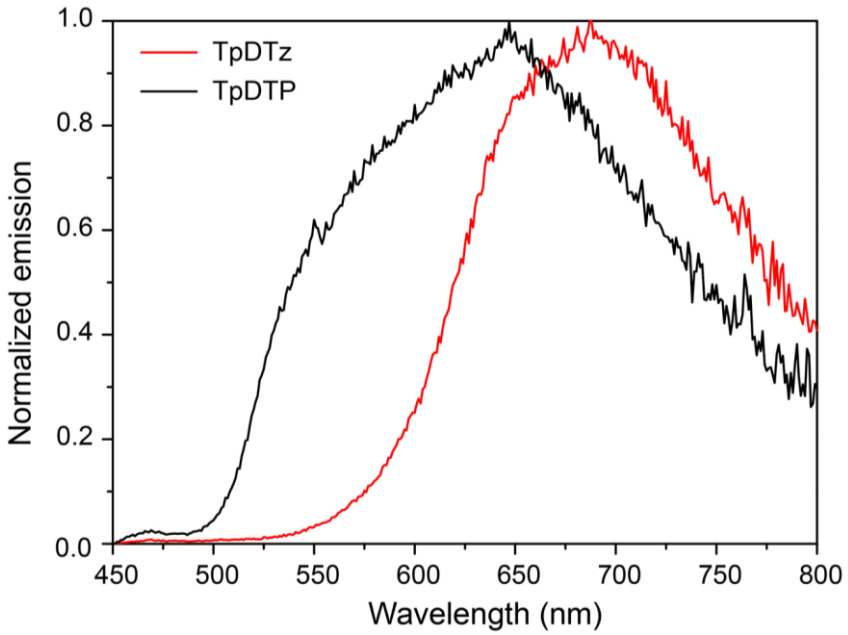

Figure B-19. Comparison of the emission spectra for TpDTz and TpDTP COF measured in the solid state.

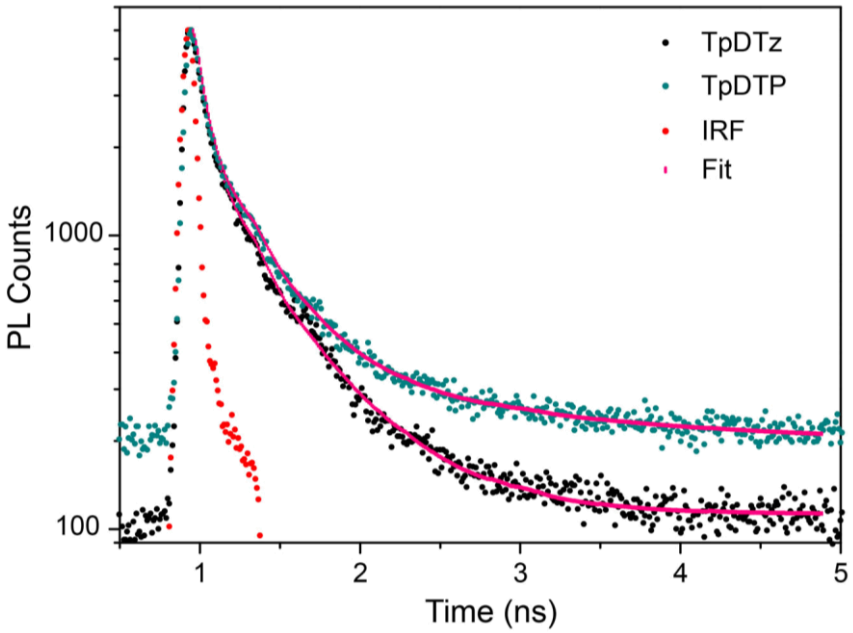

Figure B-20. Time-correlated single-photon counting (TCSPC) experiments for TpDTz and TpDTP COF in the solid state. Samples were excited with a λ_{exc} = 380 nm laser and emission was measured at λ_{em} = 650 nm. The fluorescence decays can be fitted with triexponential functions and the amplitude weighted average lifetime for TpDTz COF is 94 ps [τ = 33 ps (44.3%), 79 ps (46.9%), 0.49 ns (8.6%)] and TpDTP COF is 115 ps [τ = 55 ps (87.4%), 0.34 ns (13%), 1.59 ns (1.4%)] respectively.

B.8 Cyclic Voltammetry

Aqueous cyclic voltammetry experiments were conducted on an Ametek VersaStat MC (VersaStat 3 Model 500) potentiostat with an FTO working, a platinum wire counter and a saturated calomel (SCE) reference electrode in double-deionized water (ultra-pure type 1, 18 MΩ) under argon atmosphere. In the standard procedure 30 µmol of $Ni(OAc)_2 \cdot 4H_2O$ and 60 µmol of 2-Mercaptoethanol (ME) were dissolved in 20 mL of double-deionized water. Prior to the measurement the solution was degassed by purging with argon for 10 min. Reduction onset potentials (E_{onset}) were extracted from the x-intercept of the linear fits in the voltammograms (Figure B-21). Under our conditions we found the reduction onset potential of the NiME complex to be -0.75 V vs. SCE, which is comparable to the value reported by Zhang *et. al.* with a glassy carbon working electrode and in aqueous solution.[20]

Non-aqueous cyclic voltammetry experiments were conducted on the same potentiostat with a modified FTO working, a platinum wire counter and a platinum wire pseudo-reference electrode, referenced to SCE using Ferrocene (Fc) as an internal standard ($E_{1/2,Fc}$ = 0.40 V vs. SCE).[21] Modified FTO electrodes were prepared similarly to recent procedures by L.-Z. Peng *et. al*. and P.-F. Wei *et. al.*[22,23] The corresponding **TpDTz** COF (2 mg) was suspended in a mixture of deionized water (50 µL), isopropanol (30 µL) and 5% Nafion-117 solution (20 µL) by sonication for 60 min. 10 µL of this suspension were drop casted on plasma-cleaned FTO electrodes (5 × 5 mm) and dried overnight on a heating plate at 60 °C (air). After purging the electrochemical cell with argon for 10 min, a fresh modified electrode was submerged in the electrolyte solution for each measurement. Reduction onset potentials (E_{onset}) were extracted from the x-intercept of the linear fits in the voltammograms (Figure B-22). Together with the optical bandgap ($E_{g,opt}$) this value was used to estimate valence band (VB) and conduction band (CB) edges vs. the vacuum level[24-26] according to the following equations:

$$E_{CB} = -(E_{onset\ vs.\ SCE} - E_{1/2,Fc} + 5.1)\ eV$$

$$E_{VB} = E_{CB} - E_{g,opt}$$

Energy levels of the material vs. vacuum level were calculated as E_{CB} = -3.46 eV and E_{VB} = -5.53 eV and are comparable to values reported for polymers comprising thiazolo[5,4-*d*]thiazole (TzTz) units.[27]

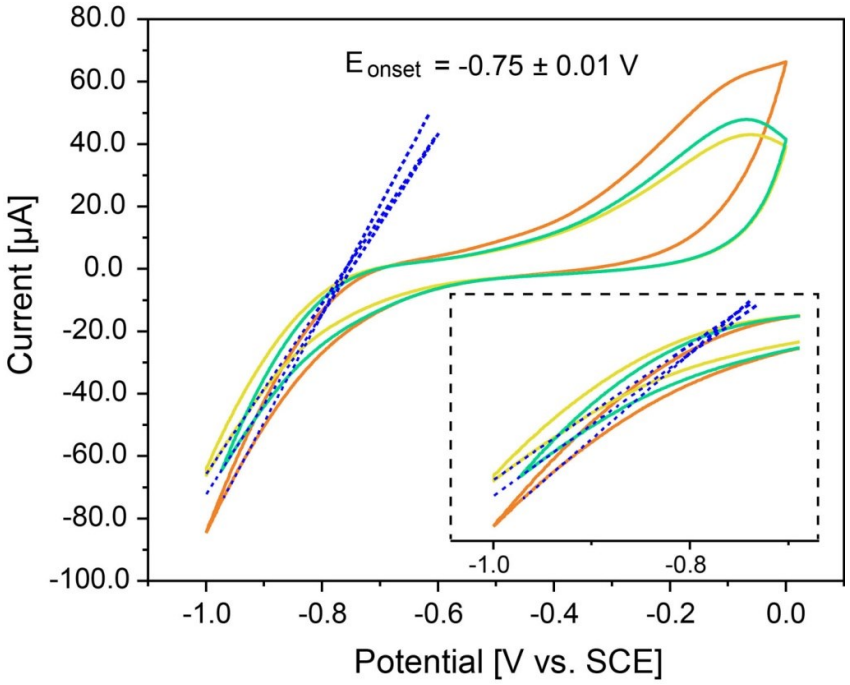

Figure B-21. Cyclic voltammograms of NiME complex with FTO working electrodes in degassed deionized water at a scan rate of 100 mV/s. The different colors refer to three successive measurements (orange to green). Between each measurement the FTO working electrode was polished.

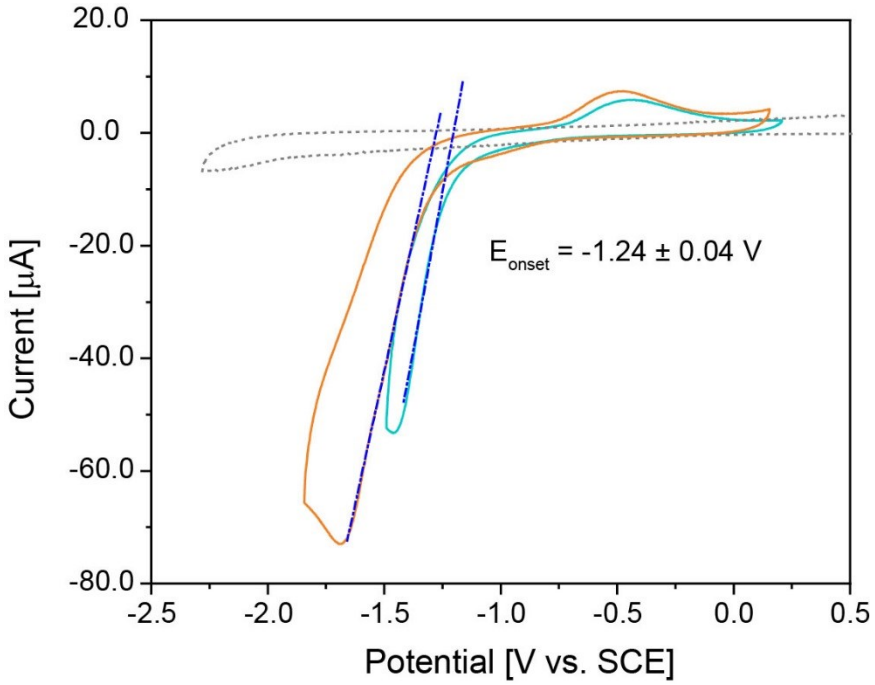

Figure B-22. Cyclic voltammogram of TpDTz COF-modified FTO working electrodes in 0.1M NBu4PF6 in anhydrous acetonitrile at a scan rate of 100 mV/s. (Grey: background without COF).

B.9 Details of photocatalysis experiments and optimizations

Experimental set-up: The photocatalytic activity of each system was measured in a novel continuous flow cell configuration of a volume of 350 mL (Figure B-22). Its main components are a jacketed glass reactor with three gas tight metal-glass KF flange ports (front: gas in, right: pressure control, and left: continuous GC injection), a top quartz-glass flanged window; and peripheral controllers and gauges to ensure that the reactor's pressure, temperature and inflow were constant during the illumination time. In addition to this, the optical design of the cell from previous publications[17] of our group was preserved in order to have a clear light pathway, ensuring a homogeneous spot at the liquid-gas interface (around 3.6 cm^2) with a total light intensity of 100 mW/cm^2 (Thorlabs Thermo power sensor) with an AM 1.5 filter installed. The light source used was a Xe lamp (Newport, 300 W) equipped with a water filter and a dichroic mirror.

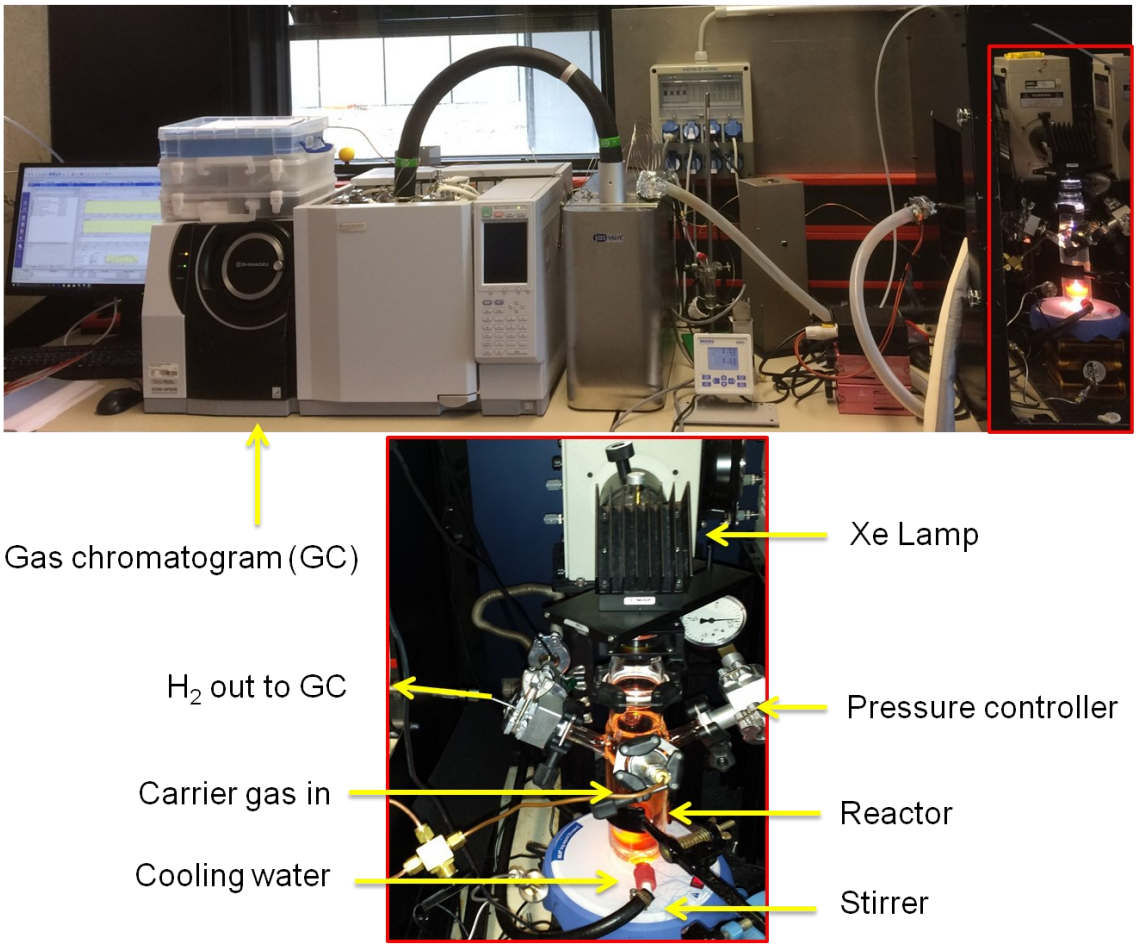

Figure B-23. Photograph of the designed photocatalytic continuous flow reactor assembly.

Reactor media preparation and control: In a standard experiment the reactor was loaded with a suspension of 5 mg of COF, *in situ* formed co-catalyst [1.4 µL of ME and 0.5 mg of $Ni(OAc)_2.4H_2O$], on 10 mL of DI water and sacrificial solution (10% v/v, TEOA) [Note: The pH of the solution was adjusted to 8.5 using HCl for all the photocatalysis experiments explained hereafter unless otherwise specified]. The initial purge of the system was 6 cycles of vacuuming and backfilling with carrier gas (He 6.0 purity) the reactor hold-up, with a range of pressure for such cycles of 100 mbar to 1100 mbar, which should theoretically dilute the initial O_2 and N_2 atmospheric concentration in the headspace down to 1-10 ppm levels. Once the media was initially purged, a backpressure controller (Brooks SLA5820 + 0251 PLC-Power supply) was turned on to keep the static pressure gauge of the headspace with a set point of 0.5 bar overpressure, the total mass inflow of He 6.0 was set to 30 $Ncm^3\ min^{-1}$ (Cellkraft P-2 series), and the water jacket temperature was set to 25 °C using a thermostat (LAUDA ECO RE 415 S). By this time also, the PLC of the heating tape used to control the transfer line temperature to the GC auto sampler was set to 70 °C (XtremeFLEX® BS0 + SDCEJD PLC).

Hydrogen rate determination in continuous flow: Once the reactor pressure, inflow, reactor temperature, and transfer line set points are stable (after approximately 1 min), the GC auto sampler valve is rotated and changed to continuous flushing of two duplicate sampling loops of 250 µL (Shimadzu-JAS Ventilbox). After 5 min flushing the loops, the gas sample at the loops is equivalent to the one in the reactor, time by which a first zero Hydrogen point is analyzed and the lamp lid is uncovered simultaneously. Under this steady illumination and media conditions, the auto sampler box rotates two other Valco-valves to inject the sampling loops content to the GC columns once every hour. The auto sampler keeps the loops and transfer lines at 70 °C to avoid influence of moisture in calibration, and the valve actuators are Helium-housed to prevent O_2 and N_2 leakages. The GC oven contains a duplicated circuit with MS-5a sieve columns with a Barrier Discharge Ionization (BID) and a mass spectrometer (MS) attached to each line (Shimadzu GCMSBID QP-2020). Under this scheme, where total mass in the reactor reaches a steady balance through the main mass and pressure controllers, the balances in the well-mixed portion of the gas system are the following:

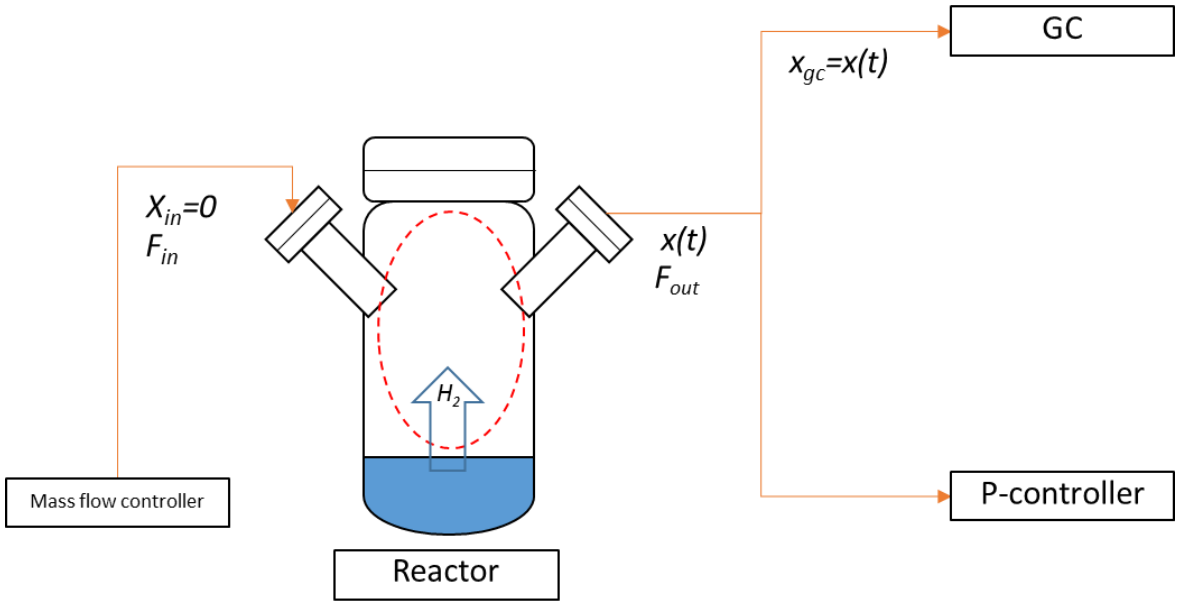

Figure B-24. Schematic diagram of the designed continuous flow photocatalytic reactor system.

$$F_{out} = R_{H_2} + F_{in} \qquad \text{Equation B-1}$$

$$N_t \frac{dx}{dt} = R_{H_2} - \left(F_{in} + R_{H_2}\right)x \qquad \text{Equation B-2}$$

Where:

F_{in} : Controlled molar Helium (99.9999% purity) in flow in [mol/h]

R_{H2} : Total Hydrogen production rate in [mol/h]

F_{out} : Controlled total molar out flow in [mol/h]

N_t : Total mol in the headspace at time t=0

x : Hydrogen molar fraction at the outlet, measured after a splitter with GCMSBID

Simply, after some reactor retention times, this is when the total mol (N_T) of the headspace have been flushed several times, the system will be stationary and the experimental Hydrogen elution rate can be calculated in steady state as:

$$R_{H_2} = \frac{F_{in} \times x_{H_2 ppm} \times 10^{-6}}{\left(1 - x_{H_2 ppm} \times 10^{-6}\right)} \qquad \text{Equation B-3}$$

Ideal reactor headspace mixing time-scale: The experimental elution Hydrogen rate (R_{H2}) data can be considered a pure reaction rate, qualitatively, after the first sampling point at t=1 [hour]. However, drastic changes or rapid time-scales observed from its trend could lead to a significant quantitative correction, due to the lack of steady state and loss of information while the hydrogen balance in the reactor is still at transient state during approximately the first one or two illumination hours. To quantify the time-scale of the ideal mixing process, the hydraulic retention time of the headspace expression was used (t_r). However, the total mol in the headspace using the ideal gas law is calculated using a reactor real "mixing volume" (V_{mix}), which is a volume estimation that accounts for physical mixing effects (forced convection and diffusion to dead volumes of the system), which in our case was measured experimentally under different flow conditions (from 15 to 100 [$Ncm^3\ min^{-1}$]) during elution curve experiments. The deviations from the ideal-mixing assumptions are embedded in this number, and its average is 430 [ml]. The difference with the geometrical volume of 350 mL is in accordance with dead volumes and diffusion lengths of ~1 [cm]. The expressions to quantify the transient-state are depicted below in Equation B-4 and Equation B-5.

$$t_r = \frac{N_t}{F_{in}} \qquad \text{Equation B-4}$$

$$N_t = V_{mix}\left(\frac{P_R}{R \times T_R}\right) \qquad \text{Equation B-5}$$

Where,

V_{mix} : Experimental reactor headspace mixing volume

P_r : Controlled reactor pressure (1.5 [bar] absolute)

T_r : Controlled reactor temperature (25 [°C])

R : Ideal gas law constant (8.314 [$Joule\ mol^{-1}\ K^{-1}$])

A more simplified relation for t_r can be obtained rearranging those terms, which is an inverse proportion with a factor of 20 [min] at 30 [$Ncm^3\ min^{-1}$]. Then, in regular experiments at 30 [$Ncm^3\ min^{-1}$], after 1 hour at least three retention times have passed

thus from the first measured point the H_2 balance can be considered mathematically stationary like in Equation B-3.

Reaction modeling and rate limiting steps (RLS): Looking at the experimental photocatalytic HER rates, we identified an overall reaction trend of a unique asymptotic activation triggered by light, seemingly due to a light-enhanced catalytically active nickel cluster species [R] (also refers to the resting state of the catalyst), the absence of hydrogen evolution in the dark, and a pseudo linear activity loss at longer time-scales. To find its more precise functionality that is realistic and simple enough to explain the observed trends, we theorized a homogeneous catalytic system similar to other nickel catalysts in the literature,[S20] but using COFs as heterogeneous photosensitizers (PS). Resembling a dye/molecular-catalyst photocatalytic tandem, such heterogeneous part is a fast recombination limited regime where the excited states are in a fast light absorption/charge-recombination equilibrium (COF^*), and a subsequent quenching step (k_q) forms a reduced state ($COF^{\bullet-}$) of the PS, which then triggers a relatively slow electron transfer step to the resting state of the catalyst to form the intermediate active species [I]; it must be noticed that this would be equally valid if this fast cycle was modelled assuming oxidative quenching instead. Under these assumptions, the fraction of PS that is excited and reduced occurs in a k_q^{-1} characteristic time (fast), and the "bottleneck" of the heterogeneous cycle will be the electron transfer step to the species [R]. In this way, the heterogeneous cycle will be rapidly pseudo-stationary and the controlling variables of this overall reaction will be the evolution of [R] and [I] in time. On the other hand, the nickel catalyst formation, activation, and deactivation are assumed as a fully homogeneous process that starts with a rapid formation of a first coordinated complex [Ni--L] (K_{eq}), and a transport-limited (k_{T1}, k_T^{-1}) formation of a fully functional nickel cluster [R]. This last assumption of transport limitation in the formation of [R] is not arbitrary since it qualitatively explains why the catalyst activation curve is unambiguously triggered by light, and why it is not changed significantly by stirring the media in dark longer before illumination. It also explains why the *on/off* cycles after illumination do not show an evident activation time, because the hold-up of [R] and [I] achieved due to a light-shifted equilibrium after the first illumination cycle is "locked' in the absence of light. Although a slow HER step (k_{HER}) could also partially provide explanation for this behavior, it is

immediately ruled out because in this context of slow activation, a slow k_{HER} constant would involve a symmetric relaxation of the system in the off cycle and thus dark hydrogen production.

Having drafted the minimum steps to qualitatively capture the complexity of our system, the next step to get a quantitative model is to assume that reaction occurs homogeneously in our liquid medium and following mass action law in all the steps, similar to a microkinetics approach, with the only exception of light excitation ($h\nu$) that is a zeroth order step, and the activation step (k_a) that is an apparent only first order process to [R]. The dynamic evolution of the species' concentrations in the liquid system in time is mathematically depicted below:

$$\frac{d[R]}{dt} = k'_T \times$$

$$\frac{d[I]}{dt} = k_a \times [R] - (k_{HER} + k_d) \times [I]$$

$$\frac{d[D]}{dt} = k_d \times [I]$$

$$k'_T = \frac{\left(\frac{1}{1 + 1/K_{eq}}\right)}{\left(\frac{1}{1 + 1/K_{eq}}\right) + 1} k_T$$

With

$$[R](t = 0) = 0$$
$$[I](t = 0) = 0$$
$$[D](t = 0) = 0$$

After re-scaling, the problem can be reduced to a non-dimensional linear non-homogeneous ODE system, popping out an inner solution where d[I]/dt is different from zero at early times, and an outer solution where [I] is stationary and [R] achieves its maximum value due to the shifted equilibrium under illumination. Finally, using a matched

asymptotic expansion perturbation approach a solution can be obtained (truncated up to the 2nd order term).

$$R_{H2} = [\varepsilon^3\beta\{1 - exp(-tk_d/\varepsilon^3\beta)\} + \varepsilon(\{1 - exp(-tk_d/\varepsilon)\} + \gamma\{\alpha(exp(-tk_d/\varepsilon) \times tk_d/\varepsilon - 1) + (\alpha - 1)exp(-tk_d/\varepsilon) - tk_d/\varepsilon + 1\})] \times \gamma \quad \text{Equation B-6}$$

Where:

ε : k_a/k_{HER} ratio (<1)

β : k_d/k_a ratio (<1)

α : $k'_T/k_{T\text{-}1}$ ratio (<1)

γ : $k'_T/(\varepsilon\ k_d)$ ratio (if transport limited <1, and <1/(1+ α))

$[Ni(OAc)_2]_0$: initial concentration of $Ni(OAc)_2$

V_L : Reactor liquid volume

Since the full solution contains at least five parameters to be fitted to the observed data simultaneously within the entire experimental time domain, a simpler composite solution was derived from Equation B-6 to fit more independently the three main trends observed experimentally (delay time, activation time, and deactivation time). The time-derivatives of the outer solution expressions in Equation B-6 are equivalent to the ones of Equation B-6 in the limit of an activation intermediate time t~(k_a^{-1}), and longer deactivation time t~(k'^{-1}_d).

$$R_{H2} = \begin{cases} R_{H2,max}\left(1 - exp\left(\frac{-t - t_0}{t'_a}\right)\right)\left(\frac{1}{1 + (t - t_0)/t'_d}\right), if\ t \geq t_0 \\ 0\ , if\ t < t_0 \end{cases} \quad \text{Equation B-7}$$

Where

$R_{H2,max}$: apparent total ([μmol h^{-1}]) or normalized ([μmol h^{-1} g^{-1}]) reaction kinetic constant (~$\boldsymbol{k_{HER}}$ k'_T k_d^{-1})

t_0 : apparent dark HER step delay time [h] ($\sim \boldsymbol{k}_{\mathbf{HER}}^{-1}$)

t'_a : apparent activation time constant [h] ($=k_a^{-1}$)

t'_d : apparent deactivation time constant [h] ($\sim k_T'^{2}\ k_d^{-1} k_a^{3} \boldsymbol{k}_{\mathbf{HER}}^{-2}$)

The rate expression of a fully activated catalyst during light *on/off* experiments and band-pass filter experiments was found to be a single step function, with a fixed reaction constant at time t=0 when the light is turned on. For dye experiments, the fitting was found to be also a step function but with an exponential decay with time-scale t_d.

Rate function trends fitting and mathematical refinement: Regardless of the analytical expression to describe the experimentally observed rate R_{H2}, the Equation B-2 and Equation B-6 were still solved simultaneously using a matched asymptotic perturbation approximation to fully subtract the transient state of the reactor on the experimental HER rate data, based on the non-dimensional re-scaling of such non-linear ordinary differential equation (ODE) system in three different time-scales. Such approach made corrections to the steady state assumption depicted in Equation B-3 only in the order of 3 small parameters t_r/t'_a (~10%), $R_{H2,max}/F_{in}$ (~0.01%), and t'_d/t'_a (~5%). Considering the expansion up to the 2nd terms, the error of the approximation was less than 1% compared to the numerical solution. Then, the parameters of the pure rate expression in Equation B-6 t_0, t_a, t_d, and $R_{H2,max}$ were fitted using Matlab *fmin* minimizing the total squared error.

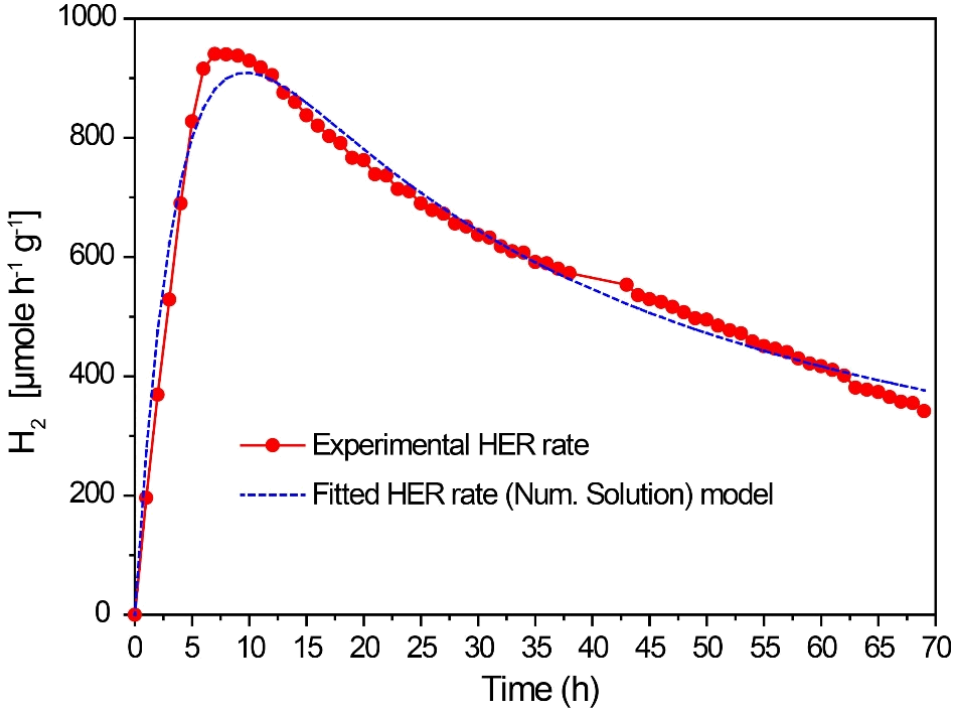

Figure B-25. Correlation of the experimental and mathematical function fitting model (numerical solution) of sustained photocatalytic H_2 evolution rate from water using **TpDTz** COF-NiME co-catalyst over 70 h under AM 1.5 light irradiation [5 mg of **TpDTz** COF in 10 ml of water with TEoA (10 vol%, pH=8.5), 0.5 mg of $Ni(OAc)_2.4H_2O$ and 1.4 µL of ME].

A comparative table with the model fit of experimental data is presented in Table B-2. The standard error (SE non-linear) of these coarse-grain fits are below 5%, proving a high degree of correlation between these simplifications and the experimental data. The other previously described more qualitative behavior can also be explained using aforesaid simplified models, including the unique catalyst activation and the *on/off* cycle trends observed in our COF catalytic system, the difference in performance of the same NiME co-catalyst by changing the photosensitizer (PS) of the system, and the absence of H_2 evolution in the dark. The model in Equation B-6 also predicts the Kinetic-Isotope-Effect (KIE) while using D_2O instead of water under identical reaction conditions. In Figure 5b and derived from Equation B-6, it is expected that the increase of the mass of the protons will decrease the first-order reaction constant k_{HER}, producing a larger initial time delay t'_0 for the HER dark cycle transient state, a larger deactivation time t'_d, a smaller reaction constant $R_{H2,max}$, but preserving roughly the catalyst activation time constant t'_a, which we observe in both experiments' fitted parameters. From this last experiment, we can give

additional support to our first claim that k_{HER} is not the liming step of the catalytic cycle, and that the electron transfer step is overall controlling the activation of the catalyst when using our COF as an heterogeneous PS.

Table B-2. Mathematical HER rate function fitted parameters for different photocatalytic experiments.

Experiments	t'_0 [h]	t'_a [h]	t'_d [h]	$R_{H2,max}$ [μmol h^{-1} g^{-1}]	SE (%)
TpDTz-NiME-H_2O	0	4.2	24.6	1432	3.3
TpDTz-NiME-D_2O	2.3	3.8	58.7	924	4.7
EB-NiME-H_2O	--	--	0.76	106965	4.7
TpDTz-NiME- H_2O (on/off)	0	4.0	128.3	664	4.0
TpDTz-NiME-H_2O-400	--	--	--	11.9	5.4
TpDTz-NiME-H_2O-500	--	--	--	50.7	1.2
TpDTz-NiME-H_2O-550	--	--	--	41.1	1.0
TpDTz-NiME-H_2O-600	--	--	--	6.7	4.6

Turnover number (TON) and turnover frequency (TOF) calculation: The amount of H_2 produced in a certain interval of time can be calculated as the integral of the rate function in time within the interval. Said calculation can be done by integrating numerically the experimental rate points, or mathematically using the fitted Equation B-6. The minimum average TON number until full catalyst depletion ($t \rightarrow \infty$) can be calculated as the total produced molecules of H_2 per the maximum number of active centers in the system (projected TON). Assuming that eventually all the (Ni) species become active, the expression for the TON number is Equation B-7. Additionally, the average turnover frequency (TOF) of the system at a certain time can be obtained directly from the HER rate experimental data using the same normalizing factor [$Ni(OAc)_2.4H_2O$] in Equation B-7.

$$\boldsymbol{TON} = \int_{t=0}^{\infty} R(t)dt \Big/ \mathrm{Ni(OAC)_2.4H_2O} \qquad \text{Equation B-8}$$

Volatile (TEoA and ME) losses in continuous flow: Due to continuous flow purging of the reactor headspace, it is necessary to have an estimation of the maximum loss of volatiles in the system, whether it is due to vaporization at the liquid-gas interface or sacrificial agent depletion. This calculation fully rules out potential influences of the continuous flow sampling or long illumination in the observed kinetic trend, particularly in long experiments when deactivation is visible. Said calculation is a numerical integration of the volatiles (ME or TEoA) elution plus SED depletion rates (TEoA), assuming that there are no mass transfer limitations, and the operational controlled in-flow is completely saturated at the vapour pressure of the solution interface. Such calculation gives a maximum limit for total depletion of both chemicals, and after 72 hours is less than 1% of the initial loading for TEoA (considering hole-scavenging rate) and 6% for ME. Furthermore, these amounts were used to calculate make-up experiments where such loss was replenished (O_2 degassed) back to the reactor after long experiments. After injection of such make-up amounts, the kinetic trends were not significantly affected, confirming that deactivation of the system is due to different means, therefore more related to the COF-co-catalyst interaction.

Apparent quantum yield (AQY) determination and band-pass filter experiments: The AQY of each experiment is calculated as the total number of monoatomic hydrogen production divided by the number of incident photon flux. The photon flux was calculated from relations between light intensity, illumination area, and previously characterized lamp spectra. For BP (± 20 [nm]) filter experiments with central wavelength (WL) of 400, 500, 550, 600, this relation was also used and the light intensity at the interface for each band was measured as depicted in our previous publication.[17] For experiments with activation and deactivation time-scales, the AQY is a function in time and the asymptotic maximum H_2 rate was considered.

$$AQY(\%) = 100 \times \left(\frac{R_{H2}}{\phi}\right)$$ Equation B-9

$$\phi = I \times \pi r^2 \times \left(\frac{\int_{\lambda_1}^{\lambda_2} f(\lambda')d\lambda'}{I_0} \right)$$

Equation B-10

Where:

ϕ : photon flux at experimental conditions

f : previously measured photon distribution spectral function at intensity I_0 (BP or AM 1.5)

λ_1,λ_2 : wavelength range in [nm] (BP or AM 1.5)

I,I_0 : experimental and reference light intensity in [mW cm^{-2}]

r : radius of interface illumination area (1.08 [cm])

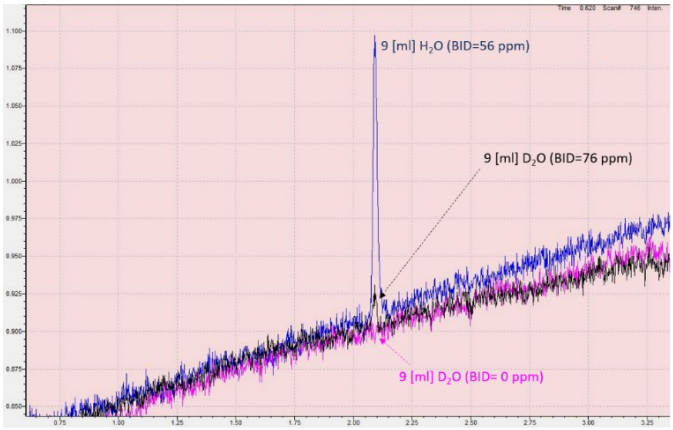

Figure B-26. m/z = 2 TIC at H_2/D_2 GC retention time (2.07 [min]), of H_2O (blue) and D_2O (black) photocatalytic experiments at the HER rate maximum point (in violet zero hydrogen baseline). In the legends the parallel total BID quantified signal for H_2/D_2 is shown.

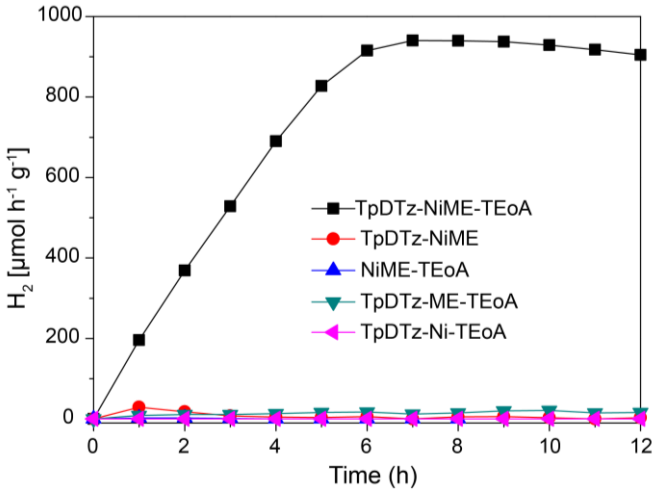

Figure B-27. Control experiments of photocatalytic H_2 evolution from water using **TpDTz** COF under AM 1.5 light irradiation [black square: 5 mg of **TpDTz** COF in total 10 ml of aqueous solution containing water with TEoA (10 vol.%, pH= 8.5), 0.5 mg of $Ni(OAc)_2.4H_2O$ and 1.4 µL of ME; red circle: 5 mg of **TpDTz** COF in total 10 ml of water (without TEoA), 0.5 mg of $Ni(OAc)_2.4H_2O$ and 1.4 µL of ME; blue triangle: 10 ml of aqueous solution containing water with TEoA (10 vol.%, pH= 8.5), 0.5 mg of $Ni(OAc)_2.4H_2O$, and 1.4 µL of ME; green triangle: 5 mg of **TpDTz** COF in total 10 ml of aqueous solution containing water with TEoA (pH= 8.5) and 1.4 µL of ME; pink triangle: 5 mg of **TpDTz** COF in total 10 ml of aqueous solution containing water with TEoA (10 vol.%, pH= 8.5), and 0.5 mg of $Ni(OAc)_2.4H_2O$].

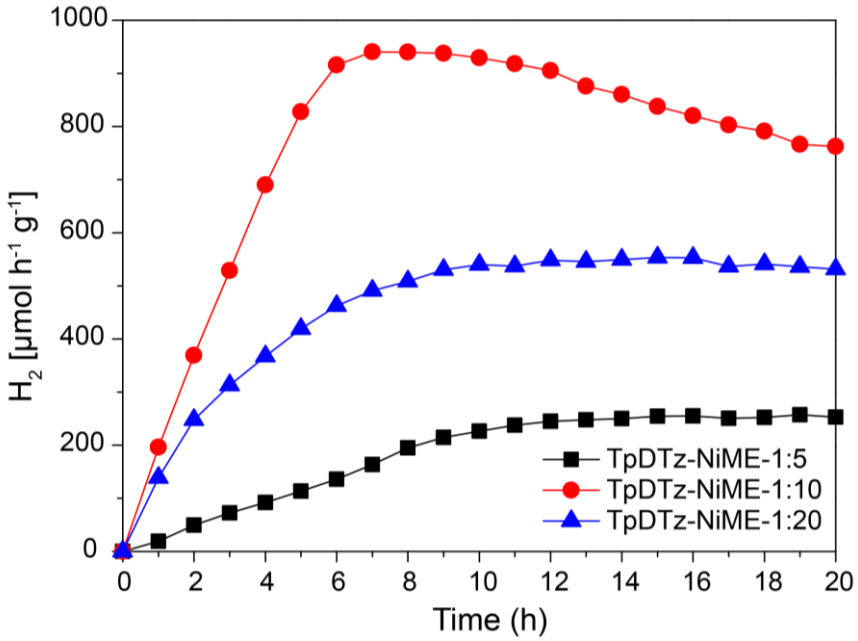

Figure B-28. Photocatalytic H_2 evolution from water using **TpDTz** COF under AM 1.5 light irradiation [5 mg of **TpDTz** COF in 10 ml of water with TEoA (10 vol.%, pH=8.5), the numbers 1: 5, 1: 10 and 1: 20 refers to the equivalent ratio of $Ni(OAc)_2.4H_2O$, 0.5 mg (2 µmol) and ME [0.7 µL (10 µmol), 1.4 µL (20 µmol) and 2.8 µL (40 µmol) respectively].

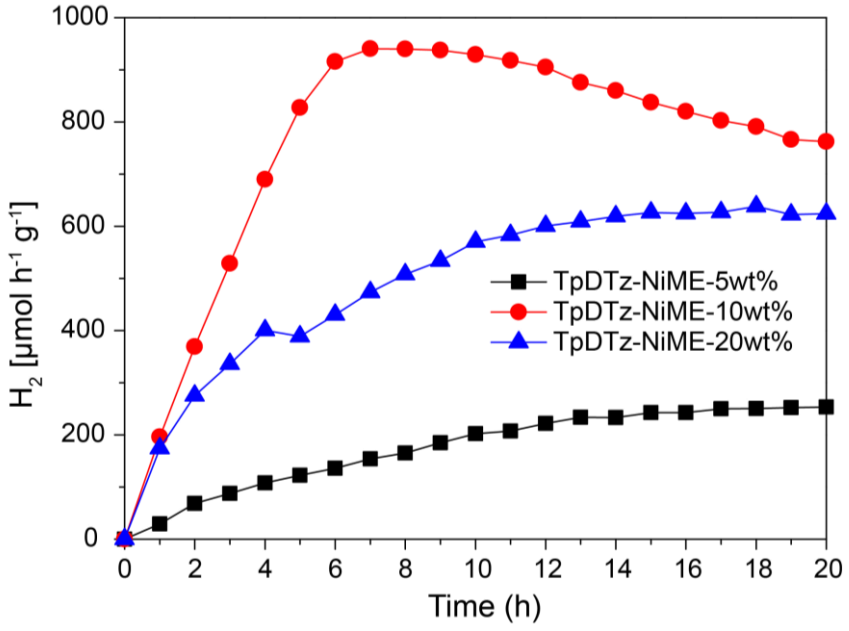

Figure B-29. Photocatalytic H_2 evolution from water using **TpDTz** COF under AM 1.5 light irradiation [5 mg of **TpDTz** COF in 10 ml of water with TEoA (10 vol.%, pH=8.5), with different wt.% of NiME co-catalyst with respect to the **TpDTz** COF].

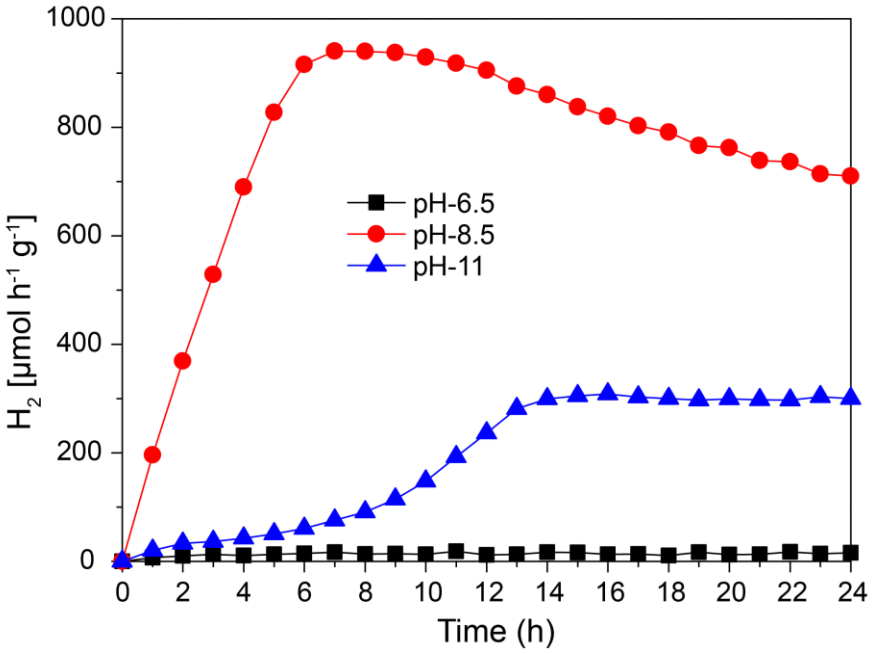

Figure B-30. Photocatalytic H_2 evolution from water using **TpDTz** COF under AM 1.5 light irradiation [5 mg of **TpDTz** COF in 10 ml of water with TEoA (10 vol.%, pH= 6.5, 8.5, and 11, adjusted using HCl), 0.5 mg of $Ni(OAc)_2.4H_2O$ and 1.4 µL of ME].

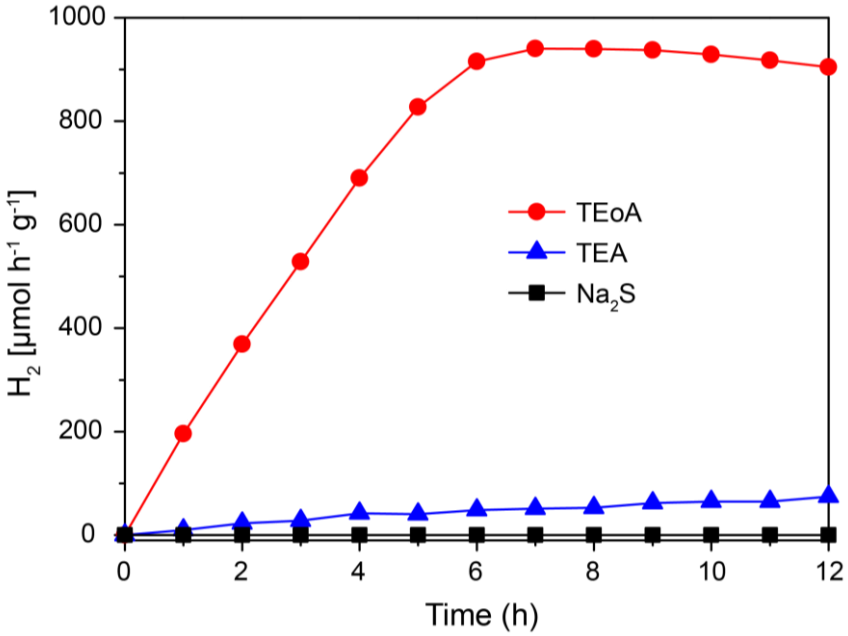

Figure B-31. Photocatalytic H_2 evolution from water using **TpDTz** COF under AM 1.5 light irradiation [5 mg of **TpDTz** COF in total 10 ml of aqueous solution containing water with different sacrificial electron donors (10 vol%) such as TEoA, TEA and Na_2S, 0.5 mg of $Ni(OAc)_2.4H_2O$ and 1.4 µL of ME]. Solution pH= 8.5 was adjusted only for TEoA and TEA containing systems.

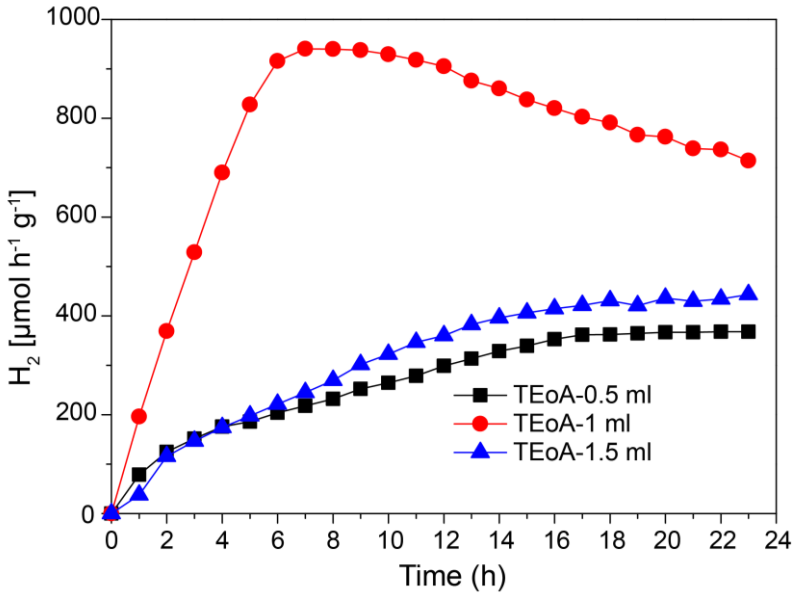

Figure B-32. Photocatalytic H_2 evolution from water using **TpDTz** COF under AM 1.5 light irradiation [5 mg of **TpDTz** COF in total 10 ml of aqueous solution containing water with different amount of TEoA (pH= 8.5), 0.5 mg of $Ni(OAc)_2.4H_2O$ and 1.4 µL of ME].

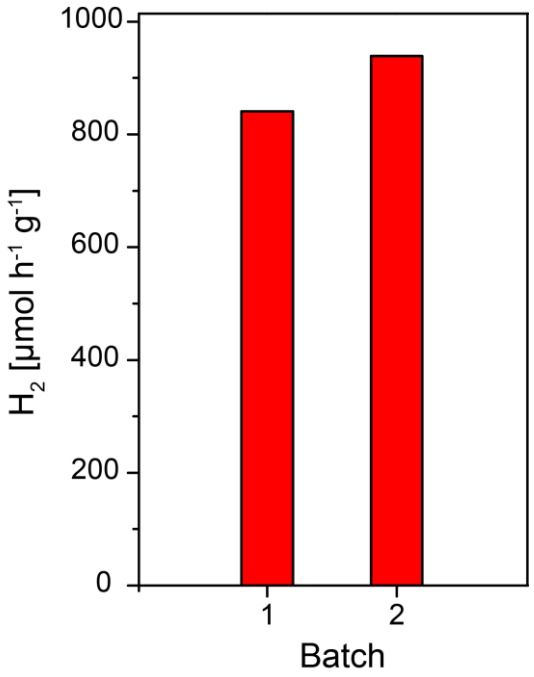

Figure B-33. H_2 evolution experiments for two different batches for **TpDTz** COF showing batch-to-batch reproducibility of the measurement [5 mg of **TpDTz** COF in total 10 ml of aqueous solution containing water with TEoA (10 vol.%, pH= 8.5), 0.5 mg of $Ni(OAc)_2.4H_2O$ and 1.4 µL of ME].

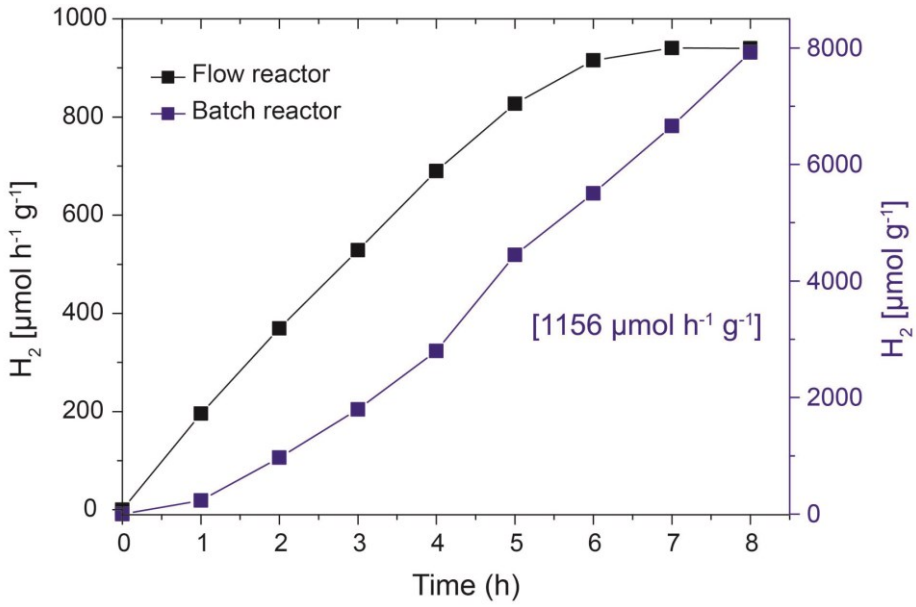

Figure B-34. A comparison of the photocatalytic H_2 evolution from water using **TpDTz** COF and NiME co-catalyst measured in both batch reactor and continuous flow reactor systems using AM 1.5 light irradiation [5 mg of **TpDTz** COF in 10 ml of water with TEoA (10 vol.%, pH=8.5), 0.5 mg of $Ni(OAc)_2.4H_2O$ and 1.4 μL of ME].

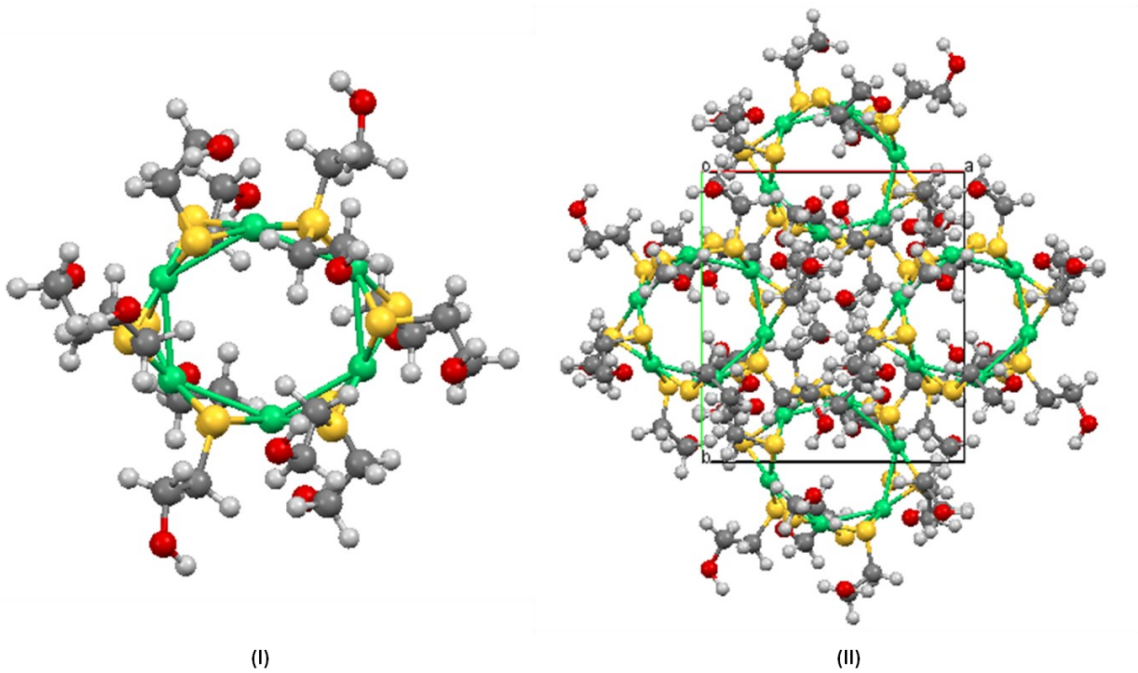

Figure B-35. The optimized molecular cyclic hexameric structure of NiME complex (I) and packing arrangement (II) generated using BIOVIA Materials Studio 2017. Note that the single crystal structure of cyclic hexameric NiME and analogous $Ni_6(SCH_2CH_2Ph)$ complex has been reported by other groups.[28,29]

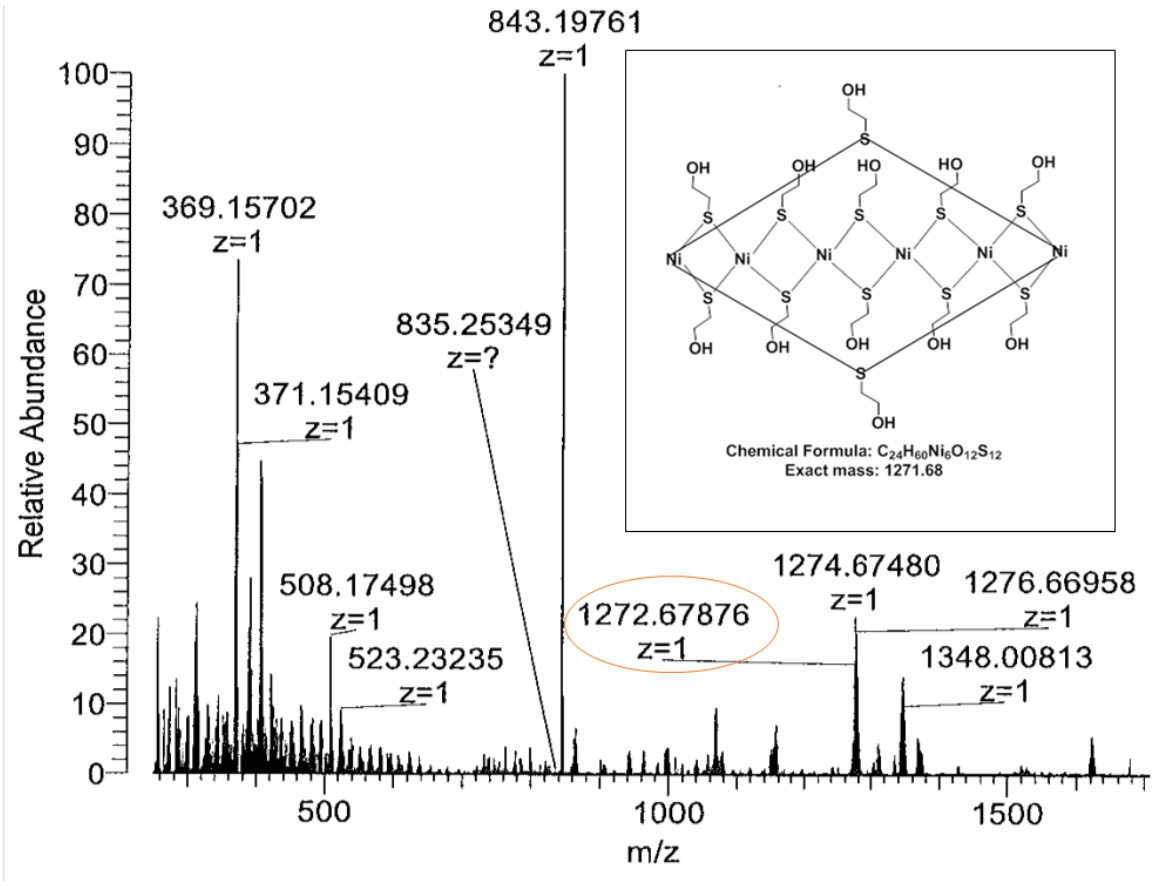

Figure B-36. ESI$^+$ mass spectrum of in situ synthesized NiME complex in water (Exact Mass: 1271.68, the circled peak corresponds to the complex mass).

Table B-3. A comparison of H_2 evolution activity of different COF-based photocatalytic systems reported in the literature.

COF	HEC	Solvent	SED	Illumination	Activity (μmol h^{-1} g^{-1})	AQE (%)	Ref
TpDTz	NiME*	Water	TEoA	AM 1.5	941	0.2 at 400 nm	#
sp^2c-COF_{ERDN}	Pt	Water	TEoA	> 420 nm	2120	0.48 at 495 nm	30
sp^2c-COF	Pt	Water	TEoA	> 420 nm	1360	-	30
TP-BDDA	Pt	Water	TEoA	> 395 nm	324	1.8 at 520 nm	31
FS-COF+WS5F	Pt	Water	Sodium ascorbate	> 420 nm	16300	2.2 at 600 nm	32
FS-COF	Pt	Water	Sodium ascorbate	> 420 nm	10100	3.2 at 420 nm	32
A-TEBPY-COF	Pt	PBS Buffer at pH 7	TEoA	AM 1.5	98	-	33
N_2-COF	Co-1*	4:1 ACN/Water	TEoA	AM 1.5	782	0.16 at 400 nm	34
N_2-COF	Co-2*	4:1 ACN/Water	TEoA	AM 1.5	414	-	34
COF-42	Co-1*	4:1 ACN/Water	TEoA	AM 1.5	233	-	34
PTP-COF	Pt	PBS Buffer at pH 7	TEoA	AM 1.5	83.8	-	35, 36
N_3-COF	Pt	PBS Buffer at pH 7	TEoA	> 420 nm	1703	0.44 at 450 nm	17
N_2-COF	Pt	PBS Buffer at pH 7	TEoA	> 420 nm	438	0.19 at 450 nm	17
N_1-COF	Pt	PBS Buffer at pH 7	TEoA	> 420 nm	90	0.077 at 450 nm	17
N_0-COF	Pt	PBS Buffer at pH 7	TEoA	> 420 nm	23	0.001 at 450 nm	17

TFPT-COF	Pt	Water	TEoA	> 420 nm	1970	2.2-3.9 at 500 nm	36

HEC: Hydrogen evolution catalyst; SED: Sacrificial electron donor; AQE: Apparent quantum efficiency. *(Molecular co-catalyst) and # (This work). The contents in the table has been arranged in a reverse chronological order according to the year of discovery of the photocatalytic system.

B.10 Post-photocatalysis characterizations

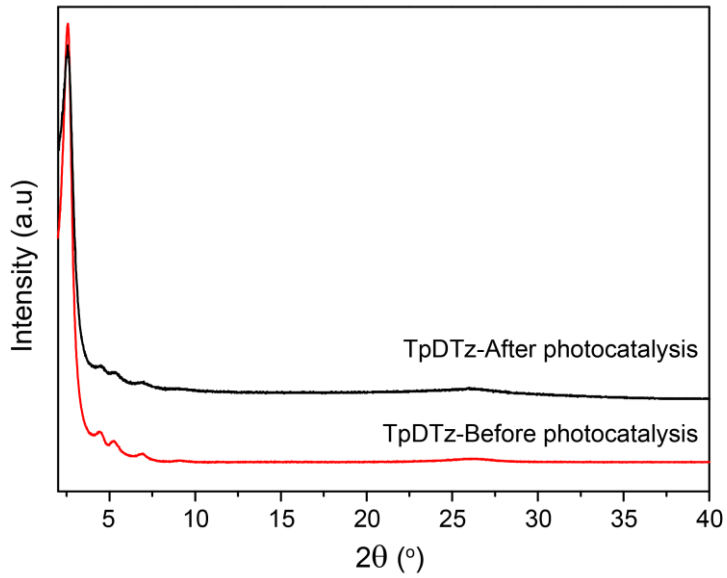

Figure B-37. Experimental PXRD (red) pattern of the pristine **TpDTz** COF showing the good match with the PXRD pattern of the recovered **TpDTz** COF after the long term (72 h) photocatalysis experiment, indicating only little loss of crystallinity.

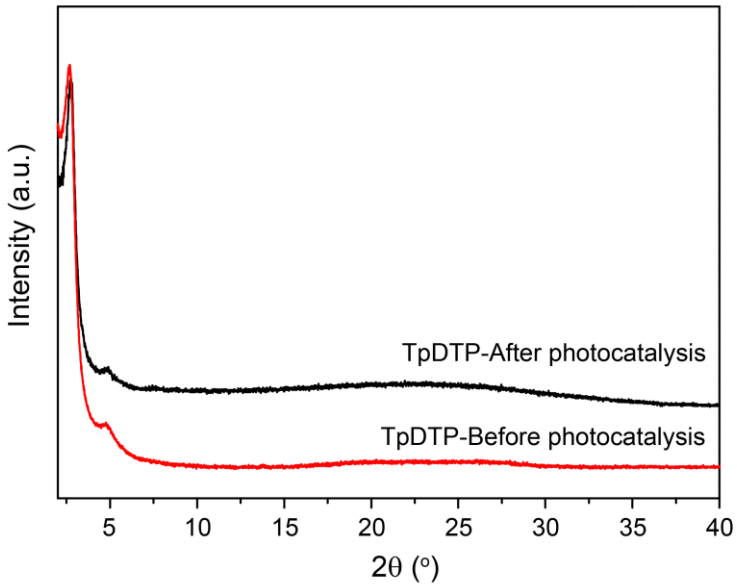

Figure B-38. Experimental PXRD (red) pattern of the pristine **TpDTP** COF showing the match with the PXRD pattern of the recovered **TpDTP** COF after the photocatalysis experiment, indicating only minor loss of crystallinity.

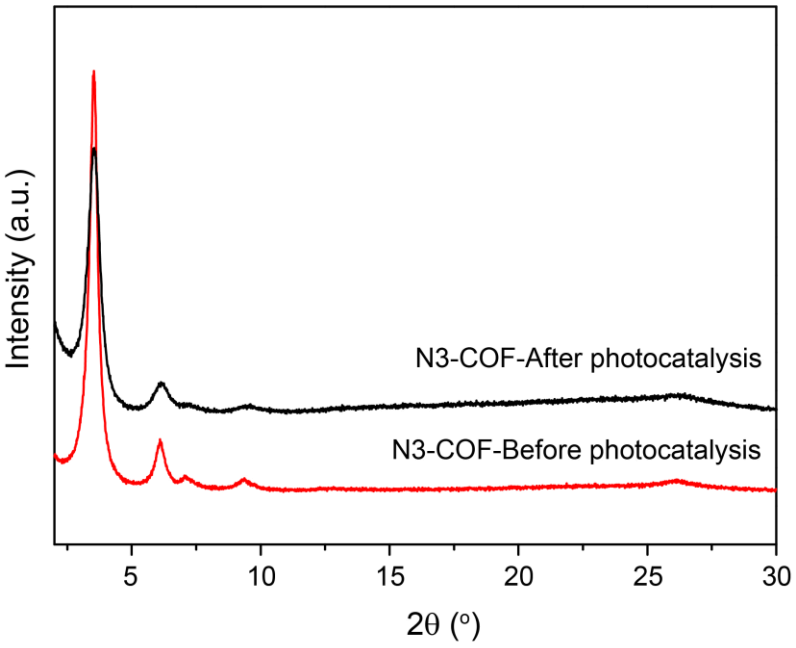

Figure B-39. Experimental PXRD (red) pattern of the pristine **N3-COF** showing the match with the PXRD pattern of the recovered **N3-COF** after the photocatalysis experiment, indicating only minor loss of crystallinity.

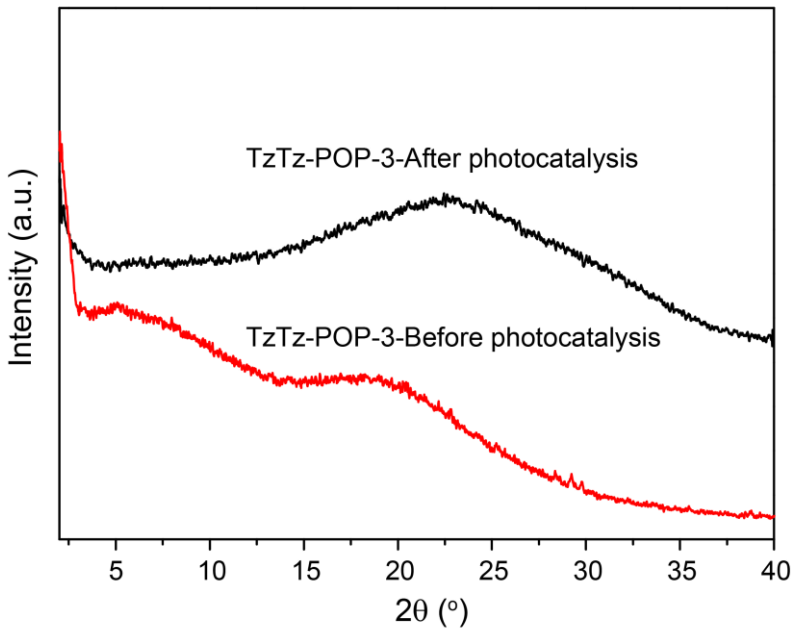

Figure B-40. Experimental PXRD (red) pattern of the pristine TzTz-POP-3 and the PXRD pattern of the recovered TzTz-POP-3 after the photocatalysis experiment.

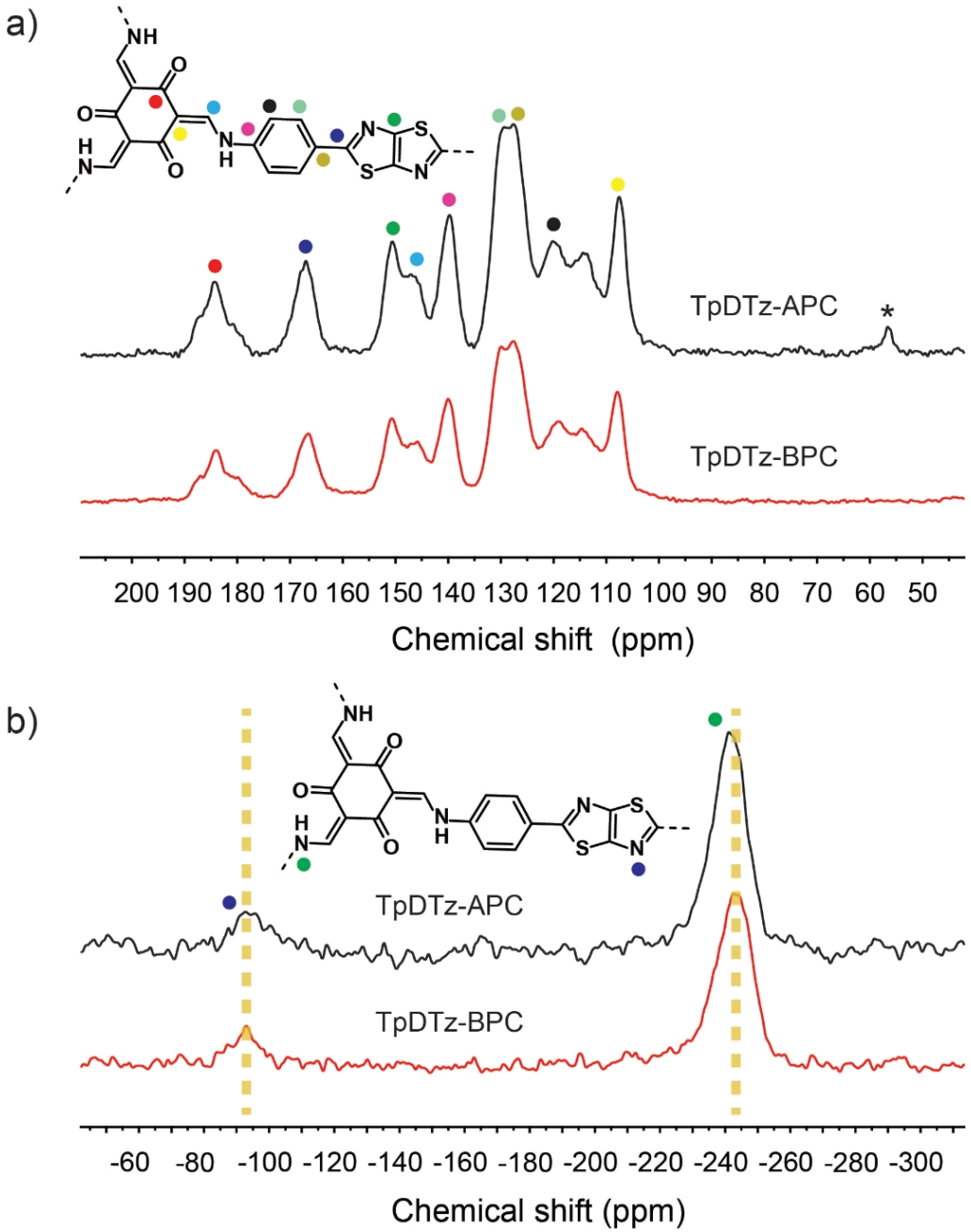

Figure B-41. (a) ^{13}C and **(b)** ^{15}N CP–MAS ssNMR of the pristine **TpDTz** COF sample in comparison with the ssNMR of the recovered **TpDTz** COF sample after the long-term (72 h) photocatalysis experiment. The almost perfect match of the spectra signifies the stability of the COF photoabsorber during photocatalysis and suggests the absence of any significant chemical interaction between the COF framework and NiME co-catalyst. *The ^{13}C signal (56.6 ppm) corresponds to trapped 2-mercaptoethanol (ME) inside the **TpDTz** COF pore in the recovered **TpDTz** COF sample after photocatalysis. This signal may point towards a persistent chemical interaction between the framework and the ligands of the co-catalyst.

Before photocatalysis

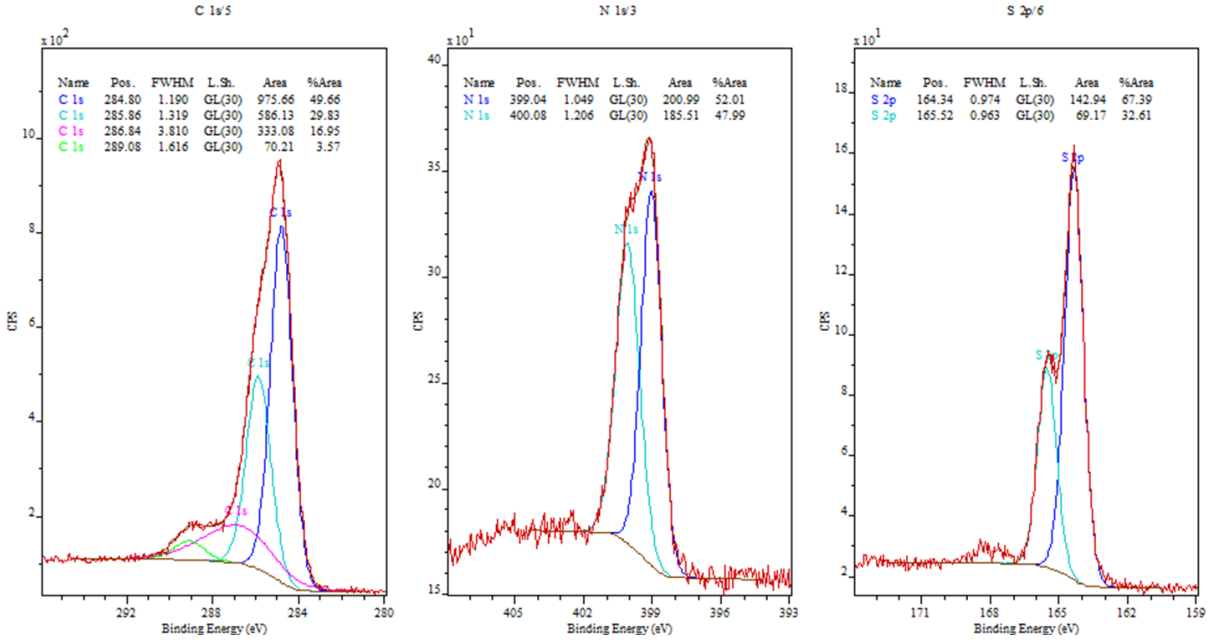

After photocatalysis

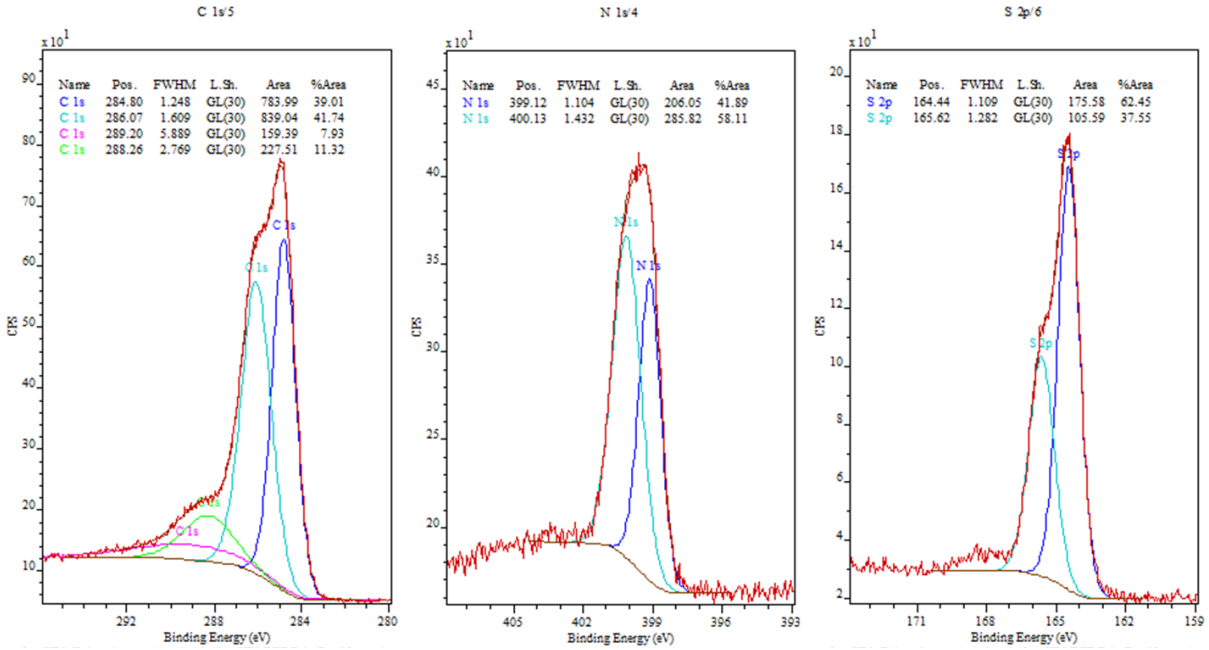

Figure B-42. Comparison of the X-ray photoelectron spectra (XPS) of pristine **TpDTz** COF with the recovered **TpDTz** COF after the long-term (72 h) photocatalysis experiment. Both samples confirm the presence of 2 different nitrogen species corresponding to TzTz and enamine (—C–NH) and one kind of sulfur (TzTz), which indicates that there is no significant structural change of COF during photocatalysis.

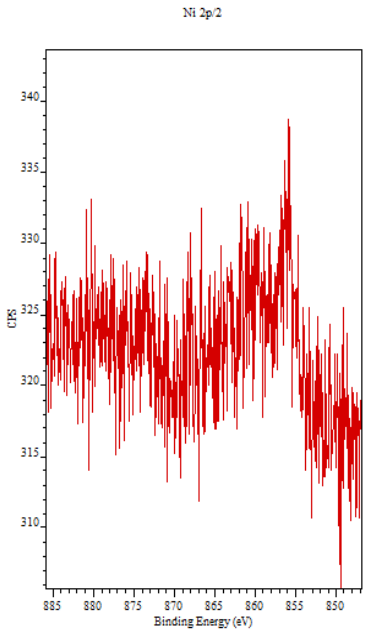

Figure B-43. Ni signal in XPS of the recovered **TpDTz** COF sample after the long-term (72 h) photocatalysis experiment. This result indicates that traces of Ni are still present in the recovered sample after photocatalysis. The amount of Ni was so little that it was not possible to do any fitting to determine the binding energies.

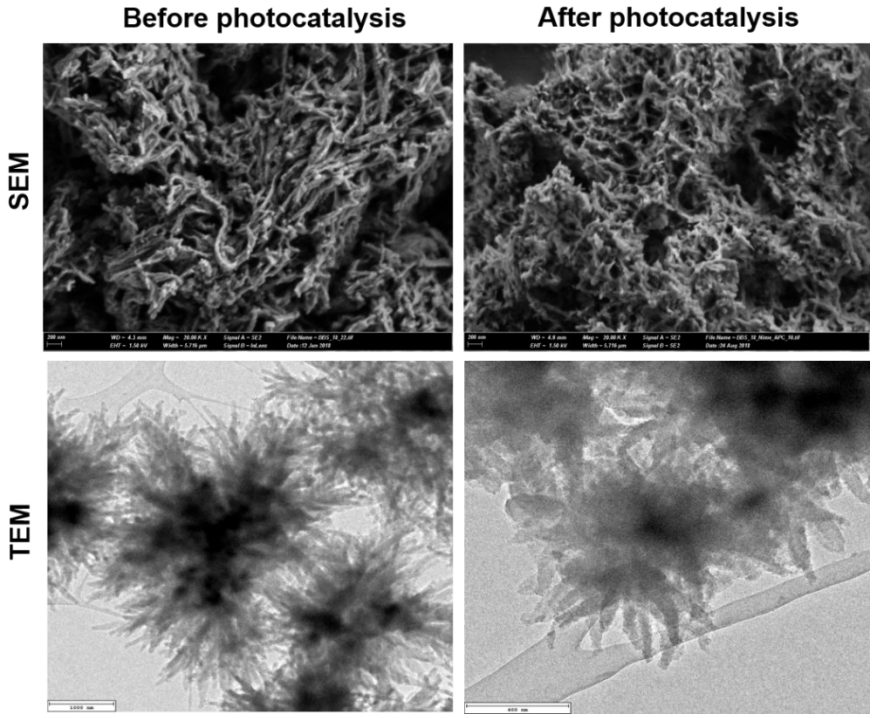

Figure B-44. Comparison of the SEM (scale bar 200 nm) and TEM images (scale bar 1 µm and 0.4 µm) of the pristine **TpDTz** COF and recovered **TpDTz** COF after the long term (72 h) photocatalysis experiment.

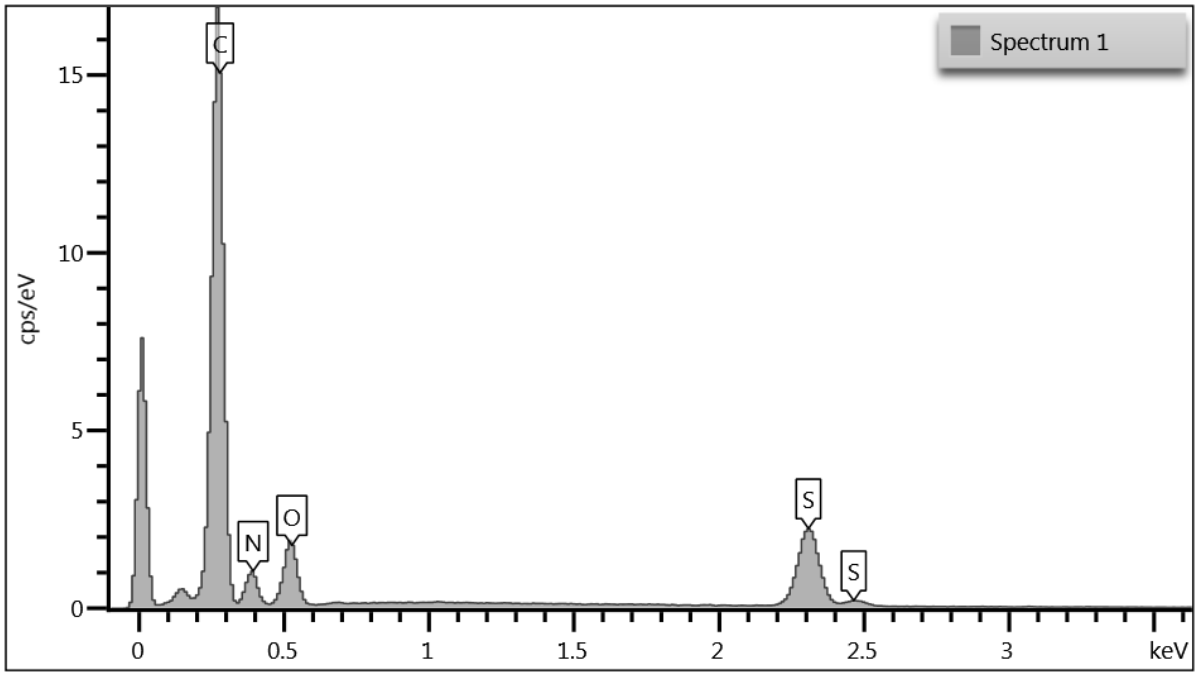

Figure B-45. EDAX profile of the pristine TpDTz COF.

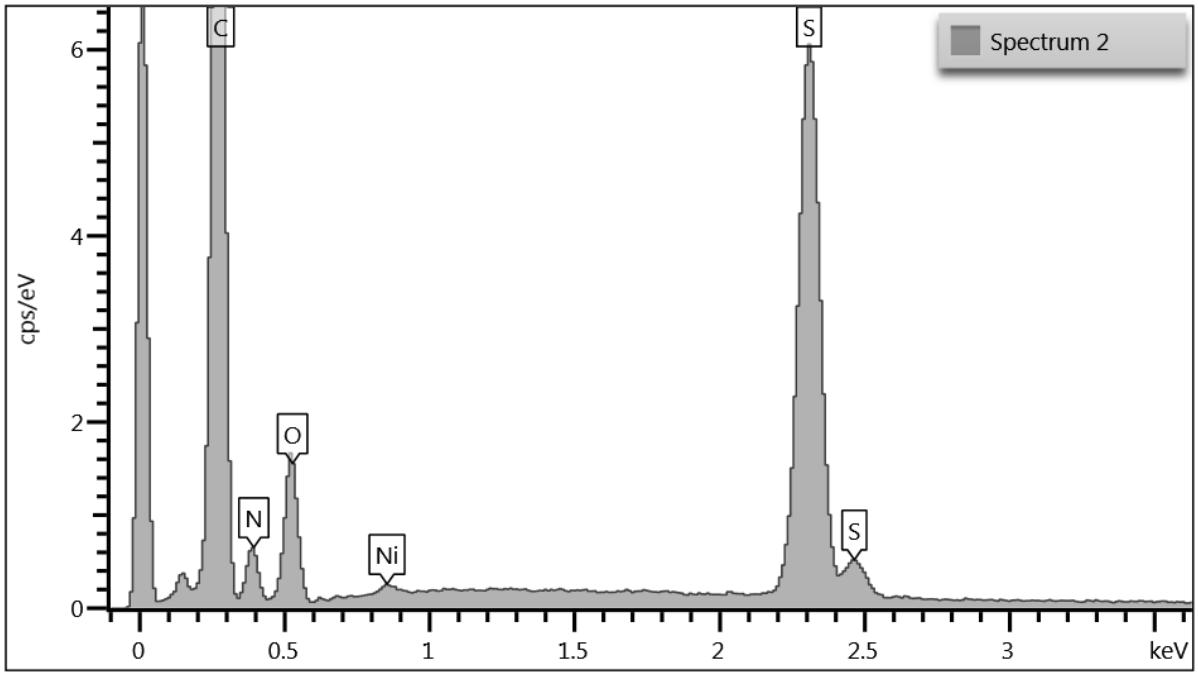

Figure B-46. EDAX profile of the recovered **TpDTz** COF after the long term (72 h) photocatalysis experiment. This information signifies that a trace amount of Ni (~1%) is still present in the recovered sample after photocatalysis. Note that from ICP measurement the total Ni content of 0.4% was found for the recovered sample after photocatalysis.

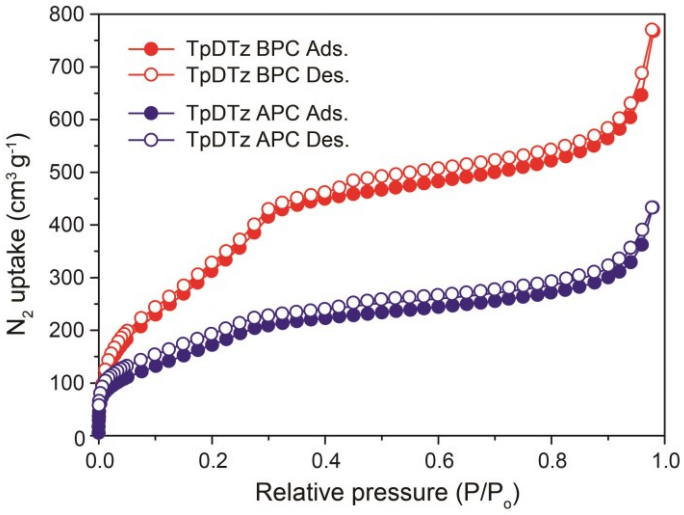

Figure B-47. Comparison of the Ar adsorption-desorption isotherms recorded at 87 K of TpDTz COF before photocatalysis (BPC) and after photocatalysis (APC). The Ar adsorption isotherms suggests that the BET surface area of recovered TpDTz COF (after 72 h of photocatalysis) is decreased by ~40% compared to the pristine TpDTz COF sample, which could be due to some trapped co-catalyst components, TEoA (boiling point of ME is 157 oC and TEoA is 208 oC) inside the COF pores and/or partial exfoliation of COF layers, though was not clearly visible in TEM images.

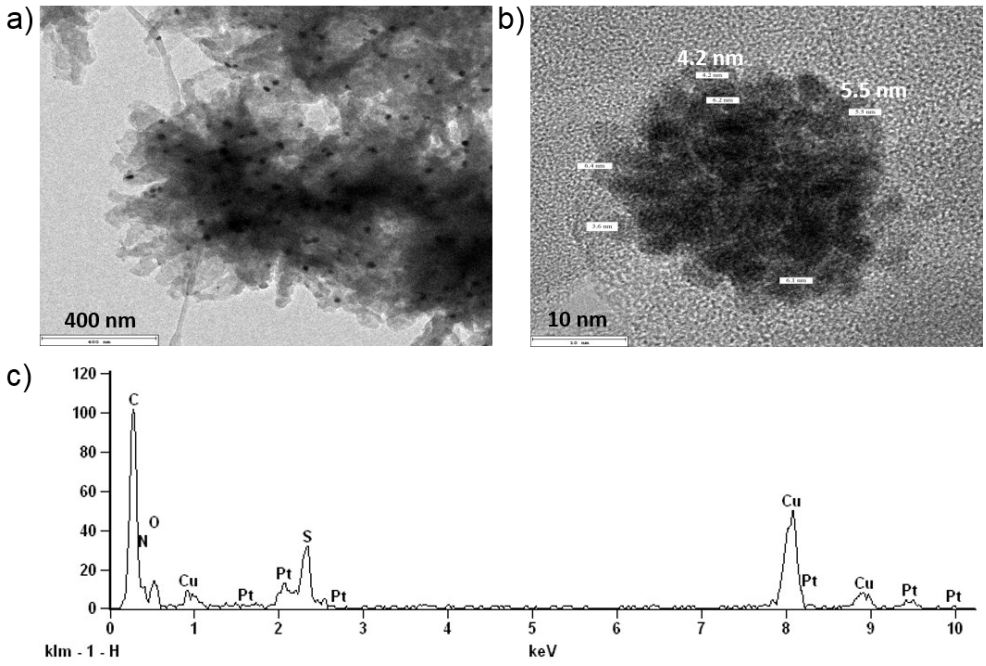

Figure B-48. a), b) TEM images and **c)** EDAX profile of the recovered TpDTz COF after the photocatalysis experiment in water with Pt as co-catalyst and TEoA as SED. These results confirm that the Pt nanoparticles are uniformly photo-deposited on TpDTz COF.

B.11 Quantum-chemical calculations

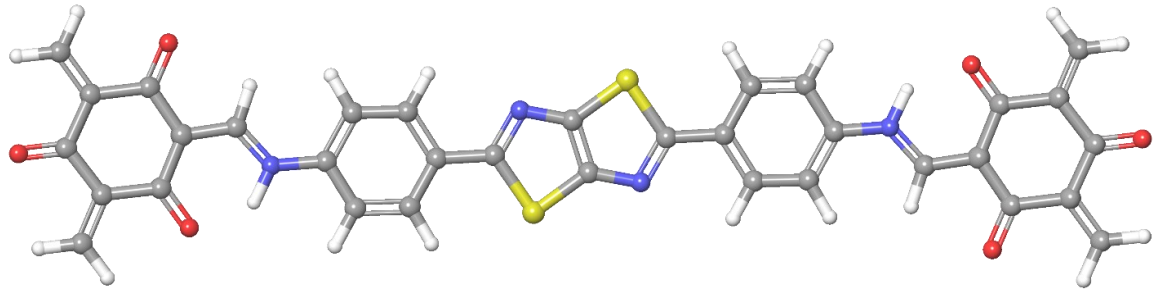

Figure B-49. Optimized structure of the TpDTz-NMR model system obtained on PBE0-D3/def2-TZVP level of theory.

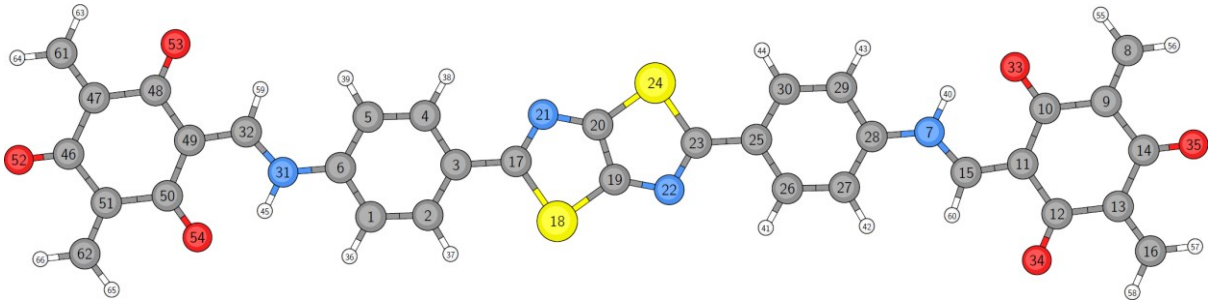

Figure B-50. Atom numbers for the optimized structure of the TpDTz-NMR model system.

Table B-4. Calculated ^{13}C-NMR chemical shifts with TMS as reference for the optimized TpDTz-NMR model system, obtained on B97-2/pcS-2//PBE0-D3/def2-TZVP level of theory. Corresponding atom numbers are shown in Figure B-50.

Number	Atom	NMR Chemical Shielding [ppm]	NMR Chemical Shift [ppm]
1	C	60.0	126.8
2	C	52.2	134.7
3	C	47.3	139.5
4	C	50.4	136.4
5	C	67.4	119.5
6	C	39.8	147.1
8	C	36.3	150.5
9	C	39.7	147.1
10	C	-5.9	192.8
11	C	72.9	113.9
12	C	-0.3	187.1
13	C	40.7	146.2
14	C	-3.0	189.8
15	C	30.2	156.6
16	C	35.3	151.6
17	C	10.1	176.8
19	C	26.6	160.2
20	C	26.6	160.2
23	C	10.1	176.8
25	C	47.3	139.5
26	C	50.4	136.4
27	C	67.4	119.5
28	C	39.8	147.1
29	C	60.0	126.8
30	C	52.2	134.7
32	C	30.2	156.6

46	C	-3.0	189.8
47	C	40.7	146.2
48	C	-0.3	187.1
49	C	72.9	113.9
50	C	-5.9	192.8
51	C	39.7	147.1
61	C	35.3	151.6
62	C	36.3	150.5

Table B-5. Calculated ^{15}N-NMR chemical shifts with nitromethane as reference for the optimized TpDTz-NMR model system, obtained on B97-2/pcS-2//PBE0-D3/def2-TZVP level of theory. Corresponding atom numbers are shown in Figure B-50.

Number	Atom	NMR Chemical Shielding [ppm]	NMR Chemical Shift [ppm]
7	N	92.1	-235.0
21	N	-54.0	-88.9
22	N	-54.0	-88.9
31	N	92.1	-235.0

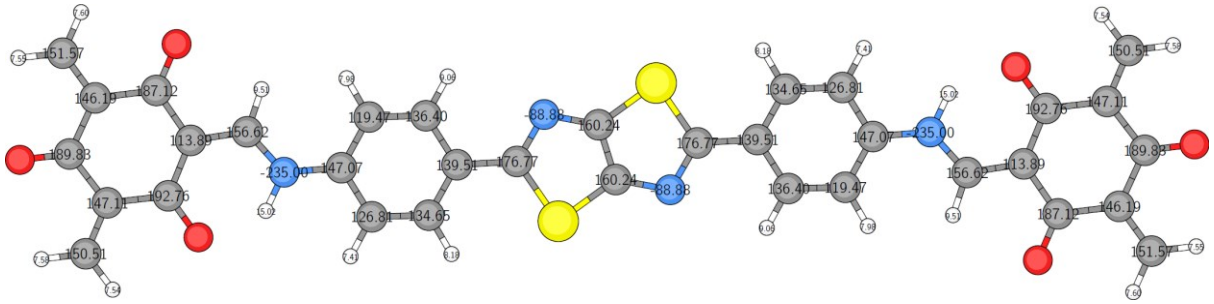

Figure B-51. Calculated ^{13}C- and ^{15}N-NMR chemical shifts overlaid on the optimized structure of the TpDTz-NMR model system.

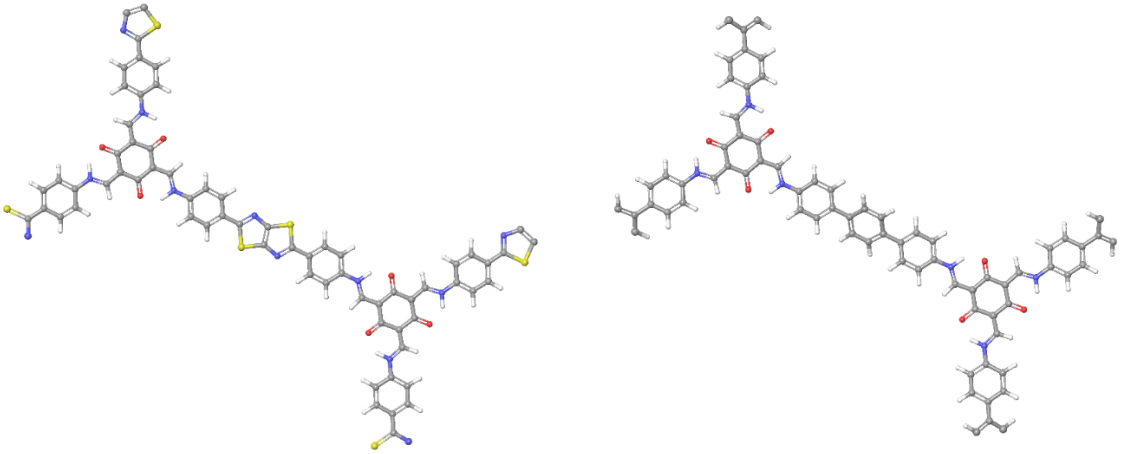

Figure B-52. Structures of the unit cell of the TpDTz (left) and TpDTP (right) model systems, obtained from a 2D periodic optimization on RI-PBE-D3/def2-TZVP level of theory.

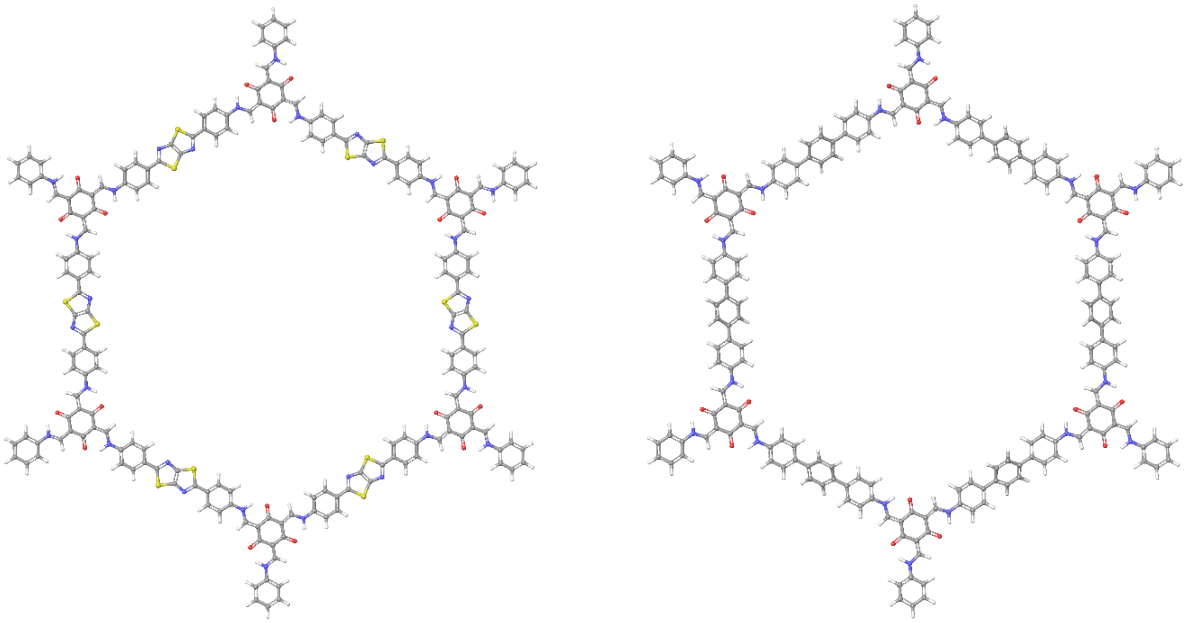

Figure B-53. Structures for the TpDTz (left) and TpDTP (right) pore model, cut from a supercell, obtained from a 2D periodic optimization on RI-PBE-D3/def2-TZVP level of theory.

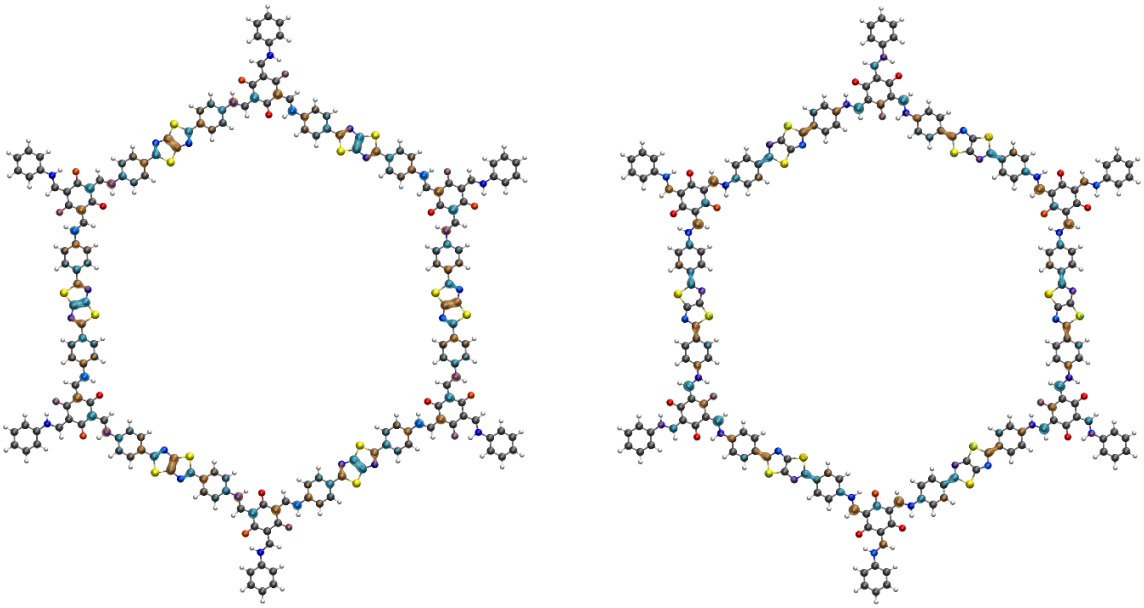

Figure B-54. Calculated molecular orbitals for the TpDTz pore model, HOMO on the left, LUMO on the right, both obtained on RI-PBE-D3/def2-TZVP//RI-PBE-D3/def2-TZVP level of theory.

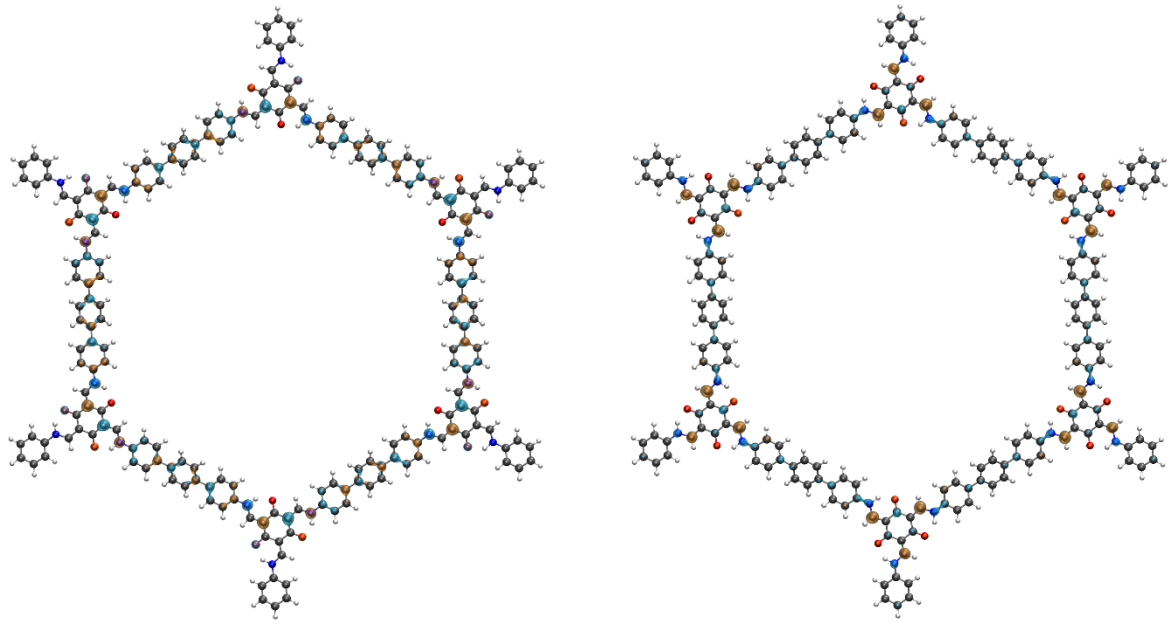

Figure B-55. Calculated molecular orbitals for the TpDTP pore model, HOMO on the left, LUMO on the right, both obtained on RI-PBE-D3/def2-TZVP//RI-PBE-D3/def2-TZVP level of theory.

Table B-6. Calculated orbital energies for the TpDTz and TpDTP pore models, obtained on RI-PBE-D3/def2-TZVP//RI-PBE-D3/def2-TZVP level of theory.

	HOMO		LUMO		Kohn-Sham Gap	
	[H]	[eV]	[H]	[eV]	[H]	[eV]
TpDTP	-0.180676	-4.92	-0.123913	-3.37	0.056763	1.54
TpDTz	-0.181172	-4.93	-0.111931	-3.05	0.069241	1.88

Table B-7. Comparison of calculated Vertical Cation Stabilization Energies (VCSE) and Vertical Anion Stabilization Energies (VASE) within and across the TpDTP and TpDTz pore model systems, obtained on RI-PBE-D3/def2-TZVP//RI-PBE-D3/def2-TZVP level of theory.

Radical Cation					Neutral
	ΔVCSE [eV]	ΔVCSE [H]	VCSE [H]	Total Energy [H]	Total Energy [H]
TpDTP	0.00	0.000000	0.198489	-9959.775926	-9959.974415
TpDTz	-0.03	-0.001179	0.197311	-14921.694520	-14921.891831
Radical Anion					Neutral

	ΔVASE [eV]	ΔVASE [H]	VASE [H]	Total Energy [H]	Total Energy [H]
TpDTP	0.00	0.000000	-0.095393	-9960.069809	-9959.974415
TpDTz	-0.34	-0.012558	-0.107951	-14921.999782	-14921.891831

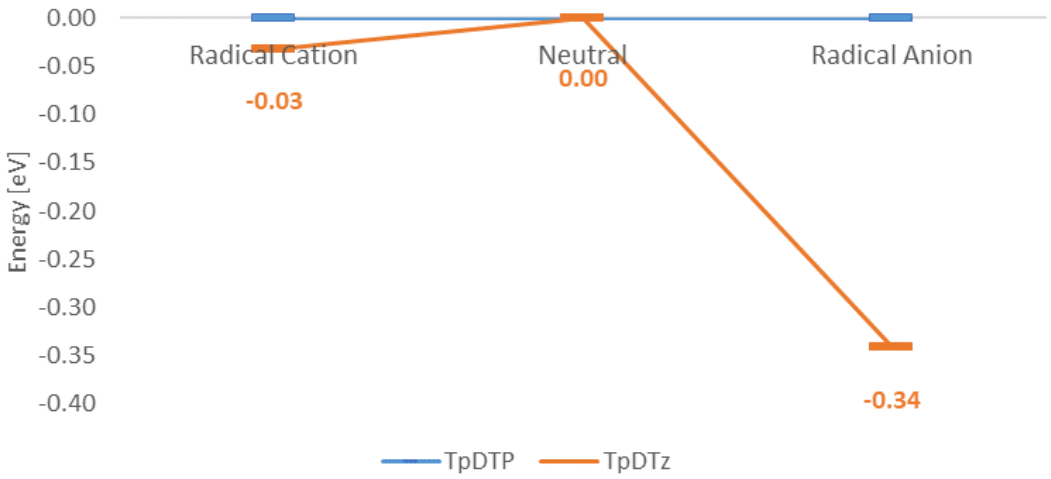

Figure B-56. Comparison of calculated Ionization Potentials (IP) and Electron Affinities (EA), calculated via Vertical Cation Stabilization Energies (VCSE) and Vertical Anion Stabilization Energies (VASE), across the TpDTP and TpDTz pore model systems in reference to the TpDTP model system, obtained on RI-PBE-D3/def2-TZVP//RI-PBE-D3/def2-TZVP level of theory.

Table B-8. Calculated orbital energies, VCSE and VASE for the TpDTz and TpDTP pore models, obtained on RI-PBE-D3/def2-TZVP//RI-PBE-D3/def2-TZVP level of theory, in comparison with experimentally obtained cyclovoltammetric data.

	Ionization Potential (IP)	Electron Affinity (EA)

	HOMO Energy [eV]	Exp. E_{VB} [eV]	*calculated as* VCSE [eV]	LUMO Energy [eV]	Exp. E_{CB} [eV]	*calculated as* VASE [eV]
TpDTP	-4.92	-	5.40	-3.37	-	-2.60
TpDTz	-4.93	-5.53	5.37	-3.05	-3.46	-2.94

Table B-9. Calculated excitation energies for the TpDTz pore model, obtained on TD-PBE0-D3/def2-TZVP//RI-PBE-D3/def2-TZVP level of theory.

State [#]	Excitation Energy [eV]	Oscillator Strength	Occupied Orbital	Virtual Orbital	Orbital Contribution [%]
1	2.30	0.000013	HOMO	LUMO	32.2
2	2.39	8.990903	HOMO	LUMO+1	26.4
3	2.40	8.996927	HOMO	LUMO+2	26.4
4	2.55	0.000006	HOMO-3	LUMO	15.8
5	2.55	0.000001	HOMO-4	LUMO	15.8

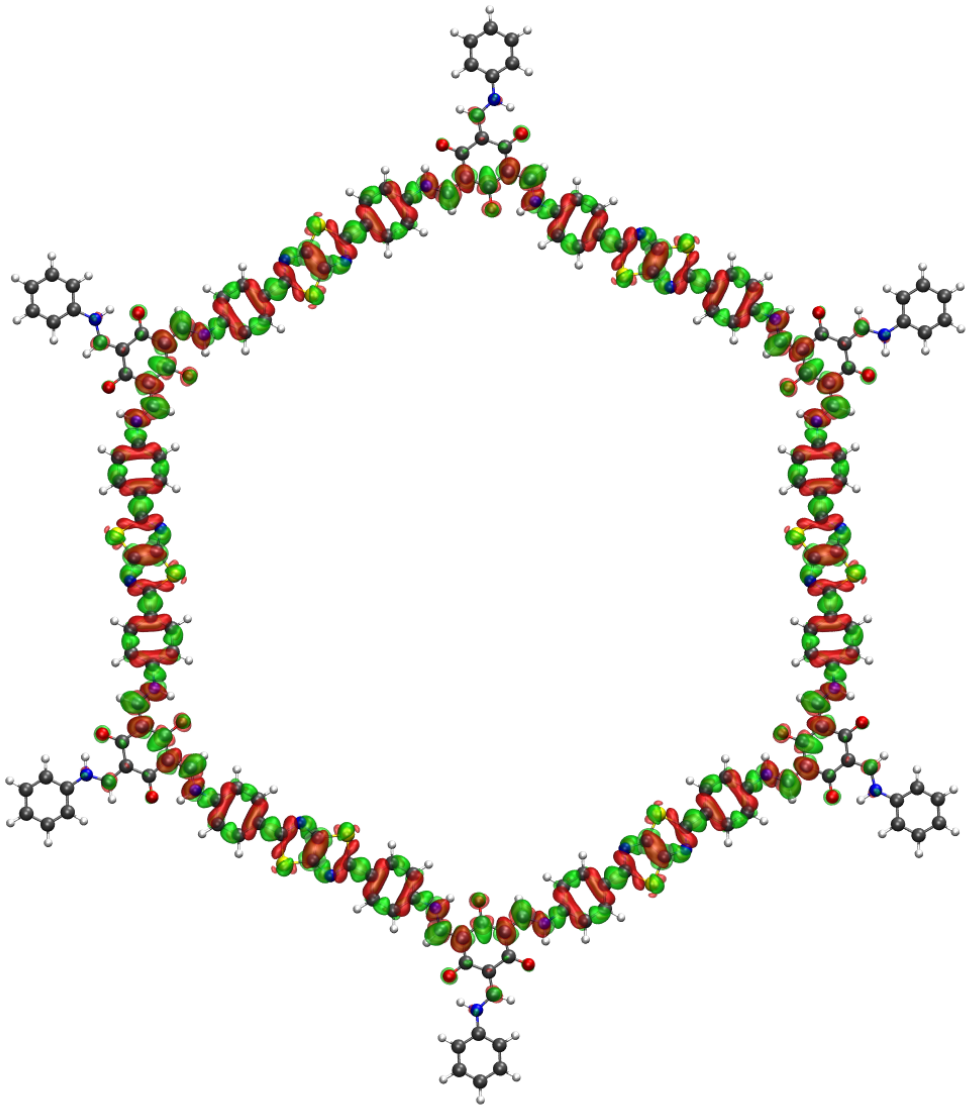

Figure B-57. Difference density for the lowest excited state for the TpDTz pore model, obtained on TD-PBE0-D3/def2-TZVP//RI-PBE-D3/def2-TZVP level of theory.

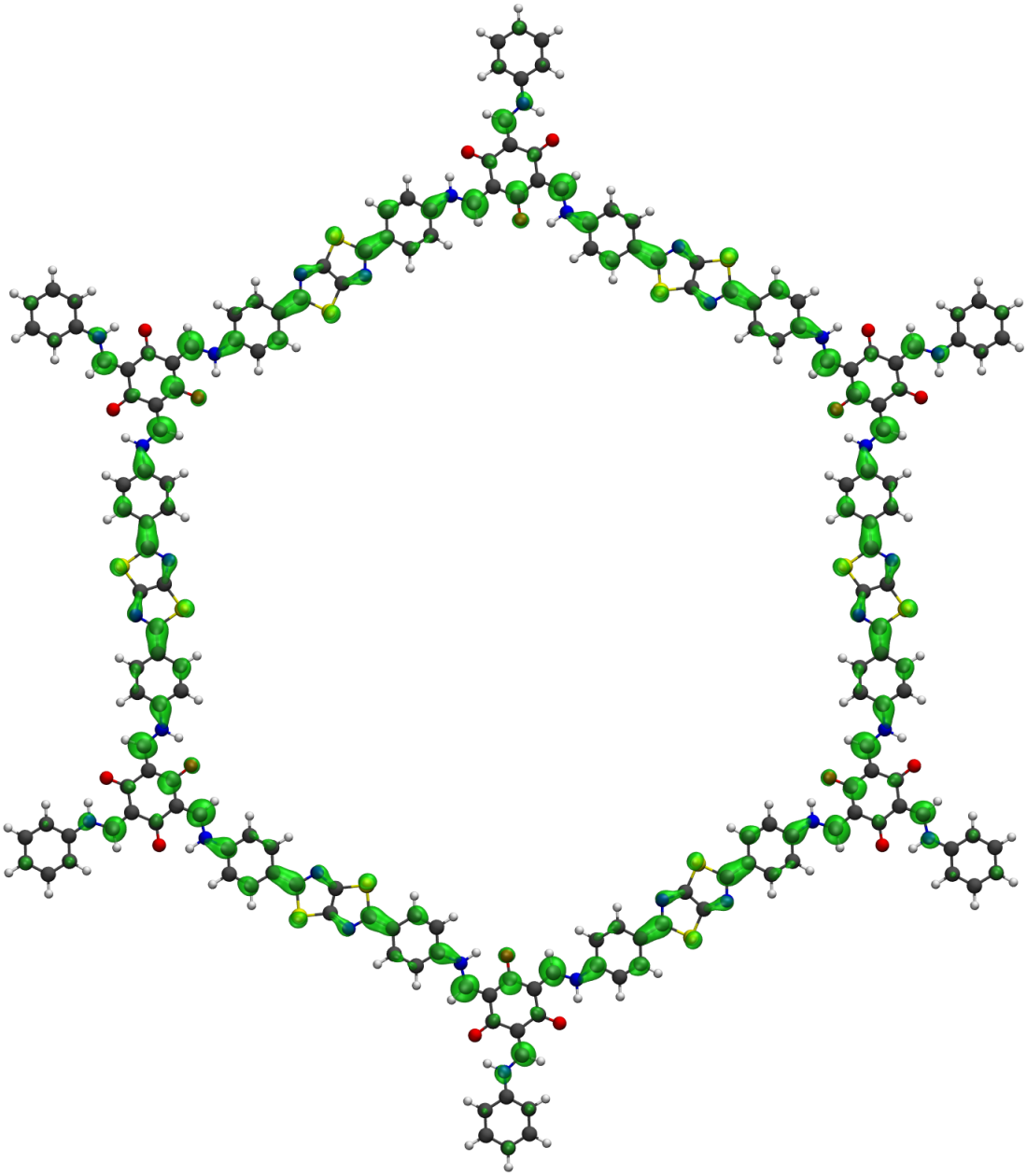

Figure B-58. Spin density for the radical anionic state for the TpDTz pore model, obtained on RI-PBE/def2-TZVP//RI-PBE-D3/def2-TZVP level of theory.

B.12 References

1. Chong JH, Sauer M, Patrick BO, MacLachlan MJ. Highly Stable Keto-Enamine Salicylideneanilines. *Organic Letters* 2003, **5**(21)**:** 3823-3826.
2. Adamo C, Barone V. Toward reliable density functional methods without adjustable parameters: The PBE0 model. *The Journal of Chemical Physics* 1999, **110**(13)**:** 6158-6170.
3. Ernzerhof M, Scuseria GE. Assessment of the Perdew–Burke–Ernzerhof exchange-correlation functional. *The Journal of Chemical Physics* 1999, **110**(11)**:** 5029-5036.
4. Grimme S, Antony J, Ehrlich S, Krieg H. A consistent and accurate ab initio parametrization of density functional dispersion correction (DFT-D) for the 94 elements H-Pu. *The Journal of Chemical Physics* 2010, **132**(15).
5. Schäfer A, Huber C, Ahlrichs R. Fully optimized contracted Gaussian basis sets of triple zeta valence quality for atoms Li to Kr. *The Journal of Chemical Physics* 1994, **100**(8)**:** 5829-5835.
6. Wilson PJ, Bradley TJ, Tozer DJ. Hybrid exchange-correlation functional determined from thermochemical data and ab initio potentials. *The Journal of Chemical Physics* 2001, **115**(20)**:** 9233-9242.
7. Jensen F. Segmented Contracted Basis Sets Optimized for Nuclear Magnetic Shielding. *Journal of Chemical Theory and Computation* 2014, **11**(1)**:** 132-138.
8. Ahlrichs R, Bär M, Häser M, Horn H, Kölmel C. Electronic structure calculations on workstation computers: The program system turbomole. *Chemical Physics Letters* 1989, **162**(3)**:** 165-169.
9. TURBOMOLE V7.3 2018, a development of University of Karlsruhe and Forschungszentrum Karlsruhe GmbH, 1989-2007, TURBOMOLE GmbH, since 2007; available from \\ http://www.turbomole.com.
10. Kussmann J, Ochsenfeld C. Pre-selective screening for matrix elements in linear-scaling exact exchange calculations. *The Journal of Chemical Physics* 2013, **138**(13).
11. Kussmann J, Ochsenfeld C. Preselective Screening for Linear-Scaling Exact Exchange-Gradient Calculations for Graphics Processing Units and General Strong-

Scaling Massively Parallel Calculations. *Journal of Chemical Theory and Computation* 2015, **11**(3)**:** 918-922.

12. Cakmak G, Nuss J, Jansen M. LiB6O9F, the First Lithium Fluorooxoborate - Crystal Structure and Ionic Conductivity. *Zeitschrift für anorganische und allgemeine Chemie* 2009, **635**(4-5)**:** 631-636.
13. Bruker Suite. Madison, WI: Bruker AXS Inc.; 2013.
14. Sheldrick GM. SADABS — Bruker AXS area detector scaling and absorption. Germany: University of Göttingen.
15. Sheldrick GM. A short history ofSHELX. *Acta Crystallographica Section A Foundations of Crystallography* 2007, **64**(1)**:** 112-122.
16. Sheldrick GM. Crystal structure refinement withSHELXL. *Acta Crystallographica Section C Structural Chemistry* 2015, **71**(1)**:** 3-8.
17. Vyas VS, Haase F, Stegbauer L, Savasci G, Podjaski F, Ochsenfeld C*, et al.* A tunable azine covalent organic framework platform for visible light-induced hydrogen generation. *Nature Communications* 2015, **6**(1).
18. Biswal BP, Becker D, Chandrasekhar N, Seenath JS, Paasch S, Machill S*, et al.* Exploration of Thiazolo[5,4-d

]thiazole Linkages in Conjugated Porous Organic Polymers for Chemoselective Molecular Sieving. *Chemistry - A European Journal* 2018, **24**(42)**:** 10868-10875.

19. Das A, Han Z, Brennessel WW, Holland PL, Eisenberg R. Nickel Complexes for Robust Light-Driven and Electrocatalytic Hydrogen Production from Water. *ACS Catalysis* 2015, **5**(3)**:** 1397-1406.
20. Zhang W, Hong J, Zheng J, Huang Z, Zhou J, Xu R. Nickel–Thiolate Complex Catalyst Assembled in One Step in Water for Solar H2 Production. *Journal of the American Chemical Society* 2011, **133**(51)**:** 20680-20683.
21. Connelly NG, Geiger WE. Chemical Redox Agents for Organometallic Chemistry. *Chemical Reviews* 1996, **96**(2)**:** 877-910.
22. Peng L-Z, Liu P, Cheng Q-Q, Hu W-J, Liu YA, Li J-S*, et al.* Highly effective electrosynthesis of hydrogen peroxide from oxygen on a redox-active cationic covalent triazine network. *Chemical Communications* 2018, **54**(35)**:** 4433-4436.

23. Wei P-F, Qi M-Z, Wang Z-P, Ding S-Y, Yu W, Liu Q*, et al.* Benzoxazole-Linked Ultrastable Covalent Organic Frameworks for Photocatalysis. *Journal of the American Chemical Society* 2018, **140**(13)**:** 4623-4631.
24. Cardona CM, Li W, Kaifer AE, Stockdale D, Bazan GC. Electrochemical Considerations for Determining Absolute Frontier Orbital Energy Levels of Conjugated Polymers for Solar Cell Applications. *Advanced Materials* 2011, **23**(20)**:** 2367-2371.
25. Calik M, Auras F, Salonen LM, Bader K, Grill I, Handloser M*, et al.* Extraction of Photogenerated Electrons and Holes from a Covalent Organic Framework Integrated Heterojunction. *Journal of the American Chemical Society* 2014, **136**(51)**:** 17802-17807.
26. Zhao W, Zhuang X, Wu D, Zhang F, Gehrig D, Laquai F*, et al.* Boron-π-nitrogen-based conjugated porous polymers with multi-functions. *Journal of Materials Chemistry A* 2013, **1**(44).
27. Qi F, Song J, Xiong W, Huo L, Sun X, Sun Y. Two wide-bandgap fluorine-substituted benzotriazole based terpolymers for efficient polymer solar cells. *Dyes and Pigments* 2018, **155:** 126-134.
28. Gould RO, Harding MM. Nickel and palladium complexes of 1-hydroxyethane-2-thiol and analogues. Part I. Crystal structure of cyclohexakis[bis-(μ-1-hydroxyethane-2-thiolato)-nickel(II)]. *J Chem Soc A* 1970, **0**(0)**:** 875-881.
29. Kagalwala HN, Gottlieb E, Li G, Li T, Jin R, Bernhard S. Photocatalytic Hydrogen Generation System Using a Nickel-Thiolate Hexameric Cluster. *Inorganic Chemistry* 2013, **52**(15)**:** 9094-9101.
30. Jin E, Lan Z, Jiang Q, Geng K, Li G, Wang X*, et al.* 2D sp2 Carbon-Conjugated Covalent Organic Frameworks for Photocatalytic Hydrogen Production from Water. *Chem* 2019, **5**(6)**:** 1632-1647.
31. Pachfule P, Acharjya A, Roeser J, Langenhahn T, Schwarze M, Schomäcker R*, et al.* Diacetylene Functionalized Covalent Organic Framework (COF) for Photocatalytic Hydrogen Generation. *Journal of the American Chemical Society* 2018, **140**(4)**:** 1423-1427.

32. Wang X, Chen L, Chong SY, Little MA, Wu Y, Zhu W-H*, et al.* Sulfone-containing covalent organic frameworks for photocatalytic hydrogen evolution from water. *Nature Chemistry* 2018, **10**(12)**:** 1180-1189.
33. Stegbauer L, Zech S, Savasci G, Banerjee T, Podjaski F, Schwinghammer K*, et al.* Photocatalysis: Tailor - Made Photoconductive Pyrene - Based Covalent Organic Frameworks for Visible - Light Driven Hydrogen Generation (Adv. Energy Mater. 24/2018). *Advanced Energy Materials* 2018, **8**(24).
34. Banerjee T, Haase F, Savasci G, Gottschling K, Ochsenfeld C, Lotsch BV. Single-Site Photocatalytic H2 Evolution from Covalent Organic Frameworks with Molecular Cobaloxime Co-Catalysts. *Journal of the American Chemical Society* 2017, **139**(45)**:** 16228-16234.
35. Haase F, Banerjee T, Savasci G, Ochsenfeld C, Lotsch BV. Structure–property–activity relationships in a pyridine containing azine-linked covalent organic framework for photocatalytic hydrogen evolution. *Faraday Discussions* 2017, **201:** 247-264.
36. Stegbauer L, Schwinghammer K, Lotsch BV. A hydrazone-based covalent organic framework for photocatalytic hydrogen production. *Chem Sci* 2014, **5**(7)**:** 2789-2793.

Appendix C. Supplementary and Experimental Section/Methods - Chapter 5

The work in this chapter was reproduced and adapted from the supplemental material of:

Toward Standardized Photocatalytic Oxygen Evolution Rates Using RuO_2@TiO_2 as a Benchmark

Hugo A. Vignolo-González*, Sourav Laha, Alberto Jiménez-Solano, Takayoshi Oshima, Viola Duppel, Peter Schützendübe and Bettina V. Lotsch

C.1 Materials

Aeroxide P25 (formerly TiO_2 Degussa P25) nanoparticles (Evonik, Sigma-Aldrich) were pre-treated before and after Ru deposition in a vacuum oven at 60°C for at least 8 h to remove the presence of potential physisorbed organics. Fresh P25 stock was then stored under regular clean conditions. $RuCl_3 \cdot xH_2O$ (Alfa Aesar, 99.99%) was used as a precursor for both hydrothermal and photodeposition methods. Different amounts of precursor were weighed and stored in an inert atmosphere. Stock solution of Ru precursor was then prepared at 1 mg mL^{-1} and kept no longer than 1 month to ensure stability. TSPP ($Na_4P_2O_7 \cdot 10H_2O$; Supelco) stock was prepared at a concentration of 500 mM. For photocatalytic testing, potassium iodate KIO_3 (Aldrich, 99.5%) or sodium persulfate $Na_2S_2O_8$ (Aldrich, 98%) were weighed directly before the experiment together with the sample. Stock solutions were prepared with Milli-Q water.

C.2 Ruthenium deposition

For hydrothermally RuO_2 deposited on P25 nanoparticles, 20 mL of Milli-Q water and 20 mg of P25 were stirred and ultrasonicated for 15 min in a microwave vial with magnetic stir bar. Ru stock solution was then added at different amounts and in duplicates, and the vials were closed.[40,41] Two different methods were employed. For the microwave method (HT-MW), vials were prepared and placed one by one in a microwave synthesis oven (Biotage Initiator+) at 150°C for 10 h. Using the second method, vial suspension samples and its duplicates were placed all together at the same temperature and time in a home-made heating plate with stirrer and a heating block. For *ex situ* photodeposited samples (PD), two different scaled photoreactor cells were employed to replicate literature methods: the first was 35 mg of P25 in 70 mL of Milli-Q water at 10 mM KIO_3 at the optimal

Ru content; the second was an identical suspension but with the volume scaled to 500 mL.[12,38,39] Solutions were sonicated for 15 min before entering the cell. The purging procedure of the photoreactor cell was identical to that reported in our previous publication, but with the difference of a degassing bubbling line entering the stirred liquid medium to degas O_2 to the headspace in continuous flow and track the produced O_2 with a photoluminescence sensor (PST9 flow-through photoluminescence sensor probe + Fibox [Presens]), and some modifications that facilitated powder recovery at the end of the experiment.[1] Once the headspace purging was finished, the bubbling was started and the O_2 was monitored until the baseline was reached, after which the light was turned on (Newport, housed Xe lamp simulator). The irradiation condition is a standard ACB quality simulated AM 1.5G, 1-sun condition (Figure C-15). The solution was irradiated until the OER rate maximum remained constant for around 30 min, and the suspension was recovered. Typically, the induction time for the Ru precursor to be completely deposited is around 0.5 min mL^{-1} of suspension. For metallic Ru-deposited samples, the same cell as that of our previous publication was used but with 16 mL of Milli-Q water, 4 mL of methanol, 10 mg of P25, and Ru precursor amount. Reaction was stopped when the hydrogen evolution reaction (HER) maximum was obtained and kept for 1 h tracking of H_2 with the BID detector of the on-line GC analysis. Finally, for all the methods (PD, HT-MW, and HT-HB), the samples were centrifuged in Teflon tubes at 15,000 rpm and then washed/suspended with Milli-Q water and ultrasonicated briefly, repeating this cycle three times. On completion, the centrifuged slurry was dried off overnight in a vacuum oven, mortar ground, and stored in glass vials sorted by batches. P25 controls were produced by using no Ru precursor and following the entire procedure described above.

C.3 Sample characterization

UV-vis spectroscopy (Cary 5000, Agilent), ICP-OES analysis (Vista Pro Axial, Varian), TEM (Philips CM30 ST, 300kV, LaB_6 cathode), TEM-FFT, and TEM-EDX (Noran System Seven Si(Li) detector) were performed as previously reported by our group.[1–3]

DLS measurements were performed using Malvern Zetasizer-Nano equipment, with 13 runs per measurement after full decay of the measured autocorrelation function and after

ensuring suitable polydispersity. Each measurement was performed in duplicates using freshly prepared suspension exactly as for photocatalytic activity testing.

PXRD patterns were collected at room temperature on a laboratory powder diffractometer in Debye-Scherrer geometry (Stadi P-Diffraktometer [Stoe]), Cu-Kα1 radiation from a primary monochromator. The samples were sealed in 0.3-mm diameter borosilicate glass capillaries (Hilgenberg glass no. 0140), which were spun during the measurements. Each pattern was measured in a 2θ range from 5° to 80° applying a total scan time of 1 h.

For XPS, measurements were carried out in a Thermo VG Thetaprobe system (Thermo Fisher Scientific, USA) employing Al Kα radiation ($h\nu$ = 1,486.68 eV) produced with an electrical power of 100 W. The X-ray spot size on the sample was about 1 cm in diameter. The analyzer aperture circle on the sample was approximately 1 mm diameter. During measurements, the base pressure of the XPS was 1×10^{-9} mbar. To compensate for possible peak shifts originating from surface charging, we used Ar ions from a flood gun. The necessary Ar flux inlet was set to a chamber pressure of 3×10^{-7} mbar. Survey spectra were recorded with a pass energy of 200 eV, and more detailed spectra were carried out with a pass energy of 50 eV and step width of 0.05 eV. The Ti 2p and Ru 3p peaks were measured with 100 scans to reduce the noise to an acceptable value. The C 1s and the O 1s peaks were measured with 60 scans. All binding energies were calibrated with respect to the C 1s peak position. The measurements were fitted using the fitting routines included in the XPS software Avantage and CasaXPS.

XPS peak analysis was conducted in relation to deconvolution of peaks shown in Figure C-5, Table C-2, and Figure 5-4. As the Ru 3p core level XPS spectra overlap with the Ti 2p signal, the spectra of the Ru^0 1.0/P25-PD, Ru1.0/P25-HT-HB, and Ru0.15/P25-PD∗ were compared with the blank P25 (Figure 5-4B). The Ti $2p_{1/2}$ and Ti $2p_{3/2}$ peaks of P25 appear at 458.6 eV and 464.6 eV, respectively, which is in agreement with literature reports.[4] Only a single Ru $3p_{3/2}$ peak is observed in Ru^0 1.0/P25-PD at 459.8 eV, which is likely due to Ru(0). In contrast, the spectra of the PD and HT samples can clearly be deconvoluted to more than two peaks, which are observed due to the presence of Ru in these samples in different oxidation states. In Ru1.0/P25-HT-HB, two Ru $3p_{3/2}$ peaks appear at 460.0 eV and 463.5 eV, which indicate the presence of both metallic Ru (Ru(0)) and Ru(IV) in the sample.[5] The spectrum of Ru0.15/P25-PD∗ exhibits two Ru $3p_{3/2}$ peaks centered around

459.7 eV and 463.7 eV, which support the presence of both Ru(0) and Ru(IV) in the sample. It can be argued that the presence of traces of metallic Ru could indirectly alter the intrinsic activity of the RuO_2/P25 junction. However, we photocatalytically measured P25 blanks modified with metallic Ru (Figure C-1a), finding almost no difference compared with non-modified P25. Furthermore, as the sample Ru0.15/P25-PD and Ru0.15/P25-PD* were thoroughly surveyed during TEM imaging, along with the observed RuO_2 species, a few rare and isolated spots of photocatalytically inactive amorphous metallic Ru were identified on the sample Ru0.15/P25-PD (Figure C-6). RuO_2 is the active species responsible for OER activity in both HT and PD methods. Besides a higher active surface area of the material obtained by the PD method, the PD samples may be more active because of their lack of crystallinity when formed at room temperature and the fact that they are highly dispersed. In fact, after heat treatment (200°C, 2 h in air) of Ru0.15/P25-PD samples, we have found that photocatalytic OER activity drastically drops to the same levels of the HT samples, as this treatment is associated with further RuO_2 crystallization in some literature concerning this junction.[6]

C.4 Photocatalytic experimental setup

Photocatalytic reactions were performed in a glass cell with a top quartz optical window similar to our group's previous publication,[1] coupled to the same GC analytics (Shimadzu-JAS autosampler + Shimadzu GCMS QP-2020), plus the redundant PST9 in between the reactor and GC sampling line. The main upgrade is the reduction of total volume to 24 mL (height 8 cm, radius 1 cm) maintaining the gas-tight glass to metal standard and the same incident light at 1 sun under AM 1.5G conditions when the cell is filled with 10–12 mL of suspension (when doing r_{opt} measurements at less solution volume, the reactor was moved up/down to keep the same irradiance). In addition to regular stirring, the bottom is a fritted glass of porosity 3 or 4.5 (nominal bubble size from 10 to 40 μm), from where the gas enters directly the liquid medium, producing additional means of liquid-gas transport. The inflow of 4.6-purity helium was controlled by a mass flow controller (Bronkhorst low dP series), and at the headspace the overpressure was maintained in continuous flow at 0.5 bar with a back-pressure flow controller (Brooks SLA5820 + 0251 PLC-Power supply). This cell was also jacketed and the temperature of the cooling water

was set to 25°C using a thermostat (Lauda Eco RE 415 S). At regular operation helium flow conditions of 10–20 NmL min^{-1}, the characteristic times measured for mass transfer coefficients (PST6 trace photoluminescence sensor for dissolved oxygen [Presens]) in our reactor geometries are 30 s and 110 min (50 min under vigorous stirring) with and without a bubbling condition, respectively.[7] On the other hand, the retention time of the gas in the headspace assuming ideal mixing is calculated and measured as around 1.5 min, which means that in the absence of bubbles the response of the reactor when the light is turned on is mass transfer limited, while with bubbling the response of the reactor is moderately headspace mixing limited. Although literature hints that a more thorough modeling and algorithms are required to calculate the O_2 that remains dissolved in the liquid during OER experiments in liquid phase and the precise time when the reactor reaches a steady flow,[8] plugging the numbers of our reactor in such algorithms suggests that the rule of thumb of our previous HER publications in continuous flow that—in the absence of material induction time—after two retention times (in this new reactor ~2 min), the evolution of oxygen measured by our instrument at the outflow port is equivalent to OER and the dissolved oxygen that remains unmeasured in liquid phase is less than 1% of the total molar fraction of O_2 measured on-line via headspace. Thus the on-line OER analysis is similar to our previous publication and corresponds to the mass balance of oxygen in the system in steady state[1]:

$$r_{O_2} = \frac{F_{in} \times \Delta x_{O_2 ppm} \times 10^{-6}}{\left(1 - \Delta x_{O_2 ppm} \times 10^{-6}\right)} \qquad \text{Equation C-1}$$

where F_{in} is controlled molar helium (99.996% purity) in flow (mol h^{-1}); r_{O2} is total OER production rate (10^{-6} µmol h^{-1}); $\Delta x_{O2,ppm}$ is oxygen molar fraction delta at the reactor outlet, measured immediately with PST9 sensor and downstream a splitter with GC-MS-BID. The delta is the raw readout measured after illumination minus the measured baseline in darkness immediately before illumination.

Initially, our reactor design contained liquid oxygen sensors (Clark electrode and photoluminescence sensor) for photocatalytic measurements also, but they were not used further, since both Clark electrodes and photoluminescence sensors in the liquid phase

were prone to serious compensation issues at the trace levels of our measurements, and significantly impeded the cleaning of our high-throughput screening regime. Furthermore, after the mass transfer calculations mentioned above, and after verifying that under certain special photocatalytic conditions the increase in liquid oxygen was null, such sensors were proven irrelevant.

C.5 Photocatalytic activity screening and in-situ RuO_2 PD procedure

Suspensions were prepared using 10 mL of Milli-Q water containing 5 mg of sample (P25 or previously activated P25 samples), 10 mM KIO_3, and the desired volume of TSPP stock. The suspensions were then ultrasonicated for 15 min and finally, in the case of *in situ* RuO_2 deposition, the desired volume of Ru(III) stock solution was added. The reactor assembled without solution was vacuumed and pressurized two times to displace initial air hold-up, and flowed at the regular controlled helium flow and controlled overpressure until a stable baseline of around 5 ppm of O_2 in the headspace was obtained. Then, under a mild overpressure, the reactor was quickly opened and the solution was inserted and vacuumed one more time until the same baseline was obtained, and at the time all process values of instrumentation reached the set points. Finally, the light was turned on (Figure C-15) together with the first point taken in darkness by the GC-MS-BID autosampler in the case of complementary measurements. The delta of O_2 was then tracked on-line with the PST9 sensor, and the GC autosampler kept measuring under different routines that minimize the GC analysis time. Additionally, in case of %Ru loading optimization, a Hamilton gas-tight syringe was kept in the reactor ready to inject more Ru precursor repeating light-off/light-on cycles to obtain the OER maxima at each point. After trying this method to obtain optimal %Ru loading *in situ*, the %Ru contents around the maxima were repeated in different vials independently, whose numbers are expressed as error bars in Figure C-2. The optimal %Ru loading was identified using a polynomial fit of the data, giving a value of 0.15 Ru(III)/P25 w/w % for PD later used in scaled experiments to obtain *ex situ* deposited optimal samples. In the case of r_{opt} experiments of previously Ru-activated P25 optimal samples, consecutively different volumes of suspension were introduced in the reactor and moved accordingly to keep the liquid-gas interface at the same distance from the lamp. For optimal samples for which no full OER rate versus

suspension volume curve was reported, two points were tried at 8 mL and 10 mL to ensure that the nominal amount of 10 mL was around the r_{opt} value.

C.6 Quantum efficiency and O_2 isotope counting measurements

For the labeled water experiment, the long time on-stream (14 h) experiment in Figure 5-7 and Figure 5-8 was repeated exactly but at half the suspension volume and using a weight ratio of one-quarter the ^{18}O-labeled water (97 atom %, Sigma-Aldrich) to Milli-Q water. The photocatalytic activity procedure was then repeated identically, measuring O_2 concentrations with the BID detector and tracking molecule counting (MIC) at the MS channels m/z = 32, m/z = 34, and m/z = 36. Such channels' response was integrated around the O_2 retention time to obtain an additional total O_2 response using regular MS calibration. Qualitatively, the peaks are shown in Figure C-9 to demonstrate that labeled O_2 species appear only when labeled water was used. Quantitative isotopic distribution was obtained by integrating such peaks, and discounting the $^{32}O_2$ mass response in darkness to the one after illumination, after which the percentage of area of channels m/z = 34 and m/z = 36 to total O_2 area was calculated. As MS response is proportional to amount of substance, such area percentage is representative of the actual distribution of O_2 species (percentage values displayed in Figure 5-8), and later contrasted to predicted distributions by using a mean field approximation for the case with and without KIE in Table C-3. For quantum efficiency experiments, the same reactor was adapted to an alternative design that is jacketless to place a spectrophotometer collecting fiber together with a cosine corrector (Ocean Optics FX-XR1-ES) perpendicular to the outer surface of the reactor. The integration settings were fine-tuned to avoid sensor saturation and maximize signal-to-noise ratio, and the fiber was tried at different angular positions during quick illumination intervals to ensure optimal photon collection. The experiment in Figure 5-7 was then repeated and the OER activity was recorded to ensure no major deviation from reported trends using the regular reactor while collecting different spectra of side-scattered light with the lamp turned on. After recording, the fiber was moved down 1 mm per step to complete a 32-mm profile. The experimental data that show a good agreement with the optical model predictions are presented in Figure C-13.

C.7 Optical models

To simulate the light propagation in our reactor under the same conditions of the photocatalysis experiment, we employ a theoretical approach based on the Monte Carlo method together with scattering Mie theory similar to that reported by some of us in previous works.[9–12] The model considered here consists of a cylindrical glass reactor with a quartz window (mimicking the one used in the experiment) that contains the TiO_2 nanoparticle suspension under study (Figure C-12), in which each material considered (glass, quartz, water, and TiO_2) is described by the complex refractive index:

$$\tilde{n}(\lambda) = n(\lambda) + ik(\lambda) \qquad \text{Equation C-2}$$

where λ corresponds to the incident wavelength. For the nanoparticle suspension, the volumetric effective medium approximation is considered; it is at this point where the TiO_2 concentration of the suspension under study is introduced into the model together with the agglomerate size (Figure C-10). This approach allows us to follow the trajectory of each photon individually (Figure C-11). These trajectories are described by the Fresnel coefficients at the interfaces and by the Mie theory when the photon interacts with TiO_2 nanoparticles.[9] By monitoring the trajectories of all the photons (Figure C-11), we can sketch the reflectance, transmittance, and absorptance spectra of the system under study (Figure 5-9). Furthermore, the parasitic absorption due to the solvent or the walls of the reactor itself can also be evaluated. Moreover, the information of the trajectories of each photon individually allows us to know the spatial and spectral distributions of the absorption processes (Figure C-14). To ensure the convergence of all these distributions, the system is pumped with 10^6 photons for each wavelength.

C.8 Supplementary figures and tables

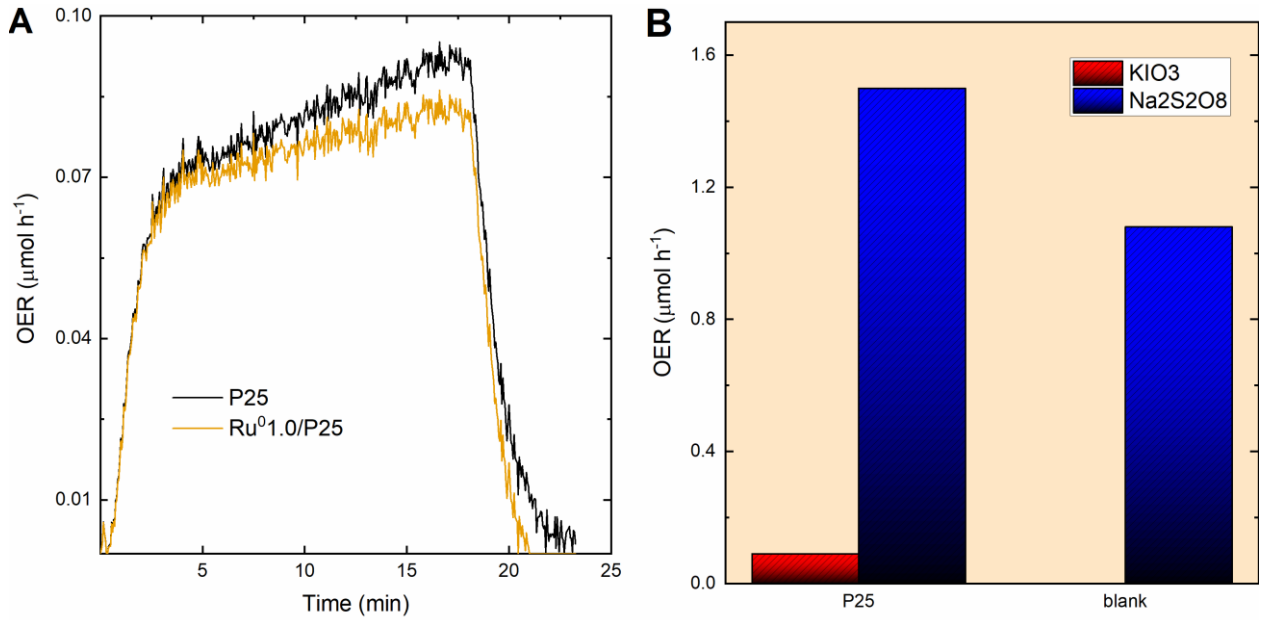

Figure C-1. OER blanks. **(a)** P25 and metallic Ru XPS reference (Ru01.0/P25 – PD) background at typical reaction conditions. Suspension conditions: 5 mg sample, 10 mL water (10 mM KIO3, 0-1 mM TSPP). Other blanks not included due to response below Lower Detection Limit (LDL): 10 mM KIO3 + light; water + light, 10 mM KIO3 + 5 mg nanosilica + light, Ru01.0/P25 – PD + SEA + TSPP + no light (dark or cut-off filter 420 nm). P25 controls during different deposition process without metal precursor were recovered at identical conditions as active samples and tried for activity testing and characterization, with identical response to fresh P25. **(b)** SEA OER response to illumination in the presence (P25) and absence (blank) of photoabsorber. KIO3 (10 mM) condition is AM 1.5G illumination, 10 mL suspension with a concentration of and 1 mM TSPP as dispersing agent for both blank and photoabsorber, and suspension density of 0.5 mg mL-1 for P25. Na2S2O8 (20 mM) condition is a Xe lamp full arc illumination at 150 mW cm-2, 10 mL suspension with no dispersing agent for both blank and photoabsorber, and suspension density of 1 mg mL-1 for P25.

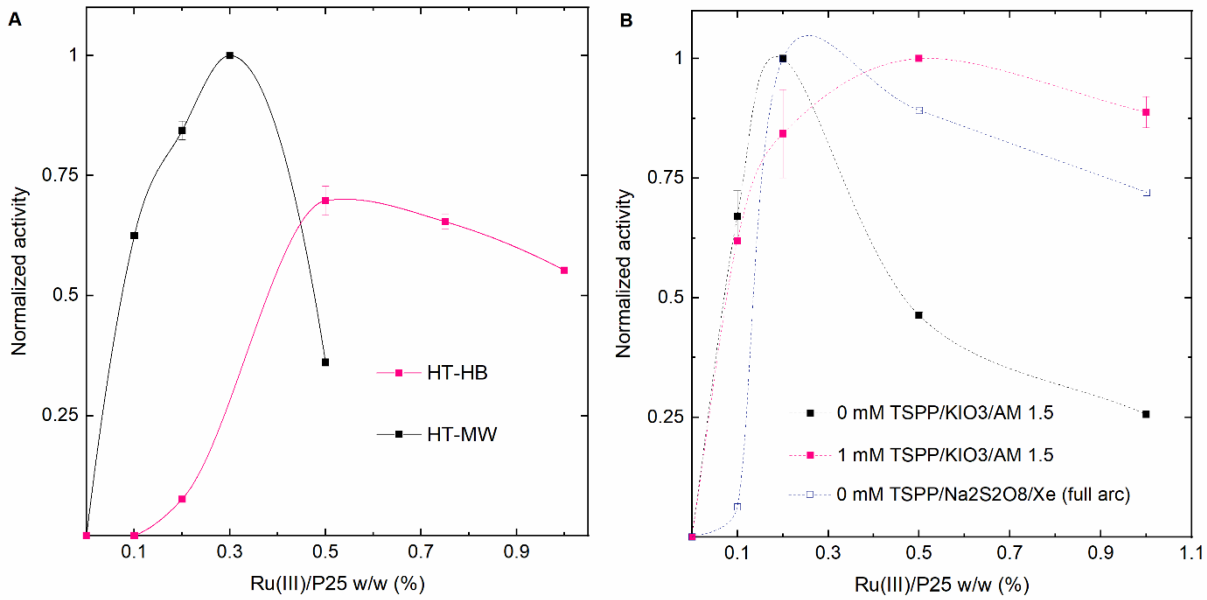

Figure C-2. Ru loading optimization curves. (a) P25 Ex-situ HT deposited P25/RuO2 samples OER activity testing. Suspension conditions: 5 mg sample, 5 mL water (10 mM KIO3, 0 mM TSPP), and full arc Xe lamp illumination (Data points are presented as mean ± SEM of duplicated batches). **(b)** In-situ Ru(III) PD+OER in activity testing setup vs P25. Suspension conditions: 5 mg sample, 10 mL water (10 mM KIO3, 0-1 mM TSPP), and AM 1.5G or full arc Xe lamp (~ 150 mW cm-2) illumination.

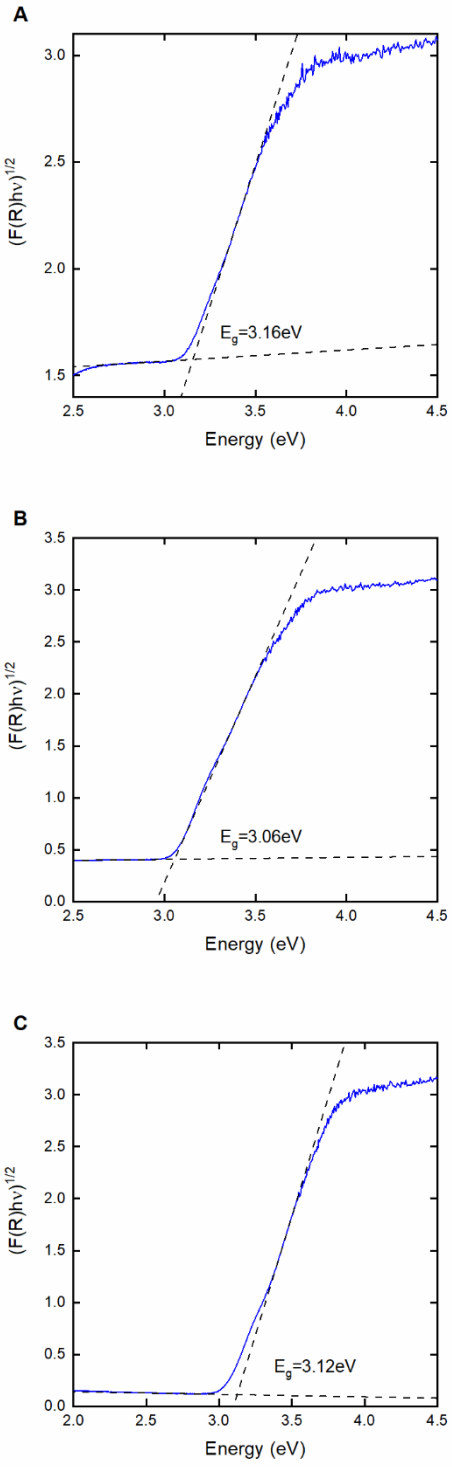

Figure C-3. UV-visible spectra of P25 deposited with RuO2. Tauc plots obtained from diffuse reflectance measurements of samples **(a)** Ru1.0/P25-HT-HB, **(b)** Ru0.15/P25-PD*, and **(c)** P25 control.

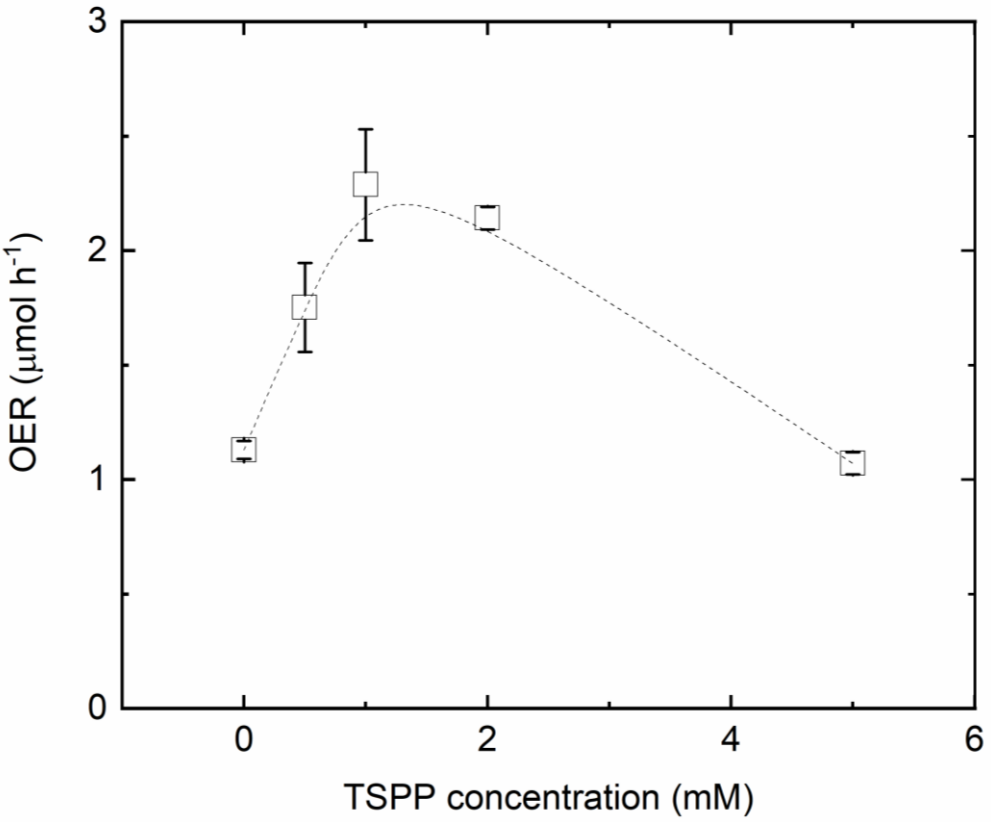

Figure C-4. Dispersant (TSPP) optimization. P25 and reaction media vials were prepared at different levels of TSPP around the optimal precursor Ru loading obtained at 1 mM TSPP (0.5% w/w Ru(III)/P25, 10 mM KIO_3, {0; 0.5; 1; 5} mM TSPP) (Data points are presented as mean ± SEM of duplicated measurements).

Table C-1. ICP-OES Ruthenium contents vs nominal contents. Nominal values are amount of Ru precursor during deposition step. In descending order, the samples correspond to optimal ex-situ PD using dispersing agent (1 mM TSPP); optimal ex-situ PD using no dispersing agent; RuO_2 XPS; and metallic Ru XPS reference. P25 controls displayed no traces of precursor, sacrificial, or dispersant agent. Standard deviation (σ) is presented in % of the mean ICP value.

Sample name	nominal Ru %w/w content	ICP mean %	σ/mean %	Yield %
0.15Ru/P25 – PD*	0.15	0.08	1.22	55
0.15Ru/P25 - PD	0.15	0.08	4.15	52
Ru1.0/P25-HT-HB	1.0	0.43	0.12	43
$Ru^0$1.0/P25-PD	1.0	0.39	0.77	39

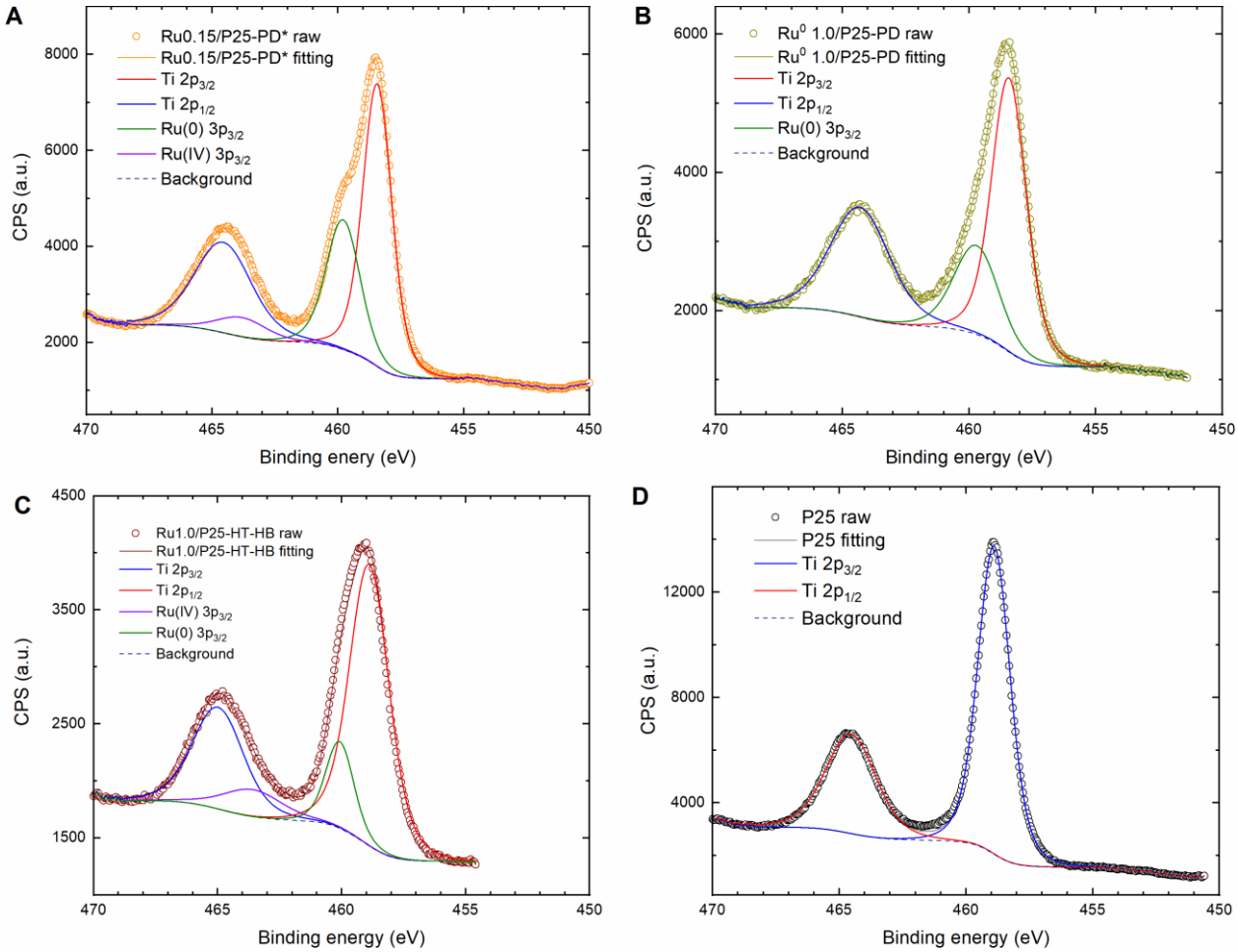

Figure C-5. Full XPS spectra of optimal PD sample, and RuO_2 and metallic Ru references. (a) Ru0.15/P25-PD*, (b) Ru01.0/P25-PD, (c) Ru1.0/P25-HT-HB, (d) P25 control.

Table C-2. XPS quantitative analysis. Calculated from Figure C-5 for Ru containing samples.

	Ru0.15/P25 – PD*	**Ru1.0/P25 - HT-HB**	**$Ru^0$1.0/P25 - PD**
Ru 3p I (position) (eV)	459.7	460.0	459.8
Ru 3p I (area) (a.u.)	4922	1160	3059
Ru 3p II (position) (eV)	463.7	463.5	--
Ru 3p II (area) (a.u.)	1064	758	--

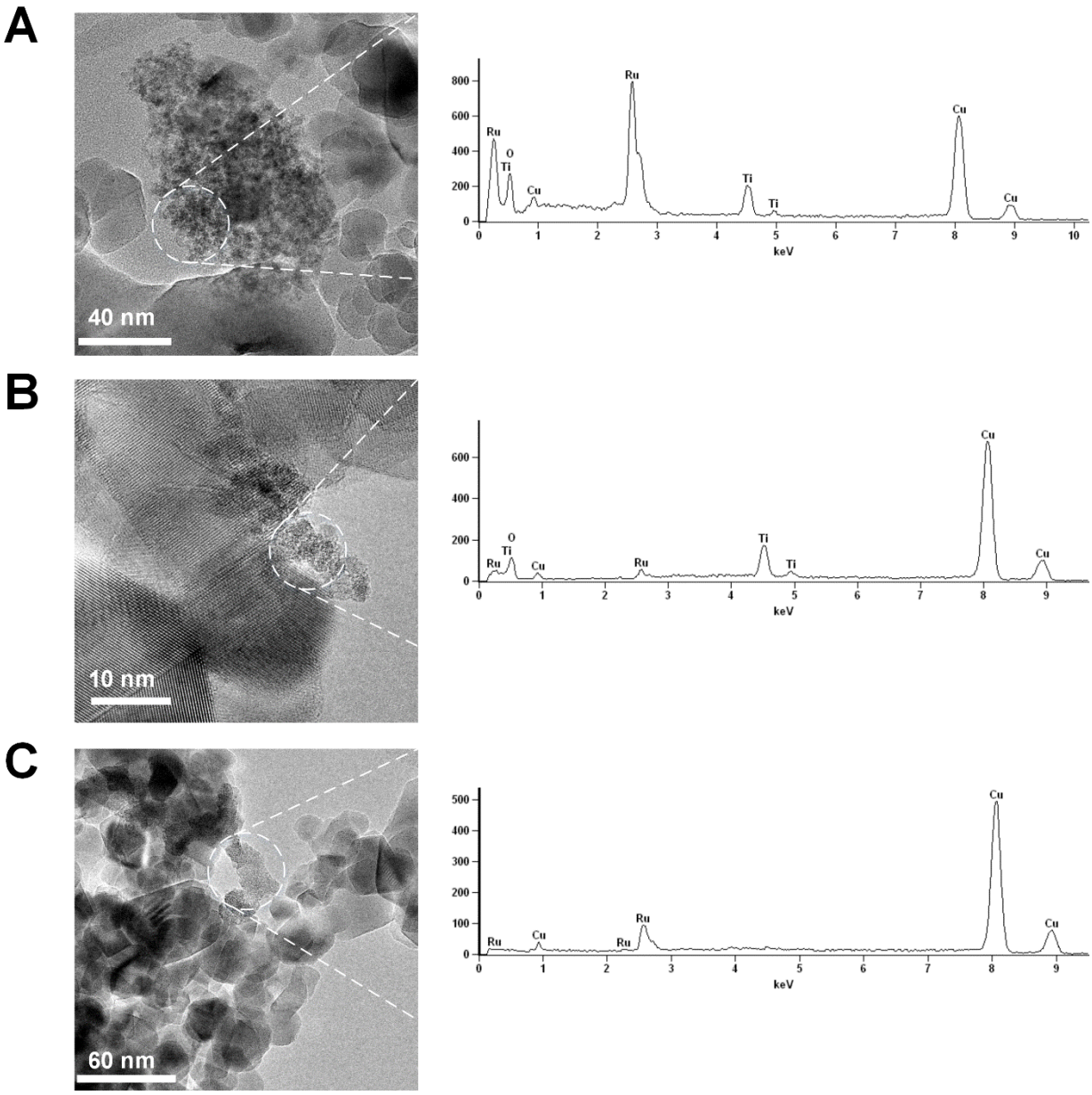

Figure C-6. TEM-EDX raw spectra. **(a)** Ru0 1.0/P25-PD (metallic Ru XPS reference, scale bar: 40 nm), **(b)** Ru1.0/P25-HT-HB (RuO2 XPS reference, scale bar: 10 nm), **(c)** Ru0.15/P25-PD (amorphous metallic Ru zone, scale bar: 60 nm).

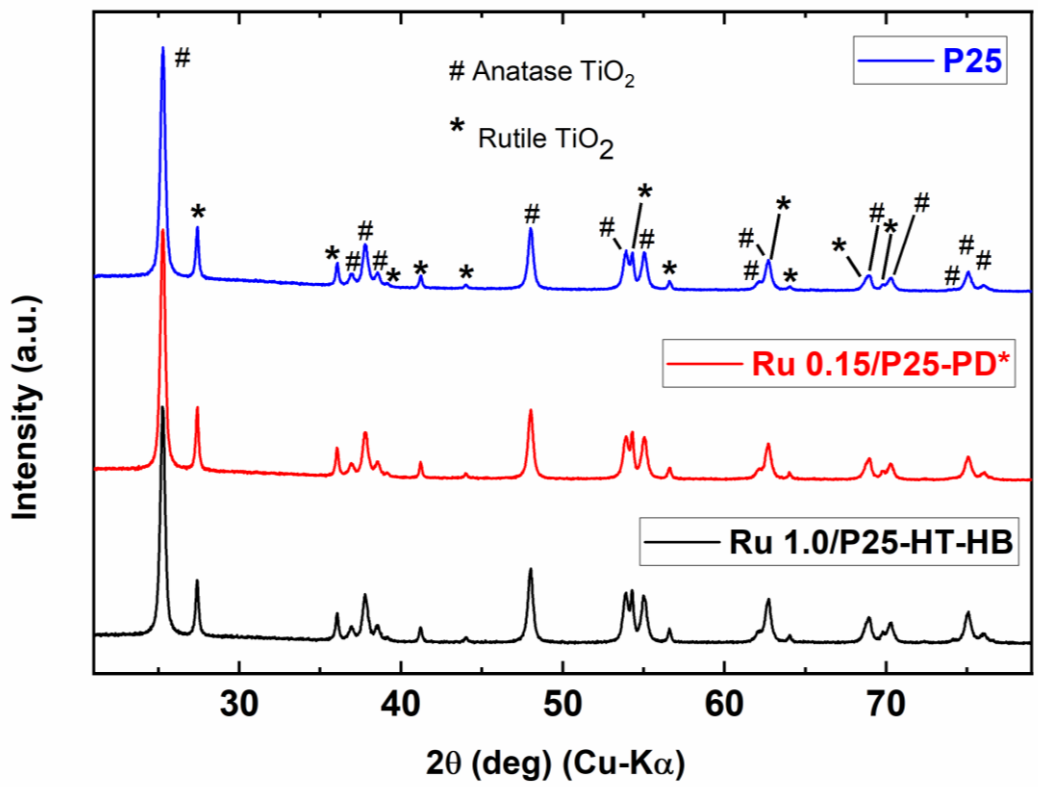

Figure C-7. PXRD pattern of P25 deposited with RuO2. X-ray powder diffractogram of samples Ru1.0/P25-HT-HB, Ru0.15/P25-PD*, and P25 control. Both anatase and rutile TiO2 peaks are marked for P25.

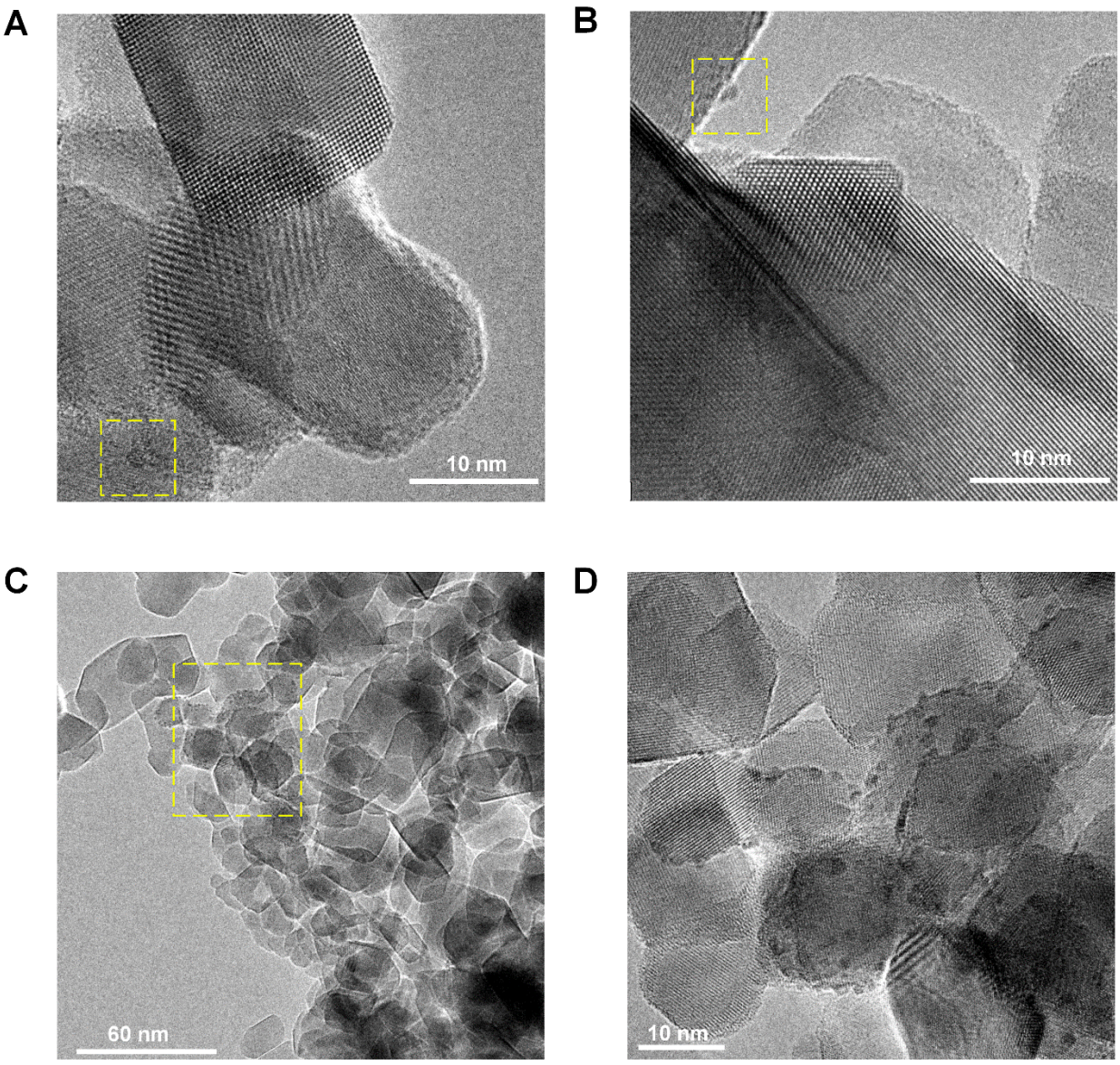

Figure C-8. TEM images of Ru species zones on P25. (a), (b) After ex-situ PD at 0.5 mg mL-1, AM 1.5 filter, and 1 mM TSSP (Ru0.15/P25-PD*, scale bar: 10 nm). **(c), (d)** After ex-situ PD at 0.5 mg mL-1, full arc illumination, and no TSSP (Ru0.15/P25-PD, scale bar: 60 and 10 nm respectively).

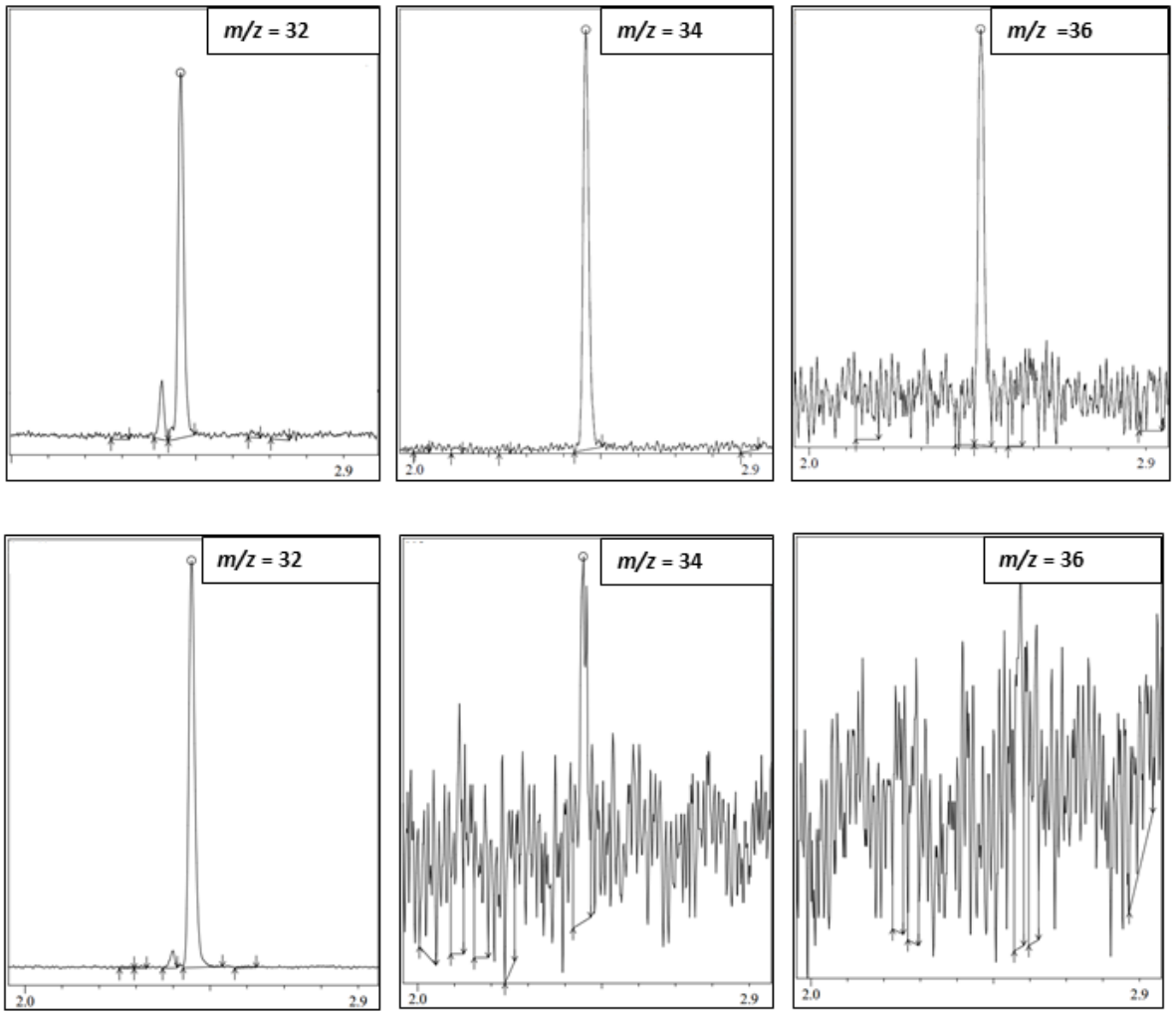

Figure C-9. Raw MS response around O2 GC retention time. m/z = 32 ($^{32}O_2$), m/z = 34 ($^{16}O^{18}O$) and m/z = 36 ($^{36}O_2$) counting peaks at O2 retention time (2.45 min) obtained after 12 minutes of sample illumination, Top row: when using a ratio of 1/3 in weight of $H_2^{18}O$ to H_2O (complement BID quantification), Bottom row: under normal reaction conditions as in Figure 5-7. Integration of peaks is proportional to analyte mass and calibration of MS and quantitative BID detector is considered for ppm calculation. Isotopic distribution is obtained by % of ΔA of the species to total integrated O2 area (A) of channels m/z = 32, 34, 36, where ΔA is obtained subtracting areas measured in dark background.

Table C-3. Ratios of labeled O_2 species (m/z = 34 and m/z = 36) to O_2 normal mass (m/z = 32). Theoretical distribution without Kinetic Isotope Effect (Column: Theoretical no KIE) is predicted using only the mean field approximation (MFA) in molar fraction of labeled water molecules (no KIE). If reaction rate limiting step (RLS) is at the bottleneck predicted by reference literature[59], using a MFA and the ratio $k_{RLS1}/k_{RLS2}\sim(m_2/m_1)^{½}$ for reaction probability correction, a KIE distribution is obtained (Column: Theoretical with KIE). Error columns are calculated in % relative to experimental average observation.

$x/^{32}O_2$	Experimental (average)	Theoretical No KIE	Theoretical KIE	Error % (no KIE)	Error % (KIE)
$^{18}O^{16}O$	0.54	0.67	0.55	18.9	1.2
$^{36}O_2$	0.08	0.11	0.07	31.4	-1.9

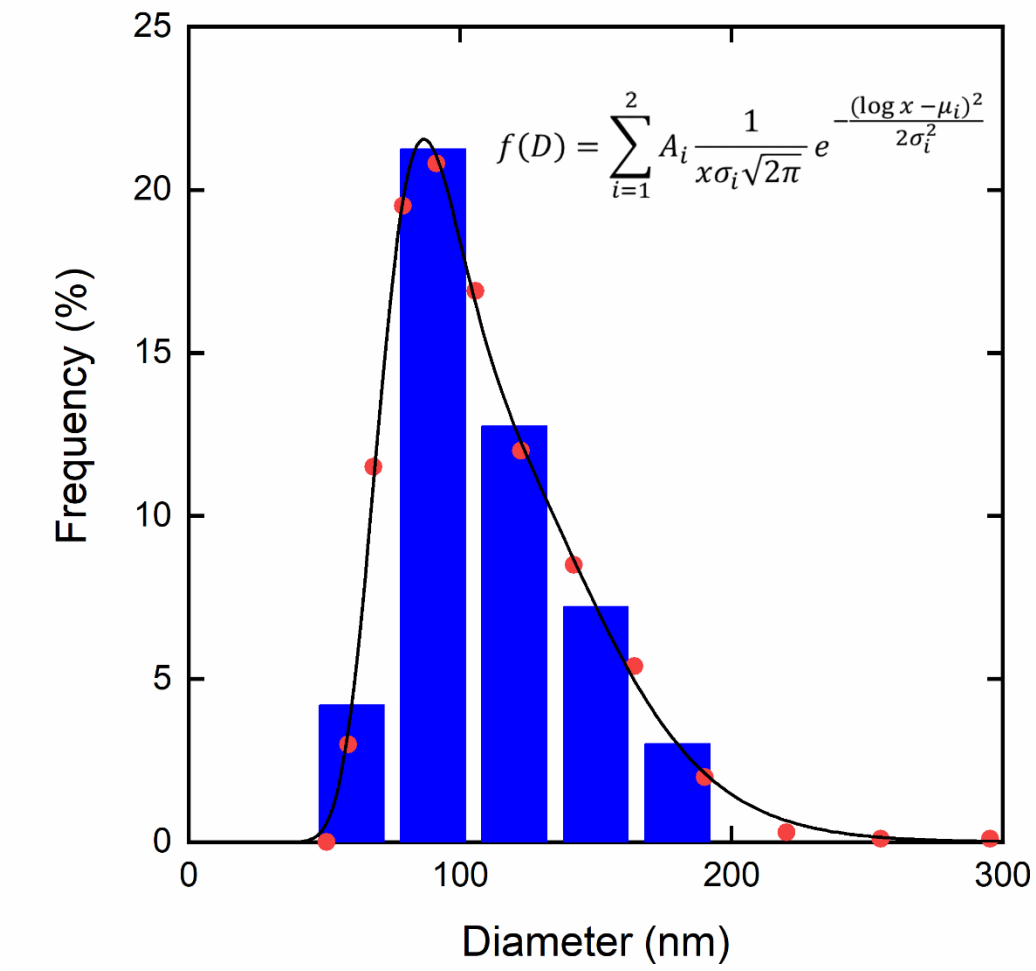

Figure C-10. Redefinition of Dynamic light scattering (DLS) particle size distributions (dots) of Ru0.15/P25-PD* nanoparticles. The solid line is the fit to the double log-normal size distribution f(D) of inset equation. The histogram bars represent the sizes and frequencies used as input for the Monte Carlo calculation of light propagation in the suspension.

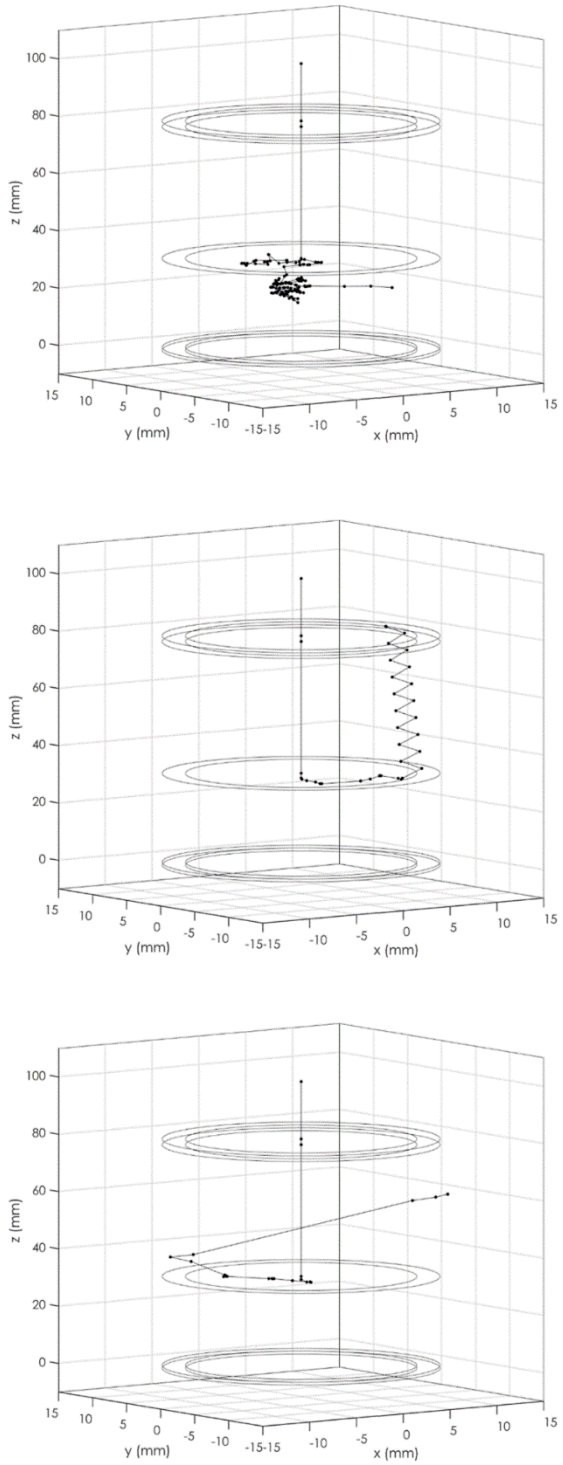

Figure C-11. Photon trajectories in optical modeling. From top to bottom, absorbed, back-scattered and side-scattered. Representation of 80 mm reactor filled with 10 mL of the considered suspension integrating scattering centers with size distribution shown in Figure C-10 and a concentration of 0.01586 vol% of nanoparticles. The photon enters the reactor at z = 80 mm and the interface air-suspension is located at z = 32 mm.

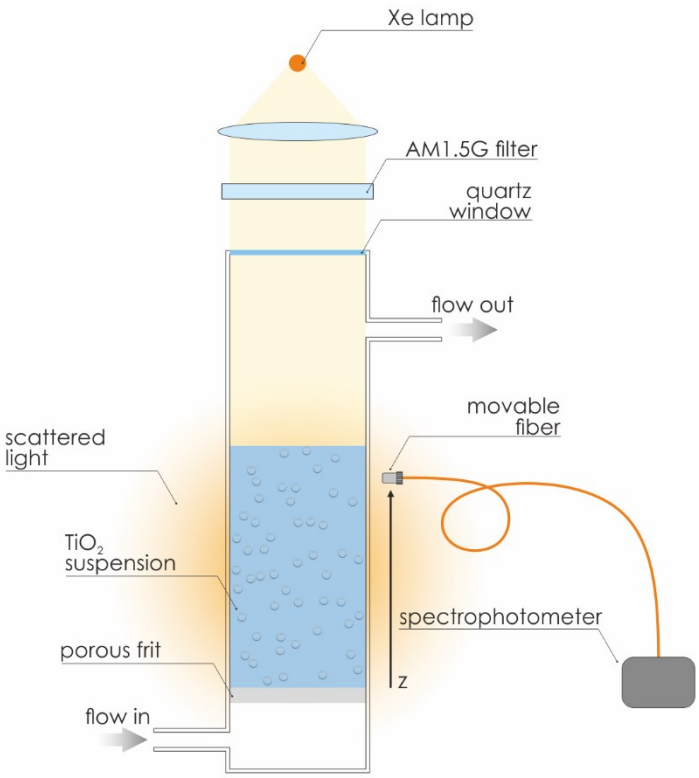

Figure C-12. Quantum efficiency experimental setup.

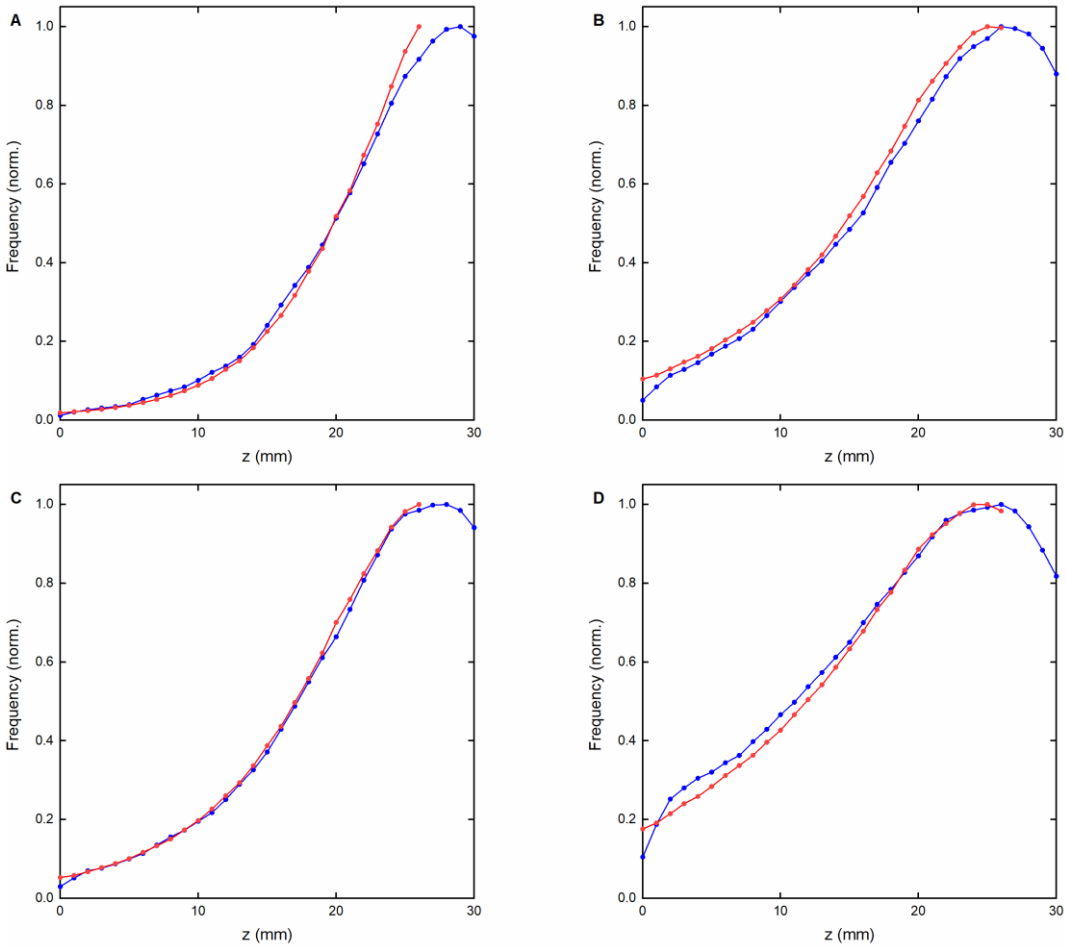

Figure C-13. Experimental (red) and theoretical (blue) distribution of monochromatic scattered light at different wavelengths and positions. **(a)** 400 nm, **(b)** 500 nm, **(c)**, 600 nm, **(d)** and 700 nm. At reactor outer walls as a function of the distance to the air-suspension interface plane, as described in Figure C-12.

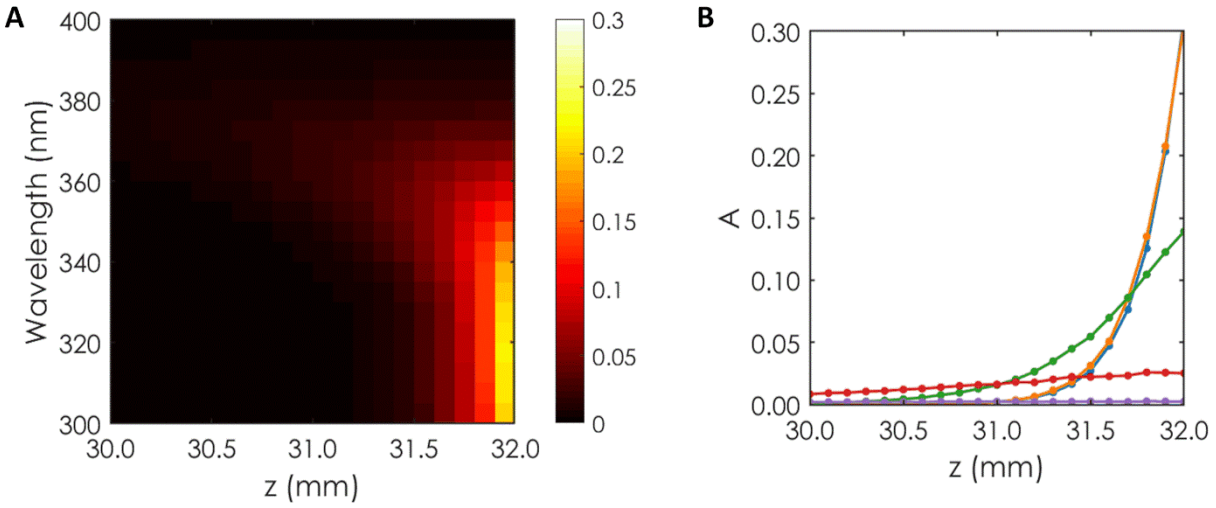

Figure C-14. Modeled solution absorptance vs depth vs wavelength. (a) Contour plot showing the absorption profile as a function of the wavelength of the TiO_2 along an 80 mm reactor filled with 10 mL of the considered suspension integrating scattering centers with size distribution shown in Figure C-10 and a concentration of 0.016 vol%. The air-suspension interface is located at z = 32 mm. **(b)** Absorption profile of some specific wavelengths. λ = 300 nm (blue), λ = 325 nm (orange), λ = 350 nm (green), λ = 375nm (red) and λ = 400 nm (purple).

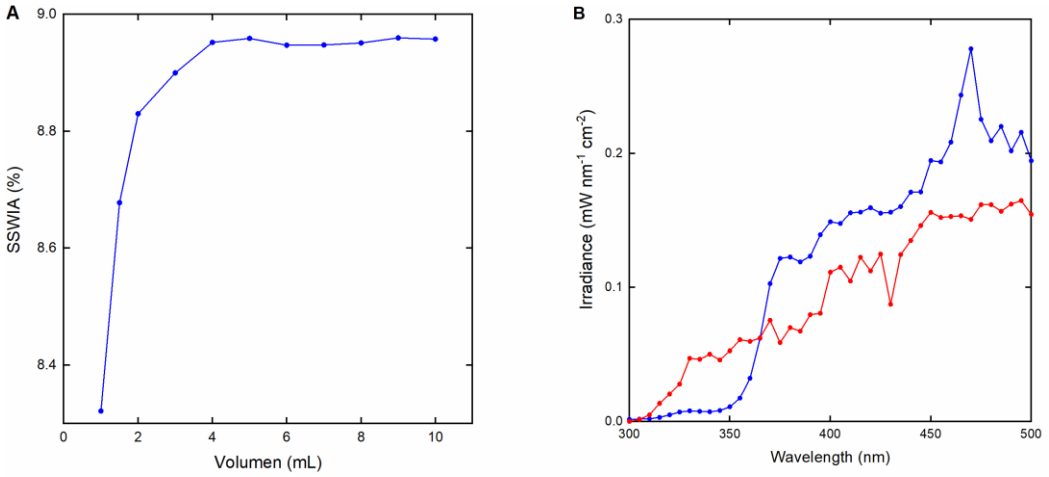

Figure C-15. Incident light and absorbed photon characterization. (a) Predicted Solar Spectrum Weighted Integrated Absorptance (SSWIA) for the real system as function of the suspension volume (point data point at 10 mL had experimental validation by measuring side-scattered light as shown in Figure C-12 and Figure C-13). **(b)** Incident light lamp spectrum (blue) used in the study, together with AM1.5G (ASTM G-173-03) solar irradiance spectrum (red).

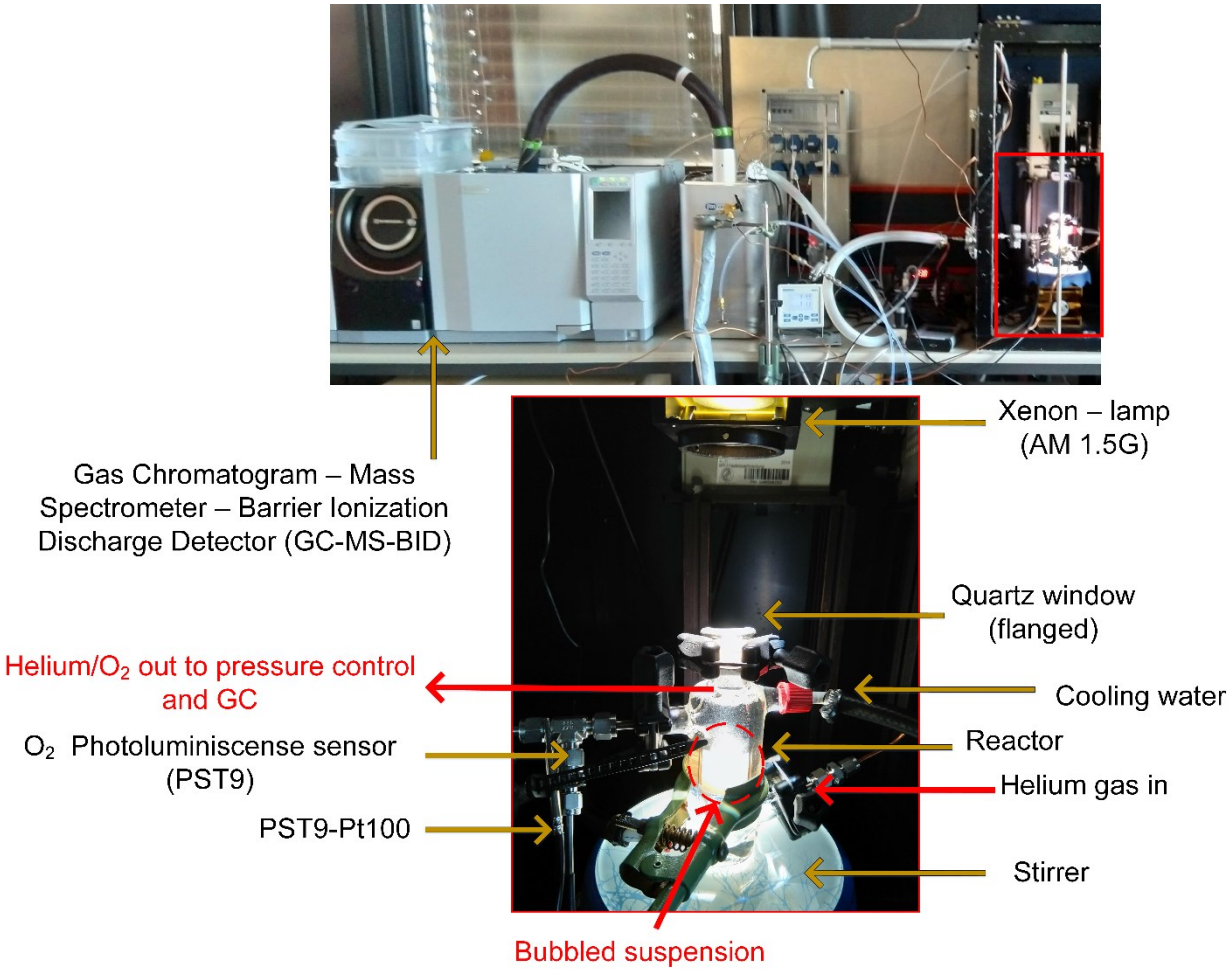

Figure C-16. Photograph of the designed photocatalytic OER continuous flow reactor assembly.

C.9 References

1. Biswal, B. P. *et al.* Sustained Solar H2 Evolution from a Thiazolo[5,4-d]thiazole-Bridged Covalent Organic Framework and Nickel-Thiolate Cluster in Water. *J Am Chem Soc* **141**, 11082–11092 (2019).
2. Laha, S. *et al.* Ruthenium Oxide Nanosheets for Enhanced Oxygen Evolution Catalysis in Acidic Medium. *Adv Energy Mater* **9**, 1803795 (2019).
3. Banerjee, T. *et al.* Single-Site Photocatalytic H2 Evolution from Covalent Organic Frameworks with Molecular Cobaloxime Co-Catalysts. *J Am Chem Soc* **139**, 16228–16234 (2017).
4. Wang, M. *et al.* Low-temperature fabrication of brown TiO2 with enhanced photocatalytic activities under visible light. *Chemical Communications* **52**, 2988–2991 (2016).
5. Morgan, D. J. Resolving ruthenium: XPS studies of common ruthenium materials. *Surface and Interface Analysis* **47**, 1072–1079 (2015).
6. Xiang, G., Shi, X., Wu, Y., Zhuang, J. & Wang, X. Size effects in Atomic-Level Epitaxial Redistribution Process of RuO2 over TiO2. *Sci Rep* **2**, 801 (2012).
7. Lewis, R. S. & Deen, W. M. Kinetics of the Reaction of Nitric Oxide with Oxygen in Aqueous Solutions. *Chem Res Toxicol* **7**, 568–574 (1994).
8. Hernández, S. *et al.* A new method for studying activity and reaction kinetics of photocatalytic water oxidation systems using a bubbling reactor. *Chemical Engineering Journal* **238**, 17–26 (2014).
9. Li, Y. *et al.* Maximized performance of dye solar cells on plastic: a combined theoretical and experimental optimization approach. *Energy Environ Sci* **9**, 2061–2071 (2016).
10. Sudiarta, I. W. & Chylek, P. Mie-scattering formalism for spherical particles embedded in an absorbing medium. *Journal of the Optical Society of America A* **18**, 1275–1278 (2001).
11. Miranda-Muñoz, J. M., Esteso, V., Jiménez-Solano, A., Lozano, G. & Míguez, H. Finite Size Effects on Light Propagation throughout Random Media: Relation between Optical Properties and Scattering Event Statistics. *Adv Opt Mater* **8**, 1901196 (2020).

12. Miranda-Muñoz, J. M. *et al.* Efficient bifacial dye-sensitized solar cells through disorder by design. *J Mater Chem A Mater* **4**, 1953–1961 (2016).

Appendix D. Supplementary and Experimental Section/Methods - Chapter 6

The work in this chapter was reproduced and adapted from the supplemental material of: **Morphology matters: 0D/2D WO3 Nanoparticle-Ruthenium Oxide Nanosheet Composites for Enhanced Photocatalytic Oxygen Evolution Reaction Rates** Hugo Hugo A. Vignolo-González, Andreas Gouder, Sourav Laha, Viola Duppel, Sol Carretero-Palacios, Alberto Jiménez-Solano, Takayoshi Oshima, Peter Schützendübe, Bettina V. Lotsch.

D.1 Materials

Commercial WO_3 nanoparticle powders were used without further purification (Sigma-Aldrich, 99.99%, particle size < 100 nm). For ruthenium oxide nanosheet (RONS) synthesis, Na_2CO_3, Ru and RuO_2 were purchased at standard reactant grade purity from commercial suppliers. For benchmark OER rate standardization, Aeroxide® P25 (formerly TiO_2 Degussa P25) nanoparticles (Evonik, Sigma-Aldrich) were purchased and treated as in our previous work.[1] Tetra sodium pyrophosphate $Na_4P_2O_7 \cdot 10H_2O$ (TSPP, Supelco) was used as dispersing agent for the P25 benchmark (RuO_2/TiO_2 benchmark). $RuCl_3 \cdot H_2O$ (Alfa Aesar, 99.99%) was used as a precursor for the WO_3 impregnation with both of ruthenium oxide nanoparticles (RONP), and in-situ deposition methods on P25 and WO_3. $RuCl_3 \cdot H_2O$ was treated as previously reported and kept as a solution stock (1 mg mL^{-1}).[1] For photocatalytic testing, potassium iodate KIO_3 (Aldrich, 99.5%) or sodium persulfate $Na_2S_2O_8$ (Aldrich, 98%) were weighted right before the experiment together with the sample. Stock solutions for synthesis and photocatalytic screening were prepared with ultrapure water. For dye experiments, Tris(2,2-bipyridyl)ruthenium(II) chloride hexahydrate ($[Ru(bpy)_3]^{2+}$) was purchased from a commercial supplier and stored in dry/dark conditions (Sigma-Aldrich).

D.2 Synthesis and exfoliation of ruthenium oxide nanosheets (RONS)

The nanosheets were prepared by exfoliation of proton exchanged $NaRuO_2$ as described in the literature.[2,3] A mixture of Na_2CO_3:Ru:RuO_2 = 2:1:3 was heated at 900 °C for 12 h under the constant flow of Ar in a tube furnace to obtain $NaRuO_2$ with a small amount of unreacted Ru. The tube furnace was previously baked at 120°C for 1 h and evacuated 5

times with Ar to ensure minimal amount of H_2O and O_2. After baking, the furnace was cooled down to 70 °C and the sample was inserted in an alumina boat at positive pressure, evacuation was repeated with Ar 5 times, and the synthesis temperature ramp started under constant flow of Ar. The $NaRuO_2$ crystallizes in the α-$NaFeO_2$ structure with space group *R*3*m* (no. 166) (*a* = 3.046(8) Å, *c* = 16.377(4) Å), which was tracked with powder X-ray diffraction (PXRD, Figure D-1). The resulting mixture was directly treated with HCl (1 M) solution for five days (daily acid exchange) to obtain a mixture of $H_xNa_yRuO_2 \cdot zH_2O$ and Ru, which was characterized with *Scanning Electronic Microscopy Electron Dispersive Spectra* (SEM-EDX) showing only traces of Na left. According to our previous work, the proton exchanged sample was then shaken in tetrabutylammonium hydroxide (TBAOH) solution (0.02 M, H:TBAOH = 1:2) for 10 days, and ultrasonicated for 30 min daily the first 5 days to obtain a stable dark green colored colloidal suspension of nanosheets. In addition, for exfoliation, two methods were developed using a vortexing device. For preparing extensive amounts of nanosheet colloid necessary for photocatalytic screening, the same solution was first ultrasonicated 15 min, and vortexed overnight at room temperature. The suspension was then ultrasonicated an additional 1 h. This high throughput method had almost identical results in terms of nanosheet size and activity, but with better reproduction, shorter times, and roughly 4 times more material exfoliated. A second method to control the size of nanosheets was performed using the same initial steps of quick ultrasonication and overnight vortexing (8 h) but removing the unexfoliated residues with centrifugation before ultrasonication. In this second method, ultrasonication was then applied separately at different times on using the previously vortexed/exfoliated stock solution. Exfoliation efficiency and nanosheet colloidal size were tracked in-situ with UV-Vis transmission and *Dynamic Light Scattering* (DLS) Measurements, which is later described in this section. The unexfoliated residues, unreacted Ru, and excess TBAOH were separated by repeated centrifugations, when necessary, at 2200 RPM for 30 min at 16 °C, keeping only the supernatant. For samples requiring almost full removal of TBAOH, for example dye photocatalysis experiments, TBAOH was further removed with centrifugation at 22000 RPM for 30 min at 16 °C, discarding supernatant, and repeating the procedure after redispersing the sedimented nanosheets in ultrapure water.

D.3 WO_3 impregnation with cocatalyst

An aliquot of previously exfoliated RONS suspension of a known concentration (~ 0.1 mg mL^{-1}) was poured onto a porcelain dish containing WO_3 powder (50 mg) and ultrapure water (3 mL), and sonicated 5 min at room temperature to form a stable slurry of the nanocomposite (RONS/ WO_3). The slurry pH control was ignored but measured around pH = 8, due to the necessary presence of TBAOH amount to remain RONS stably suspended until the end of the drying off process. Acidic pH adjustment of the slurry is not possible due to the violent precipitation of RONS. The slurry was then dried off while manually stirring on the dish. The temperature at the bottom of the dish was maintained around 100 °C by vapor coming from a water boiling bath, which was heated and stirred on a heating plate. The wet WO_3 impregnation with RONP (RONP/ WO_3) was performed identically but with $RuCl_3 \cdot H_2O$ as Ru source, which was done by replacing the RONS colloid by a $RuCl_3 \cdot H_2O$ stock solution (1 mg mL^{-1}) volume required to produce the desired wt% Ru load. In some cases, a stock of TBAOH solution was also randomly added to the impregnation of RONP/WO_3 samples, to simulate potential effects of TBAOH during impregnation of RONS/WO_3. However, no differences were observed on RONP/WO_3 samples activity when TBAOH was added during impregnation. TBAOH was also added to pure WO_3 for blank impregnation to obtain WO_3 blanks + TBAOH after calcination, showing no traces of carbon in Fourier-transform IR spectroscopy (FT-IR) measurements after calcination (Figure D-3). RONS/WO_3 and RONP/WO_3 impregnated samples were adjusted to nominal %wt Ru/WO_3 loadings of 0.05, 0.1, 0.2, 0.4, 0.6, 1, 2 and 3. ICP-OES elemental analysis was later used to confirm the Ru content of the powders. The nominal Ru loading of RONP/WO_3 samples is calculated from the $RuCl_3 \cdot H_2O$ aqueous stock solution concentration (1 mg mL^{-1}), and the adjusted volume of this stock that is added to WO_3. The nominal Ru loading of RONS/WO_3 samples is obtained similarly, but the RONS colloid concentration is estimated from UV-vis transmission measurements performed in-situ before the WO_3 impregnation, procedure which is described at the end of this section. Finally, samples were scratched out to a mortar, finely ground with a pestle, and calcinated at 400 °C for 1.5 h. PtO_x and $RuO_2 \cdot H_2O$ samples were produced similarly but following literature conditions.[4–6] PtO_x impregnation was performed identically at different cocatalyst loadings, but using H_2PtCl_6 as precursor, and calcinated at 550 °C for 2 h. The WO_3

impregnation with $RuO_2 \cdot H_2O$ was identical to RONP, but the fine powder collected from the mortar was dispersed in 25 ultrapure water and centrifuged at 22000 RPM for 20 min to wash Cl^- ions out. Then the sample was dried in vacuum oven at 50 °C with no calcination step.

D.4 Sample characterization

UV-Vis diffuse reflectance spectroscopy (Cary 5000, Agilent) of powders for band gap calculations, *inductively coupled plasma – optical emission spectroscopy* (ICP-OES) elemental analysis (Vista Pro Axial, Varian), and FT-IR spectra (PerkinElmer UATR TWO) were performed as previously reported by our group.[1,2,7]. For *transmission electron microscopy* (TEM), powders were ground and suspended in butanol, distributed onto a holey carbon/copper grid, and studied with a Philips CM 30 ST microscope (300 kV, LaB6 cathode). Images were taken with a TVIPS TemCam-F216 CMOS Camera. The program EM-Menu 4.0 Extended was used to perform TEM-*fast Fourier transform* (TEM-FFT). *TEM-energy dispersive X-ray* spectroscopy (TEM-EDX) was performed with a Noran System Seven [NSS] Si(Li) detector. *Dynamic light scattering* (DLS) measurements and *surface zeta-potential* were performed using a Malvern Zetasizer-Nano equipment. In DLS mode, 13 runs per measurement are recorded after full decay of the measured auto-correlation function, and after ensuring suitable polydispersity. RONS (0.1 mg mL^{-1} and 0.03 mg mL^{-1}) and WO_3 (0.5 mg mL^{-1} and 2 mg mL^{-1}) suspensions were prepared under impregnation conditions with 5-minute ultrasonication. Mixtures of RONS and WO_3 were freshly prepared prior measurements in duplicates. TBAOH residues were washed out from RONS by means of centrifugation (RONS*). In *zeta potential* mode, 100 runs per measurement were recorded to get a zeta-potential distribution. WO_3 (0.5 mg mL^{-1}) and RONS (0.1 mg mL^{-1}) suspensions were prepared with a solution of ultrapure water and NaCl (10 mM). Suspensions were freshly prepared in duplicates and ultrasonicated for 5 min before the measurements. HCl or NaOH stock solutions were added for pH adjustment (Mettler Toledo seven compact for pH gauge). *Powder X-ray diffraction* (PXRD) patterns were collected at room temperature on a laboratory powder diffractometer in Debye-Scherrer geometry (Stadi P-Diffraktometer [Stoe]), Mo-Kα1 radiation from primary monochromator. The samples were sealed in 0.2 mm diameter borosilicate glass capillaries (Hilgenberg

glass No. 0140), which were spun during the measurements. Each pattern was measured in a 2θ range from 5° to 40° (0° to 90° for WO_3 samples) applying a total scan time of 1 h. *X-ray photoelectron spectroscopy* (XPS) measurements were carried out in a Thermo VG Thetaprobe system (Thermo Fisher Scientific, USA) employing Al Kα radiation (hv = 1486.68 eV) produced with an electrical power of 100 W. The X-ray spot size on the sample was about 1 cm in diameter. The analyzer aperture circle on the sample was approx. 1 mm in diameter. During measurements, the base pressure of the XPS was $1x10^{-9}$ mbar. To compensate for possible peak shifts originating from surface charging, we use Ar ions from a flood gun. The necessary Ar flux inlet was set to a chamber pressure of $3x10^{-7}$ mbar. Survey spectra were recorded with a pass energy of 200 eV and more detailed spectra were carried out with a pass energy of 50 eV and step width of 0.05 eV. The C 1s and the O 1s peaks were measured with 60 scans. All binding energies were calibrated with respect to the C 1s peak position at 285 eV. The measurements were fitted using the fitting routines included in the XPS software Avantage and CasaXPS.

AFM of ruthenium oxide nanosheets (RONS). Atomic force microscopy (AFM) topography measurements on the nanosheets were performed with an MFP-3D Standalone AFM (Asylum Research) operated in tapping mode. The dimensions of the nanosheets were analyzed via the software Gwyddion (2.55) by applying a height filter of 5 nm.

SEM and SEM-EDX of RuO_2 nanosheets. *Scanning electron microscopy* (SEM) and *energy dispersive X-ray spectroscopy* (EDX) analysis was performed to track Na content of RONS precursor before and after proton exchange ($NaRuO_2$ and $H_xNa_yRuO_2 \cdot zH_2O$). This was performed as in our previous publication.[2] SEM and SEM-EDX analysis of exfoliated RONS and RONS impregnated on WO_3 ($RONS/WO_3$) was performed on a Merlin instrument (Zeiss) equipped with an Ultim Extreme detector (Oxford). Images and EDX spectra were obtained at 1.5 kV and 5 kV, respectively.

D.5 Optical characterization details

Optical characterization of RONS colloids for impregnation. Concentration of RONS colloids was estimated with UV-Vis spectroscopy (Cary 60, Aglient). To correlate in-situ measured

transmittance (T) of RONS colloids for the WO_3 impregnation with the RONS colloid concentration, an initial calibration was performed. This calibration consists of the following: after complete exfoliation, at first a RONS colloidal suspension was centrifuged at 2000 RPM for 30 min to remove unexfoliated RONS residues. The centrifuged stock volume (~20 mL) was divided in two. One half of the suspension volume was drop-casted onto Ti wafers in triplicate, dried-off at 120 °C, and calcinated for 2 h at 400 °C. The Ti wafers were weighed before and after drop-cast to calculate the average of initial RONS suspension concentration (C_0, subtracting TBAOH calculated residue). The other half of the suspension volume was measured in transmittance (T) in the range of 300-800 nm in a 3 mL quartz cuvette (1 cm x 1 cm x 3 cm). Dilutions of the suspension were consecutively measured in T until the difference with a background transmittance (T_0) was only 1%. T_0 was obtained from a blank cuvette containing only 3 mL of ultrapure water and TBAOH (20 mM) (Figure D-4a). Given that RONS colloids are translucid, light absorption through the colloid was approximated to Lambert- Beer Law (1 cm optical path length). Absorbance is defined as $-\text{Log}_{10}(T/T_0)$ at $\lambda=365 \pm 5$ nm. This calibration was performed for two independent synthesis batches of RONS. Molar absorption coefficients (ε) can be obtained from a linear fit with the previously measured C_0 (Figure D-4b). The average of ε = 471 mL mg^{-1} cm^{-1} was assigned for later RONS exfoliated batches used for impregnation. With measurements of T and aforesaid calibrated ε, the RONS suspension concentration was estimated in-situ for each exfoliated batch, and the aliquot volume for impregnation on WO_3 was set according to the desired nominal cocatalyst loading (%wt Ru). RONS/WO_3 and RONP/WO_3 cocatalyst nominal loadings were corroborated later with ICP-OES elemental analysis (Figure D-4c).

Optical characterization of RONS, RONS/WO_3 and RONP/WO_3 for photocatalysis. Suspension absorptance ($A(\lambda)$ = 100% - (%$T(\lambda)$ + %$R(\lambda)$)) of RONS colloids, and RONS/WO_3 and RONP/WO_3 samples was measured with UV-Vis spectroscopy, with an integrating sphere in absorption mode (Cary 5000, Agilent). For WO_3 composites, a suspension volume (10 mL) was prepared at same conditions as in photocatalysis (10 mM KIO_3, 0.5 mg mL^{-1}), and sonicated for 5 min. A volume of this suspension (3 mL) was then transferred into a quartz cuvette (1 cm optical depth), and measured $A(\lambda)$ in the range of

300-800 nm. Background for absorptance ($A_0(\lambda)$) was measured with a blank cuvette containing only ultrapure water and KIO_3 (10 mM). For pure RONS colloids, $A_0(\lambda)$ was estimated with a blank cuvette containing only ultrapure water and TBAOH (20 mM). The pure RONS colloid suspension concentration was adjusted from a stock of a known initial concentration (~ 0.5 mg mL^{-1}), to reach an equivalent Ru concentration in suspension as in the cuvettes containing impregnated RONS/WO_3 suspensions. RONS/WO_3 samples are confirmed their Ru content by ICP-OES elemental analysis (Figure D-4c). Such Ru adjusted suspension densities of pure RONS colloid are then abbreviated as the nominal cocatalyst load of RONS/WO_3 samples in %wt Ru, like in Figure D-16, Figure D-17, and Figure 6-4c. Absorptance of Ru species ($A_{Ru}(\lambda)$) can be calculated directly as $A_{Ru}(\lambda) = 1- (1 - A(\lambda))/(1 - A_0(\lambda))$ for pure RONS colloids. Likewise, in the wavelength range of 500 to 800 nm, absorptance of Ru species on RONS/WO_3 and RONP/WO_3 samples can be calculated from the measured $A(\lambda)$ and the $A(\lambda)$ of bare WO_3 ($A_{WO3}(\lambda)$). $A_{WO3}(\lambda)$ at different bare WO_3 suspension densities used for background subtraction (0.5 mg mL^{-1}) is presented in Figure D-17a. In the wavelength range of 300 to 500 nm light absorption on WO_3 takes place. $A(\lambda)$ of RONS/WO_3 and RONP/WO_3 samples like in photocatalysis (10 mM KIO_3, 0.5 mg mL^{-1}) is presented in Figure D-17b considering the wavelength range of 300 to 500 nm, and WO_3 light absorption. We do not deconvolute this simultaneous cocatalyst and WO_3 light absorption. Instead, we extrapolate the average fraction of cocatalyst light absorption of RONP/WO_3 and RONS/WO_3 samples obtained by UV-Vis in the wavelength range of 500 to 800 nm (Figure D-16a). This fraction is defined as f_{RuO2}. For such extrapolation to photocatalysis conditions (~ 400 to 500 nm), we take into consideration the light absorption behavior of pure RONP and RONS. From optical modelling of pure RONP (Figure D-18c), we expect that the experimentally measured RONP average light absorption between 500 and 800 nm (Figure D-16a) will roughly decrease 5% between 400 and 500 nm. UV-Vis experiments performed on pure RONS show that the average light absorption between 500 and 800 nm will roughly increase 40% (i.e., at 3 %wt Ru) between 400 and 500 nm (Figure D-17c). We then assume that f_{RuO2} of RONP/WO_3 and RONS/WO_3 samples measured between 500 and 800 nm (Figure D-16a), will have the same relative increase at the wavelength range of 400 to 500 nm as their pure cocatalyst components. The probability of parasitic light absorption in photocatalysis is then approximated to this

estimation of f_{RuO2} at the wavelength range of 400 to 500 nm. This approximation does not calculate the actual fraction of light absorption on the WO_3, nor the different suspension geometries used in photocatalysis experiments. Regardless these simplifications, the f_{RuO2} presented in Figure 6-4c (400 to 500 nm) is still a valid estimation of the highest possible probability of parasitic light absorption in photocatalysis — the experimentally measured f_{RuO2} in the absence of light absorption on WO_3 can only decrease when the latter is present.

Optical modelling of photon fate. In a first scenario, photon absorptance after interaction with pure RONS or RONP is modelled to describe the difference in absorptance observed between pure RONS and RONP/WO_3 samples at equivalent Ru suspension concentration (Figure D-16b). This modelling ignored the presence of WO_3, and consisted of estimating the absorptance of individual RONP and RONS, by means of Finite Difference Time Domain (FDTD) numerical simulations, using the reported refractive index (n) and absorption coefficient (k) of RONP and RONS,[8,9] and presented in Figure D-18a and Figure D-18b, respectively. The RONP and RONS geometry used for absorptance simulation corresponds to the average of their observed dimension in TEM and SEM images (RONP: spheres of 5 nm radius, RONS: 500 nm x 500 nm x 1 nm sheet). The obtained absorptance of each nanostructure was then normalized by volume of material simulated. To compute the absorptance (defined as the fraction of source power absorbed in volume) of individual RONS and RONP, we employed FDTD numerical simulations by using the commercial software Ansys FDTD Lumerical. An FDTD simulation box of 1200 x 1200 x 1200 nm^3 was considered, and an auto-non uniform mesh accuracy of 4 with a conformal variant 1 mesh refinement type was set. Symmetry boundary conditions were applied along the x and y directions, while stretched coordinate perfect-matching layers (PML) with 24 layers and a standard profile along the direction of illumination in the z-axis were used. To avoid instabilities, the override simulation bandwidth for mesh generation was enabled and fixed to the operation wavelength. The Advanced Method with a Pabs_adv monitor of a fixed size was applied to both the computation of the absorptance of individual RONS and RONP so that a direct comparison of the optical properties of the two structures is possible. Within this approach, the absorptance is calculated as $P_{abs}=-0.5\ \omega|E|^2\ \mathrm{imag}(\varepsilon)$, with ω

being the angular frequency, $|E|^2$ the intensity of the electric field, and imag(ε) the imaginary part of the corresponding permittivity, defined as imag(ε) = 2·n·k. Finally, nanostructures were illuminated with a Total-Field Scattered-Field (TFSF) source impinging at normal incidence on either a RONS placed perpendicularly along the x-y plane, or a RONP in air. For the RONS, a mesh override region of 0.08 nm along the z-direction based on the nanostructure with a buffer of 2 nm was considered, while for the RONP, the mesh override region was applied along the three directions and fixed to 0.1 nm with a buffer of 10 nm. The resulting absorptance after volume normalization is presented in Figure D-18c.

In a second scenario, photon scattering angular profiles after interaction with WO_3 nanoparticles are modeled to describe the difference in absorptance observed between pure RONS and RONS/WO_3 samples at equivalent Ru suspension concentration (Figure D-16c). Modelling of scattering angular profiles consisted of simulated stochastic photon trajectories using the reported complex refractive index of WO_3.[1,10–13] This model assumes only aqueous media around the WO_3 nanoparticles, and an arbitrary 180° reference for the photon incidence. The WO_3 optical properties used in this model are presented in Figure D-19. We ignore in this scenario that the presence of RONS or RONP may distinctively influence the calculated scattering and light absorption cross section on bare WO_3 (Q_{sc} and Q_{abs}, Figure D-19b and Figure D-19c). Therefore, in this scenario, we restrict the following analysis only to the fraction of scattered light by WO_3 and its potential interaction with a RONS or RONP based on geometrical aspects. The model's extrapolation describing the difference in bias between the RONS/WO_3 and RONP/WO_3 geometries are described in Figure D-20a, which illustrates the probability of forward scattering in RONS/WO_3 composites. The forward scattering probability was calculated using the angular profiles in Figure D-19d, assuming the limiting and simplified case described in the top panel of Figure D-20a. This is, a WO_3 NP centered on the RONS surface, a large RONS lateral size and a photon incidence angle of 180° (angular sweep from 270° to 90°). We calculate then the average forward scattering probability after simulating multiple scattering events using this simplified model, which is presented in Figure D-20b for different wavelengths and WO_3 nanoparticle size. However, the angular sweep for integration depends on three variables: the actual photon incidence angle, the relative

position of the WO_3 NP on the RONS surface, and the RONS geometry. We alternatively calculated then the average forward scattering probability after simulating multiple scattering events at different random values for those three variables, which showed no observable difference to the results presented in Figure D-20b.

D.6 Photo- electrocatalysis experimental details

Photocatalysis setup. Photocatalytic reactions were performed in a bubbled glass cell with a top quartz optical window identical to our group's previous publication, coupled to the same Gas Chromatography (GC) analytics equipped with a Barrier Ionization Discharge (BID) and Mass Spectrometer (MS) detectors (Shimadzu-JAS autosampler + Shimadzu GCMSBID QP-2020), plus the redundant O_2 photoluminescence flow through sensor (Presens PST9) in between reactor and GC sampling line.[1] Two reaction cells were employed. The high throughput cell has a total volume of 24 mL (Height: 8 cm, radius: 0.9 cm, maximum suspension volume of 10 to 12 mL), and an incident light resulting from an attenuated AM 1.5G spectrum at the gas-liquid interface provided with a AAA solar simulator (Newport 94023A). The high throughput cell operated at a 35% lower attenuated integrated intensity from the original AM 1.5G spectra (65 mW cm^{-2}), preserving the original AM 1.5G normalized spectral distribution and homogeneity as it can be seen in Figure D-24. The finer optics cell has a total volume of 50 mL (Height: 8 cm, radius: 1.3 cm, maximum suspension volume of 12 to 14 mL), and same illumination but at nominal integrated power (100 mW cm^{-2}, Figure D-24). The in-flow of Helium 4.6 purity was controlled with mass flow controller (Bronkhorst low dP series), and at the headspace the over-pressure is maintained in continuous flow (0.15 barg) with a back-pressure flow controller (Brooks SLA5820 + 0251 PLC-Power supply). This cell is jacketed and temperature controlled (25 °C) with water from a thermostat and recirculator (LAUDA ECO RE 415 S). Helium in-flow (99.996% purity) setpoints are maintained ensuring rapid liquid-to-gas mass transfer, fast response at detectors, and according to material activity (20 to 40 NmL min^{-1}).[1] Prior to experiments, the reactor is evacuated without suspension 6-times ensuring the headspace maximum gas purity, then the suspension is introduced under positive pressure and high flow, bubbled through for a minimum of 15 min, and then the baseline was recorded. After the signal of the PST9 instrument asymptotically reaches a

stable minimum readout (5 ppmv, purging rate < 0.2 ppmv min^{-1}), illumination and GC dark sampling starts. After illumination, the O_2 headspace concentration becomes steady in around 2 to 5 min, the moment at which the maximum OER is recorded with the PST9 instrument and contrasted with a second GC point obtained after 12 min of illumination. Detection limits at the lowest flow of Helium are 0.05 µmol h^{-1} for PST9, and 2 µmol h^{-1} for GCMSBID. In all reported statistics of OER measurements (for example Figure 6-3a and Figure 6-4c), when detection limits allow redundant quantification, both GCMSBID and PST9 readouts are averaged in the calculation of error bars. Then the online OER rates are calculated by mass balance of oxygen in the system in steady state according to

$$r_{O_2} = \frac{F_{in} \times \Delta x_{O_2 ppm} \times 10^{-6}}{\left(1 - \Delta x_{O_2 ppm} \times 10^{-6}\right)} \qquad \text{Equation D-1}$$

F_{in} : Controlled molar Helium (99.996% purity) in flow in (mol h^{-1})

r_{O2} : Total OER production rate in (10^{-6} µmol h^{-1})

$\Delta x_{O2,ppm}$: Oxygen molar fraction delta at the reactor outlet, measured immediately with PST9 sensor and downstream a splitter with GCMSBID. The delta is the raw readout measured after illumination less the measured baseline in dark right before illumination.

Photonic efficiency experiments. Suspensions were prepared using ultrapure water (10 mL), sample powder (5 mg of RONS/WO_3 or RONP/WO_3) and KIO_3 (10 mM). DLS measurements determined that WO_3 agglomerate size is below 1 µm when its particle concentration in ultrapure water is less than 0.5 mg mL^{-1} after calcination. A concentration of 0.5 mg mL^{-1} of photocatalyst was set as the nominal suspension concentration for all experiments using WO_3 as the light harvester support to avoid agglomeration influences in optics. For the RuO_2/TiO_2 benchmark, ex-situ deposited sample was prepared according to our previous work.[1] The RuO_2/TiO_2 benchmark measurements were performed with the sample dispersed in ultrapure water containing (5 mg, 10 mL), KIO_3 (10 mM), and TSPP (40 mM). Suspensions were ultra-sonicated for 15 min before injection at mild overpressure to the previously purged photocatalytic reactor with helium. The light was

turned on together with the first point taken in dark by the GCMSBID autosampler in case of complementary measurements. Then the delta of O_2 was tracked online with the PST9 sensor and the GC autosampler kept measuring under with GC analysis time of 10 min. After illumination, the maximum recorded r_{O2} in time for each sample was then used to estimate photonic efficiency of the sample according to

$$\xi_e(\lambda_i, \lambda_j)\% = \frac{4 \times r_{O_2}}{I_0(\lambda_i, \lambda_j)} \qquad \text{Equation D-2}$$

$I_0(\lambda_i, \lambda_j)$: Incident photon rate at a specified wavelength range between λ_i and λ_j (i.e. 10^{-6} μmol of photons h^{-1}, or 10^{-6} E h^{-1}). Presented in Figure D-24.

Optimal photonic efficiency (ξ_e) is defined when the addition of more sample suspension produces no further increase in measured r_{O2}. When both cells are filled with 10-12 mL suspension, light attenuation is roughly asymptotic, the condition used in our previous work to define ξ_e of the sample (or alternatively optimal photocatalytic rate r_{opt}). [1] In Figure D-23a where the full trend of ξ_e is presented, reactions were performed at stepwise addition of suspension volume into the finer optics cell, with reactor moved up/down to keep nominal irradiance and recording r_{O2} at each level. In the case RuO_2/TiO_2 benchmark is performed in a specific cell, the ξ_e of different samples can be normalized for comparison with other samples measured in other reactor geometries, for example among different laboratories, to obtain a relative optimal photonic efficiency (ξ'_e), as

$$\xi'_e(\lambda_i, \lambda_j) = \left. \frac{r_{opt,x}}{I_{0,x}(\lambda_i, \lambda_j)} \middle/ \frac{r_{opt,0}}{I_0} \right. \qquad \text{Equation D-3}$$

I_0 : Incident photon rate for OER benchmark at near AM 1.5G conditions

$I_{0,x}(\lambda_i, \lambda_j)$: Incident photon rate for a material x to be normalized, at a specified wavelength range between λ_i and λ_j . Equal to I_0 if AM 1.5G is also used for material x.

Error bars in graphs containing ξ_e and other photocatalysis indicators represent *mean ± standard error of the mean* of the activity of two independent batches of sample. The value of activity for each batch of sample is the average of two duplicated photocatalytic OER rate measurements on the same batch (including redundant GC measurements when possible). Typical instrumental error in photocatalytic OER rate measurements is around ± 3%. In the case of synthesized ruthenium oxide nanosheets (RONS), each synthesis batch has an additional replica of the wet WO_3 impregnation for activity measurements.

Apparent Quantum Yield (AQY). Suspensions were prepared using ultrapure water (10 mL), sample powder (5 mg of RONS/WO_3 or RONP/WO_3) and KIO_3 (10 mM). Then, r_{O2} was tracked by inserting a cut-on filter on top of the Quartz window, whose change in illumination spectra is presented in Figure D-24. The order of the cut-on filters installed was 550, 495, 445, 420, 395 and 330 nm. The subtraction of consecutive filters power distribution is used to calculate the representative λ of the band, and the incremental photon counting and r_{O2} were used to obtain the external efficiency according to

$$AQY(\lambda)\% = \frac{4 \times r_{O_2}}{I_0(\lambda)} \qquad \text{Equation D-4}$$

$I_0(\lambda)$: Incident photon rate at a specified wavelength λ (i.e. 10^{-6} μE h^{-1})

The incident photon rate $I_0(\lambda)$ (in 10^{-6} μE h^{-1} units) can be calculated for a wavelength band (for photonic efficiency or AQY) as

$$I_0(\lambda) = \frac{3600 \times \pi r^2}{N_a} \int_{\lambda_1}^{\lambda_2} I'(\lambda) \frac{\lambda}{hc} d\lambda \qquad \text{Equation D-5}$$

λ : Photon wavelength (m)

$I'(\lambda)$: Incident measured power distribution at interface (W m^{-3})

h : Planck constant (6.62×10^{-34} J s)

c : Speed of light (3×10^9 m s^{-1})

N_a : Avogadro number (6.02×10^{23} mol^{-1})

r : Reactor radius (m)

Other Performance indicators and useful acronyms definitions used in this article can be found in literature, i.e., Turnover Number (TON).[1,7,14–17]

Dye experiments. Dye experiments using $[Ru(bpy)_3]^{2+}$ instead of WO_3 as light harvester were performed in the same photocatalytic setup and high throughput cell. Suspensions were prepared using ultrapure water (10 mL), $[Ru(bpy)_3]^{2+}$ powder (5.5 mg), $Na_2S_2O_8$ (10 mM) and a RONS colloid volume. For dye experiments, the RONS colloid were washed out to remove TBAOH as much as possible due to the hole-scavenging nature of TBAOH in solution. TBAOH is removed by centrifuging the RONS colloid at low speed for 1 h (< 2000 RPM) to remove unexfoliated material, then the supernatant is collected and centrifuged at high speed (20.000 RPM) for 1 h. The supernatant is discarded, the centrifuge tube is replenished the equivalent volume in ultra-pure water and centrifuged again at high speed for 1 h. The latter step is repeated until agglomeration of RONS due to the absence of TBAOH starts being visible (typically two cycles). Only 2 min of ultrasonication was necessary to homogenize the aqueous mixture of dye, sacrificial agent, and washed RONS colloid. For nanosheet size dependent OER experiments, the colloid amount was exfoliated only with a vortexing device, unexfoliated material was removed and TBAOH washed out accordingly. Then DLS of the clarified RONS colloids was measured to track in-situ the change of size, and UV-Vis in transmission mode was performed to ensure that each vial at different ultrasonication times contained the same RONS concentration. The dynamic trend of OER rates was tracked online with the PST9 sensor only due to rapid changes. The maximum signal recorded was reported as the OER rate in dye experiments.

Oxygen Isotope counting measurements. For the labeled water experiment, the photocatalysis experiment in Figure D-23a was repeated exactly as for reporting optimal photonic efficiency. A suspension (12 mL) containing RONS/WO_3 (3 %wt Ru, 0.5 mg mL^{-1}) was prepared and placed in the OER cell previously described for finer optics. O_2 concentration in the headspace before and after illumination was measured with the BID detector, and molecule counting was tracked by means of Multiple Ion Chromatogram (MIC) at the MS channels m/z = 32, m/z = 34 and m/z = 36. Then, the reactor was opened

and ^{18}O labeled water was added (2 mL, 97% atom, Sigma-Aldrich). The photocatalytic activity procedure was then repeated identically, tracking BID and MS response change in MIC channels. The response of m/z = 32, m/z = 34 and m/z = 36 channels was recorded and integrated around the O_2 retention time twice to get an average of MIC channel response after OER rates stabilization. Qualitatively, the peaks are shown in Figure D-22 to demonstrate that labeled O_2 species appear only when labeled water was used. Quantitative isotopic distribution was obtained by integrating such peaks and discounting the $^{32}O_2$ mass response in dark to the one after illumination, and then the % of Area of channels m/z = 34 and m/z = 36 to total O_2 Area was calculated for 5 different light-on/light-off cycles. As the MS response is proportional to amount of substance and assumed to be invariant to these slight changes of oxygen molecules, such %A is representative of the actual distribution of O_2 species (%values displayed in Table D-2).

(Photo)electrochemistry experiments. All (photo)electrochemical measurements were performed with a self-made photoelectrochemical reactor equipped with a quartz glass for illumination. The aqueous electrolyte containing Na_2SO_4 (0.1 M) was purged with argon (> 99 %) prior to each measurement to remove oxygen. A saturated Ag/AgCl electrode (RE-1CP, ALS Japan) was used as reference and gold foil (Sigma Aldrich) as counter electrode. Measurements were performed with a multichannel potentionstat (Autolab M204, NOVA). The sample was illuminated using a solar simulator (LightLine A4, Sciencetech) which provides simulated sunlight with AAA quality (AM1.5G). Photoelectrodes were prepared by drop-casting plasma cleaned FTO templates (1 cm x 1 cm) with 50 µL of a suspension of ultra-pure water and the previously impregnated WO_3 samples used in photocatalysis (5 mg mL^{-1}). The photoelectrodes were subsequently dried at 60°C, and annealed at 400°C for 1.5 h.

D.7 Optical modelling analysis

In a first scenario, we consider the single event of photons first reaching exposed RONS and RONP, this is assuming that the optical cross section of WO_3 in impregnated samples does not influence cocatalyst interaction with light. We performed numerical simulations to estimate the absorptance of individual RONP and RONS using the reported properties

of both materials (see details of optical modelling in Methods Section).[8,9] The optical properties of RONP and RONS, and their normalized absorptance using an equivalent volume of both materials as a function of photon wavelength, are presented in Figure D-18. Figure D-18c shows that the modeled normalized absorptance (500-800 nm) of a RONS (500 nm x 500 nm x 1 nm) does not differ drastically from the one of an equivalent volume of RONP (477 nanoparticles, 5 nm radius). On the one hand, the model confirms that pure RONS are more transparent than RONP down to a photon wavelength of approximately 600 nm. Around this wavelength, a crossover of RONP and RONS absorptance is predicted by the model. On the other hand, this relative increase of absorptance of pure RONS in the UV range is observed in UV-vis experiments (Figure D-17c), but when comparing pure RONS with RONP/WO_3 (Figure D-16b), no absorptance crossover is observed at least down to photon wavelengths of 500 nm. This disagreement may be explained by the likely inaccuracy of the material optical properties (real and imaginary part of the complex refractive index),[8,9] and the oversimplified RONP and RONS geometries used as model inputs, and by the different effects present in suspension when measuring the absorptance of RONS and RONP experimentally.

Considering all the different optics phenomena in real suspensions, we use the experimental data in Figure D-16b to quantitatively calculate the cocatalyst light absorption of RONS/WO_3 and RONP/WO_3 samples, in the 500–800 nm wavelength range. For later estimations of parasitic light absorption in photocatalysis, we extrapolate this cocatalyst light absorption to the 400–500 nm wavelength range using the trends observed experimentally on pure RONS (Figure D-17c), and the RONP modelled absorptance (Figure D-18c). The overall lower absorptance in the 500–800 nm wavelength range of RONS/WO_3 versus pure RONS, is explained in the next scenario. In the second scenario, we consider the single event of photons reaching the WO_3 component of the photocatalyst composites first, i.e., a WO_3 NP shielding a RONS, this is assuming that the optical cross section of the cocatalyst does not influence WO_3 interaction with light. In both RONP/WO_3 and RONS/WO_3 samples the probability of scenario 1 versus scenario 2 cannot be quantified trivially. Still, RONP are relatively small and always exposed to photons on the surface of WO_3, thus it can be deducted that in RONP/WO_3 samples, the scenario 2 may be approximated to an event almost independent of the scenario 1; meaning that most

photons absorbed or scattered by WO_3 have not interacted previously with RONP. The scenario 1 in RONP/WO_3 samples may be approximated to an event partially dependent of scenario 2; meaning that photons absorbed or scattered by RONP may or may have not interacted first with WO_3. Differently, in the RONS/WO_3 samples, the scenario 1 at an optically shielded RONS may be approximated to an event almost fully dependent of the scenario 2. In the case the opposite type of shielding occurs, meaning that RONS are fully wrapping the surface of WO_3 NP, the scenario 1 at the RONS shielding the WO_3 NP may be approximated to an event much less dependent of the scenario 2. Therefore, when comparing pure RONS and RONS/WO_3 suspensions, if a non-negligible fraction of WO_3 NP is shielding the RONS in the RONS/WO_3 samples, the fate of photons undergoing the scenario 2 will strongly influence cocatalyst light absorption. The additional existence of the scenario 2 in RONS/WO_3 samples and the possibility that a fraction of RONS is optically shielded explains qualitatively why cocatalyst light absorption on RONS/WO_3 is overall less than on pure RONS suspensions (Figure D-16c). In this second scenario, we later further analyze the scattering trajectories of such photons to gain quantitative insight into their influence on RONS light absorption, for which we perform stochastic optical modeling using reported properties of WO_3 (see details of optical modelling in Experimental Section).[1,10,11] The optical properties of WO_3, and the modeled total scattered photons probability and its angular distributions as a function of WO_3 nanoparticle size and photon wavelength are presented in Figure D-19. The modeled trends of WO_3 absorption and scattering cross sections (Q_{abs} and Q_{sc}, respectively), whose sum is proportional to the probability of light interaction with WO_3 in RONS/WO_3 samples, are presented in Figure D-19b and Figure D-19c. Q_{abs} and Q_{sc} show an increase around the wavelength range at which pure RONS absorptance starts increasing more evidently (~500 nm according to experimental RONS absorptance data in Figure D-17c). This agrees with the RONS relatively less steep increase in absorptance towards the UV region when are impregnated on WO_3 as in RONS/WO_3 samples. Altogether, even in the wavelength range (towards 500 nm) where RONS are slightly less transparent, the RONS/WO_3 samples show significant less cocatalyst light absorption when compared to RONP/WO_3 (Figure D-16a). If extrapolated to photocatalysis conditions, together with RONS high transparency, the fraction of the RONS that is optically shielded by WO_3 NP also contributes to decrease parasitic light absorption on

RONS/WO_3 samples. RONS that are optically shielded by WO_3 NP may only interact with photons that have already interacted with WO_3, which will favor light absorption on WO_3 over parasitic light absorption by the shielded RONS. From the light interaction with WO_3 only the absorbed photons trigger photocatalytic OER rates. However, we cannot access from UV-Vis experiments (i.e., in Figure D-17b) or optical modelling the fraction of light that is parasitically absorbed when light absorption on WO_3 is also present. Therefore, with the sole purpose to quantitatively prove the likely existence of RONS optically shielded by WO_3 NPs, we now restrict the analysis in this second scenario to the wavelength range where WO_3 only scatters photons.

The relation between the modeled trajectories of the photons scattered by WO_3 and its interaction with a shielded RONS and a randomly distributed RONP is depicted in Figure D-20a. In the RONS case, forward scattering is defined as the sum of all the trajectories of the photons scattered by WO_3 that are still heading to the shielded RONS. A hypothetical probability of forward scattering of 100% means that the fate of all photons after scattering on WO_3 is to interact with the shielded, or partially shielded, RONS. Therefore, a forward scattering probability of 100% would mean that the existence of RONS shielded or partially shielded by WO_3 NPs in RONS/WO_3 samples has no effect in reducing cocatalyst light absorption from what is observed in pure RONS samples at wavelengths above the optical band gap of WO_3. As it is observed in Figure D-16c, there is significant drop in cocatalyst light absorption at equivalent Ru in suspension when comparing RONS/WO_3 and pure RONS samples, which hints that the forward scattering probability is not 100%. As depicted in Figure D-20a for an idealized RONS/WO_3 geometry, the forward scattering probability can be estimated from integrating the angular probability distribution in Figure D-19d using a variable angular sweep for integration. We calculate then the average forward scattering probability which is presented in Figure D-20b (see details of averaging in Methods Section). For example, for the most representative WO_3 particle size (100 nm) and at the limit of pure scattering of WO_3 ($\lambda \sim 450$ - 500 nm), the average probability of backward scattering (*100% - forward*) is roughly 30% (Figure D-20b). This implies that the proposed 0D/2D photocatalyst geometry assuming a RONS optically shielded by WO_3 NPs, predicts roughly a 30% reduction of cocatalyst light absorption in the wavelength range of 500 to 800 nm from the one of pure RONS. In that range, this calculation (Figure

D-20b) that assumes RONS being shielded by WO_3 roughly agrees with UV-Vis absorptance measurements of RONS/WO_3 suspensions and RONS colloids in Figure D-16c, which show a similar extent of cocatalyst light absorption decrease (i.e., 36% at 500 nm and 3 %wt Ru). Therefore, we prove that a fraction of RONS/WO_3 is RONS optically shielded by WO_3 NPs.

Shielded RONS in photocatalysis are not prevented from interaction with photons solely by means of backwards scattering — which becomes less crucial in photocatalysis since photons backward scattered by WO_3 may as well leave the suspension — but by means of light absorption on WO_3. As the RONS optically shielded by WO_3 NPs are strongly dependent of the outcome of light interaction with WO_3, in photocatalysis only a relatively small fraction of photons of wavelength below 500 nm will be left to forward scatter on WO_3 and interact with the RONS ($Q_{abs} > Q_{sc}$ in this range, Figure D-19). Hence, RONS optically shielded by WO_3 NPs may decrease parasitic light absorption of RONS/WO_3 during photocatalysis beyond the registered high transparency of the RONS versus RONP.

In contrast, due to the RONP isotropic nature and random distribution on WO_3, the RONP has in average equal probability of interacting with the photons scattered by the WO_3 surface in all directions, as explained in Figure D-20a. Hence, we do not further interpret parasitic light absorption on RONP/WO_3 suspensions with respect to the aspects of light scattering on WO_3 just discussed. RONP are also less dependent of the photon fate after scenario 2 and hance the cocatalyst light absorption of RONP/WO_3 samples measured at wavelengths above 500 nm (Figure D-20a) may not decrease significantly by means of competitive light absorption on WO_3 during photocatalysis.

D.8 Good practices in reporting OER rates in photocatalysis

Along with the screening of RONS/WO_3 and RONP/WO_3 relative differences in photonic efficiency, their quantitative reliability is ensured with good practices to report OER rates adopted during the production of this article.[1,15,16,18] These reported guidelines reduce the electron acceptor (KIO_3) decomposition contribution to OER rates, and facilitate comparison of photonic efficiencies with other research groups by reporting a RuO_2/TiO_2 benchmark, like in Figure 6-3A.[1,19] Also, following such standards, in situ $H_2{}^{18}O$ experiments were performed to correlate measured O_2 with water oxidation, whose results

are presented in Table D-2 and Figure D-22 for RONS/WO_3 samples. The good agreement between measured distributions of isotopes of $^{16}O^{16}O$ (77.2%), $^{16}O^{18}O$ (21.1%), and $^{18}O^{18}O$ (1.7%) compared to the ideal prediction in the absence of kinetic isotope effects ($^{16}O^{16}O$ = 76.3%; $^{16}O^{18}O$ = 22.1%; $^{18}O^{18}O$ = 1.6%), rules out the possibility of sacrificial decomposition or leakages contribution to the reported OER rates herein.[1]

Unless stated differently, all OER rates presented herein were obtained in a high throughput OER cell.[1] In addition to this high throughput OER cell, we have performed additional photocatalytic measurements in a cell that better accomplishes technical requirements for photocatalytic performance accreditation (finer optics cell).[18] In Figure D-23a, the full trend of optimal photonic efficiency using the finer optics cell is shown for RONS/WO_3, RONP/WO_3 and the RuO_2/TiO_2 benchmark samples. In this finer optics cell the diameter was widened to 2.6 cm, which decreased the suspension depth (l) to optical depth (d_λ) ratio at equal suspension volume compared to the old cell. This lower l/d_λ ratio better shows the light extinction effect in photocatalytic rates at step wise addition of 2 mL of photocatalytic suspension, for optimal photonic efficiency screening. The finer optics geometry, as expected, reduces the (asymptotic) optimal photonic efficiency values of the samples compared to Figure 6-3A. However, it better displays part of their linear increase per catalyst mass regime.[20] Mass normalization of photocatalytic OER rates for inter-laboratories comparison has been discussed in literature as unreliable in most cases, but it has also been reported that it may still provide a rough criterion for comparison to other research groups within geometries like in our finer optics cell.[1,15,16,18,20] We on the other hand advocate strongly for comparison in terms of internal quantum efficiencies or quantum yields when possible. Internal quantum efficiencies of RONS/WO_3 and RONP/WO_3 samples are not reported in this article because relative comparison of their OER rates builds upon the same light harvester (WO_3). Nevertheless, more generally, in absence of internal measurements, we alternatively propose the *relative optimal photonic efficiency* concept using a RuO_2/TiO_2 benchmark to report OER rates (ξ_e). The reported ξ_e of the RuO_2/TiO_2 benchmark reported in our high throughput OER cell at AM 1.5G conditions is a measure that remained constant at the lower integrated power used for OER measurements in this article (65 mW cm^{-2}).[1] Regardless of changes in the absolute values of ξ_e of the samples when measured in the high throughput (65 mW cm^{-2}) and finer

optics OER cell (100 mW cm^{-2}), when normalized with the RuO_2/TiO_2 benchmark, activities of RONS/WO_3 (ξ_e = 0.15) and RONP/WO_3 (ξ_e = 0.8) are almost invariant. This encourages the use of ξ_e as a way of comparing OER rates among different groups. Complementary to normalization of photocatalytic rates, in the absence of internal measurements apparent quantum yield (AQY) is another necessary performance indicator according to accreditation principles, which was performed in our finer optics OER cell for RONS/WO_3 and RONP/WO_3 and presented in Figure 23b.[1,15,18]

D.9 Electrochemistry and photoelectrochemistry analysis

Linear Sweep Voltammetry (LSV) measurements were performed on WO_3, RONS/WO_3, RONP/WO_3, and PtO_x/WO_3. LSV allows independent measurements of water oxidation (anodic currents) and IO_3^- reduction (cathodic currents) trends (see details LSV in Experimental Section). A chopped illumination method (AM 1.5G) was used for the anodic (oxidative) current measurement to measure the photocurrent resulting from photoexcited electron extraction from WO_3. This is a direct measure of the photoexcited holes performing the desired photoelectrocatalytic OER process. Results in Figure 6-3b show that at a potential above 0 V *vs.* Ag/AgCl, RONS/WO_3 exhibit an increasing photocurrent when compared to RONP/WO_3 (10 and 4 μA cm^{-2} at a potential of 0.5 V *vs.* Ag/AgCl, respectively). We attribute the increase of photocurrent with potential to an increasing driving force for photogenerated electron extraction up until the onset for electrocatalytic water oxidation is reached. In Figure D-25a, we show the reduction reaction in dark LSV measurements in the absence and presence of KIO_3 (10 mM) in the electrolyte. RONS/WO_3 and RONP/WO_3 show similar cathodic (reductive) current onsets starting at a potential of approx. 0.1 V *vs.* Ag/AgCl while, as expected, PtO_x/WO_3 displays a much steeper current onset at a potential of -0.2 V *vs.* Ag/AgCl.[4,6] RONS/WO_3 also shows the smallest cathodic current for electrocatalytic IO_3^- reduction, which we interpret as RONS/WO_3 having the smallest artificial boost in OER photocatalysis. At the same time, compared to RONP/WO_3 and PtO_x/WO_3, the RONS/WO_3 sample shows electrocatalytic water oxidation current (Figure D-25b) at the smallest potential onset (+1 V vs. Ag/AgCl; compared to +1.1 V vs. Ag/AgCl for RONP), suggesting the most efficient photoelectrocatalytic water oxidation process. These findings reinforce the idea that the enhancement of

photocatalytic OER rates using RONS/WO_3 must be linked to better optical properties and lower overpotential of water splitting for RONS. The electrocatalytic measurements also present additional evidence to XPS measurements of the fundamental difference in Ru oxidation state between RONS and RONP, because the Ru(III) species also present in the RONS perform better in the catalytic process than the anhydrous RuO_2 constituting the RONP (Ru(IV)).[2] We evidence this with the shift in water oxidation onset in the dark LSV measurement, which has previously been reported and attributed to the RuOOH constituent of the RONS (Figure D-25b).[2] Additionally, other potential RONP and RONS chemical differences not captured by XPS measurements, for example traces of $RuO_2 \cdot nH_2O$ in RONP or RONS would have an impact on the enhancement of cathodic currents, like PtO_x does, which is not observed in either of them by dark LSV measurements.[6,27]

D.10 RONS size-dependent photocatalysis studies

Lateral size controlled RONS colloids were impregnated at equal loading on WO_3 using a previously prepared RONS colloid stock. The stock was previously exfoliated using only a vortexing device and sediments were removed via centrifugation (see details of RONS exfoliation in Experimental Section). It was observed previously that pure vortexing is an effective way to obtain unilamellar sheets with minimum changes on the original lateral dimension. The low Ru loading (~ 0.25 %wt, Figure D-26) was chosen to prevent significant nanosheet restacking during impregnation. Nanosheets with different lateral sizes were obtained by varying the ultrasonication time of the unique RONS colloid stock, which was separated into four different vials. Subsequent ultrasonication of the vials proved effective in decreasing the sheet lateral dimension, which we confirm via atomic force microscopy (AFM) images. Examples of AFM images used to measure RONS lateral size can be found in Figure D-27. To quantitatively know more about the most active RONS abundance, we performed an AFM systematic screening of the colloids tuned to maximize single layer nanosheets deposited on Si/SiO_2 wafers, right before the WO_3 impregnation. Quantitative AFM lateral size distributions obtained from different random spots on the wafers are displayed in Figure 6-4b, for the same samples screened in Figure 6-4a. The optimal RONS stock ultrasonication duration suggests that the decrease in nanosheet lateral size is beneficial for the photocatalytic OER rates obtained on the RONS/WO_3

samples. However, it comes at the expense of another colloid property seemingly unfavorable for the WO_3 impregnation as will be shown in the following. The most significant decrease in nanosheet lateral size from roughly 1 µm to 200 nm corresponds to the 1 h of ultrasonication of the colloid stock. Past this sonication time, the size distribution shows little change in size but a likely increase in agglomeration (Figure D-27 and Figure D-28). This suggests that at very small nanosheet lateral sizes, the RONS colloid becomes unstable and TBA^+ ions no longer prevent restacking and/or agglomeration. Hence, an excessive ultrasonication power of RONS at 20 mM TBAOH seemingly results in temporary nanosheet agglomerate breakdown, yet only a marginal decrease in the nanosheet lateral sizes. By applying a cut-on filter on the measured nanosheets height (2 nm) (see AFM images in Figure D-27), we can qualitatively show a minimal reduction of nanosheet lateral size from 2 to 3 h of ultrasonication time. RONS restacking creates inaccessible cocatalyst active sites when impregnated on WO_3. This compromise between lateral size reduction and agglomeration arises from the limitations of the ultrasonication technique used to reduce the nanosheet lateral size. RONS agglomeration during ultrasonication is seemingly reduced with the increase of TBAOH concentration (50 mM), as seen in Figure 6-4a.

The exfoliation method to control RONS size is effective in limiting the fraction of less active nanosheets with lateral sizes > 1 µm, but due to its low exfoliation efficiency (~ 5%) is impractical for extensive photocatalysis screening. Photocatalytic screening of RONS/WO_3 samples produced with the exfoliation method to control RONS size is only explored in Section 2.2.2. Still, screening of photonic efficiencies (Figure 6-3a) and OER rates versus RONS loading (Figure 6-4c) of RONS/WO_3 samples implicitly exploit the benefit of a high amount of RONS edges. For such RONS/WO_3 samples screening, the two high throughput exfoliation methods used to produce the RONS colloids later impregnated on WO_3 result in a broad nanosheet lateral size distribution. This distribution includes the 100 - 400 nm range targeted in Figure 6-4a and Figure 6-4b as the most active size before RONS agglomeration occurs. Optimization of these high throughput exfoliation methods resulted in the RONS/WO_3 impregnated samples benchmarked in Figure 6-4a (see details of RONS exfoliation in Experimental Section). Such methods are still subject to further

optimization to achieve a better compromise of reproducibility, exfoliation efficiency, and size control beneficial for photocatalysis applications.

D.11 Supplementary figures and tables

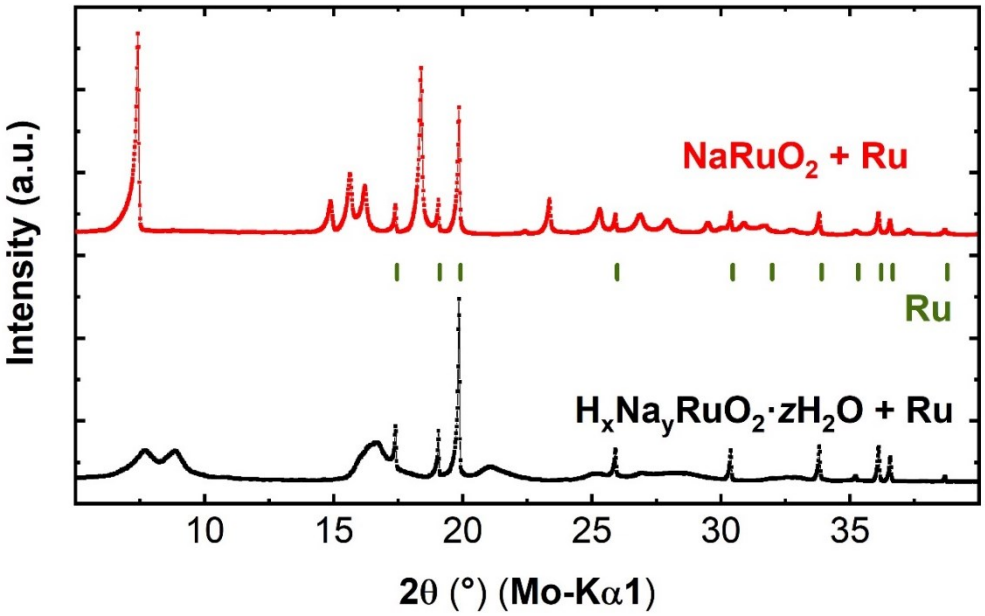

Figure D-1. *Powder X-ray Diffraction* (PXRD) patterns of $NaRuO_2$ (red) and $H_xNa_yRuO_2.zH_2O$ (black), which are obtained from the RONS precursor synthesis and subsequent proton exchange, respectively. Displayed Ru peak positions are obtained from the literature (green).[21] Ru containing precursor is later removed during RONS exfoliation from $H_xNa_yRuO_2.zH_2O$.

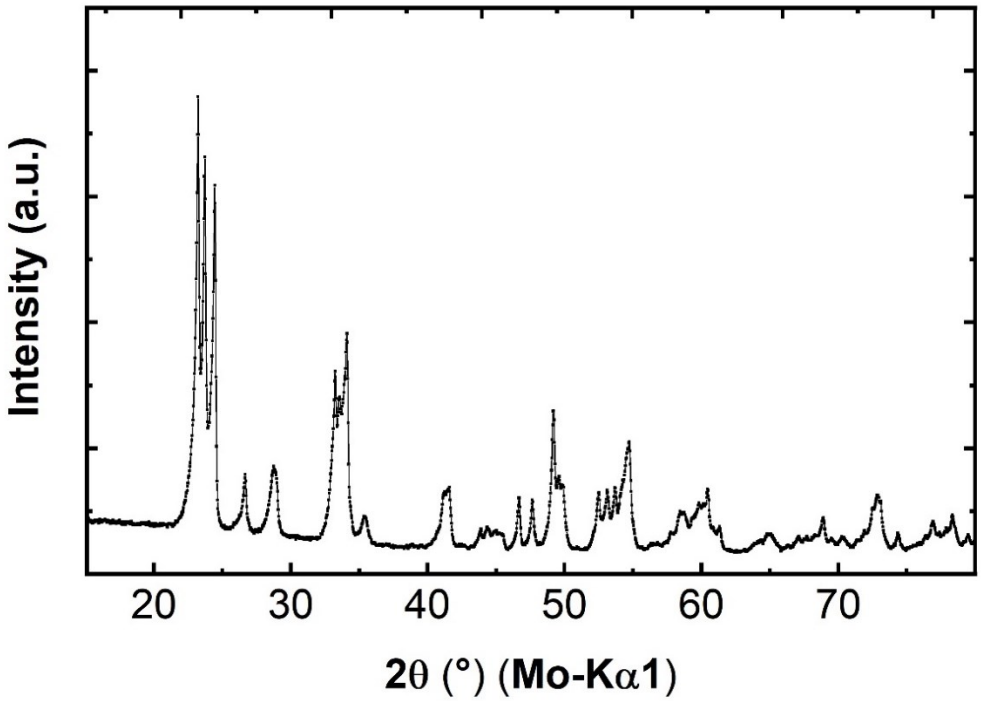

Figure D-2. PXRD patterns of commercial WO_3 powder after calcination at 400 °C. PXRD patterns of WO_3 impregnated with ruthenium oxide nanosheets (RONS/WO_3, 3 %wt Ru) and ruthenium oxide nanoparticles (RONP/WO_3, 3 %wt Ru) show no observable difference to the ones of commercial WO_3 (due to low cocatalyst loading).

Table D-1. Summary of photocatalytic OER rates on WO_3 composites obtained in the literature.

WO_3 composite	*Reaction conditions*	*Activity/Efficiency*	*Year*
WO_3 nanoparticles	$AgNO_3$ 50 mM, 8 mg mL^{-1} photocatalyst	Qualitative photocatalytic oxygen evolution reaction (OER) rates	1984[22]
WO_3 nanoparticles, decorated with PtO_x (0.5 %wt Pt) nanoparticles, and Pt–TaON sample (0.3 wt% Pt, as HER photocatalyst)	$NaIO_3$ 5 mM 250 mL suspension, 200 mg Pt-TaON photocatalyst, 300 mg Pt-WO_3 photocatalyst, pH 6.5	Overall water splitting, Apparent quantum efficiency, AQE (λ < 420 nm) = 0.5%	2011[5]
WO_3 nanoparticles, decorated with PtO_x (0.5 %wt Pt) and RuO_x (0.001 %wt Ru) nanoparticles	$NaIO_3$ 10 mM 100 mL suspension, 100 mg photocatalyst pH 5.9	OER, Apparent quantum yield, AQY(λ = 420 nm) = 14.4%	2012[4]
50 – 100 nm WO_3 nanoparticles (oxygen defective)	$AgNO_3$ 10 mM, 120 mL suspension, 30 mg photocatalyst, no pH adjustment	OER, AQY(λ = 420 nm) = 0.14 %	2019[23]
100 – 300 nm WO_3 nanoparticles (oxygen defective, facet engineered)	$AgNO_3$ 10 mM, 100 mL suspension, 50 mg photocatalyst, no pH adjustment	OER, AQY(λ = 420 nm) = 15.3 %	2019[24]

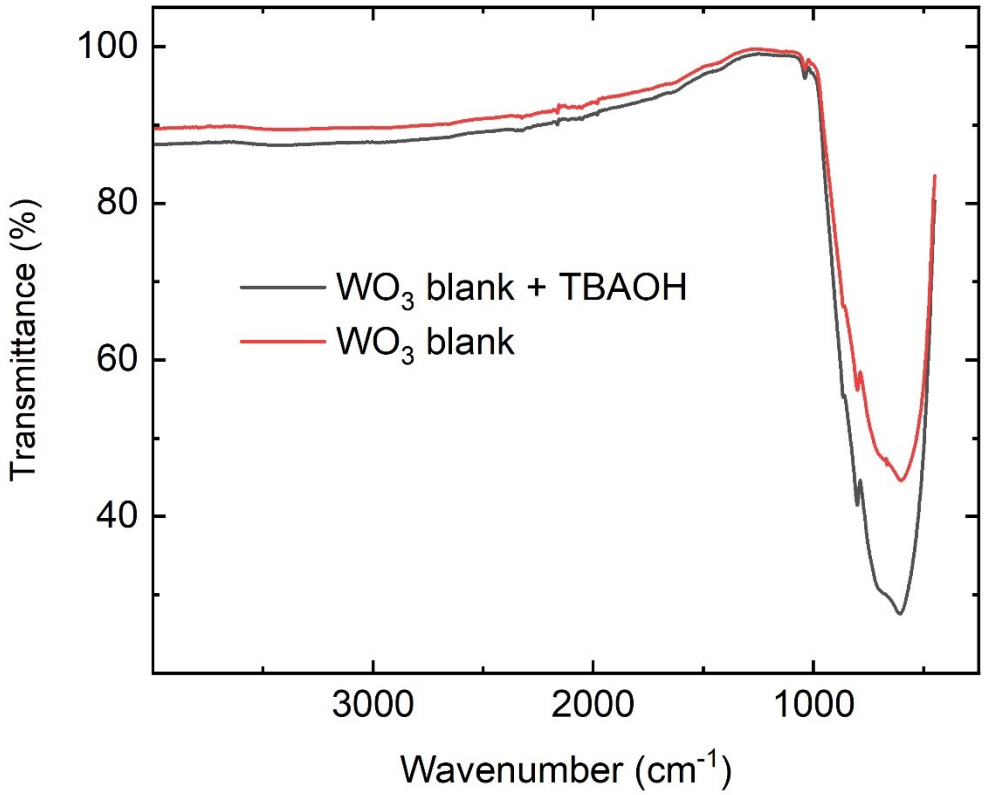

Figure D-3. FT-IR spectra of WO_3 blank samples after impregnation and calcination. Samples were obtained in absence and presence of TBAOH (WO_3 blank and WO_3 blank + TBAOH, respectively). TBAOH amount added to WO_3 blank during impregnation is equivalent to the one used at the WO_3 impregnation with RONS (at nominal %wt Ru/WO_3 loadings of 3%). Only a broad band is obtained around 676 cm^{-1} in both samples, which corresponds to the stretch of O-W modes.[25] No carbon residue is observed.

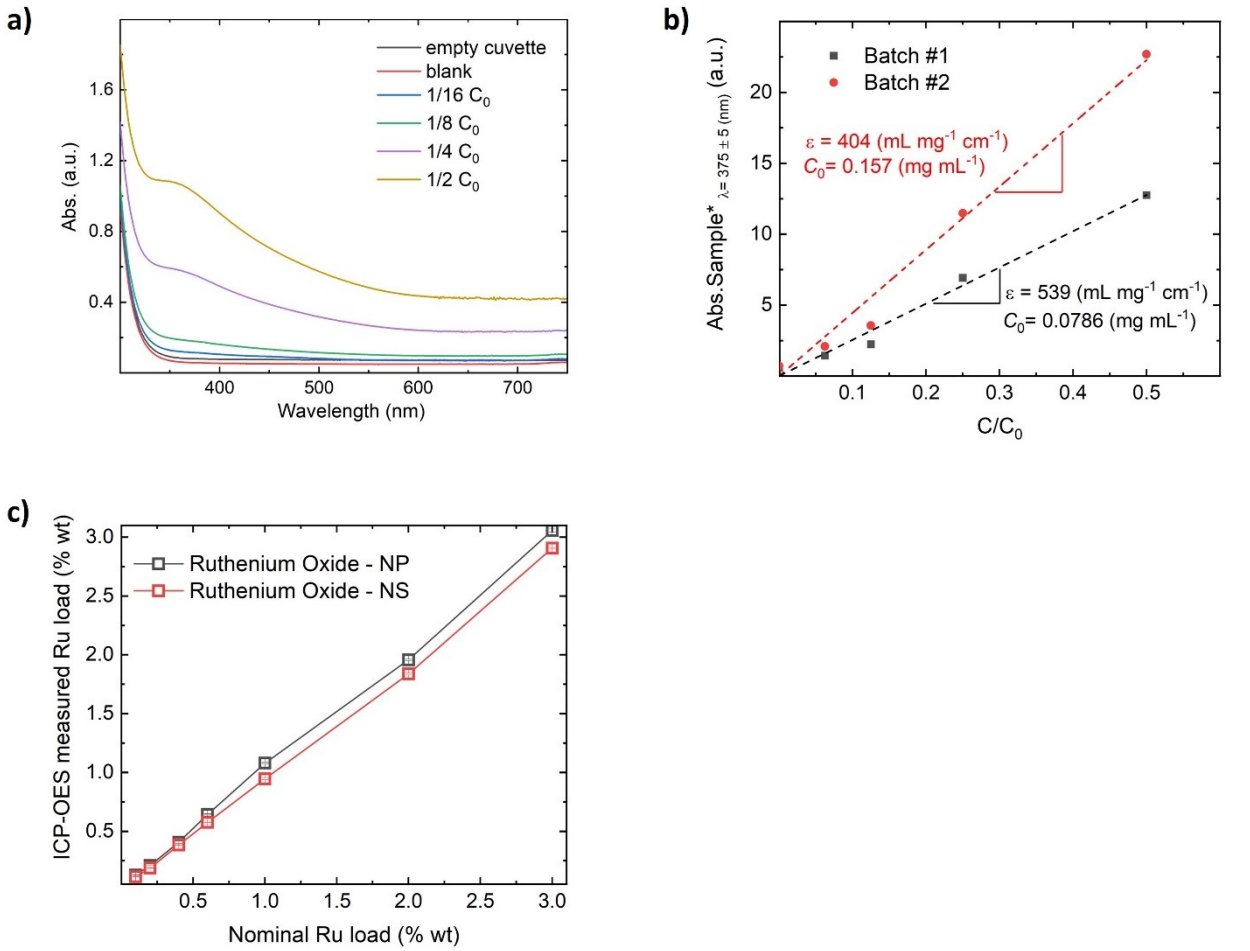

Figure D-4. UV-Vis spectroscopy for ruthenium oxide nanosheets (RONS) colloidal suspension concentration estimations. **(a)** UV-Vis spectra of 3 mL of RONS colloid at 20 mM TBAOH (Absorbance = $-\log_{10}(T)$, Y-axis). Initial concentration of suspension colloid was measured with drop-casting and microbalance (approximately 0.15 mg mL^{-1}, C_0 of batch #1). **(b)** corrected absorbance curve versus RONS colloidal suspension dilution (C/C_0, x-axis) including background absorbance T_0 ($Abs.sample^* = -\log_{10}(T/T_0)$, Y-axis). Slope from linear fitting plus C_0 is used to calculate the apparent molar absorption coefficient (ε). **(c)** Ru loading (Y-axis) determined by ICP elemental analysis of RONS/WO_3 and RONP/WO_3, versus nominal Ru loading calculated with UV-Vis of RONS colloidal suspensions, average ε (471 mL mg^{-1} cm^{-1}), and adjusted volume for the WO_3 impregnation. Nominal Ru loading of RONP is calculated from previously prepared $RuCl_3 \cdot H_2O$ stock solution (1 mg mL^{-1}) and adjusted volume for the WO_3 impregnation. The error between nominal and ICP-OES measured Ru loading of RONS/WO_3 and RONP/WO_3 samples is in average 7% and 6%, respectively.

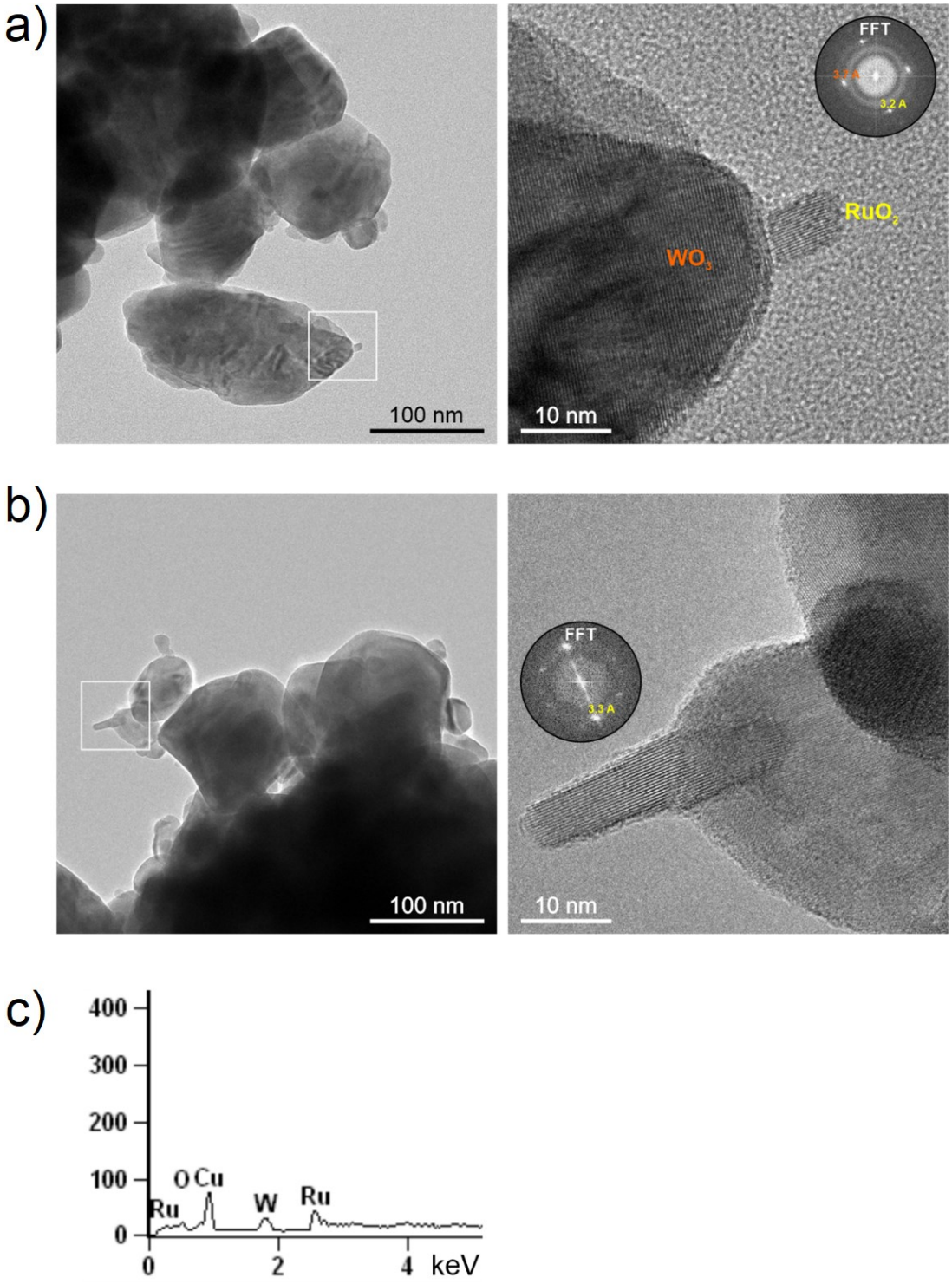

Figure D-5. Additional transmission electron microscopy (TEM) images of RONP/WO_3 sample after $RuCl_3 \cdot xH_2O$ wet impregnation (0.4 %wt Ru). (**a**) Layout and zoom-in image used for fast Fourier transformation (TEM-FFT) analysis in Figure 6-2c. ~100 nm particles correspond to WO_3. **(b)** Layout and zoom-in of areas containing slightly elongated RONP. **(c)** TEM- electron dispersive X-ray (TEM-EDX) analysis on RONP displayed in (b).

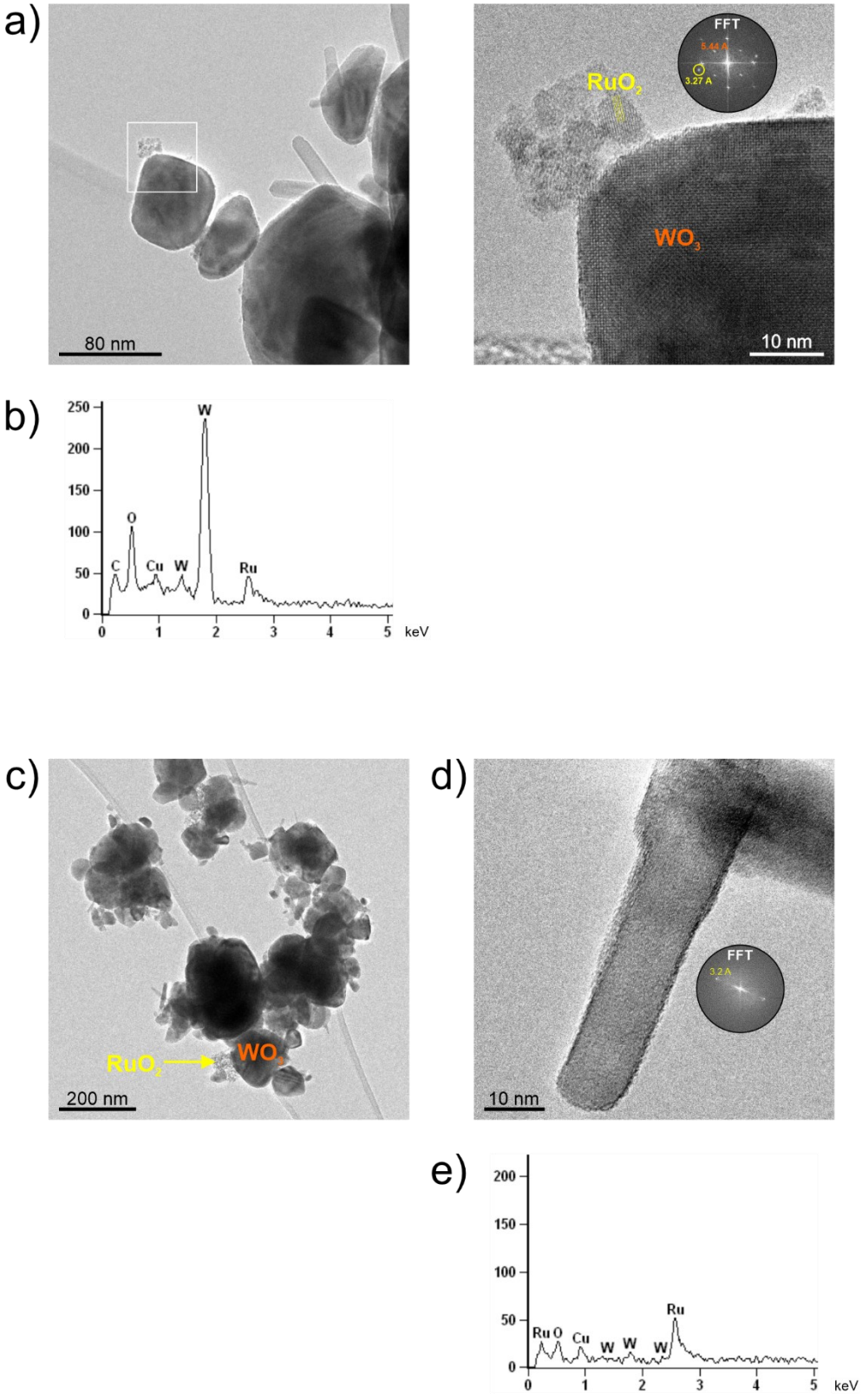

Figure D-6. Additional transmission electron microscopy (TEM) images of RONP/WO_3 sample after $RuCl_3 \cdot xH_2O$ wet impregnation (3 %wt Ru). (a) Layout and zoom-in image showing the d-spacings obtained by FFT of the regions containing RONP (d-spacing = 3.27 Å). **(b)** TEM-EDX analysis on RONP displayed in (a). **(c)** Dispersion of RONP on WO3. **(d)** Zoom-in of areas containing elongated RONP. **(e)** TEM-EDX analysis on RONP displayed in (d).

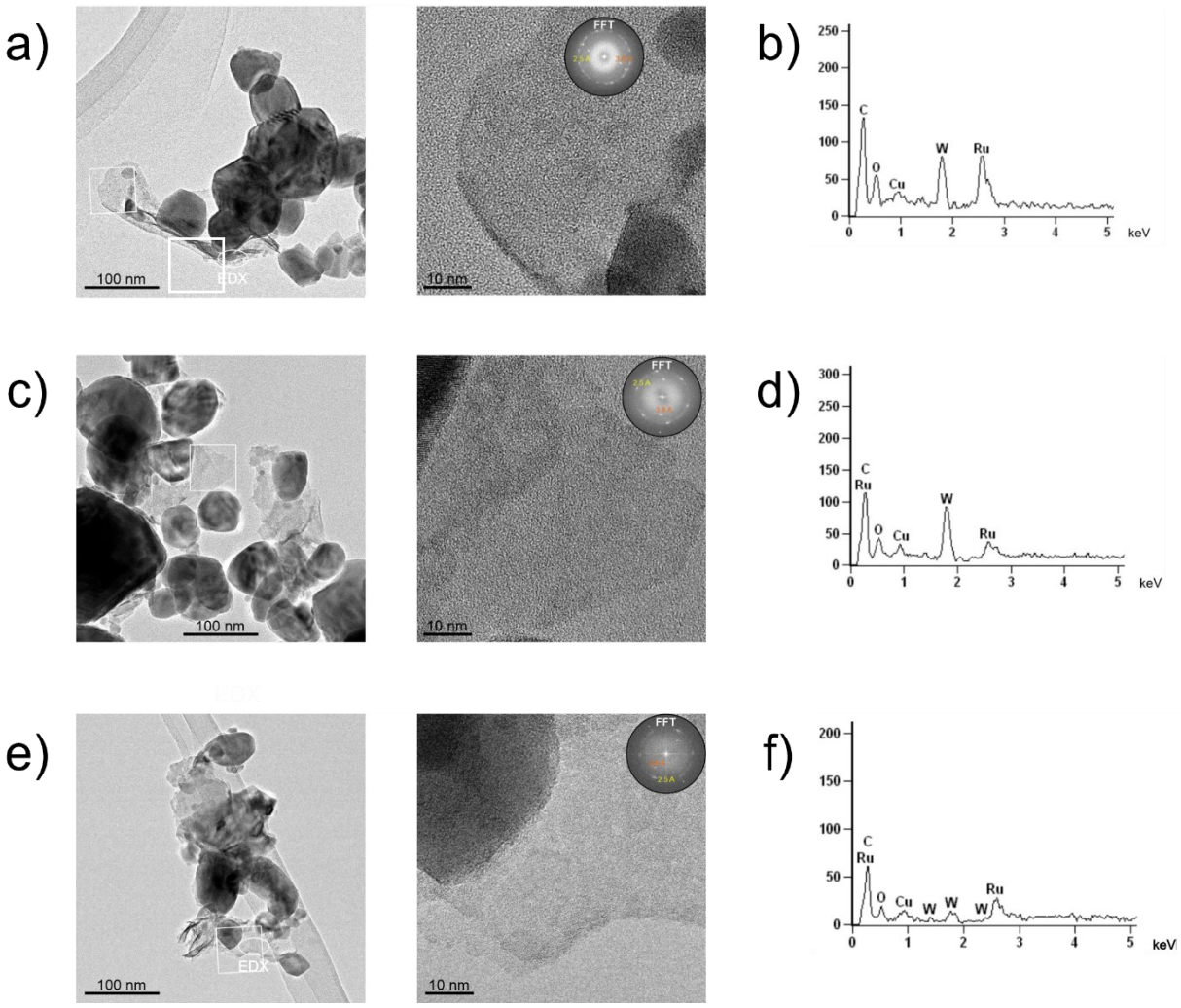

Figure D-7. Additional transmission electron microscopy (TEM) images of RONS/WO3 sample after RONS wet impregnation (3 %wt Ru). (a) Layout and zoom-in image showing the d-spacings obtained by FFT of the regions containing RONS (d-spacing = 2.5 Å), used in Figure 4e. **(b)** TEM-EDX analysis on RONS displayed in a. **c)** Additional layout and zoom-in image showing the d-spacings obtained by FFT of the regions containing RONS (d-spacing = 2.5 Å). **(d)** TEM-EDX analysis on RONP displayed in c. **(e)** Additional layout and zoom-in image showing the d-spacings obtained by FFT of the regions containing RONS (d-spacing = 2.5 Å). **(f)** TEM-EDX analysis on RONP displayed in e.

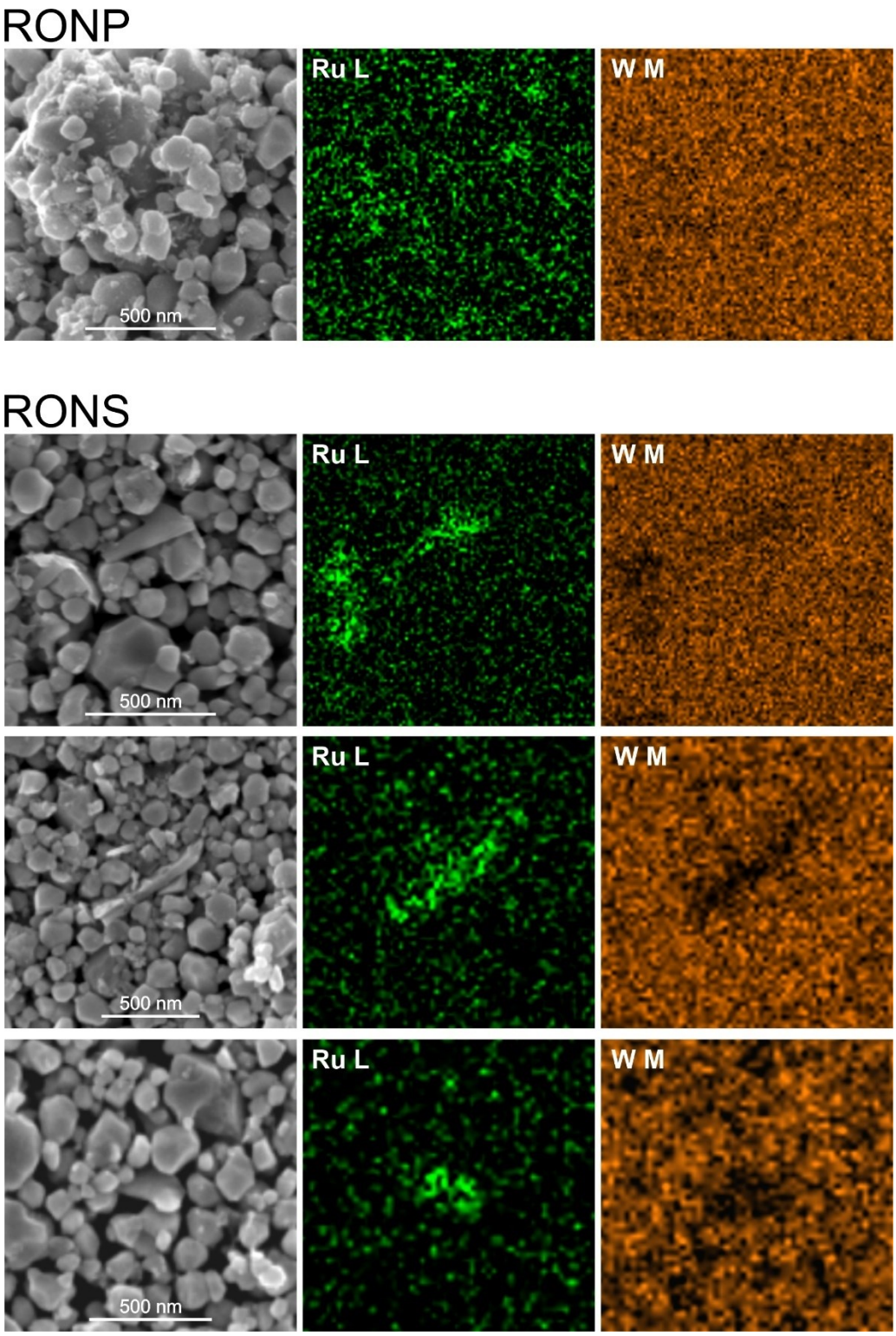

Figure D-8. Additional SEM image snapshots and SEM-EDX elemental maps of RONP/WO3 (3 %wt Ru) and RONS/WO3 (3 %wt Ru) samples after wet impregnation of WO3.

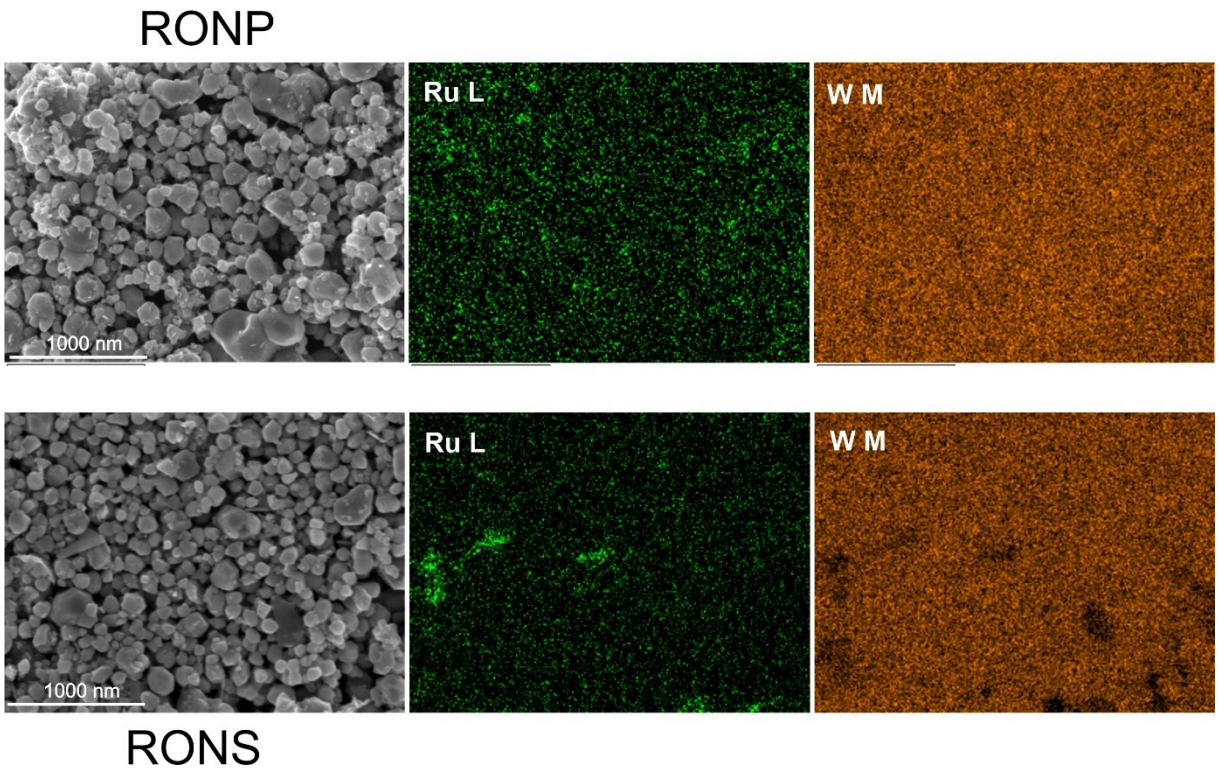

Figure D-9. Additional SEM image snapshots and SEM-EDX elemental maps at lower magnification of RONP/WO_3 (3 %wt Ru) and RONS/WO_3 (3 %wt Ru) samples after wet impregnation of WO_3.

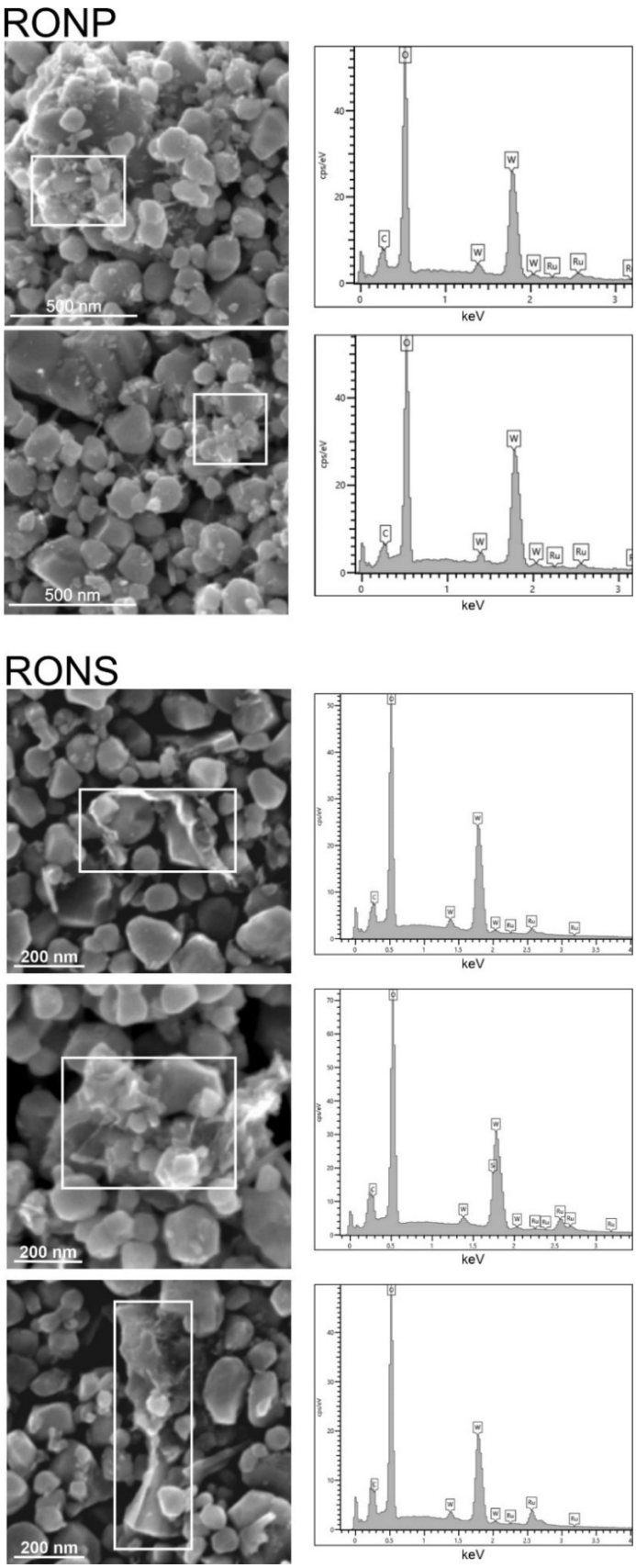

Figure D-10. Additional SEM image snapshots and SEM-EDX analysis of RONP/WO_3 (3 %wt Ru) and RONS/WO_3 (3 %wt Ru) samples after wet impregnation of WO_3.

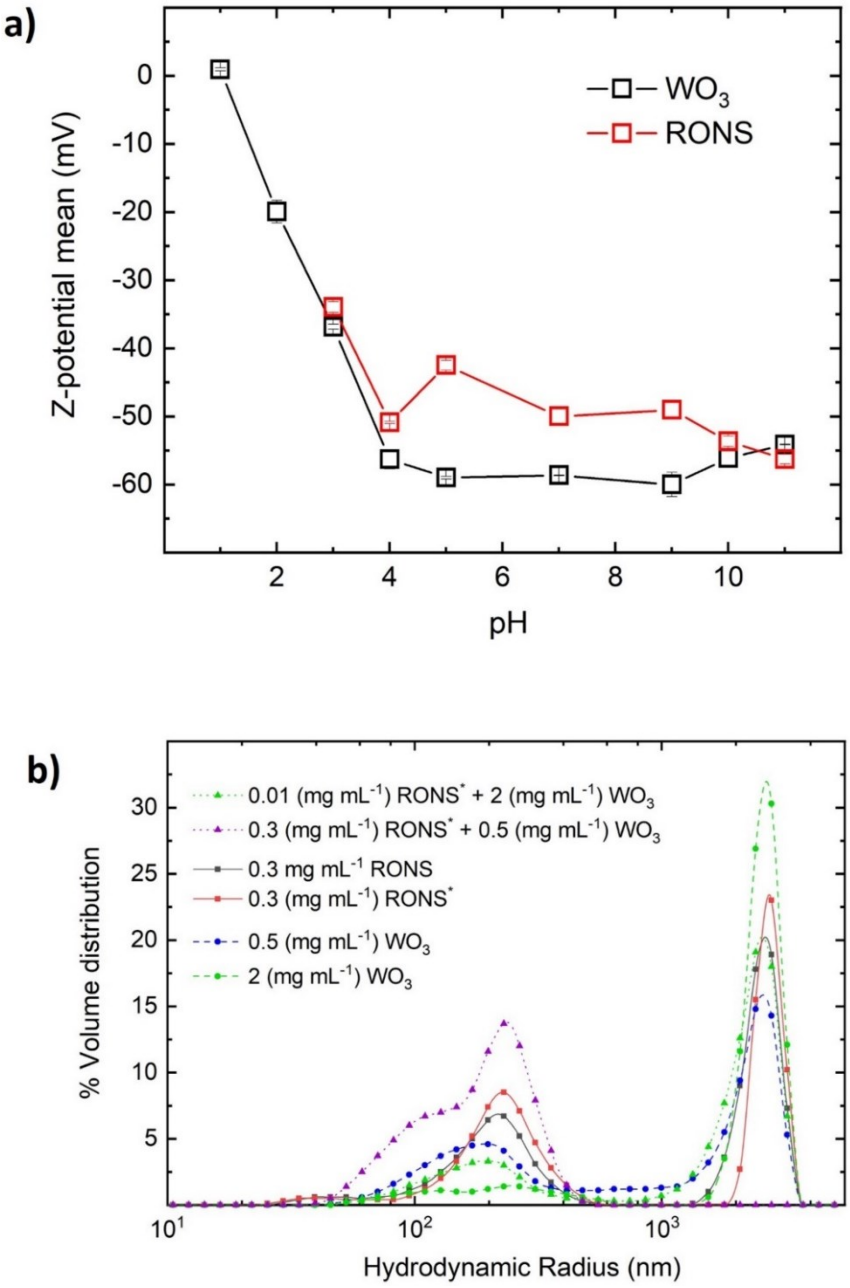

Figure D-11. (a) Zeta-potential average versus pH of a suspension containing WO3 nanoparticles (0.5 mg mL-1) and ruthenium oxide nanosheets (RONS, 0.1 mg mL-1), measured at 10 mM NaCl. **(b)** DLS volume distribution of colloid mixtures in a 3 mL cuvette at different concentrations and blends of RONS suspension in 20 mM TBAOH. Washed RONS colloid contains < 0.2 mM TBAOH (RONS*). DLS blends are like the slurry formed during wet impregnation. The agglomerate peak of pure WO3 suspension (2 mg mL-1) with hydrodynamic radius around 2 µm (green dot curve) decreases significantly after addition of 100 µL aliquot of RONS* colloid (0.01 mg mL-1, green triangle curve). A simultaneous increase in the nanosheet hydrodynamic radius distribution region around 200 nm is also detected after addition of the RONS* colloid, albeit the signal of pure RONS* at 0.01 mg mL-1 is not detectable. Second experiment is a blend of a less dense WO3 suspension (0.5 mg mL-1, blue dot curve) and denser RONS* colloid (0.3 mg mL-1, red dot curve). This second blend (violet triangle curve) also shows the trend of the large micron size agglomerates of pure WO3 and RONS* being completely displaced to the 200 nm region. DLS measurements show only qualitative trends of WO3 and RONS adhesion due to the anisotropy of the RONS.

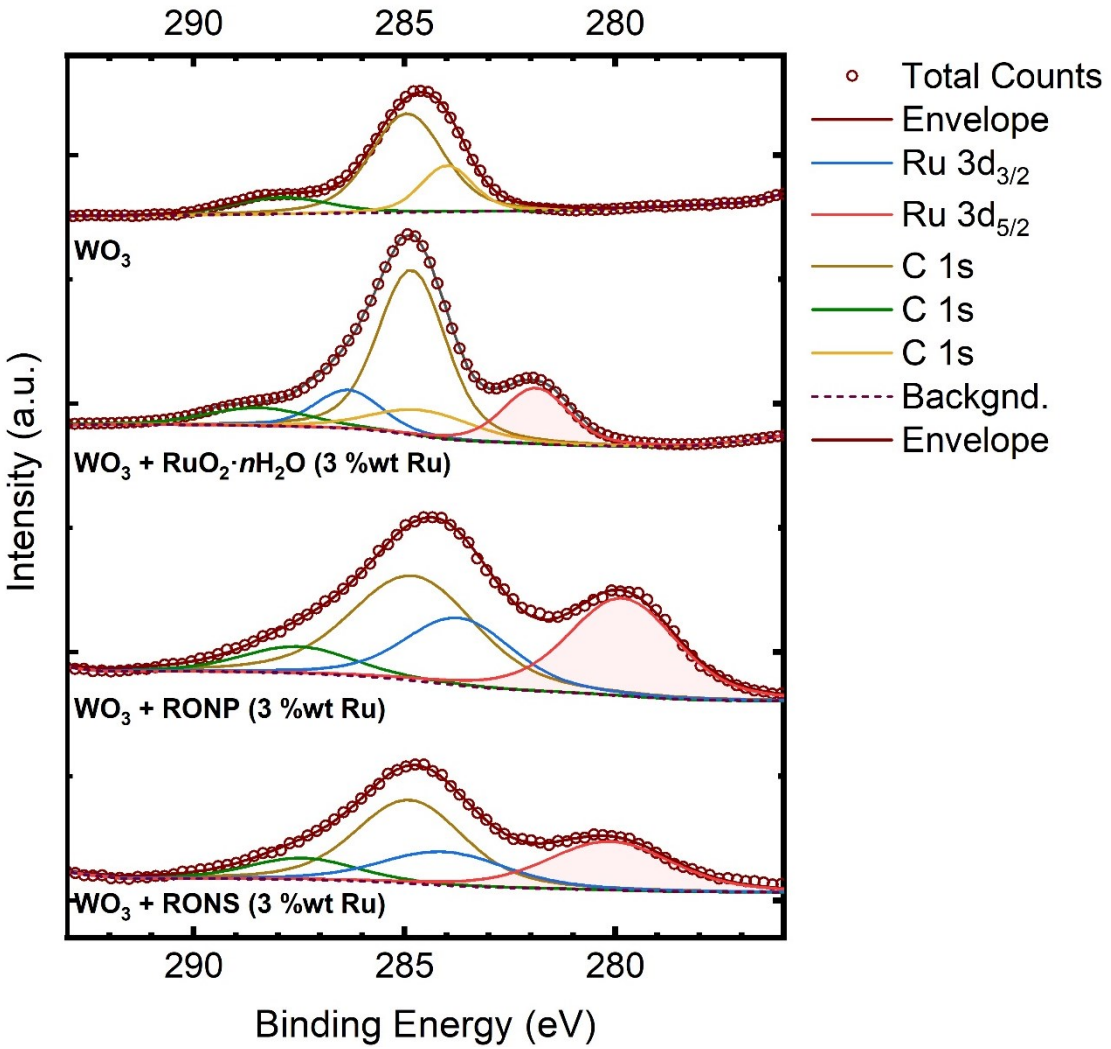

Figure D-12. X-ray photoelectron spectra (XPS) of impregnated WO_3 samples before OER photocatalytic screening. From top to bottom: WO3 reference, RuO2·*n*H2O/WO3 (3 %wt Ru), RONP/WO3 (3 %wt Ru), RONS/WO3 (3 %wt Ru). Area under the Ru 3d5/2 signal is filled. The pure WO3 reference sample was measured with and without further thermal treatment, showing no observable differences due to the impregnation conditions. The fitted Ru 3d5/2 signal of RONP and RuO2·*n*H2O match the peak position (~280.7 and 282 eV, respectively) reported for the same materials in the literature.3 The fitted Ru 3d5/2 signal of RONS should be a superposition of Ru(III) and Ru(IV) distinctive peaks.4,5 Yet, the RONS/WO3 displays only an apparent single peak centered around 280.7 eV due to the low amount of Ru loading and WO3 background. As the RONS are surrounded by WO3 particles in RONS/WO3, it is difficult to get a prominent XPS signal from the sample to further look for other chemical differences between RONS/WO3 and RONP/WO3 after impregnation.

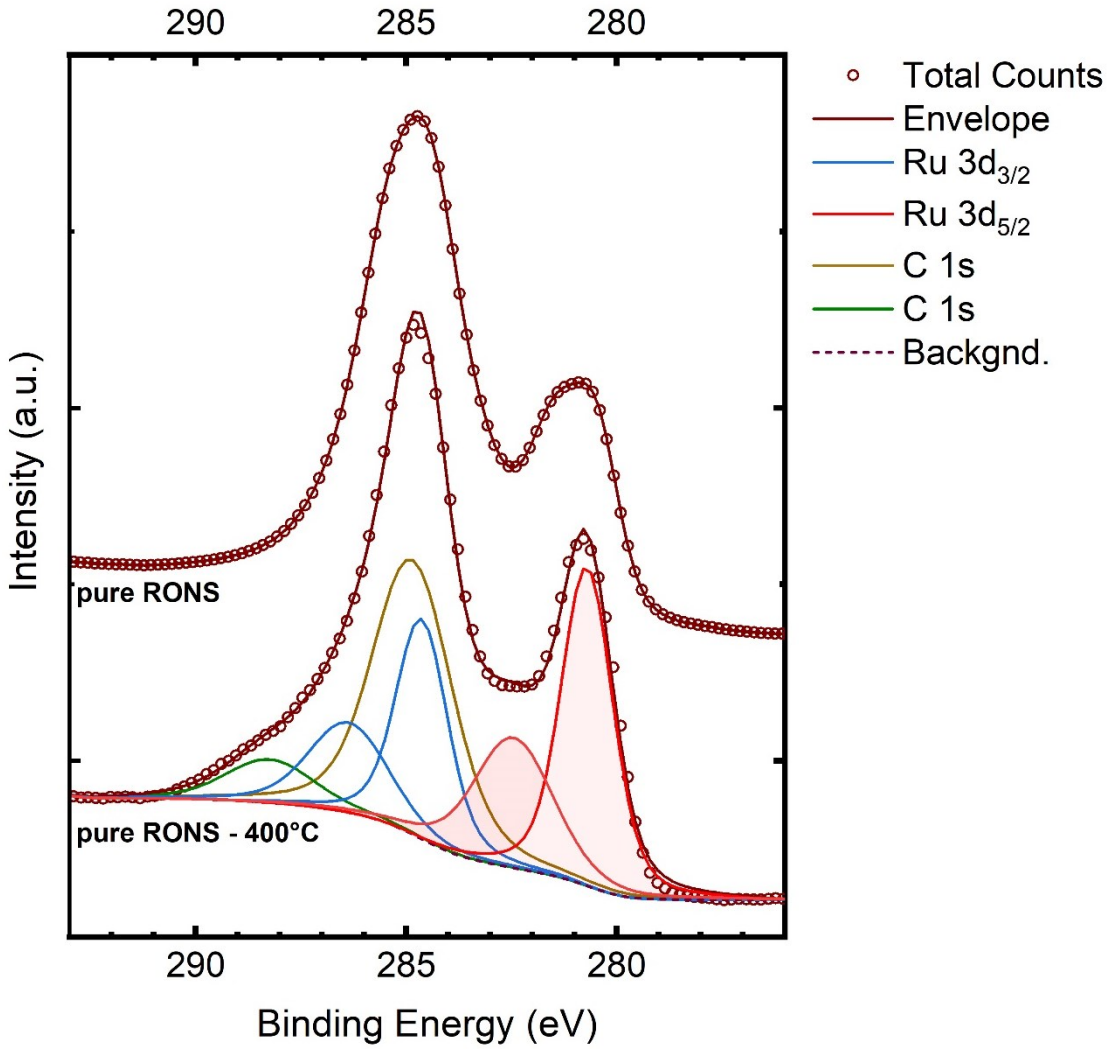

Figure D-13. X-ray photoelectron spectra (XPS) of pure exfoliated RONS before the WO_3 impregnation samples used for OER photocatalytic screening. From top to bottom: pure exfoliated RONS reference before (pure RONS) and after (pure RONS-400°C) being exposed to identical conditions as the impregnated WO3 samples in Figure D-10 (400 °C, 1.5 h). Area under the Ru 3d5/2 signal is filled. Although the fitted Ru 3d5/2 signal of RONS/WO3 displays only a single peak centered around 280.7 eV (Figure D-10), the RONS' Ru(III) and Ru(IV) distinctive peaks are observed when XPS was performed on pure exfoliated RONS after calcination. The fitted Ru 3d5/2 signal of pure RONS after calcination matches the Ru(IV) and Ru(III) peaks positions (~280.8 and 282.3 eV, respectively) reported for the same material in the literature.4,5 The XPS data overlay of pure RONS before calcination (envelope and total counts) shows qualitatively no significant changes due to the thermal treatment used for the WO3 impregnation. These observations agree with the Ru 3d5/2 peak position and thermal stability of the RONS reported in our previous work, which implies that the RONS impregnated on WO3 corresponds to that same water oxidation cocatalyst.4,5

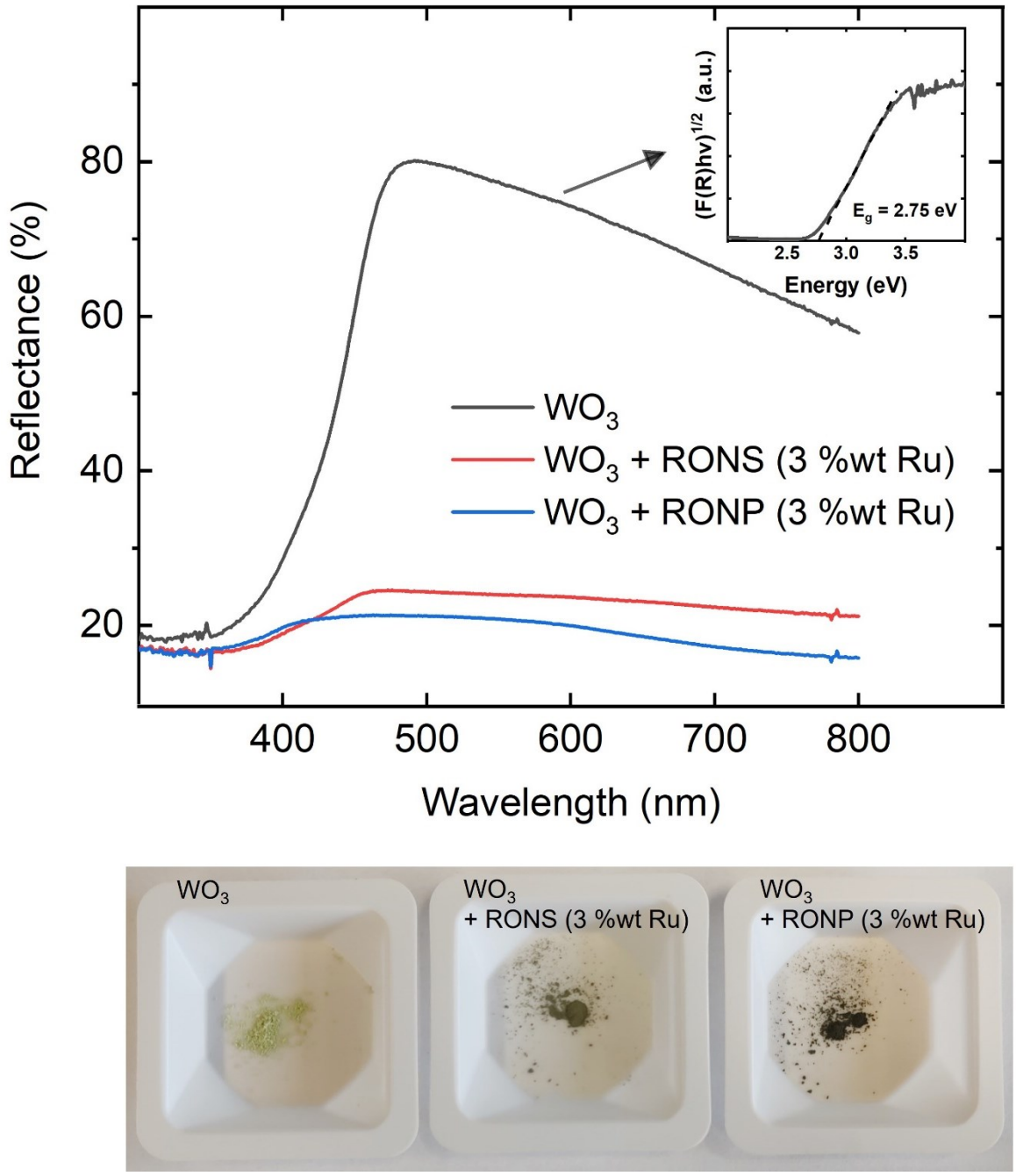

Figure D-14. (top) UV-Vis powder diffuse reflectance spectra (DRS) of impregnated and bare WO3 samples. Inset, Tauc plot obtained from bare WO3 DRS data (optical band gap: 2.75 eV). **(bottom)** Picture of 10 mg of the measured powders.

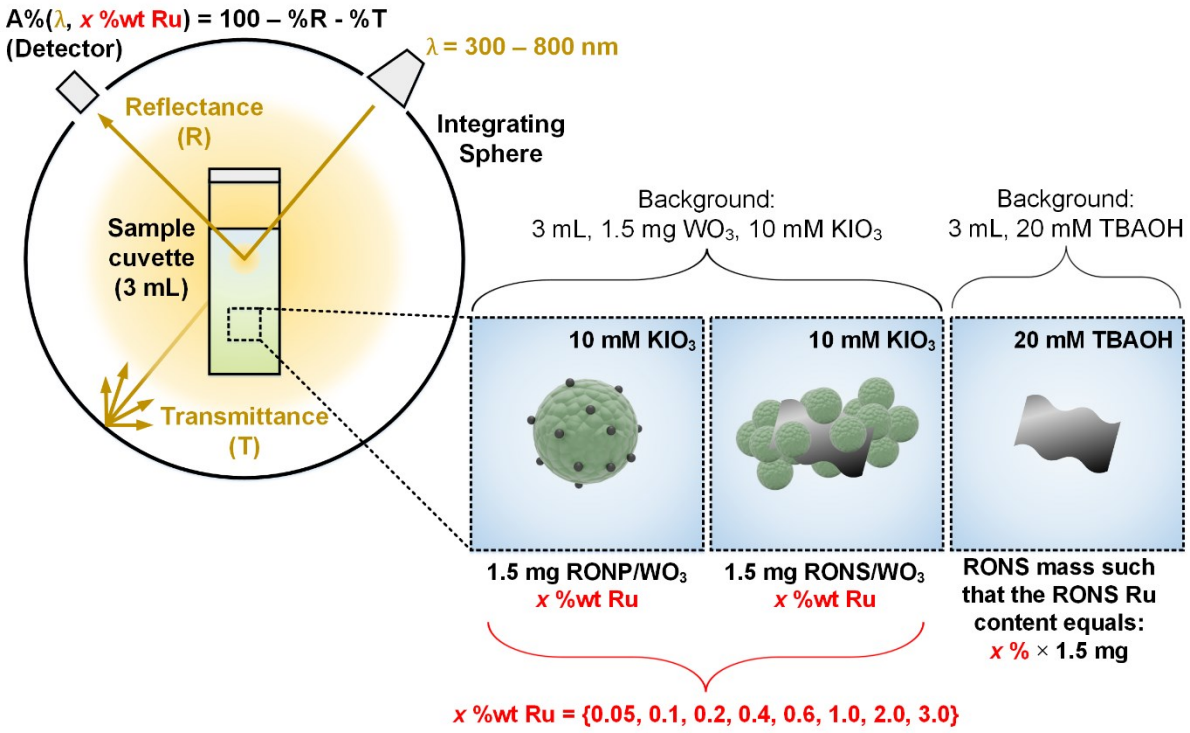

Figure D-15. Depiction of UV-Vis diffuse transmission spectroscopy experiments on pure RONS colloidal suspension, and RONS/WO_3 and RONP/WO_3 nanoparticulate suspensions. Suspension absorptance (*A*) is measured in an integrating sphere, using a quartz cuvette containing 3 mL of suspension. *A* of pure RONS colloidal suspension is background subtracted from the *A* of a blank cuvette containing water and 20 mM TBAOH ($A_{corrected} = 1 - (1 - A_{sample})/(1 - A_{background})$). Likewise, *A* of RONS/WO_3 and RONP/WO_3 suspensions (0.5 mg mL^{-1}, 10 mM KIO_3) are background subtracted from the *A* of a blank cuvette containing water, bare WO_3, and electron acceptor (0.5 mg mL^{-1}, 10 mM KIO_3). Mass of Ru in suspension is equivalent among the three types of samples at each Ru loading level. Ru loading levels are expressed as Ru content on WO_3 samples (%wt Ru: 0.05, 0.1, 0.2, 0.4, 0.6, 1.0, 2.0, and 3.0).

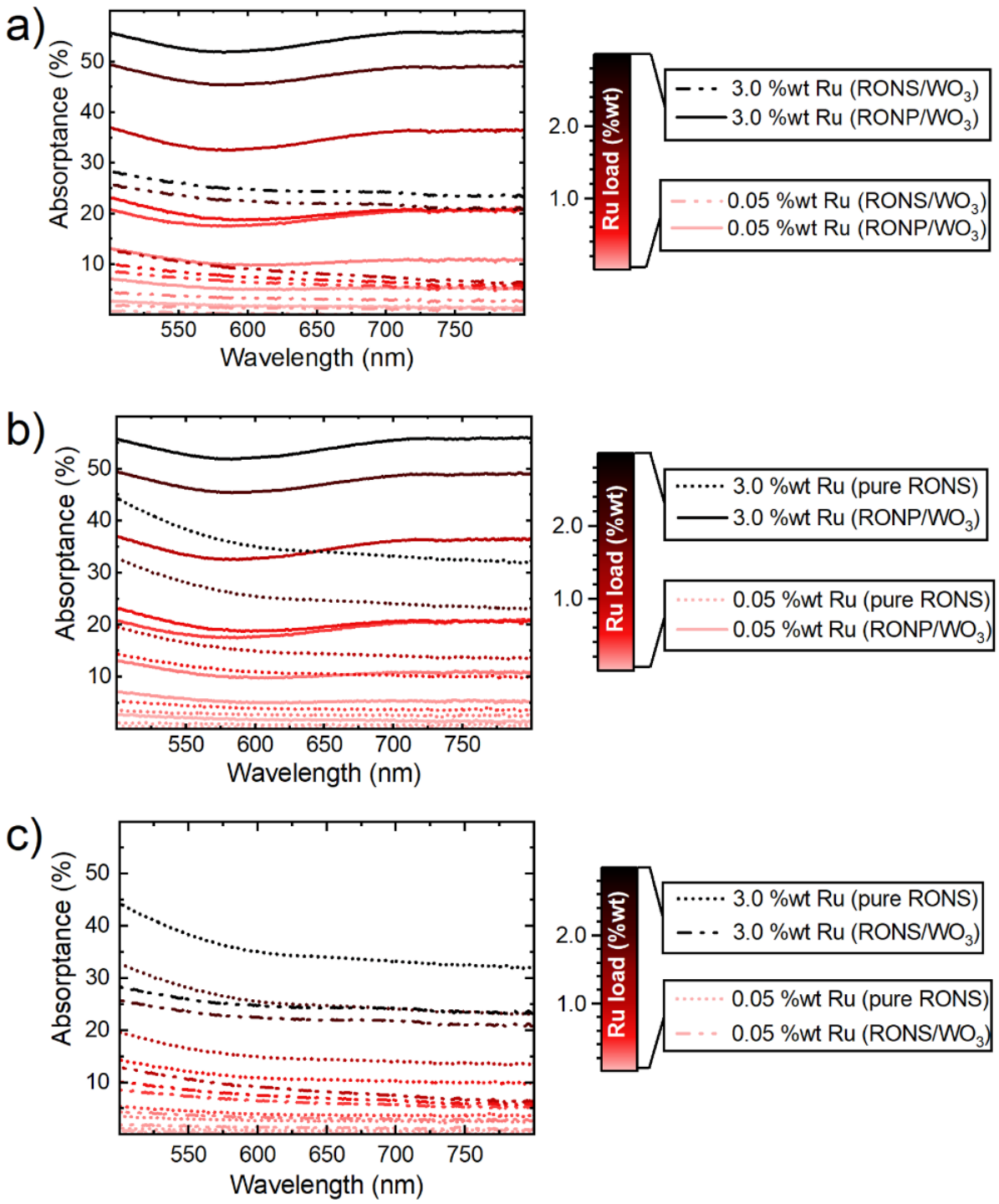

Figure D-16. UV-Vis spectroscopy (500-800 nm) of pure RONS colloidal suspension, and RONS/WO_3 and RONP/WO_3 nanoparticulate suspensions. The displayed suspension absorptance (*A*) is corrected (background subtraction) so that it only corresponds to the absorptance of RONP and RONS in suspension, as explained in Figure D-13. Mass of Ru in suspension is equivalent among the three types of samples at each Ru loading level (solid lines: RONP/WO_3, dashed-dotted lines: RONS/WO_3, dotted lines: pure RONS). Ru loading levels are expressed as Ru content on WO_3 samples (%wt Ru: 0.05, 0.1, 0.2, 0.4, 0.6, 1.0, 2.0, and 3.0), and displayed as the color progression of the curves (color bar on the right). **(a)** Overall absorptance difference of WO_3 supported RONP and RONS, **(b)** optical transparency of pure RONS versus RONP/WO_3, and **(c)** comparison of WO_3 supported RONS versus pure RONS for shielding effect screening.

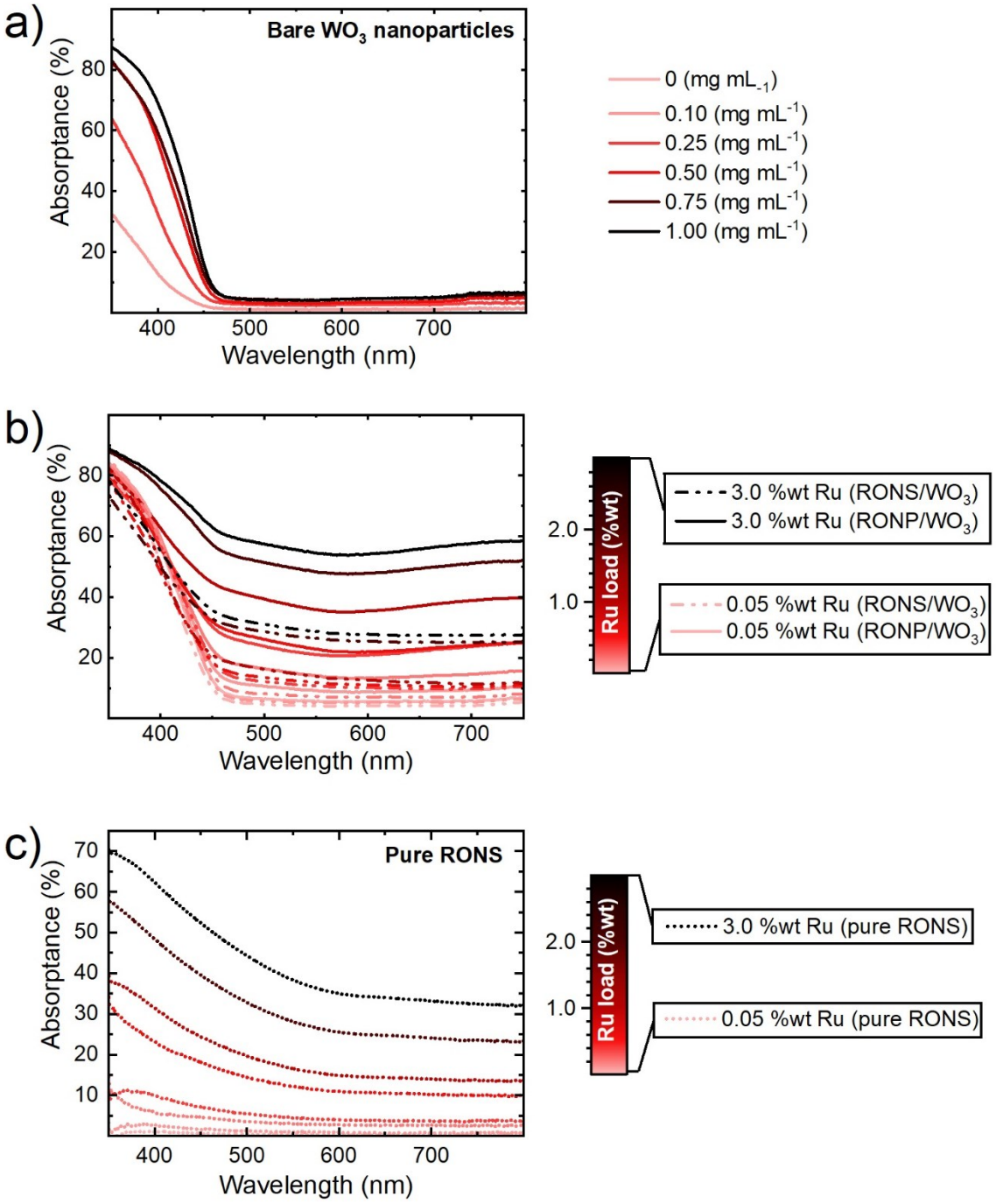

Figure D-17. UV-Vis spectroscopy (350-800 nm) of **(a)** bare WO_3 nanoparticulate suspensions at different concentrations and in the presence of sacrificial electron acceptor (10 mM KIO_3), **(b)** the RONS/WO_3 and RONP/WO_3 nanoparticulate suspensions, which is the same data in Figure D-14a but including the WO_3 absorptance background (0.5 mg mL^{-1}), and **(c)** pure RONS, which is the same data in Figure D-14b and Figure D-14c but extended to the UV range. Suspensions absorptance is measured in an integrating sphere, using a quartz cuvette containing 3mL suspension. Absorptance of suspensions in (a) and (b) are background subtracted from the absorptance of a blank cuvette containing only water and electron acceptor (10 mM KIO_3). Absorptance of pure RONS colloidal suspensions in (c) are background subtracted from the absorptance of a blank cuvette containing water and 20 mM TBAOH.

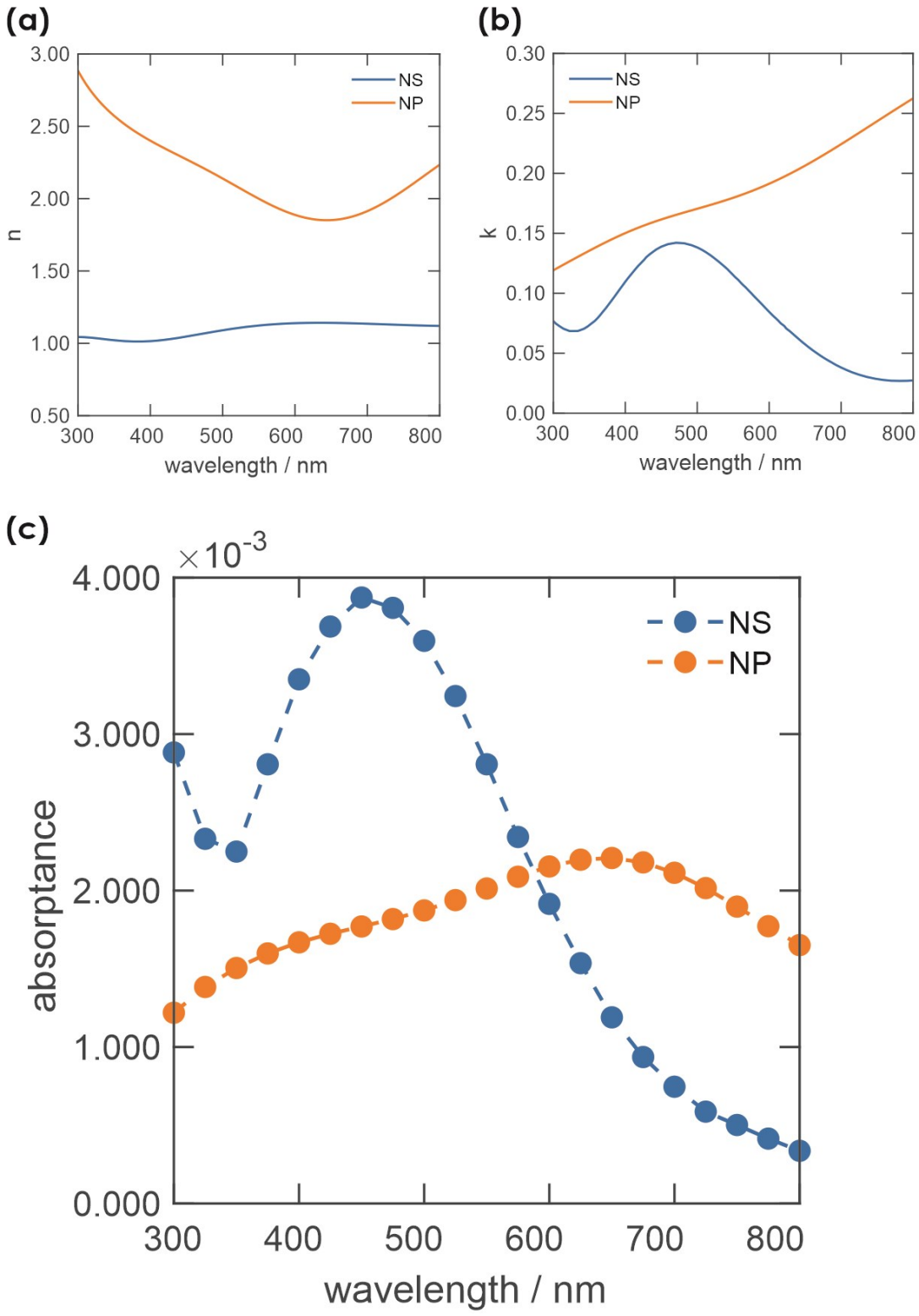

Figure D-18. Spectral dependence of the real (a) and imaginary part (b) of the complex refractive index ($n + i \cdot k$) of the RONP (orange) and RONS (blue) materials employed in the calculations.[6,7] **(c)** Absorptance of 1 RONS (500 nm x 500 nm x 1 nm) versus the absorptance of a number of RONP (spheres of 5 nm radius) totaling a volume equivalent to 1 RONS (which corresponds to 477 RONP), calculated using finite difference time domain numerical analysis of individual RONS and RONP embedded in air, and photons perpendicular to the RONS plane.

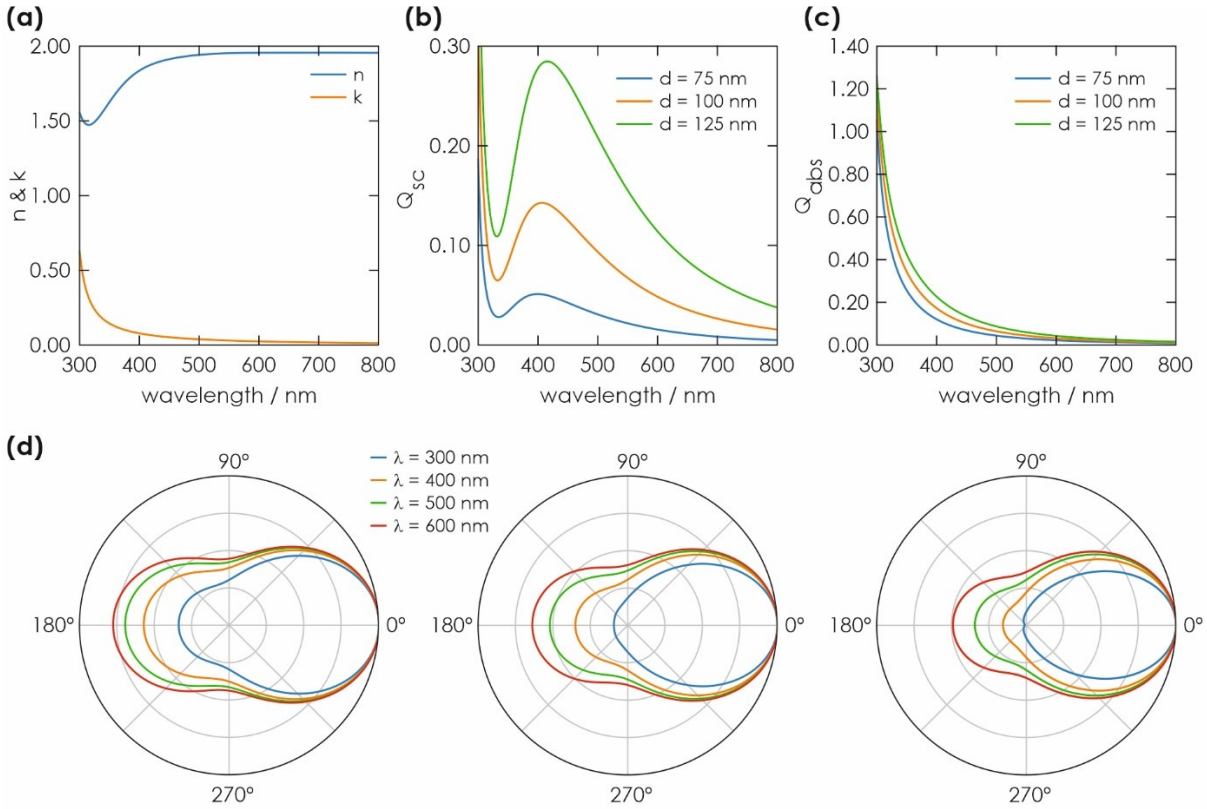

Figure D-19. (a) Spectral dependence of the real (blue) and imaginary part (orange) of the complex refractive index ($n + i{\cdot}k$) of the WO_3 employed in the calculations.[10] The refractive index of water is considered constant at a value of n = 1.33. **(b)** Scattering and **(c)** absorption cross sections of spherical nanoparticles of diameter d = 75 nm (blue), d = 100 nm (orange) and d = 125 nm (green) made from WO_3 embedded in an aqueous medium. **d)** Angular distribution of scattered light for a photon incidence direction at 180° (λ= 300 nm (blue), λ = 400 nm (orange), λ = 500 nm (green) and λ = 600 nm (red)) of nanoparticles of diameter d = 75 nm (left panel), d = 100 nm (middle panel) and d = 125 nm (right panel) made from WO_3 embedded in an aqueous medium.

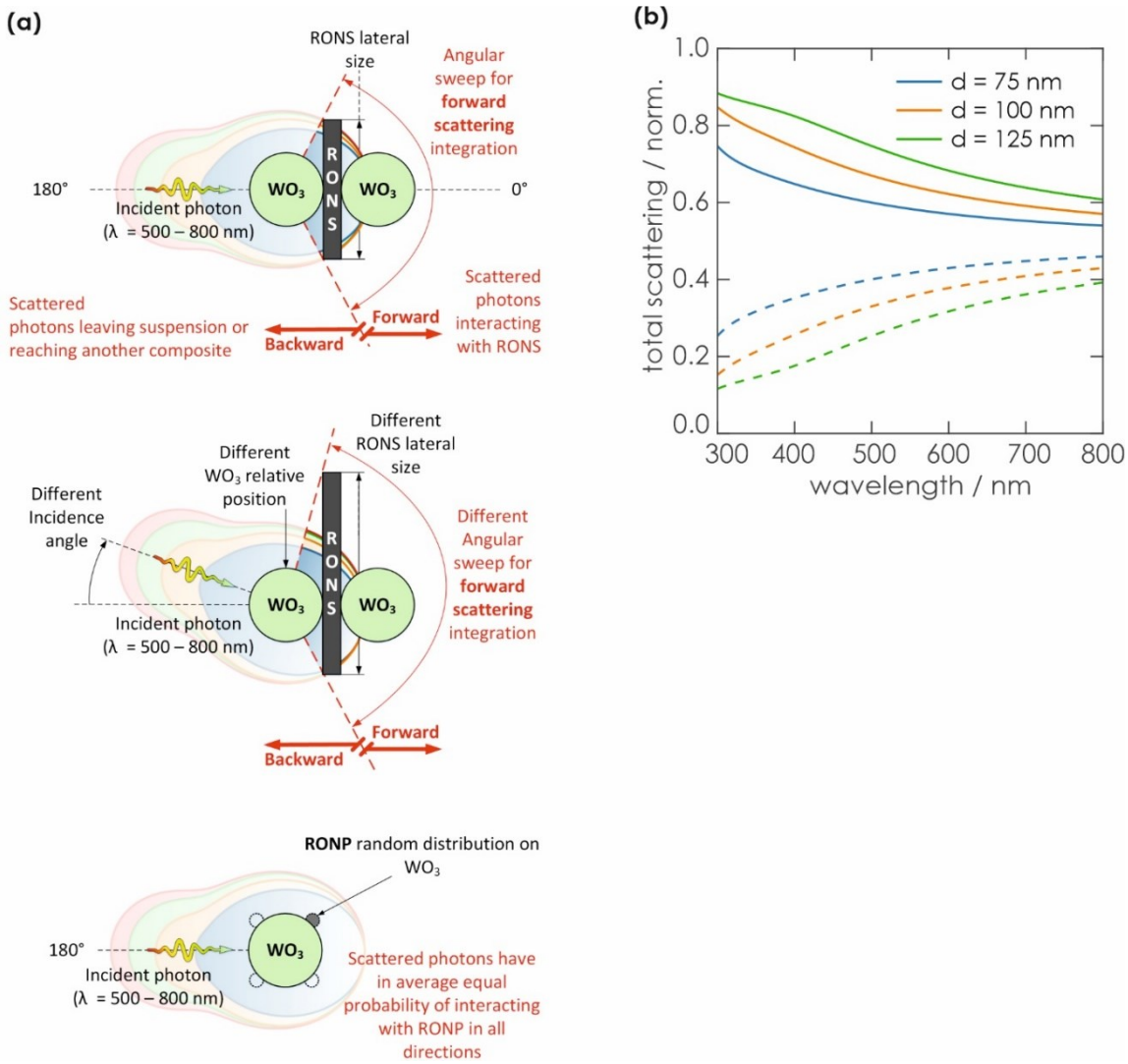

Figure D-20. (a) Forward and backward scattering depiction of an incident photon on WO_3 in RONS/WO_3 (top, middle) and RONP/WO_3 (bottom) samples. In top and bottom panel, the photon incidence angle normal to the RONS plane is arbitrarily set to 180°, as in Figure D-19d. As RONPs are uniformly and randomly distributed on WO_3, scattered photons have in average the same probability of interacting with RONP in all directions. In RONS/WO_3 samples, forward scattering is defined as the sum of all scattered photon trajectories that lead to photon interaction with the inner RONS. The forward scattering probability is calculated from the angular probability distribution integration in Figure D-19d (described as the colored background), where the angular sweep for integration depends on the photon incidence angle (rotation of the 180° angle reference in Figure D-19d), the relative position of the WO_3 NP on the RONS surface, and the RONS lateral size (assumed square in lateral dimensions). While the depicted RONS lateral size to WO_3 NP diameter aspect ratio is 1:2 (top) and 1:3 (bottom), the experimentally measured aspect ratio ranges from 1:2 to 1:10, which results in an average angular sweep for forward scattering integration close to 180°, as described in the top panel. **(b)** Average forward (solid) and backward (dashed, *100% - forward*) total scattering probability of spherical nanoparticles of diameter d = 75 nm (blue), d = 100 nm (orange) and d = 125 nm (green) made from WO_3 embedded into an aqueous medium. The average forward scattering probability is calculated from the angular probability distribution in Figure D-19d and the limiting case described in (a) for a large RONS lateral size, a WO_3 NP centered on the RONS surface, and a photon incidence angle of 180° (angular sweep from 270° to 90°). The angular sweep for integration was also varied for multiple scattering event simulating a random photon incidence angle (between 90° and 270°), a random RONS lateral size (between 200 and 1000 μm), and a random position of the WO_3 NP on the RONS, obtaining no significant differences.

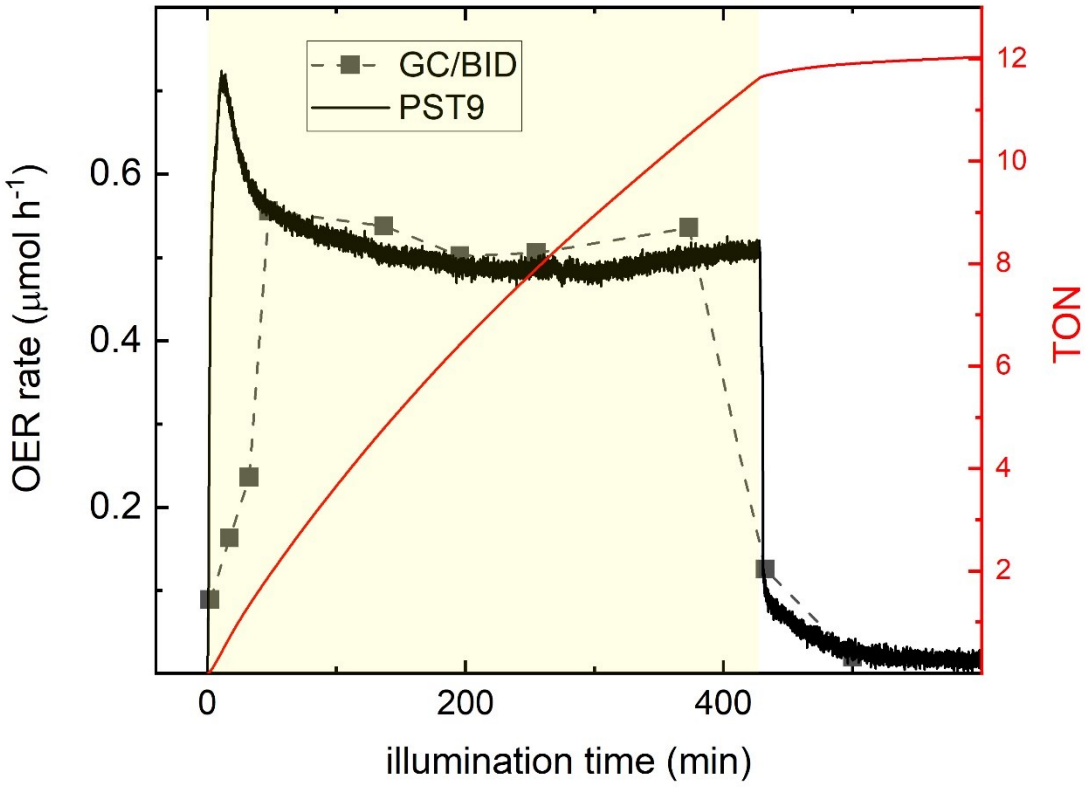

Figure D-21. Photocatalytic stability of RONS/WO_3 (1 %wt Ru). After the initial drop in activity after 10 min of illumination, it remains stable for 7 h under continuous illumination reaching a turnover number (TON) of 12. The maximum activity of RONS/WO_3 in time was almost fully recovered after redispersing and illuminating the suspension at the end of the experiment. This observation suggests that the loss of activity after 30 min is only due to suspension sedimentation or mass transfer limitations, and that RONS/WO_3 is stable under photocatalysis conditions. Photocatalysis conditions: 10 mL ultrapure water, 10 mM KIO_3, 0.5 mg mL^{-1} of sample and AM 1.5 Illumination.

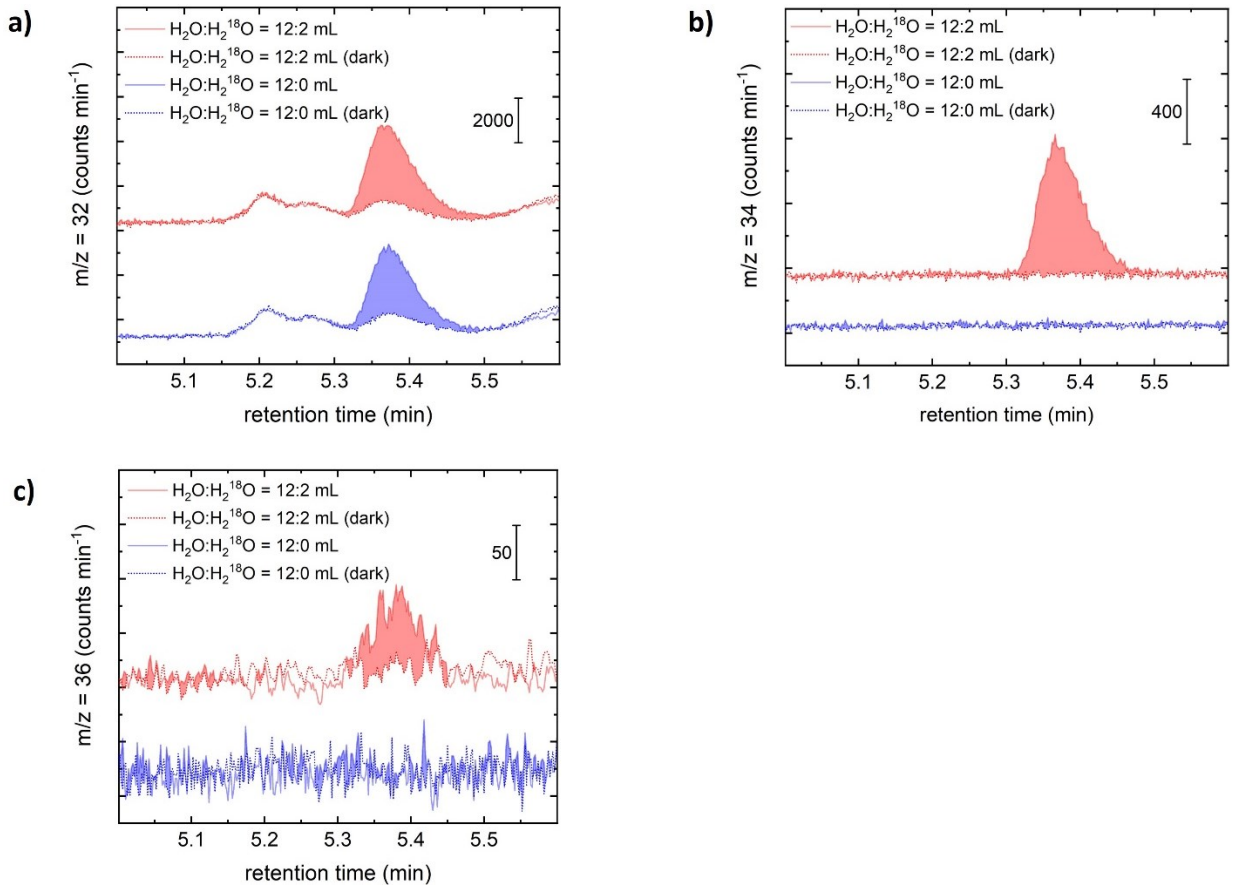

Figure D-22. (a) m/z = 32 ($^{32}O_2$), **(b)** m/z = 34 ($^{16}O^{18}O$) and **(c)** m/z = 36 ($^{36}O_2$). Blue indicates regular photocatalytic experiments using 12 mL suspension as in Figure D-23a. Red indicates same photocatalytic experiments but with an additional 2 mL of $H_2{}^{18}O$ (97% isotopic purity). Counting rate at the multiple ion chromatograph channels (MIC, y-axis) is obtained at O_2 gas chromatograph (GC) retention time (5.47 min), before (dotted line) and after (solid lines) sample illumination at same conditions. Integration of peaks is displayed as the shaded area between signal after illumination and dark baseline, which is roughly proportional to O_2 molecules coming from photocatalytic OER (ΔA). Isotopic distribution is obtained by % of ΔA of the species to total integrated ΔA of channels m/z = 32, 34, 36.

Table D-2. Integral analysis of O peaks described in Figure D-22. The result summarizes the isotopic distribution in percentage (*Experimental mean*), after five light-on/light-off cycles. Value for each cycle is the average of two points at stable OER signal after illumination. *Standard error (SE) of the mean* in % is presented for the 5 cycles. Theoretical values are calculated from random water oxidation using the molar fraction of $H_2{}^{18}O$.

Species	Experimental mean (avg)	SE of the mean %	theoretical
$^{16}O^{16}O$	77.2	0.3	76.3
$^{16}O^{18}O$	21.1	0.2	22.1
$^{18}O^{18}O$	1.7	0.2	1.6

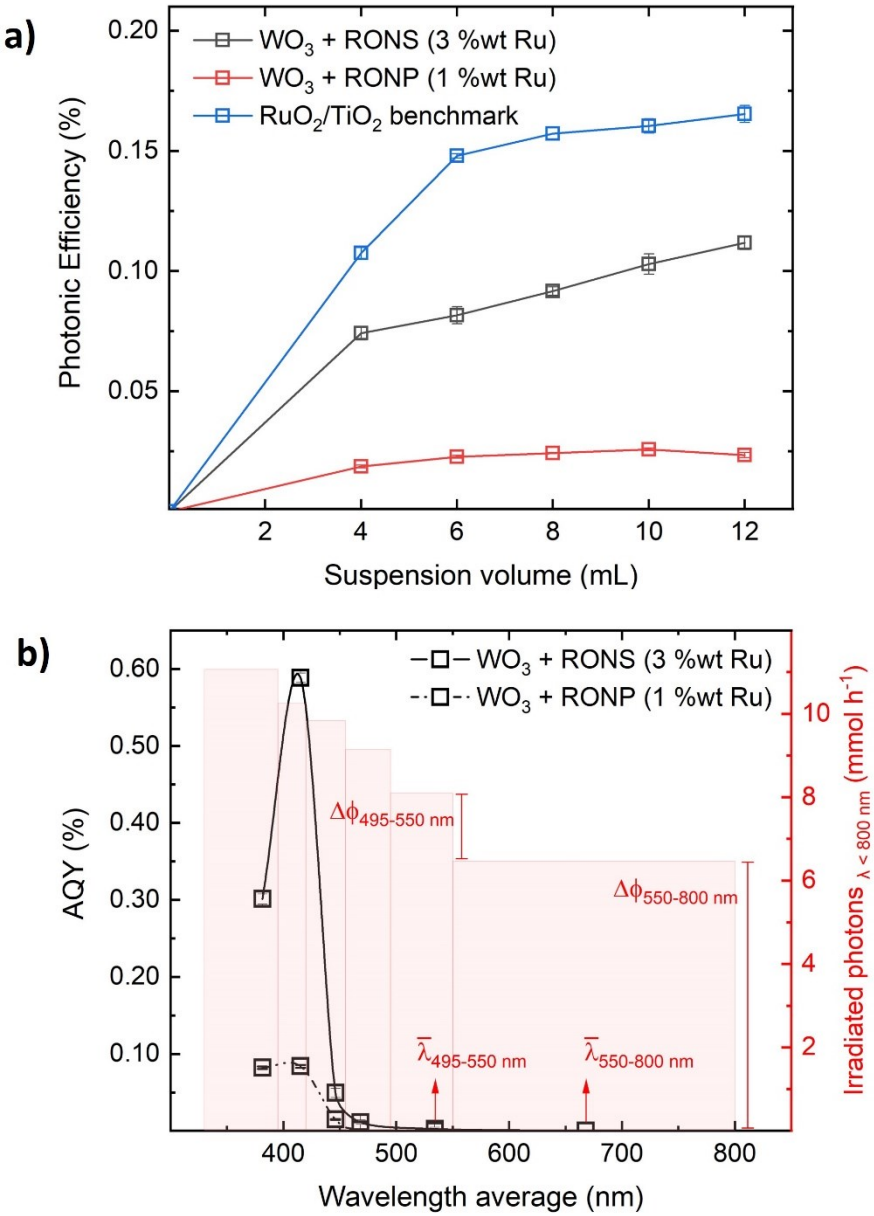

Figure D-23. Photocatalytic OER rate standardization of RONS/WO_3 (3 %wt Ru) and RONP/WO_3 (1 %wt Ru). Photoreactor cell for finer optics employed. **(a)** Optimal photonic efficiency curves contrasted with RuO_2/TiO_2 benchmark.[1] Photocatalysis conditions: step-wise addition of 2 mL suspension containing ultrapure water, 10 mM KIO_3, and 0.5 mg mL^{-1} of sample. AM 1.5 Illumination (100 mW cm^{-2}). Error bars represent mean ± SE of the mean of the average activity of two independent batches of sample (see details in Experimental Section); **(b)** *Apparent quantum yield* (AQY) curves. AQY is obtained as the ratio of the differential OER rate increase to the differential photon counting (ΔΦ) after exchanging cut-on filters, from longer to shorter wavelength (cut-on filters spectra in Figure D-24). In primary axis (black), AQY is graphed versus the average wavelength ($\bar{\lambda}$) of the band between cut-on filters. In secondary axis (red), cumulative frequency distribution bar graph of irradiated photons (λ< 800 nm) versus the wavelength band between cut-on filters. Photocatalysis conditions: 10 mL suspension containing ultrapure water, 10 mM KIO_3, and 0.5 mg mL^{-1} of sample. AM 1.5 Illumination (100 mW cm^{-2}), with external cut-on filters. Error bars represent mean ± standard error of the mean of the average activity of two independent batches of sample (see details in Experimental Section).

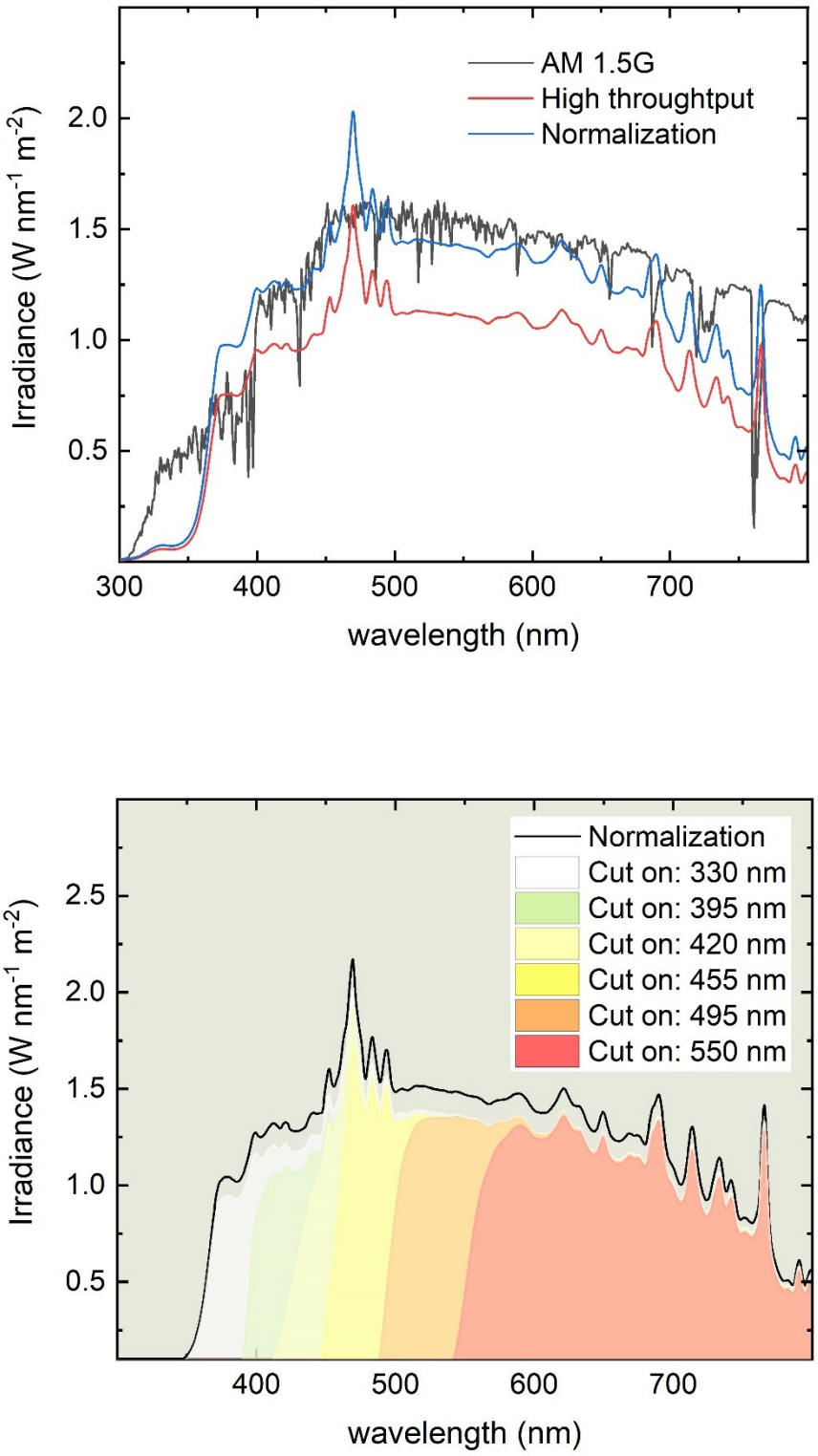

Figure D-24. Incident light lamp spectrum (blue and red) used in the study, together with AM1.5G (ASTM G-173-03) solar irradiance spectrum (black). Cut on filters are represented as colored areas (bottom).

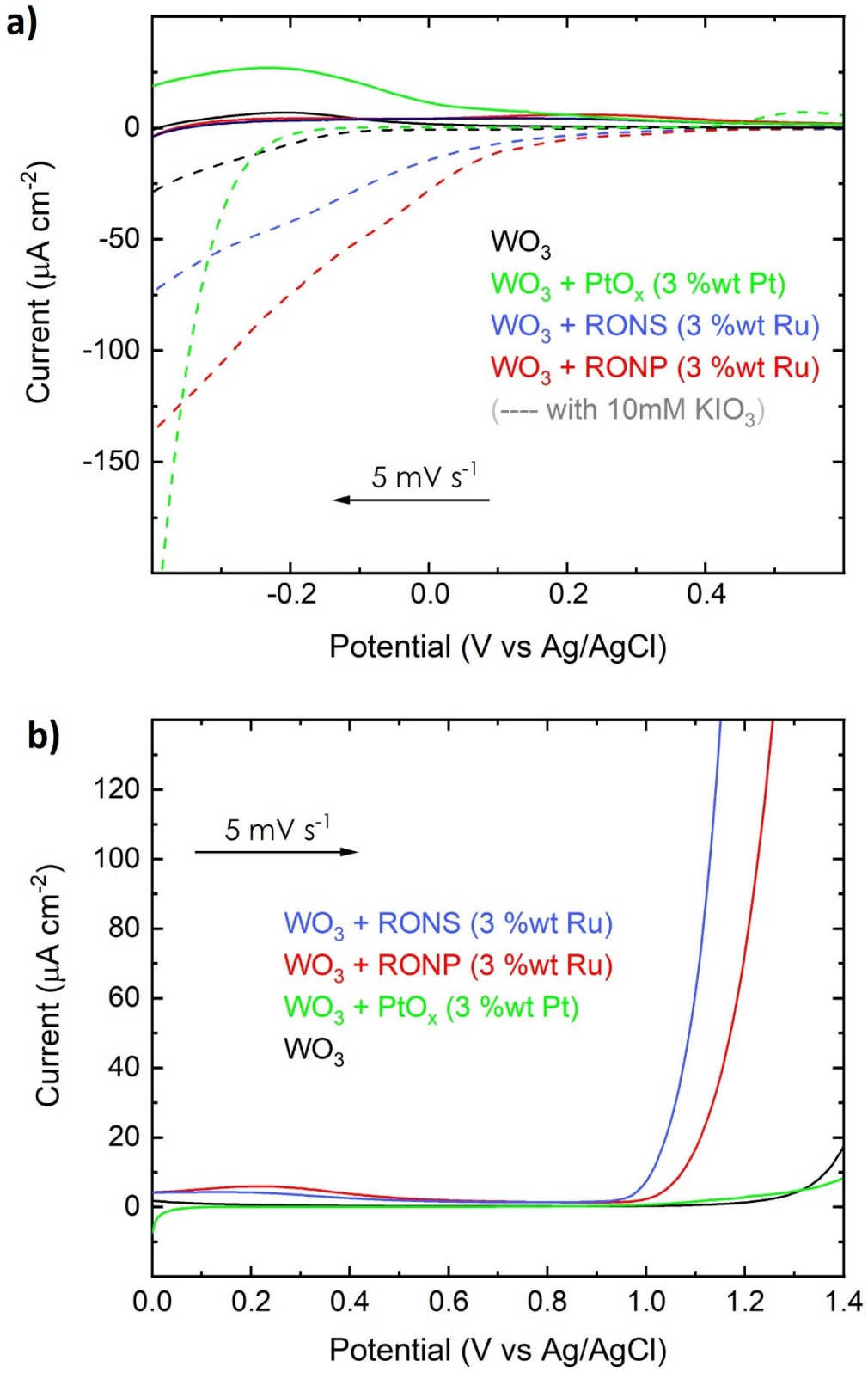

Figure D-25. (a) Cathodic currents (LSV) for WO_3 + cocatalyst electrodes in 0.1 M aqueous Na_2SO_4 solution, containing no (solid lines) or 10 mM KIO_3 (dashed lines). The positive current bump for the WO_3+PtO_x sample when no KIO_3 is present results most likely from contaminates which were not completely removed during a prior activation CV measurement. **(b)** Dark anodic currents (LSV). Scan rate: 5 mV s^{-1}.

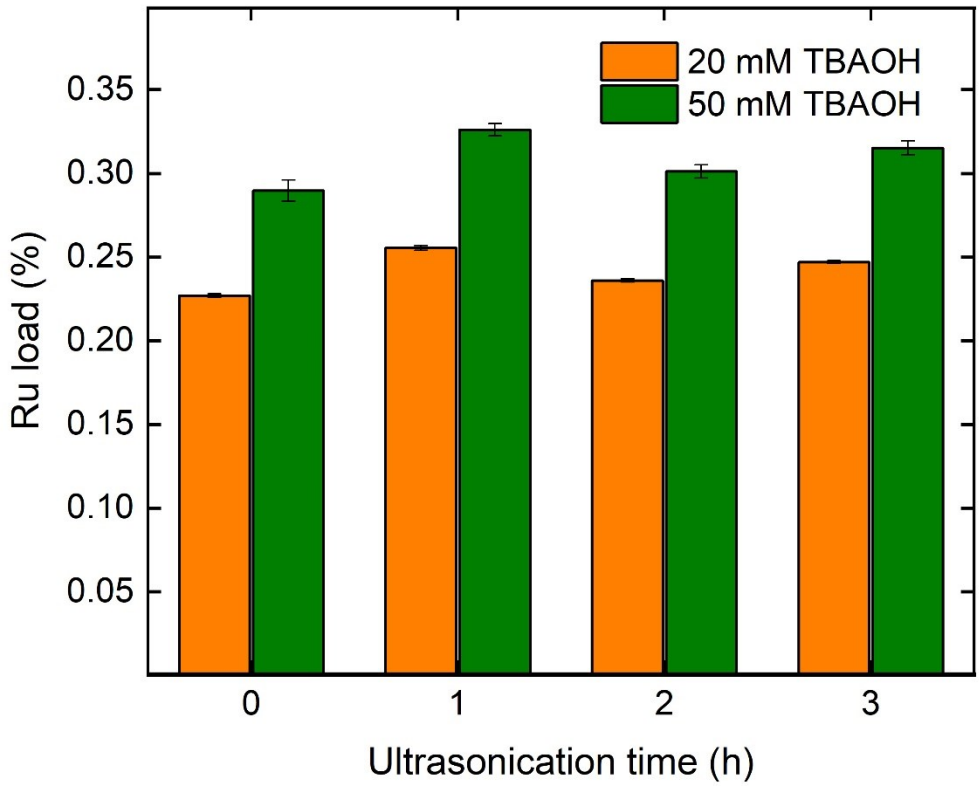

Figure D-26. Ruthenium loadings from Inductively Coupled Plasma (ICP) analysis of size controlled nanosheets experiments.

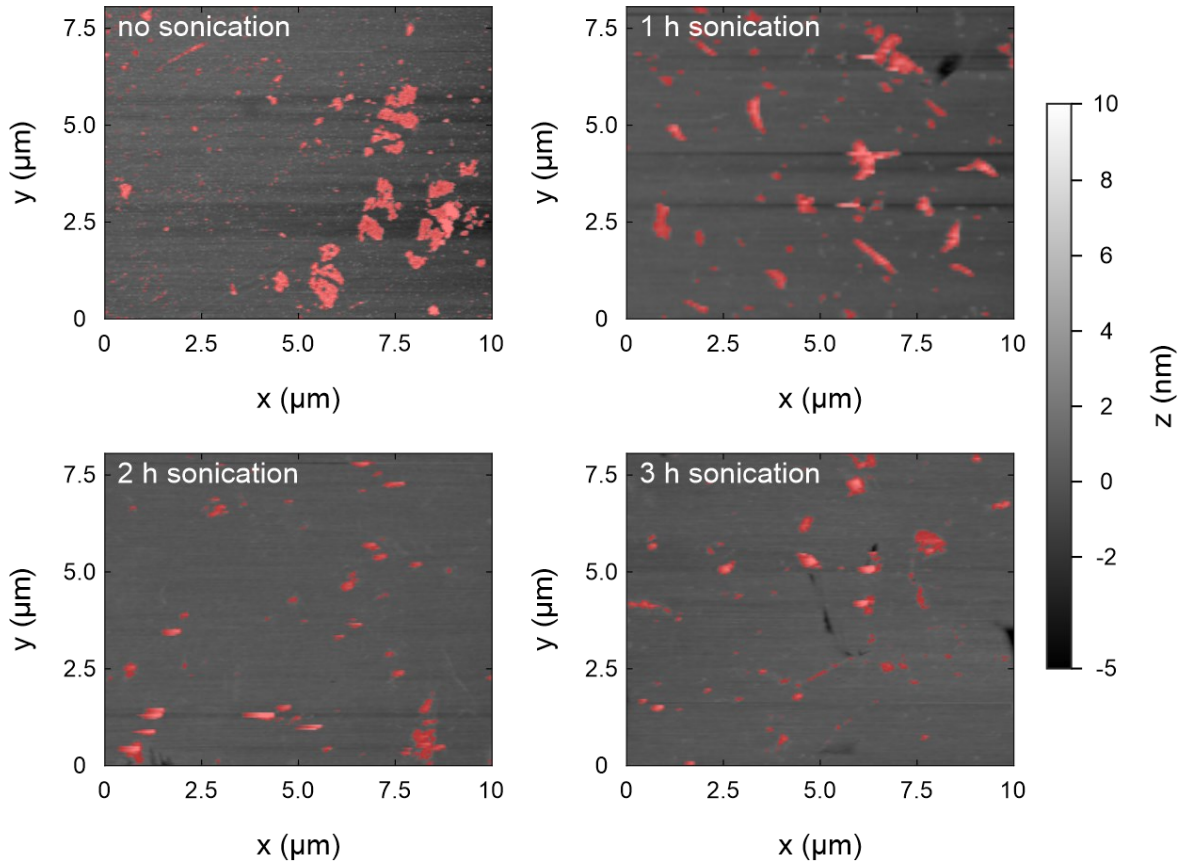

Figure D-27. AFM raw images of the vortexed/exfoliated RONS at different ultrasonication times and 20 mM TBAOH. Red shaded areas are marked with a height filter (> 5 nm) to quantify thickness of nanosheets.

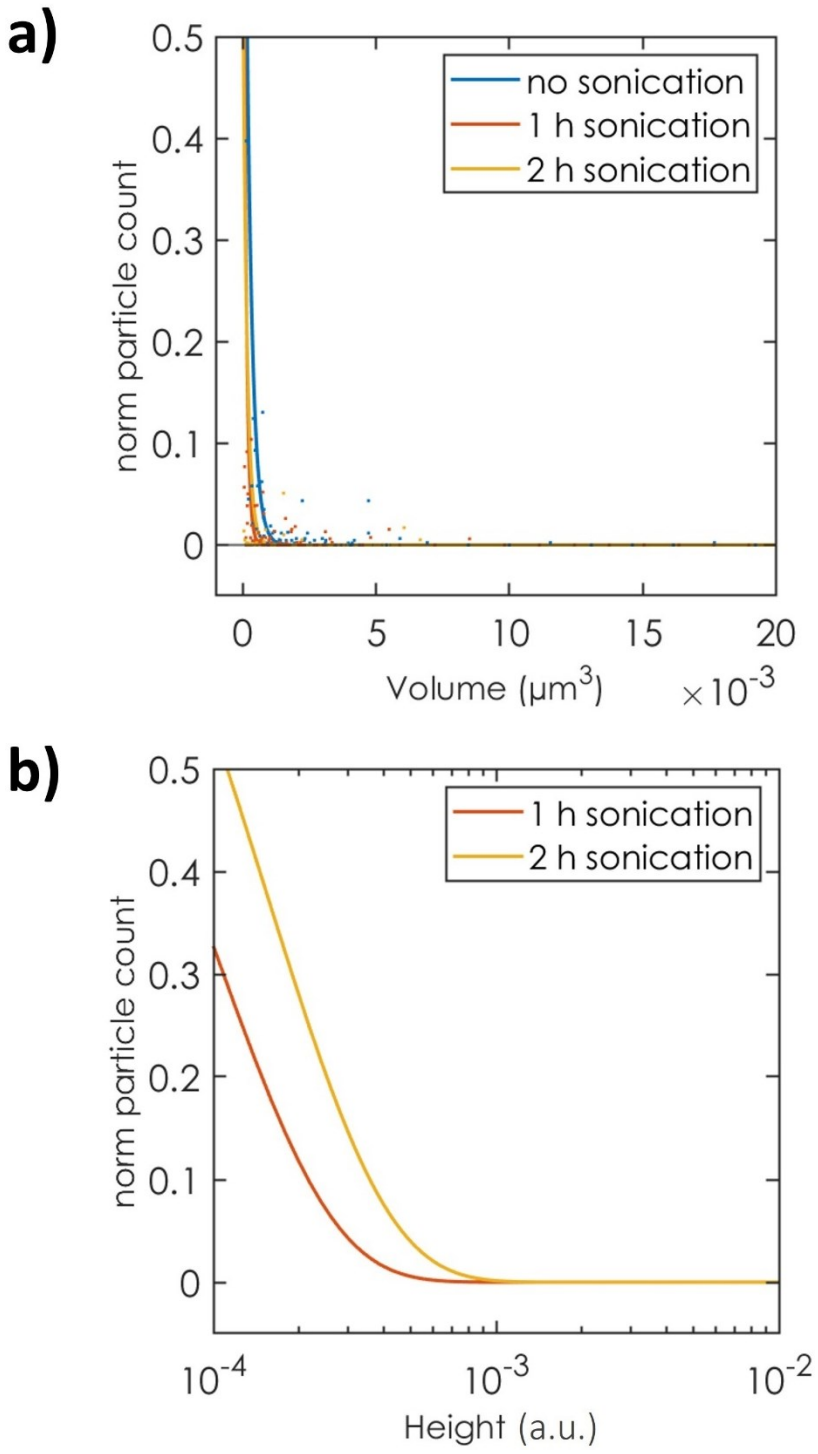

Figure D-28. (a) Nanosheet volume distribution from AFM images of the vortexed/exfoliated RONS at different ultrasonication times and 20 mM TBAOH (x-axis in Figure 6-4a). **(b)** Nanosheet extrapolated height distribution (in arbitrary units) at 1 and 2 h of ultrasonication times and 20 mM TBAOH, calculated from the ratio of exponential fittings of the RONS volume distribution in (a) to the area distribution of the RONS in Figure 6-4b. Qualitatively, AFM images of vortexed/exfoliated RONS samples at 0 and 3 h of ultrasonication time display the lowest and highest average nanosheet height, respectively. This result suggests that apparent nanosheet height of vortexed/exfoliated RONS increases monotonically with ultrasonication time.

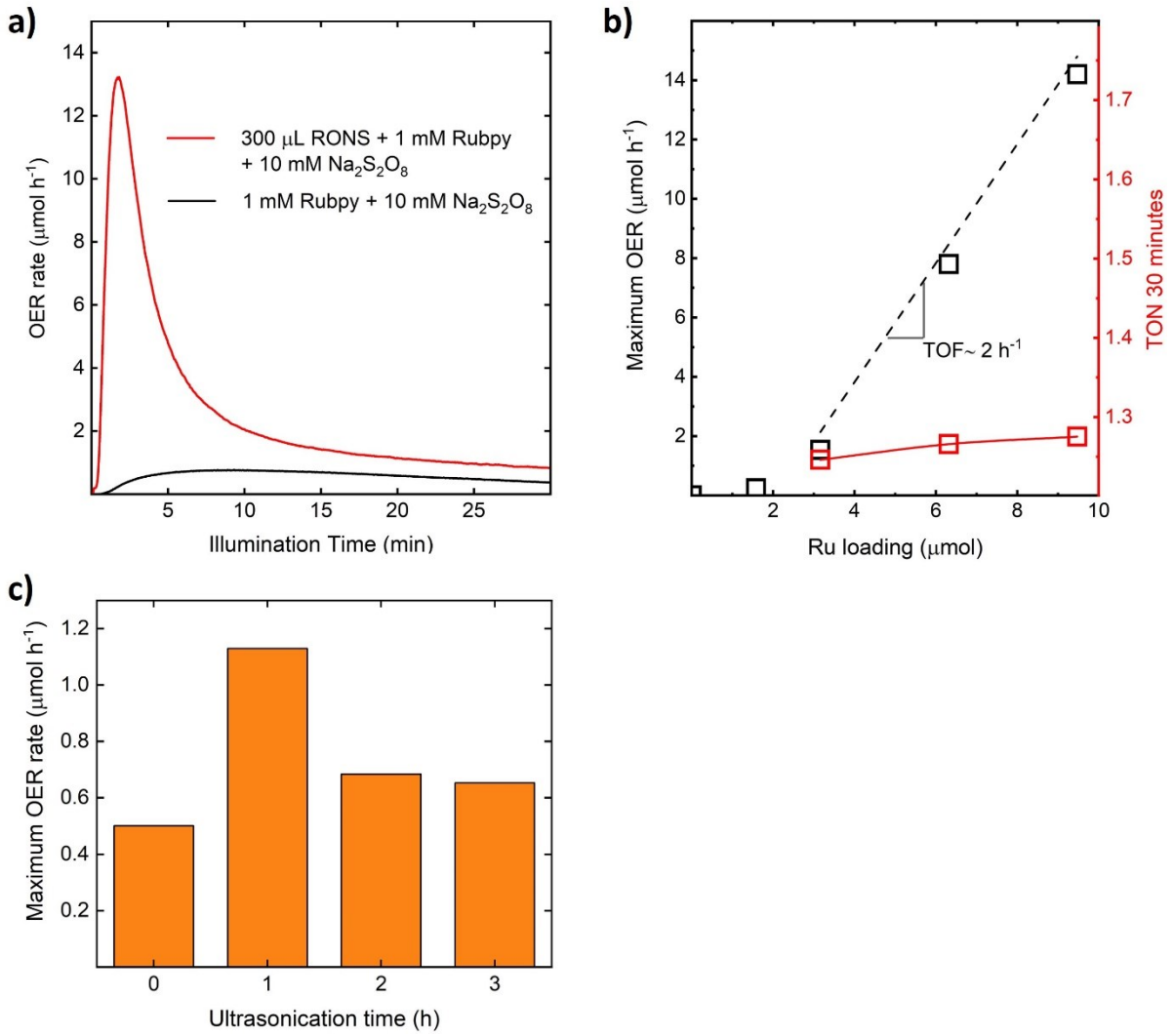

Figure D-29. (a) Black curve: dynamic OER rate of blank 10 mL suspension containing dye ($[Ru(bpy)_3]^{2+}$, 1 mM) and sacrificial electron acceptor ($Na_2S_2O_8$, 10 mM), after AM 1.5G illumination. In black: identical as blank suspension but to the suspension was added 300 μL of RONS colloid (approximately 10 μmol of Ru). Blanks of pure persulfate (10 mM), and RONS plus persulfate (10 μmol of Ru and 10 mM, respectively) yielded no significant OER signal. **(b)** Summary of Turnover Frequency (TOF, primary axis) and Turnover Number (TON integrated from TOF in time, secondary axis) at different RONS loadings at identical photocatalysis conditions. **(c)** Maximum OER rate obtained at identical photocatalysis conditions versus different RONS colloid ultrasonication times. RONS vials contained equal Ru loading (1 μmol) and volume (5 mL), which was obtained after exfoliation with a vortexing device and separated into 4 vials. Each vial was ultrasonicated different times (x-axis), TBAOH washed out, condensed, mixed with photocatalytic suspension, and photocatalytic OER rate was recorded (y-axis).

D.12 References

1. Vignolo-González, H. A. *et al.* Toward Standardized Photocatalytic Oxygen Evolution Rates Using RuO2@TiO2 as a Benchmark. *Matter* **3**, 464–486 (2020).
2. Laha, S. *et al.* Ruthenium Oxide Nanosheets for Enhanced Oxygen Evolution Catalysis in Acidic Medium. *Adv Energy Mater* **9**, 1803795 (2019).
3. Fukuda, K. *et al.* Synthesis of nanosheet crystallites of ruthenate with an α-NaFeO 2-related structure and its electrochemical supercapacitor property. *Inorg Chem* **49**, 4391–4393 (2010).
4. Ma, S. S. K., Maeda, K., Abe, R. & Domen, K. Visible-light-driven nonsacrificial water oxidation over tungsten trioxide powder modified with two different cocatalysts. *Energy Environ Sci* **5**, 8390–8397 (2012).
5. Abe, R., Higashi, M. & Domen, K. Overall water splitting under visible light through a two-step photoexcitation between TaON and WO3 in the presence of an iodate-iodide shuttle redox mediator. *ChemSusChem* **4**, 228–237 (2011).
6. Suzuki, H., Nitta, S., Tomita, O., Higashi, M. & Abe, R. Highly Dispersed RuO_2 Hydrates Prepared via Simple Adsorption as Efficient Cocatalysts for Visible-Light-Driven Z-Scheme Water Splitting with an IO_3^-/I^- Redox Mediator. *ACS Catal* **7**, 4336–4343 (2017).
7. Biswal, B. P. *et al.* Sustained Solar H2 Evolution from a Thiazolo[5,4-d]thiazole-Bridged Covalent Organic Framework and Nickel-Thiolate Cluster in Water. *J Am Chem Soc* **141**, 11082–11092 (2019).
8. El-Tantawy, F. *et al.* Optical properties of nanostructured ruthenium dioxide thin films via sol–gel approach. *Journal of Materials Science: Materials in Electronics* **28**, 52–59 (2017).
9. Hong, H. *et al.* Enhanced interfacial electron transfer between thylakoids and RuO2 nanosheets for photosynthetic energy harvesting. *Sci Adv* **7**, 1–13 (2021).
10. Saygin-Hinczewski, D., Hinczewski, M., Sorar, I., Tepehan, F. Z. & Tepehan, G. G. Modeling the optical properties of WO3 and WO3–SiO2 thin films. *Solar Energy Materials and Solar Cells* **92**, 821–829 (2008).

11. Li, Y. *et al.* Maximized performance of dye solar cells on plastic: a combined theoretical and experimental optimization approach. *Energy Environ Sci* **9**, 2061–2071 (2016).
12. Miranda-Muñoz, J. M., Esteso, V., Jiménez-Solano, A., Lozano, G. & Míguez, H. Finite Size Effects on Light Propagation throughout Random Media: Relation between Optical Properties and Scattering Event Statistics. *Adv Opt Mater* **8**, 1901196 (2020).
13. Miranda-Muñoz, J. M. *et al.* Efficient bifacial dye-sensitized solar cells through disorder by design. *J Mater Chem A Mater* **4**, 1953–1961 (2016).
14. Braslavsky, S. E. *et al.* Glossary of terms used in photocatalysis and radiation catalysis (IUPAC Recommendations 2011). *Pure and Applied Chemistry* **83**, 931–1014 (2011).
15. Kisch, H. & Bahnemann, D. Best Practice in Photocatalysis: Comparing Rates or Apparent Quantum Yields? *Journal of Physical Chemistry Letters* **6**, 1907–1910 (2015).
16. Qureshi, M. & Takanabe, K. Insights on measuring and reporting heterogeneous photocatalysis: Efficiency definitions and setup examples. *Chemistry of Materials* **29**, 158–167 (2017).
17. Gottschling, K. *et al.* Rational Design of Covalent Cobaloxime–Covalent Organic Framework Hybrids for Enhanced Photocatalytic Hydrogen Evolution. *J Am Chem Soc* **142**, 12146–12156 (2020).
18. Wang, Z. *et al.* Efficiency Accreditation and Testing Protocols for Particulate Photocatalysts toward Solar Fuel Production. *Joule* **5**, 344–359 (2021).
19. Schneider, J. & Bahnemann, D. W. Undesired Role of Sacrificial Reagents in Photocatalysis. *J. Phys. Chem. Lett.* **4**, 3479–3483 (2013).
20. Kunz, L. Y. *et al.* Artificial inflation of apparent photocatalytic activity induced by catalyst-mass-normalization and a method to fairly compare heterojunction systems. *Energy Environ Sci* **12**, 1657–1667 (2019).
21. Persson, K. Materials Data on Ru (SG:194) by Materials Project. **4**, (2016).
22. Erbs, W., Desilvestro, J., Borgarello, E. & Graetzel, M. Visible-light-induced oxygen generation from aqueous dispersions of tungsten(VI) oxide. *J Phys Chem* **88**, 4001–4006 (1984).

23. Chew, Y. H. *et al.* Engineering surface oxygen defects on tungsten oxide to boost photocatalytic oxygen evolution from water splitting. *Chemical Communications* **55**, 6265–6268 (2019).
24. Yang, Y. *et al.* Oxygen vacancy-mediated WO3 nanosheets by etched {200} facets and the efficient visible-light photocatalytic oxygen evolution. *New Journal of Chemistry* **43**, 16391–16395 (2019).
25. Bai, S. *et al.* Synthesis mechanism and gas-sensing application of nanosheet-assembled tungsten oxide microspheres. *J. Mater. Chem. A* **2**, 7927–7934 (2014).
26. Morgan, D. J. Resolving ruthenium: XPS studies of common ruthenium materials. *Surface and Interface Analysis* **47**, 1072–1079 (2015).

Acronyms

AFM	Atomic force microscopy
AYQ	Apparent quantum yield
BID	Barrier ionization discharge
COF	Covalent organic framework
DLVO	Derjaguin, Landau, Verwey, and Overbeek
EDL	Electrical double layer
EDX	Energy dispersive X-ray
EQE	External quantum efficiency
FFT	Fourier fast transform
FID	Flame ionization detector
GC	Gas chromatography
HEC	Hydrogen evolution catalyst
HEP	Hydrogen evolution photocatalyst
HER	Hydrogen evolution reaction
HOMO	Highest occupied molecular orbital
IQE	Internal quantum efficiency
LSV	Linear sweep voltammetry
LUMO	Lowest unoccupied molecular orbital
LVRPA	Local volumetric rate of power absorption
MS	Mass spectrometry
OEC	Oxygen evolution catalyst

OEP	Oxygen evolution photocatalyst
OER	Oxygen evolution reaction
PDRS	Powder diffuse reflectance spectroscopy
PEM	Proton exchange membrane
POWS	Photocatalytic overall water splitting
PV	Photovoltaic
PXRD	Powder X-ray diffraction
QY	Quantum yield
RLS	Rate limiting step
RONP	Ruthenium oxide nanoparticle
RONS	Ruthenium oxide nanosheet
SEA	Sacrificial electron acceptor
SED	Sacrificial electron donor
SEM	Scanning electron microscopy
STC	Solar to chemical
STH	Solar to hydrogen
TCD	Thermal conductivity detector
TEM	Transmission electron microscopy
XPS	X-ray photoelectron spectroscopy

List of Figures and Tables